

UNIVERSITAT POLITÈCNICA DE VALÈNCIA
DEPARTAMENTO DE INGENIERÍA TEXTIL Y PAPELERA



UNIVERSITAT
POLITÈCNICA
DE VALÈNCIA

**RECUPERACIÓN DEL COLORANTE DE AGUAS RESIDUALES
TEXTILES MEDIANTE NANOARCILLAS PARA SU
REUTILIZACIÓN COMO PIGMENTOS Y NUEVOS BAÑOS DE
TINTURA**

TESIS DOCTORAL

Presentada por:

Daniel López Rodríguez

Dirigida por:

Dra. Bàrbara Micó Vicent

Dra. Eva Bou Belda

Mayo 2023

Agradecimientos

En primer lugar, a mis hijos Martín y Alba, que se han convertido en el faro de mi vida y siempre consiguen hacer que olvide los problemas que surgen en el camino llenando mi vida de alegría. A mi mujer por ayudarme a hacer posible este trabajo, apoyarme y aguantar mis largas y nada sintetizadas charlas sobre el tema. A mi padre que siempre está y estará a mi lado para lo que necesite, por su infinita paciencia conmigo su apoyo incondicional y por ser el padre más orgulloso del mundo cuando habla de su hijo.

Un hueco indispensable en este apartado va para mis directoras Bàrbara y Eva. En lo personal gracias Bàrbara por ser mi amiga desde hace tantos años y haberme hecho pasar ratos tan agradables, en lo académico has sido una directora excelente y eficiente. Gracias Eva por compartir la ilusión de los nuevos hallazgos conmigo y transmitirme esas ganas de seguir avanzando. Sin tu dedicación y profesionalidad esto no habría sido posible. Además, gracias por ser una gran compañera de departamento y ayudarme en todo.

Ha habido una persona que ha estado preocupado por mi tesis casi como si fuera un director más, muchas gracias, Jordi Jordán por tu seguimiento y ayuda, para mi eres mucho más que un gran amigo. Otra persona que ha participado desde el primer momento y a la que le debo mucho es Marilés quien con gran acierto propuso la temática de este trabajo y que además siempre me ha ayudado en todo lo que he necesitado. Como no indispensable acordarme de Manuel Zamorano, siempre dispuesto a ayudarme en todo lo necesario en el laboratorio.

Dedicatoria

Quiero dedicar este trabajo a mi abuelo José, la vida nos dejó poco tiempo para compartir y te marchaste pronto de mi lado, pero aun así has dejado una huella infinita en mí para toda mi vida y sigues vivo en mis recuerdos.

Resumen

La preocupación por la salud del planeta ha aumentado drásticamente y los efluentes textiles son de los más contaminantes en la industria a nivel mundial. Los procesos de ennoblecimiento textil y en especial los de tintorería, vierten grandes cantidades de residuos de difícil tratamiento como los colorantes. Las nanoarcillas pueden limpiar las aguas residuales de colorantes gracias a su capacidad de adsorción. En este trabajo fue posible analizar y cuantificar la cantidad de iones metálicos sustituidos por colorantes aniónicos cuando se adsorben, y determinar la cantidad óptima de nanoarcilla que debe utilizarse para adsorber todo el colorante. Las pruebas demostraron la cantidad específica de nanoarcilla que debe utilizarse y cómo optimizar los procesos posteriores de separación y procesamiento de la nanoarcilla. Se utilizó hidrotalcita como material adsorbente. En esta investigación se utilizaron diversos tipos colorantes, directos, reactivos, catiónicos y dispersos. Los patrones de difracción de rayos X (DRX) permitieron comprobar la recuperación de la forma de la hidrotalcita y confirmaron la adsorción de los colorantes. Se utilizó un análisis FTIR, XPS y EDX para comprobar la presencia de grupos característicos de los colorantes en los híbridos resultantes. Las pruebas termogravimétricas (TGA) corroboraron la adsorción del colorante y la mejora de la solidez térmica. La reflectancia solar total (TSR) mostró una mayor protección frente a la radiación UV-VIS-NIR. Gracias a los trabajos realizados, se ha podido establecer el punto máximo de adsorción de la hidrotalcita. Además, mediante la utilización de nanotecnologías han podido colorear sustratos textiles con nuevas técnicas de estampación aprovechando colorantes que se han desechado de baños de tintura no agotados. Las estampaciones obtenidas se someten a pruebas de solidez del color para compararlas con estampaciones más convencionales. Se realizaron mediciones del color mediante espectrofotómetros de reflexión para valorar el resultado del color tanto de los híbridos como de los textiles estampados exitosamente. Las pruebas de TGA-DTGA realizadas previamente a las estampaciones sobre los híbridos, permite adelantarse a los resultados de ciertas pruebas de solidez del color a la luz o el planchado, las cuales se ven mejoradas gracias a la acción de la hidrotalcita. Otro uso de las nanoarcillas híbridas obtenidas de la adsorción de colorantes es el de realizar nuevos baños de tintura para sustratos textiles. Mediante el uso del nanoadsorbente hidrotalcita, han logrado adsorber

y recuperar colorantes de diferente carga como aniónicos, catiónicos y no iónicos para reutilizarlos de forma exitosa en nuevos baños de tinte. Las tinturas realizadas sobre tejidos de algodón, poliéster y acrílico han sido sometidas a diferentes pruebas de degradación del color para ver su viabilidad como productos finales, utilizando la espectroscopía de reflexión para la medida del atributo de color antes y después de los ensayos, mostrando resultados muy coherentes a los de una tinte convencional.

Resum

La preocupació per la salut del planeta ha augmentat dràsticament i els efluents tèxtils són dels més contaminants en la indústria a nivell mundial. Els processos d'ennobliment tèxtil i especialment els de tintoreria, aboquen grans quantitats de residus de difícil tractament com els colorants. Les nanoargiles poden netejar les aigües residuals de colorants gràcies a la seua capacitat d'adsorció. En aquest treball va ser possible analitzar i quantificar la quantitat d'ions metàl·lics substituïts per colorants aniònics quan es adsorben, i determinar la quantitat òptima de nanoarcilla que ha d'utilitzar-se per a adsorbir tot el colorant. Les proves van demostrar la quantitat específica de nanoargila que ha d'utilitzar-se i com optimitzar els processos posteriors de separació i processament de la nanoargila. Es va utilitzar hidrotalcita com a material adsorbent. En aquesta investigació es van utilitzar diversos tipus de colorants, directes, reactius, catiònics i dispersos. Els patrons de difracció de raigs X (DRX) van permetre comprovar la recuperació de la forma de la hidrotalcita i van confirmar l'adsorció dels colorants. Es va utilitzar una anàlisi FTIR, XPS i EDX per a comprovar la presència de grups característics dels colorants en els híbrids resultants. Les proves termogravimètriques (TGA) van corroborar l'adsorció del colorant i la millora de la solidesa tèrmica. La reflectància solar total (TSR) va mostrar una major protecció enfront de la radiació UV-VIS-NIR. Gràcies als treballs realitzats, s'ha pogut establir el punt màxim d'adsorció de la hidrotalcita. A més, mitjançant la utilització de nanotecnologies han pogut acolorir substrats tèxtils amb noves tècniques d'estampació aprofitant colorants que s'han rebutjat de banys de tintura no esgotats. Les estampacions obtingudes se sotmeten a proves de solidesa del color per a comparar-los amb estampacions més convencionals. Es van realitzar mesuraments del color mitjançant espectrofotòmetres de reflexió per a valorar el resultat del color tant dels híbrids com dels tèxtils estampats reeixidament. Les proves de TGA-DTGA realitzades prèviament a les estampacions sobre els híbrids, permet avançar-se als resultats d'unes certes proves de solidesa del color a la llum o el planxat, les quals es veuen millorades gràcies a l'acció de la hidrotalcita. Un altre ús de les nanoargiles híbrides obtingudes de l'adsorció de colorants és el de realitzar nous banys de tintura per a substrats tèxtils. Mitjançant l'ús del nanoadsorbent hidrotalcita, han aconseguit adsorbir i recuperar colorants de

diferent càrrega com a aniónics, catiónics i no iònics per a reutilitzar-los de manera reeixida en nous banys de tintura. Les tintures realitzades sobre teixits de cotó, polièster i acrílic han sigut sotmeses a diferents proves de degradació del color per a veure la seua viabilitat com a productes finals, utilitzant la espectroscòpia de reflexió per a la mesura de l'atribut de color abans i després dels assajos, mostrant resultats molt coherents als d'una tintura convencional.

Abstract

Concern for the health of the planet has increased dramatically and textile effluents are among the most polluting in the industry worldwide. Textile finishing processes, especially dyeing, discharge large quantities of difficult-to-treat wastes such as dyestuffs. Nanoclays can clean wastewater of dyes thanks to their adsorption capacity. In this work it was possible to analyze and quantify the amount of metal ions substituted by anionic dyes when adsorbed, and to determine the optimum amount of nanoclay to be used to adsorb all the dye. The tests demonstrated the specific amount of nanoclay to be used and how to optimize the subsequent processes of separation and processing of the nanoclay. Hydrotalcite was used as the adsorbent material. Various types of dyes, direct, reactive, cationic and disperse dyes were used in this investigation. X-ray diffraction (XRD) patterns verified the recovery of the hydrotalcite form and confirmed the adsorption of the dyes. FTIR, XPS and EDX analysis were used to check the presence of characteristic groups of the dyes in the resulting hybrids. Thermogravimetric tests (TGA) corroborated dye adsorption and enhanced thermal robustness. Total solar reflectance (TSR) showed enhanced protection against UV-VIS-NIR radiation. Thanks to the work carried out, it was possible to establish the maximum adsorption point of hydrotalcite. In addition, by using nanotechnologies it is possible to color textile substrates with new printing techniques, taking advantage of dyes that have been discarded from dye baths that have not been exhausted. The prints obtained are subjected to color fastness tests to compare them with more conventional prints. Color measurements were performed using reflection spectrophotometers to assess the color performance of both hybrids and successfully printed textiles. The TGA-DTGA tests performed prior to printing on the hybrids allows to anticipate the results of certain color fastness tests to light or ironing, which are improved thanks to the action of the hydrotalcite. Various types of dyes, direct, reactive, cationic and disperse dyes were used in this investigation. X-ray diffraction (XRD) patterns verified the recovery of the hydrotalcite form and confirmed the adsorption of the dyes. FTIR, XPS and EDX analysis were used to check the presence of characteristic groups of the dyes in the resulting hybrids. Thermogravimetric tests (TGA) corroborated dye adsorption and enhanced thermal robustness. Total solar reflectance (TSR) showed enhanced protection against UV-VIS-NIR radiation. Thanks to the work carried out, it was possible to establish

the maximum adsorption point of hydrotalcite. In addition, by using nanotechnologies it is possible to color textile substrates with new printing techniques, taking advantage of dyes that have been discarded from dye baths that have not been exhausted. The prints obtained are subjected to color fastness tests to compare them with more conventional prints. Color measurements were performed using reflection spectrophotometers to assess the color performance of both hybrids and successfully printed textiles. The TGA-DTGA tests performed prior to printing on the hybrids allows to anticipate the results of certain color fastness tests to light or ironing, which are improved thanks to the action of the hydrotalcite.

Índice de General

Capítulo 1 Introducción	2
1.1. Justificación	2
1.2. Aguas residuales de efluentes textiles	4
1.3. Coloración de materias textiles	6
1.3.1. Materias Colorantes	7
1.3.1.1 Colorantes	7
1.3.1.2. Pigmentos	12
1.3.2. Tintura de materias textiles	13
1.3.2.1. Tintura por agotamiento	14
1.3.2.2. Tintura por impregnación	16
1.3.3. Estampación de materias textiles	19
1.3.3.1. Fases de la estampación	19
1.3.3.2. Métodos de estampación	21
1.3.3.3. Procesos de estampación. Aplicación de pastas	23
1.3.4. Solidez del color	25
1.3.4.1. Solidez del color al frote	26
1.3.4.2. Solidez del color al lavado	27
1.3.4.3. Solidez del color al planchado	28
1.3.4.4. Solidez del color a la luz artificial	29
1.3.4.5. Solidez del color a la luz natural	31
1.3.5. Color percibido	33
1.3.6. Color psicofísico	34
1.3.7. Color psicométrico	36
1.3.8. Kubelka-Munk	38
1.4. Nanoarcillas	39
1.4.1. Uso de nanoarcillas para la limpieza de aguas residuales textiles	40
1.4.2. Hidrotalcita	42

1.4.3. Adsorción de colorante mediante Hidrotalcita.....	43
Capítulo 2 Hipótesis y Objetivos	62
2.1. Hipótesis.....	62
2.2. Objetivos	62
Capítulo 3 Publicaciones.....	66
3.1. Adaptación del artículo: Uses of Nanoclays and Adsorbents for Dye Recovery: A Textile Industry Review	68
3.1.1. Introduction	68
3.1.2. Sewage Treatment	72
3.1.2.1. General Textile Recovery	72
3.1.2.2. With Nanotechnologies	73
3.1.3. Reused Waste Water Dyes.....	88
3.1.3.1. Pigment	89
3.1.3.2. Dyes.....	89
3.1.4. Conclusions	91
3.2. Adaptación del artículo: Direct and Reactive Dyes Recovery in Textile Wastewater Using Calcinated Hydrotalcite	122
3.2.1. Introduction	123
3.2.2. Materials and Methods.....	124
3.2.3. Results and Discussion	125
3.2.3.1. UV absorption	125
3.2.3.2. Color measurements.....	126
3.2.3.3. Total solar reflectance (TSR)	127
3.2.3.4. Thermogravimetry	128
3.2.3.5. X-ray diffraction (XRD)	131
3.2.4. Conclusions	131
3.3. Adaptación del artículo: The Optimal Concentration of Nanoclay Hydrotalcite for Recovery of Reactive and Direct Textile Colorants.....	138
3.3.1. Introduction	138
3.3.2. Results	140
3.3.2.1. Final Concentrations in Solution	140

3.3.2.2. Color Measurements.....	143
3.3.2.3. Total Solar Reflectance (TSR)	145
3.3.2.4. Thermogravimetry (TGA)	150
3.3.2.5. X-ray Diffraction (XRD)	154
3.3.2.6. Fourier Transform Infrared Spectroscopy FTIR-ATR Analysis	155
3.3.2.7. Morphology Scanning and Transmission Electron Microscopy (SEM-TEM)	161
3.3.3. Discussion.....	163
3.3.4. Materials and Methods.....	165
3.3.4.1. Materials	165
3.3.4.2. Methods	166
3.4. Adaptación del artículo: Printing with hydrotalcite hybrid nanoclays and dispersed, reactive, direct dyes	178
3.4.1. Introduction	178
3.4.2. Materials and methods	180
3.4.3. Results and discussion	189
3.4.3.1. Final concentration in solution	189
3.4.3.2. Hybrid colour measurements	189
3.4.3.3. Total solar reflectance (TSR)	191
3.4.3.4. Thermogravimetry (TGA)	194
3.4.3.5. X-ray diffraction (XRD)	197
3.4.3.6. Fourier transform infrared spectroscopy FTIR-ATR analysis.....	198
3.4.3.7. X-ray photoelectron spectroscopy (XPS).....	202
3.4.3.8. Scanning Electron Microscopy Energy + Dispersive X-ray spectroscopy (SEM-EDX)	204
3.4.3.9. Measurement of printing colour.....	204
3.4.3.10. Colour Fastness	206
3.4.3.11. Scanning Electron Microscopy (SEM).....	212
3.4.4. Conclusions	213
3.5. Adaptación del artículo: Dyeing with Hydrotalcite Hybrid Nanoclays and Disperse, Basic and Direct Dyes.....	224

3.5.1. Introduction	224
3.5.2. Results	226
3.5.2.1. Dye Adsorption Performance.....	226
3.5.2.2. Hybrid Color Measurements.....	226
3.5.2.3. X-ray Diffraction (XRD)	228
3.5.2.4. Fourier Transform Infrared Spectroscopy FTIR-ATR Analysis	231
3.5.2.5. Colour Measurement of the Dyes.....	234
3.5.2.6. Colour Fastness	235
3.5.2.7. Scanning Electron Microscopy (SEM).....	237
3.5.2.8. BET Surface Area and Porosity Measurements	238
3.5.3. Discussion.....	239
3.5.4. Materials and Methods.....	240
3.5.4.1. Materials	240
3.5.4.2. Synthesis Methods.....	242
3.5.4.3. Characterisation	245
Capítulo 4 Discusión de los resultados	258
4.1. Adsorción de colorantes textiles.....	259
4.1.1. Material adsorbente	259
4.1.2. Calcinación de la hidrotalcita	260
4.1.2.1. Difracción de rayos-X (XRD)	261
4.1.2.2. Análisis mediante espectroscopia infrarroja por transformada de Fourier FTIR-ATR	264
4.1.2.3. Mediciones de superficie y porosidad (BET).....	265
4.1.3. Síntesis de híbridos colorante/arcilla.....	266
4.1.4. Rendimiento de adsorción	269
4.1.5. Caracterización del híbrido	270
4.1.5.1. Medida del color	270
4.1.5.2. Reflectancia solar total.....	272
4.1.5.3. Termogravimetría (TGA)	274
4.1.5.4. Difracción de Rayos-X (XRD).....	280

4.1.5.5. Espectroscopia infrarroja por transformada de Fourier FTIR-ATR.....	281
4.2. Estampación con híbridos de arcilla-colorante.....	285
4.2.1. Espectroscopia de fotoelectrones de rayos X (XPS).....	286
4.2.2. Microscopía electrónica de barrido Espectroscopía de rayos X de energía + dispersión (SEM-EDX).....	289
4.2.3. Estampaciones	289
4.2.4. Medida del color de las estampaciones híbridas.....	292
4.2.5. Solideces.....	294
4.2.6. Microscopia electrónica de barrido (SEM).....	300
4.3. Tintura con híbridos de arcilla-colorante.....	301
4.3.1. Método de tintura. Desorción	301
4.3.2. Medida del color de las tinturas	303
4.3.3. Solideces.....	305
4.3.4. Microscopia electrónica de barrido (SEM).....	307
Capítulo 5 Conclusiones.....	318
Capítulo 6 Futuras líneas de investigación	324

Índice de Figuras

Figura 1.1. Evolución publicaciones de para las palabras clave “dyes nanoclay” y “wastewater nanoclay”. (fuente webofscience.com).....	3
Figura 1.2. Autoclave para tintura por agotamiento	15
Figura 1.3. Foulard (fuente: Gester total testing solution)	17
Figura 1.4. Fases de la tintura	18
Figura 1.5. Fases de la estampación	21
Figura 1.6. Procesos de estampación.....	23
Figura 1.7. Estampación por rodillos cilíndricos huecos	24
Figura 1.8. Escala de grises a) índice de descargar; b) índice de degradación.....	25
Figura 1.9. Instrumento normalizado para realizar la solidez al frote, crockmeter. (fuente James Heal)	27
Figura 1.10. Instrumento normalizado para realizar la solidez del color al lavado, Linitest. (fuente James Heal)	28
Figura 1.11. Plancha de presión (fuente: youtube)	29
Figura 1.12. Instrumento normalizado para realizar la solidez del color a la luz, Xenotest. (fuente: directindustry).....	31
Figura 1.13. Rueda de color, croma, tono y luminosidad (fuente: https://es.wikipedia.org/wiki/Modelo_de_color_HSL)	32
Figura 1.14. Diagrama Cromaticidad (fuente: https://es.wikipedia.org/wiki/Gama_de_color)	36
Figura 1.15. Espacio CIELAB	37
Figura 1.16. Porcentajes de pérdidas de colorantes en efluentes.....	41
Figura 1.17. Hidrotalcita SEM.....	43
Figura 1.18. Preparación de Hidrotalcita, adsorción y reutilización.	44
Figure 3.1.1. Loss in the effluent percentage.....	70
Figure 3.1.2. Montmorillonite (MMT) SEM.....	76
Figure 3.1.3. Zeolite SEM (left) and TEM (right).....	79
Figure 3.1.4. Zeolite adsorption of dye	79
Figure 3.1.5. Halloysite SEM (left) and TEM (right) images	80
Figure 3.1.6. Sepiolite Type 2:1 two tetrahydric silica layers, and another octahedric....	82
Figure 3.1.7. Sepiolite SEM	84
Figure 3.1.8. Laponite aqueous dispersion and dye adsorption.....	86
Figure 3.1.9. Hydrotalcite SEM.....	87
Figure 3.1.10. XRD from Hydrotalcite after heat treatment, 600 °C, 3 h (HC): original hydrotalcite (HC) and hydrotalcite reconstructed after a natural dye (from beetroot) adsorption in different bath conditions (L9R7).....	88
Figure 3.1.11. Dye desorption process	90

Figure 3.2.1. a) HC SEM b) HC TEM	124
Figure 3.2.2. CIE-L*a*b* color space diagrams of the (1-4) samples	126
Figure 3.2.3. Reflectance (%) for the (1-4) samples; 190-2500 nm.	127
Figure 3.2.4. TGA for the original dyes and hydrotalcite	129
Figure 3.2.5. TGA for each hybrid sample.....	130
Figure 3.2.6. TGA for hydrotalcite and Sample 1	130
Figure 3.2.7. XRD for Hydrotalcite, Hydrotalcite calcined and hybrid pigments (Samples 1-4)	131
Figure 3.3.1. LSD Fisher means plot (95% confidence intervals) from Ads(%) as the response variable	143
Figure 3.3.2. Graphic CIELAB plots for hybrid pigments synthesized under 1–16 conditions using the D65 illuminant and the CIE-1931 XYZ standard observer. Left, CIE-a * b * color diagram; right, CIE-Cab * L * color chart.....	145
Figure 3.3.3. TSR (%) for each hybrid at maximum and minimum dye loading.....	147
Figure 3.3.4. TSR (%) for RED 23 dye hybrid	148
Figure 3.3.5. Total Solar Reflectance (TSR (%)) for each sample	149
Figure 3.3.6. LSD Fisher means plot (95% confidence intervals) from TSR (%) as the response variable	150
Figure 3.3.7. TGA and DTGA of Direct Blue 199 free and adsorbed	151
Figure 3.3.8. TGA and DTGA of Direct Blue 71 free and adsorbed	152
Figure 3.3.9. TGA and DTGA of Direct Red 23 free and adsorbed	152
Figure 3.3.10. TGA and DTGA of Reactive Yellow DR free and adsorbed	153
Figure 3.3.11. XRD for hydrotalcite, hydrotalcite calcinated, Samples 1–4 and Samples 9–12.....	155
Figure 3.3.12. FTIR of uncalcined hydrotalcite (H) and calcined hydrotalcite (HC)	156
Figure 3.3.13. FTIR of Direct Blue 199, Sample 2 and Sample 11	157
Figure 3.3.14. FTIR of Direct Blue 71, Sample 3 and Sample 12	158
Figure 3.3.15. FTIR of Direct Red 23, Sample 1 and Sample 10	159
Figure 3.3.16. FTIR of Yellow DR, Sample 4 and Sample 9	160
Figure 3.3.17. Semi-quantitative analysis and incorporation of new functional groups	161
Figure 3.3.18. SEM micrographies of different HC samples: (a) HC original; (b) HC calcinated; (c) HC reconstructed. TEM micrographies of different HC samples: (d) HC original; (e) HC calcinated; (f) HC reconstructed	162
Figure 3.3.19. Basic structure of hydrotalcite.....	163
Figure 3.3.20. (a) Direct Blue 199; (b) Direct Blue 71; (c) Direct Red 23; (d) Reactive Drimaren Yellow.....	165
Figure 3.4.1. a) Direct Blue 199 [25], b) Reactive Drimarene Yellow [26], c) Disperse Red 1	181

Figure 3.4.2. SEM micrographies of different H samples: a) H original b) HC calcinated c) HC reconstructed. TEM micrographies of different H samples: d) original H e) HC calcinated f) HC reconstructed.....	182
Figure 3.4.3. Graphic CIELAB plots for hybrid pigments synthesised using the D65 illuminant and the CIE-1931 XYZ standard observer. Left: CIE-a * b * colour diagram; right: CIE-Cab * L * colour chart.....	191
Figure 3.4.4. Total Solar Reflectance (TSR (%)) for each sample	193
Figure 3.4.5. TSR(%) for each hybrid.....	194
Figure 3.4.6. TGA and DTGA of for each dye, each hybrid and hydrotalcite	196
Figure 3.4.7. XRD for Hydrotalcite, Hydrotalcite calcinated, samples 4-6.....	198
Figure 3.4.8. FTIR comparasion of Uncalcined Hydrotalcite (H) and Calcined Hydrotalcite (HC).....	199
Figure 3.4.9. FTIR of DB199, RYD, DR1 and samples 4, 5 and 6.....	201
Figure 3.4.10. XPS Hydrotalcite, samples 4, 5 and 6.....	202
Figure 3.4.11. EDX Hydrotalcite, samples 4, 5 and 6	204
Figure 3.4.12. Graphic CIELAB plots for hybrid printed using the D65 illuminant and the CIE-1931 XYZ standard observer. Left: CIE-a * b * colour diagram; right: CIE-Cab * L * colour chart.....	205
Figure 3.4.13. Sample prints 4, 5 and 6.....	206
Figure 3.4.14. Pairwise comparison of colour fastness values by grey-scale index.....	209
Figure 3.4.15. Fisher's 95% LSD mean comparison plot, for the means obtained in the degradation fastness tests, according to the type of test and printing, with or without HC	211
Figure 3.4.16. Fisher's LSD 95% mean comparison plot for the means obtained in the degradation fastness tests, according to the type of dye and printing, with or without HC	212
Figure 3.4.17. a) Sample 5, b) Sample 17 after washing, c) Witness Sample 17 after washing	213
Figure 3.5.1. Graphic CIELAB plots for hybrid pigments synthesised using the D65 illuminant and the CIE-1931 XYZ standard observer. (Left): CIE-a * b * color diagram; (right): CIE-Cab * L * color chart.	227
Figure 3.5.2. Diffraction patterns of the hydrotalcite without calcining (H), the hydrotalcite after the calcination at 600 °C for 4 h	229
Figure 3.5.3. XRD for Hydrotalcite, Hydrotalcite calcinated at 600 °C for 4 h., samples HDB199, HBY2, HDR1, H2DB199, H2BY2 and H2DR1 in the range of 10° to 12.5°.....	230
Figure 3.5.4. FTIR comparison of Uncalcined Hydrotalcite (H) and Calcined Hydrotalcite (HC).....	232
Figure 3.5.5. FTIR of DB199, BY2, DR1 and samples HDB199, HBY2, HDR1, H2DB199, H2BY2 and H2DR1.....	233

Figure 3.5.6. Graphic CIELAB plots for hybrid dyed using the D65 illuminant and the CIE-1931 XYZ standard observer. (Left): CIE-a * b * color diagram; (right): CIE-Cab * L * color chart	235
Figure 3.5.7. Colour fastness values by greyscale index.	237
Figure 3.5.8. (a) SEM sample TDB199, (b) SEM sample TBY2, (c) SEM sample TDR1	238
Figure 3.5.9. (a) Direct Blue 199, (b) Basic Yellow 2, (c) Disperse Red 1.....	240
Figure 3.5.10. SEM micrographs of different H samples: (a) H original (b) HC calcinated (c) HC reconstructed. TEM micrographs of different H samples: (d) H original, (e) HC calcinated (f) HC reconstructed	241
Figure 3.5.11. Dye desorption and dyeing of the textile fibre	244
Figura 4.1.1. SEM de hidrotalcita (adaptada de Figure 3.2.1).....	260
Figura 4.1.2. Micrografías SEM de diferentes muestras de H: (a) H original (b) HC calcinado (c) HC reconstruido. Micrografías TEM de diferentes muestras de H: (d) H original, (e) HC calcinado (f) HC reconstruido (adaptada de Figure 3.3.18)	261
Figura 4.1.3. Patrones de difracción de la hidrotalcita sin calcinar (H) y la hidrotalcita después de la calcinación (HC) (adaptada de Figure 3.5.2)	262
Figura 4.1.4. DRX para Hidrotalcita, Hidrotalcita calcinada y muestras híbridas 4-6 (adapta de Figure 3.4.7)	263
Figura 4.1.5. Comparación FTIR de hidrotalcita no calcinada (H) e hidrotalcita calcinada (HC) (adaptada de Figure 3.4.8)	265
Figura 4.1.6. Diagramas CIELAB gráficos para pigmentos híbridos sintetizados en condiciones 1-16 utilizando el iluminante D65 y el observador estándar CIE-1931 XYZ. Izquierda: diagrama de color CIE-a * b *; derecha: Diagrama de color CIE-Cab * L * (adaptada de Figure 3.3.2)	271
Figura 4.1.7. TSR(%) para cada híbrido con carga máxima y mínima de colorante (adapta de Figure 3.3.3)	273
Figura 4.1.8. Reflectancia Solar Total (TSR(%)) para cada muestra (adaptada de Figure 3.3.5)	274
Figura 4.1.9. TGA y DTGA de cada colorante y de la hidrotalcita	275
Figura 4.1.10. Comparación TGA y DTGA de hidrotalcita y muestra 3	276
Figura 4.1.11. TGA y DTGA de Direct Blue 199 libre y adsorbido (adaptada de Figure 3.3.7)	277
Figura 4.1.12. TGA y DTGA de Direct Blue 71 libre y adsorbido (adaptada de Figure 3.3.8)	277
Figura 4.1.13. TGA y DTGA de Direct Red 23 libre y adsorbido (adaptada de Figure 3.3.9)	278
Figura 4.1.14. TGA and DTGA of Reactive Yellow DR free and adsorbed (adaptada de Figure 3.3.10)	278

Figura 4.1.15. DRX para Hidrotalcita, Hidrotalcita calcinada, muestras 1-4 y muestras 9-12 (adaptada de Figure 3.3.11)	280
Figura 4.1.16. FTIR de Direct Blue 199, muestra 2 y muestra 11 (adaptada de Figure 3.3.13)	282
Figura 4.1.17. FTIR Direct Blue 71, muestra 3 y muestra 12 (adaptada de Figure 3.3.14)	282
Figura 4.1.18. FTIR Direct Red 23, muestra 1 y muestra 10 (adaptada de Figure 3.3.15)	283
Figura 4.1.19. FTIR Yellow DR, muestra 4 y muestra 9 (adaptada de Figure 3.3.16)	284
Figura 4.1.20. Análisis semicuantitativo y la incorporación de los nuevos grupos funcionales (adaptada de Figure 3.3.17)	285
Figura 4.2.1. a) Direct Blue 199, b) Reactive Drimarene Yellow, c) Disperse Red 1 (adaptada de Figure 3.4.1)	286
Figura 4.2.2. XPS Hidrotalcita y muestras 4, 5 y 6 (adaptada de Figure 3.4.10)	287
Figura 4.2.3. EDX Hidrotalcita, muestra 4, 5 y 6 (adaptada de Figure 3.4.11)	289
Figura 4.2.4. Estampaciones de los híbridos, muestras 4, 5 y 6 (adaptada de Figure 3.4.13)	290
Figura 4.2.5. Gráficos CIELAB para híbridos impresos utilizando el iluminante D65 y el observador estándar CIE-1931 XYZ. Izquierda: diagrama de color CIE-a* b*; derecha: Diagrama de color CIE-Cab* L* (adaptada de Figure 3.4.12).....	293
Figura 4.2.6. Comparativa a pares de los valores de solidez del color mediante índice de escala de grises (adaptada de Figure 3.4.14)	299
Figura 4.2.7. a) Muestra 5, b) Muestra 17 después del lavado y c) Testigo Muestra 17 después del lavado (adaptada de Figure 3.4.17)	300
Figura 4.3.1. Desorción del colorante y tintura de la fibra textil (adaptada de Figure 3.5.11)	302
Figura 4.3.2. Gráficos CIELAB para híbridos tintados utilizando el iluminante D65 y el observador estándar CIE-1931 XYZ. Izquierda: diagrama de color CIE-a* b*; derecha: Diagrama de color CIE-Cab* L* (adaptada de Figure 3.5.6).....	304
Figura 4.3.3. Valores de solidez del color mediante índice de escala de grises (adaptada de Figure 3.5.7)	307
Figura 4.3.4. a) SEM muestra TDB199, b) SEM muestra TBY2, c) SEM muestra TDR1 (adaptada de Figure 3.5.8)	308

Índice de Tablas

Tabla 1.1. Tratamientos de ennoblecimiento textil	6
Tabla 1.2. Clasificación tintórea de los colorantes [41]–[44].....	8
Tabla 1.3. Colorantes utilizados para formar la escala de azules del 1 al 8	30
Tabla 1.4. Grados de fijación según materia colorante.	41
Table 3.1.1 Fixation percentages of different families of colorants and their estimated loss in effluents [20]	69
Table 3.1.2. Comparison of different clays	91
Table 3.1.3. Adsorbent’s characteristics comparison	92
Table 3.2.1. Lambert-Beer line equations and R^2	125
Table 3.2.2. Difference in concentration after HC absorption.....	126
Table 3.2.3. TSR Values	128
Table 3.3.1. Differences in concentrations after HC adsorption.....	141
Table 3.3.2. Variance analysis for Ads(%) from the 42 DoE	141
Table 3.3.3. TSR Values	146
Table 3.3.4. Analisis of variance for TSR values	149
Table 3.3.5. A summary of the IR peak positions.....	160
Table 3.3.6. Lambert–Beer line equations and R^2	166
Table 3.3.7. Samples and their concentrations under experimental conditions according to the general full factorial DoE 4^2	167
Table 3.4.1. Lambert-Beer line equations and R^2	182
Table 3.4.2. Printing samples	185
Table 3.4.3. Colour fastness testing	188
Table 3.4.4. Difference in concentration after HC adsorption.....	189
Table 3.4.5. L^* , a^* , b^* , C^*_{ab} values of each dye and each hybrid.....	190
Table 3.4.6. TSR Values	192
Table 3.4.7. Binding energy H, sample 4, 5 and 6	203
Table 3.4.8. L^* , a^* , b^* , C^*_{ab} values of each printing	205
Table 3.4.9. Colour fastness values by greyscale index and discharge (SSR)	208
Table 3.4.10. Analysis of Variance from degradation results, with Fastness test and HC factors	210
Table 3.4.11. Analysis of Variance from degradation results, with Dye and HC factors.	212
Table 3.5.1. Difference in concentration after HC adsorption.....	226
Table 3.5.2. Values L^* , a^* , b^* , C^*_{ab} and h of each hybrid	227
Table 3.5.3. Values L^* , a^* , b^* , C^*_{ab} and h of each dyeing	234
Table 3.5.4. Colour fastness values by greyscale index	237
Table 3.5.5. BET surface areas, pore volumes and average pore sizes.....	239
Table 3.5.6. Lambert-Beer line equations and R^2	242

Tabla 4.1.1. Superficies, volúmenes de poros y tamaños medios de poros (adaptada de Table 3.5.5).....	266
Tabla 4.1.2. Ecuación de Lambert–Beer y R^2 (adaptada de Table 3.3.6).....	266
Tabla 4.1.3. Muestras y sus concentraciones en condiciones experimentales según General Full Factorial 4^2 (adaptada de Table 3.3.7)	268
Tabla 4.1.4. Diferencia de concentración tras la adsorción de HC (adaptada de Table 3.3.1)	270
Tabla 4.1.5. Valores TSR (adaptada de Table 3.3.3).....	272
Tabla 4.1.6. Resumen de la posición de los picos IR (adaptada de Table 3.3.5).....	284
Tabla 4.2.1. XPS Hidrocalcita y muestras 4, 5 y 6 (adaptada de Table 3.4.7).....	288
Tabla 4.2.2. Muestras de estampación (adaptada de Table 3.4.2).....	292
Tabla 4.2.3. Valores L^* , a^* , b^* , C^*ab y h de cada estampación (adaptada de Table 3.4.8)	292
Tabla 4.2.4. Pruebas de solidez (adaptada de Table 3.4.3)	295
Tabla 4.2.5. Valores de solidez del color mediante índice de escala de grises y descarga (SSR) (adaptada de Table 3.4.9)	297
Tabla 4.3.1. Valores L^* , a^* , b^* , C^*ab y h de cada tintura (adaptada de Table 3.5.3)	304
Tabla 4.3.2. Valores de solidez del color mediante índice de escala de grises (adaptada de Table 3.5.4).....	306

Recuperación del colorante de aguas residuales textiles mediante nanoarcillas para su reutilización como pigmentos y nuevos baños de tintura

Capítulo 1

Introducción

1.1. Justificación

Durante las últimas décadas la preocupación por el medioambiente, su contaminación y conservación es un asunto en gran auge y que afortunadamente toda la sociedad y los estamentos gubernamentales están tratando de paliar. No pasa desapercibido que la industria textil, especialmente la rama química, es una de las más contaminantes del planeta debido a sus tratamientos en húmedo que generan enormes cantidades de aguas residuales contaminadas [1]–[4]. Uno de los factores que más impactan en las aguas residuales textiles es el vertido de colorantes a dichas aguas. Es cierto que existen métodos para eliminar estos colorantes, pero aun así, algunos resultan difíciles de eliminar por los métodos más convencionales, como es el caso de los colorantes reactivos [5]–[7]. Así pues, la comunidad científica ha empezado a plantear el uso de nanoarcillas para la separación de los colorantes de las aguas residuales, gracias a su gran capacidad de adsorción. La ventaja de esta metodología con respecto a otras convencionales es que no se busca la eliminación y destrucción del contaminante, sino su separación y posterior reutilización, pasando de tratarse como residuo a materia prima en posteriores procesos de ennoblecimiento textil.

En la Figura 1.1. se puede ver el impacto y la evolución científica que ha tenido tanto a nivel de publicaciones el uso de nanoarcillas como elemento adsorbente:

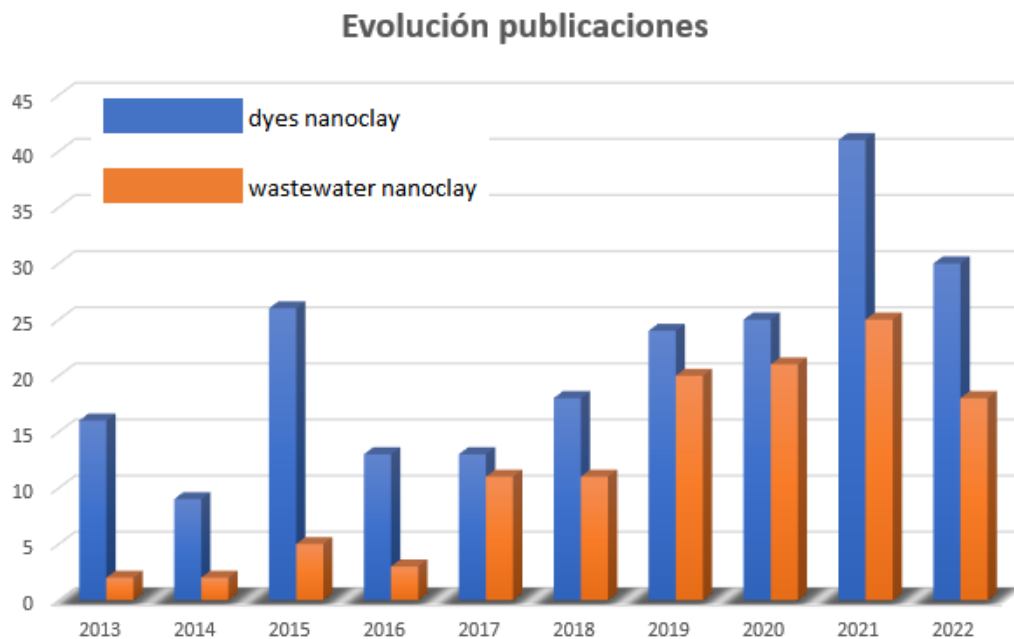


Figura 1.1. Evolución publicaciones de para las palabras clave “dyes nanoclay” y “wastewater nanoclay”. (fuente webofscience.com)

En diversos aspectos los productos textiles son de gran necesidad para la humanidad, destacando la gran relevancia de las prendas de vestir. Aun así, las toneladas que acaban desechándose y acaban en los vertederos a una gran velocidad es sorprendente (se estima un camión de basura por segundo). Tal aspecto supone un impacto ambiental de grandes dimensiones. Tanto las organizaciones no gubernamentales como los gobiernos han empezado a realizar advertencias y llamamientos a los responsables de las cadenas textiles para que estudien su rediseño, pasando de una economía lineal a una de carácter circular. Algunos de estos puntos en los que se requiere modificar el diseño son la creación de fuente de materia primas renovables, reorganizar la producción, reproducción y estrategias de reciclaje, reutilización de productos textiles, extender la vida útil de los textiles, redistribuir textiles a mercados nuevos y paralelos, etc. [8]. En los tiempos actuales se han conseguido implementar nuevas prácticas para gestionar las cadenas de suministro sostenible a las que se les ha incorporado aspectos ecológicos a las empresas, consiguiendo disminuir de

esta formar los factores que destruyen el medio ambiente tanto en los procesos de fabricación como de compra.

A la vez, la economía circular [9],[10] ha ampliado los límites de la sostenibilidad medioambiental, destacando la consideración de todos los bienes de carácter innovador consiguiendo formar una interrelación sostenible entre el crecimiento económico y el ecosistema [11]–[13]. Cuatro pilares fundamentales son los que sustentan este sistema sostenible en la industria textil y de la confección para aplicarla a una economía circular en este sector [14].

1.2. Aguas residuales de efluentes textiles

Actualmente la contaminación de los efluentes acuíferos por el vertido de productos químicos ha llegado a ser un foco de preocupación muy importante y un asunto prioritario para la sociedad, que ha llegado también a las autoridades públicas, pero por encima de todos estos y debido a la responsabilidad en todo ello, está afectando notablemente al mundo industrial [15]–[17]. Si se analiza cuáles son las causas reales de la contaminación de las aguas, se pueden distinguir diversas: diferentes residuos procedentes de la industria, explotación de minerales, los vertidos, los plaguicidas y fertilizantes químicos, el uso y explotación de la energía, los residuos radiactivos, la urbanización de las ciudades , etc [17]–[19].

La industrialización desempeña un papel fundamental en el desarrollo y crecimiento de todos los países y como otras, la industria textil es un elemento vital y emergente en diversos países. Esta industria hace uso de distintos recursos y materiales como por ejemplo el algodón o la lana (fibras naturales) o poliéster, acrílicos, poliamidas (fibras sintéticas). Dentro de la gran dimensión que tiene la industria textil se puede hacer una clasificación en dos grupos, los tejidos en seco y la de tejidos en húmedo. Como es obvio, los residuos sólidos son producidos en la industria de los tejidos en seco, mientras que los residuos líquidos son generados por el grupo de los tejidos en húmedo. Algunos ejemplos de proceso industrial que pertenecen al grupo de los tejidos húmedos pueden ser el descrudado, desencolado, blanqueo, mercerizado, la tintura o el estampado, los

cuales producen los vertidos líquidos. Durante el acabado de los textiles el agua se convierte en un elemento imprescindible para los procesos en húmedo [20].

Así pues, la industria textil es una de las mayores generadoras de aguas residuales debido a las enormes cantidades de agua que necesita utilizar en las operaciones de procesamiento en húmedo. Dichos procesos emplean diferentes productos químicos como ácidos, álcalis, tintes, peróxido de hidrógeno, almidón, agentes dispersantes de tensioactivos y jabones metálicos [21]. Así pues, haciendo una valoración de impacto medioambiental, se considera que la industria textil es la que más agua utiliza dentro del mundo industrial a nivel mundial, teniendo la gran mayoría de las aguas vertidas un grado alto de contaminación, siendo estimado por el Banco Mundial que estos procesos generan alrededor del 20% de las aguas residuales procedente de la industria [22]. Por término medio una fábrica textil realiza un consumo diario de 200 L de agua por cada Kg de tejido procesado [23].

Como ya se ha explicado, uno de los procesos en húmedo empleados en la cadena de transformación del textil es la tintura. Este proceso vierte colorantes a las aguas que acaban afectando gravemente a la función fotosintética de las plantas [24]–[26]. Además, al reducir la cantidad de luz que es capaz de penetrar en el agua e incrementar el consumo de oxígeno, acaba afectando a la vida acuática. La contaminación de estos colorantes acaba siendo letal para diversos animales marinos por la presencia de metales y cloro. La formación de partículas en suspensión afecta a las branquias de la fauna marina, acabando con su vida. Por otra parte, produce una reducción de la capacidad de las algas en la generación de alimentos y oxígeno. Ciertos estudios han demostrado que el tratamiento de aguas residuales con fuentes de luz ultravioleta ven su efectividad notablemente reducida por la presencia de estos colorantes [27]–[31].

De por sí los colorantes utilizados en las tinturas textiles no son biodegradables debido a sus compuestos aromáticos y heterocíclicos que acaban convirtiéndolos en una estructura estable y compleja no degradable, que sumados a otros componentes de matriz compleja que puedan haber en el agua, genera una sinergia contraria a degradarse de forma natural [32]. Así pues, la mineralización de los colorantes y la toxicidad

producida en la industria textil es sin duda un gran reto para la comunidad científica por lo que se trabaja en varias líneas de investigación para los tratamientos reales y eficientes de las aguas residuales textiles.

Es por ello que uno de los elementos relevantes de esta tesis es la de poder establecer métodos atractivos, eficientes y rentables para que las industrias estén dispuestas a invertir en este tipo de procesos y contribuir a la conservación del medio ambiente.

1.3. Coloración de materias textiles

Las materias textiles precisan de alguno o varios procesos de ennoblecimiento para acabar de darles las características necesarias para el uso para el que están diseñadas. El concepto de ennoblecimiento textil esta englobado por el conjunto de los tratamientos físico-químicos que acaban confiriendo a los materiales las propiedades que de por sí solos no tienen. Estos tratamientos se pueden clasificar como se observa en la Tabla 1.1.

Tabla 1.1. Tratamientos de ennoblecimiento textil

Tratamientos Previos	Coloración	Tratamientos Finales
<u>PREPARACIÓN</u>	<u>TINTURA</u>	<u>APRESTOS</u>
Descrudado	Coloración completa de la materia, penetración dentro de la fibra. Afinidad del colorante por la fibra.	Tratamientos químicos que confieren nuevas características, por ejemplo ignifugacion, antimanchas, antiestáticos.
Chamuscado		
Modificación de materias para mejorar absorción y otros procesos		
<u>BLANQUEO</u>	<u>ESTAMPACIÓN</u>	<u>ACABADOS</u>
Blanco óptico	Coloración superficial, fijación mediante el uso de ligantes.	Tratamientos mecánicos que mejorar el tacto, la caída, la fijación de las fibras.
Blanqueo de materias naturales.		

De todos los tratamientos de ennoblecimiento que se han detallado, los que incumben a este trabajo y en los que se va a centrar el estudio, son los de coloración de materias textiles. Dos grandes técnicas son las que se utilizan, la de tintura y la de estampación. Aunque el objetivo de ambas es el de conferir color a un sustrato textil, las características tanto de su aplicación como del producto final obtenido son muy diferentes.

La tintura se puede definir como el proceso mediante el cual un sustrato textil se pone en contacto con un baño que contiene una disolución o una dispersión de un material colorante, el cual en una primera fase es adsorbido por la fibra, quedando depositado de forma superficial y en una segunda fase acaba siendo absorbido del todo, mostrando un determinado grado de resistencia a volver a la fase acuosa, gracias a la fijación que tiene con la fibra. Así pues, es importante que para que se complete una tintura tiene que haber una fijación entre colorante y fibra. La tintura se puede realizar sobre un sustrato textil en cualquiera de sus formas, así pues puede tintarse sobre floca, hilo, tejido o incluso una prenda ya confeccionada y terminada [33],[34] dependiendo del sistema empleado para realizar el proceso de coloración.

Por otro lado la estampación es una técnica de coloración habitual para los tejidos con patrones o dibujos concretos, que se realizan utilizando un tipo de maquinaria específica y especial para estas labores [35]–[37]. La materia colorante se une y se fija (dependiendo de si es pigmento o colorante) a la fibra para poder protegerla de procesos posteriores de lavado y del frote. A diferencia del proceso de tintura, el color se aplica a zonas localizadas y concretas no de forma masiva, con lo que permite crear diseños complejos [38],[39].

1.3.1. Materias Colorantes

1.3.1.1. Colorantes

Cuando se habla de materias colorantes empleadas en procesos de estampación y de tintura se distinguen dos grupos diferentes. Por un lado, los colorantes, que se definen como materias orgánicas coloreadas que se pueden disolver o dispersar en el agua y que

tienen afinidad por determinadas materias textiles. Por otro lado se encuentran los pigmentos, definidos como la materia coloreada no soluble en agua y que no tienen afinidad por las materias textiles [40].

Acudiendo a la perspectiva de la tintorería los colorantes deben ser clasificados en función de la aplicación para los que se puedan utilizar sin tener en cuenta su grupo cromóforo, ni la estructura química que tengan. Así pues, se puede realizar una clasificación atendiendo a la información que se encuentra en la Tabla 1.2.

Tabla 1.2. Clasificación tintórea de los colorantes [41]–[44]

Tipo de fibra	Colorante
Celulósicas	Directos
	Azoicos insolubles
	Tina
	Sulfurosos
	De Oxidación
	Indigosolos
	Reactivos
Proteicas	Ácidos
	Premetalizados 1:1
	Premetalizados 2:1
	Al Cromo mordentables
	Reactivos
Sintéticas	Catiónicos
	Dispersos
	Ácidos (poliamida)

En esta tesis se ha hecho uso principalmente de los colorantes directos, reactivos y dispersos ya que presentan una carga diferente y de esta forma se puede hacer un estudio general al valorar los resultados de adsorción y posterior reutilización de colorantes

aniónicos, catiónicos y no iónicos. Además, estas tres familias de colorantes presentan diferentes afinidades, tipos de enlaces y métodos de tinturas distintos.

En el caso de los **colorantes directos** son de carácter aniónico una vez solubilizados, contienen grupos solubilizantes como el $-\text{SO}_3\text{Na}$, tienen elevado peso molecular en comparación con otros colorantes y tintan a las fibras celulósicas de forma directa ya que tienen una fuerte afinidad por este tipo de materias [45],[46]. Su estructura química es coplanar presentando grupos aceptores o dadores de electrones a distancia múltiplos de 10.3 \AA [44],[47],[48]. El primer colorante directo fue descubierto en 1884 y se trata del rojo Congo [49]. El grupo cromóforo que tienen este tipo de colorantes incluye los de tipo azo, estibeno, oxazina y ftalocianina, con algunos colorantes azo tiazol y complejos de cobre [50].

En cuanto a los **colorantes dispersos** son los que tintan a las fibras sintéticas, normalmente son utilizadas para la tintura del poliéster, aunque también pueden ser utilizados para la tintura de poliamida y acetato de celulosa y fibras acrílicas, aunque en estos casos la solidez en tratamientos en húmedo es baja [51]. Presentan un bajo peso molecular y no presentan grupos solubilizantes iónicos por lo que no son solubles en agua y son no iónicos. No obstante se pueden dispersar en agua con la ayuda de tensoactivos dispersantes y de ahí reciben su nombre [52],[53]. La mayoría de los colorantes dispersos se basan en estructuras azoicas; sin embargo, los colores violeta y azul se obtienen a menudo a partir de derivados de la antraquinona [53].

Según los autores R. Farouk, H.E. Gaffer [54] los **colorantes reactivos** son los únicos que están pensados para que acaben formando un enlace de tipo covalente con la materia textil durante el proceso de tintura, este es el motivo por el cual se les denomina reactivos. Este tipo de colorantes se han vuelto muy populares porque tienen muy buena resistencia a las solideces en húmedo, brillo y ofrecen una gran gama de colores [55]–[57]. En un principio fueron pensados para fibras celulósicas, pero en la actualidad existen grupos reactivos de estos colorantes que son capaces de reacción con fibras proteicas y con poliamidas [58],[59]. Según Hang Xiao [46] y otros [60],[61] los colorantes reactivos pueden ser producidos por la reacción del colorante dicloro- s -triazina, con una amina a

temperaturas en la región de 25-40° C. Esta reacción es el resultado del desplazamiento de uno de los átomos de cloro.

Otros colorantes no utilizados en esta tesis pero que merecen una mención y explicación son los que siguen a continuación:

Los **azoicos insolubles** se constituyen dentro de la misma fibra, partiendo de elementos intermedios que no tienen color. Al reaccionar entre ellos dentro de la materia textil mediante una reacción de copulación producen como resultado un colorante azoico no soluble al no contener grupos solubilizantes [62]–[64].

Colorantes Tina, son un tipo de colorantes insolubles ya que no tienen grupos solubilizantes y contienen grupos cetónicos en su estructura química, los cuales tienen la capacidad de ser reducidos [65] por un reductor, como por ejemplo, el hidrosulfito en medio básico, aunque también se puede reducir electroquímicamente [66]–[69]. Tras esta reducción forma el denominado leuco-derivado, que si es soluble en agua y es entonces cuando puede realizar la tintura sobre fibras celulósicas. Destacar que durante esta reducción el colorante cambia de color, pero al oxidarlo nuevamente con aire o H_2O_2 vuelve a su color normal al recuperar su estructura original [70].

Los **colorantes sulfurosos** son denominados de esta forma por tener azufre en su estructura química, aunque no se sabe con exactitud cuál es su estructura se propone que debe ser algo del tipo $Ar-S-S-Ar_1$. Al igual que los colorantes tina necesitan ser reducidos para solubilizarlos con el mismo proceso, tanto electroquímico [71],[72], como con la utilización de un reductor tipo hidrosulfito en medio alcalino empleando cantidades considerables de sosa caustica NaOH. Una vez solubilizados tienen afinidad por las fibras celulósicas y pueden ser coloreadas.

La aplicación de los **colorantes de oxidación** se fundamenta en la formación de un colorante insoluble en el seno de la fibra. Dicha formación se consigue al realizar una oxidación en medio ácido de compuestos que si son solubles o que se han podido solubilizar que llegan a formar un colorante de un alto peso molecular.

En lo referente a los **colorantes indigoles** hay que indicar que son un tipo de colorante tina solubilizados, obtenidos al tratarlos con ácido clorosulfónico, en medio piridina. Tras este tratamiento se convierten en sales sódicas de los sulfoésteres del leuco-derivado del colorante tina, que se haya tomado para solubilizar. Son capaces de adentrarse en la materia textil al ser solubles para posteriormente ser tratados en medio ácido recuperando la forma original del colorante desde la forma leuco y así tornarse nuevamente insoluble.

Para tinar fibras proteicas como la lana y otras como poliamida, poliamida o seda en un pH ácido comprendido entre 3 y 7 se utilizan los **colorantes ácidos** [73]. El tamaño molecular es un factor a tener en cuenta a la hora de utilizar para las fibras naturales (seda o lana) o para las fibras sintéticas (poliamida). Las moléculas pueden ser muy diferentes estructuralmente, incluir complejos metálicos y grupos sulfonados que confieren hidrosolubilidad.

También para tinar fibras proteicas, y poliamidas se utilizan los llamados **colorantes premetalizados**. En función de la estructura química se dividen en dos grupos. Los premetalizados 1:1 que contienen un átomo de metal y una molécula de colorante o los premetalizados 2:1 que en lugar de solo una tienen dos moléculas de colorante y mantienen el único átomo de metal [74]–[77].

Los **colorantes mordentables al cromo** son capaces de tinar fibras proteicas y consiguen fijarse a ellas gracias a una sal metálica de cromo o de cobre. Por lo general son colorantes de carácter ácido que poseen características especiales, como la presencia de –OH próximos a dobles enlaces y resto de ácido salicílico, que permiten que reaccionen con ciertos metales [78].

Para la tintura de fibras acrílicas se utilizan los colorantes de carácter básico denominados **colorante catiónicos**. También se emplean para la tintura de poliamida y en los sustratos de poliéster modificado. Los tintes básicos poseen un grupo amina cuaternaria el cual normalmente forma parte integral de la estructura química. En

ocasiones, un átomo de oxígeno o azufre cargado positivamente reemplaza al nitrógeno [79].

Los colorantes textiles también pueden ser clasificados en función de su estructura cromófora, que es la que le da el color específico [49],[80]. En correspondencia a estos grupos cromóforos, los colorantes pueden ser clasificados en diferentes tipos como, trifenilmetano, azo, difenilmetano, oxazina xanteno, etc. [81].

Los colorantes textiles tienen una estructura química única para cada color [49],[82]. Se pueden nombrar en función a la estructura química de su grupo cromóforo. El llamado cromóforo es un grupo de átomos presentes en las estructuras del colorante responsable de su color. El grupo de átomos se une al cromóforo llamado auxocromo que realiza el color del cromógeno [83],[84]. Los grupos cromógenos más habituales son (-C = C-), (-C = N-), (-C = O-), (-N = N-) (-NO₂) y anillos quinoídes [85]. Los auxocromos utilizables son (-CO₂H), (-NH₃), (-SO₃H) y (-OH), [49],[82],[86]. A cada colorante se le asigna un índice de color (C.I.), formado por un nombre genérico seguida de un número de constitución química [87].

1.3.1.2. Pigmentos

En cuanto a los **pigmentos orgánicos** se han estado empleado asiduamente en la industria de la estampación ya que presenta diversas ventajas, como por ejemplo la buena fotosensibilidad, la transparencia que se consigue, la alta saturación del color, el brillo y lo estable del producto final [88]–[90]. Aunque se han solucionado algunos inconvenientes como el bajo rendimiento de la dispersión, la insolubilidad y la tendencia que presentan las partículas del pigmento a formar agregados en el agua, sigue habiendo cierta limitación asu utilización debido a los problemas de solidez que presenta. No obstante se esta mejorando también en dichos problemas de solidez, pero a día de hoy sigue siendo un aspecto a tener en cuenta.

En la estampación textil, el uso de pigmentos orgánicos, en lugar de los colorantes tradicionales, ofrece las ventajas de no tener que lavarse tras el proceso, resulta un método sencillo y con una gran aplicabilidad a las fibras [91]. El tejido que ha sido

estampado con pigmentos muestra un gran color, un contorno claro y lleno de sentido tridimensional, pero también existen las deficiencias de la impresión con pigmentos, la más notoria es la sensación de aspereza al manipularlo. En la industria de la estampación pigmentaria se necesita un gran cantidad de ligantes para resolver el problema de la baja solidez del color, que se debe a la nula afinidad entre los pigmentos y los tejidos [92]–[94].

Hay un segundo método de utilización de los pigmentos para dar coloración a una materia textil, se trata de la coloración en masa, utilizado en materias sintéticas. Esta técnica consiste en añadir el pigmento cuando se tiene una disolución de polímero, en los casos de viscosa o acetato, o bien incorporarlo a un polímero fundido, como por ejemplo en la poliamida o el poliéster. De esta forma se consigue colorear el material antes de formar el hilo.

1.3.2. Tintura de materias textiles

La tintura es un proceso físico-químico en el cual un colorante que se encuentra disuelto o dispersado en medio acuoso se aproxima a la fibra para depositarse en su superficie en una fase de adsorción, para seguidamente ser totalmente absorbido y fijado en el interior del sustrato, presentando con ella resistencia a abandonar la fibra y volver al baño de tintura. Así pues, se pueden establecer varias fases en el proceso de tintura [95],[96]:

- 1- Difusión del colorante en el baño.
- 2- Adsorción del colorante en la superficie de la fibra.
- 3- Difusión/absorción del colorante superficial al interior de la fibra.
- 4- Fijación del colorante en el interior de la fibra.

En la primera etapa de difusión del colorante se deben tener en cuenta las características del colorante y la tendencia que pueda tener a formar agregados. En la segunda fase intervienen las fuerzas de atracción que tenga el colorante y la fibra y además las fuerzas iónicas que se producen en las fibras y los colorantes en disolución acuosa. En función de estas cargas pueden producirse atracciones o repulsiones entre la

fibra y el colorante. En la fase de difusión/absorción hay diferentes cinéticas en función de las características de las fibras y los colorantes, algunas tinturas pueden ser más rápidas y otras más lentas. Finalmente en la cuarta fase, en función de los enlaces que se establezcan y las fuerzas de atracción en el colorante, quedara fijado en mayor o menor medida [79].

Para los procesos de tintura se pueden elegir diferentes métodos con distintos tipos de maquinaria. Para elegir adecuadamente hay que basarse en una serie de variables que determinaran cual es el más idóneo. Algunas de estas variables son:

- Capacidad de la máquina.
- Relación de baño (R/B) a utilizar.
- Tiempo de tintura.
- Temperatura a alcanzar.
- Afinidad Colorante-Fibra.
- Formato de presentación de la materia.

Así pues, a continuación, se presentan y describen los dos grandes grupos de sistemas de tintura que se utilizan, que son las tinturas por agotamiento y las tinturas por impregnación.

1.3.2.1. Tintura por agotamiento

En un procedimiento de tintura por agotamiento la materia colorante se encuentra en una fase acuosa disuelta o dispersada en un volumen concreto, en función de la capacidad que pueda tener la máquina utilizada. Este denominado baño de tintura estará en contacto directo con el sustrato textil que también tendrá una cantidad determinada, dependiendo nuevamente de la capacidad que tenga la maquinaria. Este proceso de agotamiento se fundamenta en el proceso mediante el cual el colorante que se encuentra en el baño pasará a la fibra con un nivel de agotamiento (transferencia del baño a la fibra) mayor o menor en función de diversas variables como son el tipo de materia textil y colorante y la afinidad que ambos tengan, el tipo de máquina de tintura, el proceso, etc.

Así pues, cuando menor cantidad de colorante quede en el agua después de proceso de tintura mayor habrá sido el agotamiento.

Prácticamente todas las presentaciones de las materias textiles se pueden utilizar para una tintura en agotamiento, ya sea fibras, hilos, tejidos de punto y de calada, etc. Estos procesos por agotamiento son sistemas discontinuos que necesitan periodos de tiempo largos para que los productos y colorantes realicen todas las reacciones necesarias para llegar a completar el proceso de tintura. Este método se basa principalmente en cargar una cantidad de sustrato textil en la máquina y llevarla al denominado equilibrio con una disolución que tiene el colorante y los productos químicos auxiliares necesarios durante un periodo de tiempo que puede comprender minutos hasta horas a cierta temperatura, dependiendo de la tintura que se lleve a cabo [97]. El proceso de tintura por agotamiento tiene un mayor consumo energético por las altas temperaturas que se necesita alcanzar y a los grandes volúmenes de baño que hay que calentar (Figura 1.2.).



Figura 1.2. Autoclave para tintura por agotamiento

La tintura por agotamiento lleva implícito un proceso de desorción y absorción tanto de los colorantes como de los productos químicos auxiliares, producido por la sustantividad de estos productos a la fibra textil [98]. La tintura es un proceso exotérmico,

lo que significa que el calor de tintura es negativo y la mayoría de la energía que se utiliza es para calentar el agua [99].

Por lo general los procesos de tintura por agotamiento van precedidos de unos tratamientos de preparación previos del tejido, como son el blanqueo, descrudado, descolado o prelavados. Cada tratamiento de coloración suele ir seguido de lavados y aclarados posteriores en función de la concentración y afinidad del textil a la sustancia química que no se haya fijado. Este punto es especialmente importante en la tintura con colorantes reactivos, ya que dichos colorantes hidrolizan antes de penetrar en la fibra quedando depositada en la superficie y no eliminar ese colorante superficial produce descargas de color no deseadas cuando se usa el textil [100].

Al igual que se hablaba de los consumos de energía en el calentamiento del agua para el baño de tintura, también exigen gran cantidad de energía estos pretratamientos. Hay varios estudios que investigan y proponen modelos para reducir tanto el consumo energético como el de agua [101]–[106]. Los análisis termodinámicos de los procesos de acabado tienen una gran importancia debido al gran consumo energético que estos conllevan, siendo uno de los más relevantes en la industria textil. Una destacable propiedad de la termodinámica es la exergía que se define como el potencial de trabajo de un sistema concreto y viene a representar la cantidad de trabajo útil que se consigue cuando dicho sistema se equilibra con el entorno [107]. Esta exergía cuantifica la utilidad o calidad de una forma de energía para producir determinados cambios.

1.3.2.2. Tintura por impregnación

Lo más habitual y común que se ha encontrado en las empresas de tintura textiles son los procesos de tintura por agotamiento visto en el apartado anterior. No obstante gracias a los numerosos estudios realizados sobre los métodos de tintura por impregnación [108]–[111] que ha desembocado en la reducción de problemas y costes de fabricación se ha convertido en una técnica mucho más utilizada en los últimos años. Una de las grandes ventajas es que se ha conseguido una reducción de costes y un incremento de la producción haciéndola un método más rentable [112].

La tintura por impregnación se realiza mediante el proceso denominado como foulardado, haciendo servir un foulard. Esta operación se basa en el proceso de impregnar un sustrato textil en un baño previamente preparado que contenga una disolución determinada, en este caso concreto contendrá materia colorante. Después de ser sumergido en la cubeta de este baño, será escurrido mediante unos cilindros que hay a la salida del foulard y cuya presión es ajustada en función del tipo de tejido.

Después de conseguir una distribución uniforme del colorante sobre el textil que ha pasado por el foulard hay que conseguir una fijación de este colorante, ya que después de este proceso tan solo se ha conseguido una deposición superficial y por lo tanto no presentara unos niveles de solidez suficientes como para ser utilizado en un entorno habitual para el que está ideado. Existen varios procesos que consiguen esta difusión final del colorante a la fibra. Algunos ejemplos de ellos son el vaporizado o el calor seco (Hotflue) [113],[114] (Figura 1.3.).



Figura 1.3. Foulard (fuente: Gester total testing solution)

A modo de resumen se muestra un esquema del proceso de tintura tanto por agotamiento como por impregnación en la Figura 1.4.

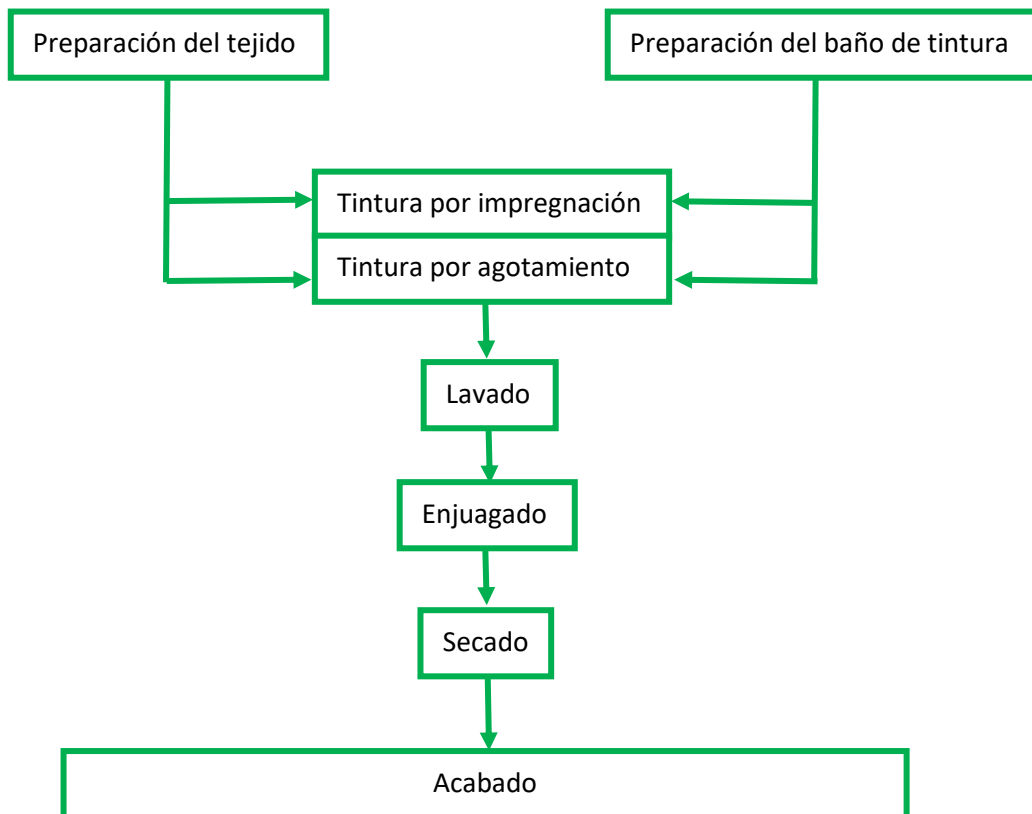


Figura 1.4. Fases de la tintura

1.3.3. Estampación de materias textiles

La estampación textil es una técnica de coloración de los sustratos textiles tan antigua como la misma civilización. El sector textil tiene una gran influencia sobre la economía de todos los países [115]. La utilización de la coloración a través de los procedimientos de tintura y estampación se convierte, por el valor añadido que aporta al producto final, en un proceso de alta relevancia [78]. El estampado es una forma de arte que se remonta a miles de años. Es uno de los métodos más diversos y significativos para incorporar colores y patrones a los materiales textiles [116]–[118]. También se puede definir como el proceso de realizar una mezcla de uno o varios colores con espesantes sintéticos o naturales para poder aplicar la pasta resultante sobre un sustrato textil [119]–[128]. Dentro de esta definición hay que incluir que el objetivo es obtener bordes nítidos en los tejidos que se aplica el motivo estampado.

El color aplicado se procesa para que quede fuertemente fijado mediante ligantes y sea capaz de resistir el lavado y el frote entre otros agentes. El tintado localizado es otra forma de definir la estampación textil, ya que a diferencia de una tintura convencional en el estampado queda solamente coloreada una parte específica [38]. Una de las grandes diferencias entre una tintura y una estampación es que en el proceso de tintura el sustrato textil es sumergido en una solución diluida de baño de tintura y el excedente de este baño es exprimido. Por otro lado, la estampación se realiza aplicando una pasta más gruesa que contiene colorantes o pigmentos con otras sustancias adicionales siguiendo un patrón de color [37],[39]. La viscosidad de la pasta de estampación es un factor de gran importancia ya que controla la cantidad de pasta que se transmite al tejido y por tanto, la cantidad que finalmente queda extendida sobre la superficie.

1.3.3.1. Fases de la estampación

Una vez definido el proceso de estampación de forma fundamental se procede a describir algunas de las fases que hay que llevar a cabo para realizar correctamente todo el proceso de coloración, se muestra un resumen en la Figura 1.5.

- a) Preparación del textil: En función de la materia textil y sus características deben someterse a unas operaciones previas como pueden ser el chamuscado, blanqueo, mercerizado, tundido en **fibras celulósicas**, blanqueado y clorado para la **lana** y en caso de **fibras sintéticas** un desaprestado, blanqueo óptico, tundido y cepillado.
- b) Elaboración de las pastas de estampación: Esta fase se suele llevar a cabo en la que se denomina comúnmente como “cocina de colores”. Los elementos básicos que componen una receta de estampación son el agua, la materia colorante, espesante y ligante. Puede añadirse otros compuestos para mejorar el proceso.
- c) Aplicación de pastas: Es simplemente la aplicación de la pasta preparada en la fase anterior para la deposición en la superficie el tejido. Como ya se verá en apartados posteriores, hay varias formas de realizar esta deposición, lo que nos definirá los procesos de estampación. Tras la aplicación se somete al tejido a un secado para que no haya roces de ningún tipo y, por ejemplo, se pierda definición en el perfil de los dibujos.
- d) Fijación del color: Son tratamientos físico-químicos que permiten la unión estable del color al sustrato textil. Por lo general los pigmentos se someten a un termofijado mediante calor seco en un rame y los colorantes a un vaporizado con calor húmedo.
- e) Acabado final: Se realiza un lavado para eliminar espesantes y otros productos seguido de un secado para finalizar el proceso.

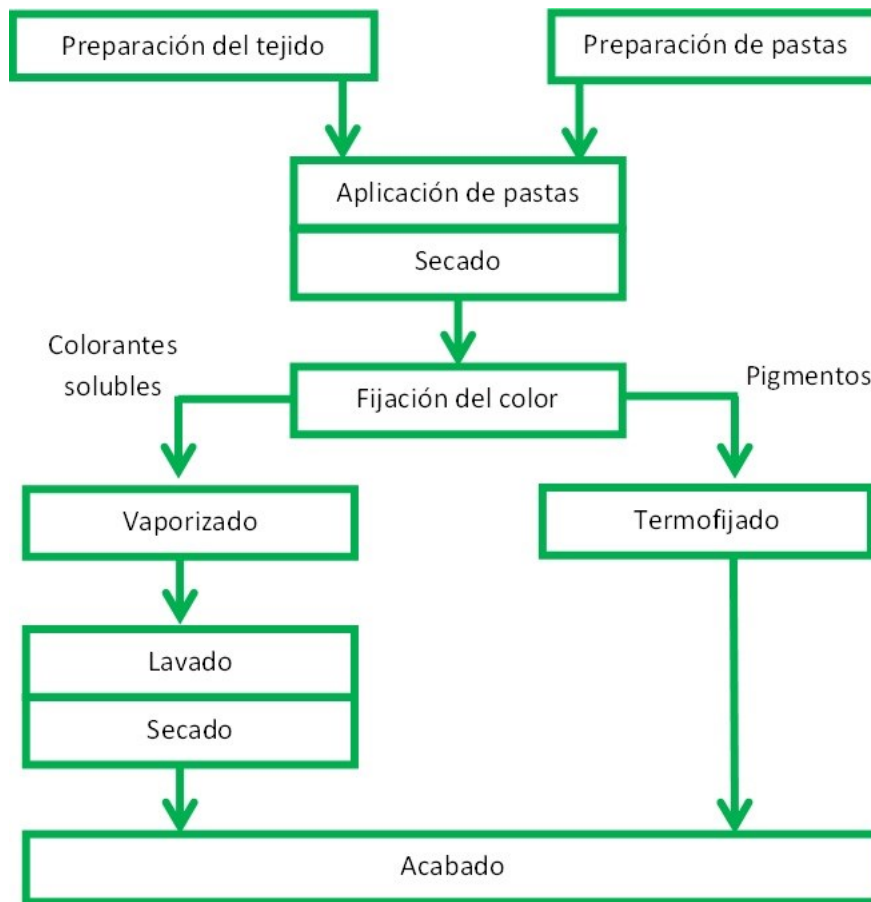


Figura 1.5. Fases de la estampación

1.3.3.2. Métodos de estampación

Se pueden distinguir claramente 3 tipos de métodos de estampación conocidos con el nombre de estampación directa, estampación por corrosión y estampación por reserva. A continuación se explican brevemente cada una [35].

- a) Estampación directa: Es el método más simple de los 3, consiste en aplicar directamente la pasta de estampación preparada en la cocina de color sobre la superficie del tejido. Se pueden utilizar tanto colorantes solubles como pigmentos en este método. Es fácilmente identificable en un tejido acabado ya que en el revés de la tela se aprecia levemente el dibujo estampado en la cara “buena” o si el tejido es muy grueso puede que no llegue a verse, ya que generalmente solo se aplica en una cara [129]–[132].

- b) Estampación por corrosión: Después de haber tintado un tejido se aplica una pasta de forma selectiva en determinadas zonas, siendo esta pasta capaz de decolorar la zona donde se haya aplicado gracias a un agente químico de corrosión del color. Los colorantes de la tintura deben ser capaces de sufrir esta corrosión. La pasta puede contener además un colorante que no sufra ese ataque corrosivo, con el que se conseguirá una sustitución del color en la zona de aplicación [133],[134].
- c) Estampación por reserva: Al igual que en la estampación por corrosión se trata de una combinación de tintura y estampación. En este caso se trata de conseguir una aplicación de una pasta de estampación que no permita la tintura del textil en esa zona donde se ha depositado, consiguiendo una reserva en blanco. Si esa pasta de estampación tiene además un colorante apropiado se conseguirá una reserva con color. Tanto en esta estampación como en corrosión si hay color en la pasta se consigue la misma intensidad por ambas caras del tejido [131],[135]–[137].
- d) Estampación combinada de reserva y corrosión: Esta técnica se ideó sobre todo para evitar los problemas de corrosión que sufría el poliéster cuando se trabaja con colorantes dispersos. El método consiste en realizar una tintura por impregnación secando a baja temperatura para no fijar el colorante, después se estampa por reserva y se realiza la fijación, no quedando fijado el colorante que está bajo la pasta de estampación.

Como ya se ha explicado anteriormente las pastas de estampación están formadas por agua, materia colorante, espesante y otros productos auxiliares. Dado que los colorantes y pigmentos ya se han explicado en la sección 1.3.1 se procede directamente a analizar los dos restantes.

- a) Espesantes: Son aquellos productos químicos (polímeros) encargados de otorgar una determinada viscosidad a la pasta de estampación. En el mercado se pueden encontrar una gran variedad con diferentes características en

función del uso que se vaya a dar, por ejemplo, hay espesantes coloidales, de emulsión o de dispersión.

- b) Productos auxiliares: Dentro de esta familia se pueden incluir a los agentes de corrosión y reserva empleados en las estampaciones vistas en este apartado. Los ligantes y fijadores como su propio nombre indica ayudaran a conseguir que el color no abandone la fibra y presente mejores solidez. También se aplican modificadores al tacto para reducir la rugosidad. Los productos higroscópicos fijaran la humedad los que evita que las pastas se resequen y mejoran la difusión del color.

1.3.3.3. Procesos de estampación. Aplicación de pastas

El sistema utilizado para aplicar la pasta de estampación sobre el textil dependerá del sistema que se utilice. Así pues, se puede establecer una clasificación de los procesos de estampación en función al sistema que se utilice para aplicar las pastas (Figura 1.6.).

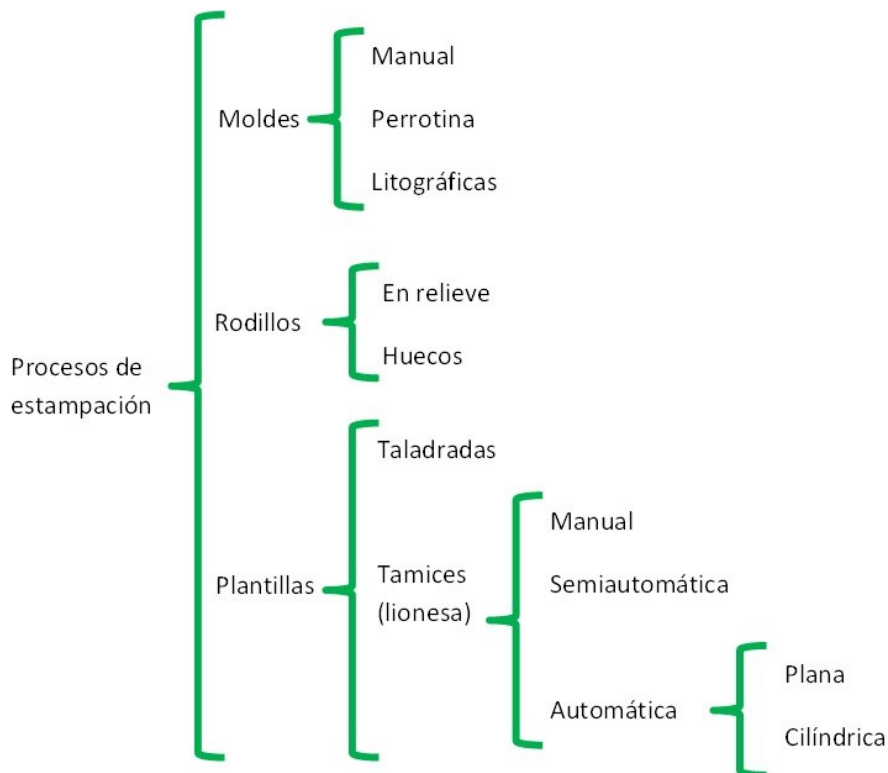


Figura 1.6. Procesos de estampación

Estampación con moldes: Se empezó realizándola manualmente con moldes de madera planos aunque con el tiempo fue tecnológicamente avanzando para utilizar perrotinas y mecanismos análogos a los que utilizan en litografía. El diseño que se quiere estampar está grabado en un molde en relieve, al tomar contacto con la pasta de color quedan impregnadas las zonas con más volumen que después se ponen en contacto con el tejido. Guarda una gran similitud con los sellos o cuños que se utilizan en oficinas.

Estampación con rodillos: Esta es uno de los métodos de fabricación de estampados más populares [138]. Fue la primera máquina que se diseñó para poder trabajar a la continua, con el consiguiente impacto productivo que trajo. Para la obtención de los motivos se emplean rodillos de cobre grabados en relieve o huecos y permiten utilizar hasta 16 colores diferentes. Las producciones pueden alcanzar los 6.000 metros por hora. En la actualidad los rodillos o cilindros huecos (Figura 1.7) son los que se siguen utilizando.



Figura 1.7. Estampación por rodillos cilíndricos huecos

Estampación con plantillas: Aquí encontramos dos tipos, la estampación con plantilla tamiz (lionesa) o con plantilla taladrada. Estas plantillas están formadas por una tela muy tensada de malla muy fina sobre la cual se realiza el diseño deseado para después impermeabilizar las zonas que no están ocupadas por el dibujo, de esta forma cuando se pone la pasta de estampación y se ejerce presión de la pasta contra la plantilla únicamente dejara pasar pasta en la zona dibujada, marcando sobre el textil. Este tipo de estampación de forma manual ha ido evolucionando a sistemas semiautomáticos y completamente automáticos.

1.3.4. Solidez del color

La pérdida o descarga de color en los textiles es una circunstancia no adversa a la calidad de un tejido. Así pues, la ISO (Organización Internacional de Normalización o Estandarización) y la AATCC (Asociación Estadounidense de Químicos y Coloristas Textiles) han diseñado diferentes ensayos estandarizados para poder simular y valorar los factores que pueden producir esta no deseada decoloración. La solidez del color se puede definir como la resistencia que presenta un textil a cambiar cualquiera de sus propiedades de color (degradación) y a la transferencia de color (descarga) a otros materiales que puedan estar junto al sustrato textil durante el uso común para el que ha sido ideado el textil. La valoración de variación del color que se provocan controladamente con estos ensayos se suelen valorar de forma visual con una escala de grises (conforme a la norma UNE-EN ISO 105-A03:2020) (Figura 1.8) de degradación y otra de descarga, pero cada vez es más habitual y objetivo realizar esta valoración de forma instrumental con un espectrofotómetro de reflexión y el cálculo con ecuaciones mejoradas [139] de acuerdo a la norma UNE-EN ISO 105-A05:1998.

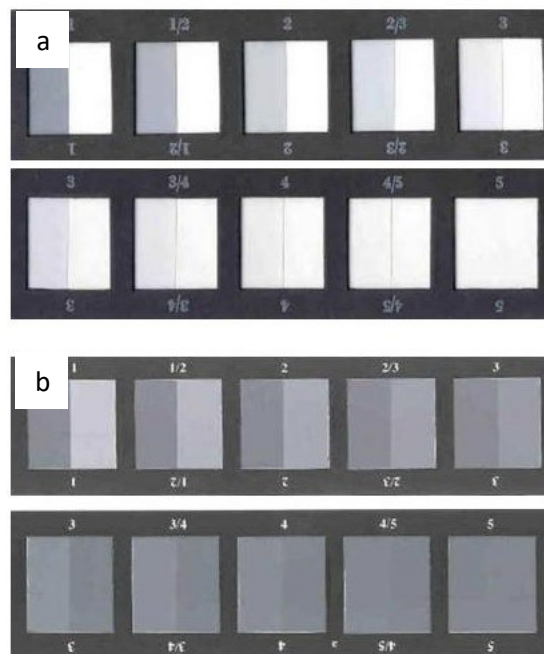


Figura 1.8. Escala de grises a) índice de descargar; b) índice de degradación

Existen alrededor de medio centenar de normas que evalúan la solidez de las materias textiles a diferentes agentes físicos y químicos que pueden degradar el color. Se debe seleccionar con sentido común cuales son las más oportunas para el uso que se le vaya a dar a cada tejido. Por ejemplo, no tendría demasiado sentido someter a pruebas de solidez a la luz natural a un tejido destinado para una funda de colchón, ya que este tipo de sustrato no va a estar expuesto a esa fuente de radiación. Sí que será muy necesario realizar ese tipo de ensayo a un tejido destinado para un toldo de un balcón ya que va a estar muchas horas expuesto directamente a esa radiación solar. Así pues, dada la extensa variedad de ensayos, se procede a explicar brevemente las más relevantes para el estudio de esta tesis.

1.3.4.1. Solidez del color al frote

Para realizar el ensayo de la solidez del color al frote se sigue la norma UNE-EN ISO 105-X12:2016:2016. Esta norma describe un método para valorar la resistencia que tiene el color de cualquier textil frente al frote y la consecuente descarga. Para realizar correctamente este ensayo se utiliza un crockmeter (Figura 1.9), el cual es una máquina fabricada exprofeso para aplicar los parámetros requeridos en la norma y realizar los ciclos necesarios para la prueba. Las muestras se frotran con un tejido testigo seco y también con uno mojado, ambos resultados se presentan por separado como solidez al frote húmedo y mojado. El testigo es un tejido de algodón blanqueado, descolado y sin aprestos, el cual realiza 20 ciclos de frote y tras los cuales se valoran tanto la degradación en el tejido a analizar como la descarga que ha habido sobre el testigo. Estos resultados se expresan en escala de grises y se puede valorar visualmente (norma ISO 105-A03:2020) o instrumentalmente (UNE-EN ISO 105-A05:1998).

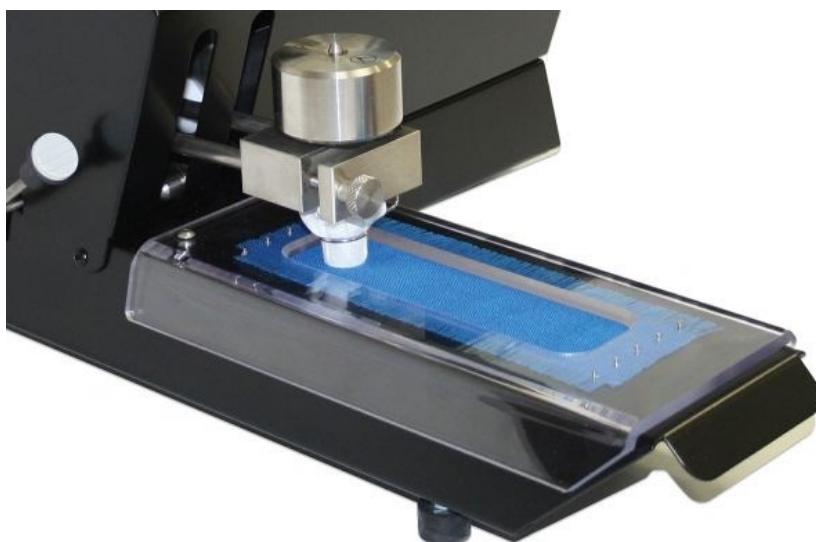


Figura 1.9. Instrumento normalizado para realizar la solidez al frote, crockmeter. (fuente James Heal)

1.3.4.2. Solidez del color al lavado

La norma UNE-EN ISO 105-C06:2010 se utiliza para valorar la solidez del color al lavado doméstico y comercial. El objeto de esta norma y sus correspondientes ensayos es definir métodos para poder conocer la solidez del color en los sustratos textiles antes los procesos de lavado doméstico o comercial haciendo uso de un detergente. Existen ensayos simples o múltiples con o sin la acción abrasiva de unas esferas metálicas. Un ensayo simple con la acción abrasiva simula un único lavado. La prueba consiste en coser junto a la probeta dos tejidos testigos de determinadas materias en función de la materia componente de la propia probeta a testear y someterlas al lavado. Una vez finalizado el ensayo se valora la descarga en los testigos y la degradación en la probeta. Como ya se ha visto en el apartado anterior la valoración se hace mediante escala de grises visual o instrumentalmente. El aparato de ensayo utilizado para realizar este ensayo recibe el nombre de Linitest (Figura 1.10) cuya descripción viene recogida en la misma norma UNE-EN ISO 105-C06:2010.



Figura 1.10. Instrumento normalizado para realizar la solidez del color al lavado, Linitest. (fuente James Heal)

1.3.4.3. Solidez del color al planchado

Para valorar la solidez del color al planchado se recurre a la norma UNE-EN ISO 105-X11:1997. El objetivo de esta norma y sus ensayos es el de poder realizar una valoración de la pérdida de color que pueda producirse en un textil por el efecto de un planchado doméstico y/o industrial con rodillos. El ensayo consiste en colocar sobre una probeta un testigo de algodón y someterla a un planchado con una plancha de presión (Figura 1.11) durante 15 segundos a una temperatura entre 110 y 200 °C. La variable temperatura dependerá de la materia componente de la probeta a ensayar. Se pueden realizar ensayos de planchado en seco, mojado y húmedo, dependiendo del uso final que se le vaya a dar al tejido. En seco no se altera ninguna de las partes, ni probeta ni testigo. En mojado se moja el testigo de algodón ajustándolo al doble de su peso inicial, y en húmedo se mojan ambas partes, tanto testigo como probeta ajustando al doble de su peso inicial.

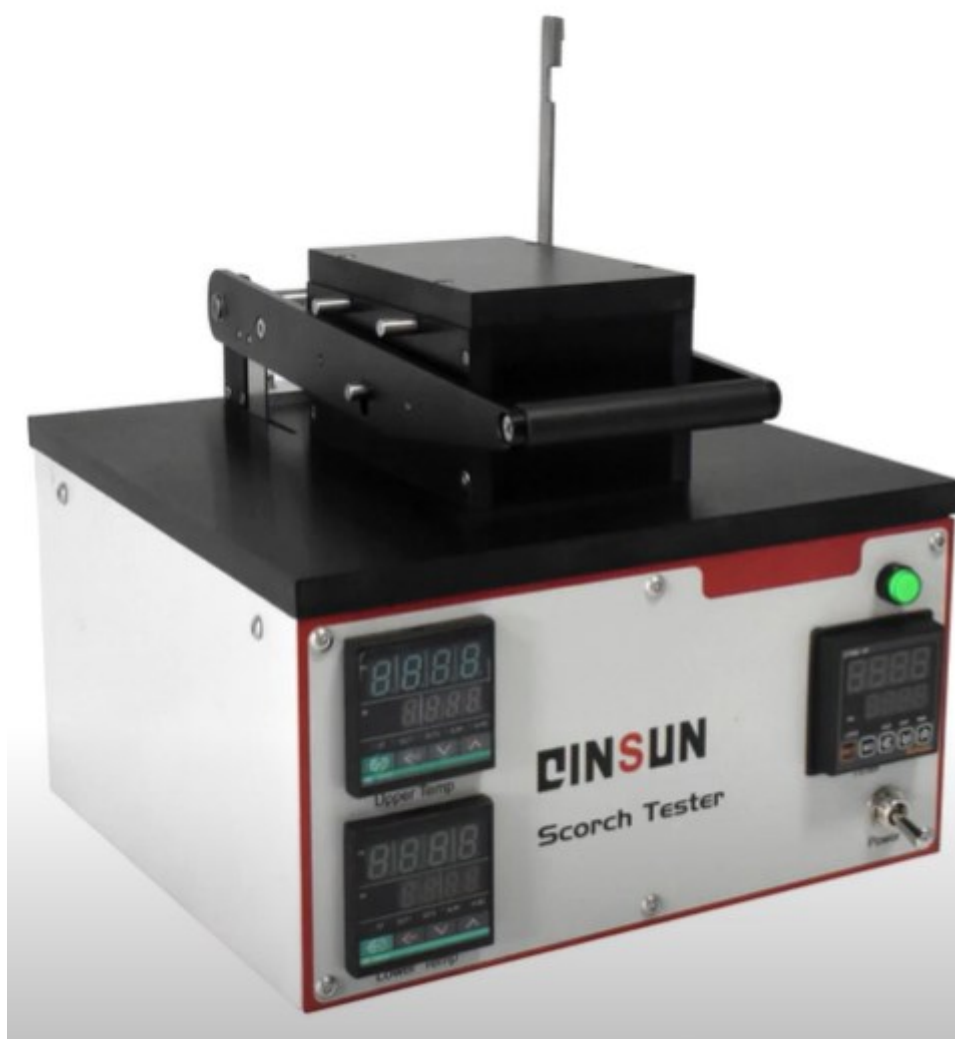


Figura 1.11. Plancha de presión (fuente: youtube)

1.3.4.4. Solidez del color a la luz artificial

Para hacer un ensayo de solidez del color a la luz artificial se utiliza un xenotest (Figura 1.12) [140]–[142] y se sigue la norma UNE-EN ISO 105-B02. En ensayo consiste en someter una probeta a la luz artificial de lámparas de xenón en unas condiciones determinadas junto a unas muestras de referencia. Estas muestras de referencia son unas escalas de azules de las que se conocen su reacción a la radiación de luz artificial. A diferencia de las escalas de grises que va del 1 al 5 la escala de azules va desde el 1 hasta

el 8. Esta escala de azules se trata de textiles de lana tintados con diferentes colorantes azules como se muestra en la Tabla 1.3.

Tabla 1.3. Colorantes utilizados para formar la escala de azules del 1 al 8

Referencia	Colorante
1	CI Acid Blue 104
2	CI Acid Blue 109
3	CI Acid Blue 83
4	CI Acid Blue 121
5	CI Acid Blue 47
6	CI Acid Blue 23
7	CI Solubilized Vat Blue 5
8	CI Solubilized Vat Blue 8

La prueba consiste en colocar la probeta junto a las referencias de la escala de azules. Se cubre una parte con una cartulina que proteja de la radiación de la lámpara y se someten a dicha radiación hasta que el contraste entre la parte expuesta y no expuesta de la probeta sea igual a un grado 4 de la escala de grises, momento en el que debe finalizar la exposición y se procede a la valoración. Para dicha valoración se compara la degradación de la probeta con la sufrida en los materiales de referencia de la escala de azules, dando como resultado aquella muestra de escala de azules que tenga la degradación más similar a la de la probeta testeada.



Figura 1.12. Instrumento normalizado para realizar la solidez del color a la luz, Xenotest. (fuente: directindustry)

1.3.4.5. Solidez del color a la luz natural

El ensayo de la solidez del color a la luz natural sigue las directrices de la norma UNE-EN ISO 105-B01. El método sigue los mismos pasos que se han descrito en el apartado anterior, pero con la diferencia que la exposición a la fuente radiante será la luz natural y no un xenotest. Se coloca la probeta junto a las referencias de la escala de azules. Se cubre una parte con una cartulina que proteja de la radiación solar y se someten a dicha exposición durante 24 h al día hasta que el contraste entre la parte expuesta y no expuesta de la probeta sea igual a un grado 4 de la escala de grises, momento en el que debe finalizar la exposición y se procede a la valoración. Para dicha valoración se compara la degradación de la probeta con la sufrida en los materiales de referencia de la escala de azules, dando como resultado aquella muestra de escala de azules que tenga la degradación más similar a la de la probeta testeada. Medida del color

La percepción o visión del color es una parte fundamental que posee el sistema visual humano. Está basado en la acción de tres clases de fotorreceptores en forma de cono que se encuentran alojados en la retina, los cuales poseen unas curvas de sintonía de longitud de onda diferentes pero que se encuentran en superposición [143]. Los datos que son recogidos por este mecanismo son enviados desde ojo hasta el cerebro humano. Hay tres canales de envío llamados blanco-negro, azul-amarillo y rojo-verde y están caracterizados de forma computacional, psicofísica y fisiológicamente.

Diferentes aspectos viales como pueden ser la orientación, movilidad y la profundidad son procesadas al mismo tiempo que el color para que nuestro cerebro tenga toda la información necesaria para construir completamente la imagen. El sistema visual puede trabajar con la misma eficacia cuando se trata de estímulos de blanco y negro o de color para casi todas las tareas psicofísicas [144]–[147].

Tal y como se percibe el color puede ser caracterizado a través de tres unidades de medida, estas son el croma la luminosidad y el tono, con los cuales se consigue identificar de forma única y puede ser distinguido de cualquier otro.

Para poder describir el color fundamental la componente que se emplea es el tono, tal y como se puede observar en la Figura 1.13. El croma cuantifica como de saturado esta un color y conforme se disminuye ese croma puede llegar a un gris. Si el croma aumenta hasta el máximo se obtendrá un color con un tono totalmente puro. Lo luminoso u oscuro que es un color vendrá determinado por la luminosidad y mostrará la intensidad de luz que posee un color pudiendo cambiar desde un blanco a un negro.

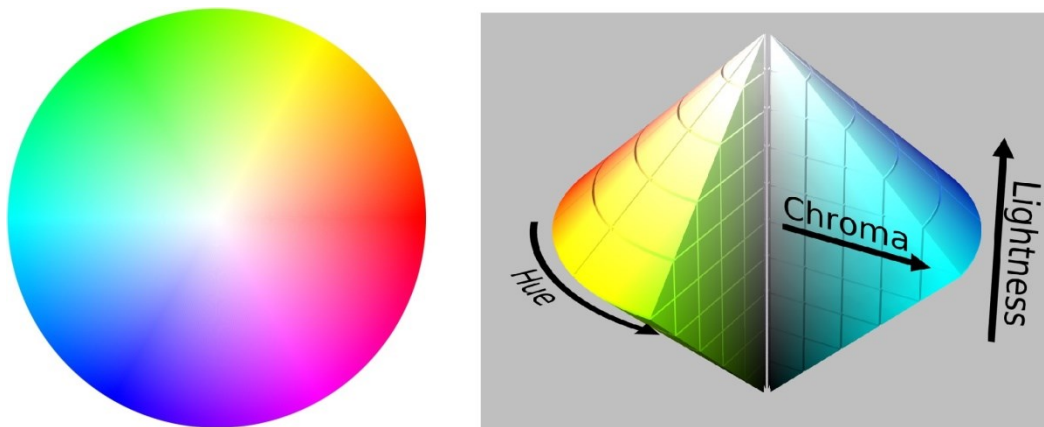


Figura 1.13. Rueda de color, croma, tono y luminosidad (fuente: https://es.wikipedia.org/wiki/Modelo_de_color_HSL)

La comunidad científica ha estandarizado diferentes espacios de color ya que existen distintas aplicaciones tanto industriales como científicas: Munsell, CIE Lab, CIE Lch, CIE XYZ, Hunter Lab [148]–[150]. El Sistema Munsell propuesto por el propio Albert Munsell se basa en una escala de color fundamentada en la propia percepción humana

del color, cuyo uso sigue vigente en la actualidad. Fue el primer sistema tridimensional propuesto y valora numéricamente las tres características del color: luminosidad, croma y tono. Además, este sistema estableció unas bases en las que fundamentaron otros sistemas más actuales como el CIE Lab.

La necesidad de 3 elementos como son la fuente de iluminación, objeto y observador, la Commission Internationale de l'Eclairage (CIE) estableció en 1931 un sistema de medición del color en el que se estandarizan tanto la fuente de iluminación como el observador. Así pues se establecen tres espacios distintos presentados por la CIE, en los que es posible representar un color a través de tres valores: CIE XYZ, CIE Lab y CIE Lch [151]. En 1931 la CIE introdujo un sistema basado en los valores triestímulos XYZ que se ha quedado en un uso muy limitado por no tener una buena correlación con los atributos visuales. Aunque el valor Y sí que tiene una correcta correlación con la luminosidad los valores X y Z no lo tienen con el croma y el tono. Es por ello que se recomienda emplear los valores (x,y) y mantener la Y para valorar la luminosidad.

1.3.5. Color percibido

Dentro del concepto de color percibido [152],[153] podemos diferenciar dos tipos. El **color percibido de una luz** que es la percepción que provoca la radiación de un color físico, y por otro lado tenemos el **color percibido de una superficie**, que se trata de la percepción que nos da la capacidad de diferenciar dos superficies de las mismas características estructurales, de forma y magnitudes [154]–[156]. Algunos de los conceptos fundamentales en cuanto al color percibido se refieren son:

- Luminosidad percibida: dícese de la cantidad de luz que percibe el ojo de un objeto que ha reflejado, emitido o transmitido cierta cantidad de radiación lumínica. Queda representado por el símbolo “Q”.
- Cromacidad percibida: nivel de cromacidad que percibe el ser humano procedente de una superficie de un objeto siendo este en mayor o menor medida cromático [157]. Se representa por el símbolo “M”.

- Claridad percibida: comúnmente conocida como la luminosidad de una superficie que es percibida. El símbolo “L” es utilizado para representar esta magnitud.
- Tono percibido: Percepción visual producida para una luz monocromática que posee un espectro no equienergético. Dentro de esta definición se puede mejorar ya que ciertos términos no quedan bien definidos [158]. Así pues se pueden definir [159]:
 - Rojo: Tono que percibe el ojo humano de una radiación electromagnética monocromática que tiene una longitud de onda de 650 nm.
 - Amarillo: Tono que percibe el ojo humano de una radiación electromagnética monocromática que tiene una longitud de onda de 580 nm.
 - Verde: Tono que percibe el ojo humano de una radiación electromagnética monocromática que tiene una longitud de onda de 520 nm.
 - Tono que percibe el ojo humano de una radiación electromagnética monocromática que tiene una longitud de onda de 450 nm.
- Saturación percibida: se trata de aquella cromacidad de una superficie que ha sido valorada en función de su luminosidad. Viene representada por el símbolo “S”.
- Cromaticidad percibida: es la percepción que recibe el ojo a causa de la combinación establecida por el tono y la saturación.

1.3.6. Color psicofísico

El propósito de la medición del color de forma numérica no busca definir directamente el color, sino que lo que intenta es establecer una relación entre el suceso psicológico que es la percepción del color y el suceso físico que es el causante de esa percepción. Así pues, es un procedimiento para establecer los sucesos físicos que

producen unos sucesos psicológicos. Este proceso o procedimiento recibe el nombre de psicofísico y las correspondientes mediciones son denominadas medidas psicofísicas algunas de las cuales se pueden explicar de la siguiente forma [160]–[163]:

- Estímulos primarios de referencia: asociación de estímulos diferentes de color que al asociarse logran el objetivo de poder igual un color determinado. Se representan simbólicamente por los símbolos [R], [G], [B].
- Valores triestímulos: como de antemano su propio nombre indica se trata de la cuantía de cada uno de tres estímulos de referencia utilizado en un sistema tricromático establecido. Al igual que los estímulos primarios de referencia se simboliza con la R, G, B.
- Observador y sistema colorimétrico CIE XYZ 1964: dado que el observador colorimétrico CIE XYZ 1931 estaba limitado a un ángulo de observación de como máximo 4º y solo servía para comparación de colores, la CIE recomendó un nuevo observador denominado CIE XYZ 1964 que podía alcanzar ángulos superiores hasta los 10º. Los valores triestímulos pasaron a ser X₁₀, Y₁₀, Z₁₀. Por lo tanto, las coordenadas de cromaticidad se calcularían como el valor triestímulo dividido entre la suma de los tres valores triestímulo (Ecuación 1).

$$x_{10} = \frac{X_{10}}{X_{10} + Y_{10} + Z_{10}} ; y_{10} = \frac{Y_{10}}{X_{10} + Y_{10} + Z_{10}} ; z_{10} = \frac{Z_{10}}{X_{10} + Y_{10} + Z_{10}}$$

Ecuación 1. Valores triestímulo

- Diagrama de cromaticidad: representación en forma de diagrama de las coordenadas de cromaticidad de los valores triestímulos x, y (Figura 1.14).

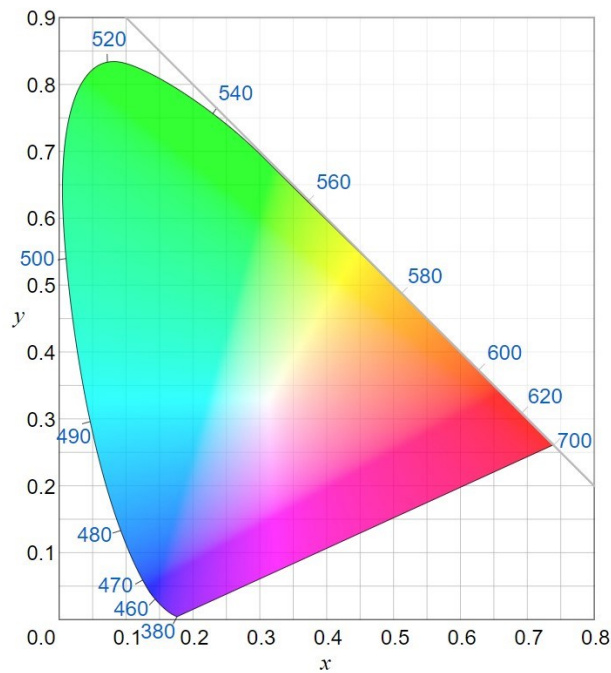


Figura 1.14. Diagrama Cromaticidad (fuente: https://es.wikipedia.org/wiki/Gama_de_color)

1.3.7. Color psicométrico

A pesar de haber definido el observador y sistema colorimétrico CIE XYZ 1964 se continuó trabajando para conseguir un espacio de color todavía más uniforme. Es cierta la gran importancia que tiene el sistema UCS para industrias que utilizan la mezcla aditiva, aunque para todos los análisis relacionados con esta tesis se utiliza las ecuaciones CIELAB (CIE L* a* b* 1976) siendo una de las más fiables para valorar los colores de las superficies de los textiles. Se procede a definir la terminología más relevante en lo referente al color psicométrico [155]:

- **Coordenadas CIE a*, b* 1976:** dichas coordenadas son calculadas para obtener una transformación no lineal de los valores triestímulo X, Y, Z [164]. Se emplean los valores X, Z correspondiente a dichos valores triestímulo del color a analizar y X_n , Y_n son los valores del color estímulo de referencia. Las ecuaciones para dicha transformación son las que se muestran en la Ecuación 2.

$$a^* = 500 \cdot \left[\sqrt[3]{\frac{X}{X_n}} - \sqrt[3]{\frac{Y}{Y_n}} \right] ; \quad b^* = 200 \cdot \left[\sqrt[3]{\frac{Y}{Y_n}} - \sqrt[3]{\frac{Z}{Z_n}} \right]$$

Ecuación 2. Cálculo de a^* y b^*

- Claridad CIE 1976: la Ecuación 5 permite calcular la luminosidad o claridad de una superficie y se representa mediante el símbolo L^* (Ecuación 3)

$$L^* = 116 \cdot \sqrt[3]{\frac{X}{Y_n}} - 16$$

Ecuación 3. Cálculo de luminosidad

- Espacio de color CIE $L^* a^* b^*$: representación tridimensional con un alto grado de uniformidad de las coordenadas L^* (luminosidad), a^* (verde-rojo), b^* (azul-amarillo) (Figura 1.15)

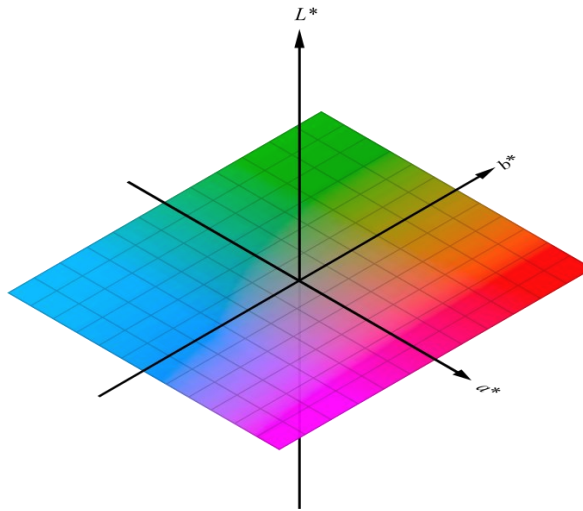


Figura 1.15. Espacio CIELAB

1.3.8. Kubelka-Munk

La teoría original de Kubelka-Munk (K-M) es una aproximación de dos flujos a la teoría general de transferencia de radiación. Se desarrolló para explicar la propagación de la luz en capas de colorantes paralelos de extensión xy infinita [165],[166]. Al contrario de lo que ocurre en una disolución, la relación de la concentración de colorante con la reflectancia o absorbancia no es una función lineal, no podemos usar unos cálculos como los de Lambert-Beer para el cálculo de concentración en disoluciones. Así pues, hay que recurrir a las ecuaciones de Kubelka-Munk.

Esta teoría se basa en definir dos tipos de flujos, por una parte, el flujo descendente (dirección $-z$) se refiere a la media de aquellos rayos que se dirigen hacia el hemisferio inferior. Por otro lado, si se hace referencia al flujo ascendente (dirección $+z$) como es de esperar serán todos aquellos rayos que toman dirección hacia el hemisferio superior. La denominación más común que se conoce hoy en día de estos flujos son los coeficientes de dispersión y absorción S y K respectivamente [167].

Los valores S y K no poseen un valor físico de forma directa, aunque aparentemente representan fracciones de luz dispersada y absorbida. Aun así, dicha apreciación no es tenida en consideración por muchos científicos, los cuales definen que S y K son propiedades físicas del sustrato. Un simple ejemplo que sustenta dicha afirmación es que S y K varían en función de la geometría de la iluminación (difusa o colimada). Si la distribución de la luz es difusa, Kubelka y Munk concluyeron que la S es el coeficiente intrínseco de dispersión ($S=s$) y la K es el coeficiente intrínseco de absorción (a) multiplicado por dos ($K=2a$). Al contrario de K y S , los valores a y s son físicamente significativas. Realizan una representación de las probabilidades de que la radiación pueda ser absorbida y dispersada por unidad de longitud de trayectoria de forma isotrópica [168]–[175].

En el caso de tener un sustrato opaco de espesor infinito teniendo en cuenta que R_{∞} es el factor de reflectancia y que este no varía al incrementar el espesor de la muestra, se podría calcular el valor de K/S según la ecuación Ecuación 4.

$$\frac{K}{S} = \frac{(1 - R_{\infty})^2}{2 \cdot R_{\infty}}$$

Ecuación 4. Ecuación Kubelka-Munk

1.4. Nanoarcillas

Nanoarcilla [76–109] es el término general utilizado para referirse a las arcillas minerales con una estructura fosilífera o laminar del orden de los nm y superficies de 50-150 nm o más. A pesar de que las nanoarcillas son de uso común, hay que tener en cuenta que no todas las dimensiones de las nanoarcillas son de tamaño nanométrico. Algunas dimensiones de arcilla clasificadas como nanoarcillas son de tamaño microscópico debido a las aglomeraciones o a su estructura, como la montmorillonta laminar, que es nano en una dimensión laminar, pero micro en la otra. La base mineral puede ser sintética o natural, y es hidrofílica. La superficie de la arcilla puede modificarse con compuestos específicos para mejorar su afinidad y hacerla compatible, por ejemplo, con los polímeros. La superficie de las nanoarcillas es muy grande, alrededor de $750 \text{ m}^2 \cdot \text{g}^{-1}$. Cuando se incorporan pequeñas cantidades de estos materiales a matrices poliméricas, el resultado se conoce como nanocompuesto. La mayoría de los colorantes utilizados en la industria textil son aniónicos, por lo que cabe esperar que las nanoarcillas aniónicas logren un mayor rendimiento de adsorción.

Las nanoarcillas estudiadas en esta tesis presentan varias ventajas, como su abundancia natural, su bajo coste y su alta capacidad de adsorción. Cuando estas nanoarcillas actúan como anfitriones inorgánicos de compuestos orgánicos, mejoran las propiedades del anfitrión orgánico para conferirle una mayor solidez frente a los entornos químicos y naturales. Estas nanoarcillas pueden sintetizarse químicamente para mejorar sus características físico-químicas. Otra firme ventaja de la síntesis química es que no hay ningún paso de purificación, que es necesario con las nanoarcillas naturales para mejorar la capacidad de adsorción.

El silicio y el oxígeno son comunes en todas las arcillas minerales. Cuando se combinan con otros elementos, como el Al, el Mg, el Fe, el Na, el Ca y el K, y dadas las múltiples formas en que estos elementos pueden vincularse, generan un gran número de configuraciones posibles. Una distinción importante en las propiedades de las arcillas minerales es la capacidad de algunas de ellas de cambiar de volumen mediante la adsorción de moléculas de agua de otros iones polares en su estructura. Esto se denomina propiedad de hinchamiento [176].

1.4.1. Uso de nanoarcillas para la limpieza de aguas residuales textiles

En las últimas décadas, las alertas medioambientales se han disparado por la creciente preocupación por el cuidado del medio ambiente. Esto se ha sumado a la posibilidad de optimizar y reducir el uso de recursos en los procesos industriales de tintura textil y ha llevado a la comunidad científica a buscar opciones para recuperar o reutilizar los colorantes de las aguas residuales textiles (Tabla 1.4 y Figura 1.16). El objetivo general de esta investigación es atrapar el colorante presente en las aguas residuales de los procesos de tintura, introduciendo un tercer elemento en el mismo baño. Se sabe que algunos compuestos o materiales son de utilidad en este proceso, como las ciclodextrinas [177], los elementos de desecho agrícola [178] y los nanocompuestos [179]; también se pueden utilizar medios físicos, como la filtración por membrana [23], entre otros muchos métodos.

El reciclaje de las aguas residuales industriales se ha convertido en una necesidad cada vez más evidente. Los esfuerzos de los gobiernos internacionales por salvaguardar el medio ambiente han contribuido a que las empresas privadas tomen cartas en el asunto y realicen importantes inversiones en estos campos [19],[148],[149],[151]-[163]. La industria textil vierte residuos orgánicos e inorgánicos que producen bioacumulación y pueden causar altos grados de toxicidad [180].

Tabla 1.4. Grados de fijación según materia colorante.

Familia Colorantes	Materia Textil	Grado de fijación (%)
Ácidos	Poliamida/Lana	80–95
Azoicos	Celulósicas	75–90
Básicos	Acrílicos	95–100
Directos	Celulósicas	70–95
Dispersos	Poliéster	90–100
Premetalizados	Lana	85–95
Reactivos	Celulósicas	60–90
Sulfurosos	Celulósicas	60–86

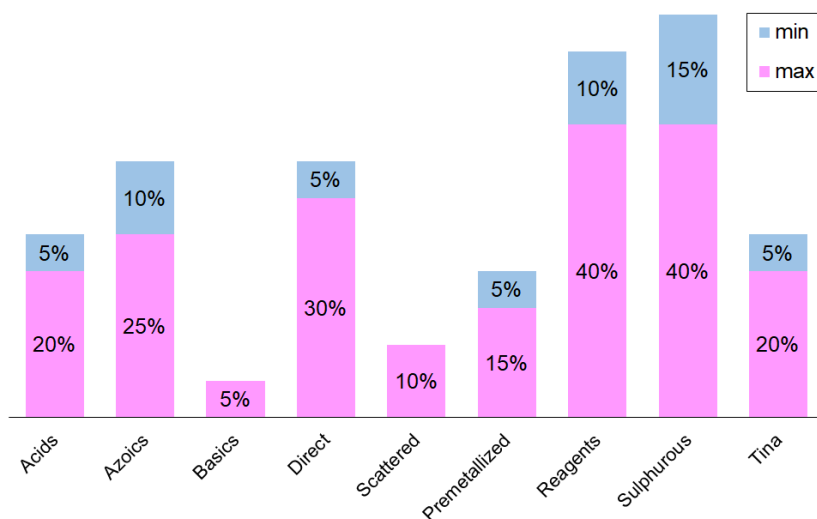


Figura 1.16. Porcentajes de pérdidas de colorantes en efluentes

La industria química textil es una de las que más afectan a las aguas residuales, y es la industria con mayor actividad química del planeta [1]. Debido a la tintura y estampado de textiles, los colorantes son uno de los contaminantes más comunes en la industria textil [2]–[4]. La concentración de colorantes en los efluentes se sitúa en torno a 50-1000 ppm [180]. La naturaleza de su composición depende del tipo de colorante, considerando la fijación y las pérdidas estimadas en el efluente, como se muestra en la Tabla 1.6. Por tanto, es muy importante mejorar la capacidad de las industrias para eliminar los colorantes de los efluentes. El desarrollo de absorbentes de bajo coste mediante la

integración de tecnología avanzada puede suponer un avance significativo en este ámbito [181].

Otras tecnologías de tratamiento de aguas textiles realizadas por medio de la nanotecnología son las siguientes: los nanosorbentes, incluidas las nanoarcillas, de las que se ocupa esta tesis, los compuestos nanosorbentes y basados en carbono, que se emplean principalmente para aguas con Ni^{2+} [182],[183] y los polímeros nanosorbentes regenerables, que se utilizan en lugar de contaminantes de tipo orgánico e inorgánico. Los compuestos de hierro y carbono también son capaces de reducir grandes cantidades de estos diferentes contaminantes [182],[184]–[186].

1.4.2. Hidrotalcita

La hidrotalcita, $\text{Mg}_6\text{Al}_2(\text{CO}_3)(\text{OH})_{16}\cdot 4(\text{H}_2\text{O})$ (Figura 1.17), se clasifica como un mineral de tamaño nanométrico porque una de las dimensiones de su lámina mide menos de 20 nm. Debido a su estructura característica, entra en la categoría de los "hidróxidos dobles estratificados" (LDH). Esta capa tiene una área específica de superficie de entre $71 \text{ m}^2\cdot\text{g}^{-1}$ y $104 \text{ m}^2\cdot\text{g}^{-1}$ [187]. Los investigadores muestran un creciente interés por estos elementos gracias a su amplia gama de aplicaciones como catalizadores, y también en medicina, adsorción, etc. [188]. Existen diferentes métodos mediante los cuales se produce la adsorción de aniones por parte de los compuestos de LDH. El más común es el que se produce por adsorción directa en dispersión [189]–[191]. La cristalinidad de un sólido limita dicha adsorción por las siguientes razones: la polaridad del medio, la temperatura, el tamaño del anión y el pH [189]–[191].

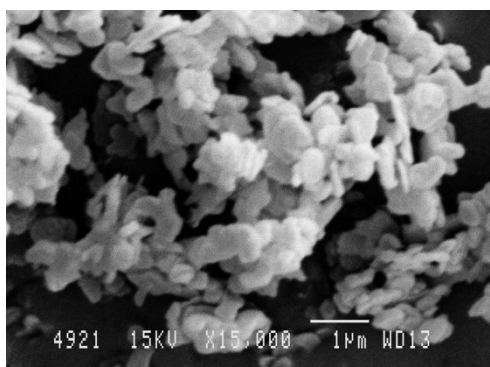


Figura 1.17. Hidrotalcita SEM

El segundo método, aunque algo más largo, pero que ofrece claras ventajas, es la calcinación. Estudios anteriores han demostrado que la hidrotalcita tiene memoria de forma tras ser expuesta a una fuente térmica elevada. Esto cambia sustancialmente su disposición laminar inicial, que se recupera durante los procesos de hidratación posteriores. Tras ser expuesta a temperaturas de 450-600°C, se reconstruye tal y como se ha descrito anteriormente gracias a los aniones presentes en la disolución y su incorporación a la nueva estructura de la nanoarcilla [192]–[194].

Un tercer y último método se basa en producir la nanoarcilla de forma sintética y en este proceso hacer que un anión determinado sea incorporado a la estructura de la hidrotalcita. A este método se le denomina coprecipitación [195].

1.4.3. Adsorción de colorante mediante Hidrotalcita

En los últimos años diferentes métodos de sorción como son la adsorción, el intercambio de iones y la biosorción han alcanzado un alto nivel de relevancia como proceso de alta eficacia para la limpieza y purificación de aguas residuales gracias a la utilización innovadora de ciertos materiales [196]. Un ejemplo de este tipo de materiales que ofrecen una proyección muy prometedora son las hidrotalcitas u otros elementos con gran similitud englobados dentro de los denominados hidróxidos dobles estratificados [197]. Dentro de estos hidróxidos dobles las más populares son las hidrotalcitas de Mg-Al donde los aniones que hay intercalados en la estructura y sus moléculas de H₂O tienen la

capacidad de poder ser intercambiadas con otro tipo de aniones, es por ello que se dicen que estas nanoarcillas son buenos intercambiados de aniones [198].

En la Figura 1.18 se muestra un esquema de cómo se prepara la hidrotalcita mediante calcinación a 600°C para poder después adsorber con mayor rendimiento los aniones (colorantes) e incorporarlos a su estructura durante la fase de recuperación de su forma. Una vez recuperada y habiendo incorporado el colorante, el híbrido obtenido colorante-arcilla ha tomado el color característico del colorante y a partir de aquí se abre un abanico de posibilidades para su reutilización en diferentes aplicaciones. Además, la presencia de la nanoarcilla en este híbrido confiere ciertas mejoras que pueden otorgar características destacables en su reutilización, como son la mejora de solidez del color en tratamientos energéticos como son la luz o el planchado.

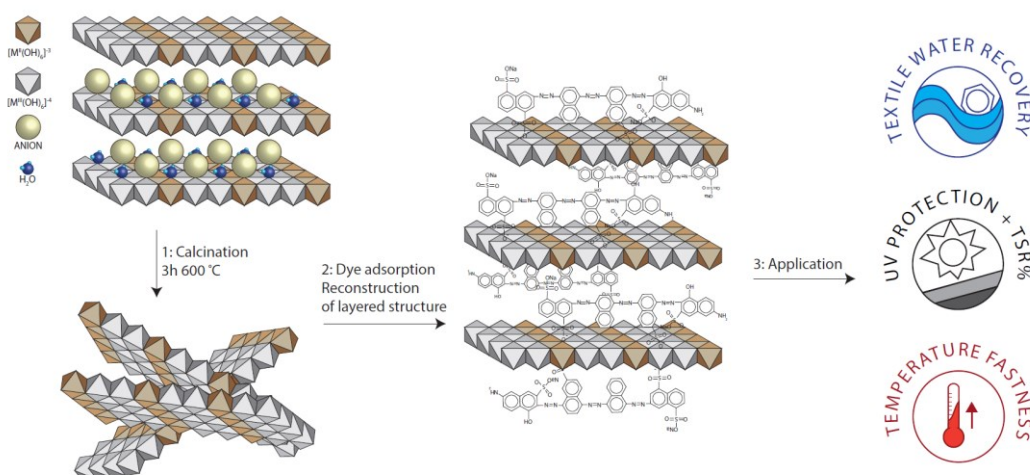


Figura 1.18. Preparación de Hidrotalcita, adsorción y reutilización.

Hay que señalar que el estado del arte sobre la que versa esta tesis esta ampliado en el Capitulo 3 de publicación, en la sección 3.1 titulada Uses of Nanoclays and Adsorbents for Dye Recovery: A Textile Industry Review. En ella se recoge una revisión de otros trabajos de investigación que tratan sobre esta temática y algunos de los resultados obtenidos.

Referencias

1. Wakkal, M.; Khiari, B.; Zagrouba, F. Textile Wastewater Treatment by Agro-Industrial Waste: Equilibrium Modelling, Thermodynamics and Mass Transfer Mechanisms of Cationic Dyes Adsorption onto Low-Cost Lignocellulosic Adsorbent. *J. Taiwan Inst. Chem. Eng.* 2019, 96, 439–452. <https://doi.org/10.1016/J.JTICE.2018.12.014>.
2. Nath, J.; Bag, S.; Bera, D.; Ray, L. Biotreatment of Malachite Green from Aqueous Solution and Simulated Textile Effluent by Growing Cells (Batch Mode) and Activated Sludge System. *Groundw. Sustain. Dev.* 2019, 8 (May 2018), 172–178. <https://doi.org/10.1016/j.gsd.2018.11.002>.
3. Bankole, P. O.; Adekunle, A. A.; Obidi, O. F.; Olukanni, O. D.; Govindwar, S. P. Degradation of Indigo Dye by a Newly Isolated Yeast, *Diutina Rugosa* from Dye Wastewater Polluted Soil. *J. Environ. Chem. Eng.* 2017, 5 (5), 4639–4648. <https://doi.org/10.1016/j.jece.2017.08.050>
4. Deniz, F.; Karaman, S. Removal of an Azo-Metal Complex Textile Dye from Colored Aqueous Solutions Using an Agro-Residue. *Microchem. J.* 2011, 99 (2), 296–302. <https://doi.org/10.1016/j.microc.2011.05.021>
5. Robinson, T.; McMullan, G.; Marchant, R.; Nigam, P. Remediation of Dyes in Textile Effluent: A Critical Review on Current Treatment Technologies with a Proposed Alternative. *Bioresour. Technol.* 2001, 77 (3), 247–255. [https://doi.org/10.1016/S0960-8524\(00\)00080-8](https://doi.org/10.1016/S0960-8524(00)00080-8).
6. Delee, W.; O'Neill, C.; Hawkes, F. R.; Pinheiro, H. M. Anaerobic Treatment of Textile Effluents: A Review. *J. Chem. Technol. Biotechnol. Int. Res. Process. Environ. Clean Technol.* 1998, 73 (4), 323–335. [https://doi.org/10.1002/\(SICI\)1097-4660\(199812\)73:4%3C323::AID-JCTB976%3E3.0.CO;2-S](https://doi.org/10.1002/(SICI)1097-4660(199812)73:4%3C323::AID-JCTB976%3E3.0.CO;2-S)
7. Lazaridis, N. K.; Karapantsios, T. D.; Georgantas, D. Kinetic Analysis for the Removal of a Reactive Dye from Aqueous Solution onto Hydrotalcite by Adsorption. *Water Res.* 2003, 37 (12), 3023–3033. [https://doi.org/10.1016/S0043-1354\(03\)00121-0](https://doi.org/10.1016/S0043-1354(03)00121-0)
8. Chen, X.; Memon, H. A.; Wang, Y.; Marriam, I.; Tebyetekerwa, M. Circular Economy and Sustainability of the Clothing and Textile Industry. *Mater. Circ. Econ.* 2021, 3 (1), 1–9. <https://doi.org/10.1007/s42824-021-00026-2>
9. Ghisellini, P.; Cialani, C.; Ulgiati, S. A Review on Circular Economy: The Expected Transition to a Balanced Interplay of Environmental and Economic Systems. *J. Clean. Prod.* 2016, 114, 11–32. <https://doi.org/10.1016/j.jclepro.2015.09.007>
10. Ashby, A. Developing Closed Loop Supply Chains for Environmental Sustainability: Insights from a UK Clothing Case Study. *J. Manuf. Technol. Manag.* 2018. <https://doi.org/10.1108/JMTM-12-2016-0175>

11. McDonough, W.; Braungart, M. Design for the Triple Top Line: New Tools for Sustainable Commerce. *Corp. Environ. Strateg.* 2002, 9 (3), 251–258. [https://doi.org/10.1016/S1066-7938\(02\)00069-6](https://doi.org/10.1016/S1066-7938(02)00069-6)
12. MacArthur, E. Towards the Circular Economy, Economic and Business Rationale for an Accelerated Transition. *Ellen MacArthur Found. Cowes, UK* 2013, 21–34.
13. Savaskan, R. C.; Bhattacharya, S.; Van Wassenhove, L. N. Closed-Loop Supply Chain Models with Product Remanufacturing. *Manage. Sci.* 2004, 50 (2), 239–252. <https://doi.org/10.1287/mnsc.1030.0186>
14. Jia, F.; Yin, S.; Chen, L.; Chen, X. The Circular Economy in the Textile and Apparel Industry: A Systematic Literature Review. *J. Clean. Prod.* 2020, 259, 120728. <https://doi.org/10.1016/j.jclepro.2020.120728>
15. Cox, M.; Négre, P.; Yurramendi, L. Industrial Liquid Effluents. *Ina. Tecnalia, San Sebastian* 2007, 283.
16. Sonune, A.; Ghate, R. Developments in Wastewater Treatment Methods. *Desalination* 2004, 167, 55–63. <https://doi.org/10.1016/j.desal.2004.06.113>
17. Rathoure, A. K. *Toxicity and Waste Management Using Bioremediation*; IGI Global, 2015.
18. Khalaf, M. N. *Green Polymers and Environmental Pollution Control*; CRC Press, 2016.
19. Morin-Crini, N.; Crini, G.; Roy, L. Eaux Industrielles Contaminées. *PUFC, Besançon* 2017, 513, 37–47.
20. Holkar, C. R.; Jadhav, A. J.; Pinjari, D. V; Mahamuni, N. M.; Pandit, A. B. A Critical Review on Textile Wastewater Treatments: Possible Approaches. *J. Environ. Manage.* 2016, 182, 351–366. <https://doi.org/10.1016/j.jenvman.2016.07.090>
21. Paul, S. A.; Chavan, S. K.; Khambe, S. D. Studies on Characterization of Textile Industrial Waste Water in Solapur City. *Int. J. Chem. Sci.* 2012, 10 (2), 635–642.
22. Kant, R. Textile Dyeing Industry an Environmental Hazard. *Natural Science*, 4, 22–26. 2011. <http://www.scirp.org/journal/PaperInformation.aspx?PaperID=17027>
23. Erkanlı, M.; Yilmaz, L.; Çulfaz-Emecen, P. Z.; Yetis, U. Brackish Water Recovery from Reactive Dyeing Wastewater via Ultrafiltration. *J. Clean. Prod.* 2017, 165, 1204–1214. <https://doi.org/10.1016/J.JCLEPRO.2017.07.195>.
24. Farquhar, G. D.; Von Caemmerer, S.; Berry, J. A. Models of Photosynthesis. *Plant Physiol.* 2001, 125 (1), 42–45. <https://doi.org/10.1104/pp.125.1.42>
25. Evans, J. R. Improving Photosynthesis. *Plant Physiol.* 2013, 162 (4), 1780–1793. <https://doi.org/10.1104/pp.113.219006>

26. Eberhard, S.; Finazzi, G.; Wollman, F.-A. The Dynamics of Photosynthesis. *Annu. Rev. Genet.* 2008, 42, 463–515. <https://doi.org/10.1146/annurev.genet.42.110807.091452>
27. Mazumder, D. Process Evaluation and Treatability Study of Wastewater in a Textile Dyeing Industry. *Int. J. Energy Environ.* 2011, 2 (6).
28. Rosa, J. M.; Fileti, A. M. F.; Tambourgi, E. B.; Santana, J. C. C. Dyeing of Cotton with Reactive Dyestuffs: The Continuous Reuse of Textile Wastewater Effluent Treated by Ultraviolet/Hydrogen Peroxide Homogeneous Photocatalysis. *J. Clean. Prod.* 2015, 90, 60–65. <https://doi.org/10.1016/j.jclepro.2014.11.043>
29. Dehghani, M. H.; Alghasi, A.; Porkar, G. Using Medium Pressure Ultraviolet Reactor for Removing Azo Dyes in Textile Wastewater Treatment Plant. *World Appl. Sci. J.* 2011, 12 (6), 797–802.
30. Georgiou, D.; Melidis, P.; Aivasidis, A.; Gimouhopoulos, K. Degradation of Azo-Reactive Dyes by Ultraviolet Radiation in the Presence of Hydrogen Peroxide. *Dye. Pigment.* 2002, 52 (2), 69–78. [https://doi.org/10.1016/S0143-7208\(01\)00078-X](https://doi.org/10.1016/S0143-7208(01)00078-X)
31. Costa, F. A. P.; dos Reis, E. M.; Azevedo, J. C. R.; Nozaki, J. Bleaching and Photodegradation of Textile Dyes by H₂O₂ and Solar or Ultraviolet Radiation. *Sol. Energy* 2004, 77 (1), 29–35. <https://doi.org/10.1016/j.solener.2004.03.017>
32. Ding, S.; Li, Z.; Wang, R. Overview of Dyeing Wastewater Treatment Technology. *Water Resour. Prot* 2010, 26, 73–78.
33. Chequer, F. M. D.; De Oliveira, G. A. R.; Ferraz, E. R. A.; Cardoso, J. C.; Zanoni, M. V. B.; De Oliveira, D. P. Textile Dyes: Dyeing Process and Environmental Impact. *Eco-friendly Text. Dye. Finish.* 2013, 6 (6), 151–176. <http://doi.org/10.5772/53659>
34. Islam, M. M.; Mahmud, K.; Faruk, O.; Billah, M. S. Textile Dyeing Industries in Bangladesh for Sustainable Development. *Int. J. Environ. Sci. Dev.* 2011, 2 (6), 428. <https://doi.org/10.7763/IJESD.2011.V2.164>
35. Kašiković, N.; Vladić, G.; Novaković, D. Textile Printing—Past, Present, Future. *Vanred. Izd.* 2016, 35.
36. Saad, F.; Hassabo, A.; Othman, H.; Mosaad, M. M.; Mohamed, A. L. A Valuable Observation on Thickeners for Valuable Utilisation in the Printing of Different Textile Fabrics. *Egypt. J. Chem.* 2022, 65 (4), 1–2. <https://doi.org/10.21608/ejchem.2021.96612.4521>
37. Abdelrahman, M.; Wahab, S.; Mashaly, H.; Maamoun, D.; Khattab, T. A. Review in Textile Printing Technology. *Egypt. J. Chem.* 2020, 63 (9), 3465–3479. <https://dx.doi.org/10.21608/ejchem.2020.23726.2418>
38. Le Marechal, A. M.; Križanec, B.; Vajnhandl, S.; Valh, J. V. Textile Finishing Industry

- as an Important Source of Organic Pollutants. In *Organic pollutants ten years after the Stockholm convention-environmental and analytical update*; IntechOpen Rijeka, 2012; pp 29–54.
39. Bakr, M.; Taha, M. A.; Osman, H.; Ibrahim, H. M. Novel Green Printing of Cotton, Wool and Polyester Fabrics with Natural Safflower Dye Nanoparticles. *Egypt. J. Chem.* 2021, 64 (11), 6221–6230. <https://dx.doi.org/10.21608/ejchem.2021.75163.3695>
 40. Gunay, M. *Eco-Friendly Textile Dyeing and Finishing*; BoD–Books on Demand, 2013.
 41. Hunger, K. *Industrial Dyes: Chemistry, Properties, Applications*; John Wiley & Sons, 2007.
 42. Lee, M.-J.; Ho, C.-C.; Lin, H.; Wang, P.; Lu, J. Solubility of Disperse Red 82 and Modified Disperse Yellow 119 in Supercritical Carbon Dioxide or Nitrous Oxide with Ethanol as a Cosolvent. *J. Supercrit. Fluids* 2014, 95, 258–264. <https://doi.org/10.1016/j.supflu.2014.08.023>
 43. Lin, H.; Ho, C.-C.; Lee, M.-J. Solubilities of Disperse Dyes of Blue 79: 1, Red 82 and Modified Yellow 119 in Supercritical Carbon Dioxide and Nitrous Oxide. *J. Supercrit. Fluids* 2004, 32 (1–3), 105–114. <https://doi.org/10.1016/j.supflu.2004.03.001>
 44. Benkhaya, S.; M’rabet, S.; El Harfi, A. A Review on Classifications, Recent Synthesis and Applications of Textile Dyes. *Inorg. Chem. Commun.* 2020, 115, 107891. <https://doi.org/10.1016/j.inoche.2020.107891>
 45. Chen, X.; Ding, K.; Jun, L. Synthesis, Identification and Application of Aldehyde Reactive Dyes. *Dye. Pigment.* 2015, 123, 404–412. <https://doi.org/10.1016/j.dyepig.2015.05.033>
 46. Xiao, H.; Zhao, T.; Li, C.-H.; Li, M.-Y. Eco-Friendly Approaches for Dyeing Multiple Type of Fabrics with Cationic Reactive Dyes. *J. Clean. Prod.* 2017, 165, 1499–1507. <https://doi.org/10.1016/j.jclepro.2017.07.174>
 47. El Harfi, S.; El Harfi, A. Classifications, Properties and Applications of Textile Dyes: A Review. *Appl. J. Environ. Eng. Sci.* 2017, 3 (3), 0–3. <https://doi.org/10.48422/IMIST.PRSM/ajees-v3i3.9681>
 48. Ferreira, E. S. B.; Hulme, A. N.; McNab, H.; Quye, A. The Natural Constituents of Historical Textile Dyes. *Chem. Soc. Rev.* 2004, 33 (6), 329–336. <https://doi.org/10.1039/B305697J>
 49. Allen, R. L. *Colour Chemistry*; Springer Science & Business Media, 2013.
 50. Chattopadhyay, D. P. Chemistry of Dyeing. In *Handbook of textile and industrial dyeing*; Elsevier, 2011; pp 150–183. <https://doi.org/10.1533/9780857093974.1.150>

51. Hassan, S. S. M.; Awwad, N. S.; Aboterika, A. H. A. Removal of Synthetic Reactive Dyes from Textile Wastewater by Sorel's Cement. *J. Hazard. Mater.* 2009, *162* (2–3), 994–999. <https://doi.org/10.1533/9780857093974.1.150>
52. Clark, M. Fundamental Principles of Dyeing. *Handb. Text. Ind. Dye. Princ. Process. types Dye*. 2011.
53. Shamey, R. Improving the Colouration/Dyeability of Polyolefin Fibres. In *Polyolefin Fibres*; Elsevier, 2009; pp 363–397. <https://doi.org/10.1533/9781845695552.2.363>
54. Farouk, R.; Gaffer, H. E. Simultaneous Dyeing and Antibacterial Finishing for Cotton Cellulose Using a New Reactive Dye. *Carbohydr. Polym.* 2013, *97* (1), 138–142. <https://doi.org/10.1016/j.carbpol.2013.04.037>
55. Jiraratananon, R.; Sungpet, A.; Luangsowan, P. Performance Evaluation of Nanofiltration Membranes for Treatment of Effluents Containing Reactive Dye and Salt. *Desalination* 2000, *130* (2), 177–183. [https://doi.org/10.1016/S0011-9164\(00\)00085-0](https://doi.org/10.1016/S0011-9164(00)00085-0)
56. Gao, Y.; Cranston, R. Recent Advances in Antimicrobial Treatments of Textiles. *Text. Res. J.* 2008, *78* (1), 60–72. <https://doi.org/10.1177/0040517507082332>
57. Churchley, J. H.; Greaves, A. J.; Hutchings, M. G.; Phillips, D. A. S.; Taylor, J. A. A Chemometric Approach to Understanding the Bioelimination of Anionic, Water-soluble Dyes by a Biomass—Part 2: Acid Dyes §. *Color. Technol.* 2000, *116* (7-8), 222–228. <https://doi.org/10.1111/j.1478-4408.2000.tb00047.x>
58. El-Zawahry, M. M.; El-Shami, S.; El-Mallah, M. H. Optimizing a Wool Dyeing Process with Reactive Dye by Liposome Microencapsulation. *Dye. Pigment.* 2007, *74* (3), 684–691. <https://doi.org/10.1016/j.dyepig.2006.04.014>
59. Lewis, D. M. The Dyeing of Wool with Reactive Dyes. *J. Soc. Dye. Colour.* 1982, *98* (5-6), 165–175. <https://doi.org/10.1111/j.1478-4408.1982.tb03631.x>
60. Qin, Y.; Yuan, M.; Hu, Y.; Lu, Y.; Lin, W.; Ma, Y.; Lin, X.; Wang, T. Preparation and Interaction Mechanism of Nano Disperse Dye Using Hydroxypropyl Sulfonated Lignin. *Int. J. Biol. Macromol.* 2020, *152*, 280–287. <https://doi.org/10.1016/j.ijbiomac.2020.02.261>
61. Fang, S.; Feng, G.; Guo, Y.; Chen, W.; Qian, H. Synthesis and Application of Urethane-Containing Azo Disperse Dyes on Polyamide Fabrics. *Dye. Pigment.* 2020, *176*, 108225. <https://doi.org/10.1016/j.dyepig.2020.108225>
62. Sarkar, S.; Banerjee, A.; Halder, U.; Biswas, R.; Bandopadhyay, R. Degradation of Synthetic Azo Dyes of Textile Industry: A Sustainable Approach Using Microbial Enzymes. *Water Conserv. Sci. Eng.* 2017, *2* (4), 121–131. <https://doi.org/10.1007/s41101-017-0031-5>

63. de Campos Ventura-Camargo, B.; Marin-Morales, M. A. Azo Dyes: Characterization and Toxicity-a Review. *Text. Light Ind. Sci. Technol.* 2013, 2 (2), 85–103.
64. Pinheiro, H. M.; Touraud, E.; Thomas, O. Aromatic Amines from Azo Dye Reduction: Status Review with Emphasis on Direct UV Spectrophotometric Detection in Textile Industry Wastewaters. *Dye. Pigment.* 2004, 61 (2), 121–139. <https://doi.org/10.1016/j.dyepig.2003.10.009>
65. Seixas De Melo, J.; Moura, A. P.; Melo, M. J. Photophysical and Spectroscopic Studies of Indigo Derivatives in Their Keto and Leuco Forms. 2004. <https://doi.org/10.1021/jp049076y>.
66. Bechtold, T.; Turcanu, A. Electrochemical Reduction in Vat Dyeing: Greener Chemistry Replaces Traditional Processes. *J. Clean. Prod.* 2009, 17 (18), 1669–1679. <https://doi.org/10.1016/j.jclepro.2009.08.004>
67. Roessler, A.; Crettenand, D. Direct Electrochemical Reduction of Vat Dyes in a Fixed Bed of Graphite Granules. *Dye. Pigment.* 2004, 63 (1), 29–37. <https://doi.org/10.1016/j.dyepig.2004.01.005>
68. Roessler, A.; Jin, X. State of the Art Technologies and New Electrochemical Methods for the Reduction of Vat Dyes. *Dye. Pigment.* 2003, 59 (3), 223–235. [https://doi.org/10.1016/S0143-7208\(03\)00108-6](https://doi.org/10.1016/S0143-7208(03)00108-6).
69. Božič, M.; Kokol, V. Ecological Alternatives to the Reduction and Oxidation Processes in Dyeing with Vat and Sulphur Dyes. *Dye. Pigment.* 2008, 76 (2), 299–309. <https://doi.org/10.1016/j.dyepig.2006.05.041>
70. Clark, R. J. H.; Cooksey, C. J.; Daniels, M. A. M.; Withnall, R. Indigo, Woad, and Tyrian Purple: Important Vat Dyes from Antiquity to the Present. *Endeavour* 1993, 17 (4), 191–199. [https://doi.org/10.1016/0160-9327\(93\)90062-8](https://doi.org/10.1016/0160-9327(93)90062-8)
71. Leghié, P.; Lelieur, J.-P.; Levillain, E. Comments on the Mechanism of the Electrochemical Reduction of Sulphur in Dimethylformamide. *Electrochem. commun.* 2002, 4 (5), 406–411. [https://doi.org/10.1016/S1388-2481\(02\)00333-8](https://doi.org/10.1016/S1388-2481(02)00333-8)
72. Paris, J.; Plichon, V. Electrochemical Reduction of Sulphur in Dimethylacetamide. *Electrochim. Acta* 1981, 26 (12), 1823–1829. [https://doi.org/10.1016/0013-4686\(81\)85170-5](https://doi.org/10.1016/0013-4686(81)85170-5)
73. Nunn, D. M. Dyeing of Synthetic-Polymer and Acetate Fibers, Dyers. Company Publications Trust, West Yorkshire 1979.
74. Larsen, S. A. Examination of Wool Top by Infra-Red Reflectance: A Note on the Influence of Dyeing. 1979. <https://doi.org/10.1080/00405007908658898>
75. Friedman, M.; Ash, J. F.; Bry, R. E.; Simonaitis, R. A. Mothproofing Wool and Wool Blends with Permethrin. *J. Agric. Food Chem.* 1979, 27 (2), 331–336.

76. Brady, P. R.; Cookson, P. G.; Bell, V. A.; Lewis, D. M. Transfer Printing of Wool. *Text. Chem. Color.* 1979, 11 (5).
77. Puchtler, H.; Waldrop, F. S. On the Mechanism of Verhoeff's Elastica Stain: A Convenient Stain for Myelin Sheaths. *Histochemistry* 1979, 62 (3), 233–247.
78. Chavan, R. B. Environmentally Friendly Dyes. *Handb. Text. Ind. Dye.* 2011, 515–561. <https://doi.org/10.1533/9780857093974.2.515>
79. Broadbent, A. D. *Basic Principles of Textile Coloration*; Society of Dyers and Colorists Bradford, UK, 2001; Vol. 132.
80. Zollinger, H. Color Chemistry: Syntheses. *Prop. Appl. Org. Dye. Pigment. Verlag Helv. Chim. Acta, Zürich* 2003, 15–65.
81. Rauf, M. A.; Meetani, M. A.; Hisaindee, S. An Overview on the Photocatalytic Degradation of Azo Dyes in the Presence of TiO₂ Doped with Selective Transition Metals. *Desalination* 2011, 276 (1–3), 13–27. <https://doi.org/10.1016/j.desal.2011.03.071>
82. Raman, C. D.; Kanmani, S. Textile Dye Degradation Using Nano Zero Valent Iron: A Review. *J. Environ. Manage.* 2016, 177, 341–355. <https://doi.org/10.1016/j.jenvman.2016.04.034>
83. Zinatloo-Ajabshir, S.; Salavati-Niasari, M. Facile Route to Synthesize Zirconium Dioxide (ZrO₂) Nanostructures: Structural, Optical and Photocatalytic Studies. *J. Mol. Liq.* 2016, 216, 545–551. <https://doi.org/10.1016/j.molliq.2016.01.062>
84. Zinatloo-Ajabshir, S.; Salavati-Niasari, M. Nanocrystalline Pr₆O₁₁: Synthesis, Characterization, Optical and Photocatalytic Properties. *New J. Chem.* 2015, 39 (5), 3948–3955. <https://doi.org/10.1039/C4NJ02106A>
85. Antoniotti, S.; Duñach, E. Direct and Catalytic Synthesis of Quinoxaline Derivatives from Epoxides and Ene-1, 2-Diamines. *Tetrahedron Lett.* 2002, 43 (22), 3971–3973. [https://doi.org/10.1016/S0040-4039\(02\)00715-3](https://doi.org/10.1016/S0040-4039(02)00715-3)
86. Welham, A. *The Theory of Dyeing (and the Secret of Life)*. 2000.
87. Gürses, A.; Açıkyıldız, M.; Güneş, K.; Gürses, M. S. Classification of Dye and Pigments. In *Dyes and pigments*; Springer, 2016; pp 31–45. https://doi.org/10.1007/978-3-319-33892-7_3
88. Haroun, A. A.; Diab, H. A.; Hakeim, O. A. Cellulosic Fabrics Printing with Multifunctional Encapsulated Phthalocyanine Pigment Blue Using Phase Separation Method. *Carbohydr. Polym.* 2016, 146, 102–108. <https://doi.org/10.1016/j.carbpol.2016.03.039>
89. Meng, X.; Qiang, L.; Su, X.; Ren, J.; Tang, F. Synthesis of Black Magnetic

- Electrophoretic Particles for Magnetic-Electric Dual-Driven Electronic Paper. *ACS Appl. Mater. Interfaces* 2013, 5 (3), 622–629. <https://doi.org/10.1021/am301984u>
90. Xu, Y.; Liu, J.; Du, C.; Fu, S.; Liu, X. Preparation of Nanoscale Carbon Black Dispersion Using Hyper-Branched Poly (Styrene-Alt-Maleic Anhydride). *Prog. Org. Coatings* 2012, 75 (4), 537–542. <https://doi.org/10.1016/j.porgcoat.2012.05.014>
91. Lin, Y.; Zhou, Y.; Xu, C.; Xie, A.; Yang, M.; Yang, S.; Chen, H. Study on Synthesis and Thickening Property of Hyperbranched Waterborne Polyurethane. *Prog. Org. Coatings* 2013, 76 (10), 1302–1307. <https://doi.org/10.1016/j.porgcoat.2013.04.001>
92. Zhang, Q.; Hu, X.; Wu, M.; Zhao, Y.; Yu, C. Effects of Different Catalysts on the Structure and Properties of Polyurethane/Water Glass Grouting Materials. *J. Appl. Polym. Sci.* 2018, 135 (27), 46460. <https://doi.org/10.1002/app.46460>
93. Xu, C.; Zhang, L.; Xu, D.; Li, M.; Zhang, Y.; Fu, S. Preparation of Reactive Nanoscale Carbon Black Dispersion for Pad Coloration of Cotton Fabric. *Color. Technol.* 2018, 134 (2), 91–99. <https://doi.org/10.1111/cote.12320>
94. Ibrahim, W.; Sarwar, Z.; Khan, A.; Hassan, A.; Azeem, A.; Nazir, A.; Jamshaid, H.; Hussain, U. A Novel Study of Comparison Properties of Pigment and Reactive Dye-Printed Cotton Fabric. *J. Nat. Fibers* 2018. <https://doi.org/10.1080/15440478.2018.1440364>
95. Varadarajan, G.; Venkatachalam, P. Sustainable Textile Dyeing Processes. *Environ. Chem. Lett.* 2016, 14 (1), 113–122. <https://doi.org/10.1007/s10311-015-0533-3>
96. Perkins, W. S. A Review of Textile Dyeing Processes. *Text. Chem. Color.* 1991, 23 (8).
97. Silvo, K.; Melanen, M.; Honkasalo, A.; Ruonala, S.; Lindström, M. Integrated Pollution Prevention and Control—the Finnish Approach. *Resour. Conserv. Recycl.* 2002, 35 (1–2), 45–60. [https://doi.org/10.1016/S0921-3449\(01\)00118-5](https://doi.org/10.1016/S0921-3449(01)00118-5)
98. Rouette, H.-K.; Lindner, A.; Schwager, B. *Lexikon Für Textilveredlung*; Laumann-Verlag, 1995.
99. Lewis, D. M. *Ancillary Processes in Wool Dyeing*; John Wiley and Sons Limited, Chichester, and Society of Dyers and Colorists ..., 2013.
100. Blackburn, R. S.; Burkinshaw, S. M. A Greener Approach to Cotton Dyeings with Excellent Wash Fastness. *Green Chem.* 2002, 4 (1), 47–52. <https://doi.org/10.1039/B111026H>
101. Schramm, W.; Jantschgi, J. Comparative Assessment of Textile Dyeing Technologies from a Preventive Environmental Protection Point of View. *Color. Technol.* 1999, 115 (4), 130–135. <https://doi.org/10.1111/j.1478->

4408.1999.tb00310.x

102. Kiran-Ciliz, N. Reduction in Resource Consumption by Process Modifications in Cotton Wet Processes. *J. Clean. Prod.* 2003, 11 (4), 481–486. [https://doi.org/10.1016/S0959-6526\(02\)00069-0](https://doi.org/10.1016/S0959-6526(02)00069-0)
103. Cay, A.; Tarakçioğlu, I.; Hepbasli, A. Exergetic Performance Assessment of a Stenter System in a Textile Finishing Mill. *Int. J. Energy Res.* 2007, 31 (13), 1251–1265. <https://doi.org/10.1002/er.1295>
104. Brenner, E.; Brenner, T.; Scholl, M. Saving Water and Energy in Bleaching Tubular Knits. *Am. Dyest. Report.* 1993, 82 (3), 5.
105. Ohno, H.; Yoshida, F.; Morimoto, M.; Hashimoto, I.; Takamatus, T. Modelling of a Dyeing Process and Its Energy Consumption Analysis. *J. Text. Mach. Soc. Japan* 1986, 32 (1), 11–17. <https://doi.org/10.4188/jte1955.32.11>
106. Kalliala, E.; Talvenmaa, P. Environmental Profile of Textile Wet Processing in Finland. *J. Clean. Prod.* 2000, 8 (2), 143–154. [https://doi.org/10.1016/S0959-6526\(99\)00313-3](https://doi.org/10.1016/S0959-6526(99)00313-3)
107. Cengel, Y. A.; Boles, M. A.; Kanoğlu, M. *Thermodynamics: An Engineering Approach*; McGraw-hill New York, 2011; Vol. 5.
108. Shah, J.; Jan, M. R.; Khitab, F. Sonophotocatalytic Degradation of Textile Dyes over Cu Impregnated ZnO Catalyst in Aqueous Solution. *Process Saf. Environ. Prot.* 2018, 116, 149–158. <https://doi.org/10.1016/j.psep.2018.01.008>
109. Abate, M. T.; Ferri, A.; Guan, J.; Chen, G.; Nierstrasz, V. Impregnation of Materials in Supercritical CO₂ to Impart Various Functionalities. *Adv. Supercrit. Fluids Technol.* 2019. <https://doi.org/10.5772/intechopen.89223>
110. Qamar, S. A.; Ashiq, M.; Jahangeer, M.; Riasat, A.; Bilal, M. Chitosan-Based Hybrid Materials as Adsorbents for Textile Dyes—A Review. *Case Stud. Chem. Environ. Eng.* 2020, 2, 100021. <https://doi.org/10.1016/j.cscee.2020.100021>
111. Kikic, I.; Vecchione, F. Supercritical Impregnation of Polymers. *Curr. Opin. Solid State Mater. Sci.* 2003, 7 (4–5), 399–405.
112. Banchemo, M. Recent Advances in Supercritical Fluid Dyeing. *Color. Technol.* 2020, 136 (4), 317–335. <https://doi.org/10.1111/cote.12469>
113. Holme, I. Innovative Technologies for High Performance Textiles. *Color. Technol.* 2007, 123 (2), 59–73. <https://doi.org/10.1111/j.1478-4408.2007.00064.x>
114. Hyde, R. F.; Thompson, G.; Stanley, K. A. Commercial and Environmental Challenges in Continuous Dyeing with Fiber Reactive Dyes. *Text. Chem. Color.* 1996, 28 (10).

115. Mansour, R. Natural Dyes and Pigments: Extraction and Applications. *Handb. Renew. Mater. Color. Finish.* 2018, 9, 75–102.
116. Ragab, M. M.; Othman, H.; Hassabo, A. G. Resist and Discharge Printing Techniques on Different Textile Based Materials. *J. Text. Color. Polym. Sci.* 2021, 18 (2), 229–237. <https://dx.doi.org/10.21608/jtcps.2021.68420.1070>
117. Clark, M. *Handbook of Textile and Industrial Dyeing: Principles, Processes and Types of Dyes*; Elsevier, 2011.
118. Zubairu, A.; Mshelia, Y. M. Effects of Selected Mordants on the Application of Natural Dye from Onion Skin (*Allium Cepa*). *Sci. Technol.* 2015, 5 (2), 26–32. DOI: 10.5923/j.scit.20150502.02
119. Hamdy, D.; Hassabo, A. G.; Othman, H. Recent Use of Natural Thickeners in the Printing Process. *J. Text. Color. Polym. Sci.* 2021, 18 (2), 75–81. <https://doi.org/10.21608/jtcps.2021.69754.1053>
120. Ebrahim, S. A.; Hassabo, A. G.; Othman, H. Natural Thickener in Textile Printing (A Mini Review). *J. Text. Color. Polym. Sci.* 2021, 18 (1), 55–64. <https://dx.doi.org/10.21608/jtcps.2021.69482.1051>
121. AlAshkar, A.; Hassabo, A. G. Recent Use of Natural Animal Dyes in Various Field. *J. Text. Color. Polym. Sci.* 2021, 18 (2), 191–210. <https://dx.doi.org/10.21608/jtcps.2021.79791.1067>
122. Ahmed, N.; Nassar, S.; M El-Shishtawy, R. Novel Green Coloration of Cotton Fabric. Part II: Effect of Different Print Paste Formulations on the Printability of Bio-Mordanted Fabric with Madder Natural Dye. *Egypt. J. Chem.* 2020, 63 (5), 1669–1677. <https://doi.org/10.21608/ejchem.2020.22637.2345>
123. Ahmed, N.; Nassar, S.; M El-Shishtawy, R. Novel Green Coloration of Cotton Fabric. Part I: Bio-Mordanting and Dyeing Characteristics of Cotton Fabrics with Madder, Alkanet, Rhubarb and Curcumin Natural Dyes. *Egypt. J. Chem.* 2020, 63 (5), 1605–1617. <https://doi.org/10.21608/ejchem.2020.22634.2344>
124. Ebrahim, S. A.; Mosaad, M. M.; Othman, H.; Hassabo, A. G. A Valuable Observation of Eco-Friendly Natural Dyes for Valuable Utilisation in the Textile Industry. *J. Text. Color. Polym. Sci.* 2022, 19 (1), 25–37. <https://dx.doi.org/10.21608/jtcps.2021.97342.1090>
125. Diao, M.; Othman, H.; Hassabo, A. G. Printing Wool Fabrics with Natural Dyes Curcuma and Alkanet (A Critique). *J. Text. Color. Polym. Sci.* 2022, 19 (1), 11–16. <https://doi.org/10.21608/jtcps.2021.86354.1076>
126. Bajaj, P.; Goyal, M.; Chavan, R. B. Synthetic Thickeners in Textile Printing: A Critique. *J. Macromol. Sci. Part C Polym. Rev.* 1993, 33 (3), 321–348. <https://doi.org/10.1080/15321799308021439>

127. Ragab, M. M.; Hassabo, A. G. Various Uses of Natural Plants Extracts for Functionalization Textile Based Materials. *J. Text. Color. Polym. Sci.* 2021. <https://dx.doi.org/10.21608/jtcps.2021.79169.1064>
128. Hamdy, D. M.; Hassabo, A. G. Various Natural Dyes from Different Sources. *J. Text. Color. Polym. Sci.* 2021, 18 (2), 171–190. <https://doi.org/10.21608/jtcps.2021.79786.1066>
129. Haggag, K.; Ragheb, A. A.; Abd EL-Thalouth, I.; Nassar, S. H.; El-Sayed, H. A Review Article on Enzymes and Their Role in Resist and Discharge Printing Styles. *Life Sci. J.* 2013, 10 (1), 1646–1654.
130. Clark, J. H. *Chemistry of Waste Minimization*; Springer Science & Business Media, 1995.
131. El-Kashouti, M.; Elhadad, S.; Abdel-Zaher, K. Printing Technology on Textile Fibers. *J. Text. Color. Polym. Sci.* 2019, 16 (2), 129–138. <https://dx.doi.org/10.21608/jtcps.2019.15989.1027>
132. Ragab, M. M.; Othman, H.; Hassabo, A. An Overview of Printing Textile Techniques. *Egypt. J. Chem.* 2022, 65 (8), 749–761. <https://doi.org/10.21608/ejchem.2022.131477.5793>
133. Seema, H. S.; Deepika, L.; Babu, A. A Comparative Study on Discharge Printing Using Conventional and Ecological Recipe. *J. Trends Text. Eng. Fash. Technol.* 2018, No. 3, 245–261.
134. Hossain, A. H.; Raman, M.; Islam, M. Overview of Piece Printing Process in Textile Industry. *J. Polym. Text. Eng.* 2015, 12.
135. Eldesoky, R. S. A. *Novel Approaches in Textile Surface Modifications for Better Printability*; The University of Manchester (United Kingdom), 2019.
136. Lewis, D. M.; Broadbent, P. J. Digital Alkali Resist Prints on Polyester. *Color. Technol.* 2017, 133 (6), 463–468. <https://doi.org/10.1111/cote.12305>
137. Klaichoi, C.; Mongkholrattanasit, R.; Rungruangkitkrai, N. Printing of Silk Fabric with Reactive Dye Using Flour of Wild Taro Corm as a Resist Printing Paste. In *Materials Science Forum*; Trans Tech Publ, 2016; Vol. 857, pp 503–506. <https://doi.org/10.4028/www.scientific.net/MSF.857.503>
138. Majumdar, A.; Das, A.; Alagirusamy, R.; Kothari, V. K. *Process Control in Textile Manufacturing*; Elsevier, 2012.
139. Bide, M. Colour Measurement and Fastness Assessment. *Colour Meas. Princ. Adv. Ind. Appl.* 2010, 196–217. <https://doi.org/10.1533/9780857090195.1.196>.
140. Aldib, M. An Investigation of an Instrument-based Method for Assessing Colour

- Fastness to Light of Photochromic Textiles. *Color. Technol.* 2015, 131 (4), 298–302. <https://doi.org/10.1111/cote.12156>
141. Hindson, W. R.; Southwell, G. Colour Fastness of Textiles to Daylight and Artificial Light. *J. Soc. Dye. Colour.* 1973, 89 (7), 254–257. <https://doi.org/10.1111/j.1478-4408.1973.tb03153.x>
 142. Kert, M.; Gorjanc, M. The Study of Colour Fastness of Commercial Microencapsulated Photoresponsive Dye Applied on Cotton, Cotton/Polyester and Polyester Fabric Using a Pad-dry-cure Process. *Color. Technol.* 2017, 133 (6), 491–497. <https://doi.org/10.1111/cote.12297>
 143. Gegenfurtner, K. R. Cortical Mechanisms of Colour Vision. *Nat. Rev. Neurosci.* 2003, 4 (7), 563–572. <https://doi.org/10.1038/nrn1138>
 144. Ford, A.; Roberts, A. Colour Space Conversions. *Westminster Univ. London* 1998, 1998, 1–31.
 145. Van Huyssteen Ellis, F.** and Lambrechts, JN**, C. The Relationship between Subsoil Colour and Degree of Wetness in a Suite of Soils in the Grabouw District, Western Cape II. Predicting Duration of Water Saturation and Evaluation of Colour Definitions for Colour-Defined Horizons. *South African J. Plant Soil* 1997, 14 (4), 154–157.
 146. Delhey, K. A Review of Gloger’s Rule, an Ecogeographical Rule of Colour: Definitions, Interpretations and Evidence. *Biol. Rev.* 2019, 94 (4), 1294–1316. <https://doi.org/10.1111/brv.12503>
 147. O’Connor, Z. Colour Harmony Revisited. *Color Res. Appl.* 2010, 35 (4), 267–273. <https://doi.org/10.1002/col.20578>
 148. Hunt, R. W. G.; Pointer, M. R. *Measuring Colour*; John Wiley & Sons, 2011. <https://doi.org/10.1002/9781119975595>
 149. Walbridge-Jones, S. Microspectrophotometry for Textile Fiber Color Measurement. *Identif. Text. Fibers* 2009, 165–180. <https://doi.org/10.1533/9781845695651.2.165>.
 150. Hu, C.; Mei, H.; Guo, H.; Zhu, J. Color Analysis of Textile Fibers by Microspectrophotometry. *Forensic Chem.* 2020, 18, 100221. <https://doi.org/10.1016/J.FORC.2020.100221>.
 151. Kandi, S. G. The Effect of Spectrophotometer Geometry on the Measured Colors for Textile Samples with Different Textures. *J. Eng. Fiber. Fabr.* 2011, 6 (4), 155892501100600420.
 152. Berthier, M.; Provenzi, E. When Geometry Meets Psycho-Physics and Quantum Mechanics: Modern Perspectives on the Space of Perceived Colors. In

- International Conference on Geometric Science of Information*; Springer, 2019; pp 621–630. https://doi.org/10.1007/978-3-030-26980-7_64
153. Provenzi, E. A Differential Geometry Model for the Perceived Colors Space. *Int. J. Geom. Methods Mod. Phys.* 2016, 13 (08), 1630008. <https://doi.org/10.1142/S0219887816300087>
154. Ingamells, W. Colour for Textiles. *Soc. Dye. Colour.* 1993, 2–5.
155. CIE, C. I. E. International Lighting Vocabulary (CIE Publ. No. 17.4). *Int. Electrotech. Vocab.* 1987.
156. Steinvall, A. English Colour Terms in Context. Umeå universitet 2002.
157. Miró Martínez, P. Técnicas Estadísticas Para El Control y La Mejora de La Calidad En El Sector Textil: Aplicación En La Manta y La Napa Termofusionada. Universitat Politècnica de València 2008.
158. Etxegarai Madina, A.; Larrabe Uribe, Z. *Teknologia Elektrikoa*; Euskara eta Eleaniztasuneko Errektoreordetza, 2012.
159. GILABERT PEREZ, E. *MEDIDA DEL COLOR/EDUARDO J. GILABERT.*; 2002.
160. Ramachandran, V. S.; Hubbard, E. M. Psychophysical Investigations into the Neural Basis of Synaesthesia. *Proc. R. Soc. London. Ser. B Biol. Sci.* 2001, 268 (1470), 979–983. <https://doi.org/10.1098/rspb.2000.1576>
161. Fiorentini, A.; Burr, D. C.; Morrone, C. M. Temporal Characteristics of Colour Vision: VEP and Psychophysical Measurements. *From Pigment. to Percept. Adv. Underst. Vis. Process.* 1991, 139–149. https://doi.org/10.1007/978-1-4615-3718-2_16
162. Crawford, B. H. The Colour Rendering Properties of Illuminants: The Application of Psychophysical Measurements to Their Evaluation. *Br. J. Appl. Phys.* 1963, 14 (6), 319. <https://doi.org/10.1088/0508-3443/14/6/302>
163. van den Berg, C. P.; Troscianko, J.; Endler, J. A.; Marshall, N. J.; Cheney, K. L. Quantitative Colour Pattern Analysis (QCPA): A Comprehensive Framework for the Analysis of Colour Patterns in Nature. *Methods Ecol. Evol.* 2020, 11 (2), 316–332. <https://doi.org/10.1111/2041-210X.13328>
164. Illumination, I. C. on. *Colorimetry: Technical Report*; Commission internationale de l’Eclairage, CIE Central Bureau, 2004.
165. Kubelka, P. New Contributions to the Optics of Intensely Light-Scattering Materials. Part I. *Josa* 1948, 38 (5), 448–457.
166. Kubelka, P. Ein Beitrag Zur Optik Der Farbanstriche (Contribution to the Optic of Paint). *Zeitschrift fur Tech. Phys.* 1931, 12, 593–601.

167. Yang, L.; Kruse, B. Revised Kubelka–Munk Theory. I. Theory and Application. *JOSA A* 2004, 21 (10), 1933–1941. <https://doi.org/10.1364/JOSAA.21.001933>
168. Alcaraz de la Osa, R.; Iparragirre, I.; Ortiz, D.; Saiz, J. M. The Extended Kubelka–Munk Theory and Its Application to Spectroscopy. *ChemTexts* 2020, 6 (1), 1–14. <https://doi.org/10.1007/s40828-019-0097-0>
169. Kokhanovsky, A. A. Physical Interpretation and Accuracy of the Kubelka–Munk Theory. *J. Phys. D. Appl. Phys.* 2007, 40 (7), 2210. <https://doi.org/10.1088/0022-3727/40/7/053>
170. Džimbeg-Malčić, V.; Barbarić-Mikočević, Ž.; Itrić, K. Kubelka-Munk Theory in Describing Optical Properties of Paper (I). *Teh. Vjesn.* 2011, 18 (1), 117–124.
171. Barrón, V.; Torrent, J. Use of the Kubelka–Munk Theory to Study the Influence of Iron Oxides on Soil Colour. *J. soil Sci.* 1986, 37 (4), 499–510. <https://doi.org/10.1111/j.1365-2389.1986.tb00382.x>
172. Vargas, W. E.; Niklasson, G. A. Applicability Conditions of the Kubelka–Munk Theory. *Appl. Opt.* 1997, 36 (22), 5580–5586.
173. Edström, P. Examination of the Revised Kubelka-Munk Theory: Considerations of Modeling Strategies. *JOSA A* 2007, 24 (2), 548–556. <https://doi.org/10.1364/JOSAA.24.000548>
174. Yang, L.; Miklavcic, S. J. Revised Kubelka–Munk Theory. III. A General Theory of Light Propagation in Scattering and Absorptive Media. *JOSA A* 2005, 22 (9), 1866–1873. <https://doi.org/10.1364/JOSAA.22.001866>
175. Tolvaj, L.; Mitsui, K.; Varga, D. Validity Limits of Kubelka–Munk Theory for DRIFT Spectra of Photodegraded Solid Wood. *Wood Sci. Technol.* 2011, 45 (1), 135–146. <https://doi.org/10.1007/s00226-010-0314-x>
176. Micó Vicent, Barbara; Martínez Verdu, F. M.; Gilabert Pérez, J. E. Optimización de La Síntesis de Nanopigmentos de Origen Natural Para Biopolímeros Mediante El Uso Del Diseño de Experimentos.
177. Semeraro, P.; Rizzi, V.; Fini, P.; Matera, S.; Cosma, P.; Franco, E.; García, R.; Ferrándiz, M.; Núñez, E.; Gabaldón, J. A.; Fortea, I.; Pérez, E.; Ferrándiz, M. Interaction between Industrial Textile Dyes and Cyclodextrins. *Dye. Pigment.* 2015, 119, 84–94. <https://doi.org/10.1016/J.DYEPIG.2015.03.012>.
178. Sana, D.; Jalila, S. A Comparative Study of Adsorption and Regeneration with Different Agricultural Wastes as Adsorbents for the Removal of Methylene Blue from Aqueous Solution. *Chinese J. Chem. Eng.* 2017, 25 (9), 1282–1287. <https://doi.org/10.1016/J.CJCHE.2017.01.012>.
179. Sanchez, L. M.; Ollier, R. P.; Gonzalez, J. S.; Alvarez, V. A. Nanocomposite Materials

- for Dyes Removal. *Handb. Nanomater. Ind. Appl.* 2018, 922–951. <https://doi.org/10.1016/B978-0-12-813351-4.00053-5>.
180. Mathew, M. L.; Gopalakrishnan, A.; Aravindakumar, C. T.; Aravind, U. K. Low – Cost Multilayered Green Fiber for the Treatment of Textile Industry Waste Water. *J. Hazard. Mater.* 2019, 365, 297–305. <https://doi.org/10.1016/J.JHAZMAT.2018.11.014>.
181. SANZ CARBONELL, J. F. TRATAMIENTO DE AGUAS TEXTILES INDUSTRIALES MEDIANTE FOTOCATÁLISIS SOLAR Y REUTILIZACIÓN EN NUEVAS TINTURAS Doctoral Thesis, Universitat Politècnica de València. 2016.
182. Chorawalaa, K. K.; Mehta, M. J. Applications of Nanotechnology in Wastewater Treatment. *Int J Innov Emerg Res Eng* 2015, 2 (1), 21–26.
183. Sayan, B.; Indranil, S.; Aniruddha, M.; Dhruvajyoti, C.; Uday, C. G.; Debashis, C. Role of Nanotechnology in Water Treatment and Purification: Potential Applications and Implications. *Int J Chem Sci Technol* 2013, 3 (3), 59.
184. Hua, M.; Zhang, S.; Pan, B.; Zhang, W.; Lv, L.; Zhang, Q. Heavy Metal Removal from Water/Wastewater by Nanosized Metal Oxides: A Review. *J. Hazard. Mater.* 2012, 211, 317–331. <https://doi.org/10.1016/j.jhazmat.2011.10.016>
185. Kumar, R.; Chawla, J. Removal of Cadmium Ion from Water/Wastewater by Nano-Metal Oxides: A Review. *Water Qual. Expo. Heal.* 2014, 5 (4), 215–226. <https://doi.org/10.1007/s12403-013-0100-8>
186. Rajput, S.; Pittman Jr, C. U.; Mohan, D. Magnetic Magnetite (Fe₃O₄) Nanoparticle Synthesis and Applications for Lead (Pb²⁺) and Chromium (Cr⁶⁺) Removal from Water. *J. Colloid Interface Sci.* 2016, 468, 334–346. <https://doi.org/10.1016/j.jcis.2015.12.008>
187. Akil, J.; Ciotonea, C.; Siffert, S.; Royer, S.; Pirault-Roy, L.; Cousin, R.; Poupin, C. NO Reduction by CO under Oxidative Conditions over CoCuAl Mixed Oxides Derived from Hydrotalcite-like Compounds: Effect of Water. *Catal. Today* 2021, No. October 2020. <https://doi.org/10.1016/j.cattod.2021.05.014>.
188. Carlino, S. Chemistry between the Sheets. *Chem. Br.* 1997, 33 (9), 59–62.
189. Bish, D. L. Anion-Exchange in Takovite: Applications to Other Hydroxide Minerals. *Bull. Mineral.* 1980, 103 (2), 170–175.
190. Miyata, S. Physico-Chemical Properties of Synthetic Hydrotalcites in Relation to Composition. *Clays Clay Miner.* 1980, 28 (1), 50–56.
191. Ulibarri, M. A.; Pavlovic, I.; Barriga, C.; Hermosin, M. C.; Cornejo, J. Adsorption of Anionic Species on Hydrotalcite-like Compounds: Effect of Interlayer Anion and Crystallinity. *Appl. Clay Sci.* 2001, 18 (1–2), 17–27. <https://doi.org/10.1016/S0169->

1317(00)00026-0

192. Zhu, M.-X.; Li, Y.-P.; Xie, M.; Xin, H.-Z. Sorption of an Anionic Dye by Uncalcined and Calcined Layered Double Hydroxides: A Case Study. *J. Hazard. Mater.* 2005, *120* (1–3), 163–171. <https://doi.org/10.1016/j.jhazmat.2004.12.029>
193. Lakraimi, M.; Legrouri, A.; Barroug, A.; Besse, J.-P. Removal of Pesticides from Water by Anionic Clays. *J. Chim. Phys. Physico-Chimie Biol.* 1999, *96* (3), 470–478. <https://doi.org/10.1051/jcp:1999154>
194. Sato, T.; Kato, K.; Endo, T.; Shimada, M. Preparation and Chemical Properties of Magnesium Aluminium Oxide Solid Solutions. *React. Solids* 1986, *2* (3), 253–260. [https://doi.org/10.1016/0168-7336\(86\)80088-2](https://doi.org/10.1016/0168-7336(86)80088-2)
195. Salomao, R.; Milena, L. M.; Wakamatsu, M. H.; Pandolfelli, V. C. Hydrotalcite Synthesis via Co-Precipitation Reactions Using MgO and Al (OH) 3 Precursors. *Ceram. Int.* 2011, *37* (8), 3063–3070. <https://doi.org/10.1016/j.ceramint.2011.05.034>
196. Mckay, G. *Use of Adsorbents for the Removal of Pollutants from Wastewater*; CRC press, 1995.
197. Sato, T.; Wakabayashi, T.; Shimada, M. Adsorption of Various Anions by Magnesium Aluminum Oxide of (MgO. 7AlO. 3O1. 15). *Ind. Eng. Chem. Prod. Res. Dev.* 1986, *25* (1), 89–92.
198. Bellotto, M.; Rebours, B.; Clause, O.; Lynch, J.; Bazin, D.; Elkaïm, E. Hydrotalcite Decomposition Mechanism: A Clue to the Structure and Reactivity of Spinel-like Mixed Oxides. *J. Phys. Chem.* 1996, *100* (20), 8535–8542. <https://doi.org/10.1021/jp960040i>

Recuperación del colorante de aguas residuales textiles mediante nanoarcillas para su reutilización como pigmentos y nuevos baños de tintura

Capítulo 2

Hipótesis y Objetivos

2.1. Hipótesis

Este trabajo de tesis doctoral parte de la hipótesis de que dada la capacidad adsorbente que tienen las nanoarcillas, se pueden adsorber colorantes textiles para después darles una reutilización y nuevo uso, como puede ser la estampación pigmentaria con el híbrido formado por la unión del colorante y la arcilla o bien desorber el colorante para realizar nuevos baños de tintura. Todo esto se podría englobar dentro la de la denominada economía circular y la sostenibilidad que tanto en sintonía con los objetivos de desarrollo sostenible.

2.2. Objetivos

Los objetivos claros de este estudio se pueden dividir en tres grandes grupos los cuales profundizan a su vez en otros secundarios. Estos se pueden dividir de la siguiente forma:

1º Conseguir adsorber colorantes textiles y comparar los resultados según las diferentes características de los colorantes. Así pues, dentro de este objetivo se pueden diferenciar algunos secundarios como:

- a) Capacidad de adsorber colorantes aniónicos, catiónicos y no iónicos.
- b) Diferencias de adsorción en función el peso molecular del colorante.
- c) Fijación del colorante dentro de la arcilla.

2º Capacidad del híbrido para formar parte de una pasta de estampación aportando color.

3º Producir una desorción del colorante para que este pase de la arcilla a la fase acuosa y poder llegar a tinter de nuevo un sustrato textil.

a) Desorber el colorante mediante aplicación de calor y en una segunda fase sometiéndolo a pH altos o bajos.

b) Extraer el colorante incorporando el compuesto arcilla-colorante en un baño de tintura esperando que el calor convectivo del agua sea suficientemente energético para romper esa unión.

Recuperación del colorante de aguas residuales textiles mediante nanoarcillas para su reutilización como pigmentos y nuevos baños de tintura

Capítulo 3

Publicaciones

Este capítulo está dedicado a recoger las publicaciones científicas que se han realizado durante la elaboración de esta tesis doctoral. Siguiendo un orden cronológico de publicación y también de orden natural para el correcto desarrollo de todo este trabajo, se empieza con la primera publicación recogida en el apartado 3.1 que se trata de un análisis del estado del arte para conocer en profundidad todos los trabajos ya realizados por la comunidad científica relacionados con esta tematica. En el apartado 3.2 se realizan una primeras pruebas para valorar la capacidad de adsorción de al hidrotalcita con ciertos colorantes y su correspondiente caracterización. Ya en la publicación que se recoge en el apartado 3.3 se realizan más pruebas de adsorción siguiendo un diseño de experimentos para poder encontrar la concentración optima de arcilla que es necesaria para adsorber todo el colorante que hay en un baño de tintura. Tras haber adsorbido y estabilizado los diferentes colorantes en la arcilla es la hora de reutilizar el húbido, para ello en la publicación 3.4 se desarrolla un método para utilizar dicho compuesto en estampaciones pigmentarias mientras que en la 3.5 se realiza una desorción y nuevo baño de tintura para tejidos de PES, CO y PAN.

Recuperación del colorante de aguas residuales textiles mediante nanoarcillas para su reutilización como pigmentos y nuevos baños de tintura

3.1. Adaptación del artículo: Uses of Nanoclays and Adsorbents for Dye Recovery: A Textile Industry Review

Artículo publicado en: López-Rodríguez, Daniel; Micó-Vicent, B.; Jordán-Núñez, Jorge; Bonet-Aracil, Marilés; Bou-Belda, Eva. (2021) Uses of Nanoclays and Adsorbents for Dye Recovery: A Textile Industry Review. Applied Sciences, 23 (11), 1 - 27. app112311422

Abstract:

Wastewater recovery is one of the most pressing contaminant-related subjects in the textile industry. Many cleaning and recovery techniques have been applied in recent decades, from physical separation to chemical separation. This work reviews textile wastewater recovery by focusing on natural or synthetic nanoclays in order to compare their capabilities. Presently, a wide variety of nanoclays are available that can adsorb substances dissolved in water. This review summarizes and describes nanoclay modifications for different structures (laminar, tubular, etc.) to compare adsorption performance under the best conditions. This adsorbent capacity can be used in contaminant industries to recover water that can be used and be recontaminated during a second use to close the production circle. It explores and proposes future perspectives for the nanoclay hybrid compounds generated after certain cleaning steps. This is a critical review of works that have studied adsorption or desorption procedures for different nanoclay structures. Finally, it makes a future application proposal by taking into account the summarized pros and cons of each nanoclay. This work addresses contaminant reuse, where part of the employed dyes can be reused in printing or even dyeing processes, depending on the fixing capacity of the dye in the nanoclay, which is herein discussed.

3.1.1. Introduction

In recent decades, environmental alerts have been triggered by increasing concerns regarding caring for the environment. This has added to the possibility of optimizing and

reducing the use of resources in industrial textile dyeing processes and has led the scientific community to look for options to recover or reuse the colorants in textile wastewater. The general objective of this research is to trap the colorant present in wastewater from dyeing processes by introducing a third element into the same bath. Some compounds or materials are known to be of use in this process, such as cyclodextrins [1], agricultural waste elements [2], and nanocomposites [3]; physical media, such as membrane filtration [4], among many other methods, can also be utilized.

Industrial wastewater recycling has become an increasingly more evident need. The efforts of international governments to safeguard the environment have contributed to private companies taking action on the matter and making important investments in these fields [1,2,4–18]. The textile industry discharges organic and inorganic waste that produces bioaccumulation and can cause high degrees of toxicity [19] (Table 3.1.1, Figure 3.1.1).

Table 3.1.1 Fixation percentages of different families of colorants and their estimated loss in effluents [20]

Family	Material	Fixation Degree (%)
Acids	Polyamide/Wool	80–95
Azoics	Cellulosic	75–90
Basics	Acrylic	95–100
Direct	Cellulosic	70–95
Scattered	Polyester	90–100
Premetallized	Wool	85–95
Reagents	Cellulosic	60–90
Sulphurous	Cellulosic	60–86

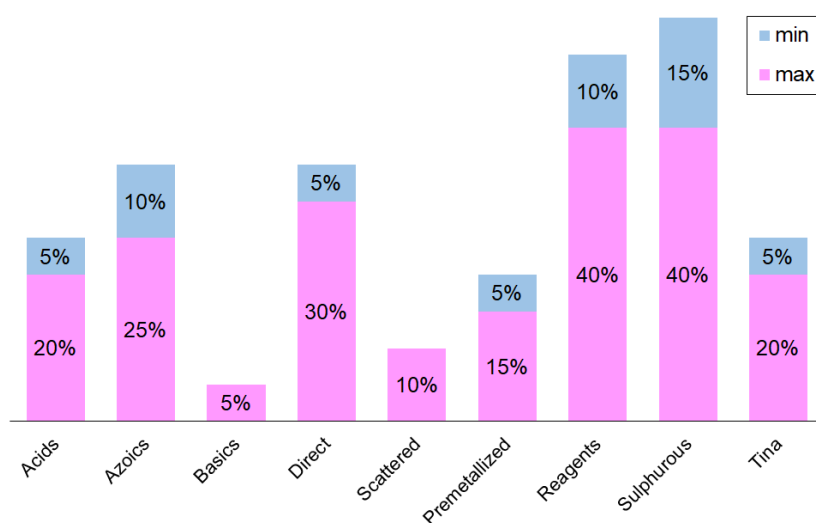


Figure 3.1.1. Loss in the effluent percentage

The textile chemical industry is one that most affects wastewater, and it is the industry with the greatest chemical activity on earth [20]. Due to textile dyeing and stamping, colorants are one of the most common contaminants in the textile industry [21]–[23]. The concentration of colorants in effluents is around 50–1000 ppm, although 10–50 ppm can also be found [19]. The nature of their composition depends on the type of dye, considering fixation and estimated losses in the effluent, as shown in Table 3.1.1. Thus, it is very important to improve industries' ability to remove colorants from effluents. The development of lowcost absorbents by integrating advanced technology can significantly advance this area [24].

Other textile water treatment technologies performed by means of nanotechnology include the following: nanosorbents, including nanoclays, which this review is concerned with; nanosorbent- and carbon-based composites, which are mainly employed for water with Ni^{2+} [25],[26]; and regenerable nanosorbent polymers, which are used instead of organic- and inorganic-type pollutants. Iron and carbon compounds are also capable of reducing large quantities of these different pollutants [25],[27]–[29].

Other technologies can also be applied, such as carbon nanotubes, which remove heavy metals, dyes, and antibiotics [30]–[32]. Another possibility is to employ membranes that, depending on pore and molecule size, can remove pollutants such as oils, dyes, and

germs by a simple procedure [30],[33]–[36]. Another well-advanced technology is photocatalysts combined with other nanoparticles, which eliminate organic compounds, dyes, germs, and antibiotics by degradation [30],[36]–[39].

The basic advantages of these technologies can be classified as follows: metal oxides, carbon nanotubes, and nanoclays are low-cost; nanotubes and membranes have high-efficiency; and membranes and photocatalysts are easily applied [30].

The textile industry employs increasingly more synthetic dyes because they are easy to use, cheap, and offer good stability, and they come in a wide range of colors compared to natural dyes [40]. Artificial dyes are synthetic organic compounds that are molecularly dispersed and bind to textile substrates thanks to intermolecular forces. More than 10,000 dyes are available on today's market. Most are not easily biodegradable, given their complex aromatic molecular structure and synthetic origin [41]. As dye baths are not biodegradable in nature, and are toxic and inhibitory, they significantly and negatively affect both water and land. The fact that certain dyes or their metabolites are toxic or mutagenic and carcinogenic should also be taken into account [42]. Records worldwide [43],[44] demonstrate the sensitive aspect of exposure to these synthetic substances at both high and low concentrations. Thus, they need to be removed before water is discharged.

For some years now, adsorption has become the most efficient technique to remove different dye types. The action of these absorbents is clearly affected by several parameters, such as dye concentration, the time the action lasts, temperature, dye particle size, and the concentration of the adsorbents, etc. Adsorption is clearly an efficient process in most physical, environmental, chemical, biological, and natural settings [45],[46]. In industry, adsorption techniques are being applied by solids acting as adsorbents to purify wastewater and polluted water. In recent decades, different types of these adsorbents have been used to remove several types of pollutants from water [47].

This paper reviews the works that have focused on highly-efficient wastewater recovery. In line with their conclusions, it proposes reusing hybrid compounds in a circular

economy concept. It shows the possibility of dye recovery using different adsorbents and presents a cheap and efficient procedure based on the advantages of nanoclays. In it, a future vision is proposed for the reuse of recovered dyes as new hybrid pigments protected by nanoclays, or via their desorption, to reuse them as dyes in other dyeing textile baths.

3.1.2. Sewage Treatment

Normal parameters exist for measuring contamination in general, which can be estimated with indicators such as biological oxygen demand at five days (BOD₅) [48]–[50] and chemical oxygen demand (COD) [51]–[54], which indicate the amounts of oxygen needed to oxidize organic matter that is capable of being oxidized either biologically (bacteria and microorganisms) or chemically. There is one other parameter, the amount of total suspended solids (TSS) [55], which provides an idea of the amount of human matter in water.

3.1.2.1. General Textile Recovery

In order to reduce water use in the textile industry, wastewater can be totally or partially reused after its deep treatment. This treatment aims to leave a low contents of organic matter, color, suspended matter, and salinity in the water. This generally requires several purification processes, among which a biological process almost always takes place because, otherwise, BOD reduction is insufficient [56].

Other water recovery processes are known, such as reverse osmosis [57]–[59], microfiltration [60]–[62], ultrafiltration [63], and distillation in multiple-effect evaporators and electrochemical processes [64]–[66], which allow the economical and profitable recovery of various products. They can also be applied for recycling various process baths, but currently their cost is not economical enough for them to be fully used for waste effluents from the textile industry.

The objective of all these purification processes is to provide treated water that is of sufficient quality to be reused in industry. In fact, several industries are already supplied with recovered surface water that has undergone a natural dilution and purification process.

In recent years, different techniques for treating textile effluents have been investigated [67]. Most of the published studies have focused on the elimination of colorants because this is the process that poses the greatest difficulty. Treating textile effluents by electrochemical techniques has been studied by several authors, with satisfactory results in color removal terms. However, this technique usually incurs high operational costs.

One of the emerging treatments for textile wastewater discoloration uses enzymatic methods [68]. Its main drawback is that the process variables must be well controlled (temperature, pH, salinity, etc.). Furthermore, enzyme separation and purification are a very delicate process. Of the physico-chemical treatments, coagulation-flocculation is the most widespread because it is very effective in removing color. This technique, however, generates a concentrated residue that requires additional treatment. Adsorption discoloration (generally with activated carbon) is influenced by several parameters, such as interactions between the dye and adsorbent, the adsorbent's surface area, and particle size, etc. It is highly efficient for a wide variety of colorants, but is a high-cost technique because the adsorbent material must be regenerated after several treatments [69],[70]. Ion exchange treatments also involve the resin regeneration problem but are not effective for all colorants. The best known physical treatments involve filtration techniques [71],[72].

Chemical oxidation treatments require the addition of oxidizing compounds such as ozone (O_3), hydrogen peroxide (H_2O_2), and permanganate (MnO_4^-). Ozone is the most widely used for its high performance in eliminating colorants, but it is not effective when treating insoluble colorants such as fat or disperse dyes.

3.1.2.2. With Nanotechnologies

The use of nanotechnologies has attracted many researchers' attention for various industrial uses [73], including wastewater recovery with different residues, such as oil. Studies have been carried out using zeolites and nanoparticles that function mainly as catalysts and adsorbents, which have been used in refineries and petrochemical plants. Studies show that nanostructured zeolite can extract up to 40% more gasoline compared to other catalysts.

Some studies have been successful in designing highly selective nanocomposite membranes using a zeolite membrane. This membrane is effective in separating O_2/N_2 molecules in air. To date, no studies have yet been conducted on the direct application of zeolites to the enhanced oil recovery (EOR) process. However, the potential of the ion-exchange nature of zeolite given its porous structure may need to be investigated. This zeolite property could be useful for adsorbing cations, especially under high salinity conditions [16].

Nanoscale adsorbents generally have advantages over other conventional bulk elements thanks to their large specific surface area and high surface reactivities [74]. For example, modified nanoclays have been used as adsorbents for non-ionic, anionic, and cationic dyes. From the differences in absorption between different chemical and morphological dye and clay structures, the adsorption forces that perform important functions have been identified.

Nanoclay can easily have an absorption capacity of more than 600 mg of substrate per gram of sorbent and may also have 90% absorption at an initial dye concentration of 6 g/L, or of 60% based on the adsorbent's weight, which indicates an extremely high dye affinity. Studies show that, with certain modifications, nanoclay, e.g., montmorillonite, could easily become an excellent adsorbent for anionic, cationic, and non-ionic dyes [75].

Nanoclays

Nanoclay [76-109] is the general term used to refer to mineral clays with a phosilicate or laminar structure in the order of nm and surfaces of 50–150 nm or more. Despite nanoclay being commonly used, we must take into account that not all nanoclay dimensions are nanosized. Some clay dimensions classified as nanoclays are microsize due to agglomerations or their structure, such as motmorillonte laminar, which is nano in one laminar dimension but micro in the other. The mineral base can be synthetic or natural, and it is hydrophilic. The clay surface can be modified with specific compounds to improve its affinity and to make it compatible with, for example, polymers. The surface area of nanoclays is very large, around $750 \text{ m}^2\cdot\text{g}^{-1}$. When small amounts of these materials are incorporated into polymeric matrices, the result is known as a nanocomposite. Most of the

dyes used in the textile industry are anionic, which is why achieving better adsorption performance can be expected from anionic nanoclays.

The nanoclays studied in this review present several advantages, such as their natural abundance, low cost, and high adsorption capacity. When such nanoclays act as inorganic hosts for organic compounds, they improve organic host properties to confer better fastness from chemical and natural environments. These nanoclays can be chemically synthesized to improve their physico-chemical characteristics. Another firm advantage of chemical synthesis is that there is no purification step, which is necessary with natural nanoclays to improve adsorption capacity.

Silicon and oxygen are common in all mineral clays. When combined with other elements, such as Al, Mg, Fe, Na, Ca, and K, and given the many ways in which these elements can be linked, they generate a large number of possible configurations. One important distinction in mineral clay properties is the ability of some to change volume by adsorbing water molecules from other polar ions in their structure. This is called the swelling property [76]. In the following, the most significant clays used for the recovery of wastewater in the textile industry will be described.

Montmorillonite (MMT)

Montmorillonite (MMT) (Figure 3.1.2) is the most abundant mineral in the smectites group. The chemical composition for montmorillonite is 80% SiO₂, 13% Al₂O₃, and 3% Fe₂O₃ [77]. It is a naturally abundant and cheap clay that offers efficient adsorbance. Its structure [78] is formed by two layers: a tetrahedric silicon one and an octahedric aluminium oxide one, which create a 2:1 diactahedral layer characterized by having a wide dehydroxylation temperature range of 500–700 °C [80–85]. MMT particle size can range between 2 μm and 0.1 μm, with a mean of around 0.5 μm, although its particle size can be smaller when exfoliated in solvent. Particles are groups of not genuine crystal silicate laminate and their specific surface area (SSA) is approximately 31.26–57.19 m²·g⁻¹ [85]. MMT possesses permanent loads thanks to the isomorphous substitutions of silicate layers, but with no homogeneous distributions [86].

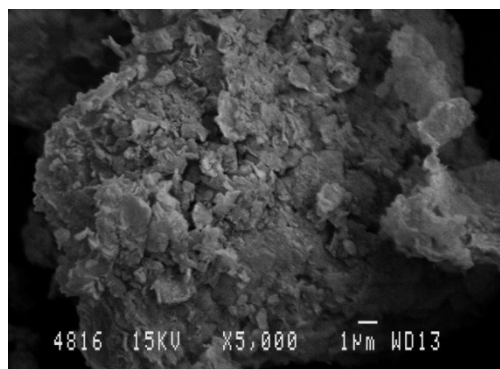


Figure 3.1.2. Montmorillonite (MMT) SEM

The porosity and ion adsorption of MMT are both well-studied characteristics. The purpose of many research works has been to achieve wider basal spacing [87]. Thanks to MMT's cation exchange capacity (CEC), whose values are approximately $90\text{--}145\text{ cmol}\cdot\text{kg}^{-1}$ [88], scientists have improved MMT's adsorption and hydration capacities. Moreover, cation exchange alters clay porosity. All this makes MMT a potential element to be used as a purifier and filter. X-ray diffraction techniques have been applied to establish a direct relation between basal spacing and adsorption capacity, and its pore size [89]. Other studies have also verified that basal spacing is affected by both load type and the position of clays. Those with loads on tetrahedral layers have narrower basal spacing, while those with loads on octahedral layers possess wider basal spacing [90].

It is worth pointing out that isomorphous substitutions of trivalent aluminum for divalent magnesium or iron (II) leave clay crystals with a negative charge, which has to be compensated with surface cations. Clay's own nature determines its swelling and ion exchange capacities in adsorption phases. Much interest has been shown to this exchange control in recent decades [91]. With MMT, this control takes place by variation in pH, and by the interlaminar space where ion exchange occurs.

In the nanoclay basal space, three different scenarios exist: when the basal space is minimum and the adsorption between the laminar nanoclay is minimum or null; when the basal space widens; and when nanoclay is totally exfoliated. This leads to a drawback: that of needing intermediate steps to improve MMT's adsorption capacity by taking into account large size-formed molecular dyes [78].

How pH affects the quantity of methylene blue dye, which clay can adsorb, has been studied. Indeed, MMT treated with acid interchanges leuco-derived dyes, and the stability of that obtained is greater when dye is placed between nanoclay layers. Some authors have concluded that treating clay with acid can allow more adsorbed dye [80],[82]–[84],[92]. In another work, Kang Peng and Huaming Yang prepared MMT by carbon hybridization to adsorb Congo Red dye [36]. MMT's hydrated carbon nanolayers were processed by saccharose calcining that, once formed, was able to adsorb 84% of the dye.

Studies have also been found that have demonstrated how the bath's ionic strength increases or decreases nanoclay adsorption capacity. Organic and inorganic salts influence the dispersion of nanoclay properties by conferring stable dispersion, coagulation, or even gel generation. As explained above, the basal space is significant for achieving the adsorption phenomenon [93]–[95].

Zeolite

Natural zeolite is a mineral widely used to treat wastewater. For the dehydrated zeolite, its chemical formula is $[Al_{12}Si_{12}O_{48}]^{12-}$ [96]. Its different specific characteristics (e.g., porosity, surface area, permeability, CEC) give it a very particular behavior [97]–[99]. Its high specific surface areas is around $200\text{--}860\text{ m}^2\cdot\text{g}^{-1}$ [100]. Having processed natural zeolite, its particle size lies between 1 mm and 12 mm. Its density is approximately double that of water, while its specific surface vastly varies and can be substantially increased by means of modifications [101]. For example, if the aim is to increase its surface, clay can be treated with nitric acid, which removes part of the aluminum from its structure to make it less crystalline and, hence, the specific surface increases [102] (Figure 3.1.3).

When analyzing its electric charge, both the total electric charge and the amount of cations in the zeolite skeleton remain quite stable in aqueous solution during the proton exchange process. Its CEC is around $563\text{ cmol}\cdot\text{kg}^{-1}$ [103]. However, zeolite possesses excellent absorption capacity because the number of exchanged ions during this process differs, and the electric field in the crystal changes [104]. Zeolite's characteristic channels and pores favor ion transport by promoting their transfer and capacity to adsorption [97],[105].

The main form by which zeolites are able to clean wastewater is by filtration and adsorption. When water pollutants pass through zeolite, they are captured, while water molecules pass through the pores [106]. Those pollutants trapped in zeolite in the previous phase are decomposed of microorganisms. After their decomposition, several plants adsorb them. In this way, the substratum is completely released from any previous impurity and can once again perform its function [107].

The zeolites used are either natural zeolites, which previous paragraphs have mentioned, or they are synthetic zeolites. When analyzing the size of component crystals, it is stressed that natural zeolites have a non-uniform crystal size because they contain other impurities, while synthetic zeolites are extremely pure, and their crystals are uniform in size. Zeolites also form differently because natural zeolites can take days or years to form, while they can be synthesized in a laboratory in just a few hours or days; their crystal size is extremely uniform, and their pore size can also be controlled by designing them according to given required specifications [108].

Synthetic zeolites can be obtained and used as artificial and natural elements. However, this does not imply that, from a cost perspective, any element is suitable for synthesization. The most widely used methods are hydrothermal [109], alkali-leaching [110], or sol-gel [111]. Each method is employed according to the desired zeolite type to be obtained. Evidently, it is necessary to bear in mind each method's limitations and advantages. In addition, certain limitations with these nanoclays should be considered, such as their non-reverse adsorption and secondary elements' steric blockage. Their porosity characteristics make high-molecule adsorption difficult [112].

The authors in [113] demonstrated that zeolite in basic or neutral medium is able to adsorb up to 99% Ni (II), which is common in pigments. In [114], the authors bound zeolite to TiO₂ to adsorb up to 99% Cd (II) in any pH medium. Figure 3.1.4 shows the process of adsorption of dye by zeolite.

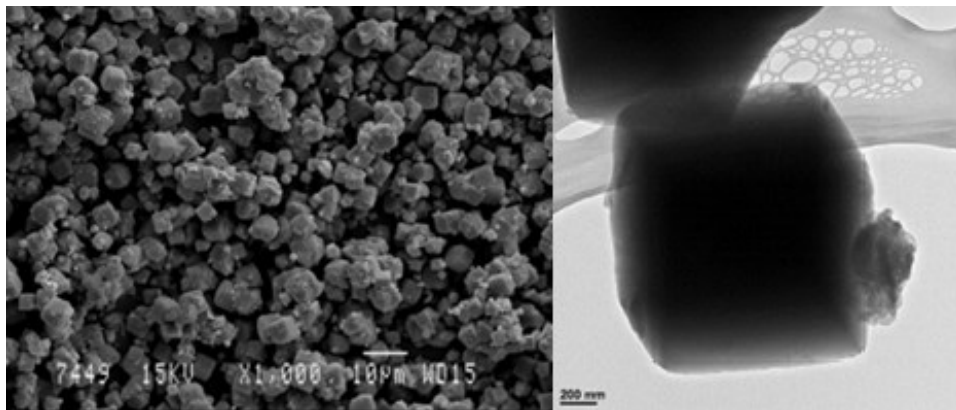


Figure 3.1.3. Zeolite SEM (left) and TEM (right)

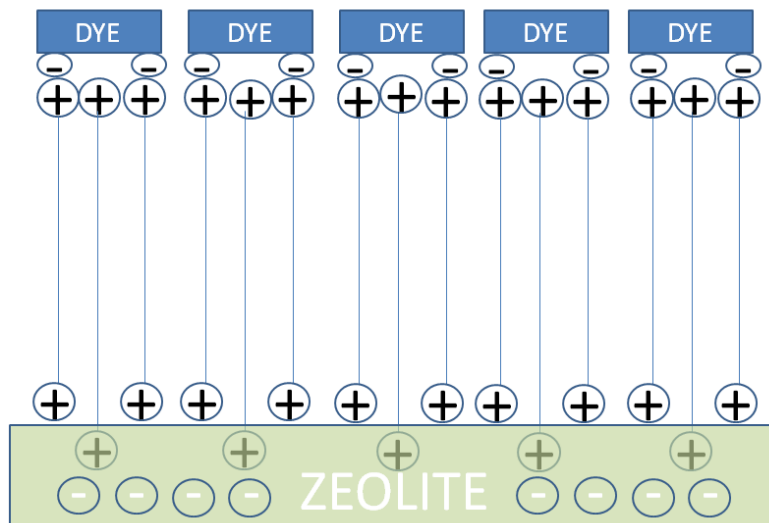


Figure 3.1.4. Zeolite adsorption of dye

Halloysite

Today, scientists are working on employing adsorption by nanotechnologies because they consider it a very efficient method to remove different types of very harmful pollutants from water. Considerable importance has been attached to clayey minerals given their natural origin, the possibility of chemically synthesizing them, and their unique characteristics [115]. Halloysite is an example of a 1:1-type clayey that abounds in nature and is classified as a biocompatible material. The diameter of halloysite nanotubes (Figure

3.1.5) is approximately 40–70 nm, and their length can be 200–2000 nm. [116]. Their specific Surface Area (SSA), $47 \text{ m}^2 \cdot \text{g}^{-1}$, and CEC, $9.45 \text{ cmol} \cdot \text{kg}^{-1}$, have been determined by the authors [117]. The interstratified phases are high-charge halloysite-smectite mixed-layered clays (CEC, 30–72 $\text{cmol} \cdot \text{kg}^{-1}$ clay) [118]. Their outer surface is negatively loaded and is composed of SiO_2 , while their inner area is positively loaded and composed of Al_2O_3 [119]. The use of halloysite nanotubes (HNT) has considerably increased thanks to them being cylindrical in nature and them having certain properties; e.g., their large area in relation to their size, drug release, low-cost, and thermal stability [116],[120]–[122].

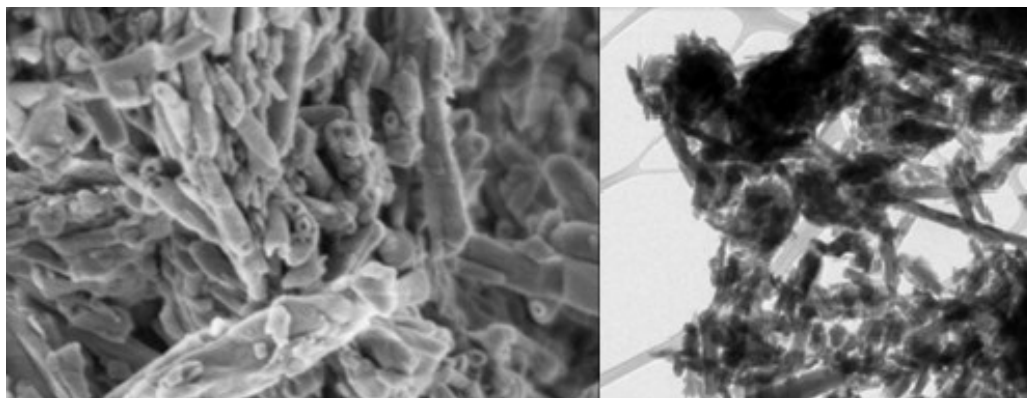


Figure 3.1.5. Halloysite SEM (left) and TEM (right) images

In order to explain their aforementioned characteristics, HNT belong to the aluminosilicates family, where one octahedric aluminum oxide layer alternates with another tetrahedric silica layer. From this mismatch in the two described layer types, a characteristic hollow tubular form of this nanoclay is generated, which confers it specific characteristics that come about because of its nanoarchitecture [123]. It is important to consider that HNT properties derive mostly from their specific geological deposit, which is explained in the consulted literature [123]–[128]. Their biocompatibility makes them very useful for adsorbing dyes [129],[130], such as methylene blue (MB) [131]–[139], azo dyes [140]–[146], triaryl and diaryl methane dyes [147]–[155], and xanthine dyes [129],[156]–[158], and also for the biosorption of heavy metals [159]. One study has eliminated Orange G from simulated and real waters by combining halloysite with ZnO nanoparticles and by photocatalytic degradation. Up to 94% dye removal was achieved [160].

One of the most frequent problems in natural halloysite is its high concentration of impurities, which must be eliminated to improve adsorption capacity. Some authors describe how adsorption performance can be enhanced by using acid treatment for 12 h and by laminar surface injection [161].

Saponite

Saponite (Sap) is a trioctahedral clayey mineral that belongs to the 2:1-type smectites group, with silicate layers that intersperse with another gibbsite layer in the following form: silicate–gibbsite–silicate. It possesses negatively charged layers that are, in turn, neutralized by other ions with positive Na^+ Mg^{2+} charges. Saponite's cation exchange capacity (CEC) has been quantified as $100 \text{ cmol}\cdot\text{kg}^{-1}$ [162]–[166]. XRD and SEM/EDX characterizations shows the clay mineral has the structural formula $^{\text{INT}}\text{Na}^{\text{TET}}[\text{Si}_7\text{Al}]^{\text{OCT}}[\text{Mg}_6]\text{O}_{20}(\text{OH})_4$ [167].

Its specific surface area (SSA) is large-sized and acidic. The specific surface area (SSA) was determined using ethylene glycol monomethyl ether, $100\text{--}115 \text{ m}^2\cdot\text{g}^{-1}$ [168]. Compared to other nanoclay minerals such as MMT, it can be stated that Sap offers greater thermal stability [169], a smaller particle size (approx. 50 nm) [162]–[166], and is simpler to delaminate and exfoliate in nanoplate units, or as individual nanolayers in aqueous solution [170]. However, the downside of natural Spa is that it is not abundantly available. When Sap is exploited, a large quantity of impurities appear in the deposits, which entails time-consuming purification that considerably increases the cost of obtaining it [171]. The chemical composition of Sap varies significantly depending on the geological process that has formed it [172]. These defects can limit its use during adsorption processes [173].

The above-described problems have led researchers to opt to synthetically obtain Sap. This process consists of synthesizing similar solids to natural Sap with a controlled chemical composition. The most conventional method followed to synthesize Sap is normally hydrothermal synthesis [174]–[180]. This method can be modified to make this synthesis microwave-assisted [181],[182].

Despite the characteristics described for both natural and synthetic Sap, Sap is not normally employed in its fundamental state without previously submitting it to modification, such as intercalation or hybridization. Researchers have put saponite swelling to best use [183]–[186] to introduce functional groups into the structure. This enables the modification of acidity and porosity, and different physico-chemical properties. Distinct hybrids have been successfully achieved by following these guidelines [187]–[190]. An increasing number of studies have demonstrated that Sap can be employed as an efficient adsorbent [190],[191]. In the work by Herney-Ramirez et al., dye Acid Orange 7 was degraded by Sap by employing H_2O_2 at 70 °C as a catalyst, which achieved over 90% degradation when clay was impregnated with Fe (II) [192].

Sepiolite

Sepiolite is a natural 2:1-type fibrous nanoclay mineral [193] whose molecular formula is $Si_{12}O_{30}Mg_8(OH)_4(H_2O)_4 \cdot 8H_2O$. Type 2:1 is defined by two tetrahedral silica layers, which are interspersed with another octahedral magnesium oxide layer. Its shape is similar to that of zeolites because it is formed by ribbon-like composites that, in turn, form an open channel. Thanks to such a structure (approx. 0.4 nm × 1 nm), it can be generated by the penetration of organic and inorganic cations. The sepiolite surface has many silanol (Si–OH) groups as a result of a discontinued silica sheet on the outer 2:1 layers [194]–[197] (Figures 3.1.6 and 3.1.7).

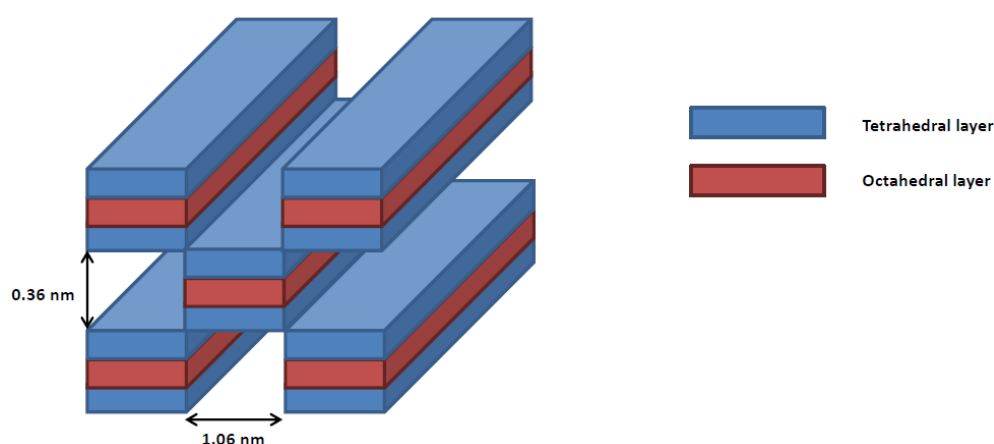


Figure 3.1.6. Sepiolite Type 2:1 two tetrahedral silica layers, and another octahedral

On the sepiolite structure, three modification/adsorption zones are distinguished: Si-OH groups along the component fiber axis; oxygen ions on the tetrahedral silica layers; and a few cationic exchange gaps. Other parameters that affect sepiolite's adsorption capacity are the load of the substance to be adsorbed and its shape and size. By bearing these parameters in mind, some researchers have found that substances presenting low-polarity and large molecular-sized molecules cannot enter sepiolite channels and, despite being adsorbed on the tetrahedral silica layer, they only represent about 40% total SSA [198]. Unlike MMT, it is possible to introduce an organic modifier into the sepiolite surface (between $400 \text{ m}^2\cdot\text{g}^{-1}$ and $500 \text{ m}^2\cdot\text{g}^{-1}$) [199].

Sepiolite is frequently industrially and scientifically commercialized as an excellent absorbent in pet latrines, and its efficiency as an adsorbent for textile industry dyes has also been demonstrated. Some studies have experimentally shown sepiolite's capacity for adsorbing different cationic dyes [200]–[203]. It adsorbs cationic substances thanks to this clay's CEC ($31,4 \text{ cmol}\cdot\text{kg}^{-1}$) [204], which also occurs through neutral gaps that favor the adsorption of cationic dyes [201]. Saturation with Na or Ca increases sepiolite's adsorption capacity for methylene blue dye [205]. However, it does not offer good adsorption results with azo acid dyes [206]. One study employed $\text{SiO}_2\text{-Mg(OH)}_2$ derived from sepiolite to remove the Cd(II) present in dye with up to 95% adsorption [207]. It worked considerably better at a neutral pH than at a basic pH, and at constant temperature ($T = 25 \text{ }^\circ\text{C}$) [208].

The pH parameter is important because it affects sepiolite's adsorption capacity. Due to isomorphous nanoclay substitutions, their structural charge can be changed by pH, which leads to hydroxyl dissociation [208].

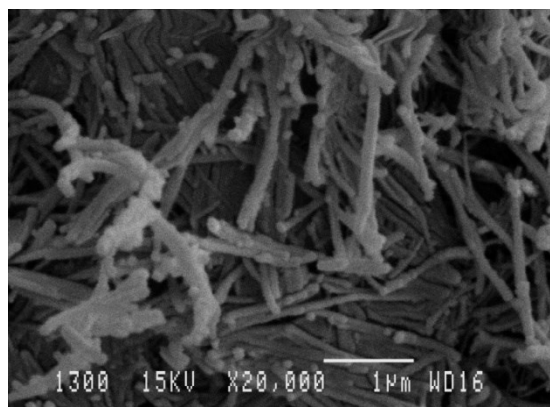


Figure 3.1.7. Sepiolite SEM

Bentonite

Bentonite (BTE) is an aluminosilicate formed by one octahedric aluminum oxide layer and two tetrahedric silicon oxide layers, which results in a 1:2-type structure with the chemical formula $\text{Al}_2\text{H}_2\text{Na}_2\text{O}_{13}\text{Si}_4$ [209],[210]. This clay is frequently employed worldwide as an adsorbent because of its excellent cost-effectiveness ratio. It is also widely available anywhere in the world. Some authors explain bentonite's high adsorption capacity with the NH_4^+ group, which is formed thanks to its high CEC, with a value generally around $40\text{--}130\text{ cmol}\cdot\text{kg}^{-1}$. Some studies conducted in 2017 by scientists revealed that raw bentonite has a NH_4^+ adsorption capacity of $19.01\text{ mg}\cdot\text{g}^{-1}$, which implies 53% adsorption efficacy, which can rise to 81% when the quantity of nanoclay is increased up to a concentration of $40\text{ g}\cdot\text{L}^{-1}$ [211]–[215].

As with many other nanoclays, modifications can be made to bentonite to change its properties. After analyzing the SSA ($45\text{--}68\text{ m}^2\cdot\text{g}^{-1}$) [216], diameter, and pore volume of BTE modified with benzylhexadecyldimethylammonium *chloride* and a natural unmodified bentonite, Tohdee and Kaewsichan concluded that, without modifications, the values of these parameters were more specific and better than those recorded after modification [217]. Moreover, cationic surfactants increased the cationic affinity of clay and their anionic adsorption. The modification made by the action of these elements only occurred on surface layers [218].

An example of these cationic surfactants appears in another study, which modified bentonite with cetrimonium bromide to give pores and a larger surface area after modifications. This led to greater adsorption capacity and, therefore, to amaranth dye removal [219]. Different parameters, such as pH [220]–[223], quantity of adsorbent [224],[225], temperature, and contact time [226]–[228] among other elements, influenced bentonite's adsorption capacity.

One study employed Zr-bentonite to remove the phosphates that abounded in textile water to adsorb them under acidic pH conditions. Removal efficiency came close to 100%, but removal efficiency lowered as pH rose. Another important factor was the quantity of NaCl in the medium because removal efficiency increased at lower NaCl concentrations. The final phosphate removal capacity in that study was 95% [229],[230].

Laponite

Laponite (Lap) is an inorganic stratified silicate element that is often used to improve the rheology of different water-based products [231]–[233]. Its capacity to react with water-based components is excellent, and its viscosity develops when such products are incorporated [234]. Some studies [235]–[237] have demonstrated that Lap can be dispersed in water (Figure 3.1.8) and can improve other elements' dispersion in solution thanks to its ability to prevent solid aggregation [238]–[242].

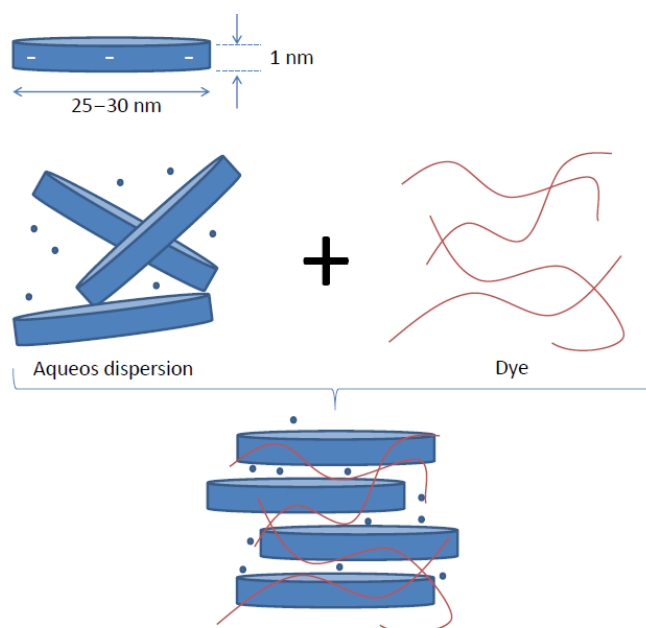


Figure 3.1.8. Laponite aqueous dispersion and dye adsorption

Synthetic Lap ($\text{Si}_8[\text{Mg}_{5.5}\text{Li}_{0.4}\text{H}_{4.0}\text{O}_{24}]^{0.7-}\text{Na}_{0.7}^+$) is a 2D clay disc-shaped silicate that is approximately 1 nm thick. Its diameter is 25 nm [243]–[245]. The raw Laponite was estimated to have an SSA of $11.7 \text{ m}^2\cdot\text{g}^{-1}$ [246]. It possesses permanent negative charges due to isomorphic substitution. Depending on the temperature, the concentration it is found at, and the curing time, it can come as a viscous gel that breaks in aqueous solution or forms a translucent fluid [247]–[250]. In the textile industry, it can act as a perfect additive for pigments because it protects them from environmental factors, such as temperature and oxygen, and improves the pigment's final stability [254–257].

Some studies have demonstrated the adsorption capacity of laponite-based hydrogels [255] and their CEC is $74 \text{ cmol}\cdot\text{kg}^{-1}$ [256]. Laponite-based hydrogel formation is due to the reticulation that occurs in the polymer. This gel can also be formed if certain components are added to it, such as H_2SO_4 or KNO_3 [247]–[250]. By means of Lap membranes, another study accomplished the removal of up to 100% of two organic dyes, namely Rhodamine B (cationic dye) and Brilliant Blue (anionic dye) [257]. To do so, a superoleophobic membrane was synthesized from hydrating polyacrylonitrile.

Hydrotalcite

Hydrotalcite, $\text{Mg}_6\text{Al}_2(\text{CO}_3)(\text{OH})_{16}\cdot 4(\text{H}_2\text{O})$ (Figure 3.1.9), is classified as a nano-sized mineral because one of the dimensions of its laminate measures less than 20 nm. Owing to its characteristic structure, it falls into the “layered double hydroxides” (LDH) category. This layer has an SSA between $71 \text{ m}^2\cdot\text{g}^{-1}$ and $104 \text{ m}^2\cdot\text{g}^{-1}$ [258]. Researchers are showing increasing interest in such elements thanks to their wide range of applications as catalysts, and also in medicine, adsorption, etc. [259]. Different methods exist by means of which the adsorption of anions by LDH composites takes place. The most common one is that produced by direct adsorption in dispersion. A solid’s crystallinity limits such adsorption for the following reasons: the medium’s polarity, temperature, anion size, and pH [260]–[262].

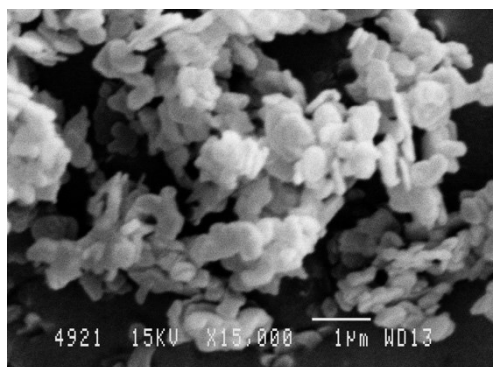


Figure 3.1.9. Hydrotalcite SEM

The second, albeit slightly more time-consuming, method, but one offering clear advantages, is calcining. Former studies have demonstrated that hydrotalcite has shape memory after being exposed to a high thermal source. This substantially changes its initial laminar arrangement, which recovers during later hydration processes. After being exposed to temperatures of $450\text{--}550 \text{ }^\circ\text{C}$, it is reconstructed as previously described thanks to the anions present in dissolution and their incorporation into the new nanoclay structure [263]–[265] (Figure 3.1.10).

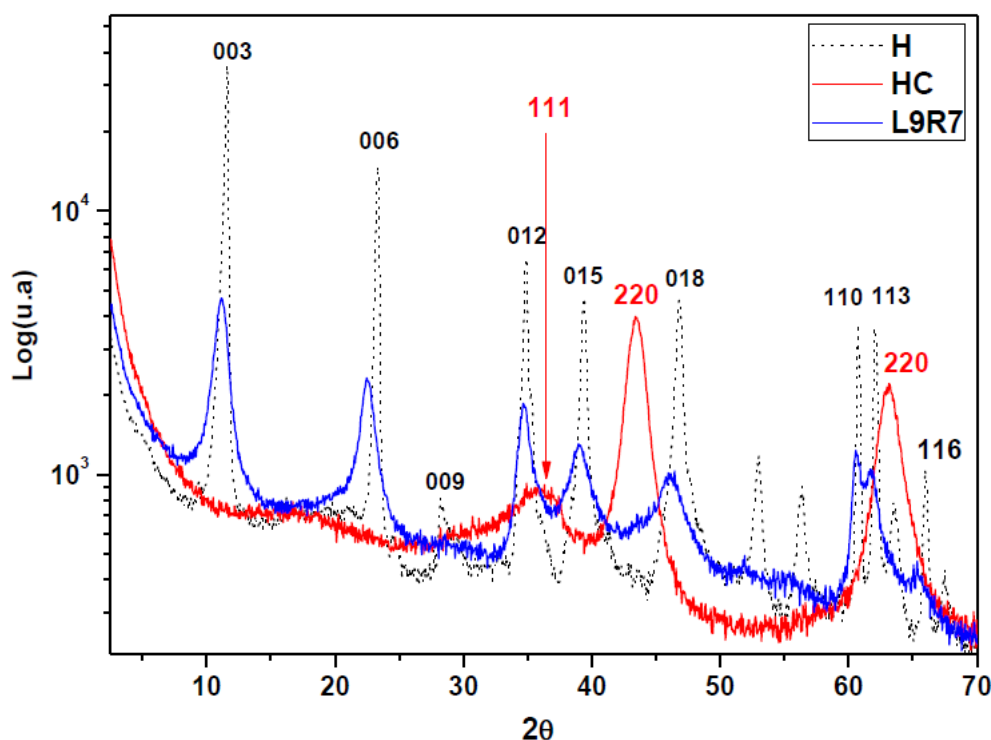


Figure 3.1.10. XRD from Hydrotalcite after heat treatment, 600 °C, 3 h (HC): original hydrotalcite (HC) and hydrotalcite reconstructed after a natural dye (from beetroot) adsorption in different bath conditions (L9R7)

3.1.3. Reused Waste Water Dyes

The third form of adsorption is coprecipitation, based on the synthesization of hydrotalcite with some anions, which are incorporated into its structure and are adsorbed [266]. Dye adsorption by cationic exchange cannot be performed in most dyes found in nature because they are anionic, which is why hydrotalcite-type clays are resorted to for this recovery [267]. Hydrotalcite's laminar structure needs to be compensated by anions being incorporated into it, which results in the aforementioned adsorption [177],[268].

Hence, high adsorbance can be accomplished, but other processes are necessary to improve this capacity to achieve the desired properties during the adsorption process. It is important to consider the CEC for this nanoclay, calculated by the authors Gasser, Mekhamer, and Abdel, Rahman in this work [269], which has a value of $8.96 \text{ cmol}\cdot\text{kg}^{-1}$.

After carrying out the different dyeing processes, wastewater is discharged without having to wait for further use. However, in view of the studies included in this article, it is possible to recover a large portion of the dyes in solution to be reused during industrial processes.

3.1.3.1. Pigment

One of the options that has been applied to the reuse these colorants is to employ them as pigments [197],[230],[270]–[274]. Once trapped inside a substrate such as clays, they can remain in this element to be later utilized during stamping processes.

In order to be used as pigments, their stability must be good, and it is necessary to ensure that the colorant does not undergo any desorption processes. Therefore, after introducing the colorant into clay, tests are carried out, during which the colorant's degree of fixation is analyzed. Only in the event of having high fixation results can its use as a pigment with no discoloration risk due to loss of colorant be guaranteed.

These pigments are very frequently used in industries, such as textiles, plastics, printing, or industrial coatings, although they have a series of properties that confer them with low stability, poor weather resistance, and poor dispersion, which mean their use is limited [275],[276]. Thus, in order to improve the described properties and defects, it is necessary to prepare stabler hybrids with colorants in clay mineral matrices [277]. By way of example, some works exist where hybrids with montmorillonite and methylene blue have been prepared, where thermal stability, photostability, and covering power have improved [278],[279].

Other works have compared the color and stability properties of dye–clay hybrids. These studies, based on a CIELAB 1976 analysis [280], conclude that the color stability of the hybrids formed by halloysite were superior to others, such as MMT and sepiolite [281], which can be attributed to each nanoclay's individual structure and chemical properties.

3.1.3.2. Dyes

Another reuse option involves employing recovered colorant during another dyeing process. In this case, the clay–dye bond must be less to allow desorption, unlike the

previous situation of utilizing a pigment. For this purpose, clays such as Lap are used [242],[282] that, according to tests, presents some degrees of desorption from 20% to 40%. Another example of a mineral that allows dye desorption is zeolite [97].

According to the bibliography, desorption processes are carried out by subjecting clay to a bath with either distilled water [282] or ethanol [197], and by means of stirring. This results in dye desorption.

A study carried out by Momina, Shahadat Mohammad, and Suzylawatilsamil [283] (Figure 3.1.11) explains how to proceed with MB desorption by subjecting the clay–dye hybrid to temperature and then using various solvents such as HCl, ethanol, nitric acid, or acetone. Their study revealed that it was not enough to apply thermal energy to break the bonds that formed during dye adsorption by clay, which they called a chemisorption process. The solvent and heating processes alone did not provide enough energy, which is why they had to apply a thermo-chemical process to regenerate the adsorbent.

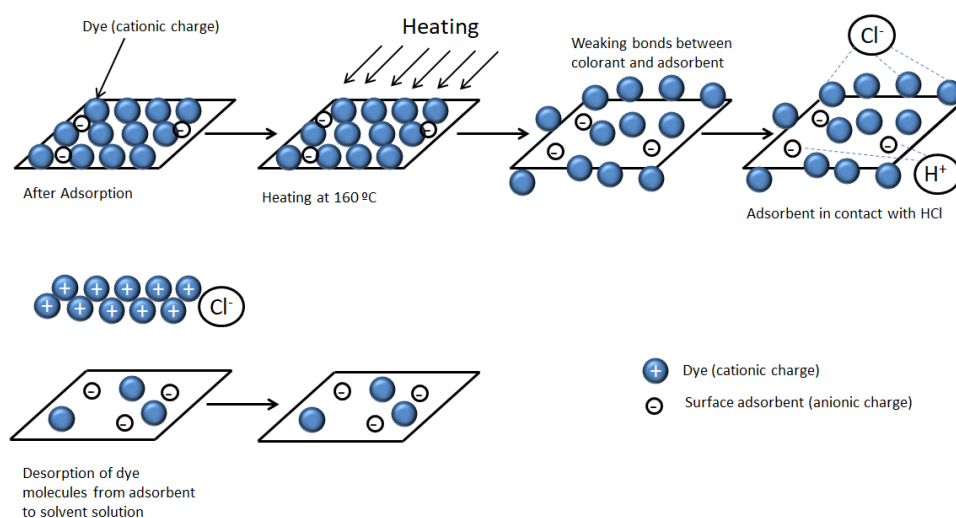


Figure 3.1.11. Dye desorption process

The process begins by heating samples to about 150–200 °C for 45 min. Accordingly, the bonds between the adsorbent and the colorant weaken. In the next step, HCl^- is introduced, which increases the charges of the positive hydrogens, which show an affinity for the clay surface and release Cl^- charges with an affinity for MB. In this way, desorption

is completed by releasing the colorant from the clay. As both elements are ionically neutralized, they do not rejoin.

As a critical aspect of this procedure, the maximum temperature that both the clay and the dye can withstand should be studied by thermogravimetric (TGA) to increase the temperature of the initial phase to a maximum and to thus weaken the bonds as much as possible and facilitate the second phase by maximizing desorption efficiency.

3.1.4. Conclusions

This article describes some of the most widespread nanoclays, referring to different sources of adsorbents research, that can be used for treating industrial wastewater (Table 3.1.2). Each clay material has specific characteristics (Table 3.1.3), which can make them more appropriate in different situations according to their subsequent utilization, cost optimization, or other factors.

Table 3.1.2. Comparison of different clays

Adsorbent	Performance	Use	Observ.	Adsorption BC *	Biblio. Ref.
Saponite	High performance	Pigment	-	Acid Orange 7 > 90%	[192],[270],[271],[284]
Montmorillonite	Thermal stability	Pigment	No desorption	Congo Red 84%	[36],[271],[272],[285]
Sepiolite	Poor stability	Pigment/Dye	Desorption in ethanol	Cd 95%	[197],[207]
Bentonite	No desorption High stability	Pigment	Low-cost. Absorbance at different pH.	Phosphates 95%	[229],[230],[273],[274]
Laponite	-	Dye	20–40% desorption	Rhodamine B% 100% Brilliant blue	[242],[257],[282]
Halloysite	Combined photocatalysis	Pigment	Novelty	90% orange G	[160],[286]
Zeolite	Regeneration for reuse	Dye	With cationic dyes	99% Ni & Cd	[97],[113],[114]
Hydrotalcite	High performance	Pigment	Low-cost	Cationic dyes	[177],[268]

* BC: Under Best Conditions.

Table 3.1.3. Adsorbent's characteristics comparison

Adsorbent	Structure	Charge	Biblio. Ref.
Saponite	Laminate	Cationic	[162]
Montmorillonite	Laminate	Cationic	[81]
Sepiolite	Channels	Cationic	[194]–[197]
Bentonite	Laminate	Cationic	[209]
Laponite	Laminate	Cationic	[243]–[245]
Halloysite	Tubular	Cationic/Anionic	[123]
Zeolite	Channels	Cationic	[97],[105]
Hydrotalcite	Laminate	Cationic	[177],[268]

From this state-of-the-art review, we found a strong nanoclay repercussion on wastewater treatment, specifically in textile wastewater with a high dye concentration. Despite the huge amount of clays and nanoclays that can be employed as adsorbents, we focused on the most widely studied nanoclays. The most well-studied ones were selected for their abundance, low-cost, and excellent adsorption efficiency. The main studied nanoclays can be found under natural conditions, and they can also be synthesized to improve their characteristics. Despite most authors supporting nanoclays for their low cost and abundance, we found that information regarding this, supported with specific numbers and comparisons to real costs, exploitation capabilities, and the real impact of exploitation or synthetic generation, was lacking. In addition, a synthetic or natural extraction comparison should be made, taking into account the purification step costs of natural clays.

Hundreds of studies have demonstrated that nanoclays are highly efficient adsorbents, and several dye structures are used during industrial processes, such as textile dyeing. The ionic exchange process that they bring about means that dye molecules are trapped in the nanoclay basal space or adhere to nanoclay surfaces. For these reasons, it is adsorption and not an absorption process that improves some of their characteristics, such as colorfastness in the event of environmental and chemical attacks, and they can be used later in textile stamping.

Nanoclay modification to improve their adsorption capacity via calcination or with surface modifiers has been widely studied. However, some authors have not considered the environmental costs of this process. The acid, basic, or thermal treatment costs should

also be considered in order to ensure that the process is clean and sustainable. On the other hand, when different authors discuss the desorption phase, they tend to give very ambiguous results; for example, they give desorption values of between 20–40%, which is not very specific because the range of variation is very wide. For future lines of enquiry, the quantification of many of the phases must be improved, for example, the preparation of materials where their adsorption capacity is improved by prior calcination, because it is not quantified to what degree the adsorption capacity improves due to previous loss of anions CO_3 .

Regarding post-dye adsorption hybrid pigment uses, we found several works that demonstrated their advantages, such as improving organic dye properties, or polymer thermal, mechanical, and thermal barrier properties, in nanocomposites. However, a textile application has not yet been studied in-depth, nor has the reuse of organic compounds after a desorption process been completely studied and described. Several factors must be considered and described, such as pH, time, and temperature, which recent works do not provide. The results obtained by these studies are ambiguous and need to be further examined. However, these studies do demonstrate that the desorption process is viable as a promising future trend.

The possibilities contained within this study and proposal are many, such as the impact on textile fibers or the desorption possibility to separately reuse dyes as raw material during dyeing processes and the use of nanoclay as an adsorbent during the wastewater cleaning process. Future applications should be considered according to the nanoclay properties described, such as cation exchange capacity (CEC) and specific surface area (SSA), etc. Each one presents specific characteristics that allow it to retain the colorant to a greater or lesser extent. Those that retain the colorant and do not present desorption will be suitable for later use in the printing industry, while those with an acceptable degree of desorption will allow a new dye bath to be made and, therefore, the residual colorant left in water can be reused.

References

1. Semeraro, P.; Rizzi, V.; Fini, P.; Matera, S.; Cosma, P.; Franco, E.; García, R.; Ferrándiz, M.; Núñez, E.; Gabaldón, J. A.; Fortea, I.; Pérez, E.; Ferrándiz, M. Interaction between Industrial Textile Dyes and Cyclodextrins. *Dye. Pigment.* 2015, *119*, 84–94. <https://doi.org/10.1016/J.DYEPIG.2015.03.012>.
2. Sana, D.; Jalila, S. A Comparative Study of Adsorption and Regeneration with Different Agricultural Wastes as Adsorbents for the Removal of Methylene Blue from Aqueous Solution. *Chinese J. Chem. Eng.* 2017, *25* (9), 1282–1287. <https://doi.org/10.1016/J.CJCHE.2017.01.012>.
3. Sanchez, L. M.; Ollier, R. P.; Gonzalez, J. S.; Alvarez, V. A. Nanocomposite Materials for Dyes Removal. *Handb. Nanomater. Ind. Appl.* 2018, 922–951. <https://doi.org/10.1016/B978-0-12-813351-4.00053-5>.
4. Erkanlı, M.; Yilmaz, L.; Çulfaz-Emecen, P. Z.; Yetis, U. Brackish Water Recovery from Reactive Dyeing Wastewater via Ultrafiltration. *J. Clean. Prod.* 2017, *165*, 1204–1214. <https://doi.org/10.1016/J.JCLEPRO.2017.07.195>.
5. Wang, L.; Zhang, W.; Wang, L.; Wu, H.; Wu, D.; Lu, S.; Huang, X. Synthesis Rod-like Mesoporous MgO Using Sodium Polystyrenesulfonate (PSS) as Structure-Direct Template and Its Application to Plumbum Absorption in Waste Water. *Mater. Lett.* 2020, No. xxxx, 129051. <https://doi.org/10.1016/j.matlet.2020.129051>.
6. Nong, G. zai; Xing, D. yue; Li, Y. jing; Zhu, T.; Wu, J. lin; Gan, W. xing; Wang, S. fei; Li, X. rong. Recycle Cooking Wood Chips with the Residue Liquid Removed out of Lignin by Calcification for Increasing Pulp Yield and Reducing Waste Water Discharge. *J. Clean. Prod.* 2020, *277*, 124028. <https://doi.org/10.1016/j.jclepro.2020.124028>.
7. Mahmoud, M. E.; Nabil, G. M.; Khalifa, M. A.; El-Mallah, N. M.; Hassouba, H. M.; Negin, C.; Ali, S.; Xie, Q.; Liu, H.; Li, X. rong; Li, M.; Zhang, Y.; Tang, K.; Liu, J.; Zheng, X.; Pei, Y.; Wang, L. L.; Zhang, W.; Wang, L. L.; Wu, H.; Wu, D.; Lu, S.; Huang, X.; Nong, G. zai; Xing, D. yue; Li, Y. jing; Zhu, T.; Wu, J. lin; Gan, W. xing; Wang, S. fei; Li, X. rong; Jadhav, S. A.; Garud, H. B.; Patil, A. H.; Patil, G. D.; Patil, C. R.; Dongale, T. D.; Patil, P. S.; Park, J.-H.; Wang, J. J.; Meng, Y.; Wei, Z.; DeLaune, R. D.; Seo, D.-C.; Erkanlı, M.; Yilmaz, L.; Çulfaz-Emecen, P. Z.; Yetis, U.; Rizvi, M. A.; Moosvi, S. K.; Jan, T.; Bashir, S.; Kumar, P.; Roos, W. D.; Swart, H. C.; Azzaz, A. A.; Jellali, S.; Akrouf, H.; Assadi, A. A.; Boussemi, L.; Sana, D.; Jalila, S.; Azzaz, A. A.; Assadi, A. A.; Jellali, S.; Bouzaza, A.; Wolbert, D.; Rtimi, S.; Boussemi, L.; Semeraro, P.; Rizzi, V.; Fini, P.; Matera, S.; Cosma, P.; Franco, E.; García, R.; Ferrándiz, M. M.; Núñez, E.; Gabaldón, J. A.; Fortea, I.; Pérez, E.; Ferrándiz, M. M.; Ranjan, P.; Verma, P.; Agrawal, S.; Rao, T. R.; Samanta, S. K.; Thakur, A. D.; Senoussi, H.; Bouhidel, K.-E.; Fatima, M.; Farooq, R.; Lindström, R. W.; Saeed, M.; Zhong, P. S.; Widjojo, N.; Chung, T.-S.; Weber, M.; Maletzko, C.; Fatima, M.; Farooq, R.; Lindström, R. W.; Saeed, M. A Review on Biocatalytic Decomposition of Azo Dyes and Electrons Recovery. *J. Clean. Prod.* 2017, *246* (xxxx), 275–281. <https://doi.org/10.1016/J.MOLLIQ.2017.09.063>.

8. Liu, H.; Li, X.; Li, M.; Zhang, Y.; Tang, K.; Liu, J.; Zheng, X.; Pei, Y. A Simple and Sustainable Beamhouse by the Recycling of Waste-Water from KCl-Dispase Synergistic Unhairing in Leather Making. *J. Clean. Prod.* 2020, No. xxxx, 124535. <https://doi.org/10.1016/j.jclepro.2020.124535>.
9. Negin, C.; Ali, S.; Xie, Q. Application of Nanotechnology for Enhancing Oil Recovery – A Review. *Petroleum* 2016, 2 (4), 324–333. <https://doi.org/10.1016/J.PETLM.2016.10.002>.
10. Zhong, P. S.; Widjojo, N.; Chung, T.-S.; Weber, M.; Maletzko, C. Positively Charged Nanofiltration (NF) Membranes via UV Grafting on Sulfonated Polyphenylenesulfone (SPPSU) for Effective Removal of Textile Dyes from Wastewater. *J. Memb. Sci.* 2012, 417–418, 52–60. <https://doi.org/10.1016/J.MEMSCI.2012.06.013>.
11. Senoussi, H.; Bouhidel, K.-E. Feasibility and Optimisation of a Batch Mode Capacitive Deionization (BM CDI) Process for Textile Cationic Dyes (TCD) Removal and Recovery from Industrial Wastewaters. *J. Clean. Prod.* 2018, 205, 721–727. <https://doi.org/10.1016/J.JCLEPRO.2018.09.026>.
12. Ranjan, P.; Verma, P.; Agrawal, S.; Rao, T. R.; Samanta, S. K.; Thakur, A. D. Inducing Dye-Selectivity in Graphene Oxide for Cationic Dye Separation Applications. *Mater. Chem. Phys.* 2019, 226, 350–355. <https://doi.org/10.1016/J.MATCHEMPHYS.2019.01.047>.
13. Mahmoud, M. E.; Nabil, G. M.; Khalifa, M. A.; El-Mallah, N. M.; Hassouba, H. M. Effective Removal of Crystal Violet and Methylene Blue Dyes from Water by Surface Functionalized Zirconium Silicate Nanocomposite. *J. Environ. Chem. Eng.* 2019, 7 (2), 103009. <https://doi.org/10.1016/J.JECE.2019.103009>.
14. Azzaz, A. A.; Assadi, A. A.; Jellali, S.; Bouzaza, A.; Wolbert, D.; Rtimi, S.; Bouselmi, L. Discoloration of Simulated Textile Effluent in Continuous Photoreactor Using Immobilized Titanium Dioxide: Effect of Zinc and Sodium Chloride. *J. Photochem. Photobiol. A Chem.* 2018, 358, 111–120. <https://doi.org/10.1016/J.JPHOTOCHEM.2018.01.032>.
15. Azzaz, A. A.; Jellali, S.; Akrou, H.; Assadi, A. A.; Bouselmi, L. Dynamic Investigations on Cationic Dye Desorption from Chemically Modified Lignocellulosic Material Using a Low-Cost Eluent: Dye Recovery and Anodic Oxidation Efficiencies of the Desorbed Solutions. *J. Clean. Prod.* 2018, 201, 28–38. <https://doi.org/10.1016/J.JCLEPRO.2018.08.023>.
16. Rizvi, M. A.; Moosvi, S. K.; Jan, T.; Bashir, S.; Kumar, P.; Roos, W. D.; Swart, H. C. Dielectric, Magnetic and Photocatalytic Activity of PolyPyrrole/Prussian Red Nanocomposite for Waste Water Treatment Applications. *Polymer (Guildf)*. 2019, 163, 1–12. <https://doi.org/10.1016/J.POLYMER.2018.12.044>.

17. Park, J.-H.; Wang, J. J.; Meng, Y.; Wei, Z.; DeLaune, R. D.; Seo, D.-C. Adsorption/Desorption Behavior of Cationic and Anionic Dyes by Biochars Prepared at Normal and High Pyrolysis Temperatures. *Colloids Surfaces A Physicochem. Eng. Asp.* 2019, 572, 274–282. <https://doi.org/10.1016/J.COLSURFA.2019.04.029>.
18. Jadhav, S. A.; Garud, H. B.; Patil, A. H.; Patil, G. D.; Patil, C. R.; Dongale, T. D.; Patil, P. S. Recent Advancements in Silica Nanoparticles Based Technologies for Removal of Dyes from Water. *Colloid Interface Sci. Commun.* 2019, 30, 100181. <https://doi.org/10.1016/J.COLCOM.2019.100181>.
19. Mathew, M. L.; Gopalakrishnan, A.; Aravindakumar, C. T.; Aravind, U. K. Low – Cost Multilayered Green Fiber for the Treatment of Textile Industry Waste Water. *J. Hazard. Mater.* 2019, 365, 297–305. <https://doi.org/10.1016/J.JHAZMAT.2018.11.014>.
20. Wakkal, M.; Khiari, B.; Zagrouba, F. Textile Wastewater Treatment by Agro-Industrial Waste: Equilibrium Modelling, Thermodynamics and Mass Transfer Mechanisms of Cationic Dyes Adsorption onto Low-Cost Lignocellulosic Adsorbent. *J. Taiwan Inst. Chem. Eng.* 2019, 96, 439–452. <https://doi.org/10.1016/J.JTICE.2018.12.014>.
21. Nath, J.; Bag, S.; Bera, D.; Ray, L. Biotreatment of Malachite Green from Aqueous Solution and Simulated Textile Effluent by Growing Cells (Batch Mode) and Activated Sludge System. *Groundw. Sustain. Dev.* 2019, 8 (May 2018), 172–178. <https://doi.org/10.1016/j.gsd.2018.11.002>.
22. Bankole, P. O.; Adekunle, A. A.; Obidi, O. F.; Olukanni, O. D.; Govindwar, S. P. Degradation of Indigo Dye by a Newly Isolated Yeast, *Diutina Rugosa* from Dye Wastewater Polluted Soil. *J. Environ. Chem. Eng.* 2017, 5 (5), 4639–4648. <https://doi.org/10.1016/j.jece.2017.08.050>
23. Deniz, F.; Karaman, S. Removal of an Azo-Metal Complex Textile Dye from Colored Aqueous Solutions Using an Agro-Residue. *Microchem. J.* 2011, 99 (2), 296–302. <https://doi.org/10.1016/j.microc.2011.05.021>
24. SANZ CARBONELL, J. F. TRATAMIENTO DE AGUAS TEXTILES INDUSTRIALES MEDIANTE FOTOCATÁLISIS SOLAR Y REUTILIZACIÓN EN NUEVAS TINTURAS Doctoral Thesis, Universitat Politècnica de València. 2016.
25. Chorawalaa, K. K.; Mehta, M. J. Applications of Nanotechnology in Wastewater Treatment. *Int J Innov Emerg Res Eng* 2015, 2 (1), 21–26.
26. Sayan, B.; Indranil, S.; Aniruddha, M.; Dhruvajyoti, C.; Uday, C. G.; Debashis, C. Role of Nanotechnology in Water Treatment and Purification: Potential Applications and Implications. *Int J Chem Sci Technol* 2013, 3 (3), 59.
27. Hua, M.; Zhang, S.; Pan, B.; Zhang, W.; Lv, L.; Zhang, Q. Heavy Metal Removal from Water/Wastewater by Nanosized Metal Oxides: A Review. *J. Hazard. Mater.* 2012, 211, 317–331. <https://doi.org/10.1016/j.jhazmat.2011.10.016>

28. Kumar, R.; Chawla, J. Removal of Cadmium Ion from Water/Wastewater by Nano-Metal Oxides: A Review. *Water Qual. Expo. Heal.* 2014, 5 (4), 215–226. <https://doi.org/10.1007/s12403-013-0100-8>
29. Rajput, S.; Pittman Jr, C. U.; Mohan, D. Magnetic Magnetite (Fe₃O₄) Nanoparticle Synthesis and Applications for Lead (Pb²⁺) and Chromium (Cr⁶⁺) Removal from Water. *J. Colloid Interface Sci.* 2016, 468, 334–346. <https://doi.org/10.1016/j.jcis.2015.12.008>
30. Cheriyaundath, S.; Vavilala, S. L. Nanotechnology-based Wastewater Treatment. *Water Environ. J.* 2021, 35 (1), 123–132. <https://doi.org/10.1111/wej.12610>
31. Gupta, V. K.; Saleh, T. A. Sorption of Pollutants by Porous Carbon, Carbon Nanotubes and Fullerene-an Overview. *Environ. Sci. Pollut. Res.* 2013, 20 (5), 2828–2843. <https://doi.org/10.1007/s11356-013-1524-1>
32. Iannazzo, D.; Pistone, A.; Zicarelli, I.; Espro, C.; Galvagno, S.; Giofré, S. V.; Romeo, R.; Cicero, N.; Bua, G. D.; Lanza, G. Removal of Heavy Metal Ions from Wastewaters Using Dendrimer-Functionalized Multi-Walled Carbon Nanotubes. *Environ. Sci. Pollut. Res.* 2017, 24 (17), 14735–14747. <https://doi.org/10.1007/s11356-017-9086-2>
33. Zhao, M.; Xu, Y.; Zhang, C.; Rong, H.; Zeng, G. New Trends in Removing Heavy Metals from Wastewater. *Appl. Microbiol. Biotechnol.* 2016, 100 (15), 6509–6518. <https://doi.org/10.1007/s00253-016-7646-x>
34. Pendergast, M. M.; Hoek, E. M. V. A Review of Water Treatment Membrane Nanotechnologies. *Energy Environ. Sci.* 2011, 4 (6), 1946–1971. <https://doi.org/10.1039/C0EE00541J>
35. Zhang, L.; Chen, B.; Ghaffar, A.; Zhu, X. Nanocomposite Membrane with Polyethylenimine-Grafted Graphene Oxide as a Novel Additive to Enhance Pollutant Filtration Performance. *Environ. Sci. Technol.* 2018, 52 (10), 5920–5930. <https://doi.org/10.1021/acs.est.8b00524>
36. Peng, K.; Yang, H. Carbon Hybridized Montmorillonite Nanosheets: Preparation, Structural Evolution and Enhanced Adsorption Performance. *Chem. Commun.* 2017, 53 (45), 6085–6088. <https://doi.org/10.1039/C7CC02334K>
37. Sharma, V.; Sharma, A. Nanotechnology: An Emerging Future Trend in Wastewater Treatment with Its Innovative Products and Processes. *Nanotechnology* 2012, 1 (2).
38. Wang, J.-C.; Lou, H.-H.; Xu, Z.-H.; Cui, C.-X.; Li, Z.-J.; Jiang, K.; Zhang, Y.-P.; Qu, L.-B.; Shi, W. Natural Sunlight Driven Highly Efficient Photocatalysis for Simultaneous Degradation of Rhodamine B and Methyl Orange Using I/C Codoped TiO₂ Photocatalyst. *J. Hazard. Mater.* 2018, 360, 356–363. <https://doi.org/10.1016/j.jhazmat.2018.08.008>

39. Zhang, X.; Ma, Y.; Xi, L.; Zhu, G.; Li, X.; Shi, D.; Fan, J. Highly Efficient Photocatalytic Removal of Multiple Refractory Organic Pollutants by BiVO₄/CH₃COO (BiO) Heterostructured Nanocomposite. *Sci. Total Environ.* 2019, *647*, 245–254. <https://doi.org/10.1016/j.scitotenv.2018.07.450>
40. Ramakrishna, K. R.; Viraraghavan, T. Dye Removal Using Low Cost Adsorbents. *Water Sci. Technol.* 1997, *36* (2–3), 189–196. [https://doi.org/10.1016/S0273-1223\(97\)00387-9](https://doi.org/10.1016/S0273-1223(97)00387-9)
41. Clarke, E. A.; Anliker, R. Organic Dyes and Pigments. In *Anthropogenic compounds*; Springer, 1980; pp 181–215. https://doi.org/10.1007/978-3-540-38522-6_7
42. Zollinger, H. Color Chemistry: Syntheses. *Prop. Appl. Org. Dye. Pigment. Verlag Helv. Chim. Acta, Zürich* 2003, 15–65.
43. Akarslan, F.; Demiralay, H. Effects of Textile Materials Harmful to Human Health. *Acta Phys. Pol. A* 2015, *128* (2B), 407–409.
44. Anliker, R. Color Chemistry and the Environment. *Ecotoxicol. Environ. Saf.* 1977, *1* (2), 211–237. [https://doi.org/10.1016/0147-6513\(77\)90037-9](https://doi.org/10.1016/0147-6513(77)90037-9)
45. Clement, R. E.; Koester, C. J.; Eiceman, G. A. Environmental Analysis. *Anal. Chem.* 1993, *65* (12), 85–116. <https://doi.org/10.1021/ac00060a007>
46. Tchobanoglous, G.; Burton, F. L.; Stensel, H. D. Wastewater Engineering. *Management* 1991, *7* (1), 4.
47. Pollard, S. J. T.; Fowler, G. D.; Sollars, C. J.; Perry, R. Low-Cost Adsorbents for Waste and Wastewater Treatment: A Review. *Sci. Total Environ.* 1992, *116* (1–2), 31–52. [https://doi.org/10.1016/0048-9697\(92\)90363-W](https://doi.org/10.1016/0048-9697(92)90363-W)
48. Andreo-Martínez, P.; García-Martínez, N.; Almela, L. Domestic Wastewater Depuration Using a Horizontal Subsurface Flow Constructed Wetland and Theoretical Surface Optimization: A Case Study under Dry Mediterranean Climate. *Water (Switzerland)* 2016, *8* (10), 1–18. <https://doi.org/10.3390/w8100434>
49. Cossu, R.; Fantinato, G.; Pivato, A.; Sandon, A. Further Steps in the Standardization of BOD₅/COD Ratio as a Biological Stability Index for MSW. *Waste Manag.* 2017, *68*, 16–23. <https://doi.org/10.1016/j.wasman.2017.06.035>
50. Cossu, R.; Lai, T.; Sandon, A. Standardization of BOD₅/COD Ratio as a Biological Stability Index for MSW. *Waste Manag.* 2012, *32* (8), 1503–1508. <https://doi.org/10.1016/j.wasman.2012.04.001>
51. Cazaudehore, G.; Schraauwers, B.; Peyrelasse, C.; Lagnet, C.; Monlau, F. Determination of Chemical Oxygen Demand of Agricultural Wastes by Combining Acid Hydrolysis and Commercial COD Kit Analysis. *J. Environ. Manage.* 2019, *250* (September), 109464. <https://doi.org/10.1016/j.jenvman.2019.109464>

52. Ghorbani, M.; Salem, S. Solar Treatment of Sewage Discharged from Industrial Estate for Reduction of Chemical Oxygen Demand over Degussa P-25 Titania. *Chemosphere* 2020, No. xxxx, 129123. <https://doi.org/10.1016/j.jenvman.2019.109464>
53. Fronczyk, J.; Radziemska, M.; Dynowski, P.; Mazur, Z.; Bazydło, M. Quality of Water in the Road Drainage Systems in the Warsaw Agglomeration, Poland. *Water (Switzerland)* 2016, 8 (10), 1–12. <https://doi.org/10.3390/w8100429>.
54. Ma, J.; Liu, L.; Xue, Q.; Yang, Y.; Zhang, Y.; Fei, X. A Systematic Assessment of Aeration Rate Effect on Aerobic Degradation of Municipal Solid Waste Based on Leachate Chemical Oxygen Demand Removal. *Chemosphere* 2021, 263, 128218. <https://doi.org/10.1016/j.chemosphere.2020.128218>.
55. Patel, N.; Ruparelia, J.; Barve, J. Prediction of Total Suspended Solids Present in Effluent of Primary Clarifier of Industrial Common Effluent Treatment Plant: Mechanistic and Fuzzy Approach. *J. Water Process Eng.* 2020, 34, 101146. <https://doi.org/https://doi.org/10.1016/j.jwpe.2020.101146>.
56. Crespi, M. Reutilización de Los Efluentes Textiles En Europa. *Boletín INTEXTER* 1989, 96, 87–106.
57. Ren, J.; Zhang, A.; Wang, X. Jo Ur Na I P Re. *Pharmacol. Res.* 2020, 104743. <https://doi.org/10.1016/j.chemosphere.2020.129345>.
58. Skuse, C.; Gallego-Schmid, A.; Azapagic, A.; Gorgojo, P. Can Emerging Membrane-Based Desalination Technologies Replace Reverse Osmosis? *Desalination* 2020, No. October, 114844. <https://doi.org/10.1016/j.desal.2020.114844>.
59. Rahimi, B.; Shirvani, H.; Asghar, A.; Farhadi, F. A Feasibility Study of Solar-Powered Reverse Osmosis Processes Kingdom of Saudi Arabia. *Desalination* 2020, No. October, 114885. <https://doi.org/10.1016/j.desal.2020.114885>.
60. Ozbey-Unal, B.; Omwene, P. I.; Yagcioglu, M.; Balcik-Canbolat, Ç.; Karagunduz, A.; Keskinler, B.; Dizge, N. Treatment of Organized Industrial Zone Wastewater by Microfiltration/Reverse Osmosis Membrane Process for Water Recovery: From Lab to Pilot Scale. *J. Water Process Eng.* 2020, 38 (September), 101646. <https://doi.org/10.1016/j.jwpe.2020.101646>.
61. Lebron, Y. A. R.; Moreira, V. R.; Furtado, T. P. B.; da Silva, S. C.; Lange, L. C.; Amaral, M. C. S. Vinasse Treatment Using Hybrid Tannin-Based Coagulation-Microfiltration-Nanofiltration Processes: Potential Energy Recovery, Technical and Economic Feasibility Assessment. *Sep. Purif. Technol.* 2020, 248 (May), 117152. <https://doi.org/10.1016/j.seppur.2020.117152>.
62. Manouchehri, M.; Kargari, A. Water Recovery from Laundry Wastewater by the Cross Flow Microfiltration Process: A Strategy for Water Recycling in Residential Buildings. *J. Clean. Prod.* 2017, 168, 227–238.

<https://doi.org/10.1016/j.jclepro.2017.08.211>.

63. Ağtaş, M.; Yılmaz, Ö.; Dilaver, M.; Alp, K.; Koyuncu, İ. Hot Water Recovery and Reuse in Textile Sector with Pilot Scale Ceramic Ultrafiltration/Nanofiltration Membrane System. *J. Clean. Prod.* 2020, 256, 120359. <https://doi.org/https://doi.org/10.1016/j.jclepro.2020.120359>.
64. Selvaraj, H.; Chandrasekaran, K.; Murugan, R.; Sundaram, M. An Integrated Biological and Electrochemical Process for Recovery of Sulfur from an Industrial Effluent Contaminated Pond Water and Its Preliminary Application in High Performance Battery. *Sep. Purif. Technol.* 2017, 180, 133–141. <https://doi.org/10.1016/j.seppur.2017.01.069>.
65. Ma, C.; Pei, S.; You, S. Closed Bipolar Electrode for Decoupled Electrochemical Water Decontamination and Hydrogen Recovery. *Electrochem. commun.* 2019, 109 (73), 106611. <https://doi.org/10.1016/j.elecom.2019.106611>.
66. Chen, P.; Yin, D.; Song, P.; Liu, Y.; Cai, L.; Wang, H.; Zhang, L. Demulsification and Oil Recovery from Oil-in-Water Cutting Fluid Wastewater Using Electrochemical Micromembrane Technology. *J. Clean. Prod.* 2020, 244, 118698. <https://doi.org/10.1016/j.jclepro.2019.118698>.
67. Buscio Olivera, V. Tratamiento y Reutilización de Efluentes de La Industria Textil Mediante Técnicas de Membranas. *TDX (Tesis Dr. en Xarxa)* 2015.
68. Cheng, D.; Liu, Y.; Ngo, H. H.; Guo, W.; Chang, S. W.; Nguyen, D. D.; Zhang, S.; Luo, G.; Liu, Y. A Review on Application of Enzymatic Bioprocesses in Animal Wastewater and Manure Treatment. *Bioresour. Technol.* 2020, 313 (May), 123683. <https://doi.org/10.1016/j.biortech.2020.123683>.
69. He, H.; Zhang, X.; Yang, C.; Zeng, G.; Li, H.; Chen, Y. Treatment of Organic Wastewater Containing High Concentration of Sulfate by Crystallization-Fenton-SBR. *J. Environ. Eng.* 2018, 144 (6), 4018041.
70. Shao, J.; Cheng, Y.; Yang, C.; Zeng, G.; Liu, W.; Jiao, P.; He, H. Efficient Removal of Naphthalene-2-Ol from Aqueous Solutions by Solvent Extraction. *J. Environ. Sci.* 2016, 47, 120–129. <https://doi.org/10.1016/j.jes.2016.03.010>
71. Ordonez, D.; Valencia, A.; Chang, N.-B.; Wanielista, M. P. Synergistic Effects of Aluminum/Iron Oxides and Clay Minerals on Nutrient Removal and Recovery in Water Filtration Media. *J. Clean. Prod.* 2020, 275, 122728. <https://doi.org/https://doi.org/10.1016/j.jclepro.2020.122728>.
72. Hube, S.; Eskafi, M.; Hrafnkelsdóttir, K. F.; Bjarnadóttir, B.; Bjarnadóttir, M. Á.; Axelsdóttir, S.; Wu, B. Direct Membrane Filtration for Wastewater Treatment and Resource Recovery: A Review. *Sci. Total Environ.* 2020, 710, 136375. <https://doi.org/https://doi.org/10.1016/j.scitotenv.2019.136375>.

73. Rh, R.; Siberian, E. Comparative Analysis of Far East Sikhotinsky.
74. Zhang, W.; Zhang, D.; Liang, Y. Nanotechnology in Remediation of Water Contaminated by Poly- and Perfluoroalkyl Substances: A Review. *Environ. Pollut.* 2019, 247, 266–276. <https://doi.org/10.1016/J.ENVPOL.2019.01.045>.
75. Yang, Y.; Han, S.; Fan, Q.; Ugbohue, S. C. Nanoclay and Modified Nanoclay as Sorbents for Anionic, Cationic and Nonionic Dyes. *Text. Res. J.* 2005, 75 (8), 622–627. <https://doi.org/10.1177/0040517505053948>.
76. Micó Vicent, Barbara; Martínez Verdu, F. M.; Gilabert Pérez, J. E. Optimización de La Síntesis de Nanopigmentos de Origen Natural Para Biopolímeros Mediante El Uso Del Diseño de Experimentos. <https://dx.doi.org/10.4995/Thesis/10251/59449>
77. Chong, A. S.; Manan, M. A.; Idris, A. K. Readiness of Lignosulfonate Adsorption onto Montmorillonite. *Colloids Surfaces A Physicochem. Eng. Asp.* 2021, 628 (June), 127318. <https://doi.org/10.1016/j.colsurfa.2021.127318>.
78. Alexandre, M.; Dubois, P. Polymer-Layered Silicate Nanocomposites: Preparation, Properties and Uses of a New Class of Materials. *Mater. Sci. Eng. R Reports* 2000, 28 (1–2), 1–63. [https://doi.org/10.1016/S0927-796X\(00\)00012-7](https://doi.org/10.1016/S0927-796X(00)00012-7)
79. Emmerich, K.; Kahr, G. The Cis-and Trans-Vacant Variety of a Montmorillonite: An Attempt to Create a Model Smectite. *Appl. Clay Sci.* 2001, 20 (3), 119–127. [https://doi.org/10.1016/S0169-1317\(01\)00065-5](https://doi.org/10.1016/S0169-1317(01)00065-5)
80. Li, J.; Cai, J.; Zhong, L.; Cheng, H.; Wang, H.; Ma, Q. Adsorption of Reactive Red 136 onto Chitosan/Montmorillonite Intercalated Composite from Aqueous Solution. *Appl. Clay Sci.* 2019, 167, 9–22. <https://doi.org/10.1016/J.CLAY.2018.10.003>.
81. Zhu, T. T.; Zhou, C. H.; Kabwe, F. B.; Wu, Q. Q.; Li, C. S.; Zhang, J. R. Exfoliation of Montmorillonite and Related Properties of Clay/Polymer Nanocomposites. *Appl. Clay Sci.* 2019, 169, 48–66. <https://doi.org/10.1016/J.CLAY.2018.12.006>.
82. T.R., G.; D., M.; P.B., U.; K., S.; Fahad, F. F.; C.M., F.; P.M., D.; M., N.; K.K., B. Montmorillonite and Phosphorus Enrichment in Sediments as the Causative Factor for Mud Bank Formation along the Southwest Coast of India. *Reg. Stud. Mar. Sci.* 2020, 40, 101517. <https://doi.org/10.1016/j.rsma.2020.101517>.
83. Zheng, R.; Liu, D.; Tang, J.; Song, Q.; Yao, Q. Analysis of Montmorillonite Affecting Coke Formation during the Thermal Conversion of Heavy Oil. *Fuel* 2020, No. November, 119687. <https://doi.org/10.1016/j.fuel.2020.119687>.
84. Yan, H.; Zhang, Z. Effect and Mechanism of Cation Species on the Gel Properties of Montmorillonite. *Colloids Surfaces A Physicochem. Eng. Asp.* 2020, No. November, 125824. <https://doi.org/10.1016/j.colsurfa.2020.125824>.
85. Hojiyev, R.; Ulcay, Y.; Çelik, M. S.; Carty, W. M. Effect of CEC Coverage of

- Hexadecyltributylphosphonium Modified Montmorillonite on Polymer Compatibility. *Appl. Clay Sci.* 2017, *141*, 204–211. <https://doi.org/10.1016/j.clay.2017.02.036>.
86. Manning, D. A. C. Handbook of Clay Science (Developments in Clay Science, 1)- Edited by F. Bergaya, BKG Theng & G. Lagaly. Wiley Online Library 2007. https://doi.org/10.1111/j.1365-2389.2007.00898_4.x
87. Capková, P.; Driessen, R. A. J.; Schenk, H.; Weiss, Z. Interlayer Porosity in Montmorillonite Intercalated with Keggin-like Cation Studied by Molecular Mechanics Simulation. *Mol. Model. Annu.* 1997, *3* (11), 467–472. <https://doi.org/10.1007/s008940050064>
88. Vazquez, A.; López, M.; Kortaberria, G.; Martín, L.; Mondragon, I. Modification of Montmorillonite with Cationic Surfactants. Thermal and Chemical Analysis Including CEC Determination. *Appl. Clay Sci.* 2008, *41* (1–2), 24–36. <https://doi.org/10.1016/j.clay.2007.10.001>.
89. Zhu, H. Y.; Gao, W. H.; Vansant, E. F. The Porosity and Water Adsorption of Alumina Pillared Montmorillonite. *J. Colloid Interface Sci.* 1995, *171* (2), 377–385. <https://doi.org/10.1006/jcis.1995.1193>
90. Laird, D. A.; Shang, C. Relationship between Cation Exchange Selectivity and Crystalline Swelling in Expanding 2: 1 Phyllosilicates. *Clays Clay Miner.* 1997, *45* (5), 681–689. <https://doi.org/10.1346/CCMN.1997.0450507>
91. Wang, C.-C.; Juang, L.-C.; Hsu, T.-C.; Lee, C.-K.; Lee, J.-F.; Huang, F.-C. Adsorption of Basic Dyes onto Montmorillonite. *J. Colloid Interface Sci.* 2004, *273* (1), 80–86. <https://doi.org/10.1016/j.jcis.2003.12.028>
92. Fahn, R.; Fenderl, K. Reaction Products of Organic Dye Molecules with Acid-Treated Montmorillonite. *Clay Miner.* 1983, *18* (4), 447–458. <https://doi.org/10.1180/claymin.1983.018.4.10>
93. Mishael, Y. G.; Rytwo, G.; Nir, S.; Crespin, M.; Annabi-Bergaya, F.; Van Damme, H. Interactions of Monovalent Organic Cations with Pillared Clays. *J. Colloid Interface Sci.* 1999, *209* (1), 123–128. <https://doi.org/10.1006/jcis.1998.5896>
94. Penner, D.; Lagaly, G. Influence of Organic and Inorganic Salts on the Coagulation of Montmorillonite Dispersions. *Clays Clay Miner.* 2000, *48* (2), 246–255. <https://doi.org/10.1346/CCMN.2000.0480211>
95. Janek, M.; Lagaly, G. Proton Saturation and Rheological Properties of Smectite Dispersions. *Appl. Clay Sci.* 2001, *19* (1–6), 121–130. [https://doi.org/10.1016/S0169-1317\(01\)00051-5](https://doi.org/10.1016/S0169-1317(01)00051-5)
96. Antúnez-García, J.; Galván, D. H.; Petranovskii, V.; Murrieta-Rico, F. N.; Yocupicio-Gaxiola, R. I.; Shelyapina, M. G.; Fuentes-Moyado, S. The Effect of Chemical

- Composition on the Properties of LTA Zeolite: A Theoretical Study. *Comput. Mater. Sci.* 2021, 196 (May). <https://doi.org/10.1016/j.commatsci.2021.110557>.
97. Mittal, H.; Babu, R.; Dabbawala, A. A.; Stephen, S.; Alhassan, S. M. Zeolite-Y Incorporated Karaya Gum Hydrogel Composites for Highly Effective Removal of Cationic Dyes. *Colloids Surfaces A Physicochem. Eng. Asp.* 2020, 586, 124161. <https://doi.org/10.1016/J.COLSURFA.2019.124161>.
98. Khaleque, A.; Alam, M. M.; Hoque, M.; Mondal, S.; Haider, J. Bin; Xu, B.; Johir, M. A. H.; Karmakar, A. K.; Zhou, J. L.; Ahmed, M. B.; Moni, M. A. Zeolite Synthesis from Low-Cost Materials and Environmental Applications: A Review. *Environ. Adv.* 2020, 2 (August), 100019. <https://doi.org/10.1016/j.envadv.2020.100019>.
99. Si, D.; Zhu, M.; Sun, X.; Xue, M.; Li, Y.; Wu, T.; Gui, T.; Kumakiri, I.; Chen, X.; Kita, H. Formation Process and Pervaporation of High Aluminum ZSM-5 Zeolite Membrane with Fluoride-Containing and Organic Template-Free Gel. *Sep. Purif. Technol.* 2021, 257 (September 2020), 117963. <https://doi.org/10.1016/j.seppur.2020.117963>.
100. Lo, A. Y.; Taghipour, F. Review and Prospects of Microporous Zeolite Catalysts for CO₂ Photoreduction. *Appl. Mater. Today* 2021, 23. <https://doi.org/10.1016/j.apmt.2021.101042>.
101. He, C.; Zhang, X.; Yu, J.; Xiang, Y.; Deng, L.; Zhao, S.; Gao, J.; Yuan, Y.; Lei, Y. Study on Adsorption Performance and Mechanism of Cr (VI) by Zn-LDHs Coating on Zeolites and Quartz Sands. *Acta Sci. Circumstantiae* 2019, 39 (2), 399–409. <https://doi.org/10.1016/j.cej.2019.122578>
102. Wang, C.; Cao, L.; Huang, J. Influences of Acid and Heat Treatments on the Structure and Water Vapor Adsorption Property of Natural Zeolite. *Surf. Interface Anal.* 2017, 49 (12), 1249–1255. <https://doi.org/10.1002/sia.6321>
103. Probst, J.; Outram, J. G.; Couperthwaite, S. J.; Millar, G. J.; Kaparaju, P. Sustainable Ammonium Recovery from Wastewater: Improved Synthesis and Performance of Zeolite N Made from Kaolin. *Microporous Mesoporous Mater.* 2021, 316 (November 2020), 110918. <https://doi.org/10.1016/j.micromeso.2021.110918>.
104. ZHU, J.; WANG, N. APPLICATIONS OF NATURAL ZEOLITES TO ENVIRONMENTAL PROTECTION [J]. *Acta Mineral. Sin.* 2003, 3. <https://doi.org/10.1515/9781501508585>
105. Kaijun, W.; Wenyan, H. E.; Kuo, F. Analysis of the Application of Typical Ion Exchange Water Treatment Technology in Low Concentration Ammonia Nitrogen Recovery. *Chinese J. Environ. Eng.* 2019, 13 (10), 2285–2301. <https://doi.org/10.12030/j.cjee.201903150>
106. Sharma, R.; Segato, T.; Delplancke, M.-P.; Terry, H.; Baron, G. V.; Denayer, J. F. M.; Cousin-Saint-Remi, J. Hydrogen Chloride Removal from Hydrogen Gas by Adsorption on Hydrated Ion-Exchanged Zeolites. *Chem. Eng. J.* 2020, 381, 122512.

<https://doi.org/10.1016/j.cej.2019.122512>

107. Shi, Y.; Sun, K. Preparation of Diphenylcarbazide-Directed CdSe Quantum Dots and Selective Determination for Cr (VI). *J. Wuhan Univ. Technol. Sci. Ed.* 2016, *31* (5), 972–976. <https://doi.org/10.1007/s11595-016-1477-6>
108. Breck, D. W. *Zeolite Molecular Sieves: Structure, Chemistry and Use*; Krieger, 1984. [https://doi.org/10.1016/S0167-2991\(08\)63608-3](https://doi.org/10.1016/S0167-2991(08)63608-3)
109. Wajima, T.; Yoshizuka, K.; Hirai, T.; Ikegami, Y. Synthesis of Zeolite X from Waste Sandstone Cake Using Alkali Fusion Method. *Mater. Trans.* 2008, *49* (3), 612–618.
110. Shoppert, A. A.; Loginova, I. V.; Chaikin, L. I.; Rogozhnikov, D. A. Alkali Fusion-Leaching Method for Comprehensive Processing of Fly Ash. *KnE Mater. Sci.* 2017, 89–96.
111. Tsujiguchi, M.; Kobashi, T.; Oki, M.; Utsumi, Y.; Kakimori, N.; Nakahira, A. Synthesis and Characterization of Zeolite A from Crushed Particles of Aluminoborosilicate Glass Used in LCD Panels. *J. Asian Ceram. Soc.* 2014, *2* (1), 27–32.
112. Perot, G.; Guisnet, M. Advantages and Disadvantages of Zeolites as Catalysts in Organic Chemistry. *J. Mol. Catal.* 1990, *61* (2), 173–196.
113. Parades-Aguilar, J.; Reyes-Martínez, V.; Bustamante, G.; Almendáriz-Tapia, F. J.; Martínez-Meza, G.; Vílchez-Vargas, R.; Link, A.; Certucha-Barragán, M. T.; Calderón, K. Removal of Nickel (II) from Wastewater Using a Zeolite-Packed Anaerobic Bioreactor: Bacterial Diversity and Community Structure Shifts. *J. Environ. Manage.* 2021, *279*, 111558.
114. Saqib, N. U.; Adnan, R.; Rahim, M.; Khan, A. Low-Cost Zeolite/TiO₂ Composite for the Photocatalytically Enhanced Adsorption of Cd²⁺ from Aqueous Solution. *J. Iran. Chem. Soc.* 2021, 1–16.
115. Lvov, Y. M.; DeVilliers, M. M.; Fakhruddin, R. F. The Application of Halloysite Tubule Nanoclay in Drug Delivery. *Expert Opin. Drug Deliv.* 2016, *13* (7), 977–986.
116. Liu, M.; Jia, Z.; Jia, D.; Zhou, C. Recent Advance in Research on Halloysite Nanotubes-Polymer Nanocomposite. *Prog. Polym. Sci.* 2014, *39* (8), 1498–1525.
117. Lazaratou, C. V.; Panagiotaras, D.; Panagopoulos, G.; Pospíšil, M.; Papoulis, D. Ca Treated Palygorskite and Halloysite Clay Minerals for Ferrous Iron (Fe²⁺) Removal from Water Systems. *Environ. Technol. Innov.* 2020, *19*, 100961. <https://doi.org/10.1016/j.eti.2020.100961>.
118. Van Ranst, E.; Kips, P.; Mbogoni, J.; Mees, F.; Dumon, M.; Delvaux, B. Halloysite-Smectite Mixed-Layered Clay in Fluvio-Volcanic Soils at the Southern Foot of Mount Kilimanjaro, Tanzania. *Geoderma* 2020, *375* (May), 114527. <https://doi.org/10.1016/j.geoderma.2020.114527>.

119. Zhao, N.; Liu, Y.; Zhao, X.; Song, H. Liquid Crystal Self-Assembly of Halloysite Nanotubes in Ionic Liquids: A Novel Soft Nanocomposite Ionogel Electrolyte with High Anisotropic Ionic Conductivity and Thermal Stability. *Nanoscale* 2016, 8 (3), 1545–1554.
120. Lazzara, G.; Cavallaro, G.; Panchal, A.; Fakhruddin, R.; Stavitskaya, A.; Vinokurov, V.; Lvov, Y. An Assembly of Organic-Inorganic Composites Using Halloysite Clay Nanotubes. *Curr. Opin. Colloid Interface Sci.* 2018, 35, 42–50.
121. Yendluri, R.; Otto, D. P.; De Villiers, M. M.; Vinokurov, V.; Lvov, Y. M. Application of Halloysite Clay Nanotubes as a Pharmaceutical Excipient. *Int. J. Pharm.* 2017, 521 (1–2), 267–273.
122. Yuan, P.; Tan, D.; Annabi-Bergaya, F. Properties and Applications of Halloysite Nanotubes: Recent Research Advances and Future Prospects. *Appl. Clay Sci.* 2015, 112, 75–93.
123. Pasbakhsh, P.; Churchman, G. J.; Keeling, J. L. Characterisation of Properties of Various Halloysites Relevant to Their Use as Nanotubes and Microfibre Fillers. *Appl. Clay Sci.* 2013, 74, 47–57.
124. Makaremi, M.; Pasbakhsh, P.; Cavallaro, G.; Lazzara, G.; Aw, Y. K.; Lee, S. M.; Milioto, S. Effect of Morphology and Size of Halloysite Nanotubes on Functional Pectin Bionanocomposites for Food Packaging Applications. *ACS Appl. Mater. Interfaces* 2017, 9 (20), 17476–17488.
125. Cavallaro, G.; Chiappisi, L.; Pasbakhsh, P.; Gradzielski, M.; Lazzara, G. A Structural Comparison of Halloysite Nanotubes of Different Origin by Small-Angle Neutron Scattering (SANS) and Electric Birefringence. *Appl. Clay Sci.* 2018, 160, 71–80.
126. Agafonov, A. V.; Kudryakova, N. O.; Ramenskaya, L. M.; Grishina, E. P. The Confinement and Anion Type Effect on the Physicochemical Properties of Ionic Liquid/Halloysite Nanoclay Ionogels. *Arab. J. Chem.* 2020, 13 (12), 9090–9104. <https://doi.org/10.1016/j.arabjc.2020.10.033>.
127. Blagojević, B.; Četojević-Simin, D.; Parisi, F.; Lazzara, G.; Popović, B. M. Halloysite Nanotubes as a Carrier of Cornelian Cherry (*Cornus Mas L.*) Bioactives. *Lwt* 2020, 134 (June). <https://doi.org/10.1016/j.lwt.2020.110247>.
128. Zhang, B.; Yuan, P.; Guo, H.; Deng, L.; Li, Y.; Li, L.; Wang, Q.; Liu, D. Effect of Curing Conditions on the Microstructure and Mechanical Performance of Geopolymers Derived from Nanosized Tubular Halloysite. *Constr. Build. Mater.* 2020, No. xxxx, 121186. <https://doi.org/10.1016/j.conbuildmat.2020.121186>.
129. Luo, P.; Zhao, Y.; Zhang, B.; Liu, J.; Yang, Y.; Liu, J. Study on the Adsorption of Neutral Red from Aqueous Solution onto Halloysite Nanotubes. *Water Res.* 2010, 44 (5), 1489–1497. <https://doi.org/10.1016/j.watres.2009.10.042>

130. Liu, W.; Fizir, M.; Hu, F.; Li, A.; Hui, X.; Zha, J.; He, H. Mixed Hemimicelle Solid-Phase Extraction Based on Magnetic Halloysite Nanotubes and Ionic Liquids for the Determination and Extraction of Azo Dyes in Environmental Water Samples. *J. Chromatogr. A* 2018, *1551*, 10–20. <https://doi.org/10.1016/j.chroma.2018.03.051>
131. Zhao, M.; Liu, P. Adsorption Behavior of Methylene Blue on Halloysite Nanotubes. *Microporous Mesoporous Mater.* 2008, *112* (1–3), 419–424. <https://doi.org/10.1016/j.micromeso.2007.10.018>
132. Luo, P.; Zhang, B.; Zhao, Y.; Wang, J.; Zhang, H.; Liu, J. Removal of Methylene Blue from Aqueous Solutions by Adsorption onto Chemically Activated Halloysite Nanotubes. *Korean J. Chem. Eng.* 2011, *28* (3), 800–807. <https://doi.org/10.1007/s11814-010-0426-x>
133. Liu, Y.; Zheng, Y.; Wang, A. Response Surface Methodology for Optimizing Adsorption Process Parameters for Methylene Blue Removal by a Hydrogel Composite. *Adsorpt. Sci. Technol.* 2010, *28* (10), 913–922.
134. Liu, L.; Wan, Y.; Xie, Y.; Zhai, R.; Zhang, B.; Liu, J. The Removal of Dye from Aqueous Solution Using Alginate-Halloysite Nanotube Beads. *Chem. Eng. J.* 2012, *187*, 210–216. <https://doi.org/10.1016/j.cej.2012.01.136>
135. Peng, Q.; Liu, M.; Zheng, J.; Zhou, C. Adsorption of Dyes in Aqueous Solutions by Chitosan–Halloysite Nanotubes Composite Hydrogel Beads. *Microporous Mesoporous Mater.* 2015, *201*, 190–201. <https://doi.org/10.1016/j.micromeso.2014.09.003>
136. Jiang, L.; Zhang, C.; Wei, J.; Tjiu, W.; Pan, J.; Chen, Y.; Liu, T. Surface Modifications of Halloysite Nanotubes with Superparamagnetic Fe₃O₄ Nanoparticles and Carbonaceous Layers for Efficient Adsorption of Dyes in Water Treatment. *Chem. Res. Chinese Univ.* 2014, *30* (6), 971–977. <https://doi.org/10.1007/s40242-014-4218-4>
137. Nguyen, T. K. L.; Cao, X. T.; Park, C.; Lim, K. T. Preparation, Characterization and Application of Magnetic Halloysite Nanotubes for Dye Removal. *Mol. Cryst. Liq. Cryst.* 2017, *644* (1), 153–159. <https://doi.org/10.1080/15421406.2016.1277465>
138. Wan, X.; Zhan, Y.; Long, Z.; Zeng, G.; He, Y. Core@ Double-Shell Structured Magnetic Halloysite Nanotube Nano-Hybrid as Efficient Recyclable Adsorbent for Methylene Blue Removal. *Chem. Eng. J.* 2017, *330*, 491–504. <https://doi.org/10.1016/j.cej.2017.07.178>
139. Farrokhi-Rad, M.; Mohammadalipour, M.; Shahrabi, T. Electrophoretically Deposited Halloysite Nanotubes Coating as the Adsorbent for the Removal of Methylene Blue from Aqueous Solution. *J. Eur. Ceram. Soc.* 2018, *38* (10), 3650–3659. <https://doi.org/10.1016/j.jeurceramsoc.2018.03.048>
140. Liu, R.; Fu, K.; Zhang, B.; Mei, D.; Zhang, H.; Liu, J. Removal of Methyl Orange by

- Modified Halloysite Nanotubes. *J. Dispers. Sci. Technol.* 2012, 33 (5), 711–718. <https://doi.org/10.1080/01932691.2011.579855>
141. Chen, H.; Zhao, J.; Wu, J.; Yan, H. Selective Desorption Characteristics of Halloysite Nanotubes for Anionic Azo Dyes. *RSC Adv.* 2014, 4 (30), 15389–15393. <https://doi.org/10.1039/C3RA47561A>
142. Chen, H.; Yan, H.; Pei, Z.; Wu, J.; Li, R.; Jin, Y.; Zhao, J. Trapping Characteristic of Halloysite Lumen for Methyl Orange. *Appl. Surf. Sci.* 2015, 347, 769–776. <https://doi.org/10.1016/j.apsusc.2015.04.167>
143. Ferrarini, F.; Bonetto, L. R.; Crespo, J. S.; Giovanela, M. Removal of Congo Red Dye from Aqueous Solutions Using a Halloysite-Magnetite-Based Composite. *Water Sci. Technol.* 2016, 73 (9), 2132–2142. <https://doi.org/10.2166/wst.2016.060>
144. Bessaha, F.; Mahrez, N.; Bendenia, S.; Kasmi, F.; Marouf-Khelifa, K.; Khelifa, A. Characterization and Spectroscopic Study of a Heat-Treated and Acid-Leached Halloysite Used in Congo Red Adsorption. *Int. J. Intell. Eng. Syst.* 2017, 10 (3), 272–279. <https://doi.org/10.22266/ijies2017.0630.31>
145. Fard, F. S.; Akbari, S.; Pajootan, E.; Arami, M. Enhanced Acidic Dye Adsorption onto the Dendrimer-Based Modified Halloysite Nanotubes. *Desalin. Water Treat.* 2016, 57 (54), 26222–26239. <https://doi.org/10.1080/19443994.2016.1160437>
146. Zango, Z. U.; Abu Bakar, N. H. H.; Tan, W. L.; Bakar, M. A. Enhanced Removal Efficiency of Methyl Red via the Modification of Halloysite Nanotubes by Copper Oxide. *J. Dispers. Sci. Technol.* 2018, 39 (1), 148–154. <https://doi.org/10.1080/01932691.2017.1301259>
147. Cavallaro, G.; Gianguzza, A.; Lazzara, G.; Milioto, S.; Piazzese, D. Alginate Gel Beads Filled with Halloysite Nanotubes. *Appl. Clay Sci.* 2013, 72, 132–137. <https://doi.org/10.1016/j.clay.2012.12.001>
148. Kiani, G.; Dostali, M.; Rostami, A.; Khataee, A. R. Adsorption Studies on the Removal of Malachite Green from Aqueous Solutions onto Halloysite Nanotubes. *Appl. Clay Sci.* 2011, 54 (1), 34–39. <https://doi.org/10.1016/j.clay.2011.07.008>
149. Bessaha, F.; Marouf-Khelifa, K.; Batonneau-Gener, I.; Khelifa, A. Characterization and Application of Heat-Treated and Acid-Leached Halloysites in the Removal of Malachite Green: Adsorption, Desorption, and Regeneration Studies. *Desalin. Water Treat.* 2016, 57 (31), 14609–14621. <https://doi.org/10.1080/19443994.2015.1063090>
150. Duan, J.; Liu, R.; Chen, T.; Zhang, B.; Liu, J. Halloysite Nanotube-Fe₃O₄ Composite for Removal of Methyl Violet from Aqueous Solutions. *Desalination* 2012, 293, 46–52. <https://doi.org/10.1016/j.desal.2012.02.022>
151. Bonetto, L. R.; Ferrarini, F.; De Marco, C.; Crespo, J. S.; Guégan, R.; Giovanela, M.

- Removal of Methyl Violet 2B Dye from Aqueous Solution Using a Magnetic Composite as an Adsorbent. *J. Water Process Eng.* 2015, 6, 11–20. <https://doi.org/10.1016/j.jwpe.2015.02.006>
152. Tao, D.; Higaki, Y.; Ma, W.; Takahara, A. Halloysite Nanotube/Polyelectrolyte Hybrids as Adsorbents for the Quick Removal of Dyes from Aqueous Solution. *Chem. Lett.* 2015, 44 (11), 1572–1574. <https://doi.org/10.1246/cl.150727>
153. Desai, S.; Pandey, A.; Dahiya, M. S. Application of Halloysite Nanotubes in Removal of Auramine Y and Auramine O Dyes. *Int. J. PharmTech. Res.* 2017, 10, 62–76. <https://doi.org/10.1504/IJEWM.2016.076427>
154. Khatri, N.; Tyagi, S.; Rawtani, D. Removal of Basic Dyes Auramine Yellow and Auramine O by Halloysite Nanotubes. *Int. J. Environ. Waste Manag.* 2016, 17 (1), 44–59. <https://doi.org/10.1504/IJEWM.2016.076427>
155. Mudhoo, A.; Gautam, R. K.; Ncibi, M. C.; Zhao, F.; Garg, V. K.; Sillanpää, M. Green Synthesis, Activation and Functionalization of Adsorbents for Dye Sequestration. *Environ. Chem. Lett.* 2019, 17 (1), 157–193. <https://doi.org/10.1016/j.chemosphere.2017.03.030>
156. Riahi-Madvaar, R.; Taher, M. A.; Fazelirad, H. Synthesis and Characterization of Magnetic Halloysite-Iron Oxide Nanocomposite and Its Application for Naphthol Green B Removal. *Appl. Clay Sci.* 2017, 137, 101–106. <https://doi.org/10.1016/j.clay.2016.12.019>
157. Massaro, M.; Colletti, C. G.; Lazzara, G.; Guernelli, S.; Noto, R.; Riela, S. Synthesis and Characterization of Halloysite–Cyclodextrin Nanosponges for Enhanced Dyes Adsorption. *ACS Sustain. Chem. Eng.* 2017, 5 (4), 3346–3352. <https://doi.org/10.1021/acssuschemeng.6b03191>
158. Zhao, Y.; Abdullayev, E.; Vasiliev, A.; Lvov, Y. Halloysite Nanotubule Clay for Efficient Water Purification. *J. Colloid Interface Sci.* 2013, 406, 121–129. <https://doi.org/10.1016/j.jcis.2013.05.072>
159. Jinhua, W.; Xiang, Z.; Bing, Z.; Yafei, Z.; Rui, Z.; Jindun, L.; Rongfeng, C. Rapid Adsorption of Cr (VI) on Modified Halloysite Nanotubes. *Desalination* 2010, 259 (1–3), 22–28. <https://doi.org/10.1016/j.desal.2010.04.046>
160. Al-Beladi, A. A.; Kosa, S. A.; Wahab, R. A.; Salam, M. A. Removal of Orange G Dye from Water Using Halloysite Nanoclay-Supported ZnO Nanoparticles. *Desalin. WATER Treat.* 2020, 196, 287–298. <https://doi.org/10.5004/dwt.2020.25923>
161. Kanani-Jazi, M. H.; Akbari, S. Amino-Dendritic and Carboxyl Functionalized Halloysite Nanotubes for Highly Efficient Removal of Cationic and Anionic Dyes: Kinetic, Isotherm, and Thermodynamic Studies. *J. Environ. Chem. Eng.* 2021, 9 (3), 105214. <https://doi.org/10.1016/j.jece.2021.105214>

162. Brigatti, M. F.; Galan, E.; Theng, B. K. G. Structures and Mineralogy of Clay Minerals. *Dev. clay Sci.* 2006, *1*, 19–86. [https://doi.org/10.1016/S1572-4352\(05\)01002-0](https://doi.org/10.1016/S1572-4352(05)01002-0)
163. Sprynskyy, M.; Sokol, H.; Rafińska, K.; Brzozowska, W.; Railean-Plugaru, V.; Pomastowski, P.; Buszewski, B. Preparation of AgNPs/Saponite Nanocomposites without Reduction Agents and Study of Its Antibacterial Activity. *Colloids Surfaces B Biointerfaces* 2019, *180* (February), 457–465. <https://doi.org/10.1016/j.colsurfb.2019.04.066>.
164. Lima, L. C. B.; Silva, F. C.; Silva-Filho, E. C.; Fonseca, M. G.; Zhuang, G.; Jaber, M. Saponite-Anthocyanin Derivatives: The Role of Organoclays in Pigment Photostability. *Appl. Clay Sci.* 2020, *191* (December 2019), 105604. <https://doi.org/10.1016/j.clay.2020.105604>.
165. Brandão Lima, L. C.; Castro-Silva, F.; Silva-Filho, E. C.; Fonseca, M. G.; Jaber, M. Saponite-Anthocyanin Pigments: Slipping between the Sheets. *Microporous Mesoporous Mater.* 2020, *300* (December 2019). <https://doi.org/10.1016/j.micromeso.2020.110148>.
166. Fatimah, I.; Nurillahi, R.; Sahroni, I.; Muraza, O. TiO₂-Pillared Saponite and Photosensitization Using a Ruthenium Complex for Photocatalytic Enhancement of the Photodegradation of Bromophenol Blue. *Appl. Clay Sci.* 2019, *183*, 105302. <https://doi.org/https://doi.org/10.1016/j.clay.2019.105302>.
167. Kenne Dedzo, G.; Rigolet, S.; Josien, L.; Ngameni, E.; Dzene, L. Functionalization of Synthetic Saponite: Identification of Grafting Sites and Application for Anions Sequestration. *Appl. Surf. Sci.* 2021, *567* (April), 150911. <https://doi.org/10.1016/j.apsusc.2021.150911>.
168. Fernández-González, M. V.; Carretero, M. I.; Martín-García, J. M.; Molinero-García, A.; Delgado, R. Peloids Prepared with Three Mineral-Medicinal Waters from Spas in Granada. Their Suitability for Use in Pelotherapy. *Appl. Clay Sci.* 2021, *202* (December 2020). <https://doi.org/10.1016/j.clay.2020.105969>.
169. Casagrande, M.; Storaro, L.; Lenarda, M.; Rossini, S. Solid Acid Catalysts from Clays: Oligomerization of 1-Pentene on Al-Pillared Smectites. *Catal. Commun.* 2005, *6* (8), 568–572. <https://doi.org/10.1016/j.catcom.2005.05.005>
170. Takagi, S.; Shimada, T.; Ishida, Y.; Fujimura, T.; Masui, D.; Tachibana, H.; Eguchi, M.; Inoue, H. Size-Matching Effect on Inorganic Nanosheets: Control of Distance, Alignment, and Orientation of Molecular Adsorption as a Bottom-up Methodology for Nanomaterials. *Langmuir* 2013, *29* (7), 2108–2119. <https://doi.org/10.1021/la3034808>
171. Carrado, K. A.; Decarreau, A.; Petit, S.; Bergaya, F.; Lagaly, G. Synthetic Clay Minerals and Purification of Natural Clays. *Dev. clay Sci.* 2006, *1*, 115–139. [https://doi.org/10.1016/S1572-4352\(05\)01004-4](https://doi.org/10.1016/S1572-4352(05)01004-4)

172. Utracki, L. A.; Sepehr, M.; Boccaleri, E. Synthetic, Layered Nanoparticles for Polymeric Nanocomposites (PNCs). *Polym. Adv. Technol.* 2007, 18 (1), 1–37. <https://doi.org/10.1002/pat.852>
173. Franco, F.; Benítez-Guerrero, M.; Gonzalez-Triviño, I.; Pérez-Recuerda, R.; Assiego, C.; Cifuentes-Melchor, J.; Pascual-Cosp, J. Low-Cost Aluminum and Iron Oxides Supported on Dioctahedral and Trioctahedral Smectites: A Comparative Study of the Effectiveness on the Heavy Metal Adsorption from Water. *Appl. Clay Sci.* 2016, 119, 321–332. <https://doi.org/10.1016/j.clay.2015.10.035>
174. Suquet, H.; Iiyama, J. T.; Kodama, H.; Pezerat, H. Synthesis and Swelling Properties of Saponites with Increasing Layer Charge. *Clays Clay Miner.* 1977, 25 (3), 231–242. <https://doi.org/10.1346/CCMN.1977.0250310>
175. Klopogge, J. T.; Komarneni, S.; Amonette, J. E. Synthesis of Smectite Clay Minerals: A Critical Review. *Clays Clay Miner.* 1999, 47 (5), 529–554. <https://doi.org/10.1346/CCMN.1999.0470501>
176. Zhang, D.; Zhou, C.-H.; Lin, C.-X.; Tong, D.-S.; Yu, W.-H. Synthesis of Clay Minerals. *Appl. Clay Sci.* 2010, 50 (1), 1–11. <https://doi.org/10.1016/j.clay.2010.06.019>
177. Jaber, M.; Komarneni, S.; Zhou, C.-H. Synthesis of Clay Minerals. In *Developments in Clay Science*; Elsevier, 2013; Vol. 5, pp 223–241. <https://doi.org/10.1016/B978-0-08-098258-8.00009-2>
178. Carniato, F.; Bisio, C.; Psaro, R.; Marchese, L.; Guidotti, M. Niobium (V) Saponite Clay for the Catalytic Oxidative Abatement of Chemical Warfare Agents. *Angew. Chemie Int. Ed.* 2014, 53 (38), 10095–10098. <https://doi.org/10.1002/anie.201405134>
179. Baldermann, A.; Dohrmann, R.; Kaufhold, S.; Nickel, C.; Letofsky-Papst, I.; Dietzel, M. The Fe-Mg-Saponite Solid Solution Series—a Hydrothermal Synthesis Study. *Clay Miner.* 2014, 49 (3), 391–415. <https://doi.org/10.1180/claymin.2014.049.3.04>
180. Zhang, C.; He, H.; Tao, Q.; Ji, S.; Li, S.; Ma, L.; Su, X.; Zhu, J. Metal Occupancy and Its Influence on Thermal Stability of Synthetic Saponites. *Appl. Clay Sci.* 2017, 135, 282–288. <https://doi.org/10.1016/j.clay.2016.10.006>
181. Trujillano, R.; Rico, E.; Vicente, M. A.; Herrero, M.; Rives, V. Microwave Radiation and Mechanical Grinding as New Ways for Preparation of Saponite-like Materials. *Appl. Clay Sci.* 2010, 48 (1–2), 32–38. <https://doi.org/10.1016/j.clay.2009.11.018>
182. Gebretsadik, F. B.; Salagre, P.; Cesteros, Y. Use of Polymer as Template in Microwave Synthesis of Saponite. Study of Several Factors of Influence. *Appl. Clay Sci.* 2014, 87, 170–178. <https://doi.org/10.1016/j.clay.2013.10.027>
183. Suquet, H.; Malard, C.; Copin, E.; Pezerat, H. Variation Du Paramètre b et de La Distance Basale d 001 Dans Une Série de Saponites à Charge Croissante: I. Etats Hydratés. *Clay Miner.* 1981, 16 (1), 53–67.

<https://doi.org/10.1180/claymin.1981.016.1.04>

184. Ferrage, E.; Lanson, B.; Michot, L. J.; Robert, J.-L. Hydration Properties and Interlayer Organization of Water and Ions in Synthetic Na-Smectite with Tetrahedral Layer Charge. Part 1. Results from X-Ray Diffraction Profile Modeling. *J. Phys. Chem. C* 2010, *114* (10), 4515–4526. <https://doi.org/10.1021/jp909860p>
185. Dazas, B.; Lanson, B.; Delville, A.; Robert, J.-L.; Komarneni, S.; Michot, L. J.; Ferrage, E. Influence of Tetrahedral Layer Charge on the Organization of Interlayer Water and Ions in Synthetic Na-Saturated Smectites. *J. Phys. Chem. C* 2015, *119* (8), 4158–4172. <https://doi.org/10.1021/jp5123322>
186. Ferrage, E. Investigation of the Interlayer Organization of Water and Ions in Smectite from the Combined Use of Diffraction Experiments and Molecular Simulations. A Review of Methodology, Applications, and Perspectives. *Clays Clay Miner.* 2016, *64* (4), 348–373. <https://doi.org/10.1346/CCMN.2016.0640401>
187. Eguchi, M.; Momotake, M.; Inoue, F.; Oshima, T.; Maeda, K.; Higuchi, M. Inert Layered Silicate Improves the Electrochemical Responses of a Metal Complex Polymer. *ACS Appl. Mater. Interfaces* 2017, *9* (40), 35498–35503. <https://doi.org/10.1021/acsami.7b13311>
188. Kurokawa, H.; Hayasaka, M.; Yamamoto, K.; Sakuragi, T.; Ohshima, M.; Miura, H. Self-Assembled Heterogeneous Late Transition–Metal Catalysts for Ethylene Polymerization; New Approach to Simple Preparation of Iron and Nickel Complexes Immobilized in Clay Mineral Interlayer. *Catal. Commun.* 2014, *47*, 13–17. <https://doi.org/10.1016/j.catcom.2013.12.009>
189. Sas, S.; Danko, M.; Bizovská, V.; Lang, K.; Bujdák, J. Highly Luminescent Hybrid Materials Based on Smectites with Polyethylene Glycol Modified with Rhodamine Fluorophore. *Appl. Clay Sci.* 2017, *138*, 25–33. <https://doi.org/10.1016/j.clay.2016.12.034>
190. Marcal, L.; de Faria, E. H.; Nassar, E. J.; Trujillano, R.; Martin, N.; Vicente, M. A.; Rives, V.; Gil, A.; Korili, S. A.; Ciuffi, K. J. Organically Modified Saponites: SAXS Study of Swelling and Application in Caffeine Removal. *ACS Appl. Mater. Interfaces* 2015, *7* (20), 10853–10862. <https://doi.org/10.1021/acsami.5b01894>
191. Sato, K.; Fujimoto, K.; Dai, W.; Hunger, M. Quantitative Elucidation of Cs Adsorption Sites in Clays: Toward Sophisticated Decontamination of Radioactive Cs. *J. Phys. Chem. C* 2016, *120* (2), 1270–1274. <https://doi.org/10.1021/acs.jpcc.5b09350>
192. Herney-Ramirez, J.; Silva, A. M. T.; Vicente, M. A.; Costa, C. A.; Madeira, L. M. Degradation of Acid Orange 7 Using a Saponite-Based Catalyst in Wet Hydrogen Peroxide Oxidation: Kinetic Study with the Fermi's Equation. *Appl. Catal. B Environ.* 2011, *101* (3–4), 197–205. <https://doi.org/10.1016/j.apcatb.2010.09.020>
193. Huggett, J. M. *Clay Minerals* ☆; Alderton, D., Elias, S. A. B. T.-E. of G. (Second E., Eds.;

- Academic Press: Oxford, 2021; pp 341–349. <https://doi.org/https://doi.org/10.1016/B978-0-12-409548-9.11855-X>.
194. Grim, R. E. *Clay Mineralogy*; LWW, 1953; Vol. 76. <https://doi.org/10.1346/CCMN.1988.0360201>
195. Ragu, S.; Dardillac, E.; Brooks, D. A.; Castro-Smirnov, F. A.; Aranda, P.; Ruiz-Hitzky, E.; Lopez, B. S. Responses of Human Cells to Sepiolite Interaction. *Appl. Clay Sci.* 2020, 194 (June), 105655. <https://doi.org/10.1016/j.clay.2020.105655>.
196. Wang, F.; Ding, Y.; Hao, M.; Fang, B.; Liang, J. Applied Clay Science Novel Fabrication of a Sepiolite Supported Cobalt-Based Catalyst via a Coprecipitation-Reduction Method. *Appl. Clay Sci.* 2020, No. July, 105909. <https://doi.org/10.1016/j.clay.2020.105909>.
197. Chen, H.; Zhang, Z.; Zhuang, G.; Jiang, R. A New Method to Prepare ‘Maya Red’ Pigment from Sepiolite and Basic Red 46. *Appl. Clay Sci.* 2019, 174, 38–46. <https://doi.org/10.1016/J.CLAY.2019.03.023>.
198. Galán, E. Properties and Applications of Palygorskite-Sepiolite Clays. *Clay Miner.* 1996, 31 (4), 443–453. <https://doi.org/10.1180/claymin.1996.031.4.01>
199. Hamid, Y.; Tang, L.; Hussain, B.; Usman, M.; Liu, L.; Ulhassan, Z.; He, Z.; Yang, X. Sepiolite Clay: A Review of Its Applications to Immobilize Toxic Metals in Contaminated Soils and Its Implications in Soil–Plant System. *Environ. Technol. Innov.* 2021, 23, 101598. <https://doi.org/10.1016/j.eti.2021.101598>.
200. Han, Z.-X.; Zhu, Z.; Wu, D.-D.; Wu, J.; Liu, Y.-R. Adsorption Kinetics and Thermodynamics of Acid Blue 25 and Methylene Blue Dye Solutions on Natural Sepiolite. *Synth. React. Inorganic, Met. Nano-Metal Chem.* 2014, 44 (1), 140–147. <https://doi.org/10.1080/15533174.2013.770755>
201. Rytwo, G.; Nir, S.; Margulies, L.; Casal, B.; Merino, J.; Ruiz-Hitzky, E.; Serratosa, J. M. Adsorption of Monovalent Organic Cations on Sepiolite: Experimental Results and Model Calculations. *Clays Clay Miner.* 1998, 46 (3), 340–348. <https://doi.org/10.1346/CCMN.1998.0460313>
202. Doke, K. M.; Khan, E. M. Equilibrium, Kinetic and Diffusion Mechanism of Cr (VI) Adsorption onto Activated Carbon Derived from Wood Apple Shell. *Arab. J. Chem.* 2017, 10, S252–S260. <https://doi.org/10.1016/j.arabjc.2012.07.031>
203. Santos, S. C. R.; Boaventura, R. A. R. Adsorption Modelling of Textile Dyes by Sepiolite. *Appl. Clay Sci.* 2008, 42 (1–2), 137–145. <https://doi.org/10.1016/j.clay.2008.01.002>
204. Hamid, Y.; Tang, L.; Hussain, B.; Usman, M.; Rehman Hashmi, M. L. ur; Bilal Khan, M.; Yang, X.; He, Z. Immobilization and Sorption of Cd and Pb in Contaminated Stagnic Anthrosols as Amended with Biochar and Manure Combined with Inorganic

- Additives. *J. Environ. Manage.* 2020, 257 (August 2019), 109999. <https://doi.org/10.1016/j.jenvman.2019.109999>.
205. Bilgiç, C. Investigation of the Factors Affecting Organic Cation Adsorption on Some Silicate Minerals. *J. Colloid Interface Sci.* 2005, 281 (1), 33–38. <https://doi.org/10.1016/j.jcis.2004.08.038>
206. Tümsek, F.; Avcı, O. Investigation of Kinetics and Isotherm Models for the Acid Orange 95 Adsorption from Aqueous Solution onto Natural Minerals. *J. Chem. Eng. Data* 2013, 58 (3), 551–559. <https://doi.org/10.1021/je301215s>
207. He, Z.; Ren, B.; Hursthouse, A.; Wang, Z. Efficient Removal of Cd (II) Using SiO₂-Mg (OH) 2 Nanocomposites Derived from Sepiolite. *Int. J. Environ. Res. Public Health* 2020, 17 (7), 2223. <https://doi.org/10.3390/ijerph17072223>
208. Santos, S. C. R.; Boaventura, R. A. R. Adsorption of Cationic and Anionic Azo Dyes on Sepiolite Clay: Equilibrium and Kinetic Studies in Batch Mode. *J. Environ. Chem. Eng.* 2016, 4 (2), 1473–1483. <https://doi.org/10.1016/j.jece.2016.02.009>.
209. Cheng, H.; Zhu, Q.; Xing, Z. Adsorption of Ammonia Nitrogen in Low Temperature Domestic Wastewater by Modification Bentonite. *J. Clean. Prod.* 2019, 233, 720–730. <https://doi.org/10.1016/j.jclepro.2019.06.079>
210. El Miz, M.; Akichoh, H.; Berraouan, D.; Salhi, S.; Tahani, A. Chemical and Physical Characterization of Moroccan Bentonite Taken from Nador (North of Morocco). *Am. J. Chem* 2017, 7 (4), 105–112.
211. Angar, Y.; Djelali, N.-E.; Kebbouche-Gana, S. Investigation of Ammonium Adsorption on Algerian Natural Bentonite. *Environ. Sci. Pollut. Res.* 2017, 24 (12), 11078–11089. <https://doi.org/10.1007/s11356-016-6500-0>
212. Kaufhold, S.; Dohrmann, R.; Weber, C. Evolution of the PH Value at the Vicinity of the Iron-Bentonite Interface. *Appl. Clay Sci.* 2020, No. November, 105929. <https://doi.org/10.1016/j.clay.2020.105929>.
213. Drobíková, K.; Štrbová, K.; Tokarčíková, M.; Motyka, O.; Seidlerová, J. Magnetically Modified Bentonite: Characterization and Stability. *Mater. Today Proc.* 2020, No. xxxx. <https://doi.org/10.1016/j.matpr.2020.10.375>.
214. Sakr, M. A.; Mohamed, M. G. A.; Wu, R.; Shin, S. R.; Kim, D.; Kim, K.; Siddiqua, S. Development of Bentonite-Gelatin Nanocomposite Hybrid Hydrogels for Tissue Engineering. *Appl. Clay Sci.* 2020, 199 (September), 105860. <https://doi.org/10.1016/j.clay.2020.105860>.
215. El-nagar, D. A.; Hereimas, D. Soil & Tillage Research Synthesis and Characterization of Nano Bentonite and Its Effect on Some Properties of Sandy Soils. *Soil Tillage Res.* 2021, 208 (November 2020), 104872. <https://doi.org/10.1016/j.still.2020.104872>.

-
216. Peng, L.; Chen, B.; Zhao, Y. Quantitative Characterization and Comparison of Bentonite Microstructure by Small Angle X-Ray Scattering and Nitrogen Adsorption. *Constr. Build. Mater.* 2020, 262, 120863. <https://doi.org/10.1016/j.conbuildmat.2020.120863>. <https://doi.org/10.1016/j.conbuildmat.2020.120863>
217. Tohdee, K.; Kaewsichan, L. Enhancement of Adsorption Efficiency of Heavy Metal Cu (II) and Zn (II) onto Cationic Surfactant Modified Bentonite. *J. Environ. Chem. Eng.* 2018, 6 (2), 2821–2828. <https://doi.org/10.1016/j.jece.2018.04.030>
218. Jiménez-Castañeda, M. E.; Medina, D. I. Use of Surfactant-Modified Zeolites and Clays for the Removal of Heavy Metals from Water. *Water* 2017, 9 (4), 235. <https://doi.org/10.3390/w9040235>
219. Munir, M.; Nazar, M. F.; Zafar, M. N. Removal of Amaranth Dye over Surfactant Modified Dull Pink Clay from Aqueous Medium. *Int. J. Environ. Anal. Chem.* 2020, 1–18. <https://doi.org/10.1080/03067319.2020.1711899>
220. Nadeem, M.; Mahmood, A.; Shahid, S. A.; Shah, S. S.; Khalid, A. M.; McKay, G. Sorption of Lead from Aqueous Solution by Chemically Modified Carbon Adsorbents. *J. Hazard. Mater.* 2006, 138 (3), 604–613. <https://doi.org/10.1016/j.jhazmat.2006.05.098>
221. Khobragade, M. U.; Pal, A. Adsorptive Removal of Mn (II) from Water and Wastewater by Surfactant-Modified Alumina. *Desalin. Water Treat.* 2016, 57 (6), 2775–2786. <https://doi.org/10.1080/19443994.2014.982195>
222. Fiol, N.; Villaescusa, I.; Martínez, M.; Miralles, N.; Poch, J.; Serarols, J. Sorption of Pb (II), Ni (II), Cu (II) and Cd (II) from Aqueous Solution by Olive Stone Waste. *Sep. Purif. Technol.* 2006, 50 (1), 132–140. <https://doi.org/10.1016/j.seppur.2005.11.016>
223. AjayKumar, A. V.; Darwish, N. A.; Hilal, N. Study of Various Parameters in the Biosorption of Heavy Metals on Activated Sludge. *World Appl. Sci. J.* 2009, 5 (5), 32–40.
224. Abbasi, S.; Foroutan, R.; Esmaili, H.; Esmailzadeh, F. Preparation of Activated Carbon from Worn Tires for Removal of Cu (II), Ni (II) and Co (II) Ions from Synthetic Wastewater. *Desalin. Water Treat* 2019, 141, 269–278. <https://doi.org/10.5004/dwt.2019.23569>
225. Cai, C.; Wu, X.; Liu, W.; Zhu, W.; Chen, H.; Qiu, J. C. D.; Sun, C.-N.; Liu, J.; Wei, Q.; Shi, Y. Selective Laser Melting of Near- α Titanium Alloy Ti-6Al-2Zr-1Mo-1V: Parameter Optimization, Heat Treatment and Mechanical Performance. *J. Mater. Sci. Technol.* 2020, 57, 51–64. <https://doi.org/10.1016/j.jmst.2020.05.004>
226. Chen, J.; Cai, Y.; Clark, M.; Yu, Y. Equilibrium and Kinetic Studies of Phosphate Removal from Solution onto a Hydrothermally Modified Oyster Shell Material. *PLoS One* 2013, 8 (4), e60243. <https://doi.org/10.1371/journal.pone.0060243>

227. Tamjidi, S.; Esmaeili, H. Chemically Modified CaO/Fe₃O₄ Nanocomposite by Sodium Dodecyl Sulfate for Cr (III) Removal from Water. *Chem. Eng. Technol.* 2019, 42 (3), 607–616. <https://doi.org/10.1002/ceat.201800488>
228. Mudzielwana, R.; Gitari, M. W.; Ndungu, P. Performance Evaluation of Surfactant Modified Kaolin Clay in As (III) and As (V) Adsorption from Groundwater: Adsorption Kinetics, Isotherms and Thermodynamics. *Heliyon* 2019, 5 (11), e02756. <https://doi.org/10.1016/j.heliyon.2019.e02756>
229. Xi, H.; Li, Q.; Yang, Y.; Zhang, J.; Guo, F.; Wang, X.; Xu, S.; Ruan, S. Highly Effective Removal of Phosphate from Complex Water Environment with Porous Zr-Bentonite Alginate Hydrogel Beads: Facile Synthesis and Adsorption Behavior Study. *Appl. Clay Sci.* 2021, 201, 105919. <https://doi.org/10.1016/j.clay.2020.105919>
230. de Queiroga, L. N. F.; França, D. B.; Rodrigues, F.; Santos, I. M. G.; Fonseca, M. G.; Jaber, M. Functionalized Bentonites for Dye Adsorption: Depollution and Production of New Pigments. *J. Environ. Chem. Eng.* 2019, 7 (5), 103333. <https://doi.org/10.1016/J.JECE.2019.103333>.
231. Herrera, N. N.; Letoffe, J.-M.; Putaux, J.-L.; David, L.; Bourgeat-Lami, E. Aqueous Dispersions of Silane-Functionalized Laponite Clay Platelets. A First Step toward the Elaboration of Water-Based Polymer/Clay Nanocomposites. *Langmuir* 2004, 20 (5), 1564–1571. <https://doi.org/10.1021/la0349267>
232. Ghadiri, M.; Hau, H.; Chrzanowski, W.; Agus, H.; Rohanizadeh, R. Laponite Clay as a Carrier for in Situ Delivery of Tetracycline. *Rsc Adv.* 2013, 3 (43), 20193–20201. <https://doi.org/10.1039/C3RA43217C>
233. Pálková, H.; Madejová, J.; Zimowska, M.; Bielańska, E.; Olejniczak, Z.; Lityńska-Dobrzyńska, L.; Serwicka, E. M. Laponite-Derived Porous Clay Heterostructures: I. Synthesis and Physicochemical Characterization. *Microporous Mesoporous Mater.* 2010, 127 (3), 228–236. <https://doi.org/10.1016/j.micromeso.2009.07.019>.
234. Bienia, M.; Danglade, C.; Lecomte, A.; Brevier, J.; Pagnoux, C. Cylindrical Couette Flow of Laponite Dispersions. *Appl. Clay Sci.* 2018, 162, 83–89. <https://doi.org/10.1016/j.clay.2018.05.030>
235. Loginov, M.; Lebovka, N.; Vorobiev, E. Laponite Assisted Dispersion of Carbon Nanotubes in Water. *J. Colloid Interface Sci.* 2012, 365 (1), 127–136. <https://doi.org/10.1016/j.jcis.2011.09.025>
236. Manilo, M. V.; Lebovka, N.; Barany, S. Combined Effect of Cetyltrimethylammonium Bromide and Laponite Platelets on Colloidal Stability of Carbon Nanotubes in Aqueous Suspensions. *J. Mol. Liq.* 2017, 235, 104–110. <https://doi.org/10.1016/j.molliq.2017.01.090>
237. Silva, J. M.; Barud, H. S.; Meneguim, A. B.; Constantino, V. R. L.; Ribeiro, S. J. L. Inorganic-Organic Bio-Nanocomposite Films Based on Laponite and Cellulose

- Nanofibers (CNF). *Appl. Clay Sci.* 2019, 168, 428–435. <https://doi.org/10.1016/j.clay.2018.12.003>
238. Le Coeur, C.; Lorthioir, C.; Feoktystov, A.; Wu, B.; Volet, G.; Amiel, C. Laponite/Poly(2-Methyl-2-Oxazoline) Hydrogels: Interplay between Local Structure and Rheological Behaviour. *J. Colloid Interface Sci.* 2021, 582, 149–158. <https://doi.org/10.1016/j.jcis.2020.07.068>.
239. Yu, D.; Li, G.; Kong, F.; Wang, H.; Liu, W.; Song, Z.; Meng, X.; Zhao, J. R. H. Encapsulation of Alkenylsuccinic Anhydride Oil Droplets in Laponite Nanoparticles Modified by Carbon Nitride Quantum Dots: Enhancement of Emulsion Stability and Paper Sizing Performance. *Appl. Clay Sci.* 2020, 191 (September 2019), 105608. <https://doi.org/10.1016/j.clay.2020.105608>.
240. Zhang, R.; Xie, L.; Wu, H.; Yang, T.; Zhang, Q.; Tian, Y.; Liu, Y.; Han, X.; Guo, W.; He, M.; Liu, S.; Tian, W. Alginate/Laponite Hydrogel Microspheres Co-Encapsulating Dental Pulp Stem Cells and VEGF for Endodontic Regeneration. *Acta Biomater.* 2020, 113 (14), 305–316. <https://doi.org/10.1016/j.actbio.2020.07.012>.
241. Elkatatny, S. Improved Carbonation Resistance and Durability of Saudi Class G Oil Well Cement Sheath in CO₂ Rich Environments Using Laponite. *J. Pet. Sci. Eng.* 2021, 196 (April 2020), 107812. <https://doi.org/10.1016/j.petrol.2020.107812>.
242. Schoonheydt, R. A.; Heughebaert, L. Clay Adsorbed Dyes: Methylene Blue on Laponite. *Clay Miner.* 1992, 27 (1), 91–100. <https://doi.org/10.1180/claymin.1992.027.1.09>.
243. Au, P.-I.; Hassan, S.; Liu, J.; Leong, Y.-K. Behaviour of LAPONITE® Gels: Rheology, Ageing, PH Effect and Phase State in the Presence of Dispersant. *Chem. Eng. Res. Des.* 2015, 101, 65–73. <https://doi.org/10.1016/j.cherd.2015.07.023>
244. Valencia, G. A.; Djabourov, M.; Carn, F.; Sobral, P. J. A. Novel Insights on Swelling and Dehydration of Laponite. *Colloid Interface Sci. Commun.* 2018, 23, 1–5. <https://doi.org/10.1016/j.colcom.2018.01.001>
245. Jatav, S.; Joshi, Y. M. Chemical Stability of Laponite in Aqueous Media. *Appl. Clay Sci.* 2014, 97, 72–77. Jatav, S.; Joshi, Y. M. Chemical Stability of Laponite in Aqueous Media. *Appl. Clay Sci.* 2014, 97, 72–77.
246. Zhang, P.; Wang, J.; Jia, Y.; Li, W.; Tan, X.; Zhang, D.; Xu, S.; Zhang, P.; Wei, C.; Miao, S. Encapsulating Spinel Nanocrystals in Laponite Cages and Applications in Molecular Oxidation of Cyclohexane. *Appl. Clay Sci.* 2019, 181 (May), 105226. <https://doi.org/10.1016/j.clay.2019.105226>.
247. Takeno, H.; Sato, C. Effects of Molecular Mass of Polymer and Composition on the Compressive Properties of Hydrogels Composed of Laponite and Sodium Polyacrylate. *Appl. Clay Sci.* 2016, 123, 141–147. <https://doi.org/10.1016/j.clay.2016.01.030>

248. Zeng, H.; Yu, Z.; Peng, Y.; Zhu, L. Environmentally Friendly Electrostatically Driven Self-Assembled LDH/GO/PVDF Composite Membrane for Water Treatment. *Appl. Clay Sci.* 2019, *183*, 105322. <https://doi.org/10.1016/j.clay.2019.105322>
249. Muller, F.; Salonen, A.; Glatter, O. Monoglyceride-Based Cubosomes Stabilized by Laponite: Separating the Effects of Stabilizer, PH and Temperature. *Colloids Surfaces A Physicochem. Eng. Asp.* 2010, *358* (1–3), 50–56. <https://doi.org/10.1016/j.colsurfa.2010.01.021>
250. van den Dungen, E. T. A.; Hartmann, P. C. Synergistic Effect of Laponite RD and Oil Soluble Surfactant in Stabilization of Miniemulsions. *Appl. Clay Sci.* 2012, *55*, 120–124. <https://doi.org/10.1016/j.clay.2011.10.015>
251. Taguchi, T.; Kohno, Y.; Shibata, M.; Tomita, Y.; Fukuhara, C.; Maeda, Y. An Easy and Effective Method for the Intercalation of Hydrophobic Natural Dye into Organo-Montmorillonite for Improved Photostability. *J. Phys. Chem. Solids* 2018, *116*, 168–173. <https://doi.org/10.1016/j.jpcs.2018.01.027>
252. Ribeiro, H. L.; de Oliveira, A. V.; de Brito, E. S.; Ribeiro, P. R. V.; Azeredo, H. M. C. Stabilizing Effect of Montmorillonite on Acerola Juice Anthocyanins. *Food Chem.* 2018, *245*, 966–973. <https://doi.org/10.1016/j.foodchem.2017.11.076>
253. Kohno, Y.; Senga, M.; Shibata, M.; Yoda, K.; Matsushima, R.; Tomita, Y.; Maeda, Y.; Kobayashi, K. Stabilization of Flavylum Dye by Incorporation into Fe-Containing Mesoporous Silicate. *Microporous mesoporous Mater.* 2011, *141* (1–3), 77–80. <https://doi.org/10.1016/j.micromeso.2010.11.004>
254. Kohno, Y.; Asai, S.; Shibata, M.; Fukuhara, C.; Maeda, Y.; Tomita, Y.; Kobayashi, K. Improved Photostability of Hydrophobic Natural Dye Incorporated in Organo-Modified Hydrotalcite. *J. Phys. Chem. Solids* 2014, *75* (8), 945–950. <https://doi.org/10.1016/j.jpcs.2014.04.010>
255. Boyaci, T.; Orakdogan, N. Poly(N,N-Dimethylaminoethyl Methacrylate-Co-2-Acrylamido-2-Methyl-Propanosulfonic Acid)/Laponite Nanocomposite Hydrogels and Cryogels with Improved Mechanical Strength and Rapid Dynamic Properties. *Appl. Clay Sci.* 2016, *121–122*, 162–173. <https://doi.org/10.1016/j.clay.2015.12.018>
256. Wang, Z.; Li, J.; Sun, Y.; Peng, J.; Wang, J.; Hao, Y.; Li, W.; Zhang, P.; Ning, W.; Miao, S. Laponite Elementary Sheets Assisted Fluorescence Resonance Energy Transfer: A Demonstration by Langmuir-Blodgett Technique. *Dye. Pigment.* 2021, *196* (June), 109800. <https://doi.org/10.1016/j.dyepig.2021.109800>
257. Prasannan, A.; Udomsin, J.; Tsai, H.-C.; Wang, C.-F.; Lai, J.-Y. Robust Underwater Superoleophobic Membranes with Bio-Inspired Carrageenan/Laponite Multilayers for the Effective Removal of Emulsions, Metal Ions, and Organic Dyes from Wastewater. *Chem. Eng. J.* 2020, *391*, 123585. <https://doi.org/10.1016/j.cej.2019.123585>

-
258. Akil, J.; Ciotonea, C.; Siffert, S.; Royer, S.; Pirault-Roy, L.; Cousin, R.; Poupin, C. NO Reduction by CO under Oxidative Conditions over CoCuAl Mixed Oxides Derived from Hydrotalcite-like Compounds: Effect of Water. *Catal. Today* 2021, No. October 2020. <https://doi.org/10.1016/j.cattod.2021.05.014>.
259. Carlino, S. Chemistry between the Sheets. *Chem. Br.* 1997, 33 (9), 59–62. <https://doi.org/10.1016/j.cej.2013.08.097>
260. Ulibarri, M. A.; Pavlovic, I.; Barriga, C.; Hermosin, M. C.; Cornejo, J. Adsorption of Anionic Species on Hydrotalcite-like Compounds: Effect of Interlayer Anion and Crystallinity. *Appl. Clay Sci.* 2001, 18 (1–2), 17–27. [https://doi.org/10.1016/S0169-1317\(00\)00026-0](https://doi.org/10.1016/S0169-1317(00)00026-0)
261. Bish, D. L. Anion-Exchange in Takovite: Applications to Other Hydroxide Minerals. *Bull. Mineral.* 1980, 103 (2), 170–175.
262. Miyata, S. Physico-Chemical Properties of Synthetic Hydrotalcites in Relation to Composition. *Clays Clay Miner.* 1980, 28 (1), 50–56. <https://doi.org/10.1346/CCMN.1980.0280107>
263. Zhu, M.-X.; Li, Y.-P.; Xie, M.; Xin, H.-Z. Sorption of an Anionic Dye by Uncalcined and Calcined Layered Double Hydroxides: A Case Study. *J. Hazard. Mater.* 2005, 120 (1–3), 163–171. <https://doi.org/10.1016/j.jhazmat.2004.12.029>
264. Lakraimi, M.; Legrouri, A.; Barroug, A.; Besse, J.-P. Removal of Pesticides from Water by Anionic Clays. *J. Chim. Phys. Physico-Chimie Biol.* 1999, 96 (3), 470–478. <https://doi.org/10.1051/jcp:1999152>
265. Sato, T.; Kato, K.; Endo, T.; Shimada, M. Preparation and Chemical Properties of Magnesium Aluminium Oxide Solid Solutions. *React. Solids* 1986, 2 (3), 253–260. [https://doi.org/10.1016/0168-7336\(86\)80088-2](https://doi.org/10.1016/0168-7336(86)80088-2)
266. Salomao, R.; Milena, L. M.; Wakamatsu, M. H.; Pandolfelli, V. C. Hydrotalcite Synthesis via Co-Precipitation Reactions Using MgO and Al (OH) 3 Precursors. *Ceram. Int.* 2011, 37 (8), 3063–3070. <https://doi.org/10.1016/j.ceramint.2011.05.034>
267. Bouraada, M.; Lafjah, M.; Ouali, M. S.; de Menorval, L. C. Basic Dye Removal from Aqueous Solutions by Dodecylsulfate-and Dodecyl Benzene Sulfonate-Intercalated Hydrotalcite. *J. Hazard. Mater.* 2008, 153 (3), 911–918. <https://doi.org/10.1016/j.jhazmat.2007.09.076>
268. Cavani, F.; Trifiro, F.; Vaccari, A. Hydrotalcite-Type Anionic Clays: Preparation, Properties and Applications. *Catal. today* 1991, 11 (2), 173–301. [https://doi.org/10.1016/0920-5861\(91\)80068-K](https://doi.org/10.1016/0920-5861(91)80068-K)
269. Gasser, M. S.; Mekhamer, H. S.; Abdel Rahman, R. O. Optimization of the Utilization of Mg/Fe Hydrotalcite like Compounds in the Removal of Sr(II) from Aqueous Solution. *J. Environ. Chem. Eng.* 2016, 4 (4), 4619–4630.

<https://doi.org/10.1016/j.jece.2016.10.027>.

270. López Arbeloa, F.; Martínez Martínez, V.; Bañuelos Prieto, J.; López Arbeloa, I. Adsorption of Rhodamine 3B Dye on Saponite Colloidal Particles in Aqueous Suspensions. *Langmuir* 2002, 18 (7), 2658–2664. <https://doi.org/10.1021/la0113163>.
271. Ogawa, M.; Takee, R.; Okabe, Y.; Seki, Y. Bio-Geo Hybrid Pigment; Clay-Anthocyanin Complex Which Changes Color Depending on the Atmosphere. *Dye. Pigment.* 2017, 139, 561–565. <https://doi.org/10.1016/J.DYEPIG.2016.12.054>.
272. Guillermin, D.; Debroise, T.; Trigueiro, P.; de Viguerie, L.; Rigaud, B.; Morlet-Savary, F.; Balme, S.; Janot, J.-M.; Tielens, F.; Michot, L.; Lalevee, J.; Walter, P.; Jaber, M. New Pigments Based on Carminic Acid and Smectites: A Molecular Investigation. *Dye. Pigment.* 2019, 160, 971–982. <https://doi.org/10.1016/J.DYEPIG.2018.07.021>.
273. McKay, G.; Ramprasad, G.; Mowli, P. Desorption and Regeneration of Dye Colours from Low-Cost Materials. *Water Res.* 1987, 21 (3), 375–377. [https://doi.org/10.1016/0043-1354\(87\)90218-1](https://doi.org/10.1016/0043-1354(87)90218-1).
274. Voudrias, E.; Fytianos, K.; Bozani, E. Sorption-Desorption Isotherms of Dyes from Aqueous Solutions and Wastewaters with Different Sorbent Materials. *Glob. NEST Journal Global NEST Int. J.* 2018, 4 (1), 75–83. <https://doi.org/10.30955/gnj.000233>.
275. Yuan, J.; Zhou, S.; You, B.; Wu, L. Organic Pigment Particles Coated with Colloidal Nano-Silica Particles via Layer-by-Layer Assembly. *Chem. Mater.* 2005, 17 (14), 3587–3594. <https://doi.org/10.1021/cm048000b>
276. Cao, L.; Fei, X.; Zhang, T.; Yu, L.; Gu, Y.; Zhang, B. Modification of CI Pigment Red 21 with Sepiolite and Lithopone in Its Preparation Process. *Ind. Eng. Chem. Res.* 2014, 53 (1), 31–37. <https://doi.org/10.1021/ie4021914>
277. Dejoie, C.; Martinetto, P.; Dooryhee, E.; Strobel, P.; Blanc, S.; Bordat, P.; Brown, R.; Porcher, F.; Sanchez del Rio, M.; Anne, M. Indigo@ Silicalite: A New Organic–Inorganic Hybrid Pigment. *ACS Appl. Mater. Interfaces* 2010, 2 (8), 2308–2316. <https://doi.org/10.1021/am100349b>
278. Raha, S.; Ivanov, I.; Quazi, N. H.; Bhattacharya, S. N. Photo-Stability of Rhodamine-B/Montmorillonite Nanopigments in Polypropylene Matrix. *Appl. Clay Sci.* 2009, 42 (3–4), 661–666. <https://doi.org/10.1016/j.clay.2008.06.008>
279. Beltrán, M. I.; Benavente, V.; Marchante, V.; Dema, H.; Marcilla, A. Characterisation of Montmorillonites Simultaneously Modified with an Organic Dye and an Ammonium Salt at Different Dye/Salt Ratios. Properties of These Modified Montmorillonites EVA Nanocomposites. *Appl. Clay Sci.* 2014, 97, 43–52. <https://doi.org/10.1016/j.clay.2014.06.001>
280. Van der Linden, E. G.; Malta, L. F. B.; Medeiros, M. E. Evaluation of Synthetic Routes

- to Pigmentary Grade Bismuth Vanadate. *Dye. Pigment.* 2011, 90 (1), 36–40. <https://doi.org/10.1016/j.dyepig.2010.11.011>
281. Wang, X.; Mu, B.; Wang, W.; Wang, Q.; Wang, A. A Comparative Study on Color Properties of Different Clay Minerals/BiVO₄ Hybrid Pigments with Excellent Thermal Stability. *Appl. Clay Sci.* 2019, 181, 105221. <https://doi.org/10.1016/j.clay.2019.105221>.
282. Yi, J.-Z.; Zhang, L.-M. Removal of Methylene Blue Dye from Aqueous Solution by Adsorption onto Sodium Humate/Polyacrylamide/Clay Hybrid Hydrogels. *Bioresour. Technol.* 2008, 99 (7), 2182–2186. <https://doi.org/10.1016/J.BIORTECH.2007.05.028>.
283. Momina; Mohammad, S.; Suzylawati, I. Study of the Adsorption/Desorption of MB Dye Solution Using Bentonite Adsorbent Coating. *J. Water Process Eng.* 2020, 34 (July 2019). <https://doi.org/10.1016/j.jwpe.2020.101155>.
284. Carretero, M. I.; Pozo, M.; Sánchez, C.; García, F. J.; Medina, J. A.; Bernabé, J. M. Comparison of Saponite and Montmorillonite Behaviour during Static and Stirring Maturation with Seawater for Pelotherapy. *Appl. Clay Sci.* 2007, 36 (1–3), 161–173. <https://doi.org/10.1016/J.CLAY.2006.05.010>.
285. Moujahid, E. M.; Lahkale, R.; Ouassif, H.; Bouragba, F. Z.; Elhatimi, W. New Organic Dye/Anionic Clay Hybrid Pigments: Preparation, Optical Properties and Structural Stability. *Dye. Pigment.* 2019, 162, 998–1004. <https://doi.org/10.1016/J.DYEPIG.2018.11.021>.
286. Nyankson, E.; Agyei-Tuffour, B.; Annan, E.; Yaya, A.; Mensah, B.; Onwona-Agyeman, B.; Amedalor, R.; Kwaku-Frimpong, B.; Efavi, J. K. Ag₂CO₃-Halloysite Nanotubes Composite with Enhanced Removal Efficiency for Water Soluble Dyes. *Heliyon* 2019, 5 (6), e01969. <https://doi.org/10.1016/J.HELIVON.2019.E01969>.

Recuperación del colorante de aguas residuales textiles mediante nanoarcillas para su reutilización como pigmentos y nuevos baños de tintura

3.2. Adaptación del artículo: Direct and Reactive Dyes Recovery in Textile Wastewater Using Calcinated Hydrotalcite

Artículo publicado en Bou-Belda, Eva; López-Rodríguez, Daniel; Micó-Vicent, B.; Bonet-Aracil, Marilés. (2022) Direct and Reactive Dyes Recovery in Textile Wastewater Using Calcinated Hydrotalcite. Materials Science Forum (163)233 - <https://www.scientific.net/MSF.1063.233>

Abstract:

Growing environmental conservation concerns have led researchers to seek the means to treat and recover wastewater. The textile industry dumps vast quantities of wastewater from textile dyes. By means of clays, dye waste can be separated and reused for other industrial processes. Clay absorption varies depending on the type of dye employed because factors like the reactivity of the dye molecule and its size are very important during the absorption process. The absorption capacity of calcined hydrotalcite at several concentrations was compared in a $0.05 \text{ g}\cdot\text{L}^{-1}$ solution of four distinct dyes: Direct Blue 199, Direct Red 23, Direct Blue 71 and Reactive Yellow. Dyes have different molecular weights because the weight of reactive dyes is considerably lighter than that of direct dyes, which is why the Lambert-Beer lines of each dye are previously considered. We worked with a $5 \text{ g}\cdot\text{L}^{-1}$ clay concentration to introduce the dye into the clay by stirring for 24 h in 100 ml of each dye solution before filtering it and leaving it to dry. In all cases, the dye absorption by nanoclay was nearly absolute and the initial solution was very clean, which are excellent results from the wastewater treatment point of view. Color measurement was performed by a Jasco V-670, double-beam spectrophotometre between 190-2700 nm. Differences in color were calculated and represented in CIE-Lab* color space diagrams. Finally, thermogravimetric (TGA) and X-ray diffraction (XRD) analyses were carried out to ensure both nanoclay-dye interactions and hydrotalcite structure recovery. No large differences were observed under these conditions, which reinforces the idea of using low nanoclay concentrations.

3.2.1. Introduction

Nanoclays have entered the textile-chemistry industry world as an element with extremely efficient absorbing characteristics that allow them to be used for treating and recovering wastewater from the textile and other industries. Thanks to their specific characteristics, nanoclays are capable of absorbing and retaining dyes from the textile industry that are not absorbed during the dyeing process. Thus their final destination is being dumped in textile effluents, which has an environmental impact.

The textile chemical industry is that which most strongly affects wastewater and is the industry that undertakes the most chemical activity in the world. [1]. Recycling industrial wastewater has become an increasingly well-known need. The concentration at which dyes are found in effluents lies around 50-1000 ppm, but can be lower at 10-50 ppm. [2]. The nanoclays surface is very large, about $750 \text{ m}^2 / \text{g}$. The outcome of introducing small quantities of these materials into polymeric matrices is called a nanocomposite [3].

Some compounds or materials are known, such as cyclodextrins [4], agricultural waste [5], nanocomposites [6] or physical means like membrane filtration [7], and many other methods aim to treat wastewater. However, most of them have not reused dyes or the treatment element, which does not promote circular economy. What is more, their complexity is much greater compared to the treatment method here discussed.

Previous works have demonstrated the efficiency of such elements and the success of corresponding trials [8-15]. Thanks to these new applications, the quantity of dyes dumped in wastewater can significantly lower, or new research lines can open up that propose how to use these dyes which, to date, have been wasted, and all this could promote the much-acclaimed circular economy. Finally, apart from cleaning textile wastewater with low clay concentrations, the created dye-clay hybrid can be employed as a pigment [8, 11, 12, 16-20], which offers a great advantage over the aforementioned methods.

3.2.2. Materials and Methods

This study used different colors. The employed direct dyes were Direct Blue 199 CI 74.180, Direct Red 23 CI 29160 and Direct Blue 71 CI 34140. Reactive Drimaren Yellow HF-3GL was utilized as the reactive dye. These dyes were chosen for their trichrome color and because they come as different types with several molecular weights.

Hydrotalcite (HC) was employed as clay and was prepared in accordance with Dos Santos R.M.M. [8]. It was calcined at 600 °C for 3 h. Figure 3.2.1 shows the HC characterization, for which a microscope (Hitachi model S3000N) with an X-ray detector (Bruker XFlash 3001 model) was used for SEM, while the JEOL JEM-2010 model and a GATAN acquisition camera (ORIOUS SC600 model) were employed for TEM imaging purposes. The SEM image shows how clay particle aggregates look like sheets owing to the structure of nanoclays, which break up after calcination. Thanks to their shape memory however, they recover after the absorption process. The TEM imaging can display amorphous areas and areas with stripes where clay sheets are seen with many small basal spaces.

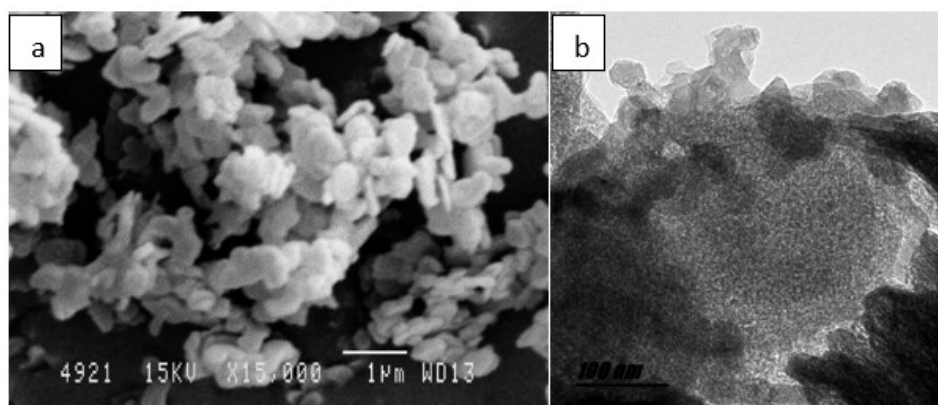


Figure 3.2.1. a) HC SEM b) HC TEM

Dilutions of all the dyes were prepared to obtain the Lambert-Beer line [9]. These lines allow the dye concentration remaining in wastewater to be known after applying clay. Table 3.2.1 shows line equations and determination coefficient R^2 .

Table 3.2.1. Lambert-Beer line equations and R²

Dye	Equation	R ²
Direct Blue 199	y = 21.784 x - 0.015	0.9982
Reactive Yellow	y = 14.943 x - 0.0021	0.9993
Direct Red 23	y = 34.357 x - 0.0148	0.9991
Direct Blue 71	y = 17,09 x - 0.0233	0.9987

For each dye, 100 mL of the 0.05 g·L⁻¹ concentration solution were taken. Next 20 g·L⁻¹ of clay were used and the mixture was placed in a magnetic stirrer [10], which was run at maximum speed for the first 2 h and then at 600 r.p.m. until the 24 h. The solution was filtered with clay for 48 h and was spectrophotometrically measured in a Zuzi spectrophotometer (model 4251/50) to calculate the dye concentration that had not been absorbed by clay [24,25]. The nanoclays with the absorbed dye were lyophilized [26,27] to completely extract water in order to be measured in a Jasco V-670 double-beam spectrophotometer between 190 and 2700 nm. Differences in color and total solar reflectance (TSR) were calculated [11]. A thermogravimetric analysis (TGA) was carried out to compare any possible variation in the degradation peaks of dyes, clays and the final hybrid [29-31]. An X-ray diffraction analysis (XRD) [32, 33] was performed to check that clay recovered its original shape before being calcined. To do so, Bruker D8-Advance XRD equipment was used (Bruker, Billerica, MA, USA) with a Göebel mirror (power: 3000W, voltage: 20-60 kV; current: 5-80 mA). Finally, measures were taken in an oxidant atmosphere at an angular rate of 1°/ min. PASO 0.05° and with 2.7°-70° angular scanning.

3.2.3. Results and Discussion

3.2.3.1. UV absorption

Our results showed that after clay had absorbed the dye, the dye concentration went from 5·10⁻² g·L⁻¹ to about 4.08·10⁻⁴ and 2.3·10⁻³ g·L⁻¹ (see Table 3.2.2).

Table 3.2.2. Difference in concentration after HC absorption

	Sample ref.	Initial conc. g·L ⁻¹	Final conc. g·L ⁻¹	% Absorption
Direct Blue 71	1	0.05	$2.30 \cdot 10^{-3}$	95.40%
Reactive Yellow	2	0.05	$4.08 \cdot 10^{-4}$	99.18%
Direct Red 23	3	0.05	$9.55 \cdot 10^{-4}$	98.09%
Direct Blue 199	4	0.05	$1.56 \cdot 10^{-3}$	96.88%

3.2.3.2. Color measurements

The color measurement of the dye-clay hybrid represented in the CIE-L* color space diagrams are found in Figure 3.2.2. The four samples have different hues close to the red, yellow and pure blue axes. A significant difference was observed between the two employed direct blue dyes. The tone in Sample 1 is more reddish than that of Sample 4, which is more greenish than the first one. Differences in colour saturation can also be seen. Sample 1 is less chromatic and darker than the other samples (except for the red one, which is slightly darker). As expected, the lightest and most chromatic sample is yellow (Sample 2).

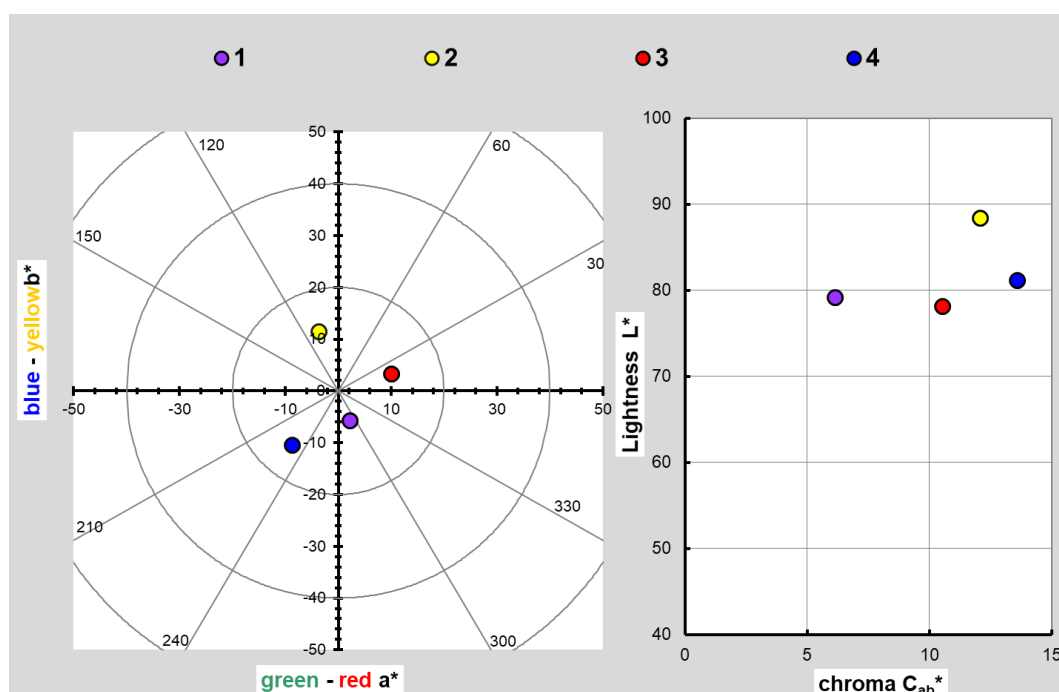


Figure 3.2.2. CIE-L*a*b* color space diagrams of the (1-4) samples

3.2.3.3. Total solar reflectance (TSR)

The total solar reflectance (TSR) absorbed by the top layer determines the heat build-up on a covered surface. The surface temperature very much depends on exposure length. To achieve cold surfaces, pigments in coatings must reflect the largest possible amount of energy. This reflection capacity is expressed as the TSR value, with 100% total reflection and zero total absorption.

Pigments with high TSR values present high reflection and low heat build-up. Conventional white coverings exhibit 75%TSR or higher which, by definition, would absorb 25% incident energy. A carbon black-based black covering might have a TSR as low as 4% and would, therefore, absorb 96% of incident solar energy.

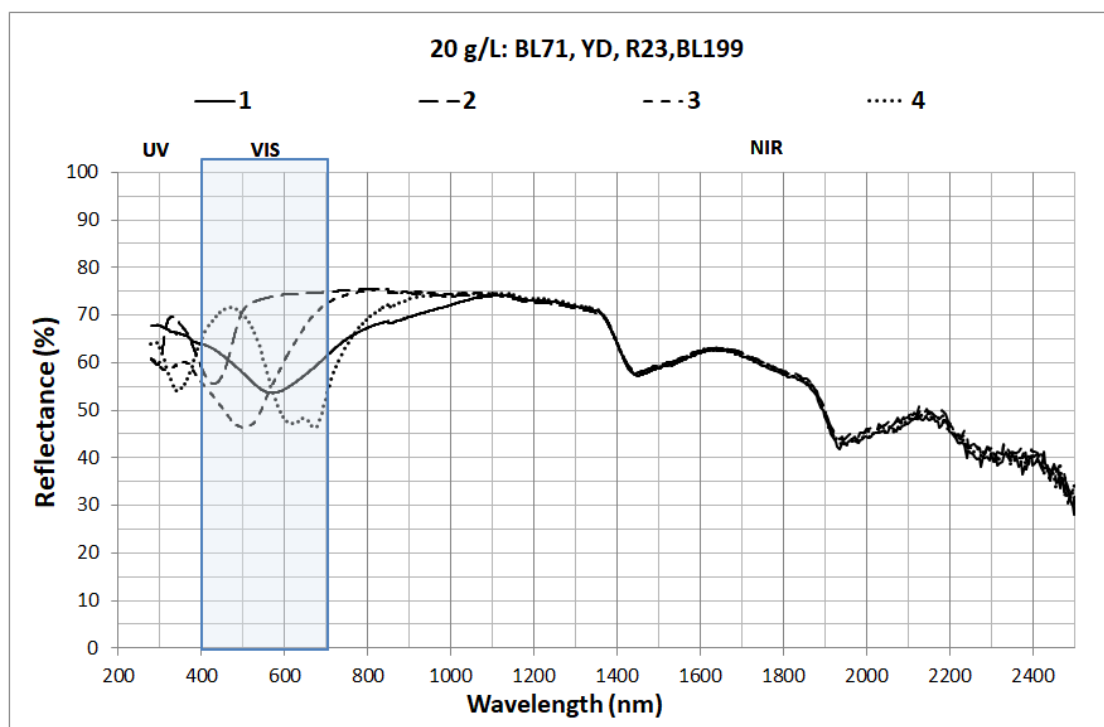


Figure 3.2.3. Reflectance (%) for the (1-4) samples; 190-2500 nm.

After performing the calculations to obtain the TSR percentages of each dye-clay hybrid, the results in Table 3.2.3 and Figure 3.2.3 were obtained. The main spectral differences fell within the visible range, which was expected owing to the dyes' characteristics. Spectral differences may also fall within the UV range, where Samples 2 and

4 obtained the highest reflectance value. Differences also appeared within the near NIR range (700-1000 nm), where Sample 4 (Direct Blue 199) had the lowest reflectance value. Within the 1000-2500 nm range, reflectance values were almost the same for all the samples owing to the nanoclay effect. These differences could explain the TSR% values and the gap in the analysed samples. As expected, the highest TSR% value was found in the yellow hybrid pigment (Sample 2) owing to the intrinsic color characteristic (light). Some interesting differences were found between the blue samples. The TSR% value of Sample 1 was 62.72%, and it was 63.45% for Sample 4. The four samples obtained high TSR% values due to the HC interaction. These hybrid pigments could be used as solar protection in various applications.

Table 3.2.3. TSR Values

Dye	Sample ref.	TSR %
Direct Blue 71	1	62.72%
Reactive Yellow	2	69.97%
Direct Red 23	3	63.85%
Direct Blue 199	4	63.45%

3.2.3.4. Thermogravimetry

According to the TGA, the dye degradation results were independently compared as were those of clay alone. The results and degradation peaks are found in Figure 3.2.4. The bottom of this figure shows curves d(YD), d(A71), d(R23), d(A199) and d(H), which derived from the first curves indicating specific degradation peaks. In view of these results, we see that Direct Blue 71 is the lowest and its degradation is the slowest, and Blue 199 strongly peaks at 367-482 °C. Red 23 and Reactive Yellow start to degrade earlier, but their drop is gradual and less marked within a range of approximately 217-556 °C.

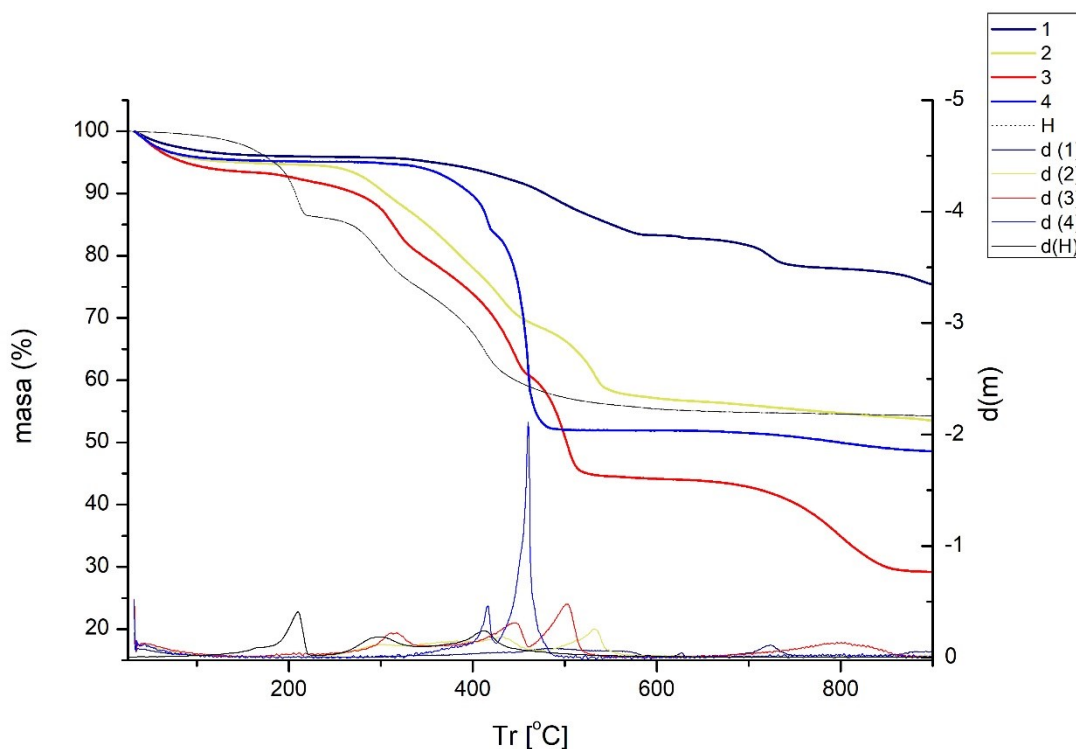


Figure 3.2.4. TGA for the original dyes and hydrotalcite

Next hybrid pigments were analyzed to see the effect of nanoclay as a host of the original dyes (Figure 3.2.5). We can see how the dye-clay interaction affected the original dye properties and how its degradation changed by temperature (Figure 3.2.5). We can observe how the first degradation peak lies at around 200°C.

Gravimetric performance was the same for the four hybrid samples because the four lines practically overlapped (Figure 3.2.5). By representing HC and only one of the HC + Dye hybrids (Figure 3.2.6), thermal performance was virtually the same as it was for HC alone. It was not easy to see the thermal degradation of the original dyes because all the hybrid pigments had a low dye content.

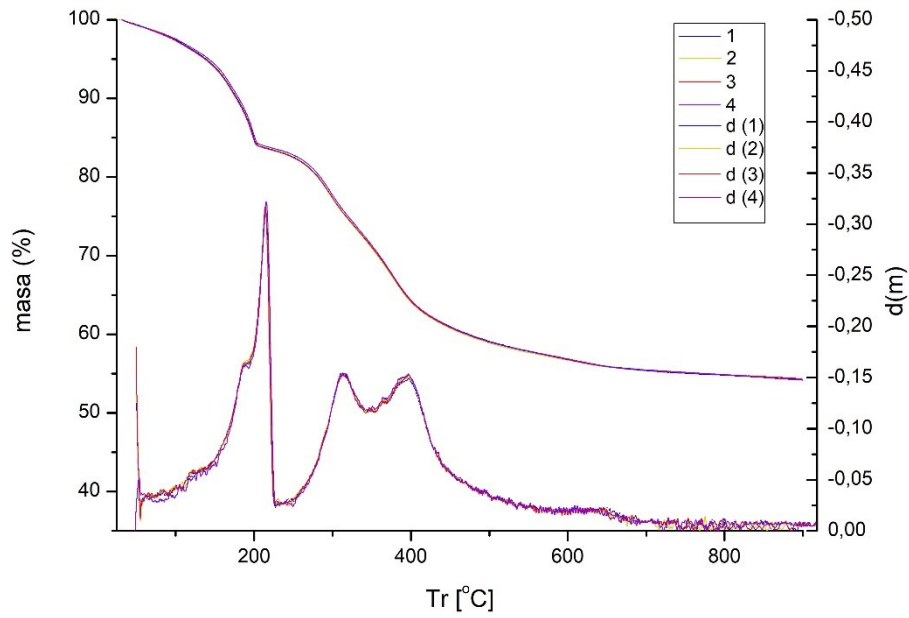


Figure 3.2.5. TGA for each hybrid sample

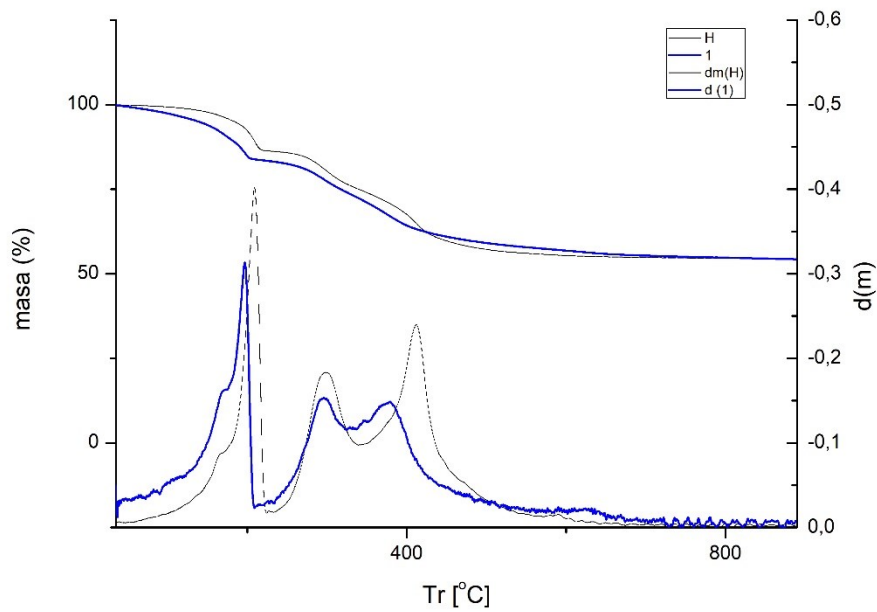


Figure 3.2.6. TGA for hydrotalcite and Sample 1

3.2.3.5. X-ray diffraction (XRD)

Thanks to X-ray diffraction, an intralaminar space opened up after clay calcination that facilitated dye penetration. The original structure became partially recomposed after the absorption process due to HC's shape memory. A peak showing the described characteristic between 11 and 12 degrees took place. As with the calcined HC, this peak disappeared because these layers opened (Figure 3.2.7). This peak slightly shifted owing to dye penetration. It can be assumed that this shift would be more marked at higher dye concentrations.

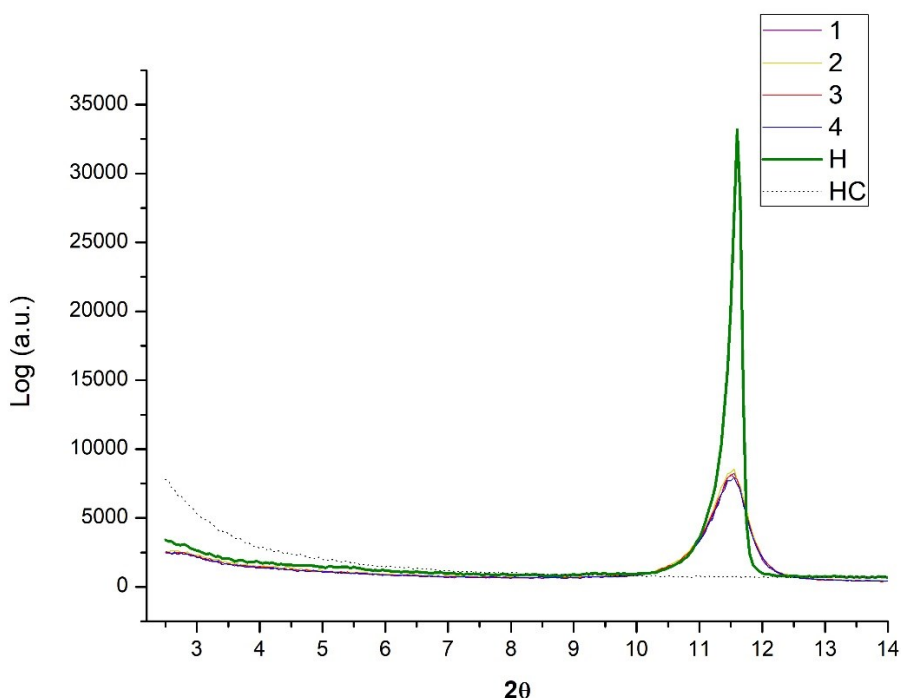


Figure 3.2.7. XRD for Hydrotalcite, Hydrotalcite calcined and hybrid pigments (Samples 1-4)

3.2.4. Conclusions

In view of our results, HC clay efficacy in absorbing reactive and direct dyes for wastewater treatment in textile dye processes was proven. The absorption percentages were considerably high because they exceeded 95% absorption in all cases. Good color fixation to clay was observed as far as its homogeneity and degree of stability are

concerned. The color intensity that resulted from the clay-dye hybrid was very low, which was not surprising because clay concentration was $20 \text{ g}\cdot\text{L}^{-1}$, while that of dyes was only $0.05 \text{ g}\cdot\text{L}^{-1}$. For future work, it is planned to calculate the adsorption kinetics of the clay to reduce the 24-hour stirring time of the solution with the dye and thus improve the process.

The TSR of the four hybrids was between 60% and 70%. As the TSR of the conventional targets was 75%, the studied samples came very close to these percentages. This reinforces the previous discussion about very low color intensity, which was very white for the white clay color.

The TGA results fell in line with this. Hybrids performed almost identically to HC alone, which means that dyes barely influenced the sample's final TGA. The hybrid's degradation peaks were the same as those of clay without having absorbed dyes. Finally thanks to the XDA, HC partially recovered its intralaminar space due to its shape memory. This should help to fix dye in clay and, therefore, the resulting hybrid stability.

References

1. M. Wakkal, B. Khiari, F. Zagrouba, Textile Wastewater Treatment by Agro-Industrial Waste: Equilibrium Modelling, Thermodynamics and Mass Transfer Mechanisms of Cationic Dyes Adsorption onto Low-Cost Lignocellulosic Adsorbent. *J. Taiwan Inst. Chem. Eng.* 2019, 96, 439–452. <https://doi.org/10.1016/J.JTICE.2018.12.014>.
2. M. L. Mathew, A. Gopalakrishnan, C. T. Aravindakumar, Aravind, U. K. Low – Cost Multilayered Green Fiber for the Treatment of Textile Industry Waste Water. *J. Hazard. Mater.* 2019, 365, 297–305. <https://doi.org/10.1016/J.JHAZMAT.2018.11.014>.
3. B. Micó Vicent, F.M. Martínez Verdu, J.E. Gilabert Pérez, Optimización de La Síntesis de Nanopigmentos de Origen Natural Para Biopolímeros Mediante El Uso Del Diseño de Experimentos. Doctoral Thesis. Universitat Politècnica de València 2015. <http://hdl.handle.net/10251/59449> (22/11/2021).
4. P. Semeraro, V. Rizzi, P. Fini, S. Matera, P. Cosma, E. Franco, R. García, M. Ferrándiz, E. Núñez, J. A. Gabaldón, I. Fortea, E. Pérez, M. Ferrándiz, Interaction between Industrial Textile Dyes and Cyclodextrins. *Dye. Pigment.* 2015, 119, 84–94. <https://doi.org/10.1016/J.DYEPIG.2015.03.012>.
5. D. Sana, S. Jalila, A Comparative Study of Adsorption and Regeneration with Different Agricultural Wastes as Adsorbents for the Removal of Methylene Blue from Aqueous Solution. *Chinese J. Chem. Eng.* 2017, 25 (9), 1282–1287. <https://doi.org/10.1016/J.CJCHE.2017.01.012>.
6. L. Sanchez, M. Ollier, R. P. Gonzalez, J. S. Alvarez, V. A. Nanocomposite Materials for Dyes Removal. *Handb. Nanomater. Ind. Appl.* 2018, 922–951. <https://doi.org/10.1016/B978-0-12-813351-4.00053-5>.
7. M. Erkanlı, L. Yilmaz, P. Z. Çulfaz-Emecen, U. Yetis, Brackish Water Recovery from Reactive Dyeing Wastewater via Ultrafiltration. *J. Clean. Prod.* 2017, 165, 1204–1214. <https://doi.org/10.1016/J.JCLEPRO.2017.07.195>.
8. M. Ogawa, R. Takee, Y. Okabe, Y. Seki, Bio-Geo Hybrid Pigment Clay-Anthocyanin Complex Which Changes Color Depending on the Atmosphere. *Dye. Pigment.* 2017, 139, 561–565. <https://doi.org/10.1016/J.DYEPIG.2016.12.054>.
9. F. López Arbeloa, V. Martínez Martínez, J. Bañuelos Prieto, I. López Arbeloa, Adsorption of Rhodamine 3B Dye on Saponite Colloidal Particles in Aqueous Suspensions. *Langmuir* 2002, 18 (7), 2658–2664. <https://doi.org/10.1021/la0113163>.
10. M. I. Carretero, M. Pozo, C. Sánchez, F. J. García, J. A. Medina, J. M. Bernabé, Comparison of Saponite and Montmorillonite Behaviour during Static and Stirring

- Maturation with Seawater for Pelotherapy. *Appl. Clay Sci.* 2007, 36 (1–3), 161–173. <https://doi.org/10.1016/J.CLAY.2006.05.010>.
11. D. Guillermin, T. Debroise, P. Trigueiro, L. de Viguerie, Rigaud, B. Morlet-Savary, F. Balme, S. Janot, J.-M. Tielens, F. Michot, L. Lalevee, J. Walter, P. Jaber, M. New Pigments Based on Carminic Acid and Smectites: A Molecular Investigation. *Dye. Pigment.* 2019, 160, 971–982. <https://doi.org/10.1016/J.DYEPIG.2018.07.021>.
 12. E. M. Moujahid, R. Lahkale, H. Ouassif, F. Z. Bouragba, W. Elhatimi, New Organic Dye/Anionic Clay Hybrid Pigments: Preparation, Optical Properties and Structural Stability. *Dye. Pigment.* 2019, 162, 998–1004. <https://doi.org/10.1016/J.DYEPIG.2018.11.021>.
 13. J.-Z. Yi, L.-M. Zhang, Removal of Methylene Blue Dye from Aqueous Solution by Adsorption onto Sodium Humate/Polyacrylamide/Clay Hybrid Hydrogels. *Bioresour. Technol.* 2008, 99 (7), 2182–2186. <https://doi.org/10.1016/J.BIORTECH.2007.05.028>.
 14. R.A. Schoonheydt, L. Heughebaert, Clay Adsorbed Dyes: Methylene Blue on Laponite. *Clay Miner.* 1992, 27, 91–100, doi:10.1180/claymin.1992.027.1.09.
 15. H. Mittal, R. Babu, A. A. Dabbawala, S. Stephen, S. Alhassan, M. Zeolite-Y Incorporated Karaya Gum Hydrogel Composites for Highly Effective Removal of Cationic Dyes. *Colloids Surfaces A Physicochem. Eng. Asp.* 2020, 586, 124161. <https://doi.org/10.1016/J.COLSURFA.2019.124161>.
 16. L. N. F. de Queiroga, D. B. França, F. Rodrigues, I. M. G. Santos, M. G. Fonseca, M. Jaber, Functionalized Bentonites for Dye Adsorption: Depollution and Production of New Pigments. *J. Environ. Chem. Eng.* 2019, 7 (5), 103333. <https://doi.org/10.1016/J.JECE.2019.103333>.
 17. H. Laguna, S. Loera, I. A. Ibarra, E. Lima, M. A. Vera, V. Lara, Azoic Dyes Hosted on Hydrotalcite-like Compounds: Non-Toxic Hybrid Pigments. *Microporous Mesoporous Mater.* 2007, 98 (1–3), 234–241. <https://doi.org/10.1016/j.micromeso.2006.09.009>.
 18. V. Rives, M. E. Pérez-Bernal, R. J. Ruano-Casero, I. Nebot-Díaz, Development of a Black Ceramic Pigment from Non Stoichiometric Hydrotalcites. *J. Eur. Ceram. Soc.* 2012, 32 (5), 975–987. <https://doi.org/10.1016/j.jeurceramsoc.2011.11.033>.
 19. X. Yu, J. Wang, M. Zhang, L. Yang, J. Li, P. Yang, D. Cao, Synthesis, Characterization and Anticorrosion Performance of Molybdate Pillared Hydrotalcite/in Situ Created ZnO Composite as Pigment for Mg-Li Alloy Protection. *Surf. Coatings Technol.* 2008, 203 (3–4), 250–255. <https://doi.org/10.1016/j.surfcoat.2008.08.074>.
 20. H. Chen, Z. Zhang, G. Zhuang, R. Jiang, A New Method to Prepare ‘Maya Red’ Pigment from Sepiolite and Basic Red 46. *Appl. Clay Sci.* 2019, 174, 38–46. <https://doi.org/10.1016/J.CLAY.2019.03.023>.

21. R. M. M. dos Santos, R. G. L. Gonçalves, V. R. L. Constantino, L. M. da Costa, L. H. M. da Silva, Tronto, J. Pinto, F. G. Removal of Acid Green 68:1 from Aqueous Solutions by Calcined and Uncalcined Layered Double Hydroxides. *Appl. Clay Sci.* 2013, 80–81, 189–195. <https://doi.org/10.1016/j.clay.2013.04.006>.
22. J. L. Bigman, Monitoring of Chemicals and Water. *Handb. Silicon Wafer Clean. Technol.* 2018, 619–657. <https://doi.org/10.1016/B978-0-323-51084-4.00011-3>.
23. M. M. F. Silva, M. M. Oliveira, M. C. Avelino, M. G. Fonseca, R. K. S. Almeida, E. C. Silva Filho, Adsorption of an Industrial Anionic Dye by Modified-KSF-Montmorillonite: Evaluation of the Kinetic, Thermodynamic and Equilibrium Data. *Chem. Eng. J.* 2012, 203, 259–268. <https://doi.org/10.1016/j.cej.2012.07.009>.
24. Huang, G.; He, J.; Zhang, X.; Feng, M.; Tan, Y.; Lv, C.; Huang, H.; Jin, Z. Applications of Lambert-Beer Law in the Preparation and Performance Evaluation of Graphene Modified Asphalt. *Constr. Build. Mater.* 2021, 273, 121582, doi:10.1016/j.conbuildmat.2020.121582.
25. J. L. Bigman, K. A. Reinhardt, *Monitoring of Chemicals and Water Elsevier Inc.*, 2018. <https://doi.org/10.1016/B978-0-323-51084-4.00011-3>.
26. C. Mensch, R. Chintala, D. Nawrocki, J. T. Blue, A. Bhambhani, Enabling Lyophilized Pneumococcal Conjugate Vaccines Through Formulation Design and Excipient Selection Suitable for A Multivalent Adjuvanted Vaccine. *J. Pharm. Sci.* 2020, 1–11. <https://doi.org/10.1016/j.xphs.2020.10.038>.
27. L. S. Castillo-Peinado, M. Calderón-Santiago, F. Priego-Capote, Lyophilization as Pre-Processing for Sample Storage in the Determination of Vitamin D3 and Metabolites in Serum and Plasma. *Talanta* 2021, 222 (September 2020). <https://doi.org/10.1016/j.talanta.2020.121692>.
28. S. Maharjan, K. S. Liao, A. J. Wang, S. A. Curran, Highly Effective Hydrophobic Solar Reflective Coating for Building Materials: Increasing Total Solar Reflectance via Functionalized Anatase Immobilization in an Organosiloxane Matrix. *Constr. Build. Mater.* 2020, 243, 118189. <https://doi.org/10.1016/j.conbuildmat.2020.118189>.
29. Y. Liu, R. Li, J. Yu, F. Ni, Y. Sheng, A. Scircle, J. V. Cizdziel, Y. Zhou, Separation and Identification of Microplastics in Marine Organisms by TGA-FTIR-GC/MS: A Case Study of Mussels from Coastal China. *Environ. Pollut.* 2020, No. xxxx, 115946. <https://doi.org/10.1016/j.envpol.2020.115946>.
30. M. Umar, M. I. Ofem, A. S. Anwar, A. G. Salisu, Thermo Gravimetric Analysis (TGA) of PA6/G and PA6/GNP Composites Using Two Processing Streams. *J. King Saud Univ. - Eng. Sci.* 2020, No. xxxx. <https://doi.org/10.1016/j.jksues.2020.09.003>.
31. I. Corazzari, F. Turci, R. Nisticò, TGA Coupled with FTIR Gas Analysis to Quantify the Vinyl Alcohol Unit Content in Ethylene-Vinyl Alcohol Copolymer. *Mater. Lett.* 2021, 284, 129030. <https://doi.org/10.1016/j.matlet.2020.129030>.

32. H. Pálková, J. Madejová, M. Zimowska, E. Bielańska, Z. Olejniczak, L. Lityńska-Dobrzyńska, E. M. Serwicka, Laponite-Derived Porous Clay Heterostructures: I. Synthesis and Physicochemical Characterization. *Microporous Mesoporous Mater.* 2010, 127 (3), 228–236. <https://doi.org/10.1016/j.micromeso.2009.07.019>.
33. W. Zhuo, Y. Xie, M. T. Benson, J. Ge, R. D. Mariani, J. Zhang, XRD and SEM/EDS Characterization of Two Quaternary Fuel Alloys (U-2.5Mo-2.5Ti-5.0Zr and U-1.5Mo-1.5Ti-7.0Zr in Wt. %) for Fast Reactors. *Mater. Charact.* 2020, 170 (September), 110696. <https://doi.org/10.1016/j.matchar.2020.110696>.

Recuperación del colorante de aguas residuales textiles mediante nanoarcillas para su reutilización como pigmentos y nuevos baños de tintura

3.3. Adaptación del artículo: The Optimal Concentration of Nanoclay Hydrotalcite for Recovery of Reactive and Direct Textile Colorants

Artículo publicado en: López-Rodríguez, Daniel; Micó-Vicent, B.; Bonet-Aracil, Marilés; Cases, Francisco; Bou-Belda, Eva. (2022) The Optimal Concentration of Nanoclay Hydrotalcite for Recovery of Reactive and Direct Textile Colorants. *International Journal of Molecular Sciences* (23)1 - 24. [ijms23179671](https://doi.org/10.3390/ijms23179671)

Abstract:

Concerns about the health of the planet have grown dramatically, and the dyeing sector of the textile industry is one of the most polluting of all industries. Nanoclays can clean dyeing wastewater using their adsorption capacities. In this study, as a new finding, it was possible to analyze and quantify the amount of metal ions substituted by anionic dyes when adsorbed, and to determine the optimal amount of nanoclay to be used to adsorb all the dye. The tests demonstrated the specific amount of nanoclay that must be used and how to optimize the subsequent processes of separation and processing of the nanoclay. Hydrotalcite was used as the adsorbent material. Direct dyes were used in this research. X-ray diffraction (XRD) patterns allowed the shape recovery of the hydrotalcite to be checked and confirmed the adsorption of the dyes. An FTIR analysis was used to check the presence of characteristic groups of the dyes in the resulting hybrids. The thermogravimetric (TGA) tests corroborated the dye adsorption and the thermal fastness improvement. Total solar reflectance (TSR) showed increased radiation protection for UV-VIS-NIR. Through the work carried out, it has been possible to establish the maximum adsorption point of hydrotalcite.

3.3.1. Introduction

The planet's resources are limited and, nowadays, managing and conserving them is of global importance. Therefore, all possible measures are being taken to make the most of these resources and not waste them. The textile chemical industry is the sector that produces the most wastewater with the greatest chemical activity on the Earth [1]. The

recycling of industrial wastewater is perceived as an ever-growing need. The concentration of dyes in effluents has been reported to be around 50–1000 ppm, although cases of lower than 10–50 ppm have been found [2].

Textile dye materials are classified into different categories depending on the dye material used, such as basic [3,4], acidic, direct, reactive, vat, and disperse dyes. Direct and reactive dye materials, in particular, are commonly produced in large amounts for textile industry printing and dyeing processes to bring color to cellulosic materials, due to their availability and range of colors [5]. Due to their toxicity, these dyes have both been extensively studied for their removal from wastewater by various techniques [6–9].

In an effort to recover all the natural resources that we enjoy, the use of nanocomposites and nanoclays has become more common in industry. When small amounts of nanoclays are incorporated into polymeric matrices, the result is called a nanocomposite [10]. Previous works have demonstrated the efficacy of this type of element and have achieved successes in corresponding trials [11–20]. The Awual group has reported a growing trend to use composite materials for the removal of different dyes, based on the specific surface area of the adsorbing agent and functionality [21–23].

It has been shown that nanoclays can be used in industry as effective absorbents for different chemical compounds, and therefore, they have been used in the purification of textile wastewater and many other industries. Thanks to their specific characteristics, they have the ability to form hybrids by absorbing and retaining residual industrial dyes that have not been absorbed during the dyeing process. These hybrids can be eliminated after filtering or even given new uses, thus, making full use of all the materials [24–26]. The properties of nanoclay allow novel applications to be defined, including applications which significantly reduce the amount of colorants that reach wastewater. This has led, in turn, to new lines of research into the possibility of reusing colorants that are not being used and are going to waste. In addition, nanoclays are an abundant and low-cost material [27,28], which makes them very cost-effective considering the cost-effectiveness ratio. Consequently, hydrotalcite was chosen for this research in view of the results of other works that have demonstrated the adsorption capacity of anionic textile dyes [24,29–33].

Hydrotalcite (HC) is a mineral that is classified as a nanoclay because its dimensions are less than 20 nm. This laminar nanoclay is of interest to the scientific community due to the different possible applications that it offers, such as in medicine, sludge cleaning, and petrochemical spills [34]. Hydrotalcite has a huge capacity to adsorb negatively charged compounds and this adsorption can be carried out using different procedures [32,35]. The most simple and effective procedure is based on the direct adsorption of compounds that are in dispersion, although there are certain limitations due to the crystallinity that the solid may present, the temperature, the pH, the size of the anions, etc. [30,36,37]. It has been shown that hydrotalcite has shape memory, which allows it to be calcined at 600 °C, and therefore, once it is in contact with an aqueous solution it recovers its shape. In this initial structure recovery process, the anions present in the solution are incorporated into the structure recovered by HC [24–26]. An alternative method involves a synthetic process in which the nanoclay incorporates a specific anion into the structure of the hydrotalcite. This method is called co-precipitation [38].

For this work, direct dyes and a reactive dye were chosen, with the aim of carrying out a study on the adsorption of the most common dyes used in cotton dyeing, since these have a loss in effluents of up to 30% [39]. In addition, when studying direct and reactive dyes, a statistical experimental design was followed to consider the influence of molecule size on the adsorption phase. Within the range of selected colorants, complete trichromy was also used, which formed part of this team's plans for future reuse work.

3.3.2. Results

3.3.2.1. Final Concentrations in Solution

The results obtained confirm that the nanoclay has a significant capacity to adsorb dyes (Table 3.3.1), as has been shown in other studies [40–44] that tested the adsorption properties of HC for removing several dyes such Congo red, acid red 1, methyl orange, and methylene blue. The tests on Samples 13–16 were completed and it was observed that the nanoclay was totally saturated and not capable of absorbing more dye. After reaching the saturation point of the nanoclay, it is possible to define the relationship “x” defined above, which is the scientific contribution of this work. Prior to these analyses, dye adsorption tests

were carried out on several real wastewaters collected from a textile dyeing industry, thus, confirming the adsorption capacity and making it possible to extrapolate the results of this work to the real industry.

Table 3.3.1. Differences in concentrations after HC adsorption

Sample Ref.	Dye	Initial Conc. g·L ⁻¹	Final Conc. g·L ⁻¹	Absorbance	Ads (%)
1	Direct Red 23	0.05	4.89×10^{-4}	0.002	99.22
2	Direct Blue 199	0.05	7.80×10^{-4}	0.002	98.43
3	Direct Blue 71	0.05	1.77×10^{-3}	0.007	96.45
4	Yellow Drimaren	0.05	5.42×10^{-4}	0.006	98.91
5	Direct Blue 71	0.05	1.60×10^{-3}	0.004	96.81
6	Yellow Drimaren	0.05	3.41×10^{-4}	0.003	99.32
7	Direct Red 23	0.05	5.47×10^{-4}	0.004	98.91
8	Direct Blue 199	0.05	8.72×10^{-4}	0.004	98.26
9	Yellow Drimaren	1	7.43×10^{-4}	0.009	99.93
10	Direct Red 23	1	5.76×10^{-4}	0.005	99.94
11	Direct Blue 199	1	8.26×10^{-4}	0.003	99.92
12	Direct Blue 71	1	1.71×10^{-3}	0.006	99.83
13	Yellow Drimaren	1	3.89×10^{-3}	0.056	99.61
14	Direct Red 23	1	1.94×10^{-3}	0.052	99.81
15	Direct Blue 199	1	2.85×10^{-3}	0.047	99.72
16	Direct Blue 71	1	5.34×10^{-3}	0.068	99.47

The adsorption for each dye shows the hybrid pigments process performance. For this reason, the total amount of dye loaded into the nanoclay as Ads(%) was used as the response variable for the DoE analysis. Table 3.3.2 shows that both of the selected factors, i.e., the dye structure and the nanoclay/dye ratio (x), are significant in the cleaning or hybrid synthesis process that it is studied. The AB interaction is not significant, which means that the trends observed in the main factors are the same as that observed in the interaction (Figure 3.3.1). There were no different behaviors observed depending on the dye structure related to the dye/clay concentration.

Table 3.3.2. Variance analysis for Ads(%) from the 42 DoE

Source	Sum of Squares	f.d.	Medium Square	F-Ratio	p-Value
A:Dye	2.59932	1	2.59932	5.06	0.0482
B:x	2.14673	1	2.14673	4.18	0.0681
AA	2.6937	1	2.6937	5.24	0.045

AB	0.0905298	1	0.0905298	0.18	0.6835
BB	1.40323	1	1.40323	2.73	0.1294
Total Error	5.13621	10	0.513621		
Total (corr.)	17.3029	15			

R-squared = 70.3159%.

As it can be observed in Figure 3.3.1, the Direct Blue 71 Sample 3, with the highest molecular weight, has less significant adsorption than the other three dyes. On the one hand, the differences are lower than 2% due to the experimental conditions. On the other hand, the differences between the nanoclay/dye concentrations show that the lowest x ratio, means more adsorbed dye, as expected, because as the dye concentration increased the adsorption grew. However, there are no significant differences between the 0.5 and 2 x levels and the 100 and 200 concentration levels.

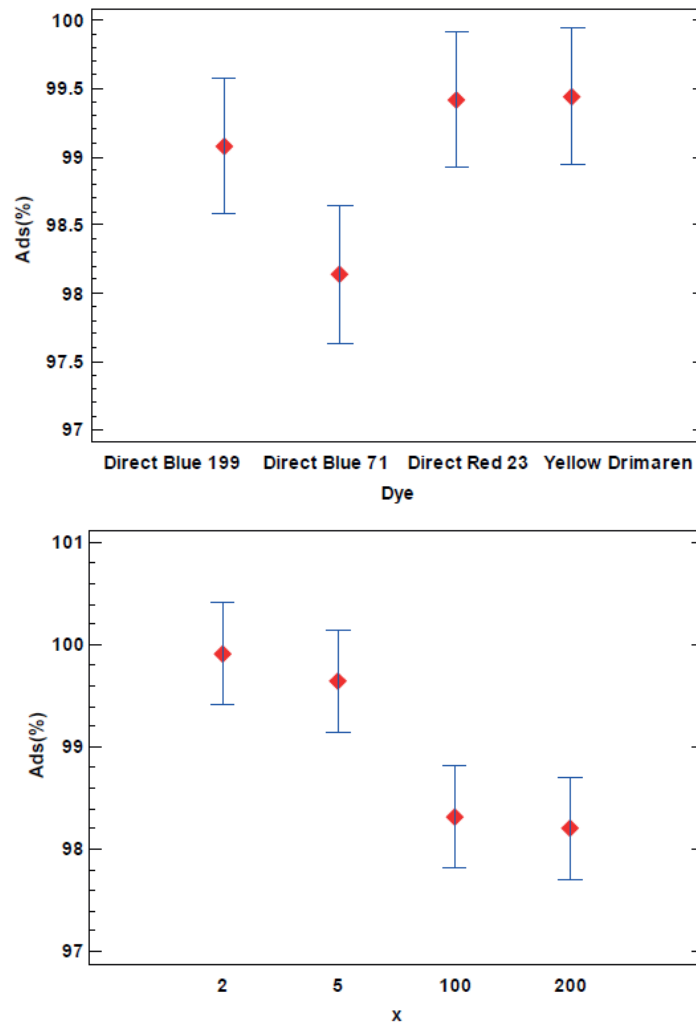


Figure 3.3.1. LSD Fisher means plot (95% confidence intervals) from Ads(%) as the response variable

3.3.2.2. Color Measurements

The color measurements of the dye-clay hybrids represented in the chromatic diagrams are shown below. For the colorimetric calculations of each hybrid pigment, the reflectance (λ) measurements were used. The main CIE 15:2004 standard [45] guidelines of the International Commission on Illumination and Color (CIE) were followed to make the absolute and relative colorimetric comparisons. The colorimetric CIELAB parameters codified by the CIE 1931 XYZ patron and D65 standard illumination were used. The CIE a^*b^* and CIE-Cab $^*L^*$ diagrams in Figure 3.3.2 show that there are changes in the hue due to the

dye and the concentration. For example, the samples with Yellow Drimaren are more yellowish at low concentrations ($x = 2$ or 0.5) than the samples at high concentrations ($x = 200$ and 100). The same phenomenon can be found in the samples with Direct Red 23.

However, the sample with $x = 2$ with the Direct Red 23, Direct Blue 71, and Direct Blue 199 are apparently achromatic as compared with the less concentrated samples at $x = 0.05$ with the same dyes. The chroma is affected by the dye concentration and the hue. With yellow samples, it is more difficult to get darker and achromatic samples, as we can see in the L^* - Cab^* highlighted areas. In addition, as the dye ratio increases (x decrease), the samples L^* is low and the chroma decrease, allowing a wider range of colors to be covered. There is a hue shift towards green in the Direct Blue 199 samples when the concentrations increase to $x = 100$ and 200 . The color range represented by the area under the L^* Cab^* diagrams is bigger with the samples with the Direct Blue 199 than the samples with the Direct Blue 71 which are less chromatic and less bright. Finally, the color range with the samples with Direct Red 23 is wider in the samples with Direct Blue 71.

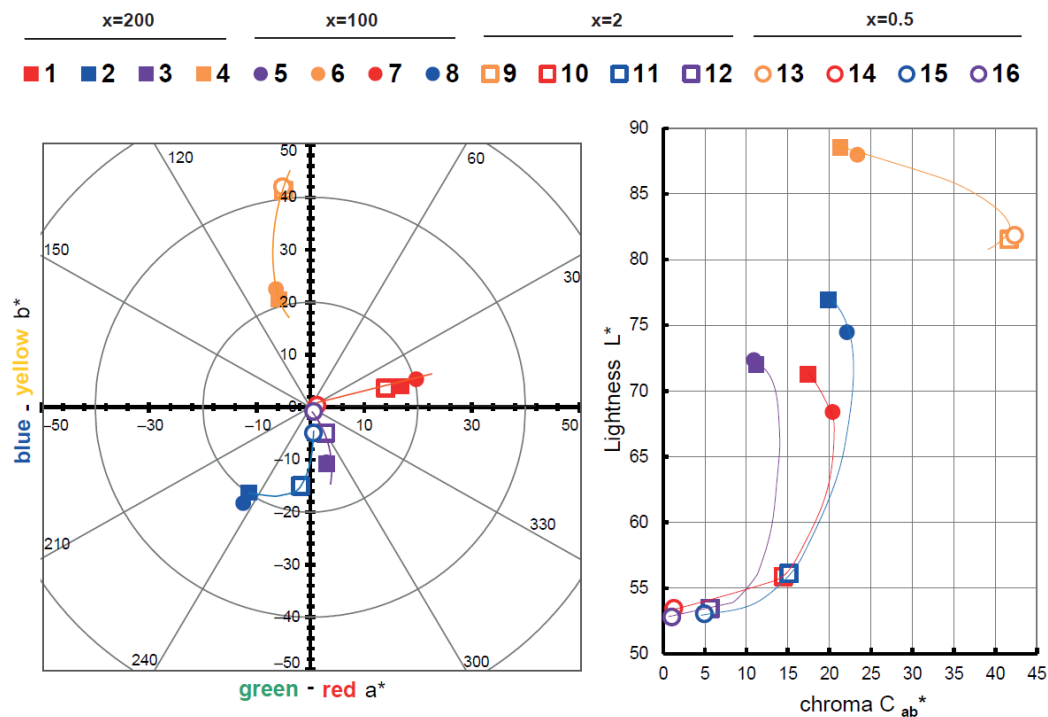


Figure 3.3.2. Graphic CIELAB plots for hybrid pigments synthesized under 1–16 conditions using the D65 illuminant and the CIE-1931 XYZ standard observer. Left, CIE-a * b * color diagram; right, CIE-Cab * L * color chart

3.3.2.3. Total Solar Reflectance (TSR)

The amount of energy that is absorbed by solar radiation in the most superficial layers of a substrate is what determines the amount of heat accumulated on that surface. One of the most determining factors for this phenomenon is the exposure time that the surface undergoes. To achieve coatings with cold surfaces, the maximum reflection of solar radiation must be achieved. This reflection capacity of a body is expressed numerically by total solar reflectance (TSR), considering 0% total absorption and 100% complete reflection.

To calculate solar reflectance, it is necessary to have the data of the solar reflectance of the raw substrate and apply the solar weighting factors for each wavelength to be analyzed. All these calculations are included in the ASTM G173-03 standards [46]. To calculate the degree of total solar absorption performed by the hybrid, (1-TSR) must be performed.

Table 3.3.3 shows a comparison from maximum ($x = 0.5$) to minimum ($x = 200$) saturation of the nanoclay after adsorption of the dye. Figure 3.3.3 represents the highest and lowest x ratio for the 4 dyes. In all these samples the visible light behavior depends on the dye structure affecting the color perception (hue, chroma and lightness). In the near infrared from 700–1400 nm the differences due to the x ratio are significant, however, from 1400–2400 nm the behavior of the samples is closer. Here the nanoclay structure has a stronger effect on the TSR (%) contribution than the dye concentration.

Table 3.3.3. TSR Values

Dye	Sample Ref.	TSR %
Direct Red 23	1	58.50
Direct Blue 199	2	58.45
Direct Blue 71	3	55.27
Yellow Drimaren	4	63.45
Direct Blue 71	5	56.27
Yellow Drimaren	6	67.49
Direct Red 23	7	55.14
Direct Blue 199	8	56.08
Yellow Drimaren	9	58.30
Direct Red 23	10	47.44
Direct Blue 199	11	36.14
Direct Blue 71	12	38.55
Yellow Drimaren	13	58.80
Direct Red 23	14	29.47
Direct Blue 199	15	29.42
Direct Blue 71	16	32.00

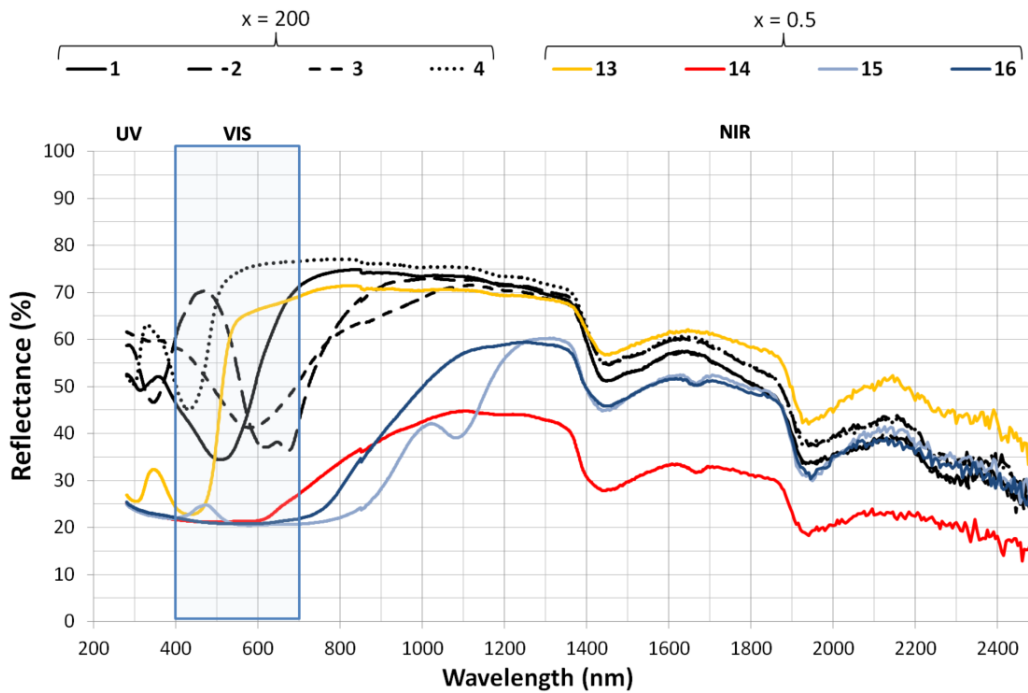


Figure 3.3.3. TSR (%) for each hybrid at maximum and minimum dye loading

In Figure 3.3.4, the Direct Red 21 dye and all its hybrids are studied to assess how this change in concentration affects the results. As can be observed, the dye concentration affects the hybrid pigment reflectances and dye ratio increases (lower x values), the reflectance factor ρ (%) decreases over all the spectra measured. The differences in the visible light between the $x = 2$ and $x = 0.05$ samples seems low, but those differences increase significantly in the near infrared from 700–2400 nm affecting the final TSR (%) value. This means that hybrid pigments with similar color perception, can obtain different TSR (%) values affecting the future applications that should be considered.

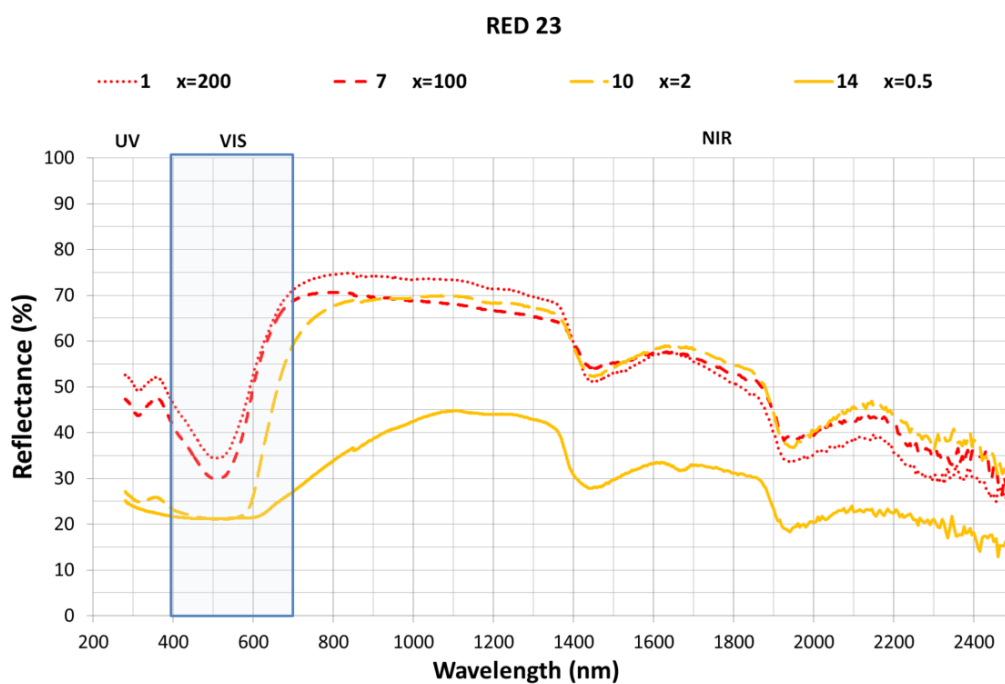


Figure 3.3.4. TSR (%) for RED 23 dye hybrid

Figure 3.3.5, shows TSR (%) values seem to be correlated with the nanoclay/dye concentration. As can be expected, the samples with low L^* values have low TSR (%) due to the lower reflectance mainly in the visible spectrum. In addition, yellow samples have more TSR (%) for the same reasons. However, more differences can be found between all the dye structures and x ratios but is not possible to know if those differences are statically significant without the variance analysis.

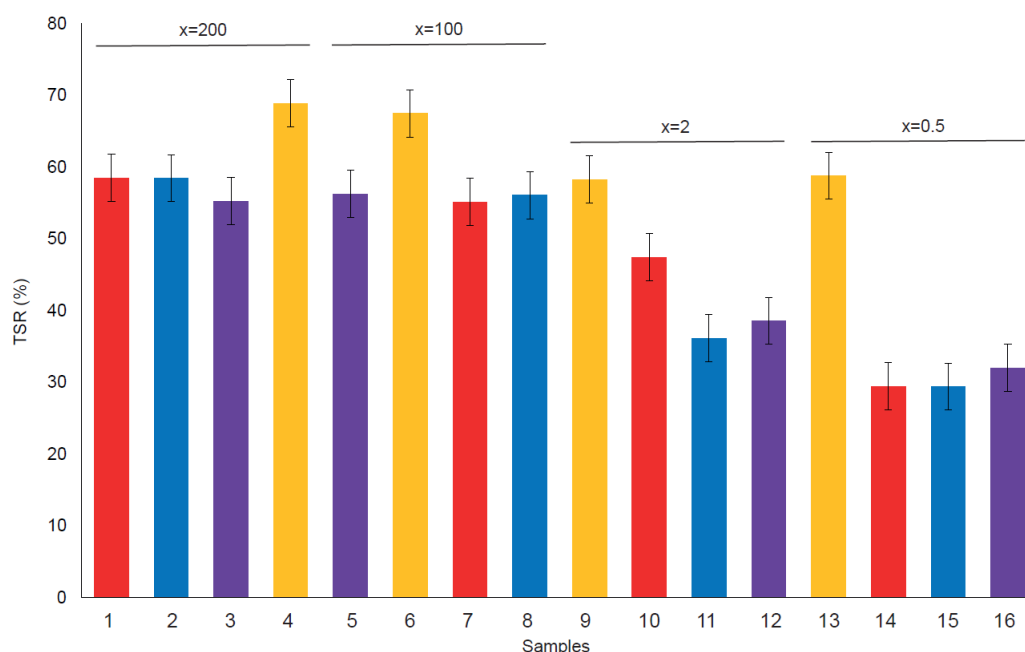


Figure 3.3.5. Total Solar Reflectance (TSR (%)) for each sample

The x ratio and the dye structure affects the TSR (%) value in the hybrid pigments, and there are no interactions between these factors as can be found in the ANOVA analysis (Table 3.3.4). The Yellow drimaren pigments has high TSR (%) values, meanwhile there are no significant differences between the blues and the reds. Also dye concentration increases, the TSR (%) decreases but there are no significant differences between $x = 2$ and $x = 0.5$, or $x = 100$ and $x = 200$. To achieve a high TSR value $x = 100$ is sufficient, and it is not a problem to increase the dye ratio from $x = 2$ to $x = 0.5$. The TSR (%) is the same and the color increases significantly as can be seen in Figure 3.3.6.

Table 3.3.4. Analisis of variance for TSR values

Source	Sum of Squares	f.d.	Medium Square	F-Ratio	p_Value
A:Dye	227.623	1	227.623	6.48	0.029
B:x	478.524	1	478.524	13.63	0.0042
AA	418.847	1	418.847	11.93	0.0062
AB	43.4298	1	43.4298	1.24	0.292
BB	178.111	1	178.111	5.07	0.048
Error total	351.007	10	35.1007		
Total (corr.)	2580.2	15			

R-squared = 86.3961%

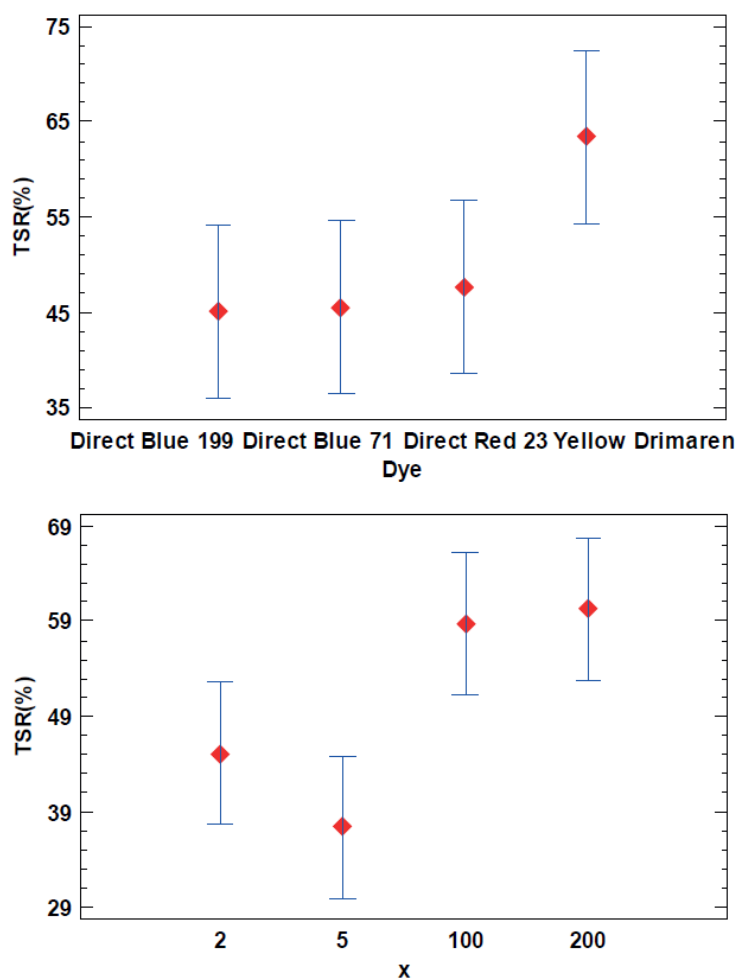


Figure 3.3.6. LSD Fisher means plot (95% confidence intervals) from TSR (%) as the response variable

3.3.2.4. Thermogravimetry (TGA)

The results obtained in the TGA are shown in Figures 3.3.7–3.3.10. Each figure shows the degradation vs. temperature curves of each colorant (B199, B71, R23, and YD) and the degradation of the nanoclay (HC) is also analyzed. The curves at the bottom of each graph show the lines $d(YD)$, $d(B71)$, $d(R23)$, $d(B199)$, and $d(HC)$, which are derived from the first curves indicating specific degradation peaks (DTGA). The results show that, on the one hand, Direct Red 23 and Reactive Yellow start to degrade earlier, but their decline is gradual and less marked within a range of approximately 217–556 °C. On the other hand, Blue 199 shows a marked peak at 367–482 °C. The degradation of Direct Blue 71 is the lowest and its degradation is the slowest.

Figure 3.3.8 shows a comparison of the TGA and DTGA of HC and Sample 3. As can be seen, hydrotalcite suffers a loss of water including physisorbed and interlamellar in the range of 100–170 °C. The second loss corresponding to the range of 170–280 °C is attributed to the loss of lamellar OH groups. The third loss, recorded between 280 and 600 °C, can be assigned to the loss of carbonate ions and combustion of the molecule fragment [47–49]. When hydrotalcite is analyzed alone without having previously adsorbed any dye, there are peaks at 208, 297, and 411 °C. The next step was to analyze the hybrid pigments after adsorption to see how the nanoclay affects thermal behavior. Figures 3.3.7 to 3.3.10 show how the initial properties of the dyes have been notably altered.

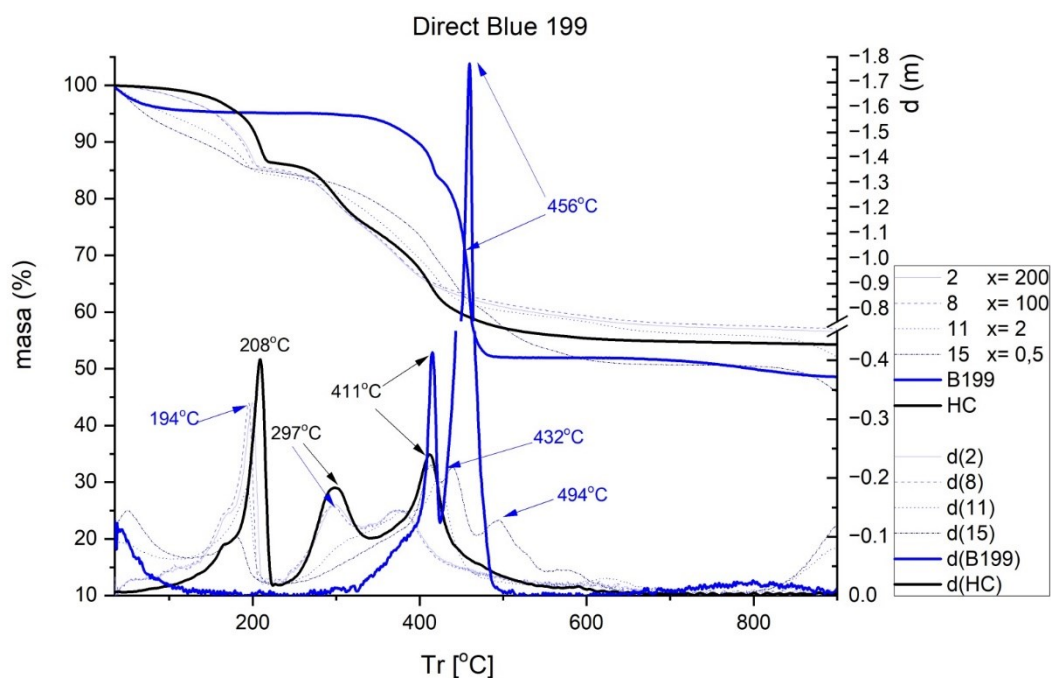


Figure 3.3.7. TGA and DTGA of Direct Blue 199 free and adsorbed

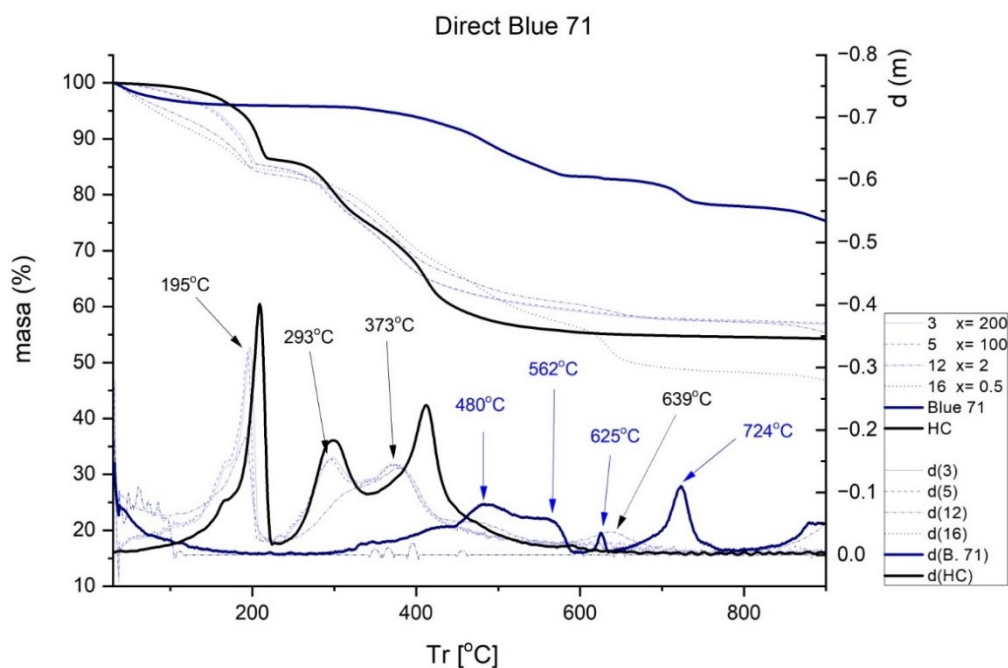


Figure 3.3.8. TGA and DTGA of Direct Blue 71 free and adsorbed

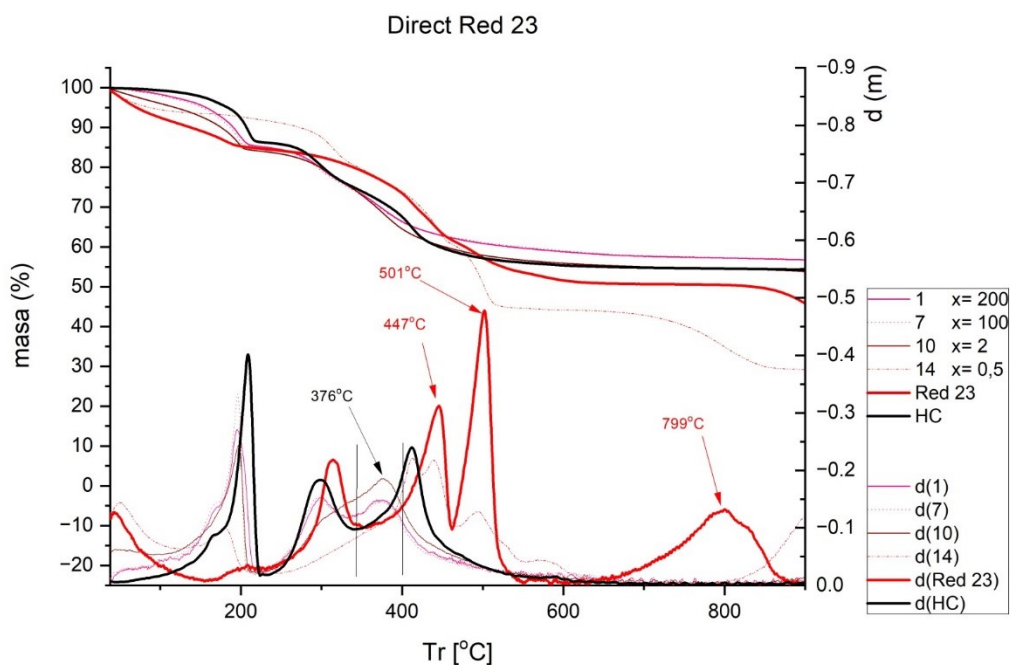


Figure 3.3.9. TGA and DTGA of Direct Red 23 free and adsorbed

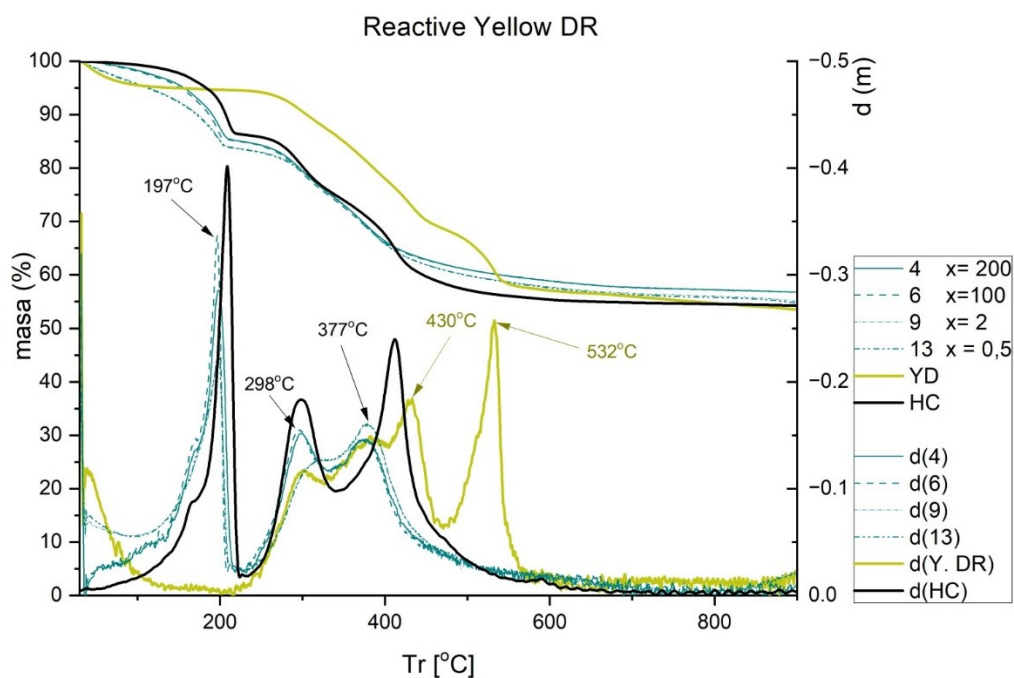


Figure 3.3.10. TGA and DTGA of Reactive Yellow DR free and adsorbed

Figure 3.3.7 shows the thermal behavior of B199. Two peaks are observed, one at 411 °C and a very prominent one at 456 °C. After adsorption on HT, the height of the original peak of the nanoclay slightly decreases in the range between 164 and 208 °C. Peaks at 297 and 411 °C are also observed, although with less loss of mass at these points. For Sample 11, two new peaks can be seen at 432 and 494 °C, most likely due to the considerable loss of mass suffered by the dye at 456 °C which is manifested in these two new peaks once adsorbed by HT.

In the case of the dye B71 (Figure 3.3.8), several peaks at around 480, 562, 625, and 724 °C are observed, which disappear after adsorption on HC, although a very mild peak is seen at 639 °C, most likely produced by the gradual degradation of the colorant between the 562 and 625 °C, which has been softened by the effect of the nanoclay. Moreover, peaks at 195, 293, and 373 °C also appear, typical of nanoclay, as seen in Figures 3.3.8 and 3.3.10 marking the peaks at 208, 297, and 411 °C.

In the hybrid formed by the Red 23 dye and the nanoclay (Figure 3.3.9), there are peaks at 447, 501, and 799 °C which completely disappear when the dye is adsorbed by the nanoclay. A single, wide peak is observed around 376 °C, which is also observed in hydrotalcite.

Finally, with Yellow DR (Figure 3.3.10), two peaks can be observed at 430 and 532 °C, which completely disappear when the hybrid is formed with the nanoclay. Again, the characteristic peaks associated with the loss of water in the nanoclay appear at 197, 298, and 377 °C, as was described in previous cases.

In previous works it has been possible to observe how the thermal stability of hybrids increased. Experimentally, it can be observed that the peaks of the dyes disappear when adsorbed by the nanoclay. It is considered that there are two reasons why the improvement of this property is achieved [50,51]. On the one hand, the laminar structure of the nanoclay has a barrier effect which reduces the volatility of the compounds and, on the other hand, there is a transfer of energy between the dye and the nanoclay when they are subjected to a temperature that is applied to the surface of the nanoclay [52,53].

3.3.2.5. X-ray Diffraction (XRD)

The X-ray diffraction results are shown in Figure 3.3.11. This figure shows how, after calcining the nanoclay, the intralaminar space has opened to facilitate the penetration of the dye, and also how, after the adsorption process, there is a partial recombination of the original structure due to memory so that hydrotalcite has shape memory [24–26,54]. After the calcination of the nanoclay, a structural collapse produced by dehydroxylation occurs inside the layers of this mineral [29]. Between 11 and 12 degrees there is a peak that shows the described characteristic and, as in the case of calcined hydrotalcite (HC), this peak disappears due to the opening of said layers.

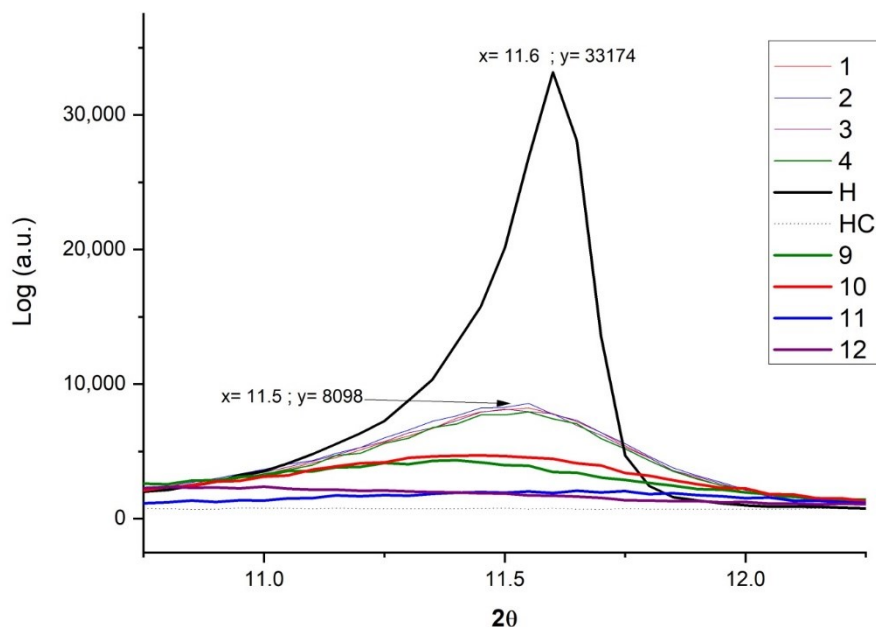


Figure 3.3.11. XRD for hydrotalcite, hydrotalcite calcinated, Samples 1–4 and Samples 9–12

At this point, it is worth noting that hydrotalcite has a crystalline structure [55,56] and colorants an amorphous form. The peak of the XRD is higher when more crystalline structures are present, but this structure is totally lost when the H is calcined to form HC it is recovered to a large extent when it is hydrated again. The experiments showed that increasing the concentration of dye adsorbed on HC causes a decrease in the XRD peak since the amount of amorphous area as compared with the crystalline area increases.

3.3.2.6. Fourier Transform Infrared Spectroscopy FTIR-ATR Analysis

With this technique, the primary aim is to see the effect that the calcination of H produces in some bands such as that of CO_3^{2-} , which can be observed in the 1365 cm^{-1} band [57], and another broad strong band found at 3426 cm^{-1} , attributed to stretching of the O-H bonds of water molecules and hydroxyl groups [44]. It is also important to note the thin but intense and clear bands that appear at 2850 and 2917 cm^{-1} produced by CH_2 stretching

vibrations [58]. As can be seen in Figure 3.3.12, after calcination, all these bands disappear, allowing a subsequent reconstruction in the dye adsorption phase.

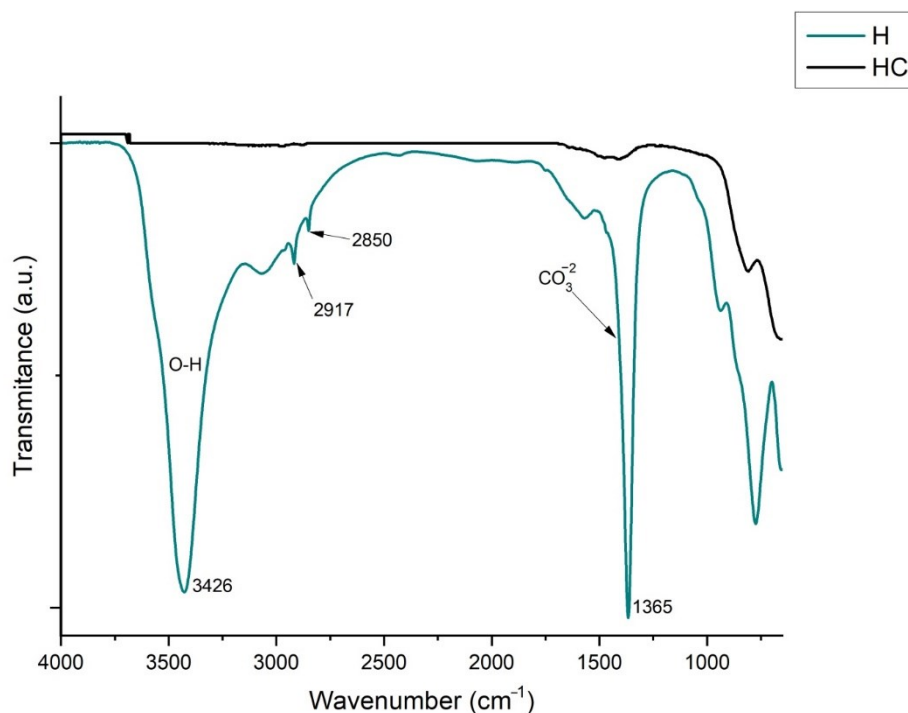


Figure 3.3.12. FTIR of uncalcined hydrotalcite (H) and calcined hydrotalcite (HC)

Figures 3.3.13–3.3.16 show the FTIR spectra obtained for dyes before and after adsorption on HC. In the case of Direct Blue 199 (Figure 3.3.13) and Direct Blue 71 (Figure 3.3.14), the peak at 1100 cm^{-1} is attributed to acetates, formates, propionates, and benzoates [59]. Previous work has indicated that the peaks between 1400 and 1640 cm^{-1} [55–58] correspond to benzene rings and that the peak shown at 1500 cm^{-1} is characteristic of the azo bond [60] which in Sample 12 can be seen smoothly shifted to 1520 cm^{-1} . Another peak can be found at 1035 cm^{-1} which corresponds to the symmetric sulfonate vibration [48]. Many of the peaks confirm the presence of the dye with more or less intensity, or do not appear at low concentrations (Samples 2 and 3), but they are appreciated when we study them in Samples 11 and 12 when we find more peaks associated with the dye adsorbed by nanoclay (look at the peaks at 1500 and 1100 cm^{-1}). In the four hybrids, an increase in the intensity of the -OH ($3420\text{--}3460\text{ cm}^{-1}$) shoulder is observed due to the loss

of water bound by hydrogen to the carbonate anions CO_3^{2-} in the basal space. This water is also replaced in the adsorption process [61].

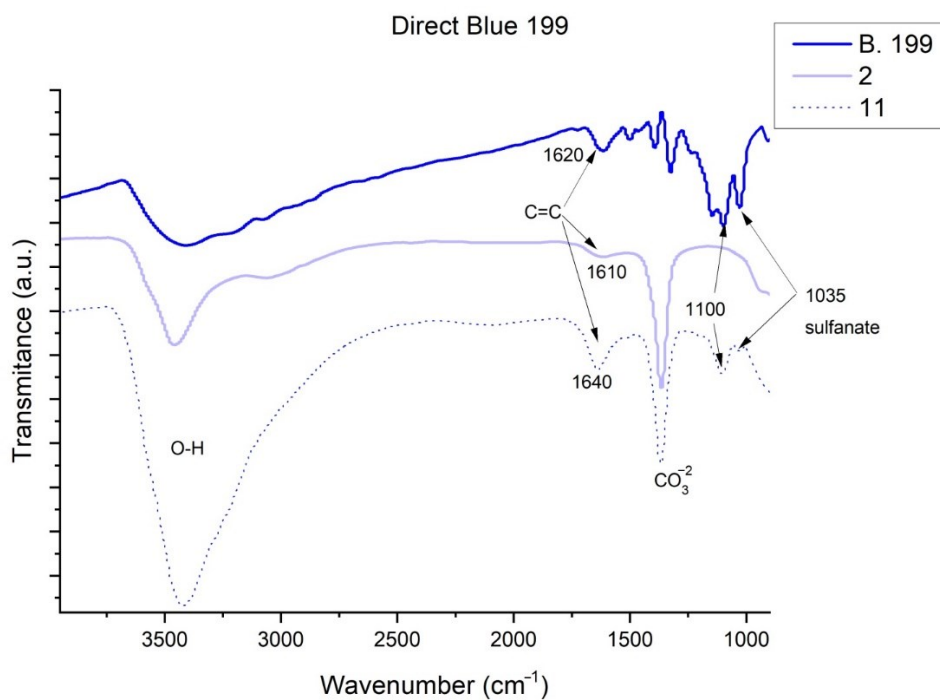


Figure 3.3.13. FTIR of Direct Blue 199, Sample 2 and Sample 11

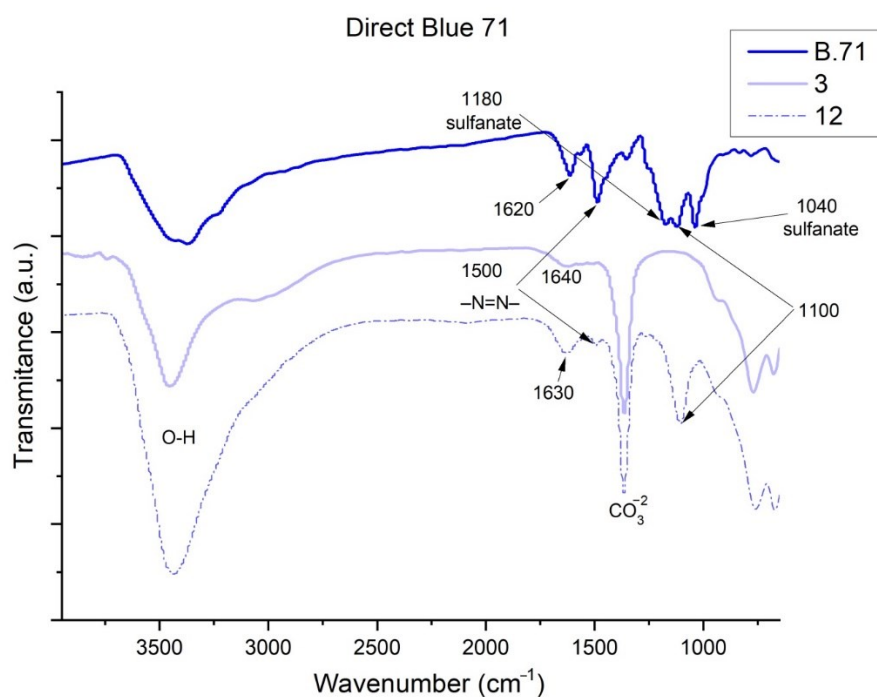


Figure 3.3.14. FTIR of Direct Blue 71, Sample 3 and Sample 12

The FTIR spectra of Direct Red 23 are shown in Figure 3.3.15. The peaks at 3308 and 3426 cm^{-1} correspond to the phenolic -OH, C-N stretching and water could be clearly observed [62–64]. Another peak is observed at 1600–1610 cm^{-1} , which corresponds to the aromatic groups -C=C-, while the peak at 1180–1170 cm^{-1} indicates the presence of single bonds of CO and OH [62–66]. The peak shown at 1480–1500 is characteristic of the azo bond [60]. Another significant peak appears at 1050 cm^{-1} , which corresponds to the bonds formed by the S-O [67,68] corresponding to the sulfonate groups $-\text{SO}_3$ from the NaSO_3 group.

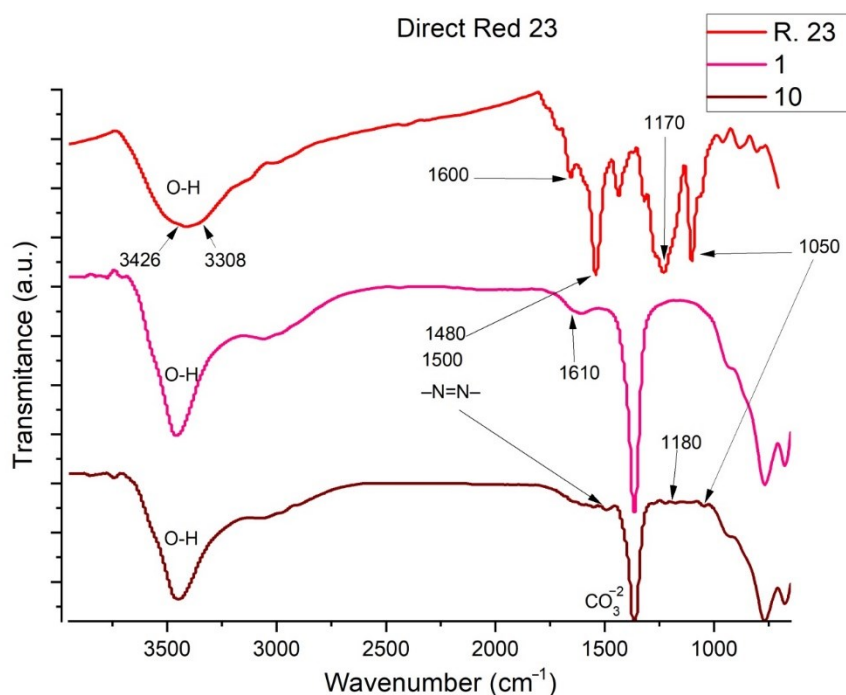


Figure 3.3.15. FTIR of Direct Red 23, Sample 1 and Sample 10

Studying the dye Reactive Yellow DR (Figure 3.3.16), again, the band of the phenolic -OH group, N-H stretching, and water is observed at 3446 cm^{-1} [62–64]. The reactive dye studied has sulfate groups that can be seen at 1110 cm^{-1} [67,68]. The peak shown at 1496 cm^{-1} is characteristic of the azo bond [60]. Other peaks are observed in Samples 4 and 9 at 1600 and 1630 cm^{-1} , respectively, which correspond to the aromatic groups -C=C- [55–58], in the colorant the peak is at 1618 cm^{-1} .

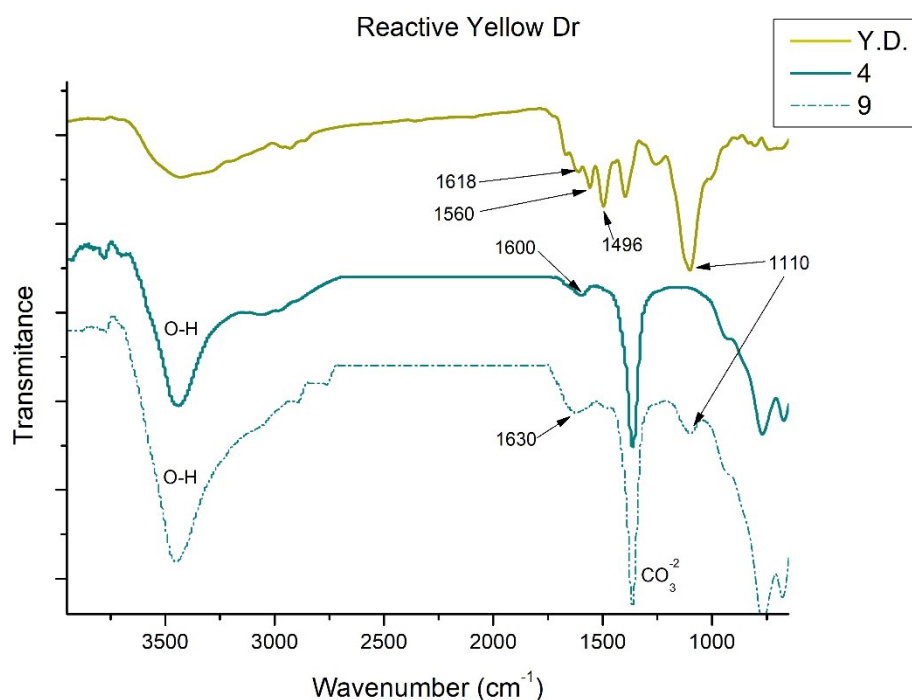


Figure 3.3.16. FTIR of Yellow DR, Sample 4 and Sample 9

Table 3.3.5 summarizes the most prominent peaks analyzed in the four hybrids. Analyzing the peaks of the OH^- and CO_3^{2-} group, a semi-quantitative analysis of the area of each of these peaks can be made calculating the area under the curve. The results obtained are shown in Figure 3.3.17. This figure shows how the amount of carbonate that was originally in the hydrotalcite has been reduced as, after the calcination and reconstruction of the nanoclay, the colorant became part of the nanoclay structure, occupying a large part of this OH^- and CO_3^{2-} band [24–26].

Table 3.3.5. A summary of the IR peak positions

	H	B199	2	11	B71	3	12	R23	1	10	YD	4	9
-OH	3426	-	3460	3420	3426	3460	3440	3308	3460	3450	3438	3442	3450
$-\text{CO}_3^{2-}$	1365	-	1370	1370	-	1370	1370	-	1370	1370	-	1370	1370
-N=N-	-	1500	-	1520	1500	-	1500	1480	-	1500	1496	-	1496
$-\text{SO}_3$	-	1035	-	1035	1180	-	1100	1050	-	1050	1110	-	1110
$-\text{C}=\text{C}-$	-	1620	1610	1640	1620	1640	1630	1600	1610	-	1618	1600	1630

By analyzing the results in more depth, it is possible to extract the estimated amount of other functional groups from the dyes that have been incorporated into the structure of the hybrids. For this, the initial quantity of carbonate in the hydrotalcite is taken into consideration along with the quantity which is later shown in the hybrids. The two quantities are subtracted, one from the other, to give the number of new groups that have been incorporated. The analysis of these results is shown in Figure 3.3.17.

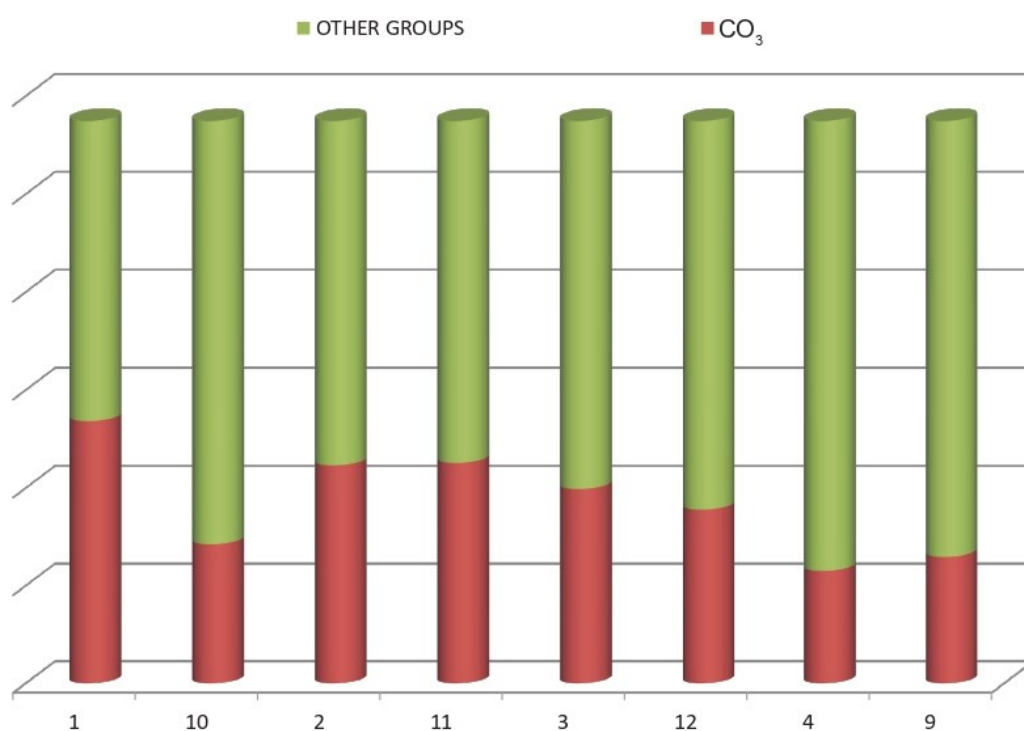


Figure 3.3.17. Semi-quantitative analysis and incorporation of new functional groups

3.3.2.7. Morphology Scanning and Transmission Electron Microscopy (SEM-TEM)

Figure 3.3.18 shows some images from the nanoclay. It is worth noting the differences between hydrotalcite before and after a calcination process was applied. Morphologically, it can be observed how, after reconstruction, the structure of the nanoclay has been recovered. This reconstruction is produced by the shape memory that the nanoclay has before and after being calcination and consequent rehydration [69].

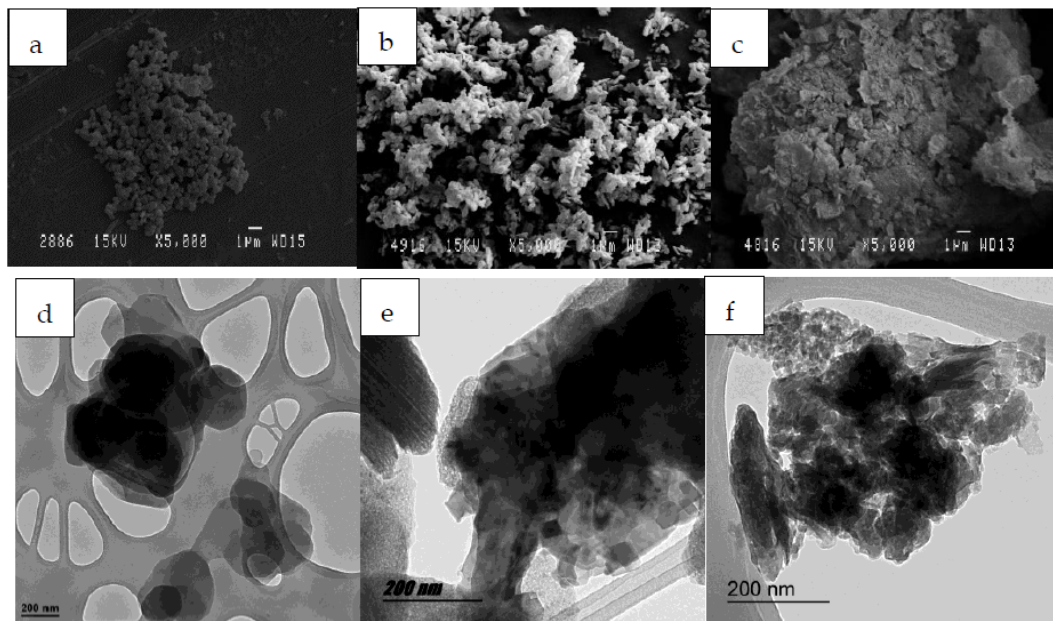


Figure 3.3.18. SEM micrographies of different HC samples: (a) HC original; (b) HC calcinated; (c) HC reconstructed. TEM micrographies of different HC samples: (d) HC original; (e) HC calcinated; (f) HC reconstructed

A closer look at the morphology of the surface of the nanoadsorbent can be seen in Figure 3.3.19. Graphically, it is possible to see how the hydrotalcite lamellae are distributed composed of lamellae separated by basal or interlamellar space between which anions and water molecules are inserted. It is in this space where the adsorbed elements are deposited and where the substitution of the anions that this nanoclay possesses by default are carried out.

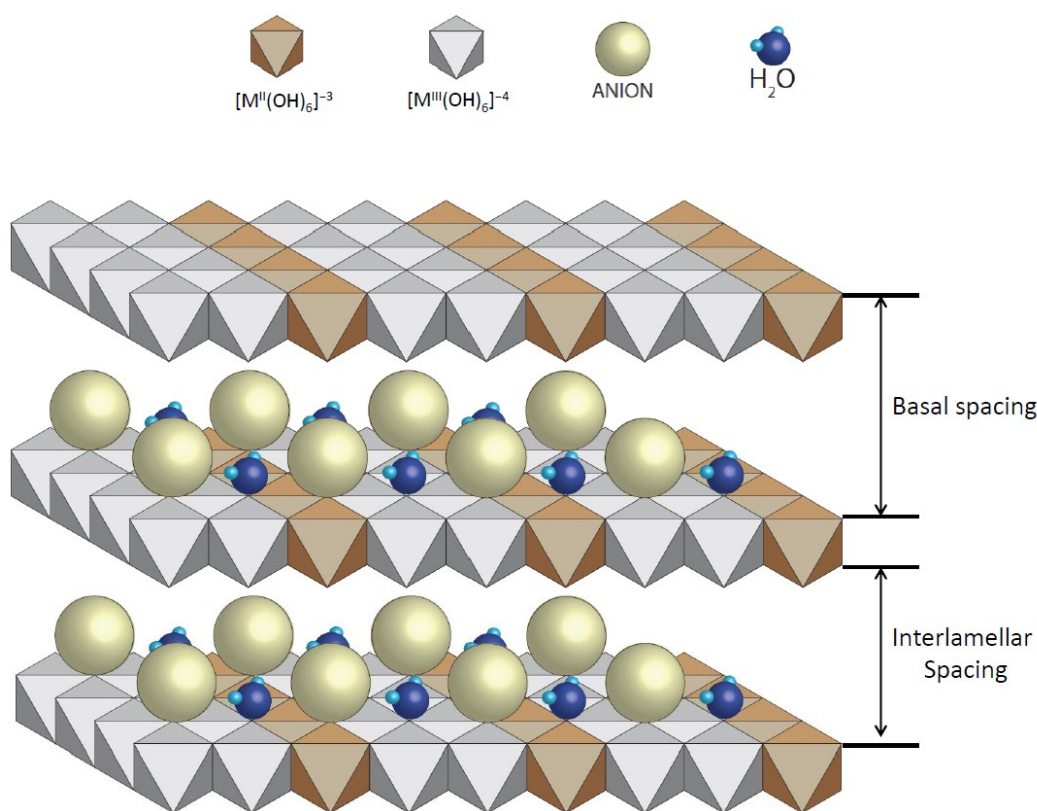


Figure 3.3.19. Basic structure of hydrotalcite [34]

3.3.3. Discussion

The mechanism of dye adsorption and shape memory recovery of HC has been demonstrated by XRD and FTIR characterization techniques. In addition, the improvement in the thermal behavior of the hybrids obtained can be observed with respect to the dyes on their own.

Thermogravimetry (TGA) also gives results that follow similar lines. The hybrids show an almost identical behavior to that of hydrotalcite alone, so the dye adsorption has very little influence on the final TGA of the hybrid. The degradation peaks of the sample are the same as those of the nanoclay without having absorbed dyes. From the other point of view, the hybrids show better resistance to temperature than the dyes on their own. Finally, using X-ray diffraction analysis, it is possible to see how the hydrotalcite partially recovers its

intralaminar space due to its shape memory. This should help the fixation of the dye within the nanoclay, and the stability of the resulting hybrid.

The XRD and FTIR characterization techniques both demonstrate the presence of the dyes in the hybrid obtained. For X-ray diffraction, it is only necessary to observe how the amorphous zone increases due to the greater presence of dye, while in the FTIR, very significant peaks of the bonds of groups such as the SO_3 sulfonate and the amino $-\text{N}=\text{N}-$ can be seen, associated with the adsorbed dyes and not found in the nanoclay. In the semi-quantitative analysis it can be seen how some functional groups such as CO_3^{2-} have been replaced by the dye.

In view of the results, the effectiveness of the HC nanoclay in absorbing the reactive and direct dyes used in this study for the purification of wastewater from textile dyeing processes has been demonstrated, and the maximum level of adsorption according to Equation (3.3.1) established in this work is $x = 0.5$. The adsorption percentages are quite high (in all cases above 95% absorption). In addition, a good fixation of the color in the nanoclay is visually appreciated, due to its homogeneity as well as its degree of stability. The intensity of the color that has resulted from the nanoclay-dye hybrid is very low, but this is not surprising considering that the nanoclay concentration was $20 \text{ g}\cdot\text{L}^{-1}$ while that of the colorants was $0.05 \text{ g}\cdot\text{L}^{-1}$. The lowest adsorption level was found in the Direct Blue 71 dye in the lowest concentrate (Sample 3), which was the dye used with the highest molecular weight. However, no significant differences were observed due to the difference in molecular weight of the direct and reactive dyes, as can be seen in Figure 3.3.4 and Table 3.3.4 which demonstrate the good adsorption capacity of H despite the differences in the molecular weight of the dyes.

Regarding the total solar reflectance (TSR) the 4 hybrids are between 60–70% of TSR. Traditional targets exhibit a total solar reflectance of 75%, so the samples studied are very close. The previous argument is reformed in which we argued that the intensity of the color is very low, looking very white due to the white color of the nanoclay. The Reactive Yellow Drimaren less concentrated samples reach higher TSR% values than the other samples.

3.3.4. Materials and Methods

3.3.4.1. Materials

Two types of anionic dyes [33], i.e., direct and reactive [70], were used for this research. The direct dyes studied were: Direct Blue 199 CI 74.180 (phthalocyanine group with molecular weight 775.17 g/mol), Direct Red 23 CI 29160 (azo dye with molecular weight 813,72 g/mol), and Direct Blue 71 CI 34140 (azo dye with 1029.88 g/mol). The reactive dye studied was: Reactive Drimaren Yellow K-2R (azo dye with molecular weight 586 g/mol) (Figure 3.3.20).

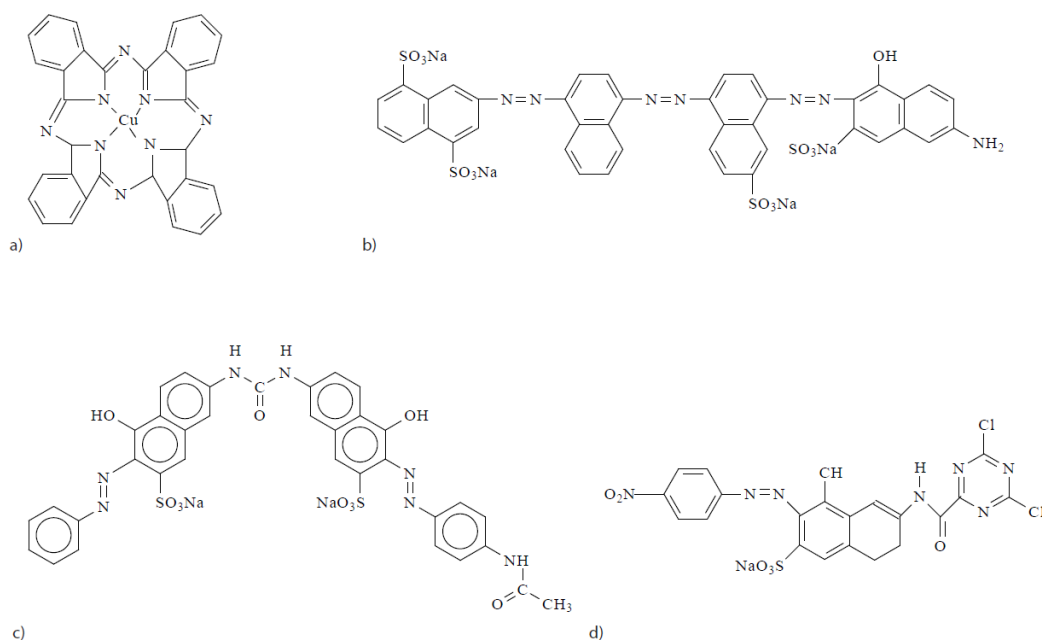


Figure 3.3.20. (a) Direct Blue 199; (b) Direct Blue 71; (c) Direct Red 23; (d) Reactive Drimaren Yellow

As adsorbing substance for the dyes, hydrotalcite $Mg_6Al_2(CO_3)(OH)_{16} \cdot 4(H_2O)$ [30,36,37] was chosen, which was calcined according to Dos Santos R.M.M. [44] destroying the structure and facilitating the penetration of the dye into the nanoclay [31]. Once the nanoclay was immersed in aqueous solution, the structure reconstructed itself due to its shape memory and the colorant was incorporated into the new structure.

3.3.4.2. Methods

In order to obtain the calibration line of dye solution concentration as a function of the absorbance, several samples of known concentrations were made to obtain the Lambert–Beer equation for each dye [71]. These equations allowed the dye concentration remaining in the wastewater (once the nanoclay has been applied) to be determined by the absorbance measurement. Table 3.3.6 shows the line equations and the regression (R).

Table 3.3.6. Lambert–Beer line equations and R²

Dye	Equation	R ²
Direct Blue 199 (B199)	$y = 21.784 x - 0.015$	0.9982
Reactive Yellow (YD)	$y = 14.943 x - 0.0021$	0.9993
Direct Red 23 (R23)	$y = 34.357 x - 0.0148$	0.9991
Direct Blue 71 (B71)	$y = 17.09 x - 0.0233$	0.9987

One of the objectives of this work was to determine the maximum amount of dye that could be absorbed. Several solutions of dyes were made at different concentrations and the ratio of HC nanoclay/dye concentration was varied following a general full factorial design of experiments (DoE) 4² (Table 3.3.7), to see what quantity of dye it could be absorbed. Table 3.3.7 shows the 16 samples and the experimental conditions. In addition, the randomization option in the dye selection was used in order to avoid experimental bias. The column “x” establishes the ratio of g·L⁻¹ of the nanoclay divided by g·L⁻¹ of the dye, according to the following formula:

$$x = \frac{\text{Clay } g \cdot L^{-1}}{\text{Dye } g \cdot L^{-1}} \quad (1)$$

Equation 3.3.1. Ratio of nanoclay/dye

Table 3.3.7. Samples and their concentrations under experimental conditions according to the general full factorial DoE 4²

Sample Ref.	Dye	g·L ⁻¹ Dye	g·L ⁻¹ Clay	x
1	Direct Red 23	0.05	10	200
2	Direct Blue 199	0.05	10	200
3	Direct Blue 71	0.05	10	200
4	Yellow Drimaren	0.05	10	200
5	Direct Blue 71	0.05	5	100
6	Yellow Drimaren	0.05	5	100
7	Direct Red 23	0.05	5	100
8	Direct Blue 199	0.05	5	100
9	Yellow Drimaren	1	2	2
10	Direct Red 23	1	2	2
11	Direct Blue 199	1	2	2
12	Direct Blue 71	1	2	2
13	Yellow Drimaren	1	0.5	0.5
14	Direct Red 23	1	0.5	0.5
15	Direct Blue 199	1	0.5	0.5
16	Direct Blue 71	1	0.5	0.5

Each sample solution of hybrid nanoclay-dye was stirred for 24 h, the first two hours at 1600 rpm and the remaining time at 600 rpm [72]. The next step was to filter the solution by gravity for 48 h through filter paper and measure with the spectrophotometer to calculate the concentration of dye that was not absorbed by the nanoclay [73,74]. The nanoclays with the dye were lyophilized [75,76] to completely extract the water.

A Jasco V-670 double UV-VIS/NIR spectrophotometer was used to calculate the total solar reflectance (TSR) [77]; measurements were performed in the range of 2700–190 nm with a frequency of 0.5 nm. The equipment described was equipped with a double grid monochromator. The first was used for the UV-VIS region (1200 grids/mm) in which the detectors were photomultiplier tubes, while the second was used for the infrared IR region (300 grids/mm) using a PbS detector. For both detectors, the changes that occurred in the grid were automated at the wavelength that the user wished. A deuterium lamp (190–350 nm) and a halogen lamp (330–2700 nm) were used as light sources. Reflectance factors $\rho(\lambda)$ were applied for the hybrid pigments within the 370–740 nm range with the D65 illuminant and the CIE-1964 standard observer, in order to calculate and compare the optical properties from each one [78].

The FTIR analysis was performed with a Nicolet 6700 Spectrometer equipped with a DTGS detector. In this case, a horizontal mono-rebound attenuated total reflection (FTIR-ATR) using a prism of ZnSe was used. A pressure control accessory was used to equalize the pressure in each sample. The average spectra were obtained after 64 scans with a resolution of 4 cm^{-1} by subtracting the background signals obtained.

A TGA analysis was also carried out to compare possible variations in the degradation peaks of the dyes [79–81]. To perform the characterization of the thermal properties of the hybrids, in this study, a thermogravimetric analyzer TGA/SDTA 851 (Mettler-Toledo Inc., Columbus, OH, USA) was used. For this, the conditions of the experiment that were established included an increase in temperature of 5°C every minute within the range from 20 to 900°C , and the oxidizing medium used was N_2/O_2 (4:1).

Finally, an X-ray diffraction (XRD) test [82,83] was carried out to verify that the nanoclay recovered its original shape before it was calcined. An XRD Bruker D8-Advance equipment (Bruker, Billerica, MA, USA) with a Göebel mirror (power 3000 W, voltage 20–60 kV, and current 5–80 mA) was used. Measurements were taken in an oxidant atmosphere at an angular speed of $1^{\circ}/\text{min}$, STEP 0.05° , and an angular scan of $2.7\text{--}70^{\circ}$. The XRD patterns allowed us to check the memory form and reconstruction of the hydrotalcite structure after the calcination process and were also used to find variations in the basal space on the nanoclay structure due to the interactions with the selected dyes.

ANOVA was used as the statistical method to determine whether the dye adsorptions (mean values) of two or more groups were different, using the dye structure and the dye/clay concentrations as factors for the analysis. The ANOVA studies were carried out with 95% confidence level. The order of use of the dyes was not correlative in order to avoid experimental bias.

References

1. Wakkal, M.; Khiari, B.; Zagrouba, F. Textile Wastewater Treatment by Agro-Industrial Waste: Equilibrium Modelling, Thermodynamics and Mass Transfer Mechanisms of Cationic Dyes Adsorption onto Low-Cost Lignocellulosic Adsorbent. *J. Taiwan Inst. Chem. Eng.* 2019, 96, 439–452. <https://doi.org/10.1016/J.JTICE.2018.12.014>.
2. Mathew, M.L.; Gopalakrishnan, A.; Aravindakumar, C.T.; Aravind, U.K. Low—Cost Multilayered Green Fiber for the Treatment of Textile Industry Waste Water. *J. Hazard. Mater.* 2019, 365, 297–305. <https://doi.org/10.1016/J.JHAZMAT.2018.11.014>.
3. Hasan, M.M.; Shenashen, M.A.; Hasan, M.N.; Znad, H.; Salman, M.S.; Awual, M.R. Natural Biodegradable Polymeric Bioadsorbents for Efficient Cationic Dye Encapsulation from Wastewater. *J. Mol. Liq.* 2021, 323, 114587. <https://doi.org/10.1016/j.molliq.2020.114587>
4. Kubra, K.T.; Salman, M.S.; Hasan, M.N. Enhanced Toxic Dye Removal from Wastewater Using Biodegradable Polymeric Natural Adsorbent. *J. Mol. Liq.* 2021, 328, 115468. <https://doi.org/10.1016/j.molliq.2021.115468>
5. Durairaj, K.; Senthilkumar, P.; Velmurugan, P.; Divyabharathi, S.; Kavitha, D. Development of Activated Carbon from Nerium Oleander Flower and Their Rapid Adsorption of Direct and Reactive Dyes. *Int. J. Green Energy* 2019, 16, 573–582. <https://doi.org/10.1080/15435075.2019.1598419>
6. Alinsafi, A.; Evenou, F.; Abdulkarim, E.M.; Pons, M.-N.; Zahraa, O.; Benhammou, A.; Yaacoubi, A.; Nejmeddine, A. Treatment of Textile Industry Wastewater by Supported Photocatalysis. *Dye. Pigment.* 2007, 74, 439–445. <https://doi.org/10.1016/j.dyepig.2006.02.024>
7. Moradi, M.; Eslami, A.; Ghanbari, F. Direct Blue 71 Removal by Electrocoagulation Sludge Recycling in Photo-Fenton Process: Response Surface Modeling and Optimization. *Desalin. Water Treat.* 2016, 57, 4659–4670. <https://doi.org/10.1080/19443994.2014.995714>
8. Shu, H.-Y. Degradation of Dyehouse Effluent Containing CI Direct Blue 199 by Processes of Ozonation, UV/H₂O₂ and in Sequence of Ozonation with UV/H₂O₂. *J. Hazard. Mater.* 2006, 133, 92–98. <https://doi.org/10.1016/j.jhazmat.2005.09.056>
9. Hebeish, A.; Ramadan, M.A.; Abdel-Halim, E.; Abo-Okeil, A. An Effective Adsorbent Based on Sawdust for Removal of Direct Dye from Aqueous Solutions. *Clean Technol. Environ. Policy* 2011, 13, 713–718. <https://doi.org/10.1007/s10098-010-0343-z>
10. Micó Vicent, Barbara; Martínez Verdu, F.M.; Gilabert Pérez, J.E. Optimización de La Síntesis de Nanopigmentos de Origen Natural Para Biopolímeros Mediante El Uso Del Diseño de Experimentos. Ph.D. Thesis, Valencia Polytechnic University, Valencia, Spain, 2016.

11. Ogawa, M.; Takee, R.; Okabe, Y.; Seki, Y. Bio-Geo Hybrid Pigment; Clay-Anthocyanin Complex Which Changes Color Depending on the Atmosphere. *Dye. Pigment.* 2017, 139, 561–565. <https://doi.org/10.1016/J.DYEPIG.2016.12.054>.
12. López Arbeloa, F.; Martínez Martínez, V.; Bañuelos Prieto, J.; López Arbeloa, I. Adsorption of Rhodamine 3B Dye on Saponite Colloidal Particles in Aqueous Suspensions. *Langmuir* 2002, 18, 2658–2664. <https://doi.org/10.1021/la0113163>.
13. Carretero, M.I.; Pozo, M.; Sánchez, C.; García, F.J.; Medina, J.A.; Bernabé, J.M. Comparison of Saponite and Montmorillonite Behaviour during Static and Stirring Maturation with Seawater for Pelotherapy. *Appl. Clay Sci.* 2007, 36, 161–173. <https://doi.org/10.1016/J.CLAY.2006.05.010>.
14. Guillermin, D.; Debroise, T.; Trigueiro, P.; de Viguerie, L.; Rigaud, B.; Morlet-Savary, F.; Balme, S.; Janot, J.-M.; Tielens, F.; Michot, L.; et al. New Pigments Based on Carminic Acid and Smectites: A Molecular Investigation. *Dye. Pigment.* 2019, 160, 971–982. <https://doi.org/10.1016/J.DYEPIG.2018.07.021>.
15. Moujahid, E.M.; Lakhale, R.; Ouassif, H.; Bouragba, F.Z.; Elhatimi, W. New Organic Dye/Anionic Clay Hybrid Pigments: Preparation, Optical Properties and Structural Stability. *Dye. Pigment.* 2019, 162, 998–1004. <https://doi.org/10.1016/J.DYEPIG.2018.11.021>.
16. Yi, J.-Z.; Zhang, L.-M. Removal of Methylene Blue Dye from Aqueous Solution by Adsorption onto Sodium Humate/Polyacrylamide/Clay Hybrid Hydrogels. *Bioresour. Technol.* 2008, 99, 2182–2186. <https://doi.org/10.1016/J.BIORTECH.2007.05.028>.
17. Schoonheydt, R.A.; Heughebaert, L. Clay Adsorbed Dyes: Methylene Blue on Laponite. *Clay Miner.* 1992, 27, 91–100. <https://doi.org/10.1180/claymin.1992.027.1.09>.
18. Mittal, H.; Babu, R.; Dabbawala, A.A.; Stephen, S.; Alhassan, S.M. Zeolite-Y Incorporated Karaya Gum Hydrogel Composites for Highly Effective Removal of Cationic Dyes. *Colloids Surfaces A Physicochem. Eng. Asp.* 2020, 586, 124161. <https://doi.org/10.1016/J.COLSURFA.2019.124161>.
19. Aregay, G.G.; Jawad, A.; Du, Y.; Shahzad, A.; Chen, Z. Efficient and Selective Removal of Chromium (VI) by Sulfide Assembled Hydrotalcite Compounds through Concurrent Reduction and Adsorption Processes. *J. Mol. Liq.* 2019, 294, 111532. <https://doi.org/10.1016/j.molliq.2019.111532>
20. Yadav, M.K.; Gupta, A.K.; Ghosal, P.S.; Mukherjee, A. PH Mediated Facile Preparation of Hydrotalcite Based Adsorbent for Enhanced Arsenite and Arsenate Removal: Insights on Physicochemical Properties and Adsorption Mechanism. *J. Mol. Liq.* 2017, 240, 240–252. <https://doi.org/10.1016/j.molliq.2017.05.082>
21. Chowdhury, M.F.; Khandaker, S.; Sarker, F.; Islam, A.; Rahman, M.T.; Awual, M.R. Current Treatment Technologies and Mechanisms for Removal of Indigo Carmine

- Dyes from Wastewater: A Review. *J. Mol. Liq.* 2020, 318, 114061. <https://doi.org/10.1016/j.molliq.2020.114061>
22. Awual, M.R. Efficient Phosphate Removal from Water for Controlling Eutrophication Using Novel Composite Adsorbent. *J. Clean. Prod.* 2019, 228, 1311–1319. <https://doi.org/10.1016/j.jclepro.2019.04.325>
23. Islam, A.; Teo, S.H.; Taufiq-Yap, Y.H.; Ng, C.H.; Vo, D.-V.N.; Ibrahim, M.L.; Hasan, M.M.; Khan, M.A.R.; Nur, A.S.M.; Awual, M.R. Step towards the Sustainable Toxic Dyes Removal and Recycling from Aqueous Solution—A Comprehensive Review. *Resour. Conserv. Recycl.* 2021, 175, 105849. <https://doi.org/10.1016/j.resconrec.2021.105849>
24. Zhu, M.-X.; Li, Y.-P.; Xie, M.; Xin, H.-Z. Sorption of an Anionic Dye by Uncalcined and Calcined Layered Double Hydroxides: A Case Study. *J. Hazard. Mater.* 2005, 120, 163–171. <https://doi.org/10.1016/j.jhazmat.2004.12.029>
25. Lakraimi, M.; Legrouri, A.; Barroug, A.; Besse, J.-P. Removal of Pesticides from Water by Anionic Clays. *J. Chim. Phys. Physico-Chimie Biol.* 1999, 96, 470–478. <https://doi.org/10.1051/jcp:1999154>
26. Sato, T.; Kato, K.; Endo, T.; Shimada, M. Preparation and Chemical Properties of Magnesium Aluminium Oxide Solid Solutions. *React. Solids* 1986, 2, 253–260. [https://doi.org/10.1016/0168-7336\(86\)80088-2](https://doi.org/10.1016/0168-7336(86)80088-2)
27. Biglari Quchan Atigh, Z.; Heidari, A.; Karimi, A.; Pezhman, M.A.; Asgari Lajayer, B.; Lima, E.C. Purification and Economic Analysis of Nanoclay from Bentonite. *Environ. Sci. Pollut. Res.* 2021, 28, 13690–13696. <https://doi.org/10.1007/s11356-020-11595-1>
28. Chihi, R.; Blidi, I.; Trabelsi-Ayadi, M.; Ayari, F. Elaboration and Characterization of a Low-Cost Porous Ceramic Support from Natural Tunisian Bentonite Clay. *Comptes Rendus Chim.* 2019, 22, 188–197. <https://doi.org/10.1016/J.CRCI.2018.12.002>
29. Cavani, F.; Trifiro, F.; Vaccari, A. Hydrotalcite-Type Anionic Clays: Preparation, Properties and Applications. *Catal. today* 1991, 11, 173–301. [https://doi.org/10.1016/0920-5861\(91\)80068-K](https://doi.org/10.1016/0920-5861(91)80068-K)
30. Bish, D.L. Anion-Exchange in Takovite: Applications to Other Hydroxide Minerals. *Bull. Mineral.* 1980, 103, 170–175.
31. Bouraada, M.; Lafjah, M.; Ouali, M.S.; de Menorval, L.C. Basic Dye Removal from Aqueous Solutions by Dodecylsulfate-and Dodecyl Benzene Sulfonate-Intercalated Hydrotalcite. *J. Hazard. Mater.* 2008, 153, 911–918. <https://doi.org/10.1016/j.jhazmat.2007.09.076>

32. Orthman, J.; Zhu, H.Y.; Lu, G.Q. Use of Anion Clay Hydrotalcite to Remove Coloured Organics from Aqueous Solutions. *Sep. Purif. Technol.* 2003, 31, 53–59. [https://doi.org/10.1016/S1383-5866\(02\)00158-2](https://doi.org/10.1016/S1383-5866(02)00158-2).
33. Bascialla, G.; Regazzoni, A.E. Immobilization of Anionic Dyes by Intercalation into Hydrotalcite. *Colloids Surfaces A Physicochem. Eng. Asp.* 2008, 328, 34–39. <https://doi.org/10.1016/j.colsurfa.2008.06.028>
34. Carlino, S. Chemistry between the Sheets. *Chem. Br.* 1997, 33, 59–62.
35. Yu, L.; Deng, J.; Wang, H.; Liu, J.; Zhang, Y. Improved Salts Transportation of a Positively Charged Loose Nanofiltration Membrane by Introduction of Poly (Ionic Liquid) Functionalized Hydrotalcite Nanosheets. *ACS Sustain. Chem. Eng.* 2016, 4, 3292–3304.
36. Miyata, S. Physico-Chemical Properties of Synthetic Hydrotalcites in Relation to Composition. *Clays Clay Miner.* 1980, 28, 50–56. <https://doi.org/10.1346/CCMN.1980.0280107>
37. Ulibarri, M.A.; Pavlovic, I.; Barriga, C.; Hermosin, M.C.; Cornejo, J. Adsorption of Anionic Species on Hydrotalcite-like Compounds: Effect of Interlayer Anion and Crystallinity. *Appl. Clay Sci.* 2001, 18, 17–27. [https://doi.org/10.1016/S0169-1317\(00\)00026-0](https://doi.org/10.1016/S0169-1317(00)00026-0)
38. Salomao, R.; Milena, L.M.; Wakamatsu, M.H.; Pandolfelli, V.C. Hydrotalcite Synthesis via Co-Precipitation Reactions Using MgO and Al(OH)₃ Precursors. *Ceram. Int.* 2011, 37, 3063–3070. <https://doi.org/10.1016/j.ceramint.2011.05.034>
39. Zhang, W.; Zhang, D.; Liang, Y. Nanotechnology in Remediation of Water Contaminated by Poly- and Perfluoroalkyl Substances: A Review. *Environ. Pollut.* 2019, 247, 266–276. <https://doi.org/10.1016/J.ENVPOL.2019.01.045>.
40. Li, B.; Zhang, Y.; Zhou, X.; Liu, Z.; Liu, Q.; Li, X. Different Dye Removal Mechanisms between Monodispersed and Uniform Hexagonal Thin Plate-like MgAl–CO₃–LDH and Its Calcined Product in Efficient Removal of Congo Red from Water. *J. Alloys Compd.* 2016, 673, 265–271. <https://doi.org/10.1016/j.jallcom.2016.02.248>
41. Zhang, C.; Yang, S.; Chen, H.; He, H.; Sun, C. Adsorption Behavior and Mechanism of Reactive Brilliant Red X-3B in Aqueous Solution over Three Kinds of Hydrotalcite-like LDHs. *Appl. Surf. Sci.* 2014, 301, 329–337. <https://doi.org/10.1016/j.apsusc.2014.02.073>
42. Shan, R.; Yan, L.; Yang, Y.; Yang, K.; Yu, S.; Yu, H.; Zhu, B.; Du, B. Highly Efficient Removal of Three Red Dyes by Adsorption onto Mg–Al-Layered Double Hydroxide. *J. Ind. Eng. Chem.* 2015, 21, 561–568. <https://doi.org/10.1016/j.jiec.2014.03.019>
43. Herald, E.; Santosa, S.J.; Triyono, T.; Wijaya, K. Anionic and Cationic Dyes Removal from Aqueous Solutions by Adsorption onto Synthetic Mg/Al Hydrotalcite-like

- Compound. Indones. J. Chem. 2015, 15, 234–241. <https://doi.org/10.22146/ijc.21190>
44. dos Santos, R.M.M.; Gonçalves, R.G.L.; Constantino, V.R.L.; da Costa, L.M.; da Silva, L.H.M.; Tronto, J.; Pinto, F.G. Removal of Acid Green 68:1 from Aqueous Solutions by Calcined and Uncalcined Layered Double Hydroxides. *Appl. Clay Sci.* 2013, 80–81, 189–195. <https://doi.org/10.1016/j.clay.2013.04.006>.
45. Grum, F.; Witzel, R.F.; Stensby, P. Evaluation of Whiteness. *JOSA* 1974, 64, 210–215. <https://doi.org/10.1364/JOSA.64.000210>
46. ASTM. Standard Tables for Reference Solar Spectral Irradiances: Direct Normal and Hemispherical on 37° Tilted Surface. *ASTM Int.* 2013, 3, 1–21. <https://doi.org/10.1520/G0173-03R20.2>.
47. Iturbe-García, J.L.; Bonifacio Martínez, J.; Granados Correa, F.; López-Muñoz, B.E. Behavior of a Hydrotalcite Type Material Obtained from MgAl Alloy for CO₂ Adsorption. *Appl. Clay Sci.* 2019, 183, 105296. <https://doi.org/https://doi.org/10.1016/j.clay.2019.105296>.
48. Extremera, R.; Pavlovic, I.; Pérez, M.R.; Barriga, C. Removal of Acid Orange 10 by Calcined Mg/Al Layered Double Hydroxides from Water and Recovery of the Adsorbed Dye. *Chem. Eng. J.* 2012, 213, 392–400. <https://doi.org/https://doi.org/10.1016/j.cej.2012.10.042>.
49. Wang, Q.; Feng, Y.; Feng, J.; Li, D. Enhanced Thermal- and Photo-Stability of Acid Yellow 17 by Incorporation into Layered Double Hydroxides. *J. Solid State Chem.* 2011, 184, 1551–1555. <https://doi.org/https://doi.org/10.1016/j.jssc.2011.04.020>.
50. Ghosh, S.K.; Brahmakumar, M.; Warriar, K.G.K.; Perumal, P.; Smitha, V.S.; Pavithran, C.; Manjumol, K.A. Rhodamine 6G Intercalated Montmorillonite Nanopigments-Polyethylene Composites: Facile Synthesis and Ultravioletstability Study. *J. Am. Ceram. Soc.* 2011, 94, 1731–1736. <https://doi.org/10.1111/j.1551-2916.2010.04326.x>
51. Raha, S.; Ivanov, I.; Quazi, N.H.; Bhattacharya, S.N. Photo-Stability of Rhodamine-B/Montmorillonite Nanopigments in Polypropylene Matrix. *Appl. Clay Sci.* 2009, 42, 661–666. <https://doi.org/10.1016/j.clay.2008.06.008>
52. Bellucci, F.; Camino, G.; Frache, A.; Sarra, A. Catalytic Charring–Volatilization Competition in Organoclay Nanocomposites. *Polym. Degrad. Stab.* 2007, 92, 425–436. <https://doi.org/10.1016/j.polymdegradstab.2006.11.006>
53. Landau, A.; Zaban, A.; Lapidés, I.; Yariv, S. Montmorillonite Treated with Rhodamine-6G Mechanochemically and in Aqueous Suspensions. *J. Therm. Anal. Calorim.* 2002, 70, 103–113. <https://doi.org/10.1023/A:1020649416016>

54. Dahdah, E.; Estephane, J.; Taleb, Y.; El Khoury, B.; El Nakat, J.; Aouad, S. The Role of Rehydration in Enhancing the Basic Properties of Mg–Al Hydrotalcites for Biodiesel Production. *Sustain. Chem. Pharm.* 2021, 22, 100487. <https://doi.org/10.1016/j.scp.2021.100487>.
55. Bernard, E.; Zucha, W.J.; Lothenbach, B.; Mäder, U. Stability of Hydrotalcite (Mg-Al Layered Double Hydroxide) in Presence of Different Anions. *Cem. Concr. Res.* 2022, 152, 106674. <https://doi.org/10.1016/J.CEMCONRES.2021.106674>.
56. Geetha Bhavani, A.; Wani, T.A.; Ma'Aruf, A.; Prasad, T. Effect of Ageing Process on Crystal Morphology of Co-Mg-Al Hydrotalcite. *Mater. Today Proc.* 2021, 44, 2277–2282. <https://doi.org/10.1016/J.MATPR.2020.12.390>.
57. Roelofs, J.C.; van Bokhoven, J.A.; Van Dillen, A.J.; Geus, J.; de Jong, K.P. The Thermal Decomposition of Mg-Al Hydrotalcites: Effects of Interlayer Anions and Characteristics of the Final Structure. *Chem. Eur. J.* 2002, 8, 5571–5579. [https://doi.org/10.1002/1521-3765\(20021216\)8:24%3C5571::AID-CHEM5571%3E3.0.CO;2-R](https://doi.org/10.1002/1521-3765(20021216)8:24%3C5571::AID-CHEM5571%3E3.0.CO;2-R)
58. Ma, Y.; Zhu, J.; He, H.; Yuan, P.; Shen, W.; Liu, D. Infrared Investigation of Organo-Montmorillonites Prepared from Different Surfactants. *Spectrochim. Acta Part A Mol. Biomol. Spectrosc.* 2010, 76, 122–129. <https://doi.org/10.1016/j.saa.2010.02.038>
59. Hafshejani, M.K.; Ogugbue, C.J.; Morad, N. Application of Response Surface Methodology for Optimization of Decolorization and Mineralization of Triazo Dye Direct Blue 71 by *Pseudomonas Aeruginosa*. *3 Biotech* 2014, 4, 605–619. <https://doi.org/10.1007/s13205-013-0192-7>.
60. Hu, C.; Jimmy, C.Y.; Hao, Z.; Wong, P.K. Photocatalytic Degradation of Triazine-Containing Azo Dyes in Aqueous TiO₂ Suspensions. *Appl. Catal. B Environ.* 2003, 42, 47–55. [https://doi.org/10.1016/S0926-3373\(02\)00214-X](https://doi.org/10.1016/S0926-3373(02)00214-X)
61. Micó-Vicent, B.; Jordán, J.; Perales, E.; Martínez-Verdú, F.; Cases, F. Finding the Additives Incorporation Moment in Hybrid Natural Pigments Synthesis to Improve Bioresin Properties. *Coatings* 2019. <https://doi.org/10.3390/coatings9010034>.
62. Kuo, C.-Y. Water Purification of Removal Aqueous Copper (II) by as-Grown and Modified Multi-Walled Carbon Nanotubes. *Desalination* 2009, 249, 781–785. <https://doi.org/10.1016/j.desal.2008.11.022>
63. Wu, C.-H. Studies of the Equilibrium and Thermodynamics of the Adsorption of Cu²⁺ onto As-Produced and Modified Carbon Nanotubes. *J. Colloid Interface Sci.* 2007, 311, 338–346. <https://doi.org/10.1016/j.jcis.2007.02.077>
64. Mahmoodi, N.M.; Salehi, R.; Arami, M.; Bahrami, H. Dye Removal from Colored Textile Wastewater Using Chitosan in Binary Systems. *Desalination* 2011, 267, 64–72. <https://doi.org/10.1016/j.desal.2010.09.007>.

65. Kuo, C.-Y.; Lin, H.-Y. Adsorption of Aqueous Cadmium (II) onto Modified Multi-Walled Carbon Nanotubes Following Microwave/Chemical Treatment. *Desalination* 2009, 249, 792–796. <https://doi.org/10.1016/j.desal.2008.11.023>
66. Lu, C.; Su, F. Adsorption of Natural Organic Matter by Carbon Nanotubes. *Sep. Purif. Technol.* 2007, 58, 113–121. <https://doi.org/10.1016/j.seppur.2007.07.036>
67. Evanson, K.W.; Urban, M.W. Surface and Interfacial FTIR Spectroscopic Studies of Latexes. I. Surfactant–Copolymer Interactions. *J. Appl. Polym. Sci.* 1991, 42, 2287–2296. <https://doi.org/10.1002/app.1991.070420820>
68. Seoudi, R.; El-Bahy, G.S.; El Sayed, Z.A. FTIR, TGA and DC Electrical Conductivity Studies of Phthalocyanine and Its Complexes. *J. Mol. Struct.* 2005, 753, 119–126. <https://doi.org/10.1016/j.molstruc.2005.06.003>
69. Lian, Z.Y.; Zhang, Y.; Wang, X.Z. Manufacturing of High Quality Hydrotalcite by Computational Fluid Dynamics Simulation of an Impinging Jet Crystallizer. *Ceram. Int.* 2022, 48, 15470–15482. <https://doi.org/10.1016/J.CERAMINT.2022.02.081>.
70. Lazaridis, N.K.; Karapantsios, T.D.; Georgantas, D. Kinetic Analysis for the Removal of a Reactive Dye from Aqueous Solution onto Hydrotalcite by Adsorption. *Water Res.* 2003, 37, 3023–3033. [https://doi.org/10.1016/S0043-1354\(03\)00121-0](https://doi.org/10.1016/S0043-1354(03)00121-0)
71. Bigman, J.L. Monitoring of Chemicals and Water. In *Handbook of Silicon Wafer Cleaning Technology*; Elsevier: Amsterdam, The Netherlands, 2018; pp. 619–657. <https://doi.org/10.1016/B978-0-323-51084-4.00011-3>.
72. Silva, M.M.F.; Oliveira, M.M.; Avelino, M.C.; Fonseca, M.G.; Almeida, R.K.S.; Silva Filho, E.C. Adsorption of an Industrial Anionic Dye by Modified-KSF-Montmorillonite: Evaluation of the Kinetic, Thermodynamic and Equilibrium Data. *Chem. Eng. J.* 2012, 203, 259–268. <https://doi.org/10.1016/j.cej.2012.07.009>.
73. Bou-Belda, E.; López-Rodríguez, D.; Micó-Vicent, B.; Bonet-Aracil, M. Direct and Reactive Dyes Recovery in Textile Wastewater Using Calcinated Hydrotalcite. In *Materials Science Forum*; Trans Tech Publ, 2022; Vol. 1063, pp 233–242. <https://doi.org/10.4028/p-31v71q>
74. Micó-Vicent, B.; Martínez-Verdú, F. M.; Novikov, A.; Stavitskaya, A.; Vinokurov, V.; Rozhina, E.; Fakhrullin, R.; Yendluri, R.; Lvov, Y. Stabilized Dye–Pigment Formulations with Platy and Tubular Nanoclays. *Adv. Funct. Mater.* 2018, 28 (27), 1703553. <https://doi.org/10.1002/adfm.201703553>
75. Mensch, C.; Chintala, R.; Nawrocki, D.; Blue, J.T.; Bhambhani, A. Enabling Lyophilized Pneumococcal Conjugate Vaccines Through Formulation Design and Excipient Selection Suitable for A Multivalent Adjuvanted Vaccine. *J. Pharm. Sci.* 2020, 110, 97–107. <https://doi.org/10.1016/j.xphs.2020.10.038>.

-
76. Castillo-Peinado, L.S.; Calderón-Santiago, M.; Priego-Capote, F. Lyophilization as Pre-Processing for Sample Storage in the Determination of Vitamin D3 and Metabolites in Serum and Plasma. *Talanta* 2021, 222, 121692. <https://doi.org/10.1016/j.talanta.2020.121692>.
 77. Maharjan, S.; Liao, K.S.; Wang, A.J.; Curran, S.A. Highly Effective Hydrophobic Solar Reflective Coating for Building Materials: Increasing Total Solar Reflectance via Functionalized Anatase Immobilization in an Organosiloxane Matrix. *Constr. Build. Mater.* 2020, 243, 118189. <https://doi.org/10.1016/j.conbuildmat.2020.118189>.
 78. Di Natale, C.; Monti, D.; Paolesse, R. Chemical Sensitivity of Porphyrin Assemblies. *Mater. Today* 2010, 13, 46–52. [https://doi.org/10.1016/S1369-7021\(10\)70127-9](https://doi.org/10.1016/S1369-7021(10)70127-9)
 79. Liu, Y.; Li, R.; Yu, J.; Ni, F.; Sheng, Y.; Scircle, A.; Cizdziel, J.V.; Zhou, Y. Separation and Identification of Microplastics in Marine Organisms by TGA-FTIR-GC/MS: A Case Study of Mussels from Coastal China. *Environ. Pollut.* 2020, 272, 115946. <https://doi.org/10.1016/j.envpol.2020.115946>.
 80. Umar, M.; Ofem, M.I.; Anwar, A.S.; Salisu, A.G. Thermo Gravimetric Analysis (TGA) of PA6/G and PA6/GNP Composites Using Two Processing Streams. *J. King Saud Univ. Eng. Sci.* 2020, 34, 77–87. <https://doi.org/10.1016/j.jksues.2020.09.003>.
 81. Corazzari, I.; Turci, F.; Nisticò, R. TGA Coupled with FTIR Gas Analysis to Quantify the Vinyl Alcohol Unit Content in Ethylene-Vinyl Alcohol Copolymer. *Mater. Lett.* 2021, 284, 129030. <https://doi.org/10.1016/j.matlet.2020.129030>.
 82. Pálková, H.; Madejová, J.; Zimowska, M.; Bielańska, E.; Olejniczak, Z.; Lityńska-Dobrzyńska, L.; Serwicka, E.M. Laponite-Derived Porous Clay Heterostructures: I. Synthesis and Physicochemical Characterization. *Microporous Mesoporous Mater.* 2010, 127, 228–236. <https://doi.org/10.1016/j.micromeso.2009.07.019>.
 83. Zhuo, W.; Xie, Y.; Benson, M.T.; Ge, J.; Mariani, R.D.; Zhang, J. XRD and SEM/EDS Characterization of Two Quaternary Fuel Alloys (U-2.5Mo-2.5Ti-5.0Zr and U-1.5Mo-1.5Ti-7.0Zr in Wt. %) for Fast Reactors. *Mater. Charact.* 2020, 170, 110696. <https://doi.org/10.1016/j.matchar.2020.110696>.

Recuperación del colorante de aguas residuales textiles mediante nanoarcillas para su reutilización como pigmentos y nuevos baños de tintura

3.4. Adaptación del artículo: Printing with hydrotalcite hybrid nanoclays and dispersed, reactive, direct dyes

Artículo publicado en: López-Rodríguez, Daniel; Micó-Vicent, B.; Jorge Jordán-Núñez; Moncho-Santonja, María; Bou-Belda, Eva. (2022) Printing with hydrotalcite hybrid nanoclays and dispersed, reactive, direct dyes. *Dyes and Pigments* (21)1 - 16. j.dyepig.2022.111022

Abstract:

By using nanotechnologies it is possible to colour textile substrates with new printing techniques using dyes that have been discarded from non-exhausted dye baths. Hydrotalcite is clay with a high adsorbent capacity that can be used for the recovery of dyes from textile wastewater. In this work, three different types of dyes will be adsorbed: direct, reactive and dispersed, the first two being anionic and the last one non-ionic. After this adsorption, the aim is to use this clay-dye hybrid to provide colour to a textile printing paste. The results obtained are subjected to colour fastness tests in order to compare them with more conventional printing processes. The hybrids are also analysed by infrared spectroscopy and x-ray diffraction characterisation techniques to check the correct adsorption and formation of the hybrid. Colour measurements are carried out using reflection spectrophotometers to evaluate the colour results of both the hybrids and the printed textiles successfully and also to analyse their TSR. Thermogravimetric analysis carried out on the hybrids allow anticipating the possible results that they may have, they present certain tests of colour fastness to light which are improved thanks to the action of the hydrotalcite.

3.4.1. Introduction

All life requires water and life would not be possible without water. It is also one of the planet's main sources of hydrogen and a potential source of energy for the future. The development of large civilisations and their industrialisation has led to increased concern about water pollution, as in the case of water where large quantities of textile dyes are discharged [1],[2]. The textile industry, besides being a fundamental pillar in the

development of the global economy, is also one of the biggest polluters of the planet, consuming around $77.5 \cdot 10^9$ tonnes of water per year [3].

Currently there is a commercial range of more than 10,000 dyes with different functional groups. Depending on the charge they may have, the different textile dyes can be classified into non-ionic, cationic and anionic dyes [4]. The presence of textile pollutants of this type causes great damage to marine life in water, as it prevents the various processes of photosynthesis and chemical oxygen demand (COD). It should also be noted that textile dyes are carcinogenic and highly toxic [5]–[7]. Furthermore, they are difficult to hydrolyse due to their resistance to light radiation, aerobic digestion and certain oxidising agents [8]. They are non-biodegradable and difficult to process due to their synthetic base and the presence of aromatic components in their chemical formula. For all these reasons, the cleaning of water by eliminating waste from industrial dyes has become one of the main environmental concerns in recent years.

The search for methods to reduce this environmental impact has led to the use of nanoclays [9]–[13]. These are a type of nanoadsorbents that are being used with great success to remove different pollutants in aqueous media. Hydrotalcite (H), which has been used in this work [14]–[18], is a laminar mixed mineral composed of an anionically charged double layer. It consists of $Mg(OH)_2$ layers within an octahedral geometrical structure. The main characteristic that gives it this adsorption property is its high anion exchange capacity [19], which is why it is frequently used in the adsorption of anionic dyes, although it can also adsorb cationic and non-ionic dyes [20].

In previous work, other researchers have used these clays with the aim of recovering dyes from wastewater for water clean-up [21]–[23] although they have not proposed any kind of reuse of the resulting hybrid. Others have been able to demonstrate the stabilisation of the dye when protected by the clay and the increase of the colour fastness to external agents [24] although they have not used the pigment obtained to colour a textile by printing techniques or any other process.

Pigmentary textile printing makes use of conventional pigments so that the printing paste has the colour conferred by the pigment, which is then transferred to the fabric and fixed by means of binders and fixatives. One of the objectives of this work is to replace this conventional pigment with clay-dye hybrids, which have obtained a high degree of totally uniform colouring due to the adsorption of the dye by the clay. In this way, the product obtained from the elimination of the dye from the textile sources is used for a new purpose and it is not necessary to make use of a new resource for printing, as it is not necessary to consume pigment as would be done in conventional printing.

The aim of this work is to trap the dye in the structure of the nanoclay in order to subsequently incorporate the hybrid obtained into a textile printing paste, allowing the colour to be incorporated by the clay-dye, thus carrying out a pigmentary type of printing. In this way, the cycle of recovery and reuse of the dye is closed, reducing the environmental impact of the dye and at the same time reusing the discarded material without generating waste. In this way, the circular economy, which is so popular these days, is achieved.

3.4.2. Materials and methods

For this research 3 types of dyes of different nature have been used: direct dye of anionic character - direct blue 199 CI 74180 (DB199) [25] (Source Clariant); reactive dye also of anionic character Yellow Drimarene K-2R (RYD) [26] (Source Clariant), and finally, Disperse Red 1 CI 11110 (DR1) [27] (Source Clariant) was used as a non-ionic disperse dye. Figure 3.4.1 shows the chemical structures of each of these dyes.

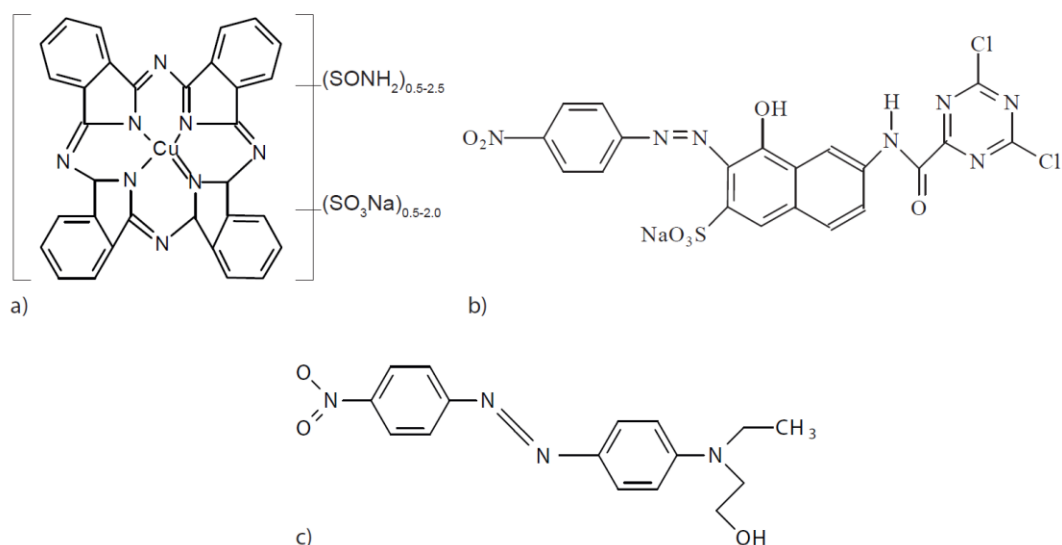


Figure 3.4.1. a) Direct Blue 199 [25], b) Reactive Drimarene Yellow [26], c) Disperse Red 1 [27]

Hydrotalcite $\text{Mg}_6\text{Al}_2(\text{CO}_3)(\text{OH})_{16}\cdot 4(\text{H}_2\text{O})$ nanoclay was used as a nanoadsorbent for the different dyes described above [16]–[18] which was previously calcined to increase its adsorption capacity, in accordance with Dos Santos R.M.M. [28]. In this calcination procedure, the H structure is destroyed and the amount of the various anions such as CO_3^{2-} is reduced. This loss of anions allows new anions to be reincorporated when the calcined hydrotalcite clay (HC) is reconstructed by being re-hydrated thanks to its shape memory. It is in this reconstruction that anionic dyes are incorporated into the clay structure during its recovery. Figure 3.4.2 shows images of the nanoclay, before calcining, after calcining and when reconstructed again during rehydration. Looking at the morphology of the different images, it can be seen that the clay structure has indeed been recovered [29].

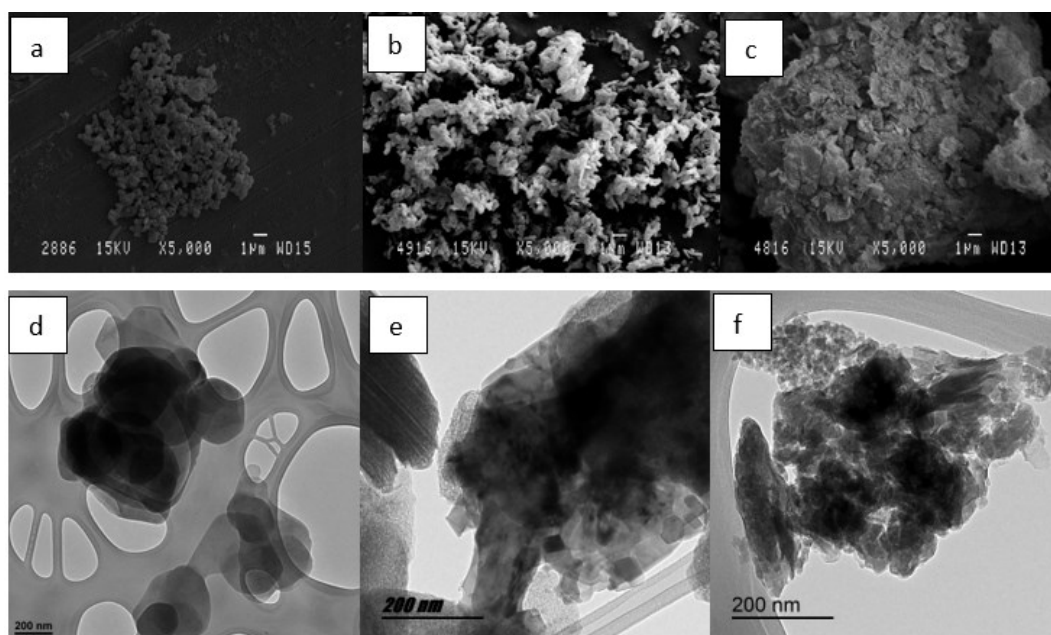


Figure 3.4.2. SEM micrographies of different H samples: a) H original b) HC calcinated c) HC reconstructed. TEM micrographies of different H samples: d) original H e) HC calcinated f) HC reconstructed

In order to know the concentration of dye remaining in a dye bath after the adsorptive action of the clay, it will be necessary to generate Lambert-Beer lines [30] to calculate this dye concentration in aqueous solution. Thus, from different dye solutions of known concentrations, several readings are taken in the transmission spectrophotometer in order to obtain the equations in Table 3.4.1.

Table 3.4.1. Lambert-Beer line equations and R^2

Dye	Equation	R^2
Direct Blue 199 (DB199)	$y = 21.784 x - 0.015$	0.9982
Reactive Yellow (RYD)	$y = 14.943 x - 0.0021$	0.9993
Disperse Red 1 (DR1)	$y = 25.411 x - 0.0244$	0.9989

As is obvious, one of the main objectives of this work is to achieve the maximum possible adsorption of the dyes by the HC clay and to leave the water free of contaminants. In the experimental adsorption phase, 3 litres of solution of each dye are made at a concentration of $1\text{g}\cdot\text{L}^{-1}$ and then $3\text{g}\cdot\text{L}^{-1}$ hydrotalcite are immediately introduced into this solution. The next step is to subject the mixture to agitation by means of a magnetic stirrer

which will run at 1600 r.p.m. during the first two hours and then it will lower the revolutions to 600 r.p.m. In this way there is a first phase of adsorption [31] in which there is more centrifugal force for the penetration of the dye, but afterwards it is ensured that the dye does not come out of the clay again, hence the reason for lowering the revolutions in an "ageing" stage of the hybrid that is being generated. Once the time described above has elapsed, the solution is filtered to separate and collect the clay from the aqueous solution, for which a filter paper is used, This is then left for 48 hours so that all the water is dispelled by gravity and is separated from the clay. After this separation, a sample of the water is collected and a new reading is taken using the transmission spectrophotometer. Using the equations in Table 3.4.1, the concentration of dye that has remained in the water and has not been adsorbed is calculated [32],[33]. The clay remaining on the filter paper is collected and freeze-dried to extract the water that could be adsorbed [34],[35] to finish extracting the water that could remain in the HC.

Once the clay has been harvested and well dried, the hybrid is printing. For this purpose, the recipe used for printing is based on: 30 g·kg⁻¹ of hybrid, 30 g·kg⁻¹ of synthetic thickener from the supplier Archroma with commercial reference Lutexal CSN liq, 10 g·kg⁻¹ of resin from the brand Color Center and referenced as Center Resin STK / 100, 10 g·kg⁻¹ of fixative from the manufacturer Archroma referenced as Lupintrol SE and deionised water to create one kilo. The prints are made on 100% cotton fabrics in the case of the hybrids obtained from direct and reactive anionic dyes and on 100% polyester in the case of the hybrid composed of non-ionic disperse dyes. In all cases, after printing, it is left to dry for 15 minutes at 60 °C and thermofixed at 180 °C for 30 seconds with a pressure plate. The results obtained are evaluated in a Minolta CM-3600d reflection spectrophotometer according to ISO 105-A05:1996 for subsequent degradation assessment, obtaining the CIE tristimulus values for the D65 illuminant and the 10° CIE standard observer.

Printing was performed with the same dyes used in adsorption to compare the results obtained. For the RYD dye, printing was performed on 100% cotton (CO) fabric with the following recipe: 50 g·kg⁻¹ of Proesgum CEL-RF thickener (alginate), 100 g·kg⁻¹ of urea, 40 g·kg⁻¹ of sodium carbonate, 10 g·kg⁻¹ of dye to have a similar shade to that of the hybrids

and deionised water was used to complete the kilo of printing paste. [36]. It should be noted that sodium carbonate Na_2CO_3 has been used for this recipe and not bicarbonate because the reactive group of the RYD dye is Trichloropyrimidine, which is the least reactive group of all, and Na_2CO_3 is used for dyes with low reactivity. After printing, it is dried at 120°C for 15 minutes and steamed at 100°C for 30 minutes. Afterwards, it is important to wash the fabric to remove the hydrolysed dye not fixed to the fabric, so initially, the products are washed with water at 60°C . This is a dilution stage in which the thickener, salt and alkali are removed from the fabrics. They are then washed in a solution of $2\text{ g}\cdot\text{L}^{-1}$ with non-ionic soap at 60°C for 30 minutes. [36],[37]. The detergent used in this wash was Solpon OWS from the manufacturer Boehme. Finally, a hot and then a cold rinse is carried out to dilute the final dye solution that is adhered to the fibres. In the cold rinse, $1\text{ g}\cdot\text{L}^{-1}$ of acetic acid is added, so that there is greater affinity with the finishing products.

The printing of direct dye DB199 was performed on a 100% CO $135\text{ g}\cdot\text{m}^{-2}$, 25 yarns $\cdot\text{cm}^{-1}$, 22 weft $\cdot\text{cm}^{-1}$ of plane weave openwork fabric for which the following recipe was used: $50\text{ g}\cdot\text{kg}^{-1}$ of proesclear thickener BDR from the manufacturer Proes Chemicals, $50\text{ g}\cdot\text{kg}^{-1}$ of urea, $10\text{ g}\cdot\text{kg}^{-1}$ of dye and deionised water to complete the kilo of printing paste. [38]. After printing, it is dried at 120°C for 15 minutes and steaming at 100°C for 30 minutes. The printing parts were rinsed at 45°C in an aqueous solution containing $2\text{ g}\cdot\text{L}^{-1}$ with non-ionic soap at 60°C for 30 minutes, and then air dried.

To complete the dye printing control battery of tests without the hybrids, a printing was carried out on a 100% polyester fabric (PES) $200\text{ g}\cdot\text{m}^{-2}$, 13 yarns $\cdot\text{cm}^{-1}$, 52 weft $\cdot\text{cm}^{-1}$ of plane weave with the DR1 disperse dye, for which the following recipe was formulated: $25\text{ g}\cdot\text{kg}^{-1}$ of neutralised dispersion thickener (synthetic), AUXICLEAR EDL, $10\text{ g}\cdot\text{kg}^{-1}$ of dye and deionised water to complete the kilo of printing paste. After printing, the printing paste is fixed at $150\text{-}160^\circ\text{C}$ for 4 minutes and then washed to remove the colloidal thickener and the unfixed dye. This washing consists of two phases: the first was done by manual mechanical action with deionised water, rubbing the fabric with the water, while in the second phase of this washing, a mixed washing (reducer and Solpon OWS detergent) was carried out to obtain greater efficiency. This second wash is with a bath composed of 2 ml-

L⁻¹ of 40% NaOH, 4 g·L⁻¹ of Na₂ S₂ O₄ and 2 ml·L⁻¹ of Solpon OWS detergent. The bath ratio will be 1/40, the temperature 60°C and the treatment time 15 minutes. As a summary, a detail of the samples used to compare the results obtained can be seen in Table 3.4.2.

Table 3.4.2. Printing samples

Sample nº	Colouring matter	Textile
1	Direct Blue 199	100% CO
2	Reactive Yellow Drimaren K-2R	100% CO
3	Disperse Red 1	100% PES
4	Hydrotalcite + Direct Blue 199	100% CO
5	Hydrotalcite + Reactive Yellow Drimaren K-2R	100% CO
6	Hydrotalcite + Disperse Red 1	100% PES

To obtain the measurements of the colour of the clay-dye hybrids and the total solar reflectance (TSR) [39] the Jasco V-670 double UV-VIS / NIR spectrophotometer was used to measure in the range 2700-190 nm using a frequency of 0.5 nm. This instrument is equipped with a double grating monochromator. The first of these monochromators is used for the UV-VIS range using 1200 grids·mm⁻¹, consisting of detectors based on a photomultiplied tube. The second grating is used for the IR infrared region with 300 grids·mm⁻¹ using a PbS detector. For both the first and the second detector, the grating has an automation system that manages the changes adapting it to the wavelength to be used at any given moment. A halogen lamp (330-2700 nm) and a deuterium lamp (190-350 nm) were used as light sources. The reflectance factors were applied for the hybrid pigments with the CIE-1964 observer and with the D65 illuminant in order to obtain the values of the optical properties and to make a comparison [40].

For the topographical analysis of the surface of the samples, a scanning electron microscope (SEM) model PHENOM (FEI Company, Eindhoven, The Netherlands) was used, working at a suitable electron acceleration of 5kV. The samples were previously prepared by sputter coating with a gold/palladium alloy in an EMITECH sputter coater mod. SC7620 (Quorum Technologies Ltd., East Sussex, UK). This coating does not affect the results obtained as the deposited thickness is only 5-7 nm.

In order to assess the thermal characteristics of the hybrids, a thermogravimetric analysis (TGA) was performed to compare the variation between the degradation peaks of the dyes and the clay-dye composites [41]–[43]. The TGA / SDTA 851 thermogravimetric analyser (Mettler-Toledo Inc., Columbus, OH, USA) was used for this characterisation. The experimental conditions of use established in this analysis were a temperature increase frequency of 5°C every minute in a study range from 20 to 900°C using an oxidation medium of N₂ :O₂ (4:1).

For the characterisation of the hybrids, the samples were tested using an infrared spectrophotometer to obtain the Fourier transform (FTIR). Given the nature of the material to be studied, a horizontal attenuated total reflection (FTIR-ATR) using a ZnSe prism was used. The test equipment used was a Jasco FTIR 4700 IRT 5200 spectrometer which is equipped with a DTGS detector sensor. A pressure accessory was also used to achieve a uniform and equalised pressure on all samples. The spectrum was obtained after a sweep of 64 scans at a resolution of 4 cm⁻¹.

Following the characterisation of the hybrids, an X-ray diffraction (XRD) test was carried out to study how the clay varies in shape and laminar structure before and after calcination and rehydration [44],[45] to study how the clay changes its shape and lamellar structure before and after being calcined and rehydrated. The equipment used was a Bruker D8-Advance XRD (Bruker, Billerica, MA, USA), with a Göebel mirror (power: 3000 W, voltage: 20-60 kV and current: 5-80 mA). Readings were taken in an oxidising atmosphere at an angular velocity of 1°/min, STEP 0.05°, and an angular sweep of 2.7-70°. This test will be of particular importance to analyse the basal space in the hydrotalcite structure produced by the adsorption of the dyes.

Finally, X-ray photoelectron spectroscopy (XPS) and Scanning Electron Microscopy Energy + Dispersive X-ray spectroscopy (SEM-EDX) techniques were used to determine and discuss the surface composition and oxidation state. For this purpose, both hydrotalcite alone and dye-loaded hybrids are analysed in order to study the changes produced upon adsorption of the dye.

X-ray photoelectron spectroscopy (XPS, NEXSA, Thermo Scientific) was used to perform surface analysis using radiation (1486.6 eV), monochromatised by a double crystal monochromator, which produces a focused X-ray spot having a diameter of 400_μm, at 6 mA × 12 kV. The alpha hemispherical analyser was used in constant energy mode with analysis step energies of 200 eV to measure the whole energy band and 50 eV in a narrow scan in order to obtain the results for certain elements. In this way XPS has been used to obtain the chemical bonding state and elemental composition of the surface of the samples. Charge compensation was achieved with the flood gun system whereby low energy electrons and low energy argon ions are obtained from a single source.

Energy dispersive X-ray (EDX) analyses were performed with a JEOL JSM-6300 scanning electron microscope. All samples were pre-coated with graphite to make the non-conductive surfaces conductive. The selected coatings were non-metallic to avoid possible interferences in the results. The EDX spectra obtained were used to obtain the elemental composition of the materials deposited on the surface of the hybrids.

The printing specimens were subjected to different tests to assess their different fastnesses. The colour fastness to washing was carried out according to the UNE-EN ISO 105-C06:1994 standard with the Linitest test apparatus, described in the UNE-EN ISO 105-C06 standard. Test number A1S was carried out at 40°C, 150 ml wash volume for 30 minutes, without adjusting the pH and with 10 steel balls to generate abrasive action. The fastness of the dyes to ironing was carried out according to the UNE-EN ISO 105-X11:1997 standard with a pressure iron. It was done dry, wet and damp as described in the standard. For all the test pieces, the ironing time was 15 seconds at a temperature of 200°C for PES fabrics and 150°C for CO fabrics, as cotton yellows at higher temperatures. For the colour fastness to rubbing, the UNE-EN ISO 105-X12:2016:2016 standard was followed using the crockmeter as test apparatus. Both dry and wet rubbing tests were carried out. Finally, with the help of a xenotest, the colour fastness to artificial light was assessed using xenon lamps according to UNE-EN ISO 105-B02 method 1 (grade 4) and the colour fastness to daylight according to UNE-EN ISO 105-B01 method 1. Table 3.4.3 shows a summary of all the specimens carried out with the different fastness tests. It is worth highlighting that the

samples 1-6 listed in Table 3.4.2 are the reference standards on which no colour degradation agent has been applied.

Table 3.4.3. Colour fastness testing

Nº	Colouring matter	Fastness test	Nº	Colouring matter	Fastness test
7	Blue Direct	ironing	31	Blue Direct	humid ironing
8	Reac. Yellow	ironing	32	Reac. Yellow	humid ironing
9	Disper. Red	ironing	33	Disper. Red	humid ironing
10	Direct Blue+HC	ironing	34	Direct Blue+HC	humid ironing
11	Reac. Yellow+HC	ironing	35	Reac. Yellow+HC	humid ironing
12	Disper. Red+HC	ironing	36	Disper. Red+HC	humid ironing
13	Blue Direct	washing	37	Blue Direct	wet rubbing
14	Reac. Yellow	washing	38	Reac. Yellow	wet rubbing
15	Disper. Red	washing	39	Disper. Red	wet rubbing
16	Direct Blue+HC	washing	40	Direct Blue+HC	wet rubbing
17	Reac. Yellow+HC	washing	41	Reac. Yellow+HC	wet rubbing
18	Disper. Red+HC	washing	42	Disper. Red+HC	wet rubbing
19	Blue Direct	rubbing	43	Blue Direct	wet ironing
20	Reac. Yellow	rubbing	44	Reac. Yellow	wet ironing
21	Disper. Red	rubbing	45	Disper. Red	wet ironing
22	Direct Blue+HC	rubbing	46	Direct Blue+HC	wet ironing
23	Reac. Yellow+HC	rubbing	47	Reac. Yellow+HC	wet ironing
24	Disper. Red+HC	rubbing	48	Disper. Red+HC	wet ironing
25	Blue Direct	artificial light	49	Blue Direct	natural light
26	Reac. Yellow	artificial light	50	Reac. Yellow	natural light
27	Disper. Red	artificial light	51	Disper. Red	natural light
28	Direct Blue+HC	artificial light	52	Direct Blue+HC	natural light
29	Reac. Yellow+HC	artificial light	53	Reac. Yellow+HC	natural light
30	Disper. Red+HC	artificial light	54	Disper. Red+HC	natural light

All the fastness tests were assessed instrumentally by means of a reflection spectrophotometer using the UNE-EN ISO 105-A05 standard and expressing the results according to grey scale values, except for the light colour fastness test, which is assessed by means of a blue scale. An instrumental evaluation of the degree of discharge of the control fabrics was also carried out following the UNE-EN ISO 105-A04 standard. For these instrumental evaluations, the Minolta CM-3600d reflection spectrophotometer was used in the 360-740 nm range with a step of 10 nm.

3.4.3. Results and discussion

3.4.3.1. Final concentration in solution

After the adsorption process described above the results obtained were excellent with adsorption percentages of more than 99% (Table 3.4.4), confirming the high capacity of HC to adsorb textile dyes thus corroborating previous works [28],[46]–[49]. Despite having ionic and non-ionic dyes, in both cases there has been almost total adsorption. For the time being, no differences can be seen in the loadings of the dyes, although it is expected that in future tests and trials differences may be seen, partly due to the characteristics of the clay.

Table 3.4.4. Difference in concentration after HC adsorption

Sample ref.	Dye	Initial conc. g·L ⁻¹	Final conc. g·L ⁻¹	Ads(%)
1	Direct Blue 199	1	6.55E-04	99.934
2	Reactive Yellow Drimaren	1	5.13E-04	99.949
3	Disperse Red 1	1	6.21E-03	99.938

3.4.3.2. Hybrid colour measurements

The measurements made to calculate the colour of the three hybrids obtained are shown in Table 3.4.5 and in Figure 3.4.3 represented in a chromatic diagram. The reflectance measurements of each of the dye-clay hybrids have been used to perform the colorimetric calculations for each pigment. The guidelines of the International Commission on Illumination CIE 15:2004 [50] of the International Commission on Illumination and Colour (CIE) have been followed in order to make an objective comparison of the absolute and relative colour values. The CIELAB colorimetric parameters encoded by the CIE 1931 XYZ standard and the standard illumination D65 were used for these calculations. The CIE a*b* and CIE-Cab*L* diagrams in Figure 3.4.3 demonstrate the colour obtained by the clays and confirm that the dye that has been removed from the solutions is now trapped in the nanoclay. The colours obtained maintain the expected shades according to the original dye used in each case, the yellow is on the axis and angle corresponding to the yellows with a slight touch towards the greens, sample 4 is in the pure blues and sample 6 in the reds with a slight yellowish touch. The saturation and luminosity of sample 5 is higher than that of

the next two samples due to the very nature of the yellow, which gives it a characteristic level of luminosity and somewhat limits the range of colours that could be obtained by increasing or decreasing the concentration of the dye in the nanoclay. However, in samples 4 and 6 (blue and red respectively), the luminosity is much lower, at L* levels of 50, so that with this saturation we have dark and chromatic hybrid pigments that provide the possibility of wider colour ranges just by decreasing the concentration or decreasing the concentration of the original dyes in the nanoclay. It goes without saying that by mixing the three types of hybrid pigments obtained, with such pure colours in terms of their shade, and these levels of saturation, the range of colours will be considerably extended.

Table 3.4.5. L*, a*, b*, C*_{ab} values of each dye and each hybrid

Sample	L*	a*	b*	C* _{ab}	h
DB199	44.94	2.03	-1.88	2.77	317.16
RYD	50.96	5.79	11.08	12.50	62.39
DR1	50.77	15.14	5.86	16.24	21.17
4	56.09	-1.77	-15.03	15.14	263.30
5	86.21	-8.75	42.61	43.50	101.61
6	50.77	15.14	5.86	16.24	21.17

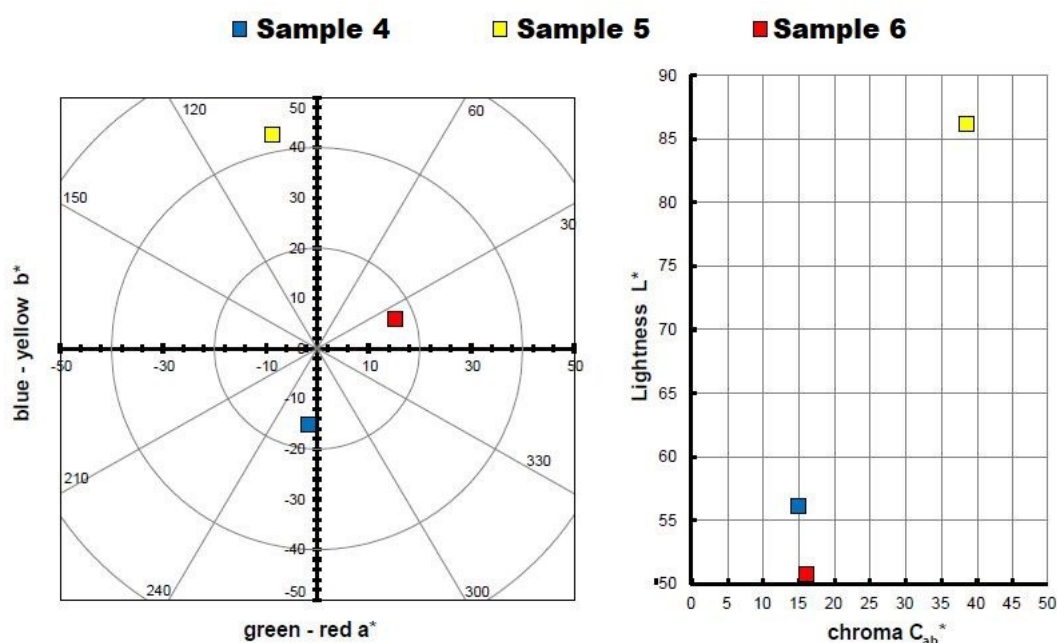


Figure 3.4.3. Graphic CIELAB plots for hybrid pigments synthesised using the D65 illuminant and the CIE-1931 XYZ standard observer. Left: CIE-a * b * colour diagram; right: CIE-Cab * L * colour chart.

3.4.3.3. Total solar reflectance (TSR)

When a coating is applied to a textile, as in the case of printing, the behaviour and resistance to external factors that this coating will have will depend largely on the amount of light radiation that it is capable of absorbing and reflecting. For this reason, a study of this radiation has been carried out using the total solar reflectance (TSR) factor. This value is determined by the amount of radiation absorbed in the outermost or surface layers of the coating. The exposure time to which the surface is subjected is one of the most relevant factors. In order to achieve bodies whose coatings have the least hot surfaces possible, the reflection of solar radiation must be maximised. The way to express this reflection capacity in numerical percentage form is called TSR, taking into account that 100% is zero adsorption and 0% is zero reflection. In order to calculate the TSR, the values of the solar light reflectance of the raw substrate are needed and then the solar weighting factors have to be applied for each value of the wavelengths to be analysed. These calculations are given in ASTM standard G173-03 [51]. In order to calculate the degree of absorption involving the hybrid, the (100-TSR) calculation must be applied.

Table 3.4.6. TSR Values

Colouring matter	Sample ref.	TSR %
Direct Blue 199	1	16.05
Reactive Yellow Drimaren K-2R	2	27.38
Disperse Red 1	3	26.93
Hydrotalcite + Direct Blue 199	4	36.14
Hydrotalcite + Reactive Yellow Drimaren K-2R	5	64.77
Hydrotalcite + Disperse Red 1	6	45.40

Table 3.4.6 shows a comparison of the TSR values of the different hybrids and dyes. The clay has a white colour and by adsorbing the dye as a result we will have a material with a much higher L* luminosity which will reflect more light and comparing each dye with its corresponding hybrid will make the TSR higher. If we compare the hybrids with each other and remember the L* values shown in Figure 3.4.3 we will see how sample 5 stands out with a much higher value than the other two, as happened with the luminosity. The second dye and hybrid is the red sample, which has a higher L* value than the blue. In all cases, the differences between the TSR% values of the original dye and the hybrid sample are significant. These results are shown in Figure 3.4.4, comparing pairs according to the dye.

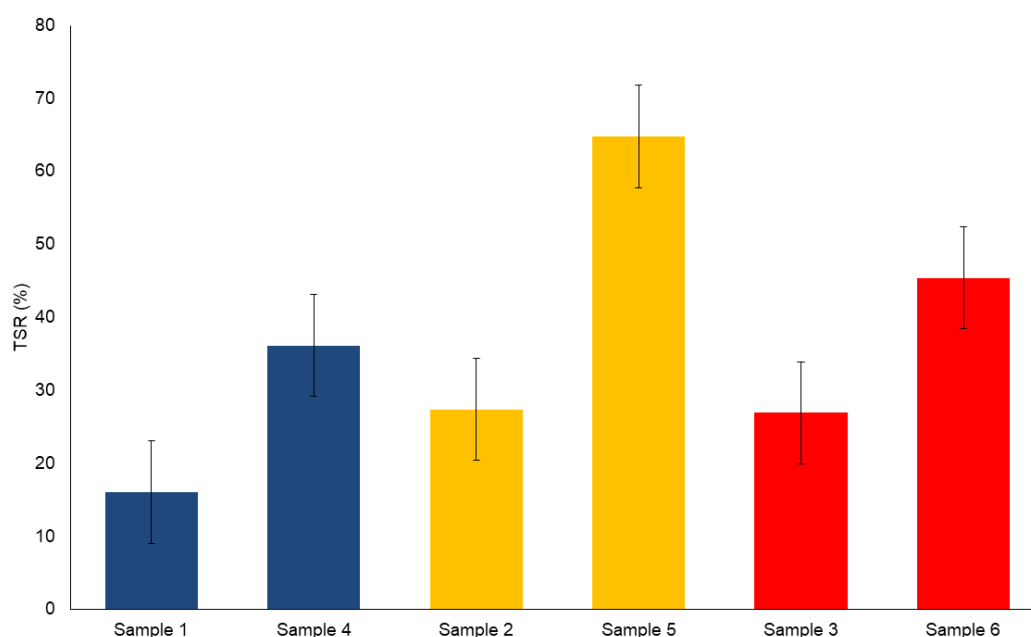


Figure 3.4.4. Total Solar Reflectance (TSR (%)) for each sample

Figure 3.4.5 presents the reflectance of each hybrid depending on wavelength. The behaviour of the samples in the ultraviolet (UV) region is very similar for hybrids 4 and 6 but very different for hybrid 5. The behaviour becomes very different in the visible spectrum between 400-700 nm and continues this difference in the near infrared (NIR) up to 1200 nm, as it is affected by factors such as the structure of the dye and the perception of colour (brightness, hue and chroma). However, in the region between 1200-1400 nm the values start to be very similar, becoming almost the same in the 1400-2400 nm area, so the main differences observed in the TSR values are due to the nature of the dye adsorbed on the nanoclays and its behaviour in the UV-visible and near infrared up to 1200nm.

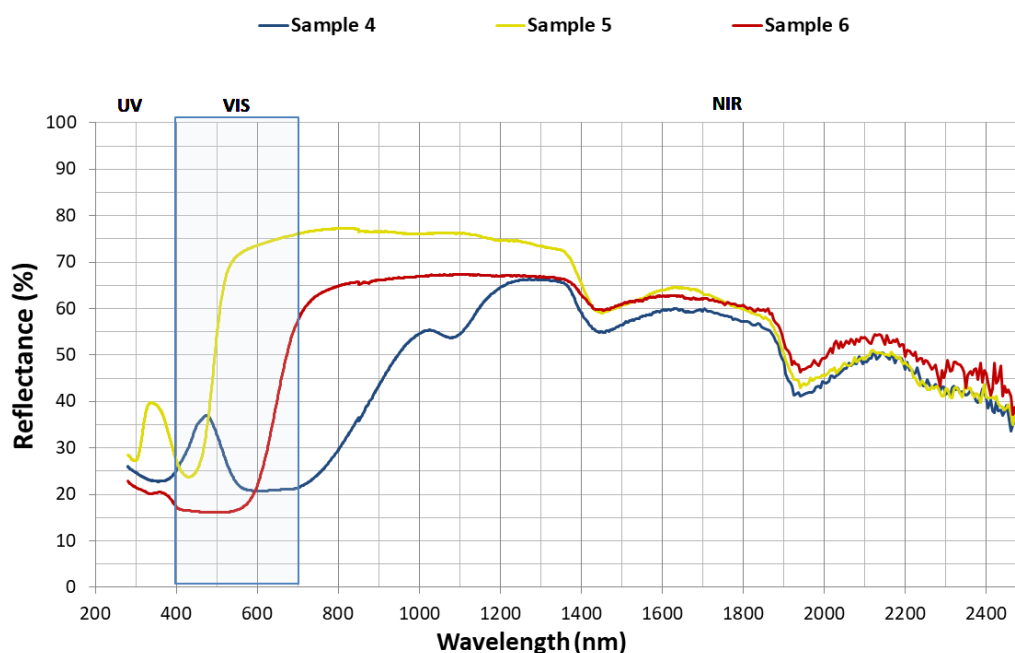


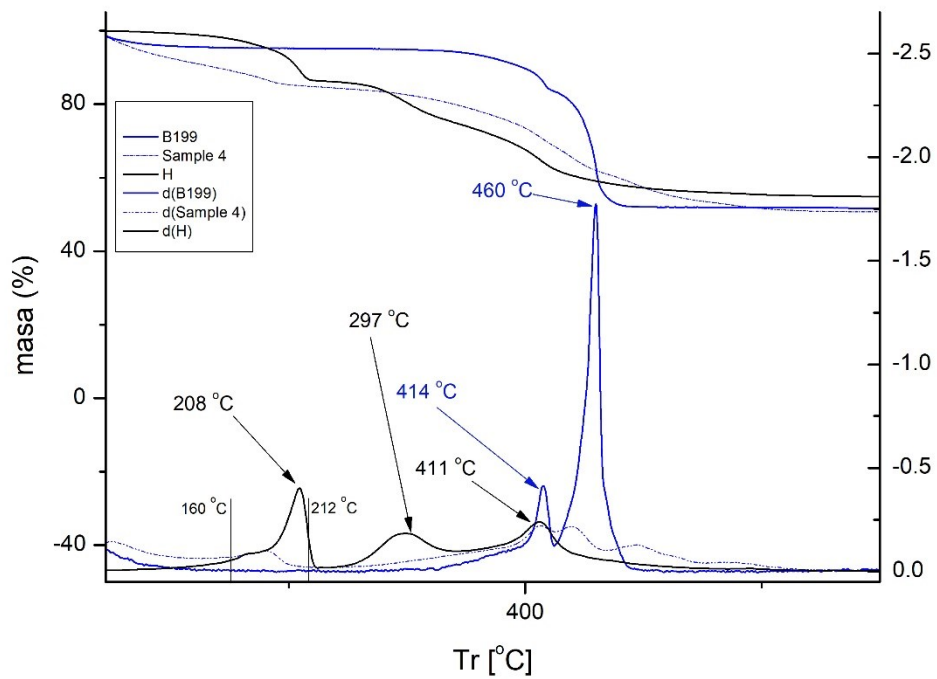
Figure 3.4.5. TSR(%) for each hybrid

3.4.3.4. Thermogravimetry (TGA)

The results of the TGA analysis are shown in Figure 3.4.6. This graph shows at the top the percentage mass loss of each sample as the temperature increases. The lower part of the figure shows the curves d(DB199), d(RYD), d(DR1), d(4), d(5), d(6) and d(H) which correspond to the derivatives (DTGA) of the upper curves, so that the specific degradation peaks can be better appreciated. It is clear that the direct and reactive (anionic) dyes have a slower degradation than the disperse. After 500 °C, the anionic dyes in this study do not degrade any more, while the non-ionic one has an abrupt drop that concludes with a degradation of up to 82%, much more noticeable than the other two dyes that degrade around 49% at the most. This shows that the disperse dye is much more sensitive to temperature, which can have consequences on fastness, which are affected by energy factors such as light.

Figure 3.4.6 shows a comparative analysis of the behaviour of the three dyes, the three hybrids and H. For hydrotalcite alone, a mass loss attributed to the evaporation of interlamellar H₂O and that which has been physisorbed can be seen in the 105-168 °C range. Following the plotted graph of the nanoclay there is another range between 172-

279 °C which corresponds to the loss of the lamellar hydroxyl -OH groups. A third mass drop observed in the range 275-605 °C is attributed to the loss of CO_3^{2-} and the combustion of the fragment molecule [52]–[54]. Notable peaks for hydrotalcite are found at 208°C due to loss of interlamellar water, 297°C and 411°C peaks attributed to loss of -OH groups [55].



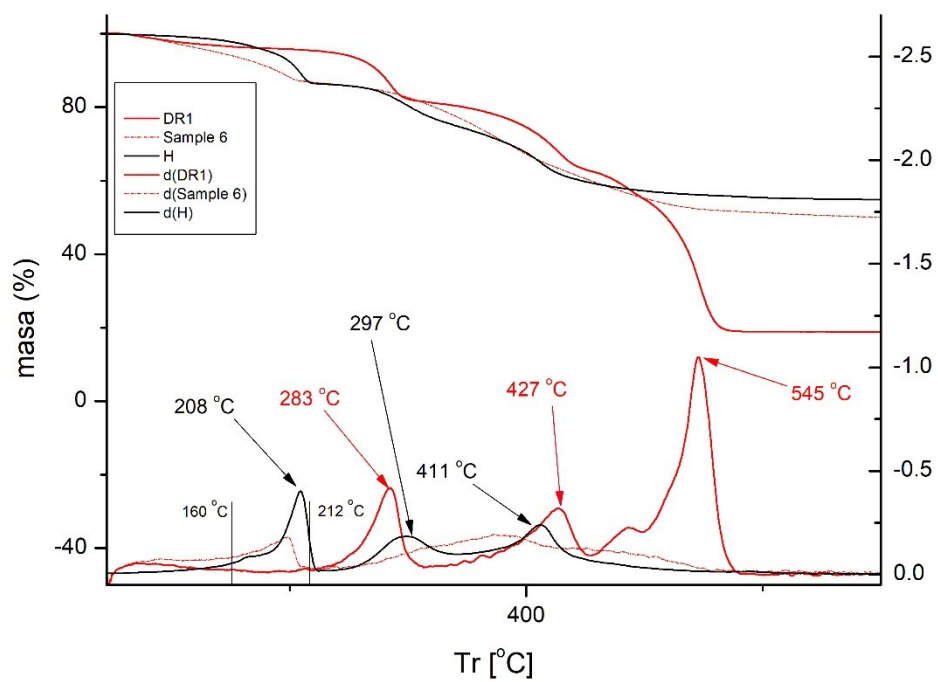
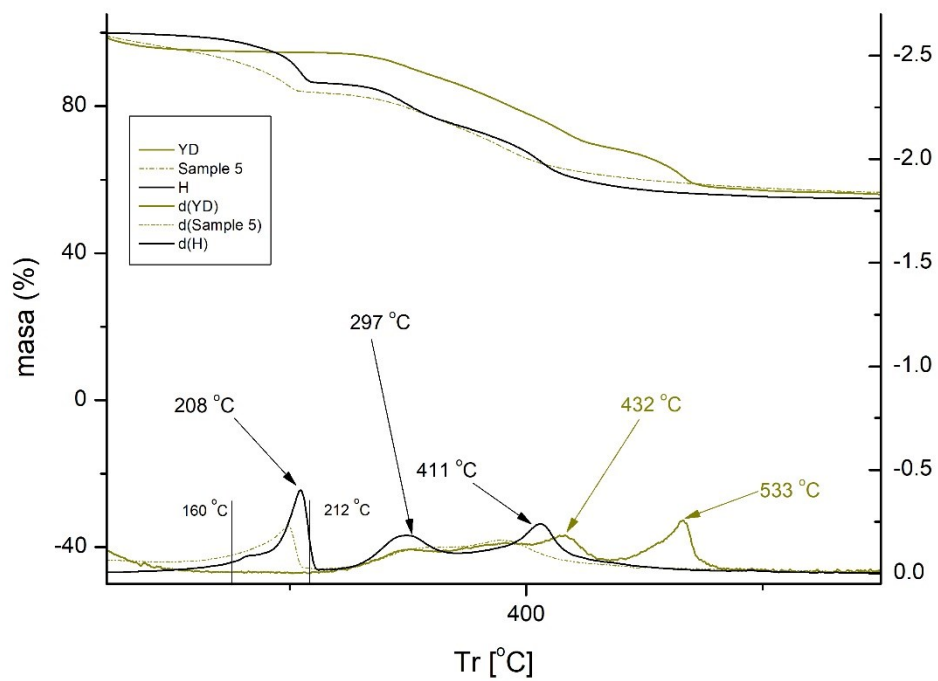


Figure 3.4.6. TGA and DTGA of for each dye, each hybrid and hydroxalcite

With regard to DB199, we can see a peak at 414°C and another very prominent one at 460°C. Sample nº4 does not have such prominent peaks, but is much more attenuated and slightly displaced, due to the protection received by the nanoclay. At the same time, it is observed that in this sample nº4 the 208°C peak of the clay is notably reduced, remaining almost in the form of a shoulder in the range of 160-212°C. In the case of the reactive dye RYD, two peaks can be clearly seen at 432 and 533°C, which disappear completely in sample nº 5. The shoulder in the 160-212°C region continues to inherit the 208°C peak of the H and also some disturbance at 297°C due to the loss of water from the nanoclay. In the case of DR1, peaks are observed at 283, 427 and 545 °C, the latter being the most intense and very significant as it shows a very strong degradation at high temperatures and produces a very significant mass loss with respect to the other dyes. After adsorption by the clay, these 3 peaks disappear completely in sample nº 6 and the shoulder appears in the range 160-212°C, typical of the clay, as in the other samples.

Studies by other researchers have shown that thanks to the effect of hydrotalcite, the thermal stability of dye-clay hybrids has been significantly increased [56],[57]. This is due, on the one hand, to the fact that the lamellar structure of the nanoclay produces a protective effect that reduces the capacity to volatilise the dye components and, on the other hand, when the composite is subjected to high temperatures, there is a transfer of energy from the dye to the clay. This transferred energy is absorbed by the nanoclay, thus reducing the energy impact on the dye [58],[59].

3.4.3.5. X-ray diffraction (XRD)

The results of analysis by X-ray diffraction can be seen in Figure 3.4.7 which shows how in the range between 11 to 12 degrees there is a prominent peak of uncalcined hydrotalcite but when calcined this peak disappears due to the exfoliation and opening of the lamellae due to the collapse that occurs due to dehydroxylation inside the layers of the mineral [60]. This opening of the lamellae is what will facilitate the penetration of the dye. After the penetration of the dye and during the rehydration of the HC, the clay recovers its original structure thanks to its shape memory, [61]–[64] incorporating dye instead of some components such as CO_3^{2-} .

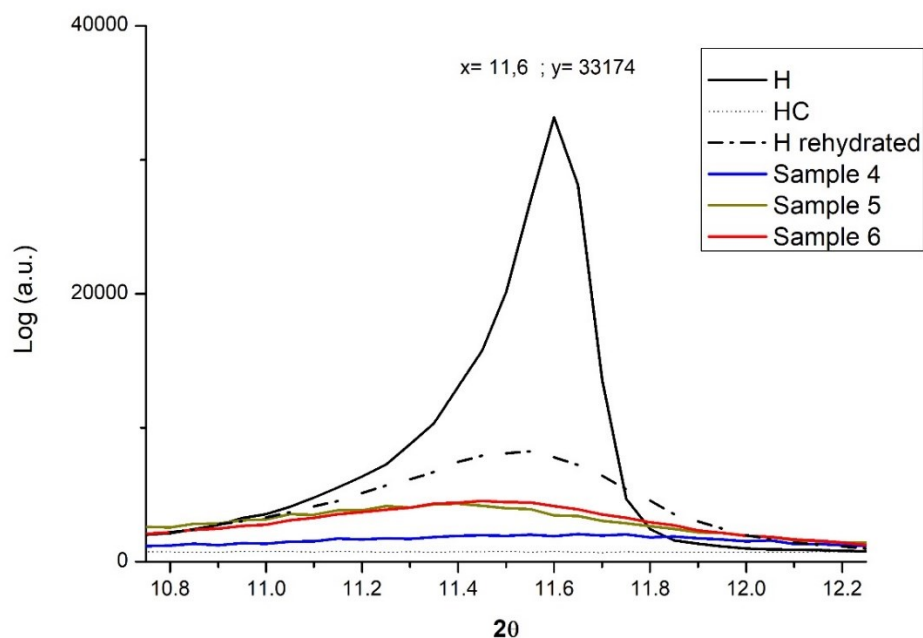


Figure 3.4.7. XRD for Hydrotalcite, Hydrotalcite calcinated, samples 4-6

Studying Figure 3.4.7 in depth it should be noted that the dyes have an amorphous form while the nanoclay has a crystalline form [65]–[67]. Therefore, the XRD peak will be more intense the more crystalline the structures are, so the more dye the clay has, the more amorphous the compound will be and the intensity of the band will decrease. Although the crystalline structure is destroyed when the H is calcined, and the peak disappears completely, it is largely recovered when it is rebuilt during rehydration. The curves of samples 4, 5 and 6 are shown with low intensity as they have a high dye loading (amorphous) and form a very flat curve.

3.4.3.6. Fourier transform infrared spectroscopy FTIR-ATR analysis

By means of this instrumental technique, information relevant to this study will be obtained. The first objective is to determine the effect of calcination on hydrotalcite. Figure 3.4.8 shows two characteristic bands, one at 1361 cm^{-1} corresponding to CO_3^{2-} [68],[69] and another between $3200\text{--}3600\text{ cm}^{-1}$ centred at 3408 cm^{-1} which is assigned to the -OH of the interlaminar water produced by the stretching of the bonds between oxygen and hydrogen

[28],[67],[69]. There are also two relevant peaks at 2850 and 2918 cm^{-1} due to the stretching vibrations of the CH_2 [70]. All these bands disappear completely or are almost completely attenuated in the case of the CO_3^{2-} band after the calcination process, which will allow the attachment of new anionic groups in the hydration reconstruction. Other observed bands are found at 767 cm^{-1} due to Al-OH translation, 640 cm^{-1} due to vibrations of NO_3^- and CO_3^{2-} and at 549 cm^{-1} due to vibrations of the Mg-O bond [55],[67].

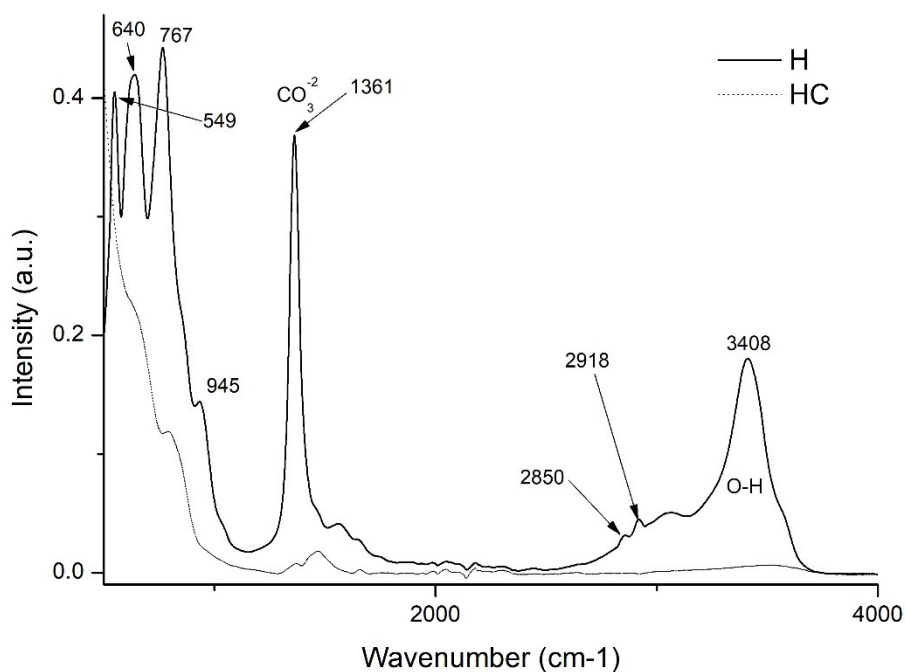
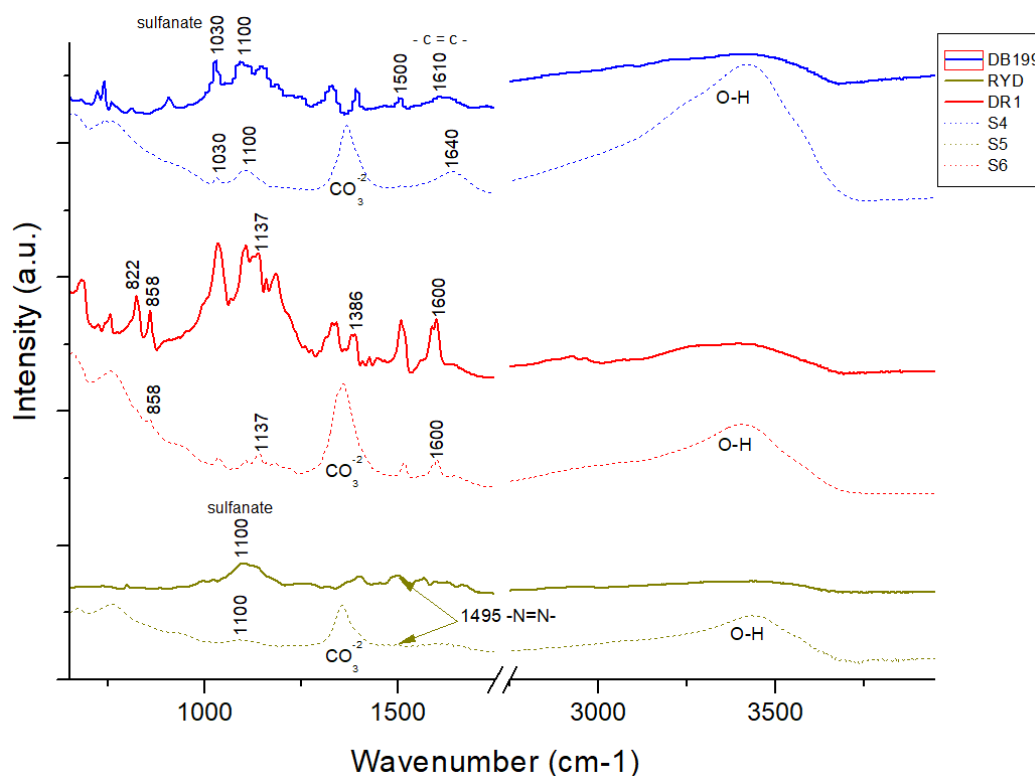


Figure 3.4.8. FTIR comparison of Uncalcined Hydrotalcite (H) and Calcined Hydrotalcite (HC)

Figure 3.4.9 shows an analysis of the spectra obtained for the three dyes studied in this work and their corresponding hybrids after adsorption on hydrotalcite. Looking closely, the hybrids show bands very characteristic of the clay, such as one at 1361 cm^{-1} corresponding to CO_3^{2-} , and another one between 3200-3600 cm^{-1} centred at 3408 cm^{-1} which is assigned to -OH. It is very interesting how after hydration and adsorption of dyes these bands that had been lost after calcination are recovered again, confirming the shape memory of this kind of solid. Regarding the CO_3^{2-} band in sample 6, this is due to the fact

that the dye used is non-ionic and therefore there is less substitution of this group during the reconstruction of the calcined clay.

Looking at the area of DB199 and its corresponding hybrid sample 4 a peak appears at 1100 cm^{-1} which is attributed to acetates, formate, propionates and benzoates [71]. Previous work by other authors [65],[66],[68],[70] explain that the peaks found between 1400 and 1640 cm^{-1} are attributed to benzene rings, while at 1030 and 1500 there is the symmetric vibration of the sulphonate group [53] and the vibration of the azo bond [72] respectively. Analysing the result of the RYD dye and its corresponding hybrid sample 5, the sulphate groups are seen in a peak at 1100 cm^{-1} [73],[74] and the characteristic azo bond at 1495 cm^{-1} [72]. The FTIR spectrum of Dispersed Red 1 shows peaks at 1600 cm^{-1} corresponding to the aromatic groups $\text{-C}=\text{C-}$, while at 1507 and 1341 cm^{-1} they are attributed to the asymmetric and symmetric stretching of NO_2 respectively [75],[76]. Other peaks at 1386 , 1142 , 858 and 822 cm^{-1} are produced by stretching of the $\text{-N}=\text{N-}$ bond, stretching of the aliphatic amine -C-N- groups, an out-of-plane bending of the C-H near NO_2 and another out-of-plane bending also of the aromatic C-H group respectively [76].



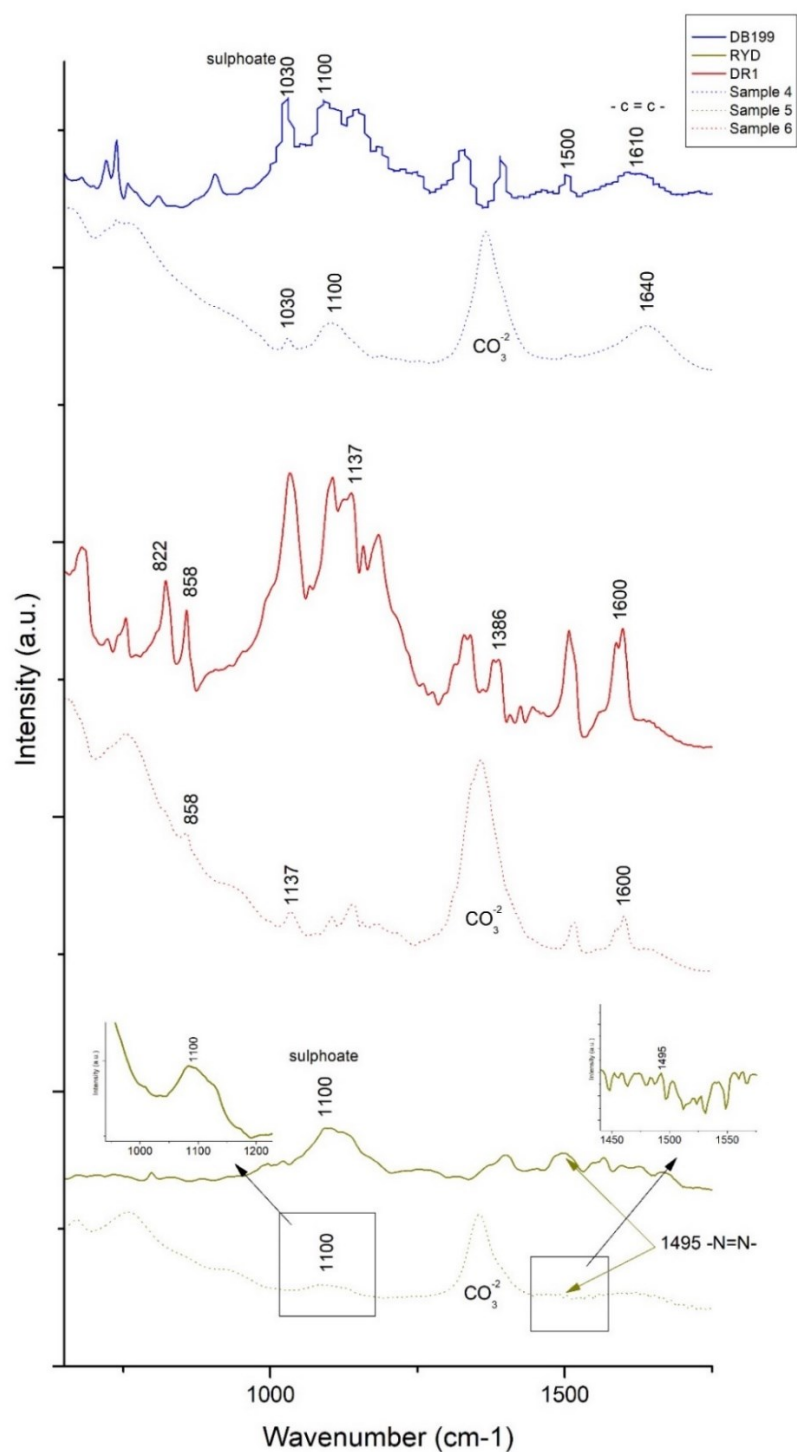


Figure 3.4.9. FTIR of DB199, RYD, DR1 and samples 4, 5 and 6

3.4.3.7. X-ray photoelectron spectroscopy (XPS)

Figure 3.4.10 and Table 3.4.7 shows the binding energy values for various atoms which are decisive for the presence of both clay and the different dyes. The presence in all the samples of C1s, O1s, Al2p3 and Mg1s in different peaks such as 285, 530, 174 and 1308 eV respectively demonstrate the presence of the Hydrotalcite. Furthermore, the presence of N1s in the peaks at 398 eV show the presence of nitrogen from each of the samples 4, 5 and 6.

On the other hand, sample 4 has Cu2p3 with peaks between 932 and 945 eV, as the direct blue 199 dye has the element copper in its structure. As for sample 5 with the yellow drimarene dye, the presence of sulphur can be distinguished by the appearance of a peak at 168.01 eV which corresponds to S2p3.

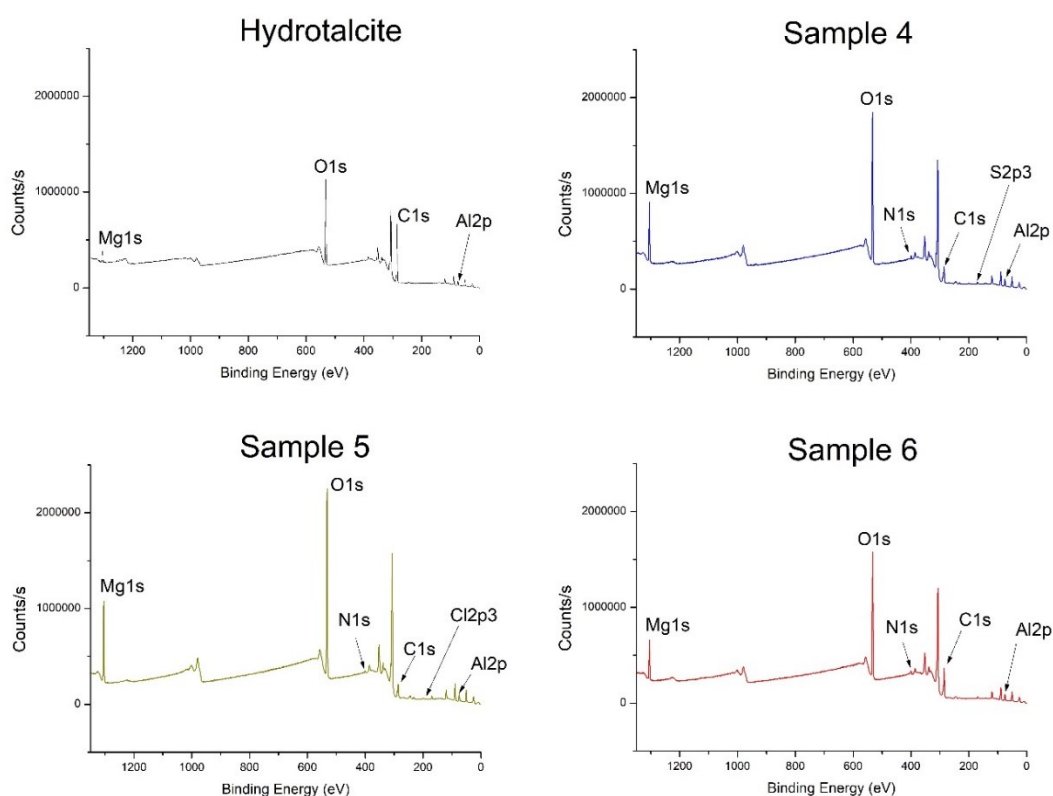


Figure 3.4.10. XPS Hydrotalcite, samples 4, 5 and 6

Recuperación del colorante de aguas residuales textiles mediante nanoarcillas para su reutilización como pigmentos y nuevos baños de tintura

Table 3.4.7. Binding energy H, sample 4, 5 and 6

Cis	Sample 4				Sample 5				Sample 6			
	B.E	FWHM eV	Area	%	B.E	FWHM eV	Area	%	B.E	FWHM eV	Area	%
Hydrotalcite	284.56	1.1	121809.04	85.68	294.64	1.41	32377.81	51.39	284.61	1.46	67532	68.39
	285.22	1.02	7726	5.44	285.59	1.12	9590.51	15.22	285.8	1.44	17364.67	17.58
	285.99	1.33	2552.77	1.80	286.47	1.6	7341.42	11.68	287.14	2	4679.13	4.75
	288.55	1.55	10054.6	7.08	288.91	1.72	13631.2	21.70	289.26	1.55	91394.44	9.28
OIs												
Hydrotalcite	530.29	1.56	39229.75	11.89	530.86	1.56	86427.73	15.12	530.7	1.49	89079.44	13.38
	531.49	1.68	278048.9	84.29	532.09	1.68	464049.21	81.28	531.75	1.7	556751.48	83.72
	532.81	1.59	12566.04	3.82	533.4	1.59	20556.34	3.60	532.47	1.99	19292.66	2.91
Al2p3												
Hydrotalcite	73.82	1.47	9947.56	100	74.48	1.37	12635.1	100	71.21	1.57	12555.1	100
Mg1s												
Hydrotalcite	1305.68	1.57	61905.82	100	1307.59	1.56	62773.06	100	1312.44	1.54	121327.91	100
N1s												
Hydrotalcite	398.65	1.5	9991.75	90.09	398.2	1.32	2056.41	30.95	399.34	1.94	10913.85	86.34
	400.12	1.36	1098.18	9.91	399.6	1.43	3676.29	56.35	401.18	1.66	17307.2	13.66
					401.51	1.56	848.35	12.70				
S2p3												
Hydrotalcite												
Cl2p3												
Hydrotalcite												
Cu2p3												
Hydrotalcite	932.8	1.95	2419.97	17.95								
	934.98	1.54	5670.67	43.59								
	937.25	3.31	1554.34	12.82								
	942.19	3.36	1620.98	12.82								
				945.17	2.54	1661.52	12.82					

3.4.3.8. Scanning Electron Microscopy Energy + Dispersive X-ray spectroscopy (SEM-EDX)

To corroborate the presence of the component elements of the hybrids, clay and different dyes, EDX was used. The spectra resulting from this analysis are shown in Figure 3.4.11. Starting with the composition of the hydrotalcite, peaks can be observed at approximately 0.35, 0.5, 1.35, 1.5 and 1.85 keV corresponding to the elements C, O, Mg, Al and Si respectively. The analysis of the hybrid samples loaded with the dyes shows the same peaks as in the hydrotalcite and other new elements that confirm the presence of the respective dyes. Thus, in sample 4 a peak appears at 2.3 keV which is attributed to sulphur (S) and at approximately 8 keV corresponding to copper (Cu). In sample 5, the presence of colour (Cl) can be assessed by the peak at 2.6 keV.

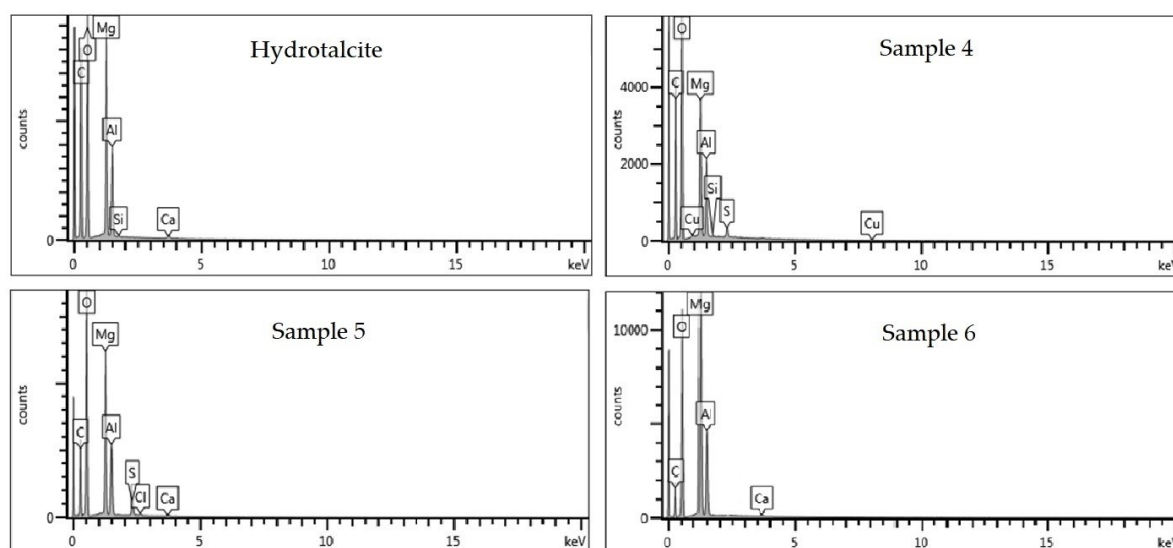


Figure 3.4.11. EDX Hydrotalcite, samples 4, 5 and 6

3.4.3.9. Measurement of printing colour

The main objective of this work was to achieve the colouring of a textile material by means of the printing technique using hybrids obtained with nanoclays as the product that provides this colour. Once this objective was achieved, the colouring of the textile substrate was calculated and evaluated. The $L^*a^*b^*$ and C^*ab values are shown in Table 3.4.8 and

represented in a chromaticity diagram in Figure 3.4.11 to show how the objective has been successfully achieved.

Table 3.4.8. L^* , a^* , b^* , C_{ab}^* values of each printing

Sample	L^*	a^*	b^*	C_{ab}^*	h
4	65.61	-18.59	-21.35	28.31	228.95
5	80.87	-3.58	56.64	56.76	93.62
6	58.59	36.18	18.07	40.44	26.54

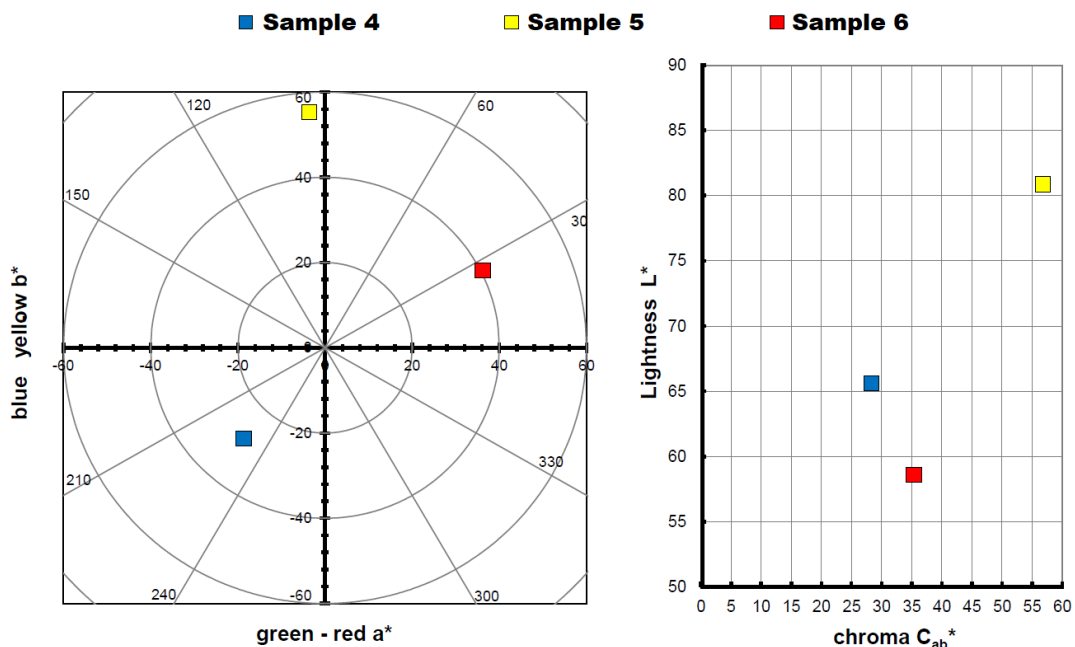


Figure 3.4.12. Graphic CIELAB plots for hybrid printed using the D65 illuminant and the CIE-1931 XYZ standard observer. Left: CIE- $a^* b^*$ colour diagram; right: CIE- $C_{ab}^* L^*$ colour chart

With regard to the colour obtained from the distribution of the dots in the diagrams shown in Figure 3.4.12, we can see in Figure 3.4.13 that the results are excellent. In yellow we have a high luminosity as is typical of this colour and shows that an intense yellow has been obtained. The tone obtained with the blue goes towards more greenish tones than those observed in the hybrid, as a result of the interaction with the textile substrate itself, whose white is not pure and provides a yellowish colouring. The same effect can be seen with the red, which shifts towards more orange tones than the original hybrid for the same

reason. In addition, when the printing pastes are mixed in the application, the lightness levels of the prints with blue and red are higher than those of the hybrid dyes analysed in the previous step. The L^* values are still between 65-55, so that the concentration of the hybrid pigments could be further reduced and a considerable colouring effect could still be seen. The saturation levels in these prints are high in all three cases providing interesting distinguishable visual effects.



Figure 3.4.13. Sample prints 4, 5 and 6

3.4.3.10. Colour Fastness

Once the objective of colouring different textile materials with nanoclays that have adsorbed dyes has been achieved, it must be verified that this colour will be able to remain on the substrates with the passage of time, despite wear and tear produced by different external agents. For this reason, different colour fastness tests have been carried out on the hybrid prints. In order to compare the results, the same tests have been carried out on samples 1, 2 and 3, remembering that these samples are prints of dyes with affinity for the component materials of the respective fabrics, the reactive and direct dyes [77]–[79] and direct dyes [80]–[82] have an affinity for cotton and the disperse dye [83]–[85] has an affinity for polyester. This affinity allows the dye to penetrate into the fibre, while in the pigment prints (samples 4, 5 and 6) the dye remains on the surface of the fabric and is bound to it by a binder [86]–[89].

Table 3.4.9 shows the results obtained for each of the different colour fastness tests. The results are expressed according to the standard greyscale (GS_c) and calculated

instrumentally according to Equation 3.4.1 using the UNE-EN ISO 105-A05. Also in Table 3.4.8 the discharges (SSR) also calculated instrumentally and calculated according to Equation 3.4.2 are shown following the UNE-EN ISO 105-A04 standard. For the artificial light and weathering colour degradation tests, a visual blue scale assessment was performed.

$$\begin{aligned} \text{a)} \quad \Delta E_f &= [(\Delta L^*)^2 + (\Delta C_f)^2 + (\Delta H_f)^2]^{1/2} \\ \text{b)} \quad \text{GS} &= 5 - [\Delta E_f / 1.7] \\ \text{c)} \quad \text{GS} &= 5 - [\log_{10} (\Delta E_f / 0.85) / \log_{10} 2] \end{aligned}$$

Equation 3.4.1. a) Colour change for the determination of the greyscale index for degradation b) GS if $\Delta E_f \leq 3.4$ c) GS if $\Delta E_f \geq 3.4$

$$\begin{aligned} \text{a)} \quad \Delta E_{GS} &= \Delta E_{CIELAB} - 0.4 (\Delta E^{*2} - \Delta L^{*2})^{1/2} \\ \text{b)} \quad \text{SSR} &= 6.1 - 1.45 \ln (\Delta E_{GS}) \\ \text{c)} \quad \text{SSR} &= 5 - 0.23 \Delta E_{GS} \end{aligned}$$

Equation 3.4.2. a) Greyscale difference b) Greyscale index 1 to 4 c) Greyscale index 4 to 5

Table 3.4.9. Colour fastness values by greyscale index and discharge (SSR)

Sample	Degradation	Discharge	Sample	Degradation	Discharge
7	2.5	5	31	3	4 – 5
8	2.5	4 – 5	32	2	4 – 5
9	4.5	3 – 4	33	5	4
10	3.5	5	34	4	5
11	3.5	5	35	2.5	5
12	0.5	3 – 4	36	1	3
13	3	4	37	3	5
14	3	4	38	4.5	2 – 3
15	4	4	39	4	5
16	0	3 – 4	40	2.5	2
17	2	4	41	4	1
18	1	3	42	2	1
19	2.5	5	43	3	4 – 5
20	4	5	44	1.5	4
21	3	4 – 5	45	4.5	4
22	3	4	46	3.5	4
23	1.5	4	47	2	4
24	3	1 – 2	48	1	
25	4 – 5	-	49	4	-
26	6	-	50	6	-
27	2 – 3	-	51	2 – 3	-
28	5	-	52	6	-
29	4	-	53	5 – 6	-
30	2	-	54	1 – 2	-

Analysing the results of the colour fastness obtained in pairs, we can see different results depending on the type of test and the type of dye. Figure 3.4.14 shows a graphic comparison of the different results obtained for each dye.

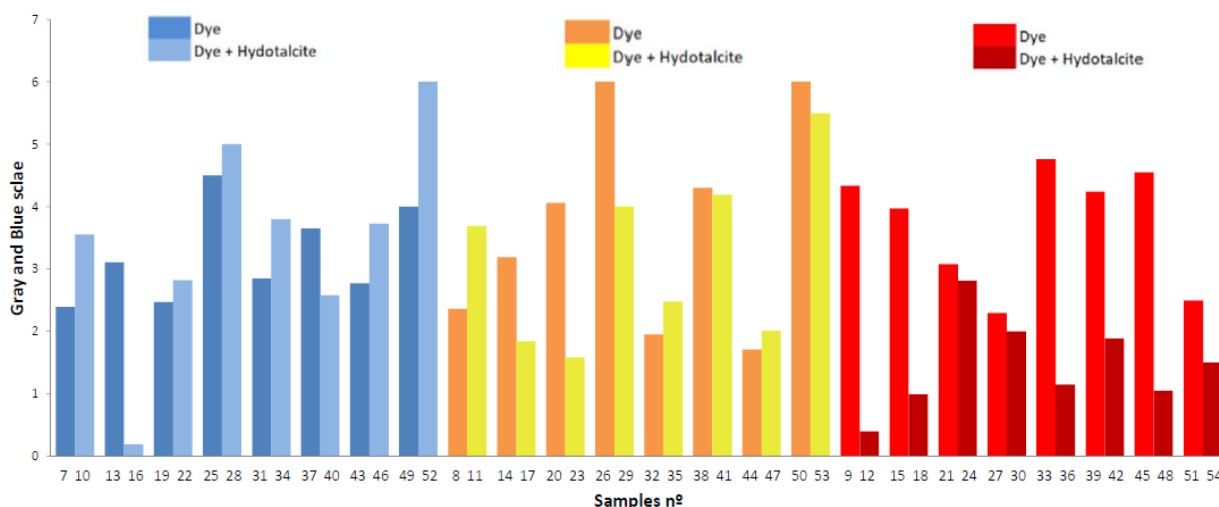


Figure 3.4.14. Pairwise comparison of colour fastness values by grey-scale index

In view of the results and this comparison, it is clear that the direct dye improves the colour fastness results for the dry ironing, dry rubbing, wet ironing, artificial light and natural light tests. These results together with those seen in the TGA show that in tests where temperature or energy is involved, the dye is protected by the clay, as reported in previous works and described in the TGA section [56]–[59] of this study. For the reactive dye, the dry, wet and damp ironing tests show improvements and it remains practically the same in the wet rubbing test. Again, in this case, as in the case of the direct dye, the clay has had a protective effect against the heat of the iron. It should be remembered that reactive dyes by themselves have very good light fastness, which is why the clay has not been able to improve this result in this test. Finally, the study of the disperse dye yields very important results, as in no case has it improved the fastness, it has even worsened considerably. It should be remembered that the disperse dye does not have an ionic charge and that hydrotalcite has above all a great affinity for adsorbing anionic elements such as reactive and direct dyes, which is why it has not exerted the same protection on the non-ionic dye as on the anionic dyes.

As stated in previous works [56]–[59], the clay has a barrier effect against the energetic agents listed above and, in addition, the energy that the dye can receive is transferred to the nanoclay, which absorbs it, thus improving the colour fastness of all those external energetic factors.

3.4.3.10.1 ANOVA

We then proceeded to corroborate whether the phenomena observed in terms of the fastnesses in the application of the synthesised hybrid materials were significant. For this purpose, a MANOVA and ANOVA study was carried out with the variables of fastness to discharge and degradation as responses, and the type of dye, the type of test and the type of printing, pigmentary or with dyes, i.e. with or without the incorporation of hydrotalcite.

We will now comment on the significant interactions, with P-values below the 0.05 significance level (Table 3.4.10), which have been found and which corroborate what was discussed in the previous section. In both discharge and degradation, the tests involving energy such as light or heat show that similar results are obtained with both types of printing, and even in some cases, such as degradation with natural light, the samples with hydrotalcite give better results on average than those printed with the original dyes (Figure 3.4.15).

Table 3.4.10. Analysis of Variance from degradation results, with Fastness test and HC factors

Source	Sum of Squares	df	Medium square	F-Ratio	P-Value
Main effects					
A: Fastness test	10.6892	5	2.13784	3.39	0.0187
B:HC	9.1809	1	9.1809	14.54	0.0008
Interactions					
AB	10.1258	5	2.02517	3.21	0.0234
Residuals	15.1527		0.631361		
TOTAL (Corrected)	45.1486				

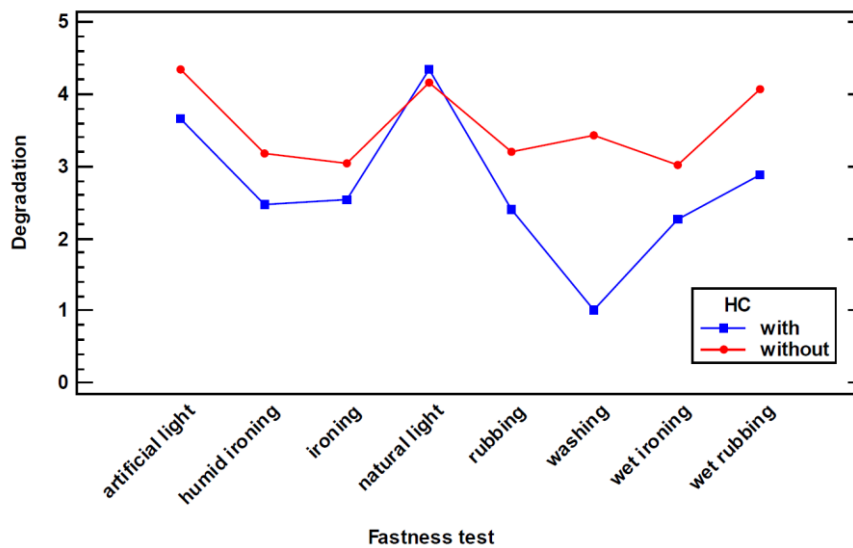


Figure 3.4.15. Fisher's 95% LSD mean comparison plot, for the means obtained in the degradation fastness tests, according to the type of test and printing, with or without HC

On the other hand, the interaction between the use of hybrid dyes or the original dyes in printing and the type of dye was also significant in terms of both average degradation and discharge, regardless of the type of test. In all cases, it is clear that the results mentioned in the previous section are corroborated, with the worst results being obtained in application with the Red dispersed dye, due to the lack of ionic charge of the same and therefore the little interaction with the nanoclay sheets. However, with ionic dyes, the results are similar and even better, as in the example in Figure 3.4.16, with the case of the direct dye, which improves its average properties in terms of degradation thanks to the protection of the nanoclay in the application. However, if only the degradation behaviour as a function of the dye is observed, the results would not be significant, as the P-value of the single effect, Dye, is above the significance level. This indicates that the observed differences in fastness behaviour between the dyes are due to the interaction with the nanoclay as stipulated (Table 3.4.11).

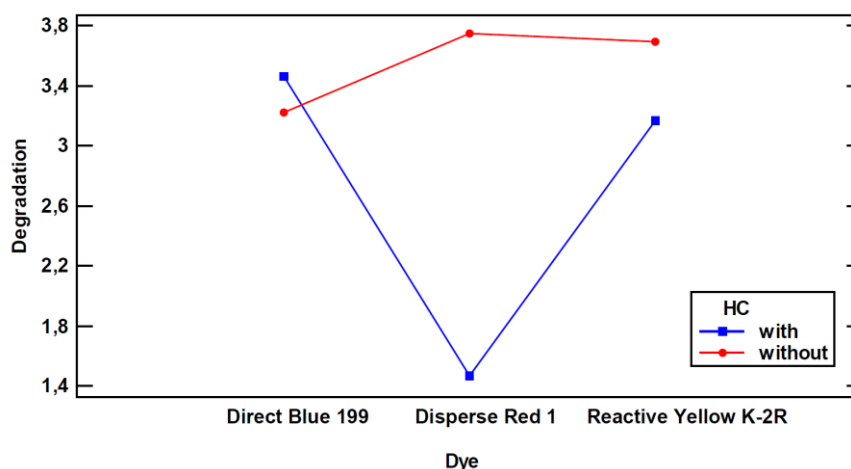


Figure 3.4.16. Fisher's LSD 95% mean comparison plot for the means obtained in the degradation fastness tests, according to the type of dye and printing, with or without HC

Table 3.4.11. Analysis of Variance from degradation results, with Dye and HC factors

Source	Sum of Squares	df	Médium square	F-Ratio	P-Value
Main effects					
A:Dye	6.47754		3.23877	1.99	0.1496
B:HC	8.75521	1	8.75521	5.38	0.0254
Interactions					
AB	13.2114		6.6057	4.06	0.0245
Residuals	68.4036	42	1.62866		
TOTAL (Corrected)	96.8478				

3.4.3.11. Scanning Electron Microscopy (SEM)

In this test, the surface topography of the samples printed with the dye-loaded clay hybrids will be analysed. In Figure 3.4.17 we can see an image of the printed sample nº 5, washed sample nº 17 and its corresponding discharge, which are significant and can be extrapolated to all the other samples, as the same conclusions are obtained. Comparing samples 5 and 17, we can see a loss of hybrid material and that part of this hybrid is now in the discharge witness. Thus, the loss of colour that has occurred and whose results have been seen in the previous section is largely due to loss of hybrid and not due to degradation of the dye itself to the different agents to which it has been exposed.

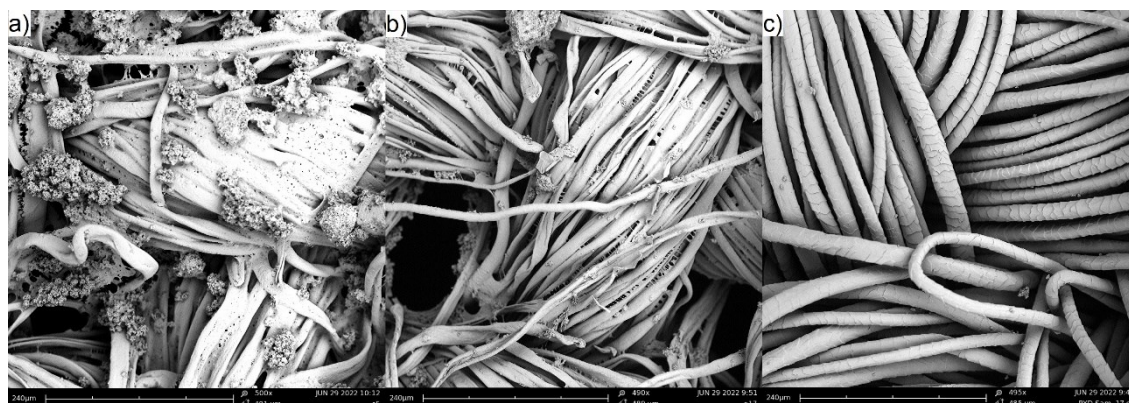


Figure 3.4.17. a) Sample 5, b) Sample 17 after washing, c) Witness Sample 17 after washing

3.4.4. Conclusions

This study has successfully developed a new method of colouring textile substrates by using nanoclay loaded with dyes from textile wastewater for printing. This novel technique has been subjected to several tests of colour fastness to washing, rubbing, ironing and light, giving satisfactory results and in some cases even improving the results obtained with conventional dye printing. Although those tests that have not given better results, it has been observed when analysing the surface by SEM that it is because the fixation of the clay to the fibre needs to be improved, which opens up the possibility of future lines of research. In the case of the non-ionic disperse dyes, the non-binding to the clay by ion exchange has significantly affected the colour fastness results, which shows the importance of this force in fixing the dye to the clay.

The adsorption capacity of H for anionic and non-ionic dyes has been confirmed and the adsorption method by calcination and its subsequent reconstruction thanks to its shape memory has been studied and validated by XRD and FTIR tests. These techniques, together with XPS and EDX, also demonstrate the presence of the dyes in the structure of the hybrid, since the increase in the amorphous zone in the XRD analysis confirms the presence of the dyes and the FTIR study shows significant peaks of certain groups that appear in the dyes such as the amino and $-SO_3^-$ sulphonate.

The increase in colour fastness in some tests such as ironing and in the case of direct dyes in natural and artificial light is closely related to the TGA results. Many of the peaks we saw in the dyes are attenuated or disappear completely in their corresponding hybrids, which confirms the barrier effect of the clay and the transfer of energy from the dye to the hydrotalcite, reducing colour degradation when we test degradation agents that involve the action of an energy source. The increase of the TSR which is between 20-40% will also influence the improvement of the light fastness.

There is no doubt that with clay-dye hybrids the textile industry is faced with a product of great potential. Due to its physical-chemical characteristics, it can be stored without any problem, transported and handled normally. This allows textile chemical manufacturers the possibility of reaching agreements with dyeing companies to recover the dye left over from dye baths and synthesise dye-loaded nanoclays for subsequent marketing. In addition, these manufacturers could improve their commercial image and that of their customers by promoting the recycling and reuse of materials and therefore the circular economy.

References

1. Karami, M.; Ghanbari, M.; Amiri, O.; Salavati-Niasari, M. Enhanced Antibacterial Activity and Photocatalytic Degradation of Organic Dyes under Visible Light Using Cesium Lead Iodide Perovskite Nanostructures Prepared by Hydrothermal Method. *Sep. Purif. Technol.* 2020, 253, 117526. <https://doi.org/10.1016/j.seppur.2020.117526>
2. Chai, W. S.; Cheun, J. Y.; Kumar, P. S.; Mubashir, M.; Majeed, Z.; Banat, F.; Ho, S.-H.; Show, P. L. A Review on Conventional and Novel Materials towards Heavy Metal Adsorption in Wastewater Treatment Application. *J. Clean. Prod.* 2021, 296, 126589. <https://doi.org/10.1016/j.jclepro.2021.126589>
3. Huang, H.; Liu, J.; Liu, H.; Evrendilek, F.; Zhang, G.; He, Y. Turning the Co-Combustion Synergy of Textile Dyeing Sludge and Waste Biochar into Emission-to-Bottom Slag Pollution Controls toward a Circular Economy. *Renew. Energy* 2022, 194, 760–777. <https://doi.org/10.1016/j.RENENE.2022.05.121>
4. Mansour, R. A. E.-G.; Simeda, M. G.; Zaatout, A. A. Removal of Brilliant Green Dye from Synthetic Wastewater under Batch Mode Using Chemically Activated Date Pit Carbon. *RSC Adv.* 2021, 11 (14), 7851–7861. <https://doi.org/10.1039/D0RA08488C>
5. Ragab, A.; Ahmed, I.; Bader, D. The Removal of Brilliant Green Dye from Aqueous Solution Using Nano Hydroxyapatite/Chitosan Composite as a Sorbent. *Molecules* 2019, 24 (5), 847. <https://doi.org/10.3390/molecules24050847>
6. Ahmed, R.; Rafia, R. R.; Hossain, M. A. Kinetics and Thermodynamics of Acid Red 1 Adsorption on Used Black Tea Leaves from Aqueous Solution. *Int. J. Sci.* 2021, 10 (06), 7–15.
7. Alqarni, S. A. The Performance of Different AgTiO₂ Loading into Poly (3-Nitrothiophene) for Efficient Adsorption of Hazardous Brilliant Green and Crystal Violet Dyes. *Int. J. Polym. Sci.* 2022, 2022. <https://doi.org/10.1155/2022/4691347>
8. Abdel-Fadeel, M. A.; Aljohani, N. S.; Al-Mhyawi, S. R.; Halawani, R. F.; Aljuhani, E. H.; Salam, M. A. A Simple Method for Removal of Toxic Dyes Such as Brilliant Green and Acid Red from the Aquatic Environment Using Halloysite Nanoclay. *J. Saudi Chem. Soc.* 2022, 26 (3), 101475. <https://doi.org/10.1016/j.jscs.2022.101475>
9. Luo, Z.; Gao, M.; Ye, Y.; Yang, S. Modification of Reduced-Charge Montmorillonites by a Series of Gemini Surfactants: Characterization and Application in Methyl Orange Removal. *Appl. Surf. Sci.* 2015, 324, 807–816. <https://doi.org/10.1016/j.APSUSC.2014.11.043>
10. Gupta, V. K.; Agarwal, S.; Olgun, A.; Demir, H. İ.; Yola, M. L.; Atar, N. Adsorptive Properties of Molasses Modified Boron Enrichment Waste Based Nanoclay for Removal of Basic Dyes. *J. Ind. Eng. Chem.* 2016, 34, 244–249. <https://doi.org/10.1016/J.IIEC.2015.11.017>

11. Carretero, M. I.; Pozo, M.; Sánchez, C.; García, F. J.; Medina, J. A.; Bernabé, J. M. Comparison of Saponite and Montmorillonite Behaviour during Static and Stirring Maturation with Seawater for Pelotherapy. *Appl. Clay Sci.* 2007, *36* (1–3), 161–173. <https://doi.org/10.1016/J.CLAY.2006.05.010>.
12. Taleb, K.; Pillin, I.; Grohens, Y.; Saidi-Besbes, S. Gemini Surfactant Modified Clays: Effect of Surfactant Loading and Spacer Length. *Appl. Clay Sci.* 2018, *161*, 48–56. <https://doi.org/10.1016/J.CLAY.2018.03.015>.
13. Olvera, R. C.; Silva, S. L.; Robles-Belmont, E.; Lau, E. Z. Review of Nanotechnology Value Chain for Water Treatment Applications in Mexico. *Resour. Technol.* 2017, *3* (1), 1–11. <https://doi.org/10.1016/J.REFFIT.2017.01.008>.
14. Akil, J.; Ciotonea, C.; Siffert, S.; Royer, S.; Pirault-Roy, L.; Cousin, R.; Poupin, C. NO Reduction by CO under Oxidative Conditions over CoCuAl Mixed Oxides Derived from Hydrotalcite-like Compounds: Effect of Water. *Catal. Today* 2021, No. October 2020. <https://doi.org/10.1016/j.cattod.2021.05.014>.
15. Carlino, S. Chemistry between the Sheets. *Chem. Br.* 1997, *33* (9), 59–62.
16. Ulibarri, M. A.; Pavlovic, I.; Barriga, C.; Hermosin, M. C.; Cornejo, J. Adsorption of Anionic Species on Hydrotalcite-like Compounds: Effect of Interlayer Anion and Crystallinity. *Appl. Clay Sci.* 2001, *18* (1–2), 17–27. [https://doi.org/10.1016/S0169-1317\(00\)00026-0](https://doi.org/10.1016/S0169-1317(00)00026-0)
17. Bish, D. L. Anion-Exchange in Takovite: Applications to Other Hydroxide Minerals. *Bull. Mineral.* 1980, *103* (2), 170–175.
18. Miyata, S. Physico-Chemical Properties of Synthetic Hydrotalcites in Relation to Composition. *Clays Clay Miner.* 1980, *28* (1), 50–56.
19. Oliveira, K. G.; Botti, R.; Kavun, V.; Gafiullina, A.; Franchin, G.; Repo, E.; Colombo, P. Geopolymer Beads and 3D Printed Lattices Containing Activated Carbon and Hydrotalcite for Anionic Dye Removal. *Catal. Today* 2022, *390–391* (December 2021), 57–68. <https://doi.org/10.1016/j.cattod.2021.12.002>.
20. Orthman, J.; Zhu, H. Y.; Lu, G. Q. Use of Anion Clay Hydrotalcite to Remove Coloured Organics from Aqueous Solutions. *Sep. Purif. Technol.* 2003, *31* (1), 53–59. [https://doi.org/10.1016/S1383-5866\(02\)00158-2](https://doi.org/10.1016/S1383-5866(02)00158-2).
21. Kamali, M.; Esmaeili, H.; Tamjidi, S. Synthesis of Zeolite Clay/Fe-Al Hydrotalcite Composite as a Reusable Adsorbent for Adsorption/Desorption of Cationic Dyes. *Arab. J. Sci. Eng.* 2022, *47* (5), 6651–6665. <https://doi.org/10.1007/s13369-022-06580-4>
22. Jie, C.; Mingming, L. I.; Chao, W.; JIANG, H.; Zhigang, L. I. U.; Hua, J. I. N. Preparation of Magnetic Hydrotalcite Composite and Its Eosin Y Adsorption Performance. *复合材料学报* 2022, *39* (5), 2288–2298.

<https://doi.org/10.13801/j.cnki.fhclxb.20210813.001>

23. Mourid, E. H.; Lakraimi, M.; Benaziz, L.; Cherkaoui, M. Water Reuse after Removing a Textile Dye Methyl Orange Using a Recyclable Hydrotalcite Material. *Moroccan J. Chem.* 2021, 9 (1), 1–9. <https://doi.org/10.48317/IMIST.PRSM/morjchem-v9i1.21114>
24. Li, S.; Mu, B.; Wang, X.; Wang, A. Recent Researches on Natural Pigments Stabilized by Clay Minerals: A Review. *Dye. Pigment.* 2021, 190, 109322. <https://doi.org/10.1016/J.DYEPIG.2021.109322>.
25. Xiong, X.-J.; Meng, X.-J.; Zheng, T.-L. Biosorption of CI Direct Blue 199 from Aqueous Solution by Nonviable *Aspergillus Niger*. *J. Hazard. Mater.* 2010, 175 (1–3), 241–246. <https://doi.org/10.1016/j.jhazmat.2009.09.155>
26. Laqbaqbi, M.; García-Payo, M. C.; Khayet, M.; El Kharraz, J.; Chaouch, M. Application of Direct Contact Membrane Distillation for Textile Wastewater Treatment and Fouling Study. *Sep. Purif. Technol.* 2019, 209 (August 2018), 815–825. <https://doi.org/10.1016/j.seppur.2018.09.031>.
27. da Silva Leite, L.; de Souza Maselli, B.; de Aragão Umbuzeiro, G.; Nogueira, R. F. P. Monitoring Ecotoxicity of Disperse Red 1 Dye during Photo-Fenton Degradation. *Chemosphere* 2016, 148, 511–517. <https://doi.org/10.1016/j.chemosphere.2016.01.053>
28. dos Santos, R. M. M.; Gonçalves, R. G. L.; Constantino, V. R. L.; da Costa, L. M.; da Silva, L. H. M.; Tronto, J.; Pinto, F. G. Removal of Acid Green 68:1 from Aqueous Solutions by Calcined and Uncalcined Layered Double Hydroxides. *Appl. Clay Sci.* 2013, 80–81, 189–195. <https://doi.org/10.1016/j.clay.2013.04.006>.
29. Lian, Z. Y.; Zhang, Y.; Wang, X. Z. Manufacturing of High Quality Hydrotalcite by Computational Fluid Dynamics Simulation of an Impinging Jet Crystallizer. *Ceram. Int.* 2022. <https://doi.org/10.1016/J.CERAMINT.2022.02.081>.
30. Bigman, J. L. Monitoring of Chemicals and Water. *Handb. Silicon Wafer Clean. Technol.* 2018, 619–657. <https://doi.org/10.1016/B978-0-323-51084-4.00011-3>.
31. Silva, M. M. F.; Oliveira, M. M.; Avelino, M. C.; Fonseca, M. G.; Almeida, R. K. S.; Silva Filho, E. C. Adsorption of an Industrial Anionic Dye by Modified-KSF-Montmorillonite: Evaluation of the Kinetic, Thermodynamic and Equilibrium Data. *Chem. Eng. J.* 2012, 203, 259–268. <https://doi.org/10.1016/j.cej.2012.07.009>.
32. B. Micó-Vicent, F. M.-V. Method for Optimising the Synthesis of Hybrid Nanopigments, 2017.
33. H. Fischer, L. F. B. Coloring Pigment, 2001.
34. Mensch, C.; Chintala, R.; Nawrocki, D.; Blue, J. T.; Bhambhani, A. Enabling Lyophilized

- Pneumococcal Conjugate Vaccines Through Formulation Design and Excipient Selection Suitable for A Multivalent Adjuvanted Vaccine. *J. Pharm. Sci.* 2020, 1–11. <https://doi.org/10.1016/j.xphs.2020.10.038>.
35. Castillo-Peinado, L. S.; Calderón-Santiago, M.; Priego-Capote, F. Lyophilization as Pre-Processing for Sample Storage in the Determination of Vitamin D3 and Metabolites in Serum and Plasma. *Talanta* 2021, 222 (September 2020). <https://doi.org/10.1016/j.talanta.2020.121692>.
 36. Kanik, M.; Hauser, P. J. Printing of Cationised Cotton with Reactive Dyes. *Color. Technol.* 2002, 118 (6), 300–306. <https://doi.org/10.1111/j.1478-4408.2002.tb00114.x>.
 37. Coloration Technology - 2006 - Ahmed - Urea Alkali-free Printing of Cotton with Reactive Dyes.Pdf. <https://doi.org/10.1111/j.1478-4408.2006.00047.x>
 38. Coloration Technology - 2006 - El-Shishtawy - Cationic Pretreatment of Cotton Fabric for Anionic Dye and Pigment Printing.Pdf. <https://doi.org/10.1111/j.1478-4408.2002.tb00367.x>
 39. Maharjan, S.; Liao, K. S.; Wang, A. J.; Curran, S. A. Highly Effective Hydrophobic Solar Reflective Coating for Building Materials: Increasing Total Solar Reflectance via Functionalized Anatase Immobilization in an Organosiloxane Matrix. *Constr. Build. Mater.* 2020, 243, 118189. <https://doi.org/10.1016/j.conbuildmat.2020.118189>.
 40. Di Natale, C.; Monti, D.; Paolesse, R. Chemical Sensitivity of Porphyrin Assemblies. *Mater. Today* 2010, 13 (7–8), 46–52. [https://doi.org/10.1016/S1369-7021\(10\)70127-9](https://doi.org/10.1016/S1369-7021(10)70127-9)
 41. Liu, Y.; Li, R.; Yu, J.; Ni, F.; Sheng, Y.; Scircle, A.; Cizdziel, J. V.; Zhou, Y. Separation and Identification of Microplastics in Marine Organisms by TGA-FTIR-GC/MS: A Case Study of Mussels from Coastal China. *Environ. Pollut.* 2020, No. xxxx, 115946. <https://doi.org/10.1016/j.envpol.2020.115946>.
 42. Umar, M.; Ofem, M. I.; Anwar, A. S.; Salisu, A. G. Thermo Gravimetric Analysis (TGA) of PA6/G and PA6/GNP Composites Using Two Processing Streams. *J. King Saud Univ. - Eng. Sci.* 2020, No. xxxx. <https://doi.org/10.1016/j.jksues.2020.09.003>.
 43. Corazzari, I.; Turci, F.; Nisticò, R. TGA Coupled with FTIR Gas Analysis to Quantify the Vinyl Alcohol Unit Content in Ethylene-Vinyl Alcohol Copolymer. *Mater. Lett.* 2021, 284, 129030. <https://doi.org/10.1016/j.matlet.2020.129030>.
 44. Pálková, H.; Madejová, J.; Zimowska, M.; Bielańska, E.; Olejniczak, Z.; Lityńska-Dobrzyńska, L.; Serwicka, E. M. Laponite-Derived Porous Clay Heterostructures: I. Synthesis and Physicochemical Characterization. *Microporous Mesoporous Mater.* 2010, 127 (3), 228–236. <https://doi.org/10.1016/j.micromeso.2009.07.019>.
 45. Zhuo, W.; Xie, Y.; Benson, M. T.; Ge, J.; Mariani, R. D.; Zhang, J. XRD and SEM/EDS

- Characterization of Two Quaternary Fuel Alloys (U-2.5Mo-2.5Ti-5.0Zr and U-1.5Mo-1.5Ti-7.0Zr in Wt. %) for Fast Reactors. *Mater. Charact.* 2020, 170 (September), 110696. <https://doi.org/10.1016/j.matchar.2020.110696>.
46. Li, B.; Zhang, Y.; Zhou, X.; Liu, Z.; Liu, Q.; Li, X. Different Dye Removal Mechanisms between Monodispersed and Uniform Hexagonal Thin Plate-like MgAl-CO₃--LDH and Its Calcined Product in Efficient Removal of Congo Red from Water. *J. Alloys Compd.* 2016, 673, 265–271. <https://doi.org/10.1016/j.jallcom.2016.02.248>
47. Zhang, C.; Yang, S.; Chen, H.; He, H.; Sun, C. Adsorption Behavior and Mechanism of Reactive Brilliant Red X-3B in Aqueous Solution over Three Kinds of Hydrotalcite-like LDHs. *Appl. Surf. Sci.* 2014, 301, 329–337. <https://doi.org/10.1016/j.apsusc.2014.02.073>
48. Shan, R.; Yan, L.; Yang, Y.; Yang, K.; Yu, S.; Yu, H.; Zhu, B.; Du, B. Highly Efficient Removal of Three Red Dyes by Adsorption onto Mg–Al-Layered Double Hydroxide. *J. Ind. Eng. Chem.* 2015, 21, 561–568. <https://doi.org/10.1016/j.jiec.2014.03.019>
49. Herald, E.; Santosa, S. J.; Triyono, T.; Wijaya, K. Anionic and Cationic Dyes Removal from Aqueous Solutions by Adsorption onto Synthetic Mg/Al Hydrotalcite-like Compound. *Indones. J. Chem.* 2015, 15 (3), 234–241. <https://doi.org/10.22146/ijc.21190>
50. Grum, F.; Witzel, R. F.; Stensby, P. Evaluation of Whiteness. *JOSA* 1974, 64 (2), 210–215. <https://doi.org/10.1364/JOSA.64.000210>
51. ASTM. Standard Tables for Reference Solar Spectral Irradiances : Direct Normal And. *Astm* 2013, 03 (Reapproved), 1–21. <https://doi.org/10.1520/G0173-03R20.2>.
52. Iturbe-García, J. L.; Bonifacio Martínez, J.; Granados Correa, F.; López-Muñoz, B. E. Behavior of a Hydrotalcite Type Material Obtained from MgAl Alloy for CO₂ Adsorption. *Appl. Clay Sci.* 2019, 183, 105296. <https://doi.org/10.1016/j.clay.2019.105296>.
53. Extremera, R.; Pavlovic, I.; Pérez, M. R.; Barriga, C. Removal of Acid Orange 10 by Calcined Mg/Al Layered Double Hydroxides from Water and Recovery of the Adsorbed Dye. *Chem. Eng. J.* 2012, 213, 392–400. <https://doi.org/10.1016/j.cej.2012.10.042>.
54. Wang, Q.; Feng, Y.; Feng, J.; Li, D. Enhanced Thermal- and Photo-Stability of Acid Yellow 17 by Incorporation into Layered Double Hydroxides. *J. Solid State Chem.* 2011, 184 (6), 1551–1555. <https://doi.org/10.1016/j.jssc.2011.04.020>.
55. Lopez, T.; Bosch, P.; Asomoza, M.; Gómez, R.; Ramos, E. DTA-TGA and FTIR Spectroscopies of Sol-Gel Hydrotalcites: Aluminum Source Effect on Physicochemical Properties. *Mater. Lett.* 1997, 31 (3–6), 311–316. [https://doi.org/10.1016/S0167-577X\(96\)00296-0](https://doi.org/10.1016/S0167-577X(96)00296-0)

56. Ghosh, S. K.; Brahmakumar, M.; Warriar, K. G. K.; Perumal, P.; Smitha, V. S.; Pavithran, C.; Manjumol, K. A. Rhodamine 6G Intercalated Montmorillonite Nanopigments-Polyethylene Composites: Facile Synthesis and Ultravioletstability Study. 2011. <https://doi.org/10.1111/j.1551-2916.2010.04326.x>
57. Raha, S.; Ivanov, I.; Quazi, N. H.; Bhattacharya, S. N. Photo-Stability of Rhodamine-B/Montmorillonite Nanopigments in Polypropylene Matrix. *Appl. Clay Sci.* 2009, *42* (3–4), 661–666. <https://doi.org/10.1016/j.clay.2008.06.008>
58. Bellucci, F.; Camino, G.; Frache, A.; Sarra, A. Catalytic Charring–Volatilization Competition in Organoclay Nanocomposites. *Polym. Degrad. Stab.* 2007, *92* (3), 425–436. <https://doi.org/10.1016/j.polymdegradstab.2006.11.006>
59. Landau, A.; Zaban, A.; Lapides, I.; Yariv, S. Montmorillonite Treated with Rhodamine-6G Mechanochemically and in Aqueous Suspensions. *J. Therm. Anal. Calorim.* 2002, *70* (1), 103–113. <https://doi.org/10.1023/A:1020649416016>
60. Cavani, F.; Trifiro, F.; Vaccari, A. Hydrotalcite-Type Anionic Clays: Preparation, Properties and Applications. *Catal. today* 1991, *11* (2), 173–301. [https://doi.org/10.1016/0920-5861\(91\)80068-K](https://doi.org/10.1016/0920-5861(91)80068-K)
61. Zhu, M.-X.; Li, Y.-P.; Xie, M.; Xin, H.-Z. Sorption of an Anionic Dye by Uncalcined and Calcined Layered Double Hydroxides: A Case Study. *J. Hazard. Mater.* 2005, *120* (1–3), 163–171. <https://doi.org/10.1016/j.jhazmat.2004.12.029>
62. Lakraimi, M.; Legrouri, A.; Barroug, A.; Besse, J.-P. Removal of Pesticides from Water by Anionic Clays. *J. Chim. Phys. Physico-Chimie Biol.* 1999, *96* (3), 470–478. <https://doi.org/10.1051/jcp:1999154>
63. Sato, T.; Kato, K.; Endo, T.; Shimada, M. Preparation and Chemical Properties of Magnesium Aluminium Oxide Solid Solutions. *React. Solids* 1986, *2* (3), 253–260. [https://doi.org/10.1016/0168-7336\(86\)80088-2](https://doi.org/10.1016/0168-7336(86)80088-2)
64. Dahdah, E.; Estephane, J.; Taleb, Y.; El Khoury, B.; El Nakat, J.; Aouad, S. The Role of Rehydration in Enhancing the Basic Properties of Mg–Al Hydrotalcites for Biodiesel Production. *Sustain. Chem. Pharm.* 2021, *22* (July). <https://doi.org/10.1016/j.scp.2021.100487>.
65. Bernard, E.; Zucha, W. J.; Lothenbach, B.; Mäder, U. Stability of Hydrotalcite (Mg-Al Layered Double Hydroxide) in Presence of Different Anions. *Cem. Concr. Res.* 2022, *152*, 106674. <https://doi.org/10.1016/J.CEMCONRES.2021.106674>.
66. Geetha Bhavani, A.; Wani, T. A.; Ma'Aruf, A.; Prasad, T. Effect of Ageing Process on Crystal Morphology of Co-Mg-Al Hydrotalcite. *Mater. Today Proc.* 2021, *44*, 2277–2282. <https://doi.org/10.1016/J.MATPR.2020.12.390>.
67. Wiyantoko, B.; Kurniawati, P.; Purbaningias, T. E.; Fatimah, I. Synthesis and Characterization of Hydrotalcite at Different Mg/Al Molar Ratios. *Procedia Chem.*

- 2015, *17*, 21–26. <https://doi.org/10.1016/j.proche.2015.12.115>
68. Roelofs, J. C. A. A.; van Bokhoven, J. A.; Van Dillen, A. J.; Geus, J.; de Jong, K. P. The Thermal Decomposition of Mg-Al Hydrotalcites: Effects of Interlayer Anions and Characteristics of the Final Structure. *Chem. Eur. J.* 2002, *8*, 5571–5579. [https://doi.org/10.1002/1521-3765\(20021216\)8:24%3C5571::AID-CHEM5571%3E3.0.CO;2-R](https://doi.org/10.1002/1521-3765(20021216)8:24%3C5571::AID-CHEM5571%3E3.0.CO;2-R)
69. Ziyat, H.; Elmzioui, S.; Naciri Bennani, M.; Houssaini, J.; Allaoui, S.; Arhzaf, S. Kinetic, Isotherm, and Mechanism Investigations of the Removal of Nitrate and Nitrite from Water by the Synthesized Hydrotalcite Mg–Al. *Res. Chem. Intermed.* 2021, *47* (6), 2605–2627. <https://doi.org/10.1007/s11164-021-04414-w>
70. Ma, Y.; Zhu, J.; He, H.; Yuan, P.; Shen, W.; Liu, D. Infrared Investigation of Organo-Montmorillonites Prepared from Different Surfactants. *Spectrochim. Acta Part A Mol. Biomol. Spectrosc.* 2010, *76* (2), 122–129. <https://doi.org/10.1016/j.saa.2010.02.038>
71. Hafshejani, M. K.; Ogugbue, C. J.; Morad, N. Application of Response Surface Methodology for Optimization of Decolorization and Mineralization of Triazo Dye Direct Blue 71 by *Pseudomonas Aeruginosa*. *3 Biotech* 2014, *4* (6), 605–619. <https://doi.org/10.1007/s13205-013-0192-7>.
72. Hu, C.; Jimmy, C. Y.; Hao, Z.; Wong, P. K. Photocatalytic Degradation of Triazine-Containing Azo Dyes in Aqueous TiO₂ Suspensions. *Appl. Catal. B Environ.* 2003, *42* (1), 47–55. [https://doi.org/10.1016/S0926-3373\(02\)00214-X](https://doi.org/10.1016/S0926-3373(02)00214-X)
73. Evanson, K. W.; Urban, M. W. Surface and Interfacial FTIR Spectroscopic Studies of Latexes. I. Surfactant–Copolymer Interactions. *J. Appl. Polym. Sci.* 1991, *42* (8), 2287–2296. <https://doi.org/10.1002/app.1991.070420820>
74. Seoudi, R.; El-Bahy, G. S.; El Sayed, Z. A. FTIR, TGA and DC Electrical Conductivity Studies of Phthalocyanine and Its Complexes. *J. Mol. Struct.* 2005, *753* (1–3), 119–126. <https://doi.org/10.1016/j.molstruc.2005.06.003>
75. Cui, Y.; Wang, M.; Chen, L.; Qian, G. Synthesis and Spectroscopic Characterization of an Alkoxysilane Dye Containing C. I. Disperse Red 1. *Dye. Pigment.* 2004, *62* (1), 43–47. <https://doi.org/10.1016/J.DYEPIG.2003.11.009>.
76. Taunamang, H.; Herman, H.; Tjia, M. O. Molecular Orientation in Disperse Red 1 Thin Film Produced by PVD Method. *Opt. Mater. (Amst).* 2001, *18* (3), 343–350. [https://doi.org/10.1016/S0925-3467\(01\)00169-0](https://doi.org/10.1016/S0925-3467(01)00169-0).
77. Siddiqua, U. H.; Ali, S.; Iqbal, M.; Hussain, T. Relationship between Structure and Dyeing Properties of Reactive Dyes for Cotton Dyeing. *J. Mol. Liq.* 2017, *241*, 839–844. <https://doi.org/10.1016/J.MOLLIQ.2017.04.057>.
78. Liu, Y. Reactive Dye Dimerization for Enhanced Affinity to Cotton Fibers. 2016.

79. Smith, B.; Berger, R.; Freeman, H. S. High Affinity, High Efficiency Fibre-reactive Dyes. *Color. Technol.* 2006, 122 (4), 187–193. <https://doi.org/10.1111/j.1478-4408.2006.00032.x>
80. Duffner, H.; Bach, E.; Cleve, E.; Schollmeyer, E. New Mathematical Model for Determining Time-Dependent Adsorption and Diffusion of Dyes into Fibers through Dye Sorption Curves in Combination Shades: Part II: Kinetic Data from Dyeing Cotton with a Trichrome Direct Dye System. *Text. Res. J.* 2000, 70 (3), 223–229. <https://doi.org/10.1177/004051759706701001>
81. Hauser, P. J.; Tabba, A. H. Improving the Environmental and Economic Aspects of Cotton Dyeing Using a Cationised Cotton. *Color. Technol.* 2001, 117 (5), 282–288. <https://doi.org/10.1111/j.1478-4408.2001.tb00076.x>
82. Daruwalla, E. H.; Kulkarni, G. G. Studies in the Equilibrium Dyeing of Cotton with Direct Dyes: The Determination of the Activity and Affinity of Direct Dyes for Cellulose. *Bull. Chem. Soc. Jpn.* 1964, 37 (9), 1250–1261. <https://doi.org/10.1246/bcsj.37.1250>
83. Van Der Kraan, M.; Vanesa Fernandez Cid, M.; Woerlee, G. F.; Veugelers, W. J. T.; Witkamp, G.-J. Equilibrium Study on the Disperse Dyeing of Polyester Textile in Supercritical Carbon Dioxide. *Text. Res. J.* 2007, 77 (8), 550–558. <https://doi.org/10.1177/0040517507077483>
84. Kim, T.-K.; Son, Y.-A.; Lim, Y.-J. Thermodynamic Parameters of Disperse Dyeing on Several Polyester Fibers Having Different Molecular Structures. *Dye. Pigment.* 2005, 67 (3), 229–234. <https://doi.org/10.1016/j.dyepig.2004.12.005>
85. Ketema, A.; Worku, A. Review on Intermolecular Forces between Dyes Used for Polyester Dyeing and Polyester Fiber. *J. Chem.* 2020, 2020. <https://doi.org/10.1155/2020/6628404>
86. Haggag, K.; Elshemy, N.; Hashem, A.; Mohamed, Z. Novel Synthesis of Unsaturated Pigment Anthracene Triazole Acrylate via Click Chemistry to Prepare Colored Binder for Textile Printing. *Egypt. J. Chem.* 2019, 62 (2), 325–332. <https://dx.doi.org/10.21608/ejchem.2018.4057.1356>
87. El-Molla, M. M.; Schneider, R. Development of Ecofriendly Binders for Pigment Printing of All Types of Textile Fabrics. *Dye. Pigment.* 2006, 71 (2), 130–137. <https://doi.org/10.1016/j.dyepig.2005.06.017>
88. El-Molla, M. M. Synthesis of Polyurethane Acrylate Oligomers as Aqueous UV-Curable Binder for Inks of Ink Jet in Textile Printing and Pigment Dyeing. *Dye. Pigment.* 2007, 74 (2), 371–379. <https://doi.org/10.1016/j.dyepig.2006.02.021>
89. Golob, D.; Osterman, D. P.; Zupan, J. Determination of Pigment Combinations for Textile Printing Using Artificial Neural Networks. *Fibres Text. East. Eur.* 2008, 16 (3), 68.

Recuperación del colorante de aguas residuales textiles mediante nanoarcillas para su reutilización como pigmentos y nuevos baños de tintura

3.5. Adaptación del artículo: Dyeing with Hydrotalcite Hybrid Nanoclays and Disperse, Basic and Direct Dyes.

Artículo publicado en: López-Rodríguez, Daniel; Jorge Jordán-Núñez; Gisbert Paya, Jaime; Díaz-García, Pablo; Bou-Belda, Eva. (2023) Dyeing with Hydrotalcite Hybrid Nanoclays and Disperse, Basic and Direct Dyes. *International Journal of Molecular Sciences*, 1 (24), 1 - 18. ijms24010808

Abstract:

Textile effluents are among the most polluting industrial effluents in the world. Textile finishing processes, especially dyeing, discharge large quantities of waste that is difficult to treat, such as dyes. By recovering this material from the water, in addition to cleaning and the possibility of reusing the water, there is the opportunity to reuse this waste as a raw material for dyeing different textile substrates. One of the lines of reuse is the use of hybrid nanoclays obtained from the adsorption of dyes, which allow dye baths to be made for textile substrates. This study analyses how, through the use of the nanoadsorbent hydrotalcite, dyes classified by their charge as anionic, cationic and non-ionic can be adsorbed and recovered for successful reuse in new dye baths. The obtained hybrids were characterised by X-ray diffraction and infrared spectroscopy. In addition, the colour was analysed by spectrophotometer in the UV-VIS range. The dyes made on cotton, polyester and acrylic fabrics are subjected to different colour degradation tests to assess their viability as final products, using reflection spectroscopy to measure the colour attribute before and after the tests, showing results consistent with those of a conventional dye.

3.5.1. Introduction

The textile industry is one of the most water-intensive and polluting industries. On average, a textile processing unit of an average size generates about 125 L of effluent [1]. Analysing the standard effluent from the textile industry shows that there are significant amounts of chemical oxygen demand (COD), biological oxygen demand (BOD) and dissolved solids [2],[3]. The pollution contained in these effluents is highly relevant [4] and it is, therefore, vital that these discharges are processed correctly [5]. Although there is a

growing awareness of the problem and many governments are working on solutions for this, small industries cannot comply with the measures imposed and the survival of the textile industry itself is threatened. Thus, the concept of ecological textile dyeing processes that are viable for this industry has arisen.

Textile dyes can be classified in two different ways; one is based on their molecular structure and the second depends on the method of application to the textile materials [6]. The first way of classification is usually adopted by colour chemists, using expressions such as phthalocyanine, azo and anthraquinone. While the second method is commonly used by dyers and also by colourists in the dye manufacturing industries, using expressions such as soluble direct dyes for cellulosic materials such as cotton (CO), soluble basic dyes for acrylic fibres (PAN) and non-soluble disperse dyes for polyester fibres (PES). It should be noted that the categorisation of dyes according to their application is the main characteristic used for the colour index (CI).

Due to the increasing awareness of the impact of effluent pollution, researchers are investigating new cleaning and purification techniques. Among these new techniques is the use of nanoclays [7]–[12] as adsorbents for pollutants; also known as nanoadsorbents, they are capable of collecting dyes in textile effluents and separating them from the water. In previous works, several authors have demonstrated the adsorption capacity of these clays [13]–[17], although they have not reused these clays to make new dye baths. Some clays such as Laponite [18],[19] can show desorption rates of around 20–40%. Another example where desorption has been achieved is with zeolites [20]. The literature also includes studies in which desorption is achieved with distilled water [19] or ethanol [21] and agitation, although none of these studies consider the possibility of a new dye.

In this work, Hydrotalcite (H) nanoclay is used as an adsorbent material. Hydrotalcite, $\text{Mg}_6\text{Al}_2(\text{CO}_3)(\text{OH})_{16}\cdot 4(\text{H}_2\text{O})$, is classified as a material of nanometric dimensions since its constituent lamellae have dimensions of less than 20 nm. Given the structure that it has, it falls into the “layered double hydroxides” (LDH) category. This layer has an SSA between $71 \text{ m}^2\cdot\text{g}^{-1}$ and $104 \text{ m}^2\cdot\text{g}^{-1}$ [22]. The aim of this research study is not only to trap the dye in the

clay but also to be able to use the hybrid obtained in a new dyeing process. To this end, it is hoped to achieve a desorption in which the dye can be desorbed from the clay and used for the dyeing of a textile material that is susceptible to being dyed, taking into account the affinity of this type of dye and the textile fibre to be dyed in the process. Tests are carried out with dispersed dyes that have an affinity with PES, basic dyes that dye PAN and direct dyes that are capable of dyeing CO.

3.5.2. Results

3.5.2.1. Dye Adsorption Performance

After having carried out the adsorption process of the dyes with the clay, it can be seen that the values obtained were excellent. The adsorptions are above 95%, which corroborates with the expected behaviour of hydrotalcite [23]–[27]. Although in this work, dyes of all possible polarities, anionic, cationic and non-ionic, were used, and in all cases, almost complete adsorption was achieved, as had already been seen in other studies [28]. The difference in charge of the dyes was not reflected in these first results, as high adsorption was achieved for all three classes at these dye and clay concentrations (Table 3.5.1).

Table 3.5.1. Difference in concentration after HC adsorption

Sample	Polarity	Initial Conc. g·L ⁻¹	Final Conc. g·L ⁻¹	Ads (%)
HDB199	Anionic	1	$6.57 \times 10^{-4} \pm 3.2 \times 10^{-8}$	99.316
HBY2	Cationic	1	$6.22 \times 10^{-4} \pm 1.1 \times 10^{-8}$	99.949
HDR1	Non-ionic	1	$6.32 \times 10^{-3} \pm 2.9 \times 10^{-9}$	98.122

3.5.2.2. Hybrid Color Measurements

The values obtained in the calculation of the colour of the initial clay-dye hybrids (HDB199, HBY2 and HDR1) and those collected after the dyeing of each fabric (H2DB199, H2BY2 and H2DR1) are shown in Table 3.5.2 and are also shown in a colour diagram in Figure 3.5.1. For these calculations and representation, the reflectance values (λ) of each of the samples have been used. The instructions of the CIE 15:2004 standard [29] have been used to perform these calculations with a fully objective comparison of both absolute and

relative colorimetric results. For all these calculations the illuminant used was the standardised illuminant D65 and it was necessary to use certain CIELAB colorimetric values that had been encoded by the CIE 1931 XYZ standard. Observing the CIE a^*b^* and CIE- Cab^*L^* diagrams, it can be seen that the clay has indeed achieved a very different colour tone from the original white, which is the first proof that the dye that is no longer in the aqueous solution has passed into the hydrotalcite.

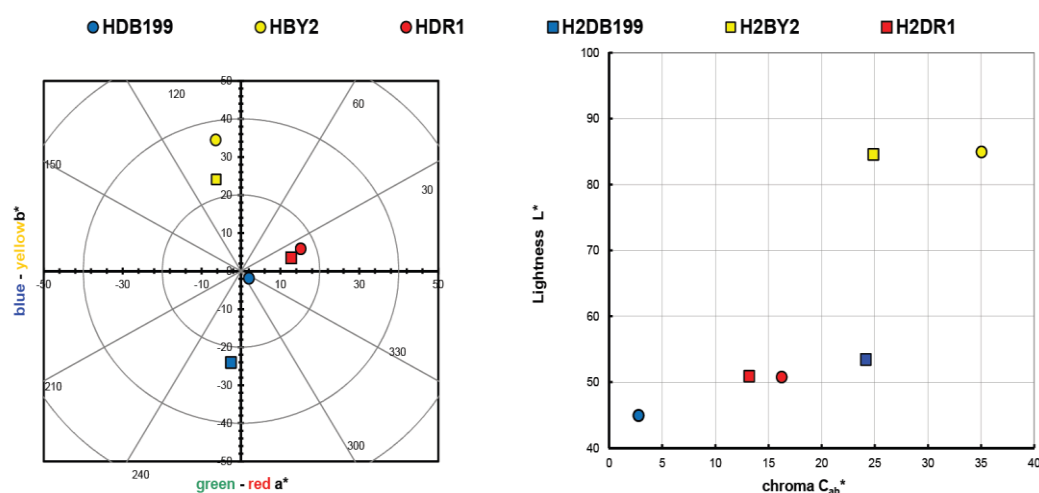


Figure 3.5.1. Graphic CIELAB plots for hybrid pigments synthesised using the D65 illuminant and the CIE-1931 XYZ standard observer. (Left): CIE- a^*b^* color diagram; (right): CIE- Cab^*L^* color chart.

Table 3.5.2. Values L^* , a^* , b^* , C^*_{ab} and h of each hybrid

Sample	L^*	a^*	b^*	C^*_{ab}	h
HDB199	44.94	2.03	1.88	2.77	317.16
HBY2	84.94	6.41	34.46	35.05	100.53
HDR1	50.77	15.14	5.86	16.24	21.17
H2DB199	53.43	-2.53	24.03	24.17	263.98
H2BY2	84.59	6.26	24.07	24.87	104.57
H2DR1	50.89	12.73	3.45	13.19	15.16

The resulting colour of the hybrids correlates with the colour that the dyes had on their own, which means that the HDB199 sample is located in the area that corresponds to pure blues. The hybrid formed by the BY2 dye identified as sample HBY2 follows an angle and is located on the axis that is assigned to yellows. Looking at the third sample HDR1 in

which the dispersed dye DR1 is found, it can be seen that it is assigned to red tones with a slight yellow influence.

Both the luminosity and the saturation of the HBY2 sample have higher values compared to the other two samples due to the characteristics of the yellow colour itself, which give it a characteristic level of luminosity and leave a certain limitation to the shade of colours that could be present if the concentration variables between the hydrotalcite and the dye itself were altered. However, in the HDB199 and HDR1 samples, a luminosity value of over 50 is observed, which implies that with this saturation the colour of the hybrids is chromatic and dark, making it possible to obtain a wider range of colours than in the case of the yellow sample by varying the clay/dye concentrations (Figure 3.5.1). Obviously, if mixtures of these three hybrids were made, given the purity of the colours in terms of their tonality and with these levels of saturation, a wide variety of colour ranges could be obtained.

3.5.2.3. X-ray Diffraction (XRD)

Regarding X-ray diffraction, the results and the comparison of hydrotalcite before (H) and after calcination (HC) can be seen (Figure 3.5.2). Looking at the H line one can see the diffraction peaks appearing at 11°, 23°, 34°, 39°, 46°, 60° and 61° which are, respectively, attributed to the crystal planes 003, 006, 012, 015, 018, 110 and 113 [30]. After calcination all these peaks disappear and diffraction peaks showing an amorphous $\text{Mg}(\text{Al})\text{O}_x$ mixed oxide structure can be seen in the HC line [31].

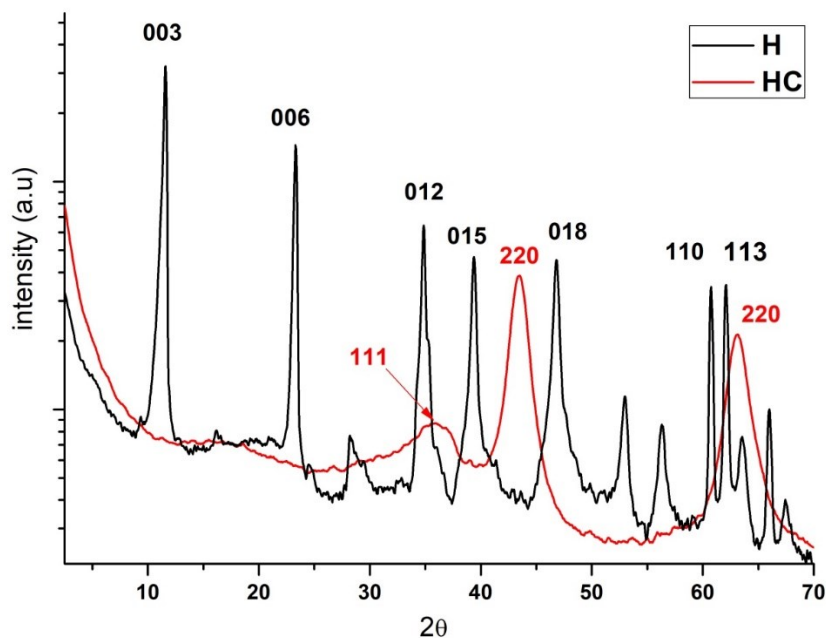


Figure 3.5.2. Diffraction patterns of the hydrotalcite without calcining (H), the hydrotalcite after the calcination at 600 °C for 4 h

Previous studies using XRD analysis of the Mg-Al supports, show a typical hydrotalcite structure ($2\theta = 11.27; 34.46^\circ$, JCPDS n° 220700) and the XRD patterns in Figure 3.5.2 demonstrate the presence of mixed oxides due to the presence of $Mg(Al^{3+})O$ of the MgO-periclase type in accordance with JCPDS n° 450946 [32]. By observing the traces of the calcined sample, we can see its correspondence with JCPDS n° 211152, which corresponds to the $MgAl_2O_4$ spinel structure [33]. Furthermore, XRD patterns of the dried Mg-Al (Figure 3.5.2) reveal two distinct crystalline phases: MgO (JCPDS 450946) and a hydrotalcite phase (JCPDS 220700).

By incorporating the HC into the dye solution, it is expected that the interaction produced between the clay and the dye will change the crystalline structure to some extent during the rehydration and reconstruction phase of the nanoclay. Figure 3.5.3 shows how this change occurs if the analysis is centred on the 003 plane at around 11° . Here, it can be seen how the peak of the uncalcined clay appears but then disappears after calcination.

The effect is produced by the collapse caused by dehydroxylation in the basal space of the nanoclay layers and exfoliation of the basal space [34]. This process will be of great help for the dye to penetrate and become fixed between the layers. Simultaneously, the penetration of the dye and the hydration of the HC take place, which will result in the reconstruction of its structure due to its shape memory [35]–[38]. In the case of anionic dyes, they will be incorporated into the structure in place of other anions that were present before calcination such as -OH- and CO_3^{2-} .

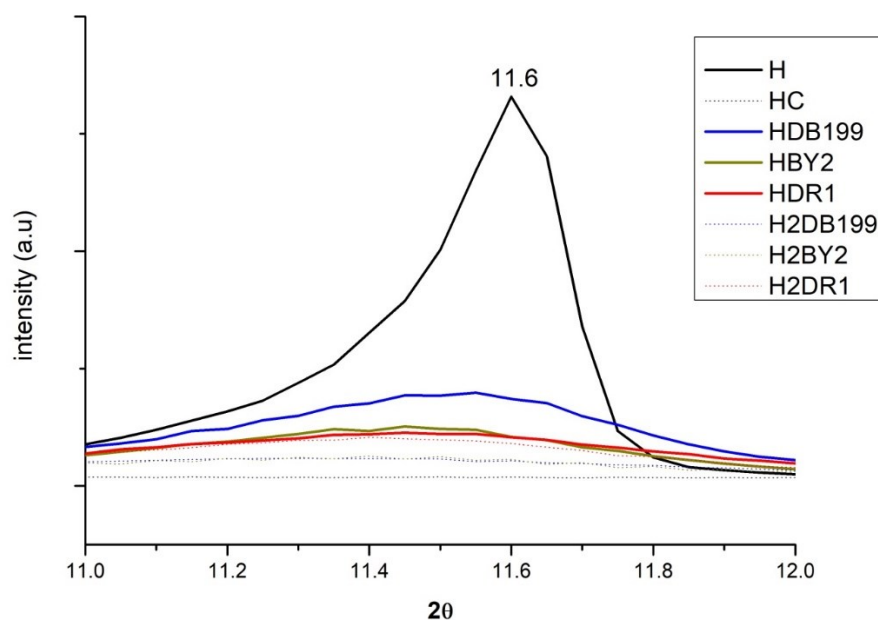


Figure 3.5.3. XRD for Hydrotalcite, Hydrotalcite calcinated at 600 °C for 4 h., samples HDB199, HBY2, HDR1, H2DB199, H2BY2 and H2DR1 in the range of 10° to 12.5°

The intensity of the band at 11° is explained by the fact that the dyes have an amorphous structure but the H has a crystalline structure [39]–[41]. As a consequence, the band will be more intense the more crystalline it is, i.e., the less dye it has, the less amorphous it will be. The HDB199, HBY2 and HDR1 curves show less intensity than H because they have a large amount of dye. However, the H2DB199, H2BY2 and H2DR1 samples have less dye and yet their intensity drops, which can be attributed to the fact that the hydrotalcite structure is being destroyed during the dyeing and desorption treatment,

in a process similar to calcination, losing its crystalline form and becoming more amorphous.

3.5.2.4. Fourier Transform Infrared Spectroscopy FTIR-ATR Analysis

By making use of the Fourier transform, some very relevant information will be obtained for this study. On the one hand, by studying and comparing the graphs in Figure 3.5.4, it is possible to analyse the differences that exist between the uncalcined hydrotalcite and how the peaks change after calcination. There are two very characteristic bands of the nanoadsorbent at 1361 cm^{-1} which are assigned to the carbonate group $-\text{CO}_3^{2-}$ [42],[43] and another one located in the range $3200\text{--}3600\text{ cm}^{-1}$ clearly centred at 3408 cm^{-1} and which is attributed to the stretching between the oxygen and hydrogen of the hydroxyl group $-\text{OH}$ [27],[41],[43] of the water between the clay laminae. The vibrations produced by methylene CH_2 [44] can be seen in the peaks at 2850 and 2918 cm^{-1} . After the destruction of the clay structure due to calcination, these bands are practically flat. This leaves the clay with a positive polarity allowing the incorporation of new anionic groups to take the place of the electronegative groups ($-\text{CO}_3^{2-}$) that have left its structure. Additionally, we note the bands produced by the Al-OH bond at 767 cm^{-1} , NO_3^- produces another peak at 640 cm^{-1} and the bond between Mg and O shows a peak at 549 cm^{-1} [41],[45].

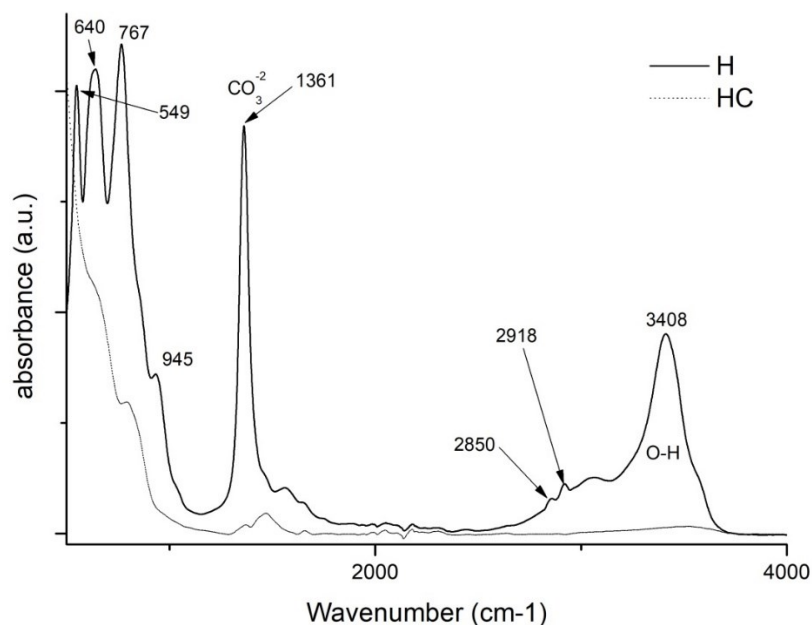


Figure 3.5.4. FTIR comparison of Uncalcined Hydrotalcite (H) and Calcined Hydrotalcite (HC)

Continuing with the analysis, Figure 3.5.5 shows the spectra offered by the three dyes and each of their hybrids after adsorption and after the dyeing process. Analysing these spectra, it can be seen that in all the hybrids the characteristic bands of the hydrotalcite are shown, as at 1361 cm^{-1} and there is the band corresponding to CO_3^{2-} and in the range of $3200\text{--}3600\text{ cm}^{-1}$ with the peak centred at 3408 cm^{-1} which corresponds to the hydroxyl group -OH [46],[47]. Once again, the appearance of these bands, which had disappeared during calcination, shows that the nanoclay has shape memory and reconstructs itself after rehydration. In the sample corresponding to the hybrid HDR1 and H2DR1, the band at 1361 cm^{-1} is more pronounced than in the samples HDB199 and HBY2, since due to the non-ionic nature of the dye, there has not been as much anionic substitution of CO_3^{2-} . In addition, this band remains constant after desorption in the case of the hybrid with disperse dye, but variations are observed in the graphs of the basic and direct dyes.

Continuing with Figure 3.5.5, it can be seen that the HDB199 sample and the DB199 dye have a band at 1100 cm^{-1} due to the formates, acetates, among others [48]. Reviewing the

literature, several studies indicate that the bands between 1400 and 1640 cm^{-1} are due to the benzenes in the dye [39],[40],[42],[44]. On the other hand, the vibration produced by the sulphonate group [49] and due to the azo bond ($\text{RN}_2\text{R}'$) [50] appear in the bands at 1030 and 1500 cm^{-1} , respectively.

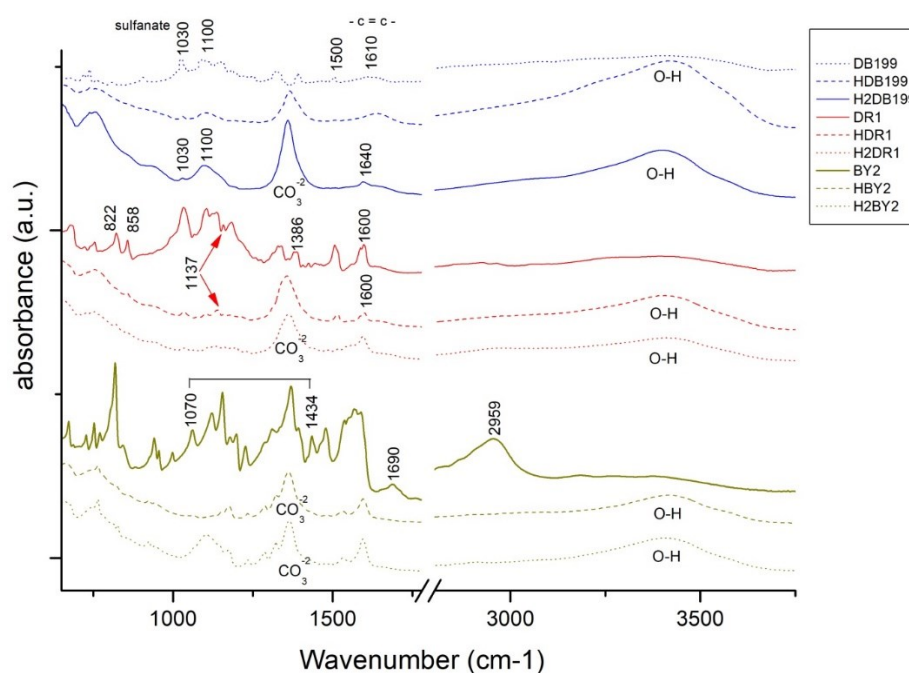


Figure 3.5.5. FTIR of DB199, BY2, DR1 and samples HDB199, HBY2, HDR1, H2DB199, H2BY2 and H2DR1

When analysing the BY2 graph, there is a zone between 1070 and 1434 cm^{-1} that can be assigned to the pyrone groups [46], which gives the basic character of the dye, and there is also a band at 1690 cm^{-1} that corresponds to carboxylic and phenolic groups [46],[51],[52]. The bands at 1227, 1370, 1478 and 2959 cm^{-1} are assigned to the aliphatic groups CH_2 and CH_3 and the bands at 752 and 765 cm^{-1} are due to the vibrations of the aromatic C-H groups [53].

Bands of the dye DR1 and its hybrids HDR1 and H2DR1 are shown at 1507 and 1341 cm^{-1} which are due to non-symmetric, and also symmetric stretching of nitrogen dioxide respectively [54],[55]. Another peak at 1600 cm^{-1} is formed by aromatic $-\text{C}=\text{C}-$ groups.




Several other bands and peaks appear at 1386, 1142 and 858 cm^{-1} , each of which is due to the bonding of N_2 , aliphatic amine -C-N- groups and by the C-H group close to nitrogen dioxide (NO_2) [55].

For the three cases of the three hybrids and dyes, there is not much variation in the bands with respect to the hybrid before and after dyeing, except in the case of H2DB199 where a more intense CO_3^{2-} band is seen. Comparing these bands with the initial bands of the dyes, it can be observed that the most relevant bands are those produced by the vibrations of the chemical structure of the hydrotalcite, although some characteristics of the dyes continue to appear at 1600 cm^{-1} in DR1, 1030 cm^{-1} in DB199 and some of the pyrone groups of BY2.

3.5.2.5. Colour Measurement of the Dyes

The main objective of this research is to carry out the dyeing of various textiles of different types by means of exhaustion dyeing using the hybrids obtained with nanoclays as the dyeing material. Once this objective has been satisfactorily achieved, the colouring obtained on the textile fabric is calculated and evaluated. Table 3.5.3 shows the results of the $L^*a^*b^*$ and C^*_{ab} values and a representation in a chromaticity diagram can also be seen in Figure 3.5.6, thus being able to express the colour obtained in each dye in a quantitative way.

Table 3.5.3. Values L^* , a^* , b^* , C^*_{ab} and h of each dyeing

Sample	Dye Shade	L^*	a^*	b^*	c^*_{ab}	h
TDB199		51.86	-29.17	-33.79	44.63	229.20
TBY2		76.23	-1.97	100.61	100.63	91.12
TDR1		32.05	49.45	28.75	57.20	30.18

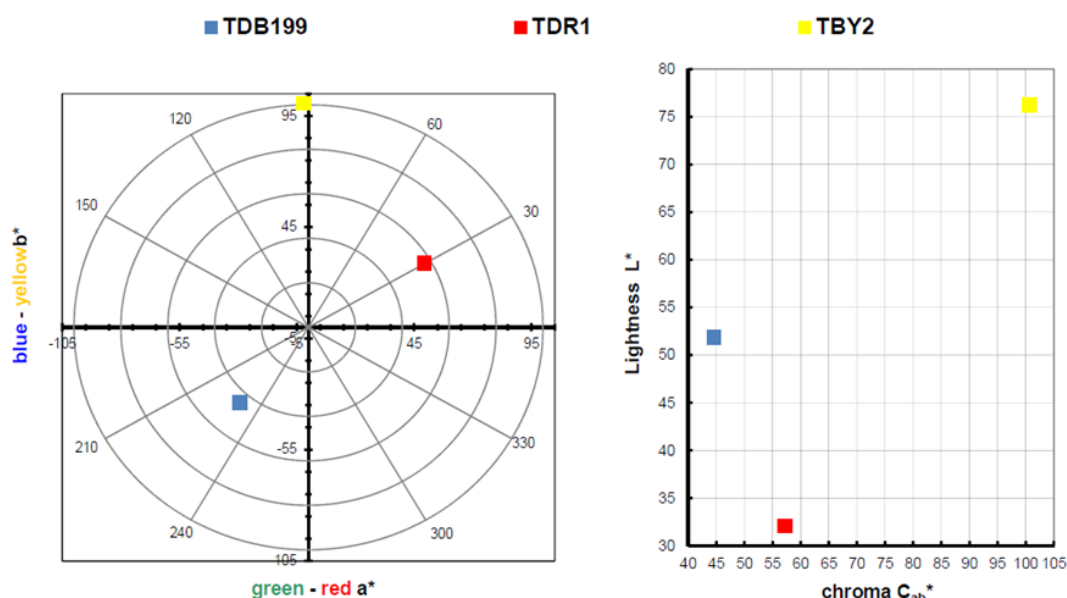


Figure 3.5.6. Graphic CIELAB plots for hybrid dyed using the D65 illuminant and the CIE-1931 XYZ standard observer. (Left): CIE-a * b * color diagram; (right): CIE-Cab * L * color chart

In view of the results obtained in the dye colour measurements, the results are totally in accordance with a conventional dye, as if the dye had been introduced directly into the bath and not a clay-dye hybrid. Take as an example the blue colour of TDB199 which takes on a slightly yellow tone due to the mixture with the cotton fabric which by its nature tends to have a yellowish tone, and this mixture produces this slightly greenish effect. On the other hand, the yellow TBY2 shows a very high luminosity above an L* of 75, something very characteristic of intense yellows. Moreover, the red TDR1 approaches very slightly orange tones also due to its union with the textile substrate, in this case, PES. It is worth noting the very high chroma level of yellow compared to the other two colours, which is situated at a value above 100, characteristic of yellow tones.

3.5.2.6. Colour Fastness

After dyeing the different textile materials used in this work, the next step was to check the capacity of that colour to remain fast in the fibre when subjected to different agents or external actions that may alter its union with the material. For this purpose, the so-called colour fastness tests are carried out. It should be remembered that hybrids have

been used whose dyes have an affinity for the specific fibre that has been introduced into the dyeing process; the direct dye shows an affinity for cellulosic materials such as cotton [56]–[58], the dyes (cationic) have an affinity for the chemical structure of PAN (anionic) [59] and in the case of polyester, they are dyed by the disperse dyes as if they were an alloy [60]–[62] since when they reach the glass transition temperature (~ 68 °C), the dye and textile join in a similar way to that of metals when they are melted. Above the glass transition of polyester, both phases are mixed at the molecular scale. These described affinities allow the dyes to be deposited on the fibre in a first adsorption phase and then to penetrate completely into the fibre in the absorption phase. This allows the colour to be well fixed, although depending on the characteristics of the dye and the nature of the fibres, they will present better or worse results of colour fastness to different agents.

The results obtained for each sample and test are shown in Table 3.5.4. These results are expressed numerically according to the grey scale (GSc) from 1 to 5, where 1 is low fastness and 5 is high fastness, all according to the standards of each test. All values have been calculated instrumentally with a reflection spectrophotometer according to UNE-EN ISO 105-A05 standard, for the colour degradation the calculations have been made using the formulas of Equation (3.5.1).

$$\Delta E_f = [(\Delta L^*)^2 + (\Delta C_f)^2 + (\Delta H_f)^2]^{1/2} \quad (1a)$$

$$GS = 5 - [\Delta E_f / 1.7] \quad (1b)$$

$$GS = 5 - [\log_{10} (\Delta E_f / 0.85) / \log_{10} 2] \quad (1c)$$

Equation (3.5.1). (a) Colour change for the determination of the greyscale index for degradation (b) GS if $\Delta E_f \leq 3.4$ (c) GS if $\Delta E_f \geq 3.4$

Table 3.5.4. Colour fastness values by greyscale index

Sample	Colour Fastness					
	Wash	Rub		Iron		
		Dry	Wet	Dry	Humid	Wet
TDB199	3–4	4–5	4	4–5	4	3–4
TBY2	4	4	4–5	2	3	3
TDR1	4–5	4–5	4–5	4	4	3–4

Figure 3.5.7 shows graphically a summary of the results obtained for each dye. The results obtained are as expected given the characteristics of each dye and material. For example, direct dyes have a low fastness to wet treatments such as washing, reactive dyes have good fastness to the same wet treatments and disperse dyes have high fastnesses in general, due to the fact that the dye and the fibre form a kind of alloy that makes it very difficult for the dye to leave the fibre.

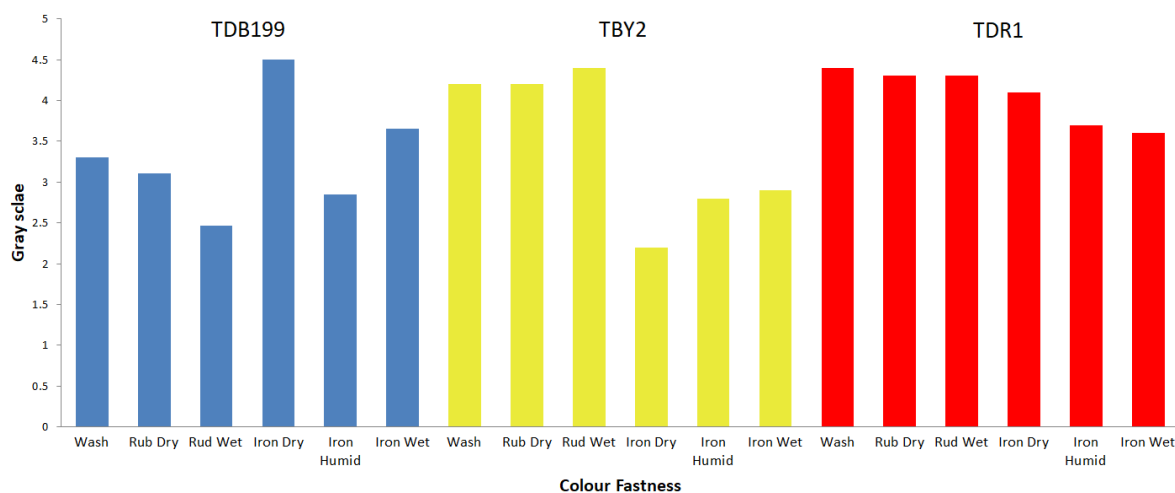


Figure 3.5.7. Colour fastness values by greyscale index.

3.5.2.7. Scanning Electron Microscopy (SEM)

The topographical analysis of the dyed fabrics will reveal whether the colour of the fabrics is due to the surface deposition of the hybrid or whether there has been an absorption of the dye by the textiles. Thus, Figure 3.5.8 shows images of PES, PAN and CO,

with which clearly show that there is hardly any hybrid residue on the surface of the fibres, but it is merely a residual quantity that in no case would be sufficient to give colour of the intensity and uniformity that the fabrics have. This analysis confirms and complements those carried out previously, showing without doubt that there has been a desorption of the dye, which has passed from the clay to the dye bath.



Figure 3.5.8. (a) SEM sample TDB199, (b) SEM sample TBY2, (c) SEM sample TDR1

3.5.2.8. BET Surface Area and Porosity Measurements

The BET surface areas, pore volumes and pore sizes are shown in Table 3.5.5. The results of hydrotalcite before and after calcination as well as after adsorption of the different dyes have been analysed and compared. The results show that surface area, pore volume and pore size increase after calcination. This is due to the fact that during calcination the clay structure opens up. Previous studies claim that these changes are due to outgassing for the catalysts produced by the decomposition of the hydrotalcite gases into their hydrated phases [63]–[65]. On the other hand, the samples that have adsorbed the dye have very similar values to those of the clay before calcination.

Table 3.5.5. BET surface areas, pore volumes and average pore sizes

Sample	Surface Area (m ² /g)	Pore Volume (cm ³ /g)	Average Pore Size (nm)
H	114.3	0.21	10.07
HC	239.6	0.37	18.7
HDR1	102.2	0.15	11.8
HDB199	93.1	0.22	10.15
HBV2	98.5	0.18	11.25

3.5.3. Discussion

In this work, a new method of dyeing textile fabrics by reusing the dye-hydrotalcite hybrids formed by the adsorption of dyes obtained from discharged textile wastewater was successfully carried out. The loading process of the nanoclay was reversed to achieve the desorption of the dyes into the dye bath. This novel contribution has been analysed using colour measurements, and SEM analysis and by subjecting the specimens to different colour fastness tests. After desorption, there is still some dye left in the clay, which would allow the dyeing process to be repeated to obtain less intense colourings or to vary the clay concentrations to match the tone of the dyes used. In any case, these variables will be the subject of further research to continue this line of investigation.

The dyed fabrics have been subjected to various fastness tests, which have given fairly standard results, taking into account the type of dye and the dyed textile material. For example, it is usual to find low fastness values in wet treatments for direct dyes and high degrees of fastness in disperse dyes, since the dyeing of the latter is like an alloy produced between the dye and the polyester.

The already-known adsorption capacity of hydrotalcite for anionic pollutants has been confirmed and its ability to adsorb non-ionic and cationic elements has also been confirmed. XRD and FTIR analysis reaffirms the reconstruction capacity of this nanoclay thanks to its shape memory and the presence of the dyes incorporated in its structure. The X-ray analysis shows the increase in the amorphous zone due to the degradation of the clay with the desorption process, and the infrared analysis shows significant peaks of amino or

sulphonate groups that confirm the hypotheses of dye adsorption and reconstruction of the nanoclay in the process.

3.5.4. Materials and Methods

3.5.4.1. Materials

In this work, three dyes with different characteristics were used to test the method when there is a different polarity of the dye and the dyeing conditions are different. An anionic dye of the direct type called direct blue 199 CI 74180 (DB199), another cationic dye classified as basic with the denomination Basic Yellow 2 (BY2) C.I. 41000 and finally a non-ionic dye without polarity of the disperse class referred to as Disperse Red 1 CI 11110 (DR1) were used. Their structures are shown in Figure 3.5.9.

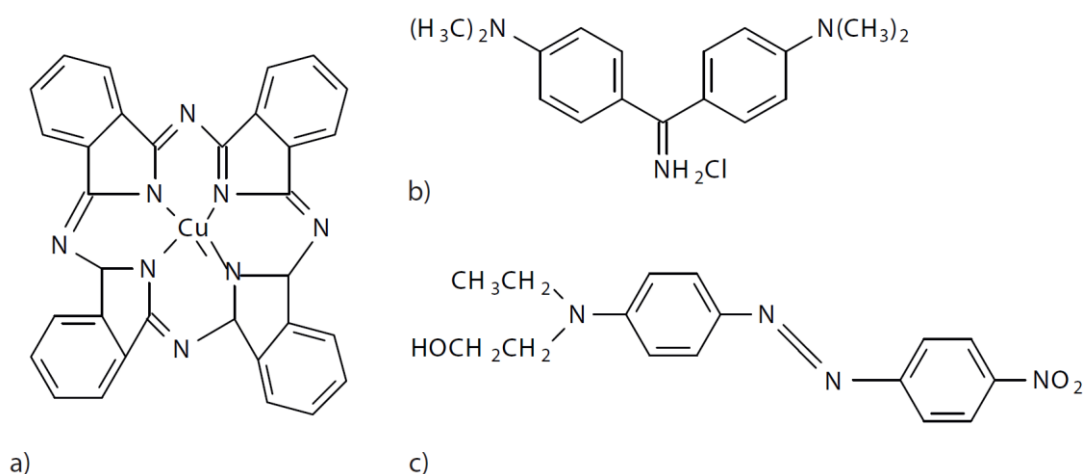


Figure 3.5.9. (a) Direct Blue 199, (b) Basic Yellow 2, (c) Disperse Red 1

Hydrotalcite $Mg_6Al_2(CO_3)(OH)_{16} \cdot 4(H_2O)$ [66]–[68] of Sigma Aldrich Gillingham (U.K), was the adsorbent used. There are different methods that can be used to achieve the adsorption of dyes in this kind of nanoclay. For this study, calcination was selected following the method described by Dos Santos R.M.M. [27]. This method, called calcination, consists of introducing the clay in a kiln at 600 °C for 3 h in order to destroy the H structure and reduce the presence of certain anions such as CO_3^{2-} carbonate, which will allow for the incorporation of new negatively charged compounds in a later reconstruction phase during

hydration thanks to the shape memory of this mineral. After this calcination process, it is considered to be calcined hydrotalcite (HC). Its lamellar structure will allow it to adsorb and fix other elements that are not anionic, so this material is not exclusive for adsorbing negatively charged pollutants.

Figure 3.5.10 shows the change in the structure of the H in the three cases described, prior to calcination, after being subjected to 600 °C for 3 h and after hydration and reconstruction. It is worth noting that in the last SEM and TEM images (Figure 3.5.10), it can be seen how the clay structure has been reconstructed [69]. Within Figure 3.5.10, image “b” shows how the structure has been destroyed by calcination and in figure “c” it can be seen how the structure has been recovered, being very similar to the original “a”. In addition, in image “e” it can be seen how the layers are further apart after calcination, which improves the adsorbent capacity as it is more likely that the adsorbate can be introduced between these layers.

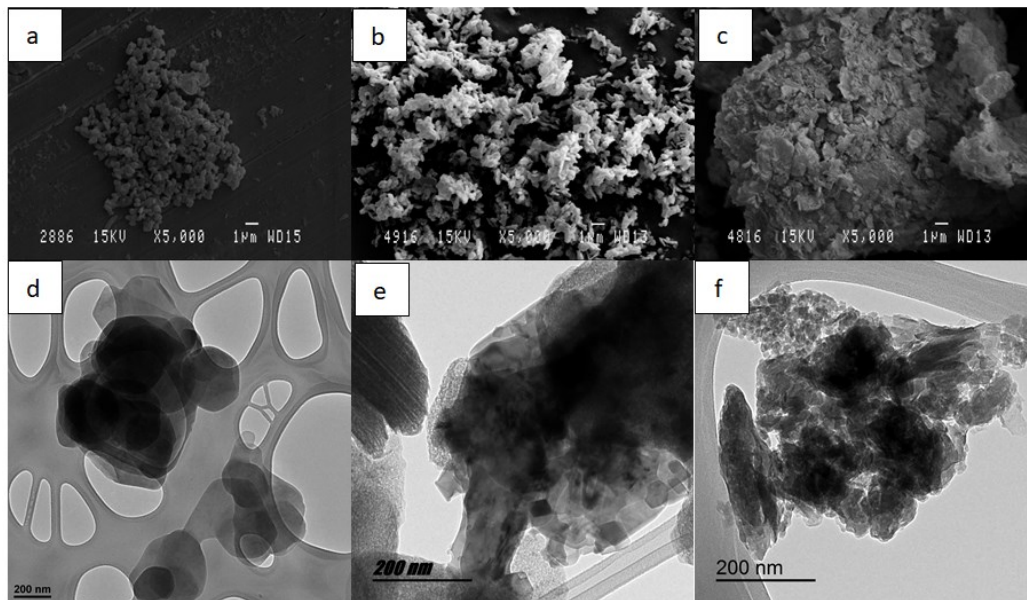


Figure 3.5.10. SEM micrographs of different H samples: (a) H original (b) HC calcinated (c) HC reconstructed. TEM micrographs of different H samples: (d) H original, (e) HC calcinated (f) HC reconstructed

3.5.4.2. Synthesis Methods

After a dyeing process by depletion, the dye remains in the dye bath; just as after the adsorption effect, the dye that has not been adsorbed may remain [47],[70]. In order to determine the amount of dye in the form of $\text{g}\cdot\text{L}^{-1}$ concentration in each of these cases, simple regression models by Lambert-Beer [71] are used beforehand. Starting from various dilutions of the dyes at controlled concentrations, the adsorbance can be measured using a transmission spectrophotometer and the equations given in Table 3.5.6 can be obtained.

Table 3.5.6. Lambert-Beer line equations and R^2

Dye	Equation	R^2
Direct Blue 199 (DB199)	$y = 21.784 x - 0.015$	0.9982
Basic Yellow 2 (BY2)	$y = 18.023 x - 0.0112$	0.9972
Disperse Red 1 (DR1)	$y = 25.411 x - 0.0244$	0.9989

The first objective to be met in the study is to achieve the maximum possible dye adsorption in order to leave the water completely clean. To assess the adsorption capacity of the hydrotalcite, 4 L of a solution of each of the dyes to be studied was prepared at a concentration of $1 \text{ g}\cdot\text{L}^{-1}$. The next step was to introduce the nanoclay into these solutions. The amount introduced was $3 \text{ g}\cdot\text{L}^{-1}$. Once the mixture is prepared, it is subjected to agitation using a magnetic stirring system in which the maximum possible speed is applied at 1600 r.p.m. for 2 h. The speed is then changed to 500 r.p.m. for a further 22 h [72]. In the first 2 h, the aim is to achieve penetration of the dye with maximum centrifugal force, but then the speed is lowered to ensure that the dye does not come out of the clay again and remains as stable as possible, allowing its accommodation in the structure of the reconstructed nanoclay.

The hybrid formed by the hydrotalcite and the dye is then separated from the water. To do this, the solution is filtered using filter paper and all the aqueous part is separated from the solid part by gravity so that the hybrid can be collected in solid form after 48 h. Samples are then taken from the water that has fallen by gravity. This water is taken to the transmission spectrophotometer where, with the absorbance reading and using the

equations in Table 3.5.5, the concentration of dye that still remains in the solution and has not been adsorbed is calculated [73],[74]. On the other hand, the solid hybrid is freeze-dried [26,27] in order to extract all the water and avoid agglutinations that could occur during drying in the oven. In this way, the hybrids identified as HDB199, HBY2 and HDR1 are obtained for the union of the dyes DB199, BY2 and DR1, respectively.

The desorption process is described as a phenomenon in which there is a transfer of the dye from the adsorbate in the solid to the liquid phase [75],[76]. Several models [77]–[79] explain different theories involving isotherms on how this desorption occurs, describing them as non-ideal and reversible adsorption/desorption systems. Another describes a system in which there is not always an interaction between neighbouring active sites due to the non-homogeneity of the nanoadsorbate, and therefore, no homogeneous adsorption. All these theories give an insight into the true nature of the adsorption/desorption process. The authors Momina, Shahadat Mohammad, and Suzylawatilsamil [80] explain a desorption model for methylene blue (MB) by first subjecting the hybrid to high temperatures to weaken the bonds and then using various solvents such as HCl, ethanol, and nitric acid or acetone. They argue that any one of these phases alone is not sufficient to produce good desorption results.

In this study, a simultaneous desorption-dyeing process is proposed, in which, based on the theory that temperature weakens the bond between the clay and the dye [80], subsequently taking advantage of the dye-fibre affinity and the dyeing process commonly used so that the dye migrates completely from the hydrotalcite to the textile fibre (Figure 3.5.11). Furthermore, in the model of this work, heat is applied by convection and not by radiation as in the model of the authors Momina, Shahadat Mohammad, and Suzylawatilsamil, as this heat is more effective at reaching more areas of the clay and is also more energetic.

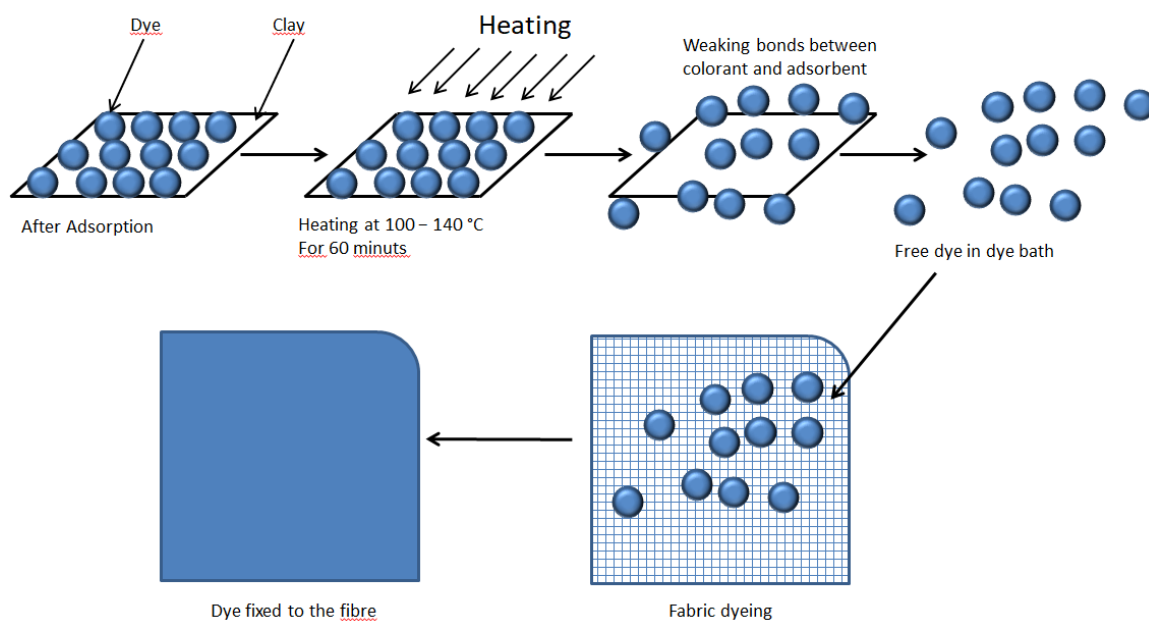


Figure 3.5.11. Dye desorption and dyeing of the textile fibre

The clay-dye hybrid is then used as a dyeing material for dyeing by exhaustion, using a bath ratio of 1/40. For the dyeing of a 100% cotton (CO) openwork fabric with a grammage of $135 \text{ g}\cdot\text{m}^{-2}$, $25 \text{ yarns}\cdot\text{cm}^{-1}$, $22 \text{ weft}\cdot\text{cm}^{-2}$ of plane weave openwork fabric, the direct dye hybrid HDB199 is used, 40% s.p.f. of clay + dye, $20 \text{ g}\cdot\text{L}^{-1}$ of sodium sulphate and three drops of a wetting agent are added to the dyeing bath to submit it to the dyeing process for 60 min at $100 \text{ }^\circ\text{C}$, obtaining the dyed fabric referenced as TDB199. For the dyeing of a 100% polyester fabric (PES) $200 \text{ g}\cdot\text{m}^{-2}$, $13 \text{ yarns}\cdot\text{cm}^{-1}$, $52 \text{ weft}\cdot\text{cm}^{-1}$ of plain weave was introduced in a bath containing 40% s.p.f. of clay + HDR1 dye, for 60 min at $140 \text{ }^\circ\text{C}$ in a closed machine with $1 \text{ g}\cdot\text{L}^{-1}$ ammonium sulphate, $0.5 \text{ g}\cdot\text{L}^{-1}$ Dekol SN dispersant after previously adjusting the pH to 4.5–5 with acetic acid, thus obtaining the sample with reference TDR1. The last dyeing was on a fabric of 100% acrylic composition (PAN) a weft knitted fabric with eight rows per centimetre and nine columns per centimetre forming an English knitted weave in whose bath 40% s.p.f. of clay+ HBY2 dye, acetic acid 2% s.p.f, $20 \text{ g}\cdot\text{L}^{-1}$ of sodium sulphate was added and processed for 40 min at $100 \text{ }^\circ\text{C}$, thus obtaining the dyed fabric referenced as TBY2. The dyeing of the polyester fabric was carried out in a closed machine due to the temperatures above $100 \text{ }^\circ\text{C}$ that must be used. The apparatus

used was the Testtherm type 9S from the manufacturer Talcatex S.A, San Sebastian de los Reyes (Spain). Conversely, the dyeing of acrylic and cotton fibre was carried out in the open machine referenced as Open Bath dye Master from the manufacturer Paramount S.A, Geneva (Switzerland). All the fabrics were washed after dyeing to eliminate any remaining dye that was not fixed to the fibres.

After the dyeing process described above, the clay that was in the dye baths was collected again to assess the desorption that it has undergone. For this purpose, the dye baths are separated from the dyed fabrics and are again filtered by gravity with filter paper, as was conducted in the previous process. The clay is analysed again after dyeing to assess its colour change and other characteristics that may have been altered after this process. From each of the hybrid samples HDB199, HBY2 and HDR1, new clay-dye hybrids are obtained from the remainder collected after the dyeing, respectively, referred to as H2DB199, H2BY2 and H2DR1.

3.5.4.3. Characterisation

The colour measurement of the obtained hybrids was studied using the Jasco V-670 double UV-VIS/NIR spectrophotometer. Measurements were carried out in the range of 2700–190 nm at a frequency of 0.5 nm. The Jasco V-670 is equipped with a double-grating monochromator. The first grating monochromator is used for the UV-VIS region serving 1200 grids·mm⁻¹ which is equipped with detectors based on a photomultiplier tube. On the other hand, the second grating is used for the rest of the spectrum studied, i.e., for the IR infrared region, but this time with 300 grids·mm⁻¹ and using a PbS detector. Both gratings are equipped with an automatic system that allows them to adapt to changes in wavelength. The light sources were a halogen lamp (330–2700 nm) and a deuterium lamp (190–350 nm). The CIE-1964 observer was used under the D65 illuminant, reflectance factors were also applied to obtain optical values for comparison [81].

A scanning electron microscope (SEM) model PHENOM (FEI Company, Eindhoven, The Netherlands) was used to perform the topographical analysis of the surface of the samples. It was operated at an acceleration of 5kV. The previous sample preparation

consists of sputtering with a palladium/gold alloy with an EMITECH sputter coater mod. SC7620 (Quorum Technologies Ltd., East Sussex, UK). As the coating thickness is only 5–7nm it will not alter the readings. For TEM imaging, a JEOL model JEM-2010 transmission electron microscope was used. The image acquisition camera is a GATAN model ORIUS SC600. It is mounted on an axis with the microscope at the bottom and is integrated into the image acquisition and processing software GATAN DigitalMicrograph 1.80.70 for GMS 1.8.0.

The clay-dye hybrids were subjected to infrared spectrophotometer analysis in order to calculate the Fourier transform (FTIR). Due to the characteristics of the material to be analysed, the horizontal attenuated total reflection technique (FTIR-ATR) was used using a ZnSe prism. The instrumentation used for the readings was the Jasco FTIR 4700 IRT 5200 spectrophotometer with a DTGS detector sensor. It was necessary to use a pressure accessory to obtain a uniform reading on each of the samples. The spectrophotometer worked at a resolution of 4 cm^{-1} and scanned 64 scans.

Continuing with the characterisation of the hybrids obtained from the clay-dye, these samples were subjected to X-ray diffraction (XRD) tests [82],[83] in order to analyse their behaviour, especially the changes in their lamellar structure during the calcination process and reconstruction during rehydration. Special attention is paid to the basal space between the hydrotalcite lamellae, which produces the adsorption of both ions and other non-ionic substances. For this purpose, the RD bruker D8-Advance (Bruker, Billerica, MA, USA) with a Göebel mirror (power: 3000 W, voltage: 20–60 kV and current: 5–80 mA) was used. The analysis was performed in an oxidising atmosphere at an angular velocity of $1^\circ/\text{min}$, STEP 0.05° , and an angular sweep of $2.7\text{--}70^\circ$. The diffraction patterns were indexed by making a comparison with the JCPDS files.

The dyeing samples of the three dyes were subjected to different fastness tests to assess their correct dyeing and subsequent behaviour. In order to check their fastness to washing, each of the samples was subjected to washing according to the UNE-EN ISO 105-C06:1994 standard using the Linitest described in this standard. The test carried out was

the A1S test described in the standard at a temperature of 40 °C for 30 min and with a bath volume of 150 mL. The pH was not adjusted and 10 steel balls were added to generate an abrasive action. Tests for colour fastness to ironing were carried out according to UNE-EN ISO 105-X11:1997 using a pressure plate. The tests were carried out in wet, damp and dry conditions as stated in the standard. The ironing time for all samples was 15 s at a temperature of 200 °C for PAN and PES fabrics, although for CO fabrics it was conducted at 150 °C, as cotton may yellow at higher temperatures. To assess the colour fastness to rubbing, the Crockmeter was used according to the UNE-EN ISO 105-X12:2016 standard. This test was carried out wet and dry as described in the standard.

Colour degradation and discharge were measured instrumentally using a Minolta CM-3600d reflection spectrophotometer in the range 360–740 nm with a step of 10 nm according to UNE-EN ISO 105-A05 for degradation and UNE-EN ISO 105-A04 for discharge. The results are expressed according to the grey scale as stated in the aforementioned standards.

BET analysis was performed to measure the surface area, pore volume and pore size using nitrogen adsorption and desorption values at –196 °C on a Micromeritics ASAP-2020. The samples are first degassed in a vacuum atmosphere at temperatures between 150 °C and 200 °C so as not to carbonise any elements in the sample [64],[65].

References

1. Bhogle, S. Case Study on Waste Water Disposal Practices and Likely Treatment Options in Textile Processing Units in Tamil Nadu. *TIDE, Bangalore* 2007.
2. Ramasany, R.; Ahmed, H. A. M.; Karthik, S. S. Development of Microbial Consortium for the Biodegradation and Biodecolorization of Textile Effluents. *J. Urban Environ. Eng.* 2012, 6 (1), 36–41.
3. Ponnusami, V.; Srivastava, S. N. Studies on Application of Teak Leaf Powders for the Removal of Color from Synthetic and Industrial Effluents. *J. Hazard. Mater.* 2009, 169 (1–3), 1159–1162. <https://doi.org/10.4090/juee.2012.v6n1.036041>
4. Ponnusami, V.; Lavanya, N.; Meenal, M.; Raj, R. A. G.; Srivastava, S. N. Application of Nitric Acid Treated Rice Husk for Sorption of Reactive Dye Reactive Black 5: Analysis Using Statistical Experimental Design. *Pollut. Res* 2008, 27, 45.
5. Pratibha, R.; Malar, P.; Rajapriya, T.; Balapournima, S.; Ponnusami, V. Statistical and Equilibrium Studies on Enhancing Biosorption Capacity of *Saccharomyces Cerevisiae* through Acid Treatment. *Desalination* 2010, 264 (1–2), 102–107. <https://doi.org/10.1016/j.desal.2010.07.011>
6. Hunger, K. *Industrial Dyes: Chemistry, Properties, Applications*; John Wiley & Sons, 2007.
7. Luo, Z.; Gao, M.; Ye, Y.; Yang, S. Modification of Reduced-Charge Montmorillonites by a Series of Gemini Surfactants: Characterization and Application in Methyl Orange Removal. *Appl. Surf. Sci.* 2015, 324, 807–816. <https://doi.org/10.1016/J.APSUSC.2014.11.043>.
8. Gupta, V. K.; Agarwal, S.; Olgun, A.; Demir, H. İ.; Yola, M. L.; Atar, N. Adsorptive Properties of Molasses Modified Boron Enrichment Waste Based Nanoclay for Removal of Basic Dyes. *J. Ind. Eng. Chem.* 2016, 34, 244–249. <https://doi.org/10.1016/J.JIEC.2015.11.017>.
9. Carretero, M. I.; Pozo, M.; Sánchez, C.; García, F. J.; Medina, J. A.; Bernabé, J. M. Comparison of Saponite and Montmorillonite Behaviour during Static and Stirring Maturation with Seawater for Pelotherapy. *Appl. Clay Sci.* 2007, 36 (1–3), 161–173. <https://doi.org/10.1016/J.CLAY.2006.05.010>.
10. Taleb, K.; Pillin, I.; Grohens, Y.; Saidi-Besbes, S. Gemini Surfactant Modified Clays: Effect of Surfactant Loading and Spacer Length. *Appl. Clay Sci.* 2018, 161, 48–56. <https://doi.org/10.1016/J.CLAY.2018.03.015>.
11. Olvera, R. C.; Silva, S. L.; Robles-Belmont, E.; Lau, E. Z. Review of Nanotechnology Value Chain for Water Treatment Applications in Mexico. *Resour. Technol.* 2017, 3 (1), 1–11. <https://doi.org/10.1016/J.REFFIT.2017.01.008>.

12. López-Rodríguez, D.; Micó-Vicent, B.; Jordán-Núñez, J.; Bonet-Aracil, M.; Bou-Belda, E. Uses of Nanoclays and Adsorbents for Dye Recovery: A Textile Industry Review. *Appl. Sci.* 2021, 11 (23), 11422. <https://doi.org/10.3390/app112311422>
13. Gasser, M. S.; Mekhamer, H. S.; Abdel Rahman, R. O. Optimization of the Utilization of Mg/Fe Hydrotalcite like Compounds in the Removal of Sr(II) from Aqueous Solution. *J. Environ. Chem. Eng.* 2016, 4 (4), 4619–4630. <https://doi.org/10.1016/j.jece.2016.10.027>.
14. Xi, H.; Li, Q.; Yang, Y.; Zhang, J.; Guo, F.; Wang, X.; Xu, S.; Ruan, S. Highly Effective Removal of Phosphate from Complex Water Environment with Porous Zr-Bentonite Alginate Hydrogel Beads: Facile Synthesis and Adsorption Behavior Study. *Appl. Clay Sci.* 2021, 201, 105919. <https://doi.org/10.1016/j.clay.2020.105919>
15. de Queiroga, L. N. F.; França, D. B.; Rodrigues, F.; Santos, I. M. G.; Fonseca, M. G.; Jaber, M. Functionalized Bentonites for Dye Adsorption: Depollution and Production of New Pigments. *J. Environ. Chem. Eng.* 2019, 7 (5), 103333. <https://doi.org/10.1016/J.JECE.2019.103333>.
16. Kanani-Jazi, M. H.; Akbari, S. Amino-Dendritic and Carboxyl Functionalized Halloysite Nanotubes for Highly Efficient Removal of Cationic and Anionic Dyes: Kinetic, Isotherm, and Thermodynamic Studies. *J. Environ. Chem. Eng.* 2021, 9 (3), 105214. <https://doi.org/10.1016/j.jece.2021.105214>.
17. Parades-Aguilar, J.; Reyes-Martínez, V.; Bustamante, G.; Almendáriz-Tapia, F. J.; Martínez-Meza, G.; Vílchez-Vargas, R.; Link, A.; Certucha-Barragán, M. T.; Calderón, K. Removal of Nickel (II) from Wastewater Using a Zeolite-Packed Anaerobic Bioreactor: Bacterial Diversity and Community Structure Shifts. *J. Environ. Manage.* 2021, 279, 111558. <https://doi.org/10.1016/j.jenvman.2020.111558>
18. Schoonheydt, R. A.; Heughebaert, L. Clay Adsorbed Dyes: Methylene Blue on Laponite. *Clay Miner.* 1992, 27 (1), 91–100. <https://doi.org/10.1180/claymin.1992.027.1.09>.
19. Yi, J.-Z.; Zhang, L.-M. Removal of Methylene Blue Dye from Aqueous Solution by Adsorption onto Sodium Humate/Polyacrylamide/Clay Hybrid Hydrogels. *Bioresour. Technol.* 2008, 99 (7), 2182–2186. <https://doi.org/10.1016/J.BIORTECH.2007.05.028>.
20. Mittal, H.; Babu, R.; Dabbawala, A. A.; Stephen, S.; Alhassan, S. M. Zeolite-Y Incorporated Karaya Gum Hydrogel Composites for Highly Effective Removal of Cationic Dyes. *Colloids Surfaces A Physicochem. Eng. Asp.* 2020, 586, 124161. <https://doi.org/10.1016/J.COLSURFA.2019.124161>.
21. Chen, H.; Zhang, Z.; Zhuang, G.; Jiang, R. A New Method to Prepare ‘Maya Red’ Pigment from Sepiolite and Basic Red 46. *Appl. Clay Sci.* 2019, 174, 38–46. <https://doi.org/10.1016/J.CLAY.2019.03.023>.

22. Akil, J.; Ciotonea, C.; Siffert, S.; Royer, S.; Pirault-Roy, L.; Cousin, R.; Poupin, C. NO Reduction by CO under Oxidative Conditions over CoCuAl Mixed Oxides Derived from Hydrotalcite-like Compounds: Effect of Water. *Catal. Today* 2021, No. October 2020. <https://doi.org/10.1016/j.cattod.2021.05.014>.
23. Li, B.; Zhang, Y.; Zhou, X.; Liu, Z.; Liu, Q.; Li, X. Different Dye Removal Mechanisms between Monodispersed and Uniform Hexagonal Thin Plate-like MgAl–CO₃--LDH and Its Calcined Product in Efficient Removal of Congo Red from Water. *J. Alloys Compd.* 2016, 673, 265–271. <https://doi.org/10.1016/j.jallcom.2016.02.248>
24. Zhang, C.; Yang, S.; Chen, H.; He, H.; Sun, C. Adsorption Behavior and Mechanism of Reactive Brilliant Red X-3B in Aqueous Solution over Three Kinds of Hydrotalcite-like LDHs. *Appl. Surf. Sci.* 2014, 301, 329–337. <https://doi.org/10.1016/j.apsusc.2014.02.073>
25. Shan, R.; Yan, L.; Yang, Y.; Yang, K.; Yu, S.; Yu, H.; Zhu, B.; Du, B. Highly Efficient Removal of Three Red Dyes by Adsorption onto Mg–Al-Layered Double Hydroxide. *J. Ind. Eng. Chem.* 2015, 21, 561–568. <https://doi.org/10.1016/j.jiec.2014.03.019>
26. Herald, E.; Santosa, S. J.; Triyono, T.; Wijaya, K. Anionic and Cationic Dyes Removal from Aqueous Solutions by Adsorption onto Synthetic Mg/Al Hydrotalcite-like Compound. *Indones. J. Chem.* 2015, 15 (3), 234–241. <https://doi.org/10.22146/ijc.21190>
27. dos Santos, R. M. M.; Gonçalves, R. G. L.; Constantino, V. R. L.; da Costa, L. M.; da Silva, L. H. M.; Tronto, J.; Pinto, F. G. Removal of Acid Green 68:1 from Aqueous Solutions by Calcined and Uncalcined Layered Double Hydroxides. *Appl. Clay Sci.* 2013, 80–81, 189–195. <https://doi.org/10.1016/j.clay.2013.04.006>.
28. Orthman, J.; Zhu, H. Y.; Lu, G. Q. Use of Anion Clay Hydrotalcite to Remove Coloured Organics from Aqueous Solutions. *Sep. Purif. Technol.* 2003, 31 (1), 53–59. [https://doi.org/10.1016/S1383-5866\(02\)00158-2](https://doi.org/10.1016/S1383-5866(02)00158-2).
29. Grum, F.; Witzel, R. F.; Stensby, P. Evaluation of Whiteness. *JOSA* 1974, 64 (2), 210–215. <https://doi.org/10.1364/JOSA.64.000210>
30. Serrano-Lotina, A.; Rodríguez, L.; Muñoz, G.; Martín, A. J.; Folgado, M. A.; Daza, L. Biogas Reforming over La-NiMgAl Catalysts Derived from Hydrotalcite-like Structure: Influence of Calcination Temperature. *Catal. Commun.* 2011, 12 (11), 961–967. <https://doi.org/10.1016/J.CATCOM.2011.02.014>.
31. Micó-Vicent, B.; Jordán, J.; Perales, E.; Martínez-Verdú, F.; Cases, F. Finding the Additives Incorporation Moment in Hybrid Natural Pigments Synthesis to Improve Bioresin Properties. *Coatings* . 2019. <https://doi.org/10.3390/coatings9010034>.
32. Millange, F.; Walton, R. I.; O'Hare, D. Time-Resolved in Situ X-Ray Diffraction Study of the Liquid-Phase Reconstruction of Mg–Al–Carbonate Hydrotalcite-like Compounds. *J. Mater. Chem.* 2000, 10 (7), 1713–1720.

<https://doi.org/10.1039/B0028270>

33. Stanimirova, T. S.; Vergilov, I.; Kirov, G.; Petrova, N. Thermal Decomposition Products of Hydrotalcite-like Compounds: Low-Temperature Metaphases. *J. Mater. Sci.* 1999, *34* (17), 4153–4161. <https://doi.org/10.1023/A:1004673913033>
34. Cavani, F.; Trifiro, F.; Vaccari, A. Hydrotalcite-Type Anionic Clays: Preparation, Properties and Applications. *Catal. today* 1991, *11* (2), 173–301. [https://doi.org/10.1016/0920-5861\(91\)80068-K](https://doi.org/10.1016/0920-5861(91)80068-K)
35. Zhu, M.-X.; Li, Y.-P.; Xie, M.; Xin, H.-Z. Sorption of an Anionic Dye by Uncalcined and Calcined Layered Double Hydroxides: A Case Study. *J. Hazard. Mater.* 2005, *120* (1–3), 163–171. <https://doi.org/10.1016/j.jhazmat.2004.12.029>
36. Lakraimi, M.; Legrouri, A.; Barroug, A.; Besse, J.-P. Removal of Pesticides from Water by Anionic Clays. *J. Chim. Phys. Physico-Chimie Biol.* 1999, *96* (3), 470–478. <https://doi.org/10.1051/jcp:1999154>
37. Sato, T.; Kato, K.; Endo, T.; Shimada, M. Preparation and Chemical Properties of Magnesium Aluminium Oxide Solid Solutions. *React. Solids* 1986, *2* (3), 253–260. [https://doi.org/10.1016/0168-7336\(86\)80088-2](https://doi.org/10.1016/0168-7336(86)80088-2)
38. Dahdah, E.; Estephane, J.; Taleb, Y.; El Khoury, B.; El Nakat, J.; Aouad, S. The Role of Rehydration in Enhancing the Basic Properties of Mg–Al Hydrotalcites for Biodiesel Production. *Sustain. Chem. Pharm.* 2021, *22* (July). <https://doi.org/10.1016/j.scp.2021.100487>.
39. Bernard, E.; Zucha, W. J.; Lothenbach, B.; Mäder, U. Stability of Hydrotalcite (Mg–Al Layered Double Hydroxide) in Presence of Different Anions. *Cem. Concr. Res.* 2022, *152*, 106674. <https://doi.org/10.1016/J.CEMCONRES.2021.106674>.
40. Geetha Bhavani, A.; Wani, T. A.; Ma'Aruf, A.; Prasad, T. Effect of Ageing Process on Crystal Morphology of Co–Mg–Al Hydrotalcite. *Mater. Today Proc.* 2021, *44*, 2277–2282. <https://doi.org/10.1016/J.MATPR.2020.12.390>.
41. Wiyantoko, B.; Kurniawati, P.; Purbaningias, T. E.; Fatimah, I. Synthesis and Characterization of Hydrotalcite at Different Mg/Al Molar Ratios. *Procedia Chem.* 2015, *17*, 21–26. <https://doi.org/10.1016/j.proche.2015.12.115>
42. Roelofs, J. C. A. A.; van Bokhoven, J. A.; Van Dillen, A. J.; Geus, J.; de Jong, K. P. The Thermal Decomposition of Mg–Al Hydrotalcites: Effects of Interlayer Anions and Characteristics of the Final Structure. *Chem. Eur. J.* 2002, *8*, 5571–5579. [https://doi.org/10.1002/1521-3765\(20021216\)8:24%3C5571::AID-CHEM5571%3E3.0.CO;2-R](https://doi.org/10.1002/1521-3765(20021216)8:24%3C5571::AID-CHEM5571%3E3.0.CO;2-R)
43. Ziyat, H.; Elmzioui, S.; Naciri Bennani, M.; Houssaini, J.; Allaoui, S.; Arhzaf, S. Kinetic, Isotherm, and Mechanism Investigations of the Removal of Nitrate and Nitrite from Water by the Synthesized Hydrotalcite Mg–Al. *Res. Chem. Intermed.* 2021, *47* (6),

- 2605–2627. <https://doi.org/10.1007/s11164-021-04414-w>
44. Ma, Y.; Zhu, J.; He, H.; Yuan, P.; Shen, W.; Liu, D. Infrared Investigation of Organo-Montmorillonites Prepared from Different Surfactants. *Spectrochim. Acta Part A Mol. Biomol. Spectrosc.* 2010, 76 (2), 122–129. <https://doi.org/10.1016/j.saa.2010.02.038>
 45. Lopez, T.; Bosch, P.; Asomoza, M.; Gómez, R.; Ramos, E. DTA-TGA and FTIR Spectroscopies of Sol-Gel Hydrotalcites: Aluminum Source Effect on Physicochemical Properties. *Mater. Lett.* 1997, 31 (3–6), 311–316. [https://doi.org/10.1016/S0167-577X\(96\)00296-0](https://doi.org/10.1016/S0167-577X(96)00296-0)
 46. de Souza, T. N. V.; de Carvalho, S. M. L.; Vieira, M. G. A.; da Silva, M. G. C.; Brasil, D. do S. B. Adsorption of Basic Dyes onto Activated Carbon: Experimental and Theoretical Investigation of Chemical Reactivity of Basic Dyes Using DFT-Based Descriptors. *Appl. Surf. Sci.* 2018, 448, 662–670. <https://doi.org/10.1016/J.APSUSC.2018.04.087>
 47. López-Rodríguez, D.; Micó-Vicent, B.; Bonet-Aracil, M.; Cases, F.; Bou-Belda, E. The Optimal Concentration of Nanoclay Hydrotalcite for Recovery of Reactive and Direct Textile Colorants. *Int. J. Mol. Sci.* 2022, 23 (17), 9671. <https://doi.org/10.3390/ijms23179671>
 48. Hafshejani, M. K.; Ogugbue, C. J.; Morad, N. Application of Response Surface Methodology for Optimization of Decolorization and Mineralization of Triazo Dye Direct Blue 71 by *Pseudomonas Aeruginosa*. *3 Biotech* 2014, 4 (6), 605–619. <https://doi.org/10.1007/s13205-013-0192-7>
 49. Extremera, R.; Pavlovic, I.; Pérez, M. R.; Barriga, C. Removal of Acid Orange 10 by Calcined Mg/Al Layered Double Hydroxides from Water and Recovery of the Adsorbed Dye. *Chem. Eng. J.* 2012, 213, 392–400. <https://doi.org/https://doi.org/10.1016/j.cej.2012.10.042>
 50. Hu, C.; Jimmy, C. Y.; Hao, Z.; Wong, P. K. Photocatalytic Degradation of Triazine-Containing Azo Dyes in Aqueous TiO₂ Suspensions. *Appl. Catal. B Environ.* 2003, 42 (1), 47–55. [https://doi.org/10.1016/S0926-3373\(02\)00214-X](https://doi.org/10.1016/S0926-3373(02)00214-X)
 51. Silverstein, R. M.; Bassler, G. C. Spectrometric Identification of Organic Compounds. *J. Chem. Educ.* 1962, 39 (11), 546.
 52. Öztürk, A.; Malkoc, E. Adsorptive Potential of Cationic Basic Yellow 2 (BY2) Dye onto Natural Untreated Clay (NUC) from Aqueous Phase: Mass Transfer Analysis, Kinetic and Equilibrium Profile. *Appl. Surf. Sci.* 2014, 299, 105–115. <https://doi.org/10.1016/J.APSUSC.2014.01.193>
 53. Çalışkan, Y.; Harbeck, S.; Bektaş, N. Adsorptive Removal of Basic Yellow Dye Using Bigadiç Zeolites: FTIR Analysis, Kinetics, and Isotherms Modeling. *Environ. Prog. Sustain. Energy* 2019, 38 (s1), S185–S195. <https://doi.org/10.1002/ep.12969>

54. Cui, Y.; Wang, M.; Chen, L.; Qian, G. Synthesis and Spectroscopic Characterization of an Alkoxysilane Dye Containing C. I. Disperse Red 1. *Dye. Pigment.* 2004, *62* (1), 43–47. <https://doi.org/10.1016/J.DYEPIG.2003.11.009>.
55. Taunamang, H.; Herman, H.; Tjia, M. O. Molecular Orientation in Disperse Red 1 Thin Film Produced by PVD Method. *Opt. Mater. (Amst).* 2001, *18* (3), 343–350. [https://doi.org/10.1016/S0925-3467\(01\)00169-0](https://doi.org/10.1016/S0925-3467(01)00169-0).
56. Duffner, H.; Bach, E.; Cleve, E.; Schollmeyer, E. New Mathematical Model for Determining Time-Dependent Adsorption and Diffusion of Dyes into Fibers through Dye Sorption Curves in Combination Shades: Part II: Kinetic Data from Dyeing Cotton with a Trichrome Direct Dye System. *Text. Res. J.* 2000, *70* (3), 223–229. <https://doi.org/10.1177/004051759706701001>
57. Hauser, P. J.; Tappa, A. H. Improving the Environmental and Economic Aspects of Cotton Dyeing Using a Cationised Cotton. *Color. Technol.* 2001, *117* (5), 282–288. <https://doi.org/10.1111/j.1478-4408.2001.tb00076.x>
58. Daruwalla, E. H.; Kulkarni, G. G. Studies in the Equilibrium Dyeing of Cotton with Direct Dyes: The Determination of the Activity and Affinity of Direct Dyes for Cellulose. *Bull. Chem. Soc. Jpn.* 1964, *37* (9), 1250–1261. <https://doi.org/10.1246/bcsj.37.1250>
59. Aspland, J. R. The Application of Basic Dye Cations to Anionic Fibers: Dyeing Acrylic and Other Fibers with Basic Dyes. *Text. Chem. Color.* 1993, *25* (6).
60. Van Der Kraan, M.; Vanesa Fernandez Cid, M.; Woerlee, G. F.; Veugelers, W. J. T.; Witkamp, G.-J. Equilibrium Study on the Disperse Dyeing of Polyester Textile in Supercritical Carbon Dioxide. *Text. Res. J.* 2007, *77* (8), 550–558. <https://doi.org/10.1177/0040517507077483>
61. Kim, T.-K.; Son, Y.-A.; Lim, Y.-J. Thermodynamic Parameters of Disperse Dyeing on Several Polyester Fibers Having Different Molecular Structures. *Dye. Pigment.* 2005, *67* (3), 229–234. <https://doi.org/10.1016/j.dyepig.2004.12.005>
62. Ketema, A.; Worku, A. Review on Intermolecular Forces between Dyes Used for Polyester Dyeing and Polyester Fiber. *J. Chem.* 2020, 2020. <https://doi.org/10.1155/2020/6628404>
63. Tichit, D.; Lhouty, M. H.; Guida, A.; Chiche, B. H.; Figueras, F.; Auroux, A.; Bartalini, D.; Garrone, E. Textural Properties and Catalytic Activity of Hydrotalcites. *J. Catal.* 1995, *151* (1), 50–59. <https://doi.org/10.1006/jcat.1995.1007>
64. Liu, Y.; Lotero, E.; Goodwin, J. G.; Mo, X. Transesterification of Poultry Fat with Methanol Using Mg-Al Hydrotalcite Derived Catalysts. *Appl. Catal. A Gen.* 2007, *331* (1), 138–148. <https://doi.org/10.1016/j.apcata.2007.07.038>.
65. Shen, J.; Tu, M.; Hu, C. Structural and Surface Acid/Base Properties of Hydrotalcite-

- Derived MgAlO Oxides Calcined at Varying Temperatures. *J. Solid State Chem.* 1998, 137 (2), 295–301. <https://doi.org/10.1006/jssc.1997.7739>.
66. Ulibarri, M. A.; Pavlovic, I.; Barriga, C.; Hermosin, M. C.; Cornejo, J. Adsorption of Anionic Species on Hydrotalcite-like Compounds: Effect of Interlayer Anion and Crystallinity. *Appl. Clay Sci.* 2001, 18 (1–2), 17–27. [https://doi.org/10.1016/S0169-1317\(00\)00026-0](https://doi.org/10.1016/S0169-1317(00)00026-0)
67. Bish, D. L. Anion-Exchange in Takovite: Applications to Other Hydroxide Minerals. *Bull. Mineral.* 1980, 103 (2), 170–175.
68. Miyata, S. Physico-Chemical Properties of Synthetic Hydrotalcites in Relation to Composition. *Clays Clay Miner.* 1980, 28 (1), 50–56. <https://doi.org/10.1346/CCMN.1980.0280107>
69. Lian, Z. Y.; Zhang, Y.; Wang, X. Z. Manufacturing of High Quality Hydrotalcite by Computational Fluid Dynamics Simulation of an Impinging Jet Crystallizer. *Ceram. Int.* 2022. <https://doi.org/10.1016/J.CERAMINT.2022.02.081>.
70. Bou-Belda, E.; López-Rodríguez, D.; Micó-Vicent, B.; Bonet-Aracil, M. Direct and Reactive Dyes Recovery in Textile Wastewater Using Calcinated Hydrotalcite. In *Materials Science Forum*; Trans Tech Publ, 2022; Vol. 1063, pp 233–242. <https://doi.org/10.4028/p-31v71q>
71. Bigman, J. L. Monitoring of Chemicals and Water. *Handb. Silicon Wafer Clean. Technol.* 2018, 619–657. <https://doi.org/10.1016/B978-0-323-51084-4.00011-3>
72. Silva, M. M. F.; Oliveira, M. M.; Avelino, M. C.; Fonseca, M. G.; Almeida, R. K. S.; Silva Filho, E. C. Adsorption of an Industrial Anionic Dye by Modified-KSF-Montmorillonite: Evaluation of the Kinetic, Thermodynamic and Equilibrium Data. *Chem. Eng. J.* 2012, 203, 259–268. <https://doi.org/10.1016/j.cej.2012.07.009>.
73. B. Micó-Vicent, F. M.-V. Method for Optimising the Synthesis of Hybrid Nanopigments, 2017.
74. H. Fischer, L. F. B. Coloring Pigment, 2001.
75. Limousin, G.; Gaudet, J.-P.; Charlet, L.; Szenknect, S.; Barthes, V.; Krimissa, M. Sorption Isotherms: A Review on Physical Bases, Modeling and Measurement. *Appl. geochemistry* 2007, 22 (2), 249–275. <https://doi.org/10.1016/j.apgeochem.2006.09.010>
76. Voudrias, E.; Fytianos, K.; Bozani, E. Sorption–Desorption Isotherms of Dyes from Aqueous Solutions and Wastewaters with Different Sorbent Materials. *Glob. Nest Int. J* 2002, 4 (1), 75–83.
77. Foo, K. Y.; Hameed, B. H. Porous Structure and Adsorptive Properties of Pineapple

- Peel Based Activated Carbons Prepared via Microwave Assisted KOH and K₂CO₃ Activation. *Microporous Mesoporous Mater.* 2012, 148 (1), 191–195. <https://doi.org/10.1016/j.micromeso.2011.08.005>
78. Daneshvar, E.; Vazirzadeh, A.; Niazi, A.; Kousha, M.; Naushad, M.; Bhatnagar, A. Desorption of Methylene Blue Dye from Brown Macroalga: Effects of Operating Parameters, Isotherm Study and Kinetic Modeling. *J. Clean. Prod.* 2017, 152, 443–453. <https://doi.org/10.1016/j.jclepro.2017.03.119>
79. Redlich, O.; Peterson, D. L. A Useful Adsorption Isotherm. *J. Phys. Chem.* 1959, 63 (6), 1024. <https://doi.org/10.1021/j150576a611>
80. Momina; Mohammad, S.; Suzylawati, I. Study of the Adsorption/Desorption of MB Dye Solution Using Bentonite Adsorbent Coating. *J. Water Process Eng.* 2020, 34 (July 2019). <https://doi.org/10.1016/j.jwpe.2020.101155>
81. Di Natale, C.; Monti, D.; Paolesse, R. Chemical Sensitivity of Porphyrin Assemblies. *Mater. Today* 2010, 13 (7–8), 46–52. [https://doi.org/10.1016/S1369-7021\(10\)70127-9](https://doi.org/10.1016/S1369-7021(10)70127-9)
82. Pálková, H.; Madejová, J.; Zimowska, M.; Bielańska, E.; Olejniczak, Z.; Lityńska-Dobrzyńska, L.; Serwicka, E. M. Laponite-Derived Porous Clay Heterostructures: I. Synthesis and Physicochemical Characterization. *Microporous Mesoporous Mater.* 2010, 127 (3), 228–236. <https://doi.org/10.1016/j.micromeso.2009.07.019>
83. Zhuo, W.; Xie, Y.; Benson, M. T.; Ge, J.; Mariani, R. D.; Zhang, J. XRD and SEM/EDS Characterization of Two Quaternary Fuel Alloys (U-2.5Mo-2.5Ti-5.0Zr and U-1.5Mo-1.5Ti-7.0Zr in Wt. %) for Fast Reactors. *Mater. Charact.* 2020, 170 (September), 110696. <https://doi.org/10.1016/j.matchar.2020.110696>

Recuperación del colorante de aguas residuales textiles mediante nanoarcillas para su reutilización como pigmentos y nuevos baños de tintura

Capítulo 4

Discusión de los resultados

Debe recordarse que los objetivos de esta tesis consisten en conseguir adsorber colorantes textiles, probar la capacidad del híbrido obtenido para integrarlo en una pasta de estampación aportando el color y producir una desorción del colorante para que este pase de la arcilla a la fase acuosa y poder llegar a tintar de nuevo un sustrato textil.

Así pues, dentro de este capítulo se van a analizar los resultados obtenidos en los diferentes trabajos para conseguir los objetivos marcados. Estos resultados siguen un orden lógico de forma que primero se verán las técnicas instrumentales y los resultados de la adsorción para una vez generado el híbrido proceder a su uso para realizar estampaciones y tinturas sobre sustratos textiles.

4.1. Adsorción de colorantes textiles

Como ya se ha comentado, el primer paso en este trabajo es el de conseguir adsorber los colorantes presentes en las aguas residuales textiles mediante el uso de nanoarcillas. Para ello se describe el proceso de preparación previa de la arcilla y las técnicas empleadas para conseguir una correcta adsorción.

4.1.1. Material adsorbente

El uso de nanotecnologías ha atraído la atención de muchos investigadores para diversos usos industriales [1], incluida la recuperación de aguas residuales con diferentes residuos. Por lo general, los adsorbentes a nanoescala presentan ventajas sobre otros elementos convencionales a granel gracias a su gran superficie específica y sus altas reactividades superficiales [2]. Por ejemplo, se han utilizado nanoarcillas modificadas como adsorbentes de colorantes no iónicos, aniónicos y catiónicos. A partir de las diferencias de adsorción entre diferentes estructuras químicas y morfológicas de colorantes y arcillas, se han identificado las fuerzas de adsorción que desempeñan funciones importantes.

En este trabajo se ha hecho uso de la nanoarcilla hidrotalcita, debido a su estructura laminar que proporciona una gran capacidad de adsorción y la fácil dispersión que facilita mucho el trabajo de laboratorio sin aglutinamientos. Nanoarcilla es el término general utilizado para referirse a las arcillas minerales con una estructura fosilicatada o laminar del orden de nm y superficies de 50-150 nm o más.

La hidrotalcita (H), $Mg_6Al_2(CO_3)(OH)_{16}\cdot 4(H_2O)$ (Figura 4.1.1) [3]–[5], se clasifica como un mineral de tamaño nanométrico porque una de las dimensiones de su laminado mide menos de 20 nm. Debido a su estructura característica, pertenece a la categoría de los "hidróxidos dobles estratificados" (LDH). Esta capa tiene un área superficial específica (SSA) comprendida entre $71\text{ m}^2\cdot\text{g}^{-1}$ y $104\text{ m}^2\cdot\text{g}^{-1}$ [6]. Los investigadores muestran un interés cada vez mayor por estos compuestos gracias a su amplia gama de aplicaciones como catalizadores, y también en medicina, adsorción, etc. [7]. Existen diferentes métodos mediante los cuales se produce la adsorción de aniones por los compuestos LDH. El más común es el que se produce por adsorción directa en dispersión. La cristalinidad de un

sólido limita dicha adsorción por la polaridad del medio, la temperatura, tamaño del anión y pH [3]–[5].

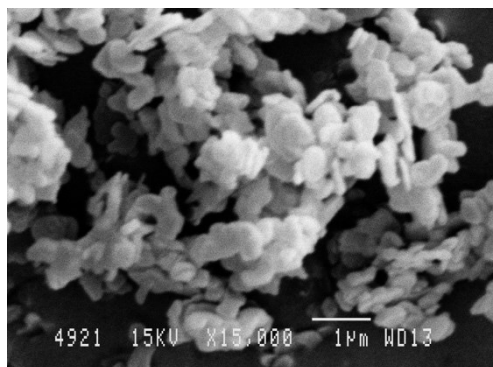


Figura 4.1.1. SEM de hidrotalcita (adaptada de Figure 3.2.1)

El segundo método es la calcinación, aunque requiere algo más de tiempo, ofrece claras ventajas. Estudios anteriores han demostrado que la hidrotalcita tiene memoria de forma tras ser expuesta a una fuente térmica elevada. Esto cambia sustancialmente su disposición laminar inicial, que se recupera durante los procesos de hidratación posteriores. Tras ser expuesta a temperaturas de 450-550 °C, se reconstruye tal y como se ha descrito anteriormente gracias a los aniones presentes en la disolución y su incorporación a la nueva estructura de la nanoarcilla [8]–[10].

4.1.2. Calcinación de la hidrotalcita

Para sintetizar los componentes híbridos de este trabajo se ha trabajado para todos los ensayos con la hidrotalcita, la cual fue calcinada previamente para incrementar su capacidad de adsorción según Dos Santos R.M.M. [11]. En ese procedimiento de calcinación se destruye la estructura de la H y se reduce la cantidad de varios aniones como el CO_3^{2-} . Esta pérdida de aniones permite reincorporar nuevos aniones cuando la arcilla hidrotalcita calcinada (HC) se reconstruye al ser hidratada nuevamente gracias a su memoria de forma. En esta reconstrucción es cuando los colorantes aniónicos se incorporan a la estructura de la arcilla durante su recuperación. La Figura 4.1.2. muestra imágenes de la nanoarcilla, antes de calcinarla, después de haber sido calcinada y al reconstruirla nuevamente en la

rehidratación. Observando la morfología de las diferentes imágenes se puede ver como la estructura de la arcilla efectivamente se ha recuperado [12].

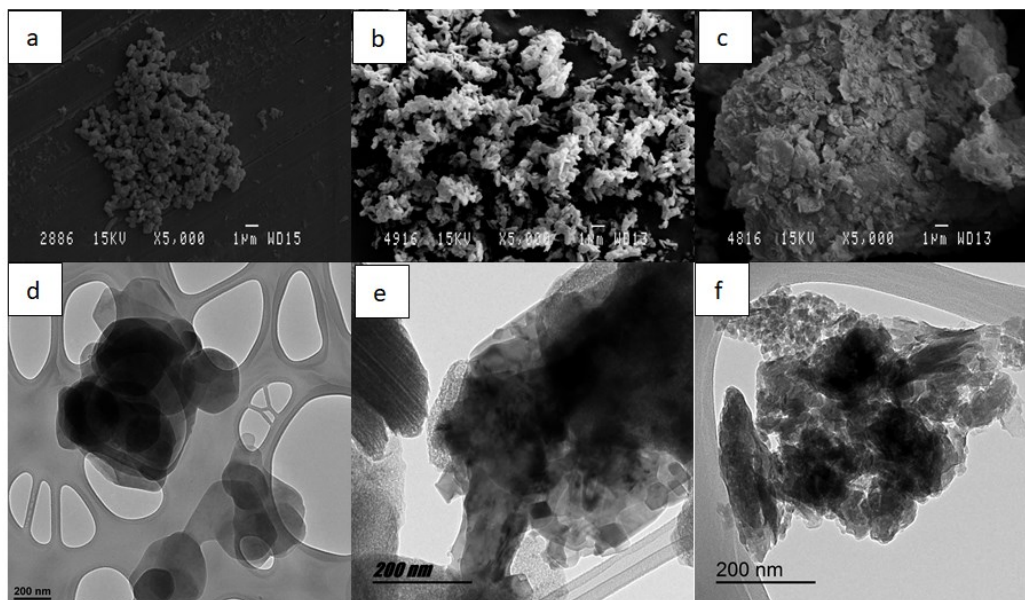


Figura 4.1.2. Micrografías SEM de diferentes muestras de H: (a) H original (b) HC calcinado (c) HC reconstruido. Micrografías TEM de diferentes muestras de H: (d) H original, (e) HC calcinado (f) HC reconstruido (adaptada de Figure 3.3.18)

4.1.2.1. Difracción de rayos-X (XRD)

Al realizar un estudio de difracción de rayos X se puede ver los resultados y la comparativa de la hidrotalcita antes (H) y después de ser calcinada (HC) en la Figura 4.1.3. Observando la línea H se pueden ver los picos de difracción que aparecen a los 11°, 23°, 34°, 39°, 46°, 60° y 61° que se atribuyen respectivamente a los planos de los cristales 003, 006, 012, 015, 018, 110 y 113 [13]. Tras la calcinación todos estos picos desaparecen y se puede ver en la línea de la HC unos picos de difracción que muestran una estructura amorfa de óxido mixto $Mg(Al)O_x$ [14].

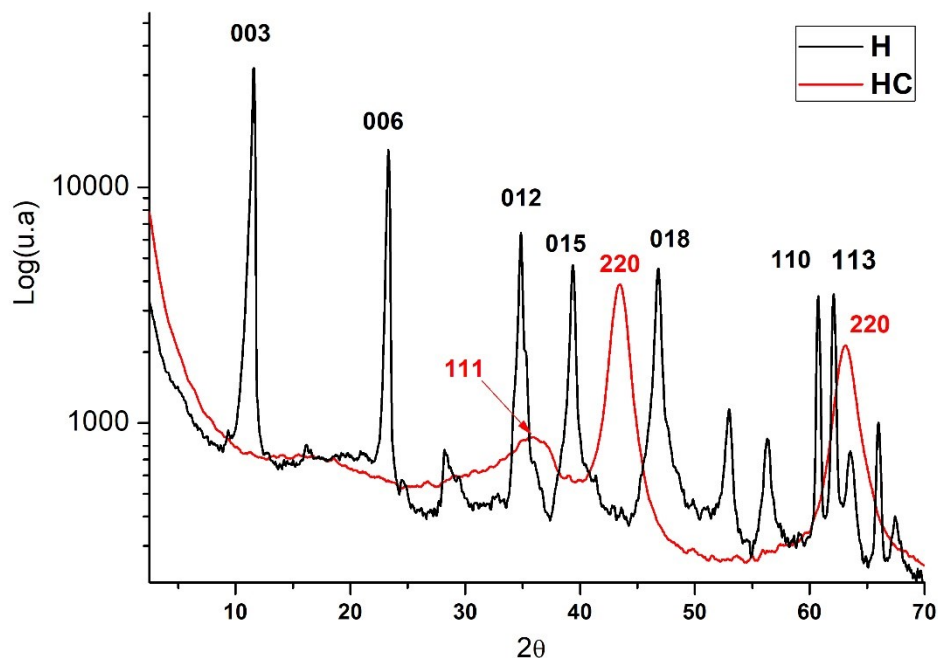


Figura 4.1.3. Patrones de difracción de la hidrotalcita sin calcinar (H) y la hidrotalcita después de la calcinación (HC) (adaptada de Figure 3.5.2)

Al incorporar la HC en la disolución de los colorantes se espera que la interacción producida entre la arcilla y el colorante haga cambiar en cierta forma la estructura cristalina durante la fase de rehidratación y reconstrucción de la nanoarcilla. En la Figura 4.1.4. se puede ver como se produce ese cambio si se centra el análisis en el plano 003 alrededor de los 11°. Ahí se observa como aparece el pico de la arcilla sin calcinar pero desaparece tras la calcinación producido provocado por el colapso que provoca la deshidroxilación en el espacio basal de las capas de la nanoarcilla y la exfoliación del espacio basal [15]. Este proceso va a servir de gran ayuda para que pueda penetrar la materia colorante y quedar fijada entre las láminas. De forma simultánea se va produciendo la penetración del colorante y la hidratación de la HC que dará como consecuencia la reconstrucción de su estructura debido a la memoria de forma que posee [8]–[10],[16]. En el caso de los colorantes aniónicos, estos se incorporarán a la estructura en lugar de otros aniones que estaban antes de la calcinación como el $-\text{OH}^-$ y el CO_3^{2-} .

Como se muestra en la Figura 4.1.4 la intensidad de la banda en los 11° se explica debido a que los colorantes poseen una estructura amorfa pero la H tiene una estructura cristalina [17]–[19]. En consecuencia, la banda variará su intensidad en función de la relación cuantitativa entre las fases cristalina (H) y amorfa (colorante). Se espera que la banda sea más intensa en aquellos compuestos que tengan una mayor proporción de fase H y menor proporción de la fase amorfa de colorante. Las curvas HDB199, HBY2 y HDR1 muestran menos intensidad que la H porque tienen una gran cantidad de colorante. Sin embargo, las muestras H2DB199, H2BY2 y H2DR1 tienen menos colorante y aun así baja su intensidad, lo que se puede atribuir a que la estructura de la hidrotalcita se está destruyendo durante el tratamiento de tintura-desorción en un proceso similar a la calcinación, perdiendo su forma cristalina y volviéndose más amorfa.

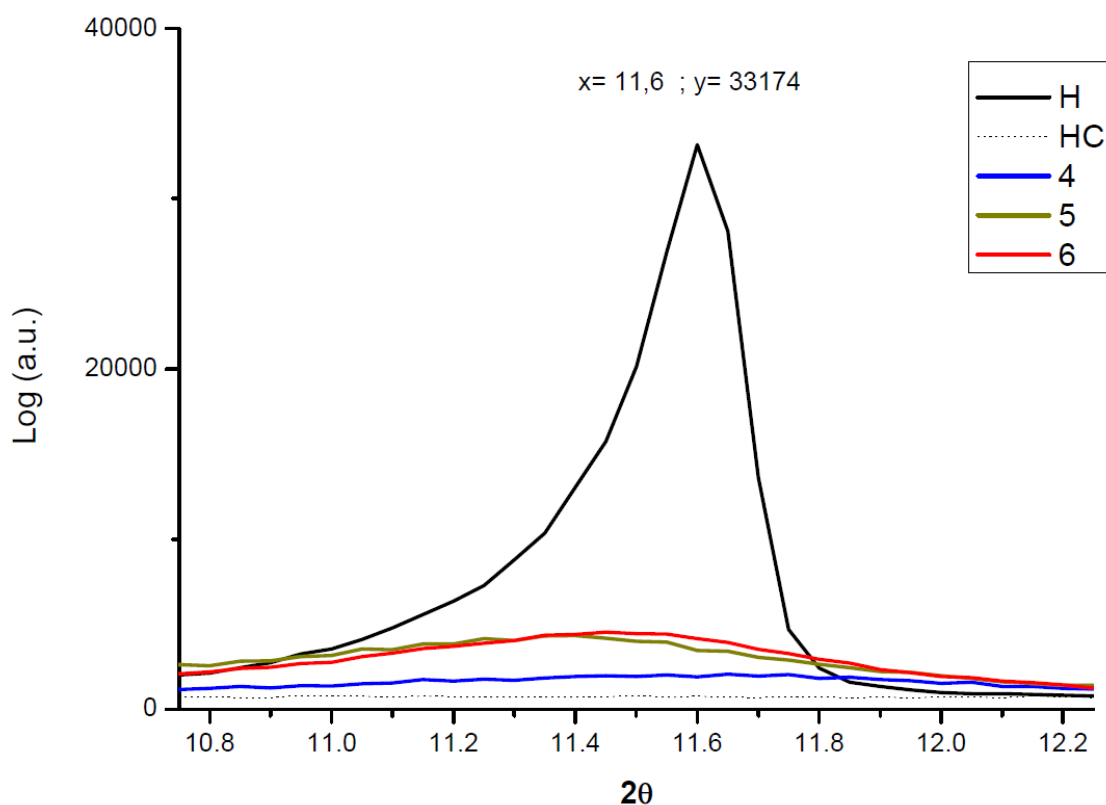


Figura 4.1.4. DRX para Hidrotalcita, Hidrotalcita calcinada y muestras híbridas 4-6 (adapta de Figure 3.4.7)

4.1.2.2. Análisis mediante espectroscopia infrarroja por transformada de Fourier FTIR-ATR

Mediante esta técnica instrumental se va a obtener información relevante para este estudio. El primer objetivo es el de determinar el efecto que la calcinación produce sobre la hidrotalcita. En la Figura 4.1.5. se ven dos bandas características, una a 1361 cm^{-1} que corresponde al -CO_3^{2-} [20],[21] y otra entre los $3200\text{-}3600\text{ cm}^{-1}$ centrada a 3408 cm^{-1} que se asigna al -OH del agua interlaminar producida por los estiramientos de los enlaces entre el oxígeno y el hidrogeno [11],[19],[21]. Asimismo se aprecian dos picos relevantes a 2850 y 2918 cm^{-1} debidos a las vibraciones de estiramiento de los grupos CH_2 [22]. Todas esas bandas desaparecen totalmente o se atenúan casi por completo en caso de la banda del -CO_3^{2-} tras el proceso de calcinación, lo que permitirá adherirse grupos aniónicos nuevos en la reconstrucción por hidratación. Otras bandas observadas se encuentran a 767 cm^{-1} por la translación del Al-OH , 640 cm^{-1} por vibraciones del NO_3^- y CO_3^{2-} y en 549 cm^{-1} por vibraciones del enlace Mg-O [19],[23].

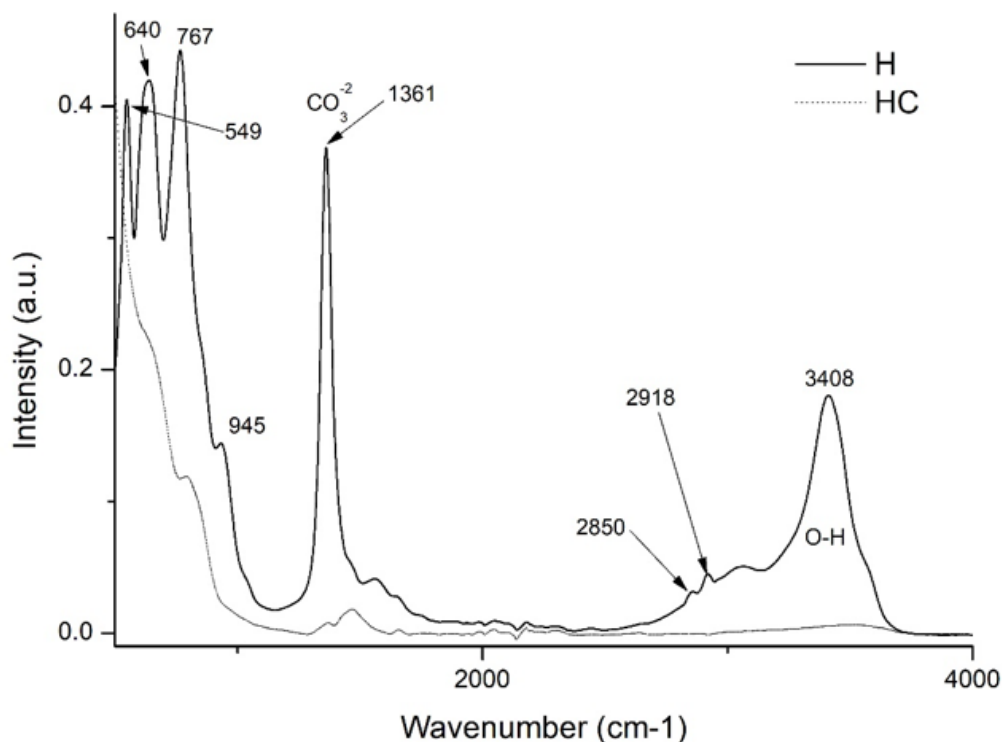


Figura 4.1.5. Comparación FTIR de hidrotalcita no calcinada (H) e hidrotalcita calcinada (HC) (adaptada de Figure 3.4.8)

4.1.2.3. Mediciones de superficie y porosidad (BET)

Las áreas superficiales BET, los volúmenes de poros y los tamaños de poros se muestran en la Tabla 4.1.1. Se han analizado y comparado los resultados de la hidrotalcita antes y después de la calcinación, así como después de la adsorción de algunos colorantes (HDR1, HDB199 Y HBY2) y su reconstrucción estructural. Los resultados muestran que el área superficial, el volumen de los poros y el tamaño de los poros aumentan tras la calcinación. Esto se debe a que durante la calcinación la estructura de la arcilla se abre. Estudios anteriores afirman que estos cambios se deben a la desgasificación de los catalizadores producida por la descomposición de los gases de la hidrotalcita en sus fases hidratadas [24]–[26]. Por otro lado, las muestras que han adsorbido el colorante tienen valores muy similares a los de la arcilla antes de la calcinación.

Tabla 4.1.1. Superficies, volúmenes de poros y tamaños medios de poros (adaptada de Table 3.5.5)

Muestra	Superficie (m ² /g)	Volumen poro (cm ³ /g)	Tamaño medio de poro (nm)
H	114.3	0.21	10.07
HC	239.6	0.37	18.7
HDR1	102.2	0.15	11.8
HDB199	93.1	0.22	10.15
HBV2	98.5	0.18	11.25

4.1.3. Síntesis de híbridos colorante/arcilla

Tras un proceso de tintura por agotamiento, el colorante permanece en el baño de tintura; al igual que tras el efecto de adsorción, el colorante que no ha sido adsorbido puede permanecer en las aguas residuales [27],[28]. Para determinar la cantidad de colorante en forma de concentración g·L⁻¹ en cada uno de estos casos, se utilizan previamente modelos de regresión simples de Lambert-Beer [29]. Partiendo de diversas diluciones de los colorantes a concentraciones controladas, se puede medir la absorbancia con un espectrofotómetro de transmisión y obtener las ecuaciones que figuran en la Tabla 4.1.2.

Tabla 4.1.2. Ecuación de Lambert–Beer y R² (adaptada de Table 3.3.6)

Colorante	Ecuación	R ²
Direct Blue 199 (B199)	$y = 21.784 x - 0.015$	0.9982
Reactive Yellow (YD)	$y = 14.943 x - 0.0021$	0.9993
Direct Red 23 (R23)	$y = 34.357 x - 0.0148$	0.9991
Direct Blue 71 (B71)	$y = 17.09 x - 0.0233$	0.9987

Uno de los objetivos de este trabajo es conocer la cantidad máxima de colorante que se puede adsorber, para lo cual se estableció la ecuación 4.1.1. Se han realizado varias disoluciones de colorantes a diferentes concentraciones y se ha variado la relación arcilla HC/concentración de colorante siguiendo un Diseño Factorial Completo General de experimentos (DoE) 4² (Tabla 4.1.3.), para ver qué cantidad de colorante puede absorber. En la Tabla 4.1.3. se muestran las 16 muestras y las condiciones experimentales. Además,

Recuperación del colorante de aguas residuales textiles mediante nanoarcillas para su reutilización como pigmentos y nuevos baños de tintura

se utilizó la opción de aleatorización en la selección del colorante para evitar sesgos experimentales. La columna "x" establece la relación de $\text{g}\cdot\text{L}^{-1}$ de arcilla dividido por $\text{g}\cdot\text{L}^{-1}$ de colorante según la Ecuación 4.1.1.

Ecuación 4.1.2. Ratio Arcilla/Colorante

$$x = \frac{\text{arcilla } \text{g} \cdot \text{L}^{-1}}{\text{colorante } \text{g} \cdot \text{L}^{-1}}$$

Table 3.3.7)

Muestra nº	Colorante	g·L ⁻¹ colorante	g·L ⁻¹ arcilla	x
1	Direct Red 23	0.05	10	200
2	Direct Blue 199	0.05	10	200
3	Direct Blue 71	0.05	10	200
4	Yellow Drimaren	0.05	10	200
5	Direct Blue 71	0.05	5	100
6	Yellow Drimaren	0.05	5	100
7	Direct Red 23	0.05	5	100
8	Direct Blue 199	0.05	5	100
9	Yellow Drimaren	1	2	2
10	Direct Red 23	1	2	2
11	Direct Blue 199	1	2	2
12	Direct Blue 71	1	2	2
13	Yellow Drimaren	1	0.5	0.5
14	Direct Red 23	1	0.5	0.5
15	Direct Blue 199	1	0.5	0.5
16	Direct Blue 71	1	0.5	0.5

Así pues, para valorar la capacidad de adsorción de la hidrotalcita se han preparado 4 L de disolución de cada uno de los colorantes a estudiar a una concentración de 1g·L⁻¹ y se prepararon cada una de las 16 muestras siguiendo las concentraciones de la Tabla 4.1.3. Una vez preparadas cada una de la mezclas se someten a agitación utilizando un sistema de agitación magnético en el que se empieza aplicando la máxima velocidad posible a 1600 r.p.m. durante 2 horas para después pasar a una velocidad de 500 r.p.m. durante 22 horas más [30]. En las primeras 2 horas se busca una penetración del colorante con la máxima fuerza centrífuga, pero después se bajan las revoluciones para conseguir que el colorante no salga de nuevo de la arcilla y quede lo más estable posible permitiendo su acomodación en la estructura de la nanoarcilla reconstruida.

A continuación, se procede a separar el híbrido formado por la hidrotalcita y el colorante del resto del agua. Para ello se somete la disolución a un filtrado utilizando papel de filtro y por gravedad toda la parte acuosa se separa de la sólida para de esta forma poder recolectar el híbrido en forma sólida transcurridas 48 horas. Después se toman muestras del agua que ha caído por gravedad. Esta agua se lleva al espectrofotómetro de transmisión

donde con la lectura de absorbancia y utilizando las ecuaciones de la Tabla 4.1.2. se calculara la concentración de colorante que todavía queda en la disolución y no se ha adsorbido [31],[32]. Por otra parte, el híbrido sólido se liofiliza [33],[34]] para poder extraer toda el agua que tuviera y evitar aglutinamientos que pudieran producirse en un secado en la estufa.

4.1.4. Rendimiento de adsorción

Los resultados obtenidos confirman la gran capacidad de la nanoarcilla para adsorber colorantes textiles (Tabla 4.1.4.), alcanzando en todos los casos porcentajes superiores al 95% de adsorción, al igual que ya se ha analizo por otros autores en otros estudios similares (29,44-47), en los que se ensayaron las propiedades de adsorción de la H para la eliminación de varios colorantes como Rojo Congo, Rojo Ácido 1, Naranja de Metilo y Azul de Metileno, etc. Las pruebas en las muestras 13-16 se completaron ya que se observó que la arcilla está totalmente saturada y no es capaz de absorber más colorante. Una vez alcanzado el punto de saturación de la arcilla, es posible definir la relación "x" expresada anteriormente.

Tabla 4.1.3. Diferencia de concentración tras la adsorción de HC (adaptada de Table 3.3.1)

Muestra nº	Colorante	Conc. ini. g·L ⁻¹	Conc. final. g·L ⁻¹	absorbancia	Ads(%)
1	Direct Red 23	0.05	4.89E-04	0.002	99.22
2	Direct Blue 199	0.05	7.80E-04	0.002	98.43
3	Direct Blue 71	0.05	1.77E-03	0.007	96.45
4	Yellow Drimaren	0.05	5.42E-04	0.006	98.91
5	Direct Blue 71	0.05	1.60E-03	0.004	96.81
6	Yellow Drimaren	0.05	3.41E-04	0.003	99.32
7	Direct Red 23	0.05	5.47E-04	0.004	98.91
8	Direct Blue 199	0.05	8.72E-04	0.004	98.26
9	Yellow Drimaren	1	7.43E-04	0.009	99.93
10	Direct Red 23	1	5.76E-04	0.005	99.94
11	Direct Blue 199	1	8.26E-04	0.003	99.92
12	Direct Blue 71	1	1.71E-03	0.006	99.83
13	Yellow Drimaren	1	3.89E-03	0.056	99.61
14	Direct Red 23	1	1.94E-03	0.052	99.81
15	Direct Blue 199	1	2.85E-03	0.047	99.72
16	Direct Blue 71	1	5.34E-03	0.068	99.47

4.1.5. Caracterización del híbrido

A continuación, se procedo con el análisis de los resultados de los híbridos obtenidos tras la adsorción de colorante por parte de la hidrotalcita. Para ello se analizarán parámetros como el color, reflectancia solar total (TSR), comportamiento térmico (TGA), FTIR, XRD, XPS o EDX.

4.1.5.1. Medida del color

En la Figura 4.1.6, se muestran las mediciones de color de los híbridos de colorante y arcilla representadas en diagramas cromáticos. Para los cálculos colorimétricos de cada pigmento híbrido se utilizaron las mediciones de reflectancia $\rho(\lambda)$. Para realizar las comparaciones colorimétricas absolutas y relativas se siguieron las principales directrices de la norma CIE 15:2004 [35] de la Comisión Internacional de Iluminación y Color (CIE). Se utilizaron los parámetros colorimétricos CIELAB codificados por el patrón CIE 1931 XYZ y la iluminación estándar D65. Los diagramas CIE a*b* y CIE-Cab*L*. La Figura 4.1.6. muestra que hay cambios en la tonalidad debidos al colorante y a la concentración. Por ejemplo, las muestras con Yellow Drimaren son más amarillentas a bajas concentraciones (x= 2 o 0,5)

que las muestras a altas concentraciones ($x=200$ y 100). El mismo fenómeno se observa en las muestras con Direct Red 23.

Sin embargo, las muestras con $x=2$ con Direct Red 23, Direct Blue 71 y Direct Blue 199 son aparentemente acromáticas en comparación con las muestras menos concentradas a $x=0.05$ con los mismos colorantes. El croma se ve afectado por la concentración de colorante y el tono. Con muestras amarillas es más difícil obtener muestras más oscuras y acromáticas como se puede ver en las zonas resaltadas L^*-Cab^* . Además, a medida que aumenta la proporción de colorante (x disminuye), el L^* de las muestras es bajo y el croma disminuye, lo que permite abarcar una gama de colores más amplia. Se observa un desplazamiento del tono hacia el verde en las muestras Direct Blue 199 cuando las concentraciones aumentan a $x=100$ y 200 . La gama de colores representada por el área bajo los diagramas $L^* Cab^*$ es mayor con las muestras con Direct Blue 199 que con las muestras con Direct Blue 71, que son menos cromáticas y brillantes. Por último, la gama de colores con las muestras con Direct Red 23 es más amplia en las muestras con Direct blue 71.

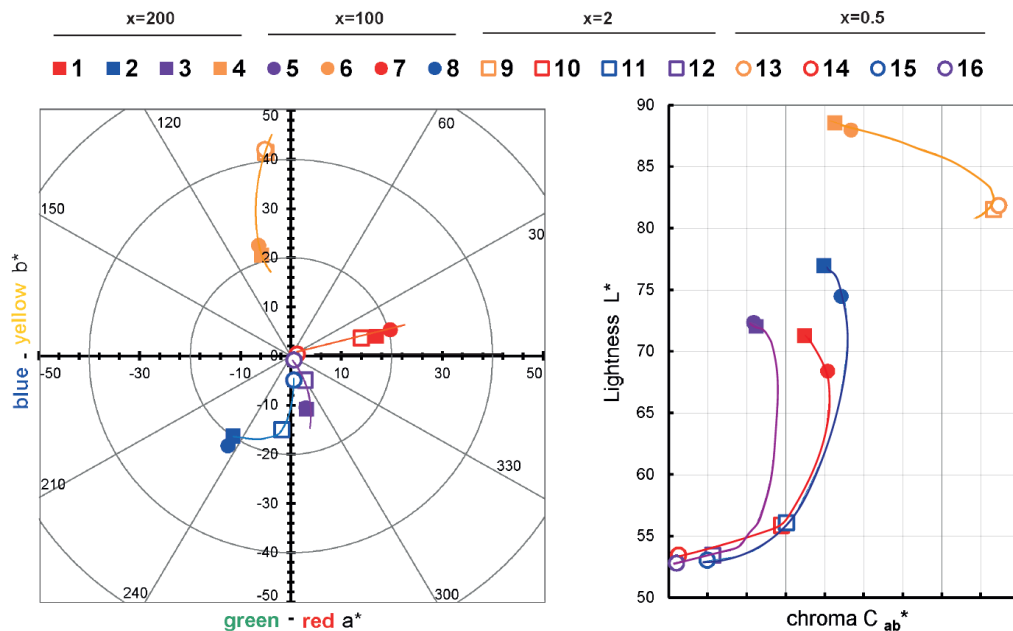


Figura 4.1.6. Diagramas CIELAB gráficos para pigmentos híbridos sintetizados en condiciones 1-16 utilizando el iluminante D65 y el observador estándar CIE-1931 XYZ. Izquierda: diagrama de color CIE- $a^* b^*$; derecha: Diagrama de color CIE- $Cab^* L^*$ (adaptada de Figure 3.3.2)

4.1.5.2. Reflectancia solar total

La cantidad de energía que absorbe un sustrato en sus capas más superficiales en forma de radiación solar es la que determina la cantidad de calor acumulada en esa superficie. Uno de los factores más determinantes de este fenómeno es el tiempo de exposición que sufre la superficie. Para conseguir recubrimientos con superficies frías, es necesario alcanzar la máxima reflexión de la radiación solar. Esta capacidad de reflexión de un cuerpo se expresa numéricamente mediante la reflectancia solar total (TSR), considerando un 0% de absorción total y un 100% de reflexión completa.

Para calcular la reflectancia solar es necesario disponer de los datos de reflectancia solar del sustrato en bruto y aplicar los factores de ponderación solar para cada longitud de onda a analizar. Todos estos cálculos están incluidos en las normas ASTM G173-03 [36]. Para calcular el grado de absorción solar total realizado por el híbrido, se debe realizar el cálculo de la operación $(1 - \text{TSR})$.

Tabla 4.1.4. Valores TSR (adaptada de Table 3.3.3)

Colorante	Ref. muestra	TSR %
Direct Red 23	1	58.50
Direct Blue 199	2	58.45
Direct Blue 71	3	55.27
Yellow Drimaren	4	63.45
Direct Blue 71	5	56.27
Yellow Drimaren	6	67.49
Direct Red 23	7	55.14
Direct Blue 199	8	56.08
Yellow Drimaren	9	58.30
Direct Red 23	10	47.44
Direct Blue 199	11	36.14
Direct Blue 71	12	38.55
Yellow Drimaren	13	58.80
Direct Red 23	14	29.47
Direct Blue 199	15	29.42
Direct Blue 71	16	32.00

La Tabla 4.1.5 muestra una comparación de la saturación máxima ($x = 0,5$) a la mínima ($x = 200$) de la arcilla tras la adsorción del colorante. La Figura 4.1.7. representa la relación “x” máxima y mínima para los 4 colorantes. En todas estas muestras, el comportamiento de la luz visible depende de la estructura del colorante y afecta a la percepción del color (tono, croma y luminosidad). En el infrarrojo cercano de 700-1400 nm las diferencias debidas a la relación x son significativas, sin embargo, de 1400-2400 nm el comportamiento de las muestras es más próximo. Aquí la estructura de la arcilla tiene un efecto más fuerte sobre la contribución del TSR (%) que la concentración de colorante.

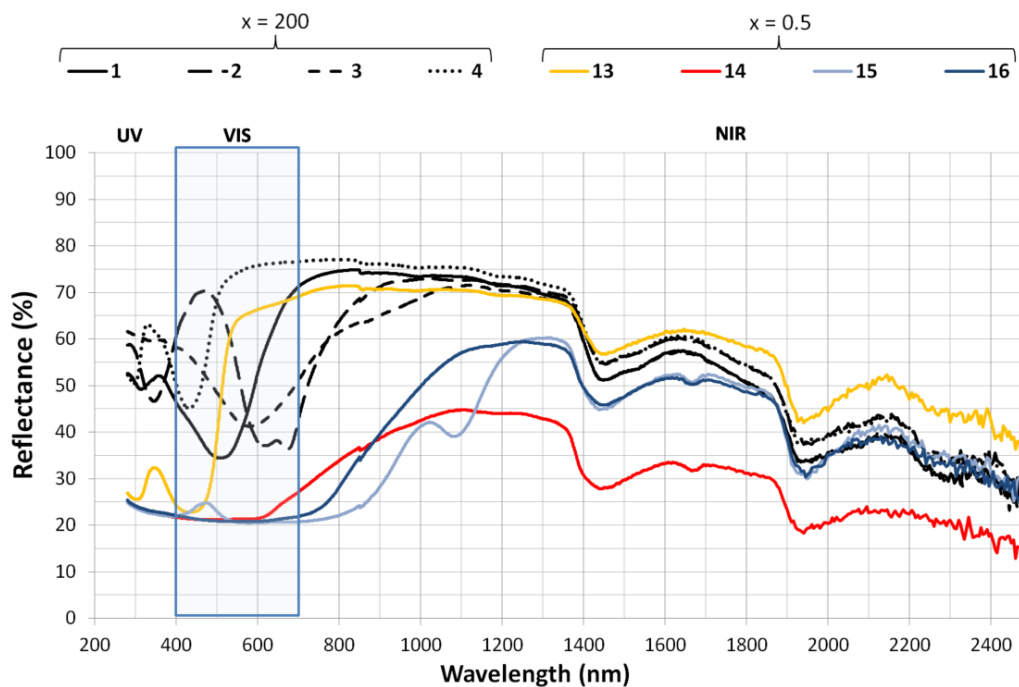


Figura 4.1.7. TSR(%) para cada híbrido con carga máxima y mínima de colorante (adapta de Figure 3.3.3)

La Figura 4.1.8 muestra que los valores de TSR(%) parecen estar correlacionados con la concentración de arcilla/colorante. Como era de esperar, las muestras con valores bajos de L^* tienen un TSR(%) bajo debido a la menor reflectancia, principalmente en el espectro visible. Además, las muestras amarillas tienen más TSR(%) por las mismas razones. Sin embargo, se pueden encontrar más diferencias entre todas las estructuras de colorantes y relaciones x, pero no es posible saber si esas diferencias son estadísticamente significativas sin el análisis de varianza.

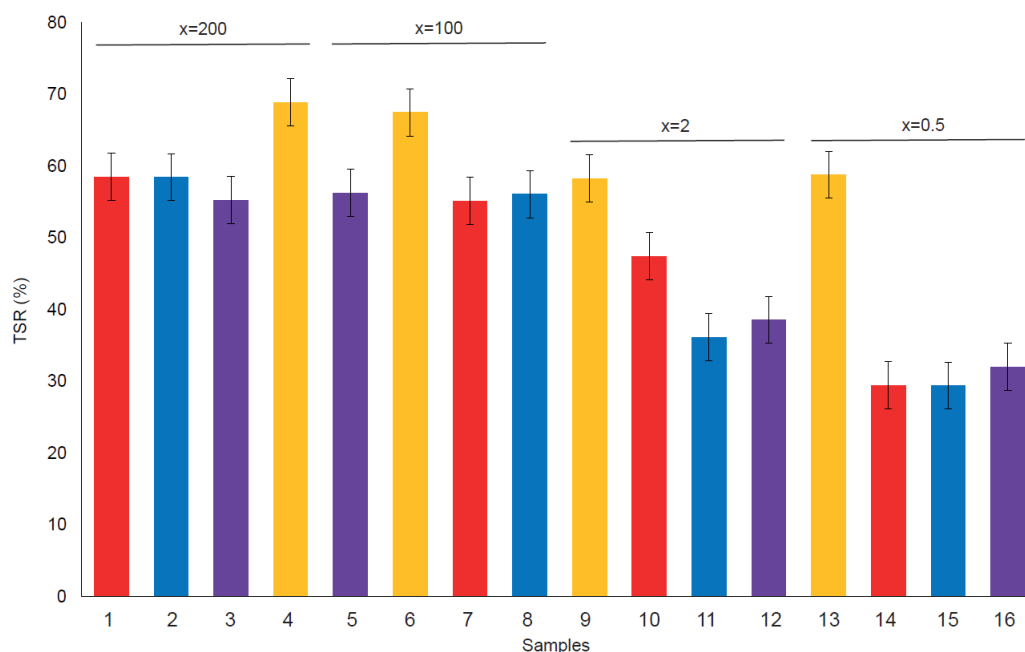


Figura 4.1.8. Reflectancia Solar Total (TSR(%)) para cada muestra (adaptada de Figure 3.3.5)

4.1.5.3. Termogravimetría (TGA)

Los resultados obtenidos en el TGA se muestran en las Figuras 4.1.9 a 4.1.14. La Figura 4.1.9 muestra las curvas de degradación frente a la temperatura de cada colorante y también se analiza la degradación de la arcilla. Las curvas de la parte inferior de este primer gráfico muestran las líneas d(YD), d(B71), d(R23), d(B199) y d(H), que se derivan de las primeras curvas que indican los picos específicos de degradación (DTGA). Los resultados muestran que el Direct Red 23 y el Reactive Yellow comienzan a degradarse antes, pero su declive es gradual y menos marcado dentro de un rango aproximado de 217-556 °C. Por otra parte, el Blue 199 muestra un pico marcado a 367-482 °C. La degradación del Direct Blue 71 es la más baja y su degradación la más lenta.

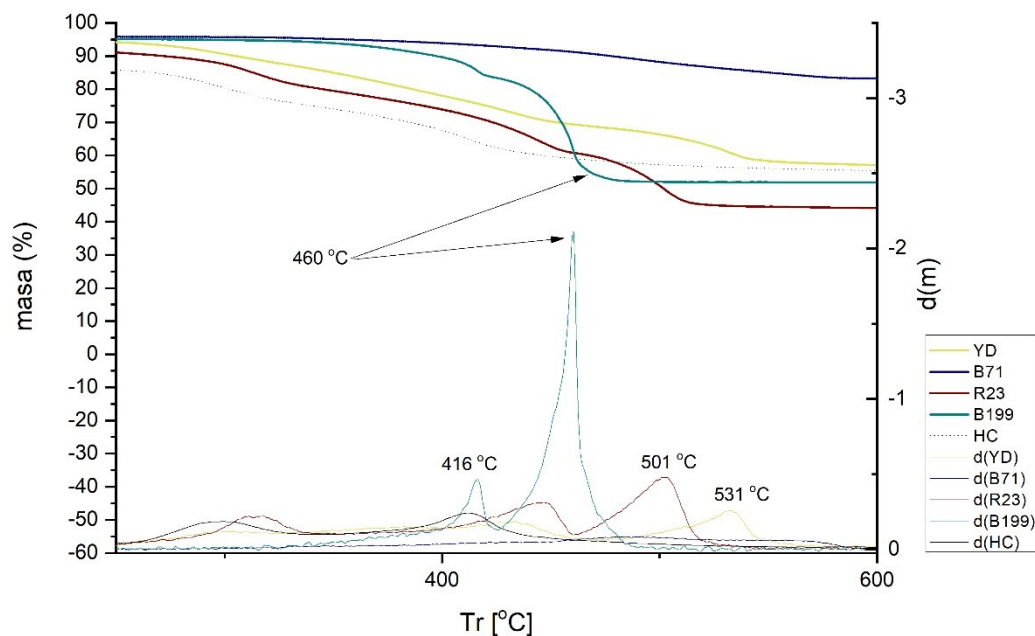


Figura 4.1.9. TGA y DTGA de cada colorante y de la hidrotalcita

La Figura 4.1.10 muestra una comparación del TGA y DTGA de HC y la muestra 3. Como puede observarse, la hidrotalcita sufre una pérdida de agua incluyendo la fisiorbida y la interlaminar en el rango de 100-170 °C. La segunda pérdida correspondiente al rango de 170-280 °C se atribuye a la pérdida de grupos -OH laminares. La tercera pérdida, registrada entre 280-600 °C, puede asignarse a la pérdida de iones carbonato y a la combustión del fragmento de molécula [37]–[39]. Cuando se analiza la hidrotalcita sola, sin haber adsorbido previamente ningún colorante, se observan picos a 208, 297 y 411 °C. La muestra 3 se analiza en detalle en la Figura 4.1.12.

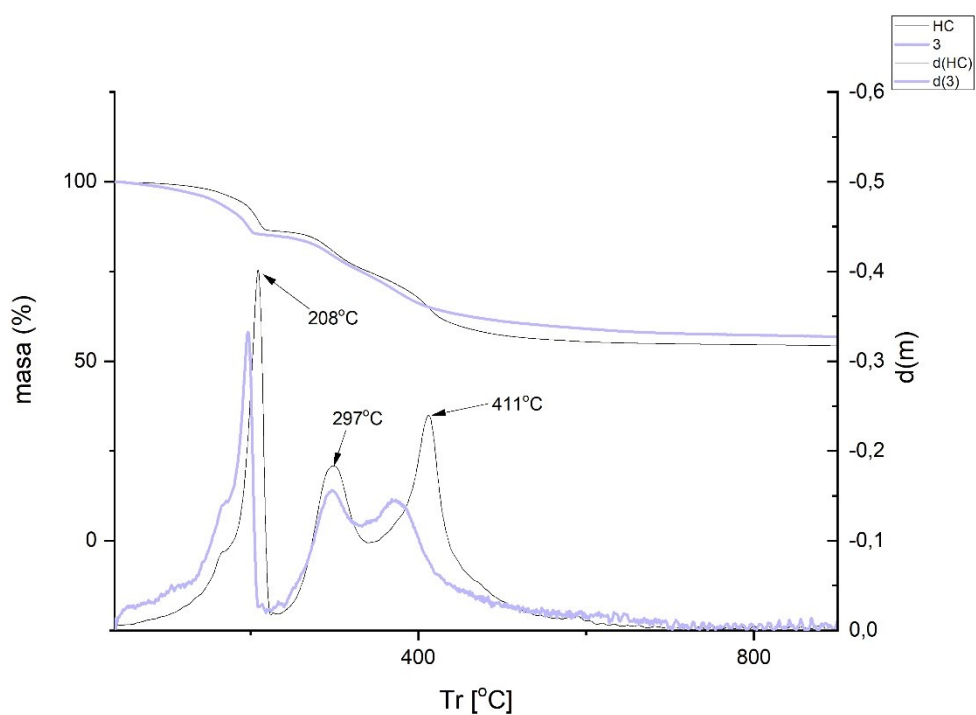


Figura 4.1.10. Comparación TGA y DTGA de hidrotalcita y muestra 3

El siguiente paso fue analizar los pigmentos híbridos tras la adsorción para ver cómo afecta la nanoarcilla al comportamiento térmico. Las figuras 4.1.11 a 4.1.14 muestran cómo se han alterado notablemente las propiedades iniciales de los colorantes.

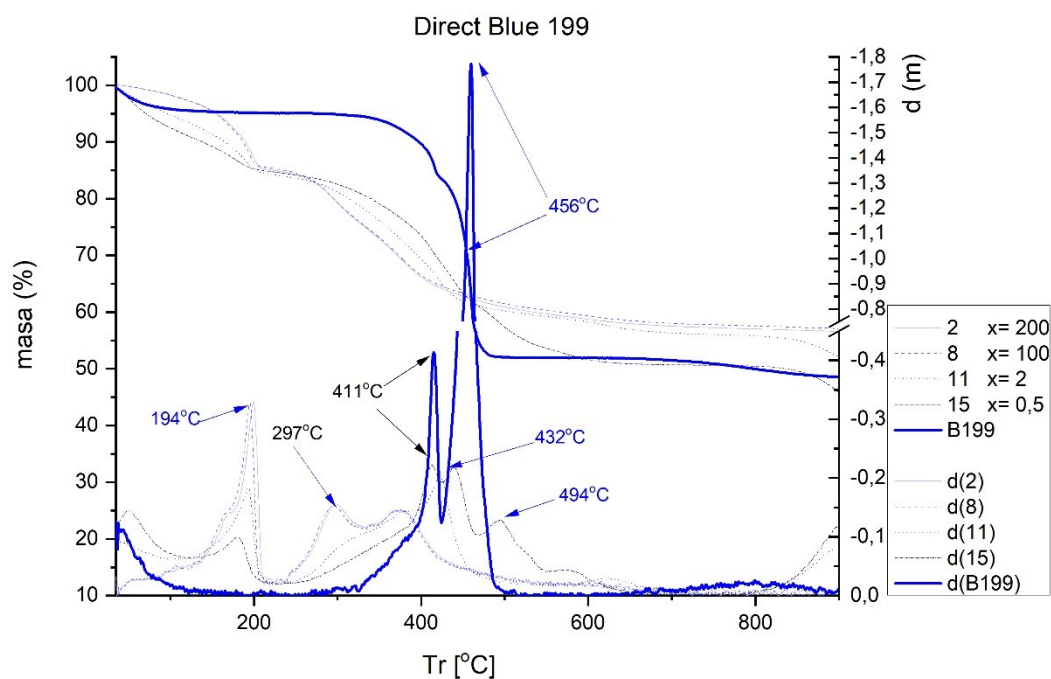


Figura 4.1.11. TGA y DTGA de Direct Blue 199 libre y adsorbido (adaptada de Figure 3.3.7)

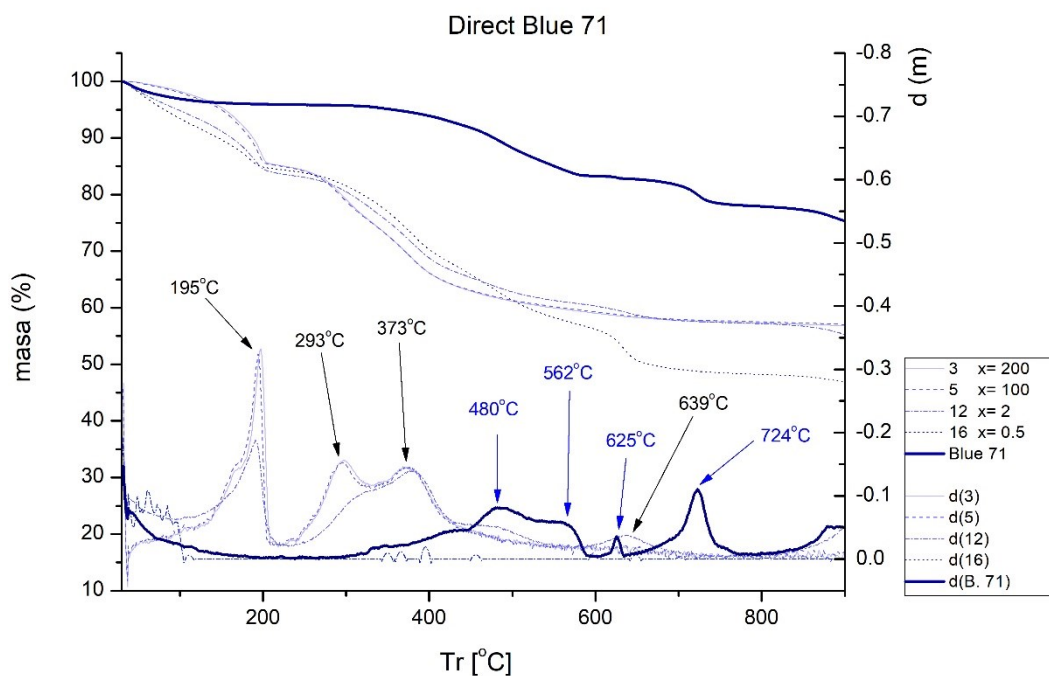


Figura 4.1.12. TGA y DTGA de Direct Blue 71 libre y adsorbido (adaptada de Figure 3.3.8)

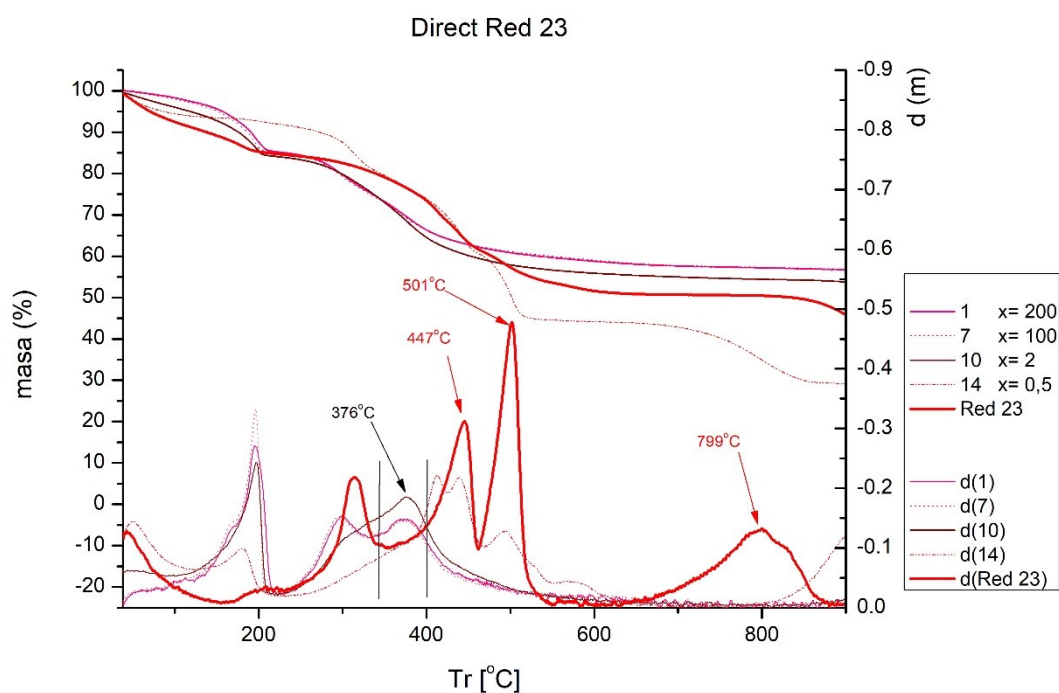


Figura 4.1.13. TGA y DTGA de Direct Red 23 libre y adsorbido (adaptada de Figure 3.3.9)

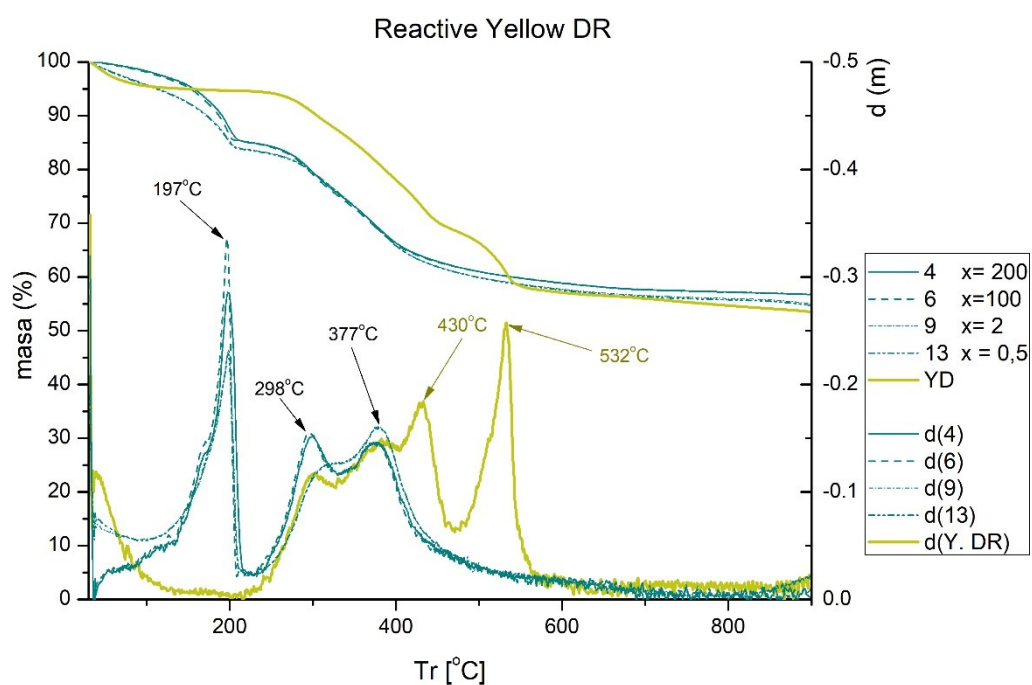


Figura 4.1.14. TGA and DTGA of Reactive Yellow DR free and adsorbed (adaptada de Figure 3.3.10)

La Figura 4.1.11 muestra el comportamiento térmico de B199. Se observan dos picos, uno a 411 °C y otro muy prominente a 456 °C. Tras la adsorción sobre HC, la altura del pico original de la arcilla disminuye ligeramente en el rango entre 164 y 208 °C. También se observan los picos a 297 y 411 °C, aunque con menor pérdida de masa en estos puntos. Para la muestra nº 11 se observan dos nuevos picos a 432 y 494 °C, muy probablemente debido a la considerable pérdida de masa sufrida por el colorante a 456 °C que se manifiesta en estos dos nuevos picos una vez adsorbido por el HC.

En el caso del colorante B71 (Figura 4.1.12), se observan varios picos en torno a 480, 562, 625 y 724 °C, que desaparecen tras la adsorción en la HC, aunque se aprecia un pico muy leve a 639 °C, muy probablemente producido por la degradación gradual del colorante entre los 562 y 625 °C, que se ha suavizado por efecto de la arcilla. Además, también aparecen picos a 195, 293 y 373 °C, típicos de la arcilla, como se observa en las Figuras 4.1.12 y 4.1.10 marcando los picos a 208, 297 y 411 °C.

En la Figura 4.1.13, correspondiente al colorante Direct Red 23 en sus estados libre y adsorbido, se observan picos en el colorante libre a 447, 501 y 799 °C que desaparecen completamente cuando el colorante es adsorbido por la arcilla. Se observa un único pico ancho en torno a 376 °C, que también se observa en la hidrotalcita.

Finalmente, con el Yellow DR (Figura 4.1.14), se observan dos picos a 430 y 532 °C, que desaparecen completamente cuando el híbrido se forma con la arcilla. De nuevo, los picos característicos asociados a la pérdida de agua en la arcilla aparecen a 197, 298 y 377 °C, tal y como se ha descrito en los casos anteriores.

En trabajos anteriores ya se ha podido observar cómo aumenta la estabilidad térmica de los híbridos. Experimentalmente se puede observar que los picos de los colorantes desaparecen cuando son adsorbidos por la arcilla. Se considera que hay dos razones por las que se consigue la mejora de esta propiedad [40],[41]. Por un lado, la estructura laminar de la arcilla tiene un efecto barrera que reduce la volatilidad de los compuestos y por otro

lado se produce una transferencia de energía entre el colorante y la arcilla cuando son sometidos a una temperatura que se aplica a la superficie de la arcilla [42],[43].

4.1.5.4. Difracción de Rayos-X (XRD)

Los resultados de la difracción de rayos X se pueden ver en la Figura 4.1.15. Esta figura muestra cómo tras la calcinación de la arcilla se ha abierto el espacio interlamilar para facilitar la penetración del colorante, y también cómo tras el proceso de adsorción se produce una recomposición parcial de la estructura original debido a la memoria, de forma que la hidrotalcita tiene memoria de forma [8]–[10],[16]. Tras la calcinación de la arcilla se produce un colapso estructural producido por deshidroxilación en el interior de las capas de este mineral [15]. Entre 11 y 12 grados se produce un pico que muestra la característica descrita y, como en el caso de la hidrotalcita (HC) calcinada, este pico desaparece debido a la apertura de dichas capas.

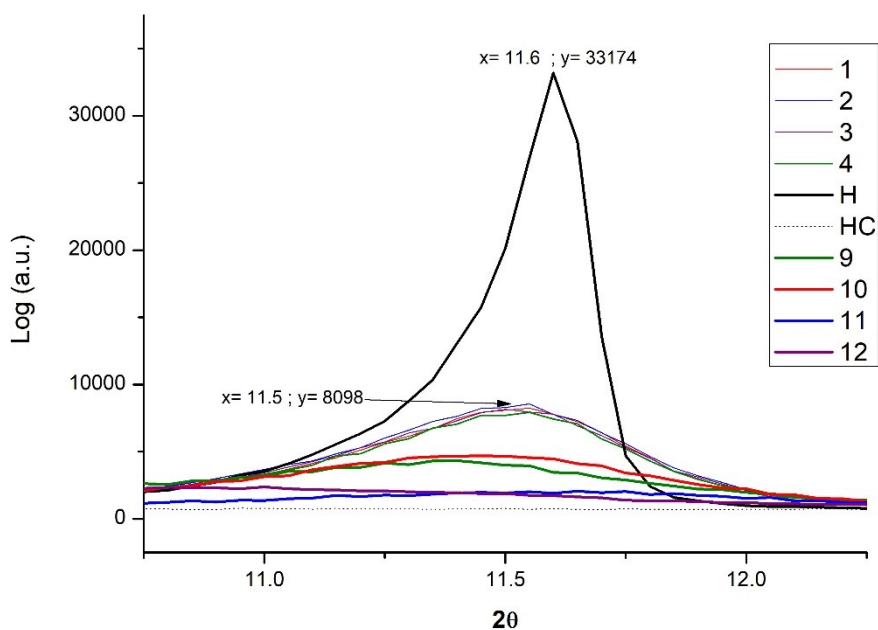


Figura 4.1.15. DRX para Hidrotalcita, Hidrotalcita calcinada, muestras 1-4 y muestras 9-12 (adaptada de Figure 3.3.11)

En este punto, cabe señalar que la hidrotalcita tiene una estructura cristalina [8],[9] y los colorantes una forma amorfa. El pico de la DRX es más alto cuando hay más estructuras cristalinas, pero esta estructura se pierde totalmente cuando el H se calcina para formar HC, pero se recupera en gran medida cuando se hidrata de nuevo. Los experimentos mostraron que el aumento de la concentración de colorante adsorbido en el HC provoca una disminución del pico de DRX, ya que aumenta la proporción de fase amorfa con respecto a la fase cristalina.

4.1.5.5. Espectroscopia infrarroja por transformada de Fourier FTIR-ATR

Las Figuras 4.1.16 a 4.1.19 muestran los espectros FTIR obtenidos para los colorantes antes y después de la adsorción sobre HC. En el caso de Direct Blue 199 (Figura 4.1.16) y Direct Blue 71 (Figura 4.1.17) el pico a 1100 cm^{-1} se atribuye a acetatos, formiatos, propionatos y benzoatos [44]. Trabajos previos indican que los picos situados entre $1400 - 1640\text{ cm}^{-1}$ [17],[18],[20],[22] corresponden a anillos bencénicos y que el pico mostrado a 1500 es característico del enlace azo [45] que en la muestra 12 puede verse suavemente desplazado a 1520 cm^{-1} . Otro pico se encuentra a 1035 cm^{-1} y corresponde a la vibración simétrica del sulfonato [38]. Muchos de los picos explicados confirman la presencia del colorante con mayor o menor intensidad, o no aparecen a bajas concentraciones (muestras 2 y 3), pero se aprecian al estudiarlos en las muestras 11 y 12 cuando encontramos más picos asociados al colorante adsorbido por la arcilla (obsérvense picos a 1500 y 1100 cm^{-1}). En los 4 híbridos se observa un aumento en la intensidad del hombro -OH ($3420-3460\text{ cm}^{-1}$) debido a la pérdida de agua unida por hidrógeno a los aniones carbonato $-\text{CO}_3^{2-}$ en el espacio basal. Esta agua también se sustituye en el proceso de adsorción [14].

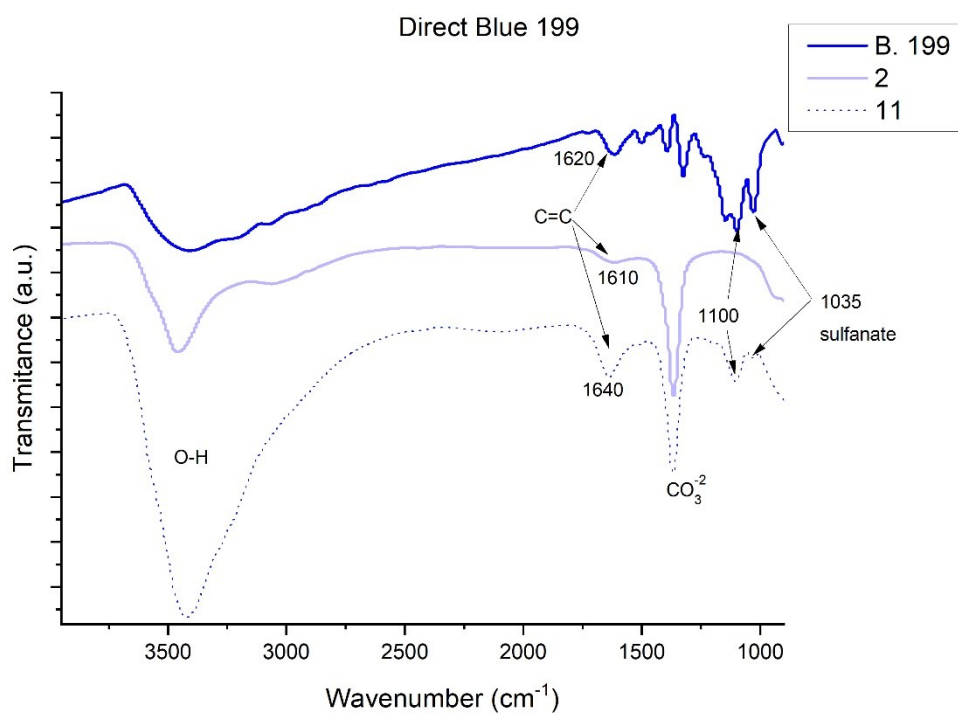


Figura 4.1.16. FTIR de Direct Blue 199, muestra 2 y muestra 11 (adaptada de Figure 3.3.13)

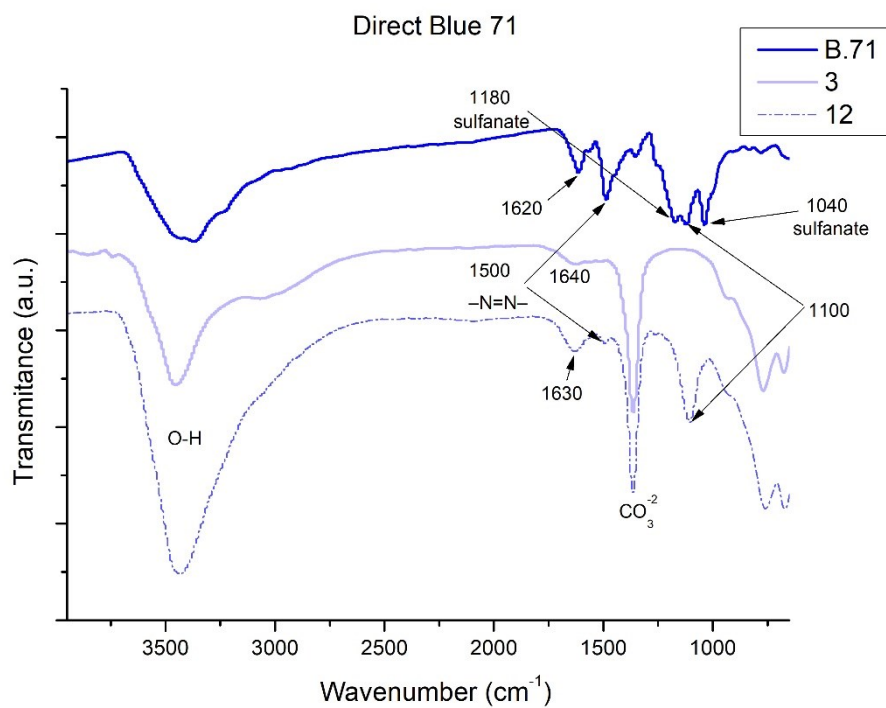


Figura 4.1.17. FTIR Direct Blue 71, muestra 3 y muestra 12 (adaptada de Figure 3.3.14)

En la Figura 4.1.18 se muestra el espectro FTIR del Direct Red 23. Los picos a 3308 y 3426 cm^{-1} corresponden a los estiramientos fenólicos -OH, C-N y agua. Los picos a 3308 y 3426 cm^{-1} corresponden a los grupos fenólicos -OH, estiramiento C-N y se puede observar claramente el agua [46]–[48]. Se observa otro pico a 1600-1610 cm^{-1} , que corresponde a los grupos aromáticos -C=C mientras que el pico a 1180-1170 cm^{-1} indica la presencia de enlaces simples de CO y OH [46]–[50]. El pico que aparece a 1480-1500 es característico del enlace azo [45]. Otro pico significativo aparece a 1050 cm^{-1} , que corresponde a los enlaces formados por el S-O [51],[52] correspondiente a los grupos sulfonato $-\text{SO}_3$ del grupo NaSO_3 .

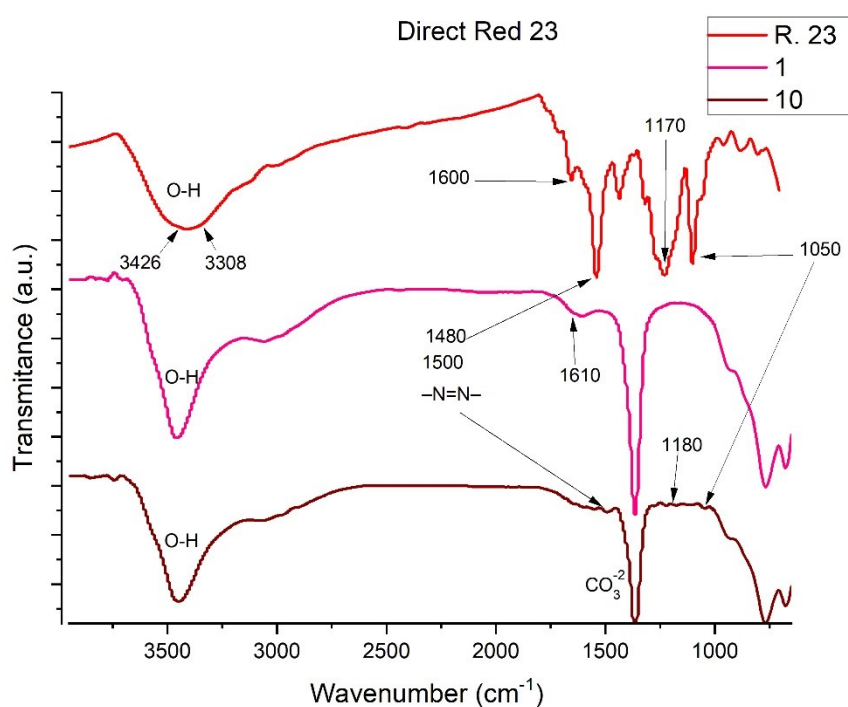


Figura 4.1.18. FTIR Direct Red 23, muestra 1 y muestra 10 (adaptada de Figure 3.3.15)

Estudiando el colorante Reactive Yellow DR (Figura 4.1.19) de nuevo se observa la banda del grupo fenólico -OH, estiramiento N-H y agua en 3446 cm^{-1} [46]–[48]. El colorante reactivo estudiado tiene grupos sulfato que se observan en los 1110 cm^{-1} [51],[52]. El pico que aparece a 1496 cm^{-1} es característico del enlace azo [45]. Otros picos que muestra el espectro en las muestras 4 y 9 en 1600 y 1630 cm^{-1} corresponden a los grupos aromáticos -C=C- (58-61), en el colorante dicho pico se sitúa en 1618 cm^{-1} .

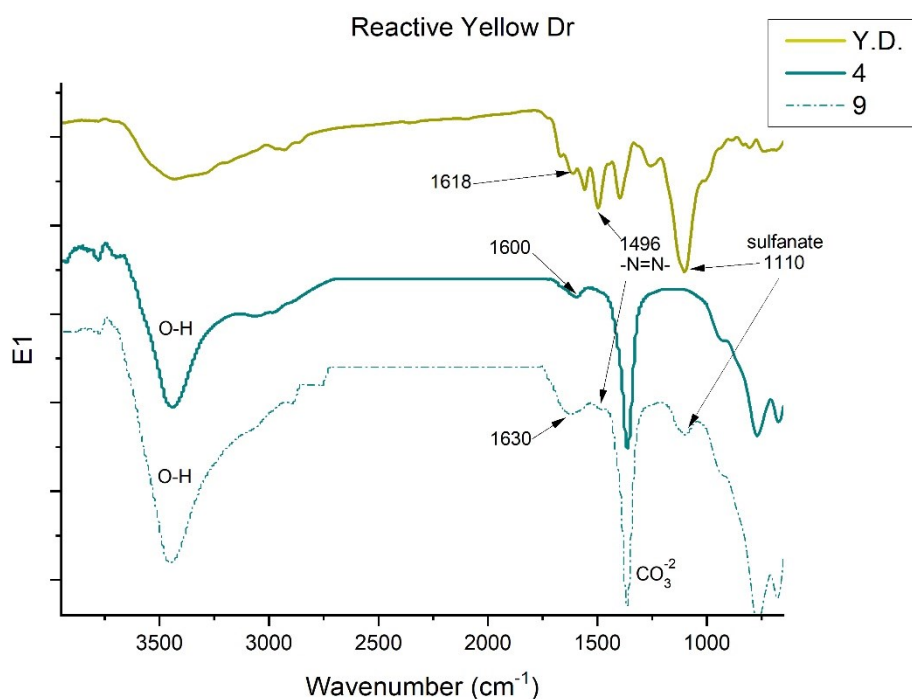


Figura 4.1.19. FTIR Yellow DR, muestra 4 y muestra 9 (adaptada de Figure 3.3.16)

Tabla 4.1.5. Resumen de la posición de los picos IR (adaptada de Table 3.3.5)

	H	B199	2	11	B71	3	12	R23	1	10	YD	4	9
-OH	3426	-	3460	3420	3426	3460	3440	3308	3460	3450	3438	3442	3450
-CO ₃ ²⁻	1365	-	1370	1370	-	1370	1370	-	1370	1370	-	1370	1370
-N=N-	-	1500	-	1520	1500	-	1500	1480	-	1500	1496	-	1496
-SO ₃	-	1035	-	1035	1180	-	1100	1050	-	1050	1110	-	1110
-C = C-	-	1620	1610	1640	1620	1640	1630	1600	1610	-	1618	1600	1630

Analizando los picos del grupo OH- y CO₃²⁻ (Tabla 4.1.6), se puede realizar un análisis semicuantitativo del área de cada uno de estos picos calculando el área bajo la curva. Los resultados obtenidos se muestran en la Figura 4.1.20. En esta figura se observa cómo la cantidad de carbonato que había originalmente en la hidrotalcita se ha reducido ya que, tras la calcinación y reconstrucción de la arcilla, el colorante ha pasado a formar parte de la estructura de la arcilla, ocupando gran parte de estas bandas OH- y CO₃²⁻ [8]–[10].

Estudiando más en profundidad los resultados es posible extraer la cantidad estimada de otros grupos funcionales del colorante que se han incorporado a la estructura

de los híbridos. Para ello, se tiene en cuenta la cantidad inicial de carbonato en la hidrotalcita junto con la cantidad que aparece posteriormente en los híbridos. La resta de uno y otro dará el número de nuevos grupos que se han incorporado (Figura 4.1.20).

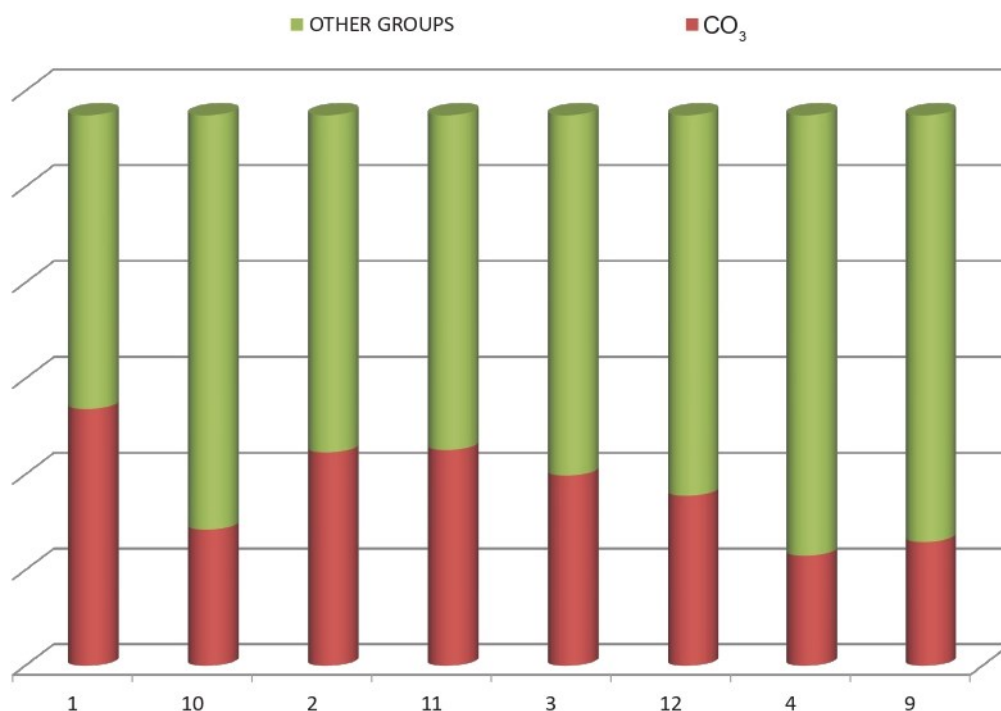


Figura 4.1.20. Análisis semicuantitativo y la incorporación de los nuevos grupos funcionales (adaptada de Figure 3.3.17)

4.2. Estampación con híbridos de arcilla-colorante

Tras optimizar y caracterizar los procesos de adsorción de colorantes textiles por parte de la hidrotalcita y conseguir híbridos estables, se seguirá con la fase de reutilización de ese híbrido para conseguir una nueva coloración de sustratos textiles. En este caso la coloración va a realizarse mediante la incorporación de ese híbrido a una pasta de estampación.

Para realizar un estudio de alcance y comparar los resultados, se han tomado 3 colorantes de diferentes características, el colorante directo Direct Blue 199 (DB199), uno

reactivo Reactive Yellow Drimarene (RYD) y otro disperso Disperse Red 1 (DR1) (Figura 4.2.1). Se han sintetizado tal y como se ha descrito en el apartado 4.1 y se han realizado diferentes pruebas de estampación sobre algodón y poliéster. Se han realizado estampaciones convencionales con estos mismos colorantes y con sus respectivos híbridos para poder comparar los resultados.

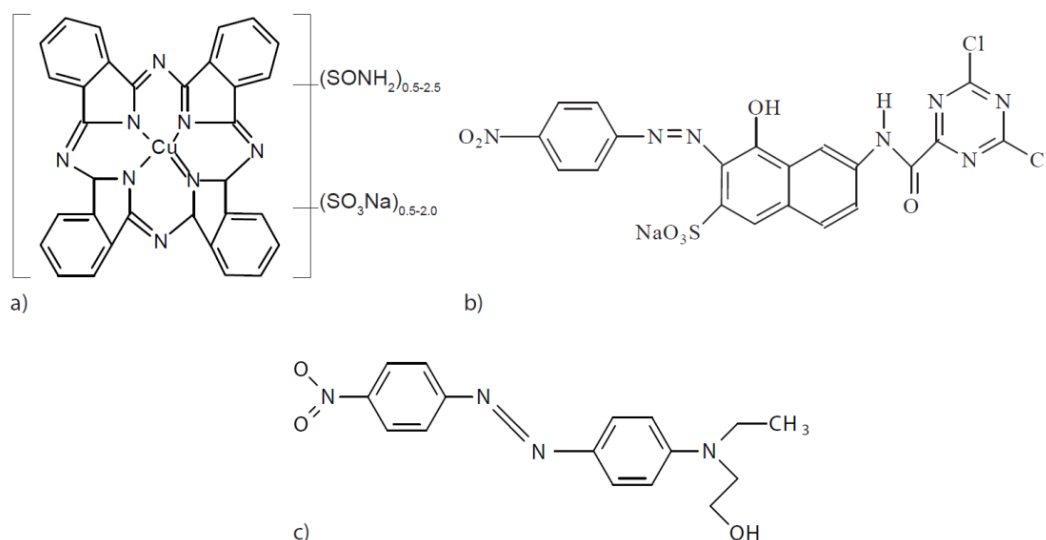


Figura 4.2.1. a) Direct Blue 199, b) Reactive Drimarene Yellow, c) Disperse Red 1 (adaptada de Figure 3.4.1)

4.2.1. Espectroscopia de fotoelectrones de rayos X (XPS)

En este caso se ha realizado un análisis XPS para comprobar la presencia de la arcilla y de los colorantes en cada uno de los híbridos. La Figura 4.2.2 y la Tabla 4.2.1 muestran los valores de energía de enlace para varios átomos que son decisivos para la presencia tanto de la arcilla como de los diferentes colorantes. La presencia en todas las muestras de C1s, O1s, Al2p3 y Mg1s en diferentes picos como 285, 530, 174 y 1308 eV respectivamente demuestran la presencia de la Hidrotalcita. Además, la presencia de N1s en los picos a 398 eV demuestran la presencia de nitrógeno de cada una de las muestras 4, 5 y 6.

Por otro lado, la muestra 4 tiene Cu₂p₃ con picos entre 932 y 945 eV, ya que el colorante azul directo 199 tiene el elemento cobre en su estructura. En cuanto a la muestra 5 con el colorante RYD, la presencia de azufre se distingue por la aparición de un pico a 168,01 eV que corresponde a S₂p₃.

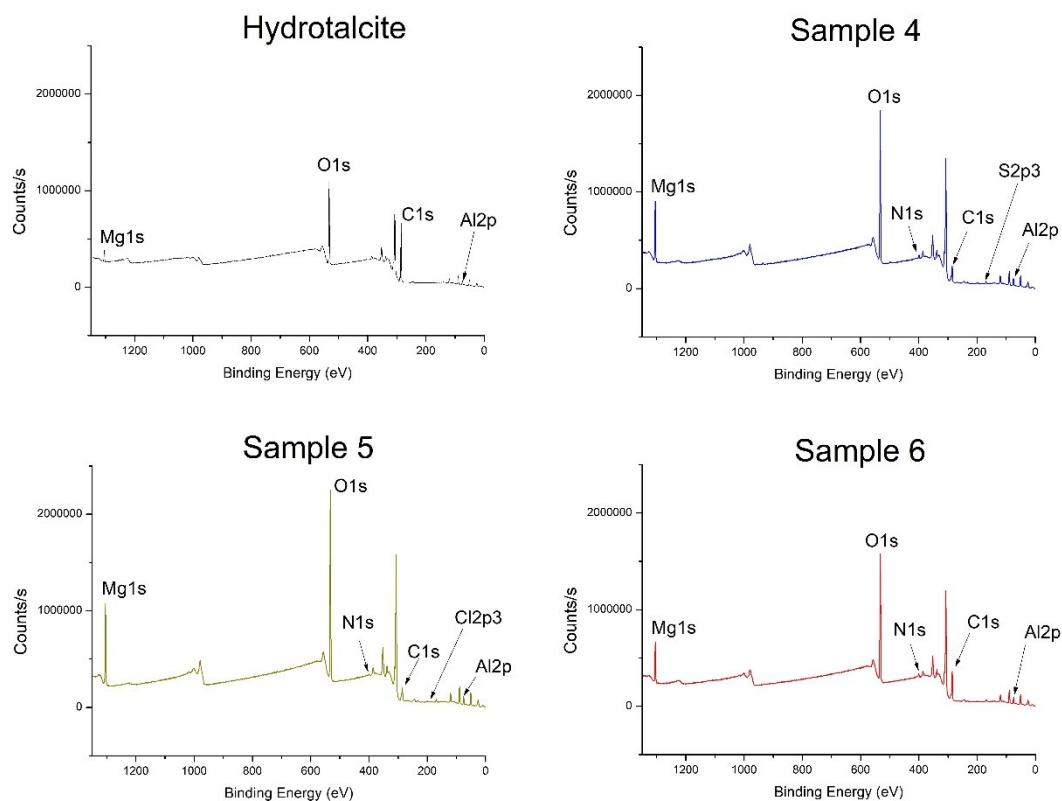


Figura 4.2.2. XPS Hidrotalcita y muestras 4, 5 y 6 (adaptada de Figure 3.4.10)

Tabla 4.2.1. XPS Hidrotalcita y muestras 4, 5 y 6 (adaptada de Table 3.4.7)

Cl	Sample 4				Sample 5				Sample 6			
	B.E	FWHM eV	Area	%	B.E	FWHM eV	Area	%	B.E	FWHM eV	Area	%
Cl1s	Hydrotalcite											
	284.56	1.1	121809.04	85.68	284.64	1.41	32377.81	51.39	284.61	1.46	67532	68.39
	285.22	1.02	7776	5.44	285.59	1.12	9590.51	15.22	285.8	1.44	17364.67	17.58
	285.99	1.33	2532.77	1.80	286.47	1.6	7341.42	11.68	287.14	2	4679.13	4.75
288.55	1.55	10054.6	7.08	288.91	1.72	13631.2	21.70	289.26	1.55	9139.44	9.28	
O1s	Hydrotalcite											
	530.29	1.56	39229.75	11.89	530.86	1.56	86427.73	15.12	530.7	1.49	89079.44	13.38
	531.49	1.68	278048.9	84.29	532.09	1.68	464049.21	81.28	531.75	1.71	383308.49	82.93
	532.81	1.59	12566.04	3.82	533.4	1.59	20556.34	3.60	533.47	1.99	19392.66	2.91
Al2p3	Hydrotalcite											
	73.82	1.47	9347.56	100	74.48	1.37	12635.1	100	74.41	1.41	10071.94	100
Mg1s	Hydrotalcite											
	1308.68	1.57	61905.82	100	1307.59	1.56	62773.06	100	1303.82	1.51	141429.97	95.2
N1s	Hydrotalcite											
	400.12	1.36	1098.18	9.91	401.51	1.56	848.35	12.70	401.18	1.66	1730.72	13.66
S2p3	Hydrotalcite											
	168.01	1.63	6512.31	100	168.01	1.63	6512.31	100	-	-	-	-
Cl2p3	Hydrotalcite											
	197.51	1.3	1573.73	65.79	199.99	1.42	826.37	34.21	-	-	-	-
Cu2p3	Hydrotalcite											
	932.8	1.95	2419.97	17.95	934.98	1.54	5670.67	43.59	-	-	-	-
Hydrotalcite	Sample 5											
	937.25	3.31	1554.34	12.82	942.19	3.36	1620.98	12.82	945.17	2.54	1661.52	12.82

4.2.2. Microscopía electrónica de barrido Espectroscopía de rayos X de energía + dispersión (SEM-EDX)

Para corroborar la presencia de los elementos componentes de los híbridos, la arcilla y los diferentes colorantes, se utilizó EDX. Los espectros resultantes de este análisis se muestran en la Figura 4.2.3. Partiendo de la composición de la hidrotalcita, se observan picos a aproximadamente 0,35, 0,5, 1,35, 1,5 y 1,85 keV correspondientes a los elementos C, O, Mg, Al y Si respectivamente. El análisis de las muestras híbridas cargadas con los colorantes muestra los mismos picos que en la hidrotalcita y otros nuevos elementos que confirman la presencia de los respectivos colorantes. Así, en la muestra 4 aparece un pico a 2,3 keV que se atribuye al azufre (S) y a aproximadamente 8 keV correspondiente al cobre (Cu). En la muestra 5, la presencia de colorante (Cl) puede evaluarse por el pico a 2,6 keV.

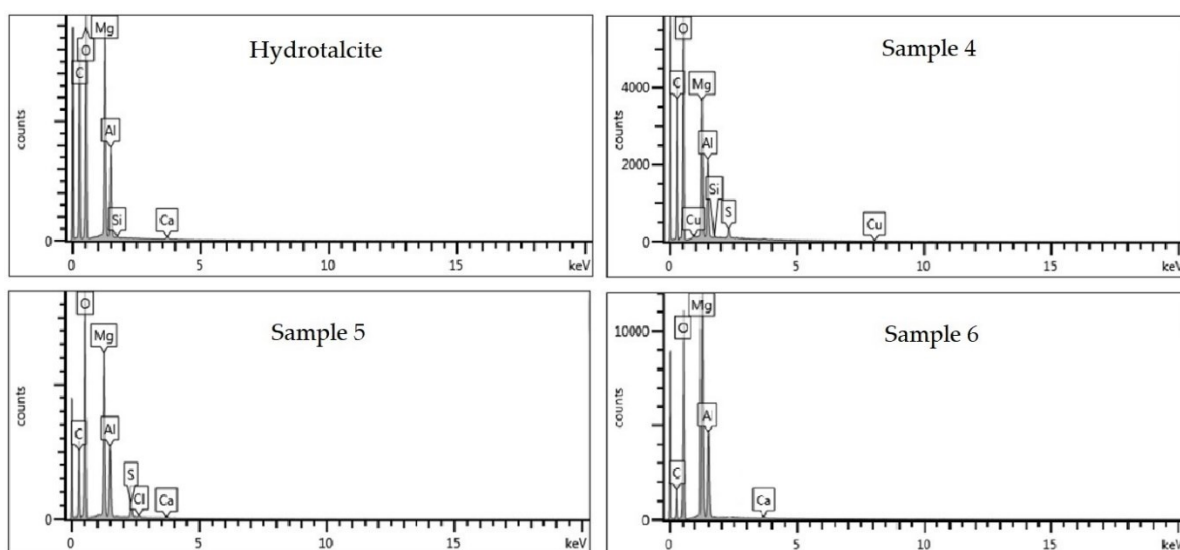


Figura 4.2.3. EDX Hidrotalcita, muestra 4, 5 y 6 (adaptada de Figure 3.4.11)

4.2.3. Estampaciones

Una vez recolectadas las arcillas y bien secadas se procede a la fase de estampación de estos híbridos Figura 4.2.4. Para ello la receta de estampación utilizada se basa en: 30 g·Kg⁻¹ de híbrido, 30 g·Kg⁻¹ de espesante sintético del proveedor Archroma con referencia comercial Lutexal CSN liq, 10 g·Kg⁻¹ de resina de la marca Color Center y referenciada como

Center Resin STK / 100, $10 \text{ g}\cdot\text{Kg}^{-1}$ de fijador del fabricante Archroma referenciado como Lupintrol SE y agua desionizada hasta completar un kilo. Las estampaciones se realizan sobre tejidos de 100% Algodón en el caso de los híbridos obtenidos a partir de colorantes aniónicos directos y reactivos y sobre 100% poliéster en el híbrido compuesto por colorante no iónicos disperso. Para todos los casos después de la estampación se deja secar 15 minutos a $60 \text{ }^\circ\text{C}$ y se termofija a $180 \text{ }^\circ\text{C}$ durante 30 segundos con una plancha de presión. Los resultados obtenidos se valoran en un espectrofotómetro de reflexión Minolta CM-3600d según la norma ISO 105-A05:1996 para su posterior valoración de la degradación, obteniendo los valores triestímulo CIE para el iluminante D65 y el observador patrón 10° CIE.



Figura 4.2.4. Estampaciones de los híbridos, muestras 4, 5 y 6 (adaptada de Figure 3.4.13)

Se realizaron estampaciones con los mismos colorantes utilizados en la adsorción para comparar los resultados obtenidos. Para el colorante RYD se realizó una estampación sobre tejido de calada de 100% algodón (CO) con la siguiente receta: $50 \text{ g}\cdot\text{Kg}^{-1}$ de espesante Proesgum CEL-RF (alginato), $100 \text{ g}\cdot\text{Kg}^{-1}$ de urea, $40 \text{ g}\cdot\text{Kg}^{-1}$ de carbonato sódico, $10 \text{ g}\cdot\text{Kg}^{-1}$ de colorante para tener un tono similar al de los híbridos y agua desionizada hasta completar el kilo de pasta de estampación [53]. Hay que señalar que para esta receta se ha empleado carbonato sódico Na_2CO_3 y no bicarbonato porque el colorante RYD tiene como grupo reactivo la Tricloropirimidina que es el grupo menos reactivo de todos y para los colorantes de baja reactividad se emplea el Na_2CO_3 . Después de la estampación se seca a $120 \text{ }^\circ\text{C}$ durante 15 minutos y se vaporiza a 100°C durante 30 minutos. Después es importante lavar el tejido para eliminar el colorante hidrolizado y no fijado al tejido. Para ello inicialmente,

los productos se lavan con agua fría y semicaliente. Esta es una etapa de dilución en la que se elimina el espesante, la sal y el álcali de las telas. Después se lavan en una disolución de $2 \text{ g}\cdot\text{L}^{-1}$ con jabón no iónico a $60 \text{ }^\circ\text{C}$ durante 30 minutos [53],[54]. El detergente utilizado en este lavado fue el Solpon OWS del fabricante Boehme. Por último, se realiza un enjuague caliente y luego frío para diluir la solución de colorante final que está adherido a las fibras, en el enjuague en frío se le coloca $1 \text{ g}\cdot\text{L}^{-1}$ de ácido acético, para que haya mayor afinidad con los productos del acabado.

En la estampación de colorante directo DB199 se realizó sobre un tejido de calada de 100% CO de $135 \text{ g}\cdot\text{m}^{-2}$, 22 pasadas/cm, 25 hilos/cm de ligamento tafetan para el cual se ha utilizado la siguiente receta: $50 \text{ g}\cdot\text{Kg}^{-1}$ de espesante Proesclear BDR del fabricante Proes Chemicals, $50 \text{ g}\cdot\text{Kg}^{-1}$ de urea, $10 \text{ g}\cdot\text{Kg}^{-1}$ de colorante y agua desionizada hasta completar el kilo de pasta de estampación [55]. Después de la estampación se seca a $120 \text{ }^\circ\text{C}$ durante 15 minutos y se vaporiza a 100°C durante 30 minutos. Las piezas estampadas se enjabonaron a $45 \text{ }^\circ\text{C}$ en una solución acuosa que contenía $2 \text{ g}\cdot\text{L}^{-1}$ con jabón no iónico a $60 \text{ }^\circ\text{C}$ durante 30 minutos, se enjuagaron y se secaron al aire.

Para completar la batería de control de estampaciones de colorantes sin los híbridos se realizó una estampación sobre un tejido de calada de 100% poliéster (PES) de $200 \text{ g}\cdot\text{m}^{-2}$, 13 pasadas/cm, 52 hilos/cm de ligamento tafetan con el colorante disperso DR1 para lo cual se formuló la siguiente receta: $25 \text{ g}\cdot\text{Kg}^{-1}$ de espesante de dispersión (sintético) neutralizado, AUXICLEAR EDL, $10 \text{ g}\cdot\text{Kg}^{-1}$ de colorante y agua desionizada hasta completar el kilo de pasta de estampación. Tras la estampación se realiza una fijación a $150\text{-}160 \text{ }^\circ\text{C}$ durante 4 minutos para después darle un lavado con el objetivo de quitar el espesante coloidal y el colorante no fijado. Este lavado consta de dos fases, la primera se hizo mediante acción mecánica manual con agua desionizada, frotando el tejido con el agua mientras que en la segunda fase de este lavado se realiza un lavado mixto (reductor y detergente Solpon OWS) para obtener mayor eficacia. Este segundo lavado es con un baño compuesto de $2 \text{ ml}\cdot\text{L}^{-1}$ de NaOH del 40%, $4 \text{ g}\cdot\text{L}^{-1}$ de $\text{Na}_2\text{S}_2\text{O}_4$ y $2 \text{ ml}\cdot\text{L}^{-1}$ de detergente Solpon OWS. La relación de baño será 1/40, la temperatura de 60°C y el tiempo de tratamiento de 15 minutos. A modo de resumen se puede ver en la Tabla 4.2.2 un detalle de las muestras realizadas para comparar

los resultados obtenidos.

Tabla 4.2.2. Muestras de estampación (adaptada de Table 3.4.2)

Muestra nº	Materia Colorante	Textil
1	Direct Blue 199	100% CO
2	Reactive Yellow Drimaren K-2R	100% CO
3	Disperse Red 1	100% PES
4	Hidrotalcita + Direct Blue 199	100% CO
5	Hidrotalcita + Reactive Yellow Drimaren K-2R	100% CO
6	Hidrotalcita + Disperse Red 1	100% PES

4.2.4. Medida del color de las estampaciones híbridas

El principal objetivo de este apartado era el de conseguir colorear un material textil mediante la técnica de estampación utilizando como producto que aportará ese color los híbridos obtenidos con nanoarcillas. Conseguido ese objetivo se calculó y valoró esa coloración del sustrato textil. A continuación, se muestran los valores $L^*a^*b^*$ h y el C^*_{ab} en la Tabla 4.2.3 y se representan en un diagrama de cromaticidad en la Figura 4.2.5 para mostrar cómo se ha cumplido el objetivo de forma exitosa.

Tabla 4.2.3. Valores L^* , a^* , b^* , C^*_{ab} y h de cada estampación (adaptada de Table 3.4.8)

Muestra	L^*	a^*	b^*	C^*_{ab}	h
4	65.61	-18.59	-21.35	28.31	228.95
5	80.87	-3.58	56.64	56.76	93.62
6	58.59	36.18	18.07	40.44	26.54

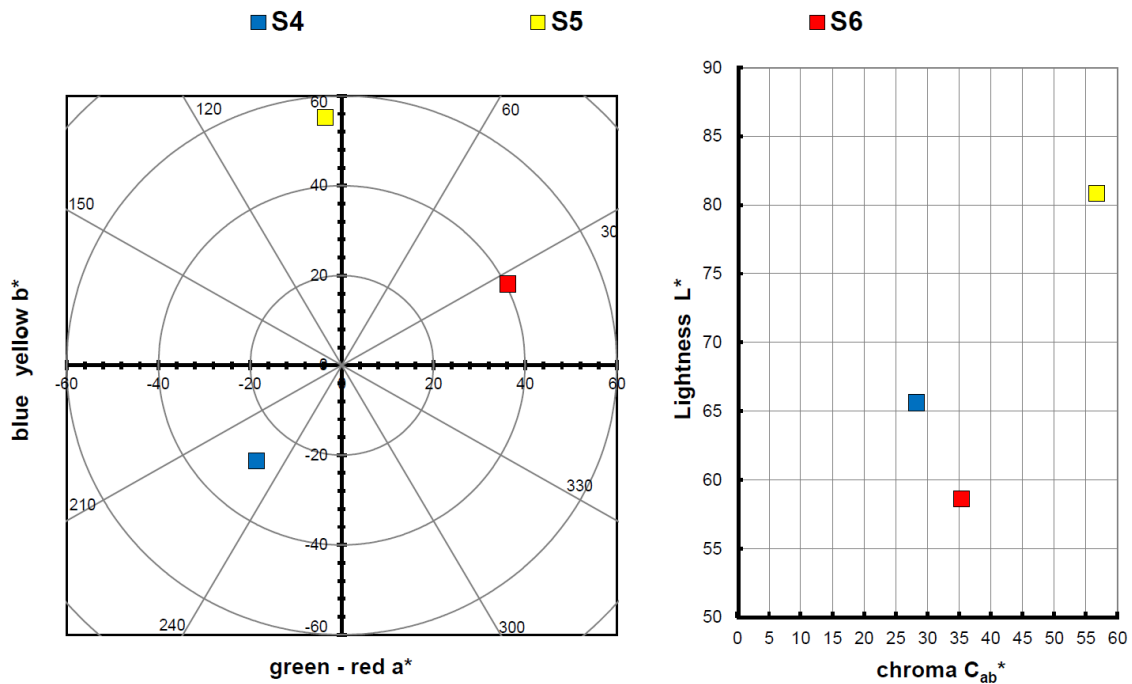


Figura 4.2.5. Gráficos CIELAB para híbridos impresos utilizando el iluminante D65 y el observador estándar CIE-1931 XYZ. Izquierda: diagrama de color CIE-a* b*; derecha: Diagrama de color CIE-Cab* L* (adaptada de Figure 3.4.12)

En lo que se refiere al color obtenido a la vista de la distribución de los puntos en los diagramas representados en la Figura 4.2.5 se observa que los resultados son excelentes. En el amarillo se consigue una alta luminosidad como es propio de este color y demuestra que se ha obtenido un amarillo intenso. El tono obtenido con el azul va hacia tonalidades más verdosas que las que se observaron en el híbrido, resultado de la interacción con el propio sustrato textil cuyo blanco no es puro y proporciona una coloración amarillenta. El mismo efecto puede apreciarse con el rojo, que se desplaza hacia tonalidades más anaranjadas que el híbrido original por el mismo motivo. Además, en la aplicación, con la mezcla de las pastas de estampación los niveles de claridad de las estampaciones con el azul y el rojo son superiores a los de los colorantes híbridos analizados en el paso previo. Se siguen teniendo valores de L^* entre 65-55 con lo que se podría disminuir aún más la concentración de los pigmentos híbridos y seguir viendo un efecto de coloración considerable. Los niveles de saturación en estos estampados son elevados en los tres casos proporcionando efectos visuales interesantes y distinguibles.

4.2.5. Solideces

Las probetas de estampación se sometieron a distintas pruebas para valorar sus diferentes solideces. La solidez del color al lavado se realizó conforme a la norma UNE-EN ISO 105-C06:1994 con el equipo de ensayo Linitest, descrito en la norma UNE-EN ISO 105-C06. Se realizó el ensayo número A1S a 40 °C, 150 ml de volumen de lavado durante 30 minutos, sin ajustar el pH y con 10 bolas de acero para generar acción abrasiva. La solidez de las tinturas al planchado se realizó conforme a la norma UNE-EN ISO 105-X11:1997 con una plancha de presión. Se hizo en seco, mojado y húmedo según se describe en la norma. Para todas las probetas el tiempo de planchado fue de 15 segundos a una temperatura de 200 °C para los tejidos de PES y a 150 °C para los de CO ya que a más temperatura el algodón amarillea.

Para la solidez del color al frote se siguió la norma UNE-EN ISO 105-X12:2016 utilizando el crockmeter como equipo de ensayo, se hizo tanto el ensayo de frote seco como frote mojado. Por último, con la ayuda de un xenotest se valoró la solidez a la luz artificial utilizando lámparas de xenón según la norma UNE-EN ISO 105-B02 método 1 (grado 4) y la solidez del color a la luz del día según la norma UNE-EN ISO 105-B01 método 1. La Tabla 4.2.4 muestra un resumen de todas las probetas realizadas con los diferentes ensayos de solideces. Recordar que las muestras del 1-6 recogidas en la Tabla 4.2.2 son los patrones de referencia sobre los que no se ha ejercido ningún agente de degradación del color.

Tabla 4.2.4. Pruebas de solidez (adaptada de Table 3.4.3)

Nº	Materia colorante	Ensayo	Nº	Materia colorante	Ensayo
7	Directo Azul	planchado	31	Directo Azul	planchado húmedo
8	Reac. Amarillo	planchado	32	Reac. Amarillo	planchado húmedo
9	Disper. Red	planchado	33	Disper. Red	planchado húmedo
10	Directo Azul+HC	planchado	34	Directo Azul+HC	planchado húmedo
11	Reac. Amarillo+HC	planchado	35	Reac. Amarillo+HC	planchado húmedo
12	Disper. Red+HC	planchado	36	Disper. Red+HC	planchado húmedo
13	Directo Azul	lavado	37	Directo Azul	frote húmedo
14	Reac. Amarillo	lavado	38	Reac. Amarillo	frote húmedo
15	Disper. Red	lavado	39	Disper. Red	frote húmedo
16	Directo Azul+HC	lavado	40	Directo Azul+HC	frote húmedo
17	Reac. Amarillo+HC	lavado	41	Reac. Amarillo+HC	frote húmedo
18	Disper. Red+HC	lavado	42	Disper. Red+HC	frote húmedo
19	Directo Azul	frote	43	Directo Azul	planchado mojado
20	Reac. Amarillo	frote	44	Reac. Amarillo	planchado mojado
21	Disper. Red	frote	45	Disper. Red	planchado mojado
22	Directo Azul+HC	frote	46	Directo Azul+HC	planchado mojado
23	Reac. Amarillo+HC	frote	47	Reac. Amarillo+HC	planchado mojado
24	Disper. Red+HC	frote	48	Disper. Red+HC	planchado mojado
25	Directo Azul	luz artificial	49	Directo Azul	luz natural
26	Reac. Amarillo	luz artificial	50	Reac. Amarillo	luz natural
27	Disper. Red	luz artificial	51	Disper. Red	luz natural
28	Directo Azul+HC	luz artificial	52	Directo Azul+HC	luz natural
29	Reac. Amarillo+HC	luz artificial	53	Reac. Amarillo+HC	luz natural
30	Disper. Red+HC	luz artificial	54	Disper. Red+HC	luz natural

Todos los ensayos de solidez se valoraron instrumentalmente mediante espectrofotometría de reflexión utilizando la norma UNE-EN ISO 105-A05 y expresando los resultados según valores de escala de grises, excepto el ensayo de solidez de color a la luz ya que se valora mediante escala de azules. También se realizó una evaluación instrumental del grado de descarga de los tejidos testigo siguiendo la norma UNE-EN ISO 105-A04. Para estas valoraciones instrumentales se utilizó el espectrofotómetro de reflexión Minolta CM-3600d en el rango de 360-740 nm con un paso de 10 nm.

En la Tabla 4.2.5 se muestran los resultados obtenidos para cada uno de los diferentes ensayos de solidez del color. Los resultados están expresados según la escala de grises normalizada (GS_c) y calculada de forma instrumental según la Ecuación 4.2.1. También en la Tabla 4.2.5 se muestran las descargas (SSR) calculadas instrumentalmente y

según la Ecuación 4.2.2. Para los ensayos de degradación del color a la luz artificial y a la intemperie se realizó una valoración visual de escala de azules.

$$\begin{aligned} \text{a)} \quad \Delta E_f &= [(\Delta L^*)^2 + (\Delta C_f)^2 + (\Delta H_f)^2]^{1/2} \\ \text{b)} \quad \text{GS} &= 5 - [\Delta E_f / 1.7] \\ \text{c)} \quad \text{GS} &= 5 - [\log_{10} (\Delta E_f / 0.85) / \log_{10} 2] \end{aligned}$$

Ecuación 4.2.1. a) Cambio de color para la determinación del índice de la escala de grises para la degradación b) GS si $\Delta E_f \leq 3.4$ c) GS si $\Delta E_f \geq 3.4$

$$\begin{aligned} \text{a)} \quad \Delta E_{GS} &= \Delta E_{CIELAB} - 0.4 (\Delta E^{*2} - \Delta L^{*2})^{1/2} \\ \text{b)} \quad \text{SSR} &= 6.1 - 1.45 \ln (\Delta E_{GS}) \\ \text{c)} \quad \text{SSR} &= 5 - 0.23 \Delta E_{GS} \end{aligned}$$

Ecuación 4.2.2. a) Diferencia de escala de grises b) Índice de la escala de grises entre 1 y 4 c) Índice de la escala de grises entre 4 y 5

Recuperación del colorante de aguas residuales textiles mediante nanoarcillas para su reutilización como pigmentos y nuevos baños de tintura

Tabla 4.2.5. Valores de solidez del color mediante índice de escala de grises y descarga (SSR)
(adaptada de

Table 3.4.9)

Muestra	Degradación	Descarga	Muestra	Degradación	Descarga
7	2.5	5	31	3	4 – 5
8	2.5	4 – 5	32	2	4 – 5
9	4.5	3 – 4	33	5	4
10	3.5	5	34	4	5
11	3.5	5	35	2.5	5
12	0.5	3 – 4	36	1	3
13	3	4	37	3	5
14	3	4	38	4.5	2 – 3
15	4	4	39	4	5
16	0	3 – 4	40	2.5	2
17	2	4	41	4	1
18	1	3	42	2	1
19	2.5	5	43	3	4 – 5
20	4	5	44	1.5	4
21	3	4 – 5	45	4.5	4
22	3	4	46	3.5	4
23	1.5	4	47	2	4
24	3	1 – 2	48	1	
25	4 – 5	-	49	4	-
26	6	-	50	6	-
27	2 – 3	-	51	2 – 3	-
28	5	-	52	6	-
29	4	-	53	5 – 6	-
30	2	-	54	1 – 2	-

Analizando a pares los resultados de las solidesces obtenidas se pueden ver diferentes resultados en función del tipo de ensayo y del tipo de colorante. En la Figura 4.2.6 se muestra gráficamente la comparativa de los diferentes resultados obtenidos para cada colorante.

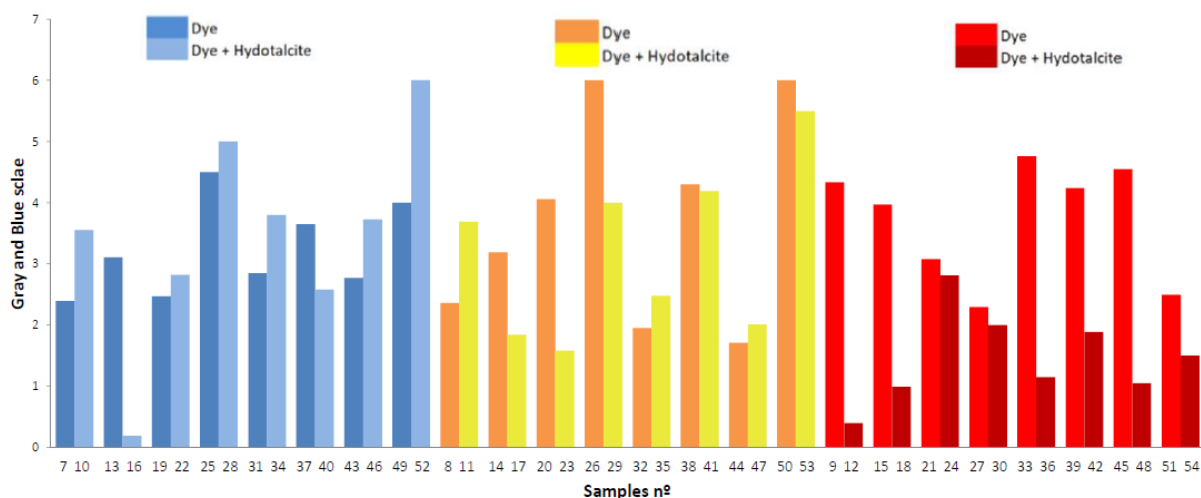


Figura 4.2.6. Comparativa a pares de los valores de solidez del color mediante índice de escala de grises (adaptada de Figure 3.4.14)

A la vista de los resultados y de esta comparativa se ve como en caso del colorante directo mejora los resultados de solidez del color para los ensayos de planchado en seco, frote en seco, planchado húmedo, planchado mojado, luz artificial y luz natural. Estos resultados acompañados con los vistos en los TGA en el apartado 4.1 demuestran que en ensayos donde hay temperatura o energía implicada el colorante es protegido por la arcilla, como se recoge en anteriores trabajos [40]–[43] y se describe en el apartado TGA de este estudio. Para el colorante reactivo mejoran los ensayos de planchado en seco, húmedo y mojado y permanece prácticamente igual en el ensayo de frote húmedo. Nuevamente para este caso igual que en el colorante directo la arcilla ha realizado un efecto protector frente al calor de la plancha.

Hay que recordar que los colorantes reactivos de por sí solos presentan muy buenas solidez a la luz, por este motivo la arcilla no ha podido mejorar ese resultado en esta prueba. Por último, el estudio del colorante disperso arroja resultados muy importantes, ya que en ningún caso ha mejorado las solidez, incluso ha empeorado considerablemente. Debe recordarse que el colorante disperso no tiene carga iónica y que la hidrotalcita tiene sobre todo una gran afinidad por adsorber elementos aniónicos como son los colorantes reactivos y directos, es por esto por lo que no ha ejercido la misma protección sobre el colorante no iónico que sobre los colorantes aniónicos.

4.2.6. Microscopia electrónica de barrido (SEM)

En este ensayo se va a analizar la topografía de la superficie de las muestras estampadas con los híbridos de arcilla cargadas de colorante. En la Figura 4.2.7 se puede ver una imagen de la muestra estampada nº5, lavada nº17 y su correspondiente descarga las cuales son significativas y extrapolables para todas las otras muestras ya que se obtienen las mismas conclusiones. Comparando la muestra 5 y 17 se observa una pérdida de material híbrido y que parte de ese híbrido se encuentra ahora en el testigo de descarga. Así pues, la pérdida de color que se ha producido y cuyos resultados se han visto en el apartado anterior se debe en gran parte por perdida de híbrido y no por degradación del propio colorante a los diferentes agentes a los que se han expuesto.

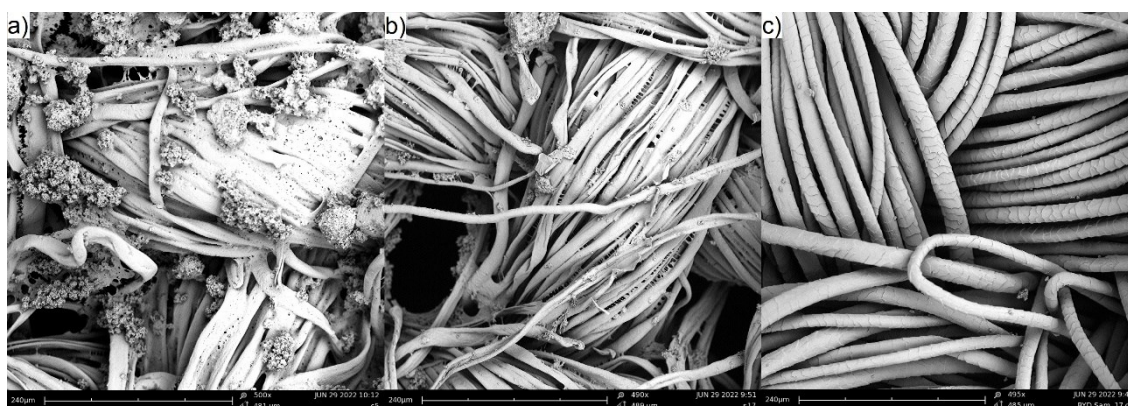


Figura 4.2.7. a) Muestra 5, b) Muestra 17 después del lavado y c) Testigo Muestra 17 después del lavado (adaptada de Figure 3.4.17)

4.3. Tintura con híbridos de arcilla-colorante

Después de haber optimizado la síntesis de híbridos y haberlos utilizado para incorporarlos a una pasta de estampación textil para su posterior aplicación se procede a ver un nuevo uso, en este caso es el de la utilización de esos híbridos para realizar nuevos baños de tintura.

Para ello se han utilizado 3 colorantes con diferentes características para comprobar el método cuando hay diferente polaridad del colorante y las condiciones de tintura son distintas. Se ha tomado un colorante aniónico del tipo directo denominado Direct Blue 199 (DB199), otro colorante catiónico clasificado como básico con la denominación Basic Yellow 2 (BY2) y por último un colorante no iónico sin polaridad de la clase disperso referenciado como Disperse Red 1 (DR1). La arcilla como en toda esta tesis sigue siendo la hidrotalcita.

4.3.1. Método de tintura. Desorción

El proceso de desorción se describe como el fenómeno en el que hay una transferencia del colorante desde el adsorbato en fase sólida a la líquida [56],[57]. Varios modelos [58]–[60] explican diferentes teorías con isoterms sobre cómo se produce esta desorción describiéndolos como sistemas de adsorción/desorción no ideales y reversibles, otro describe un sistema en el que no hay siempre una interacción entre sitios activos vecinos debido a la no homogeneidad del nanoadsorbente y por lo tanto no producirse una adsorción homogénea.

Todas estas teorías dan una idea de la verdadera naturaleza del proceso de adsorción/desorción. Los autores Momina, Shahadat Mohammad, and Suzylawatilsamil [61] explican un modelo de desorción para el Azul de metileno (MB) sometiendo en una primera fase al híbrido a temperatura para debilitar los enlaces y después utilizando diversos disolventes como HCl, etanol, ácido nítrico o acetona. Sostienen que cualquiera de estas fases por sí solo no es suficiente para producir buenos resultados de desorción.

En este estudio se plantea un proceso de desorción-tintura de forma simultánea, en la que basándose en la teoría de que la temperatura consigue debilitar la unión entre la

arcilla y el colorante [61] aprovechando posteriormente la afinidad colorante-fibra y el proceso de tintura empleado comúnmente para que este colorante acabe migrando totalmente de la hidrotalcite a la fibra textil (Figura 4.3.1). Además, en el modelo de este trabajo se aplica un calor por convección y no por radiación como en el modelo de los autores Momina, Shahadat Mohammad, and Suzyawatilsamil, siendo este calor más efectivo llegando a más zonas de la arcilla y también más energético.

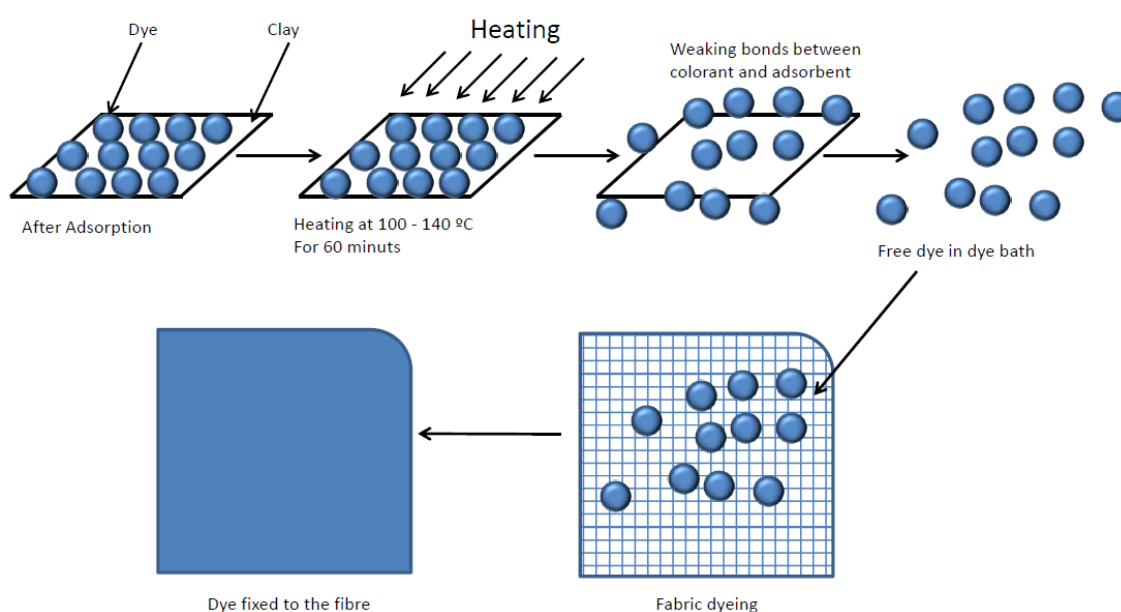


Figura 4.3.1. Desorción del colorante y tintura de la fibra textil (adaptada de Figure 3.5.11)

Así pues, el híbrido arcilla-colorante se empleará como material colorante realizando tinturas por agotamiento, todas ellas con una relación de baño 1/40. Para la tintura de un tejido de calada de algodón (CO) 100% de un gramaje de $135 \text{ g}\cdot\text{m}^{-2}$, $25 \text{ hilos}\cdot\text{cm}^{-1}$, $22 \text{ pasadas}\cdot\text{cm}^{-1}$ de tejido tafetán se emplea el híbrido del colorante directo HDB199, se añadirá al baño de tintura un 40% s.p.f de arcilla+colorante, $20\text{g}\cdot\text{L}^{-1}$ de sulfato sódico y 3 gotas de humectante para someterlo al proceso de tintura durante 60 minutos a 100°C consiguiendo el tejido tintado referenciado como TDB199.

Para la tintura de un tejido de poliéster (PES) 100% $200 \text{ g}\cdot\text{m}^{-2}$, $13 \text{ yarns}\cdot\text{cm}^{-1}$, $52 \text{ weft}\cdot\text{cm}^{-1}$ tejido tafetán introducido en un baño que contiene un 40% s.p.f de

arcilla+colorante HDR1, durante 60 minutos a 140°C en una máquina cerrada con 1g·L⁻¹ sulfato amónico, 0.5g·L⁻¹ Dispersante Dekol SN y ajustando previamente el pH a 4.5 - 5 con ácido acético, obteniendo la muestra con referencia TDR1.




La última tintura será sobre un tejido de composición 100% acrílico (PAN) un tejido de punto por trama con 8 filas por centímetro y 9 columnas por centímetro formando un ligamento de punto inglés en cuyo baño se añade un 40% s.p.f de arcilla+colorante HBY2, ácido acético 2% s.p.f, 20g·L⁻¹ de sulfato sódico y se procesara durante 40 minutos a 100°C con lo que se obtiene el tejido tintado referenciado como TBY2.

La tintura del tejido de poliéster se ha realizado en máquina cerrada debido a las temperaturas superiores a 100 °C que se deben emplear, siendo el aparato utilizado el Testtherm tipo 9S del fabricante Talcatex S.A. Por otro lado, las tinturas de fibra acrílica y algodón se realizaron en la máquina abierta referenciada como Open Bath dye Master del fabricante Paramount S.A. Todos los tejidos son lavados después de la tintura para eliminar cualquier resto de colorante no fijado a las fibras.

4.3.2. Medida del color de las tinturas

El objetivo prioritario de esta investigación es el de realizar la coloración de varios textiles de diferente naturaleza mediante la tintura por agotamiento utilizando como materia de coloración los híbridos obtenidos con nanoarcillas. Una vez que se ha conseguido de forma totalmente satisfactoria ese objetivo se procede a realizar el cálculo y valoración de esa coloración obtenida en el tejido textil. En la Tabla 4.3.1 se exponen los resultados de los valores L*a*b* h y el C*ab y también puede verse una representación en un diagrama de cromaticidad en la Figura 4.3.2 pudiendo de esta forma expresar en modo cuantitativo el color obtenido en cada tintura.

Tabla 4.3.1. Valores L^* , a^* , b^* , C^*_{ab} y h de cada tintura (adaptada de Table 3.5.3)

Muestra	Tintura	L^*	a^*	b^*	C^*_{ab}	h
TDB199		51.86	-29.17	-33.79	44.63	229.20
TBY2		76.23	-1.97	100.61	100.63	91.12
TDR1		32.05	49.45	28.75	57.20	30.18

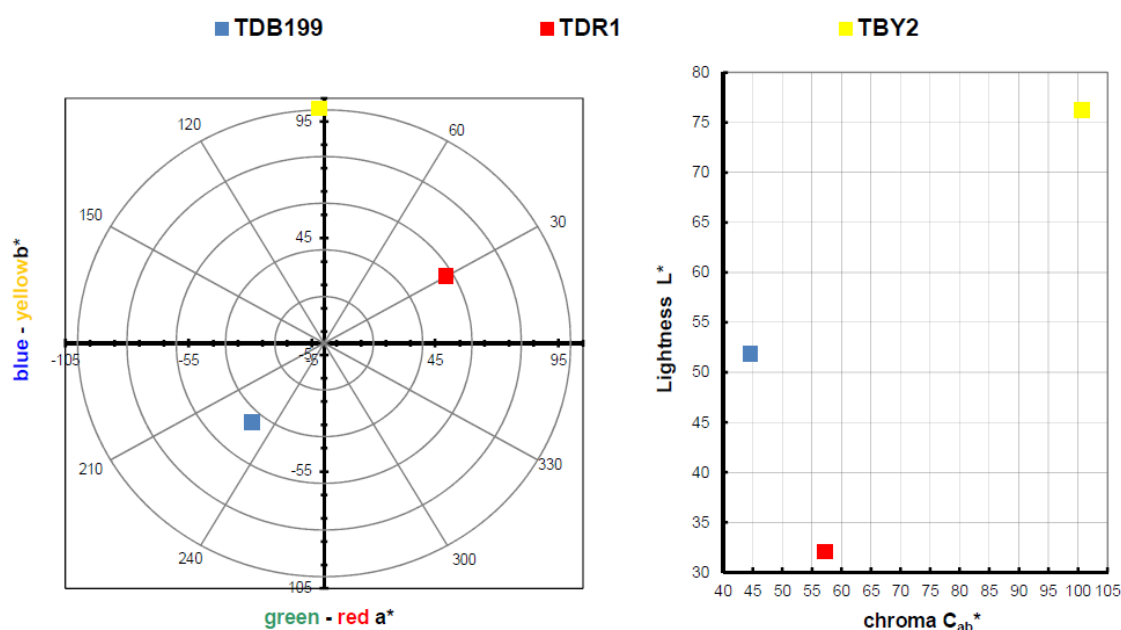


Figura 4.3.2. Gráficos CIELAB para híbridos tintados utilizando el iluminante D65 y el observador estándar CIE-1931 XYZ. Izquierda: diagrama de color CIE- $a^* b^*$; derecha: Diagrama de color CIE- $Cab^* L^*$ (adaptada de Figure 3.5.6)

A la vista de los resultados obtenidos en la medida del color de las tinturas se observan unos resultados totalmente acordes con una tintura convencional, como si en el baño se hubiera introducido directamente colorante y no un híbrido arcilla-colorante. Tómese como ejemplo el color azul del TDB199 que toma un tono ligeramente amarillo debido a la mezcla con el tejido de algodón que por su naturaleza tiende a tener un tono amarillento y esta mezcla produce ese efecto ligeramente verdoso. Por otro lado, el amarillo TBY2 muestra una luminosidad muy elevada por encima de una L^* de 75, algo muy característico de los amarillos intensos. Por su parte el rojo TDR1 se acerca hacia tonos muy ligeramente naranjas también por su unión con el sustrato textil en este caso de PES. Hay

que destacar el nivel de croma tan elevado que muestra el amarillo comparado con los otros dos colores, el cual se sitúa en un valor por encima de 100, característico de los tonos amarillos.

4.3.3. Solideces

Tras la tintura de las diferentes materias textiles utilizadas en este trabajo el siguiente paso es comprobar la capacidad que tiene ese color de permanecer en la fibra al ser sometido a diferentes agentes o acciones externas que pueden alterar su unión con la materia textil. Para ello se realizan los denominados ensayos de la solidez del color. Cabe recordar que se han utilizado híbridos cuyos colorantes tienen afinidad por la fibra específica que se ha introducido en la tintura, el colorante directo muestra afinidad por las materias celulósicas como es el caso del algodón [62]–[64], los colorantes (catiónicos) son afines a la estructura química del PAN (aniónica) [65] y en el caso del poliéster son tintados por los colorantes dispersos como si de una aleación se tratara [66]–[68] ya que al alcanzar al temperatura de transición vítrea colorante y textil se unen de forma similar a como lo hacen los metales al ser fundidos.

Estas afinidades descritas permiten que los colorantes se depositen en la fibra en una primera fase de adsorción para después penetrar completamente dentro de la fibra en la fase de absorción. Esto permite que el color quede bien fijado, no obstante, dependiendo de las características del colorante y la naturaleza de la fibra presentara mejores o peores resultados de solidez del color a diferentes agentes.

Los resultados obtenidos para cada muestra y ensayo se recogen en la Tabla 4.3.2. Dichos resultados están expresados numéricamente según la escala de grises (GS_c) de 1 a 5, siendo 1 baja solidez y 5 alta solidez, todo según se recoge en las normas de cada ensayo. Todos los valores han sido calculados de forma instrumental con un espectrofotómetro de reflexión de acuerdo con la norma UNE-EN ISO 105-A05, para la degradación del color se han realizado los cálculos utilizando las fórmulas de la ecuación 4.3.1.

- a) $\Delta E_f = [(\Delta L^*)^2 + (\Delta C_f)^2 + (\Delta H_f)^2]^{1/2}$
 b) $GS = 5 - [\Delta E_f / 1.7]$
 c) $GS = 5 - [\log_{10} (\Delta E_f / 0.85) / \log_{10} 2]$

Ecuación 4.3.1. a) Cambio de color para la determinación del índice de la escala de grises para la degradación b) GS si $\Delta E_f \leq 3.4$ c) GS si $\Delta E_f \geq 3.4$

Tabla 4.3.2. Valores de solidez del color mediante índice de escala de grises (adaptada de

Table 3.5.4)

Muestra	Lavado	Degradación				
		Frote		Planchado		
		Seco	Mojado	Seco	Humedo	Mojado
TDB199	3 - 4	4 - 5	4	4 - 5	4	3 - 4
TBY2	4	4	4 - 5	2	3	3
TDR1	4 - 5	4 - 5	4 - 5	4	4	3 - 4

En la Figura 4.3.3 se muestra gráficamente un resumen de los resultados obtenidos para cada tintura. Los resultados obtenidos son los esperados dadas las características de cada colorante y materia. Por ejemplo, los colorantes directos tienen una baja solidez a los tratamientos en húmedo como el lavado, el reactivo una buena solidez en los mismos tratamientos en húmedo y el disperso unas altas solidez en general debido a que el colorante y la fibra forman una especie de aleación que hay muy difícil que el colorante abandone la fibra.

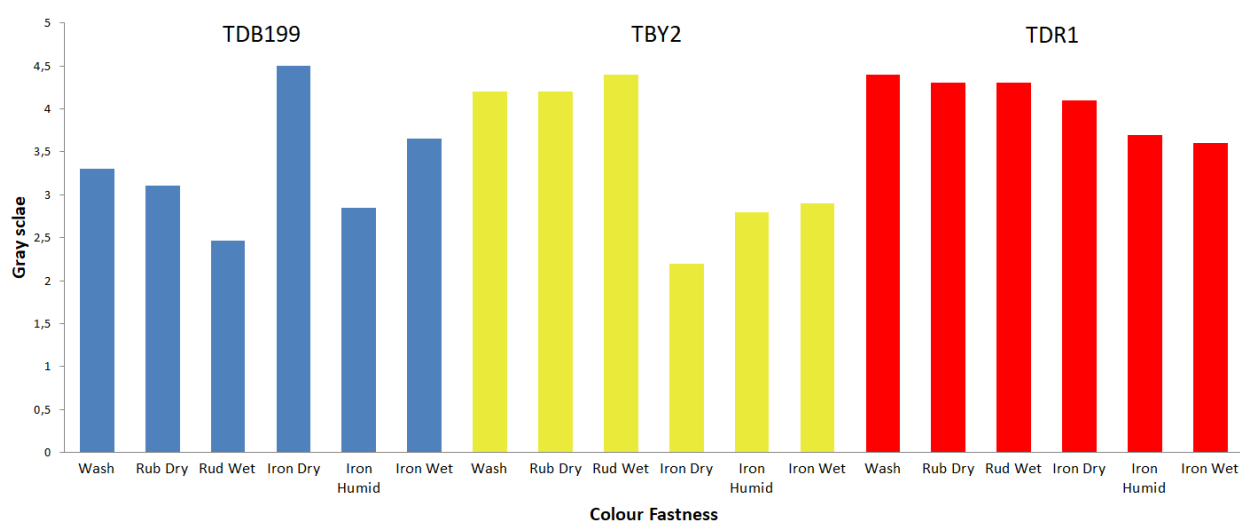


Figura 4.3.3. Valores de solidez del color mediante índice de escala de grises (adaptada de Figure 3.5.7)

4.3.4. Microscopia electrónica de barrido (SEM)

En el análisis topográfico de los tejidos tintados revelará si el color que tienen los tejidos es debido a la deposición superficial del híbrido o si ha habido una absorción del colorante por parte de los textiles. Así pues, en la Figura 4.3.4 se ven dos imágenes, una de PES y otra de CO con las que se puede asegurar que apenas hay algún resto de híbrido en la superficie de las fibras, pero es una cantidad meramente residual que en ningún caso sería suficiente como para dar color de la intensidad y uniformidad que tienen los tejidos. Este análisis confirma y complementa a los anteriores asegurando que ha habido una desorción del colorante el cual ha pasado de la arcilla al baño de tintura y de ahí a la fibra textil.

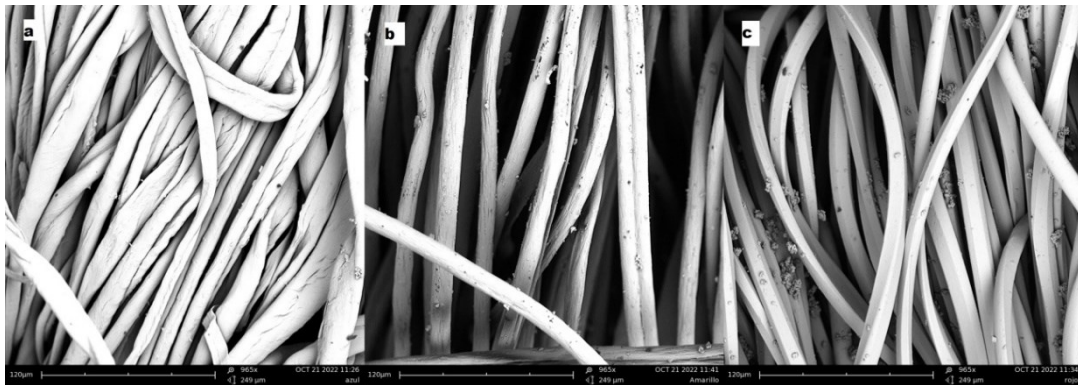


Figura 4.3.4. a) SEM muestra TDB199, b) SEM muestra TBY2, c) SEM muestra TDR1 (adaptada de Figure 3.5.8)

Referencias

Referencias

1. Rh, R.; Siberian, E. Comparative Analysis of Far East Sikhotinsky. <https://doi.org/10.3390/molecules25173774>
2. Zhang, W.; Zhang, D.; Liang, Y. Nanotechnology in Remediation of Water Contaminated by Poly- and Perfluoroalkyl Substances: A Review. *Environ. Pollut.* 2019, *247*, 266–276. <https://doi.org/10.1016/J.ENVPOL.2019.01.045>.
3. Bish, D. L. Anion-Exchange in Takovite: Applications to Other Hydroxide Minerals. *Bull. Mineral.* 1980, *103* (2), 170–175.
4. Miyata, S. Physico-Chemical Properties of Synthetic Hydrotalcites in Relation to Composition. *Clays Clay Miner.* 1980, *28* (1), 50–56. <https://doi.org/10.1346/CCMN.1980.0280107>
5. Ulibarri, M. A.; Pavlovic, I.; Barriga, C.; Hermosin, M. C.; Cornejo, J. Adsorption of Anionic Species on Hydrotalcite-like Compounds: Effect of Interlayer Anion and Crystallinity. *Appl. Clay Sci.* 2001, *18* (1–2), 17–27. [https://doi.org/10.1016/S0169-1317\(00\)00026-0](https://doi.org/10.1016/S0169-1317(00)00026-0)
6. Akil, J.; Ciotonea, C.; Siffert, S.; Royer, S.; Pirault-Roy, L.; Cousin, R.; Poupin, C. NO Reduction by CO under Oxidative Conditions over CoCuAl Mixed Oxides Derived from Hydrotalcite-like Compounds: Effect of Water. *Catal. Today* 2021, No. October 2020. <https://doi.org/10.1016/j.cattod.2021.05.014>.
7. Carlino, S. Chemistry between the Sheets. *Chem. Br.* 1997, *33* (9), 59–62.
8. Zhu, M.-X.; Li, Y.-P.; Xie, M.; Xin, H.-Z. Sorption of an Anionic Dye by Uncalcined and Calcined Layered Double Hydroxides: A Case Study. *J. Hazard. Mater.* 2005, *120* (1–3), 163–171. <https://doi.org/10.1016/j.jhazmat.2004.12.029>
9. Lakraimi, M.; Legrouri, A.; Barroug, A.; Besse, J.-P. Removal of Pesticides from Water by Anionic Clays. *J. Chim. Phys. Physico-Chimie Biol.* 1999, *96* (3), 470–478. <https://doi.org/10.1051/jcp:1999152>
10. Sato, T.; Kato, K.; Endo, T.; Shimada, M. Preparation and Chemical Properties of Magnesium Aluminium Oxide Solid Solutions. *React. Solids* 1986, *2* (3), 253–260. [https://doi.org/10.1016/0168-7336\(86\)80088-2](https://doi.org/10.1016/0168-7336(86)80088-2)
11. dos Santos, R. M. M.; Gonçalves, R. G. L.; Constantino, V. R. L.; da Costa, L. M.; da Silva, L. H. M.; Tronto, J.; Pinto, F. G. Removal of Acid Green 68:1 from Aqueous Solutions by Calcined and Uncalcined Layered Double Hydroxides. *Appl. Clay Sci.* 2013, *80–81*, 189–195. <https://doi.org/10.1016/j.clay.2013.04.006>
<https://doi.org/10.1016/j.clay.2013.04.006>

12. Lian, Z. Y.; Zhang, Y.; Wang, X. Z. Manufacturing of High Quality Hydrotalcite by Computational Fluid Dynamics Simulation of an Impinging Jet Crystallizer. *Ceram. Int.* 2022. <https://doi.org/10.1016/J.CERAMINT.2022.02.081>.
13. Serrano-Lotina, A.; Rodríguez, L.; Muñoz, G.; Martín, A. J.; Folgado, M. A.; Daza, L. Biogas Reforming over La-NiMgAl Catalysts Derived from Hydrotalcite-like Structure: Influence of Calcination Temperature. *Catal. Commun.* 2011, 12 (11), 961–967. <https://doi.org/10.1016/J.CATCOM.2011.02.014>.
14. Micó-Vicent, B.; Jordán, J.; Perales, E.; Martínez-Verdú, F.; Cases, F. Finding the Additives Incorporation Moment in Hybrid Natural Pigments Synthesis to Improve Bioresin Properties. *Coatings* . 2019. <https://doi.org/10.3390/coatings9010034>. <https://doi.org/10.3390/coatings9010034>
15. Cavani, F.; Trifiro, F.; Vaccari, A. Hydrotalcite-Type Anionic Clays: Preparation, Properties and Applications. *Catal. today* 1991, 11 (2), 173–301. [https://doi.org/10.1016/0920-5861\(91\)80068-K](https://doi.org/10.1016/0920-5861(91)80068-K)
16. Dahdah, E.; Estephane, J.; Taleb, Y.; El Khoury, B.; El Nakat, J.; Aouad, S. The Role of Rehydration in Enhancing the Basic Properties of Mg–Al Hydrotalcites for Biodiesel Production. *Sustain. Chem. Pharm.* 2021, 22 (July). <https://doi.org/10.1016/j.scp.2021.100487>.
17. Bernard, E.; Zucha, W. J.; Lothenbach, B.; Mäder, U. Stability of Hydrotalcite (Mg-Al Layered Double Hydroxide) in Presence of Different Anions. *Cem. Concr. Res.* 2022, 152, 106674. <https://doi.org/10.1016/J.CEMCONRES.2021.106674>.
18. Geetha Bhavani, A.; Wani, T. A.; Ma'Aruf, A.; Prasad, T. Effect of Ageing Process on Crystal Morphology of Co-Mg-Al Hydrotalcite. *Mater. Today Proc.* 2021, 44, 2277–2282. <https://doi.org/10.1016/J.MATPR.2020.12.390>.
19. Wiyantoko, B.; Kurniawati, P.; Purbaningtyas, T. E.; Fatimah, I. Synthesis and Characterization of Hydrotalcite at Different Mg/Al Molar Ratios. *Procedia Chem.* 2015, 17, 21–26. <https://doi.org/10.1016/j.proche.2015.12.115>
20. Roelofs, J. C. A. A.; van Bokhoven, J. A.; Van Dillen, A. J.; Geus, J.; de Jong, K. P. The Thermal Decomposition of Mg-Al Hydrotalcites: Effects of Interlayer Anions and Characteristics of the Final Structure. *Chem. Eur. J.* 2002, 8, 5571–5579. [https://doi.org/10.1002/1521-3765\(20021216\)8:24%3C5571::AID-CHEM5571%3E3.0.CO;2-R](https://doi.org/10.1002/1521-3765(20021216)8:24%3C5571::AID-CHEM5571%3E3.0.CO;2-R)
21. Ziyat, H.; Elmzioui, S.; Naciri Bennani, M.; Houssaini, J.; Allaoui, S.; Arhzaf, S. Kinetic, Isotherm, and Mechanism Investigations of the Removal of Nitrate and Nitrite from Water by the Synthesized Hydrotalcite Mg–Al. *Res. Chem. Intermed.* 2021, 47 (6), 2605–2627. <https://doi.org/10.1007/s11164-021-04414-w>
22. Ma, Y.; Zhu, J.; He, H.; Yuan, P.; Shen, W.; Liu, D. Infrared Investigation of Organo-Montmorillonites Prepared from Different Surfactants. *Spectrochim. Acta Part A*

- Mol. Biomol. Spectrosc.* 2010, 76 (2), 122–129. <https://doi.org/10.1016/j.saa.2010.02.038>
23. Lopez, T.; Bosch, P.; Asomoza, M.; Gómez, R.; Ramos, E. DTA-TGA and FTIR Spectroscopies of Sol-Gel Hydrotalcites: Aluminum Source Effect on Physicochemical Properties. *Mater. Lett.* 1997, 31 (3–6), 311–316. [https://doi.org/10.1016/S0167-577X\(96\)00296-0](https://doi.org/10.1016/S0167-577X(96)00296-0)
24. Tichit, D.; Lhouty, M. H.; Guida, A.; Chiche, B. H.; Figueras, F.; Auroux, A.; Bartalini, D.; Garrone, E. Textural Properties and Catalytic Activity of Hydrotalcites. *J. Catal.* 1995, 151 (1), 50–59. <https://doi.org/10.1006/jcat.1995.1007>
25. Liu, Y.; Lotero, E.; Goodwin, J. G.; Mo, X. Transesterification of Poultry Fat with Methanol Using Mg-Al Hydrotalcite Derived Catalysts. *Appl. Catal. A Gen.* 2007, 331 (1), 138–148. <https://doi.org/10.1016/j.apcata.2007.07.038>.
26. Shen, J.; Tu, M.; Hu, C. Structural and Surface Acid/Base Properties of Hydrotalcite-Derived MgAlO Oxides Calcined at Varying Temperatures. *J. Solid State Chem.* 1998, 137 (2), 295–301. <https://doi.org/10.1006/jssc.1997.7739>.
27. López-Rodríguez, D.; Micó-Vicent, B.; Bonet-Aracil, M.; Cases, F.; Bou-Belda, E. The Optimal Concentration of Nanoclay Hydrotalcite for Recovery of Reactive and Direct Textile Colorants. *Int. J. Mol. Sci.* 2022, 23 (17), 9671. <https://doi.org/10.3390/ijms23179671>
28. Bou-Belda, E.; López-Rodríguez, D.; Micó-Vicent, B.; Bonet-Aracil, M. Direct and Reactive Dyes Recovery in Textile Wastewater Using Calcinated Hydrotalcite. In *Materials Science Forum*; Trans Tech Publ, 2022; Vol. 1063, pp 233–242. <https://doi.org/10.4028/p-31v71q>
29. Bigman, J. L. Monitoring of Chemicals and Water. *Handb. Silicon Wafer Clean. Technol.* 2018, 619–657. <https://doi.org/10.1016/B978-0-323-51084-4.00011-3>. <https://doi.org/10.1016/B978-0-323-51084-4.00011-3>
30. Silva, M. M. F.; Oliveira, M. M.; Avelino, M. C.; Fonseca, M. G.; Almeida, R. K. S.; Silva Filho, E. C. Adsorption of an Industrial Anionic Dye by Modified-KSF-Montmorillonite: Evaluation of the Kinetic, Thermodynamic and Equilibrium Data. *Chem. Eng. J.* 2012, 203, 259–268. <https://doi.org/10.1016/j.cej.2012.07.009>.
31. B. Micó-Vicent, F. M.-V. Method for Optimising the Synthesis of Hybrid Nanopigments, 2017.
32. H. Fischer, L. F. B. Coloring Pigment, 2001. <https://doi.org/10.1016/j.dyepig.2022.111022>
33. Mensch, C.; Chintala, R.; Nawrocki, D.; Blue, J. T.; Bhambhani, A. Enabling Lyophilized Pneumococcal Conjugate Vaccines Through Formulation Design and Excipient Selection Suitable for A Multivalent Adjuvanted Vaccine. *J. Pharm. Sci.* 2020, 1–11.

<https://doi.org/10.1016/j.xphs.2020.10.038>.

34. Castillo-Peinado, L. S.; Calderón-Santiago, M.; Priego-Capote, F. Lyophilization as Pre-Processing for Sample Storage in the Determination of Vitamin D3 and Metabolites in Serum and Plasma. *Talanta* 2021, 222 (September 2020). <https://doi.org/10.1016/j.talanta.2020.121692>.
35. Grum, F.; Witzel, R. F.; Stensby, P. Evaluation of Whiteness. *JOSA* 1974, 64 (2), 210–215. <https://doi.org/10.1364/JOSA.64.000210>
36. ASTM. Standard Tables for Reference Solar Spectral Irradiances : Direct Normal And. *Astm* 2013, 03 (Reapproved), 1–21. <https://doi.org/10.1520/G0173-03R20.2>.
37. Iturbe-García, J. L.; Bonifacio Martínez, J.; Granados Correa, F.; López-Muñoz, B. E. Behavior of a Hydrotalcite Type Material Obtained from MgAl Alloy for CO2 Adsorption. *Appl. Clay Sci.* 2019, 183, 105296. <https://doi.org/https://doi.org/10.1016/j.clay.2019.105296>.
38. Extremera, R.; Pavlovic, I.; Pérez, M. R.; Barriga, C. Removal of Acid Orange 10 by Calcined Mg/Al Layered Double Hydroxides from Water and Recovery of the Adsorbed Dye. *Chem. Eng. J.* 2012, 213, 392–400. <https://doi.org/https://doi.org/10.1016/j.cej.2012.10.042>.
39. Wang, Q.; Feng, Y.; Feng, J.; Li, D. Enhanced Thermal- and Photo-Stability of Acid Yellow 17 by Incorporation into Layered Double Hydroxides. *J. Solid State Chem.* 2011, 184 (6), 1551–1555. <https://doi.org/https://doi.org/10.1016/j.jssc.2011.04.020>.
40. Raha, S.; Ivanov, I.; Quazi, N. H.; Bhattacharya, S. N. Photo-Stability of Rhodamine-B/Montmorillonite Nanopigments in Polypropylene Matrix. *Appl. Clay Sci.* 2009, 42 (3–4), 661–666. <https://doi.org/10.1016/j.clay.2008.06.008>
41. Ghosh, S. K.; Brahmakumar, M.; Warriar, K. G. K.; Perumal, P.; Smitha, V. S.; Pavithran, C.; Manjumol, K. A. Rhodamine 6G Intercalated Montmorillonite Nanopigments-Polyethylene Composites: Facile Synthesis and Ultravioletstability Study. 2011. <https://doi.org/10.1111/j.1551-2916.2010.04326.x>
42. Bellucci, F.; Camino, G.; Frache, A.; Sarra, A. Catalytic Charring–Volatilization Competition in Organoclay Nanocomposites. *Polym. Degrad. Stab.* 2007, 92 (3), 425–436. <https://doi.org/10.1016/j.polymdegradstab.2006.11.006>
43. Landau, A.; Zaban, A.; Lapidés, I.; Yariv, S. Montmorillonite Treated with Rhodamine-6G Mechanochemically and in Aqueous Suspensions. *J. Therm. Anal. Calorim.* 2002, 70 (1), 103–113. <https://doi.org/10.1023/A:1020649416016>
44. Hafshejani, M. K.; Ogugbue, C. J.; Morad, N. Application of Response Surface Methodology for Optimization of Decolorization and Mineralization of Triazo Dye Direct Blue 71 by *Pseudomonas Aeruginosa*. *3 Biotech* 2014, 4 (6), 605–619.

<https://doi.org/10.1007/s13205-013-0192-7>.

45. Hu, C.; Jimmy, C. Y.; Hao, Z.; Wong, P. K. Photocatalytic Degradation of Triazine-Containing Azo Dyes in Aqueous TiO₂ Suspensions. *Appl. Catal. B Environ.* 2003, *42* (1), 47–55. [https://doi.org/10.1016/S0926-3373\(02\)00214-X](https://doi.org/10.1016/S0926-3373(02)00214-X)
46. Kuo, C.-Y. Water Purification of Removal Aqueous Copper (II) by as-Grown and Modified Multi-Walled Carbon Nanotubes. *Desalination* 2009, *249* (2), 781–785. <https://doi.org/10.1016/j.desal.2008.11.022>
47. Wu, C.-H. Studies of the Equilibrium and Thermodynamics of the Adsorption of Cu²⁺ onto As-Produced and Modified Carbon Nanotubes. *J. Colloid Interface Sci.* 2007, *311* (2), 338–346. <https://doi.org/10.1016/j.jcis.2007.02.077>
48. Mahmoodi, N. M.; Salehi, R.; Arami, M.; Bahrami, H. Dye Removal from Colored Textile Wastewater Using Chitosan in Binary Systems. *Desalination* 2011, *267* (1), 64–72. <https://doi.org/10.1016/j.desal.2010.09.007>.
49. Kuo, C.-Y.; Lin, H.-Y. Adsorption of Aqueous Cadmium (II) onto Modified Multi-Walled Carbon Nanotubes Following Microwave/Chemical Treatment. *Desalination* 2009, *249* (2), 792–796. <https://doi.org/10.1016/j.desal.2008.11.023>
50. Lu, C.; Su, F. Adsorption of Natural Organic Matter by Carbon Nanotubes. *Sep. Purif. Technol.* 2007, *58* (1), 113–121. <https://doi.org/10.1016/j.seppur.2007.07.036>
51. Evanson, K. W.; Urban, M. W. Surface and Interfacial FTIR Spectroscopic Studies of Latexes. I. Surfactant–Copolymer Interactions. *J. Appl. Polym. Sci.* 1991, *42* (8), 2287–2296. <https://doi.org/10.1002/app.1991.070420820>
52. Seoudi, R.; El-Bahy, G. S.; El Sayed, Z. A. FTIR, TGA and DC Electrical Conductivity Studies of Phthalocyanine and Its Complexes. *J. Mol. Struct.* 2005, *753* (1–3), 119–126. <https://doi.org/10.1016/j.molstruc.2005.06.003>
53. Kanik, M.; Hauser, P. J. Printing of Cationised Cotton with Reactive Dyes. *Color. Technol.* 2002, *118* (6), 300–306. <https://doi.org/10.1111/j.1478-4408.2002.tb00114.x>.
54. Coloration Technology - 2006 - Ahmed - Urea Alkali-free Printing of Cotton with Reactive Dyes.Pdf. <https://doi.org/10.1111/j.1478-4408.2006.00047.x>
55. Coloration Technology - 2006 - El-Shishtawy - Cationic Pretreatment of Cotton Fabric for Anionic Dye and Pigment Printing.Pdf. <https://doi.org/10.1111/j.1478-4408.2002.tb00367.x>
56. Limousin, G.; Gaudet, J.-P.; Charlet, L.; Szenknect, S.; Barthes, V.; Krimissa, M. Sorption Isotherms: A Review on Physical Bases, Modeling and Measurement. *Appl. geochemistry* 2007, *22* (2), 249–275. <https://doi.org/10.1016/j.apgeochem.2006.09.010>

57. Voudrias, E.; Fytianos, K.; Bozani, E. Sorption–Desorption Isotherms of Dyes from Aqueous Solutions and Wastewaters with Different Sorbent Materials. *Glob. Nest Int. J* 2002, 4 (1), 75–83.
58. Foo, K. Y.; Hameed, B. H. Porous Structure and Adsorptive Properties of Pineapple Peel Based Activated Carbons Prepared via Microwave Assisted KOH and K₂CO₃ Activation. *Microporous Mesoporous Mater.* 2012, 148 (1), 191–195. <https://doi.org/10.1016/j.micromeso.2011.08.005>
59. Daneshvar, E.; Vazirzadeh, A.; Niazi, A.; Kousha, M.; Naushad, M.; Bhatnagar, A. Desorption of Methylene Blue Dye from Brown Macroalga: Effects of Operating Parameters, Isotherm Study and Kinetic Modeling. *J. Clean. Prod.* 2017, 152, 443–453. <https://doi.org/10.1016/j.jclepro.2017.03.119>
60. Redlich, O.; Peterson, D. L. A Useful Adsorption Isotherm. *J. Phys. Chem.* 1959, 63 (6), 1024. <https://doi.org/10.1021/j150576a611>
61. Momina; Mohammad, S.; Suzylawati, I. Study of the Adsorption/Desorption of MB Dye Solution Using Bentonite Adsorbent Coating. *J. Water Process Eng.* 2020, 34 (July 2019). <https://doi.org/10.1016/j.jwpe.2020.101155>.
62. Duffner, H.; Bach, E.; Cleve, E.; Schollmeyer, E. New Mathematical Model for Determining Time-Dependent Adsorption and Diffusion of Dyes into Fibers through Dye Sorption Curves in Combination Shades: Part II: Kinetic Data from Dyeing Cotton with a Trichrome Direct Dye System. *Text. Res. J.* 2000, 70 (3), 223–229. <https://doi.org/10.1177/004051759706701001>
63. Hauser, P. J.; Tappa, A. H. Improving the Environmental and Economic Aspects of Cotton Dyeing Using a Cationised Cotton. *Color. Technol.* 2001, 117 (5), 282–288. <https://doi.org/10.1111/j.1478-4408.2001.tb00076.x>
64. Daruwalla, E. H.; Kulkarni, G. G. Studies in the Equilibrium Dyeing of Cotton with Direct Dyes: The Determination of the Activity and Affinity of Direct Dyes for Cellulose. *Bull. Chem. Soc. Jpn.* 1964, 37 (9), 1250–1261. <https://doi.org/10.1246/bcsj.37.1250>
65. Aspland, J. R. The Application of Basic Dye Cations to Anionic Fibers: Dyeing Acrylic and Other Fibers with Basic Dyes. *Text. Chem. Color.* 1993, 25 (6). <https://doi.org/10.1111/j.1478-4408.1979.tb00210.x>
66. Van Der Kraan, M.; Vanesa Fernandez Cid, M.; Woerlee, G. F.; Veugelers, W. J. T.; Witkamp, G.-J. Equilibrium Study on the Disperse Dyeing of Polyester Textile in Supercritical Carbon Dioxide. *Text. Res. J.* 2007, 77 (8), 550–558. <https://doi.org/10.1177/0040517507077483>
67. Kim, T.-K.; Son, Y.-A.; Lim, Y.-J. Thermodynamic Parameters of Disperse Dyeing on Several Polyester Fibers Having Different Molecular Structures. *Dye. Pigment.* 2005, 67 (3), 229–234. <https://doi.org/10.1016/j.dyepig.2004.12.005>

68. Ketema, A.; Worku, A. Review on Intermolecular Forces between Dyes Used for Polyester Dyeing and Polyester Fiber. *J. Chem.* 2020, 2020. <https://doi.org/10.1155/2020/6628404>

Recuperación del colorante de aguas residuales textiles mediante nanoarcillas para su reutilización como pigmentos y nuevos baños de tintura

Capítulo 5

Conclusiones

Las hipótesis planteadas en esta tesis sugieren que se podría realizar una adsorción de los colorantes en disolución acuosa y que después se podría aprovechar el compuesto formado por la hidrotalcita y el colorante para realizar coloración de sustratos textiles, ya fuera mediante estampaciones o consiguiendo la desorción del colorante para hacer nuevos baños de tintura. En consecuencia, se plantean los objetivos de adsorber diferentes tipos de colorantes textiles, estampar los híbridos obtenidos de la fase de adsorción y conseguir una desorción del colorante que está en la arcilla para poder obtener nuevos baños de tintura y realizar la correspondiente tintura. Seguidamente, se describen las conclusiones a las que se ha llegado tras todos los resultados obtenidos en los análisis realizados.

En lo referente a la adsorción de colorante de diferentes tipos (directos, reactivos, dispersos) con diferente peso molecular y distinta polaridad (aniónicos, catiónicos y no iónicos) y estudiando la capacidad máxima de adsorción de la hidrotalcita calcinada se puede concluir lo siguiente:

El mecanismo de adsorción del colorante y la recuperación de la memoria de forma de la hidrotalcita se ha demostrado mediante técnicas de caracterización XRD, XPS, EDX y FTIR. Además, se puede observar la mejora en el comportamiento térmico de los híbridos obtenidos con respecto a los colorantes solos a la vista de los resultados del TGA.

La termogravimetría (TGA) también arroja resultados que siguen líneas similares. Los híbridos muestran un comportamiento casi idéntico al de la hidrotalcita antes de la adsorción, por lo que la adsorción del colorante tiene muy poca influencia en el TGA final del híbrido. Los picos de degradación de la muestra son los mismos que los de la arcilla sin haber absorbido colorantes. Desde el otro punto de vista, los híbridos muestran mejor

resistencia a la temperatura que los colorantes por sí solos. Por último, mediante el análisis de difracción de rayos X, es posible observar cómo la hidrotalcita recupera parcialmente su espacio interlaminar debido a su memoria de forma. Esto debería ayudar a la fijación del colorante dentro de la arcilla, y a la estabilidad del híbrido resultante.

Los análisis mediante DRX, XPS, EDX y FTIR demuestran la presencia de los colorantes en el híbrido obtenido. Para la difracción de rayos X, sólo hay que observar cómo la zona amorfa aumenta debido a la mayor presencia de colorante, mientras que por ejemplo en el FTIR, se aprecian picos muy significativos de los enlaces de grupos como el SO_3 sulfonato y el amino $-\text{N}=\text{N}-$, asociados a los colorantes adsorbidos y que no se encuentran en la nanoarcilla. En el análisis semicuantitativo se puede observar como algunos grupos funcionales como el CO_3^{2-} han sido sustituidos por el colorante.

A la vista de los resultados, se ha demostrado la eficacia de la arcilla HC en la adsorción de los colorantes reactivos, directos, dispersos y básicos utilizados en este estudio para la depuración de aguas residuales procedentes de procesos de tintura textil, siendo el nivel máximo de adsorción según la Equation 3.3.1 establecida en este trabajo de $x = 0.5$. Los porcentajes de adsorción son bastante elevados (en todos los casos por encima del 95% de absorción). Además, se aprecia visualmente una buena fijación del color en la arcilla, tanto por su homogeneidad como por su grado de estabilidad. El nivel de adsorción más bajo se encontró en el colorante Direct Blue 71 en el concentrado más bajo, que es el colorante utilizado con mayor peso molecular. Sin embargo, no se observaron diferencias significativas debido a la diferencia en el peso molecular de los colorantes, como puede verse en todos los resultados de este estudio, que demuestran la buena capacidad de adsorción de la arcilla a pesar de las diferencias en el peso molecular de los colorantes.

En cuanto a la reflectancia solar total (TSR) los híbridos con menor concentración de colorante se sitúan entre el 60 - 70% de TSR. Los blancos tradicionales presentan una reflectancia solar total del 75%, por lo que las muestras estudiadas están muy próximas. Por otro lado, a concentraciones más altas de colorante los resultados de TSR se sitúan en un rango de entre el 29% y 58% debido a los colores más intensos que se obtienen.

En el análisis de los resultados obtenidos de la estampación con nanoarcillas y la comparación de los resultados y solidez frente a estampaciones convencionales con los mismos colorantes utilizados podemos concluir:

Se ha desarrollado con éxito un nuevo método de coloración de sustratos textiles mediante la utilización de nanoarcilla cargadas con colorantes procedentes de aguas residuales textiles para realizar una estampación. Esta nueva técnica novedosa se ha sometido a varias pruebas de solidez del color al lavado, frote, planchado y luz dando resultados satisfactorios e incluso en algunos mejorando los resultados que se obtienen con una estampación convencional de colorantes. Si bien aquellos ensayos que no han dado mejores resultados se ha observado al analizar la superficie mediante SEM que es porque la fijación de la arcilla a la fibra necesita ser mejorada, lo que abre la posibilidad de futuras líneas de investigación. En el caso de los colorantes dispersos no iónicos la no unión a la arcilla por intercambio iónico ha afectado notablemente a los resultados de solidez del color, lo que demuestra la importancia que tiene esa fuerza a la hora de fijar el colorante a la arcilla.

Se ha confirmado la capacidad de adsorción de la hidrotalcita para colorantes de tipo aniónico y no iónicos y el método de adsorción mediante calcinación y su posterior reconstrucción gracias a su memoria de forma, que se ha podido estudiar y validar mediante las pruebas de XRD y FTIR. Estas técnicas también demuestran la presencia de los colorantes en la estructura del híbrido, ya que el aumento de la zona amorfa en el análisis XRD confirma la presencia de colorantes y el estudio FTIR muestra picos significativos de grupos determinados que aparecen en los colorantes como el amino y el sulfonato SO_3 .

El incremento de la solidez del color en algunos ensayos como el planchado y en el caso de los colorantes directos a la luz natural y artificial guarda una estrecha relación con los resultados del TGA. Muchos de los picos que se observaron en los colorantes se atenúan o desaparecen totalmente en sus correspondientes híbridos, lo que confirma el efecto barrera de la arcilla y la transferencia de energía del colorante a la hidrotalcita, reduciendo

la degradación del color cuando se ensayan agentes de degradación que implican la acción de una fuente de energía. El aumento del TSR, comparando colorantes y colorante+arcilla, se sitúa entre un 20-40 % lo cual también influirá en la mejora de las solideces a la luz.

Finalmente, con los trabajos experimentales realizados a la hora de realizar nuevos baños de tintura con los híbridos y la tintura de materias textiles, se obtienen las siguientes conclusiones a la vista de los resultados obtenidos:

En este trabajo de tesis doctoral se ha desarrollado exitosamente un nuevo método de tintura de tejidos textiles mediante la reutilización de los híbridos colorante-hidrotalcita formados por la adsorción de colorantes obtenidos de las aguas residuales textiles vertidas. Se ha revertido el proceso de carga de la nanoarcilla para conseguir una desorción de los colorantes al baño de tintura. Esta novedosa aportación ha sido analizada mediante medidas de color, análisis SEM y sometiendo las probetas a diferentes pruebas de solideces del color. Después de la desorción todavía ha quedado colorante en la arcilla, lo que permitiría repetir el proceso de tintura para obtener coloraciones de con menor intensidad o variar las concentraciones de arcilla para igualar el tono de las tinturas realizadas. En cualquier caso, estas variables serán objeto de nuevas investigaciones para continuar esta línea de investigación.

Los tejidos tintados han sido sometidos a diversas pruebas de solidez, las cuales han dado resultados habituales teniendo en cuenta el tipo de colorante y la materia textil tintada. Por ejemplo, es habitual encontrar bajos valores de solidez en tratamientos húmedos para colorantes directos y altos grados de solidez en los colorantes dispersos, ya que la tintura de estos últimos es como una aleación que se produce entre el colorante y el poliéster.

Así pues, a la vista de los resultados obtenidos se puede asegurar que los objetivos que se habían establecido para esta tesis se han cumplido exitosamente, llegando a desarrollar nuevos métodos de estampación y de tintura con el uso de materiales

reciclados. Además, se ha establecido un ratio de uso arcilla/colorante para optimizar los procesos de adsorción de colorante y limpieza de aguas residuales.

Recuperación del colorante de aguas residuales textiles mediante nanoarcillas para su reutilización como pigmentos y nuevos baños de tintura

Capítulo 6

Futuras líneas de investigación

Tras todo el trabajo realizado en el proceso de investigación de esta tesis se ha planteado diversas y variadas líneas de investigación que podrían seguir a este trabajo. Sirva esta propuesta para posibles investigadores posteriores que continúen esta investigación y pongan la misma pasión que hemos puesto en todo este trabajo doctoral:

- Dada la existencia de nanoarcillas de distintas tipologías, de distinta morfología, carga iónica se podrían reproducir los mismos experimentos con otras variables que ofrecen estos compuestos. Aquí se ha trabajado con hidrotalcita, pero otras arcillas como la halloisita presentan una estructura tubular en lugar de laminar y tienen doble carga iónica.
- Al igual que hay varias arcillas también quedan varios tipos de colorantes con los que experimentar y valorar su comportamiento, colorantes premetalizados, sulfuros, ácidos etc. Muchos son los que se utilizan en las industrias químicas textiles y se podrían ver beneficiados igualmente de estos métodos.
- Ciertos colorantes como los sulfurosos y los tina necesitan ser reducidos a sus derivados leuco antes de emplearse para tinter. Una vez conseguido el leuco del colorante se podría realizar el proceso de adsorción empleando una nanoarcilla determinada o evaluar el comportamiento de distintas tipologías de nanoarcilla con objeto de que el colorante no se oxide e insolubilice, protegiéndolo de que vuelvan a oxidarse y recuperar su forma original.
- Las arcillas pueden funcionar como carriers en la tintura de poliéster con colorantes dispersos, así pues, se podría estudiar y optimizar estos procesos de tintura haciendo uso de las arcillas en lugar de los carriers convencionales.

- En la extrusión de piezas con diferentes componentes plásticos se podría incorporar los híbridos para dar color a estos polímeros, de esa forma sería otra forma de reutilizar ese material reciclado y no tener que hacer uso de colorantes ex proceso para dicha coloración.
- Realizar pruebas a escala industrial real y realizar un estudio económico real teniendo en cuenta los costes materiales y de proceso.
- Cada vez es más habitual utilizar colorantes naturales en los procesos textiles, así pues, una próxima línea sería adsorber este tipo de colorantes con nanoarcillas empleando a la vez estas mismas como posibles mordientes en un proceso de tintura.